SEISMIC INITIATION OF SUBMARINE SLOPE FAILURES USING PHYSICAL MODELLING IN A GEOTECHNICAL CENTRIFUGE

STEPHEN E. COULTER

SEISMIC INITIATION OF SUBMARINE SLOPE FAILURES USING PHYSICAL MODELLING IN A GEOTECHNICAL CENTRIFUGE

by

©Stephen E. Coulter, B.A.Sc.

A thesis submitted to the

School of Graduate Studies

in partial fulfillment of the

requirements for the degree of

Master of Engineering

Faculty of Engineering and Applied Science

Memorial University of Newfoundland

April 2008

St. John's   Newfoundland & Labrador   Canada

*"I'm pickin' up good vibrations,
she's giving me the excitations."*

*- Brian Wilson, Michael Love,
& Tony Asher*

ABSTRACT

The stability of offshore slopes is a major consideration in the development of both offshore and nearshore areas. The consequences of such slope failures can include the destruction of adjacent facilities, as well as the production of dangerous tsunamis. This phenomenon poses a unique and evident threat to human populations as well as valuable infrastructure. Most of these types of failures have occurred in prehistoric times and for the most part the initiation mechanisms behind them remain unobserved. One such triggering mechanism of these failures is seismic movement or in more common terms, an earthquake.

This thesis presents a research program into the physical centrifuge modelling of the seismic initiation of submarine slope failures. The effects of impermeable layer presence, earthquake magnitude, and a phenomenon known as "seismic strengthening" are investigated. Properly scaled centrifuge modelling has been proven to be a useful tool in observing geotechnical engineering situations that would other wise be costly or impractical to investigate due to financial and time constraints.

A series of five centrifuge tests were performed on idealized slope geometries at a scale of 1:70. These tests were designed for ease of comparison with finite element analyses, with some associated compromises compared to field conditions. Generally, the test geometries consisted of a 2:1 slope constructed using Fraser River sand in a strongbox

with a rectangular inner plan area. Models were either tested with the presence of a buried and draped silt layer, an inclined silt layer featuring an approximate 5.5:1 profile, or with no silt layer present at all. Much of the equipment and procedures required for this testing at the C-CORE Centrifuge Centre were developed by the author based on the experiences from other centrifuge centres. Models were air pluviated to obtain a target relative density of 40% and then saturated with a viscous pore fluid to achieve similitude of both static and dynamic scaling laws. Following construction procedure, models were tested in the Earthquake Simulator that is situated upon the C-CORE centrifuge and spun to a test level of 70 g. The response of the models to various earthquake loadings was observed with a high-speed data acquisition system. These responses primarily consisted of short-term and long-term data collected from installed accelerometers and pore pressure transducers, as well as other instruments used to observe the vertical and horizontal displacements of the model.

Analysis consisted of examining the test data, as well as comparing analogous model tests to determine the effects mentioned above. The presence of a relatively impermeable silt layer in an appropriate orientation was found to increase the possibility of instability. A dilative response, characterized by observed upslope acceleration spikes coupled with negative spikes in pore pressure was observed in models that featured a silt layer as well as in the model that did not feature a silt layer. Seismic strengthening, through the process of densification due to the application of small seismic movements, was also observed to occur. Increased dilative response also occurred with increased earthquake

magnitude, but the increase in failure resistance caused by this dilative response was overcome by the delayed dissipation of generated excess pore pressure underneath the relatively impermeable silt layer. Slope failure was characterized by long-term horizontal and vertical slope movements that continued, and sometimes recommenced, after the cessation of earthquake shaking, short-term slope face surface heave, and the evidence of silt layer movement in post-test observations.

ACKNOWLEDGEMENTS

I must also thank COSTA-Canada, NSERC, C-CORE, and the Memorial University of Newfoundland for their financial support of this research and most of all Dr. Jacques Locat at Laval University for his supervision and encouragement of the COSTA-Canada project. I would also like to thank Dr. Peter Byrne and his fellow researchers at the University of British Columbia on the Earthquake Induced Damage Mitigation from Soil Liquefaction project for their technical assistance.

Finally, thanks to Mom, for the constant reminders.

TABLE OF CONTENTS

LIST OF FIGURES

LIST OF TABLES

LIST OF SYMBOLS

Greek Symbols

α	Slice Base Inclination
β	Soil Parameter
θ	Slope Angle
ϕ	Effective Shear Stress Parameter
ν	Velocity
σ_{v0}	Initial Total Stress
σ'_{v0}	Initial Effective Vertical Stress
σ_{normal}	Normal Vertical Stress
τ_{av}	Average Cyclic Shear Stress
$\tau_{driving}$	Driving Shear Stress
ω	Angular Rotational Speed
γ'	Effective Unit Weight
ψ	State Parameter

Lower Case

a_{max}	Maximum Acceleration
c'	Effective Shear Stress Parameter
cm	Centimetres
cSt	Centistokes
d	Distance
d_{cw}	Distance Of Counterweight From Platform Surface
d_m	Distance Of Model From Platform Surface
g	Acceleration Due To Earth's Gravity
h	Hours
h_m	Height In Model
h_p	Height In Prototype
kHz	Kilohertz
kg	Kilograms

km	Kilometres
kN	Kilonewtons
kPa	Kilopascals
kW	Kilowatts
l	Length Of Base
l_e	Effective Applied Length
m	Metres
mm	Millimetres
n	Acceleration Scaling Factor
p	Number Of Slices
r	Radius From Centre Of Rotation
r_d	Stress Reduction Coefficient
r_u	Pore Pressure Ratio
s	Seconds
u	Pore Water Pressure
u_e	Excess Pore Pressure
z	Depth Below Soil Surface

Upper Case

A	Cross-sectional Area
AC	Alternating Current
C	Celsius
$CATSCAN$	Computed Axial Tomography Scan
CPT	Cone Penetration Test
CRR	Cyclic Resistance Ratio
CSR	Cyclic Stress Ratio
CW	Counterweights
D_{10}	Particle Diameter With 10% Passing
D_{50}	Particle Diameter With 50% Passing
DC	Direct Current
E_1, E_2	Slice Normal Force
EQS	Earthquake Simulator
F_{cw}	Counterweight Force
F_{ls}	Localized Factor of Safety

F_m	Dynamic Force
F_r	Reaction Force
F_s	Factor Of Safety
F_w	Self Weight Of Centrifuge
FEM	Finite Element Methods
Hz	Hertz
HPMC	Hydroxypropyl Methylcellulose
K_α	Static Shear Stress Correction Factor
K_σ	Overburden Correction Factor
L	Litres
LVDT	Linearly Variable Differential Transformer
M_a	Mass
M_{cw}	Counterweight Mass
M_m	Model Mass
MSF	Magnitude Scaling Factor
N	Gravity Scaling Factor
N'	Normal Slice Force
N_c	Number Of Cycles
N_l	Number Of Cycle To Liquefaction
N_T	Sum Of Normal Slice Forces
PPT	Pore Pressure Transducer
PSI	Pounds Per Square Inch
R_e	Effective Centrifuge Radius
R_t	Centrifuge Radius To Top Of Model
RMS	Root Mean Square
RPM	Revolutions Per Minute
S_1, S_2	Stress States
T	Moment
T_b	Bending Moment
T_m	Dynamic Moment
T_r	Reaction Moment
V	Centrifuge Model Velocity
VELACS	Verification Of Liquefaction Analysis Using Centrifuge Studies
W	Submerged Slice Weight
W'	Effective Weight
X_1, X_2	Slice Shearing Force

1 INTRODUCTION

1.1 Background

Submarine landslides are a major factor considering the current state of offshore and nearshore development. Most of these landslides have occurred in prehistoric times and are for the most part unobserved. The consequences of such unique landslides range from the possible destruction of offshore facilities, the production of dangerous tsunamis to those that have retrogressed back onshore. Submarine landslides continue to be a potential hazard to human populations and infrastructure both offshore and nearshore.

There are several possible triggering mechanisms for these submarine landslides, including: wave loading, gas hydrate presence, and sedimentation; earthquakes are among the most common. Examples of notable earthquake-induced submarine slope failure near Canada include: the Grand Banks off of Newfoundland, the Saguenay Fjord in Quebec, off of Vancouver Island and in the Fraser River Delta in British Columbia.

Research is ongoing into the triggering mechanisms of submarine landslides in order to evaluate the risk to offshore structures, especially considering the increased interest in Canada's offshore hydrocarbon resource development over the past two decades.

Offshore investigations such as sonar and seismic profiling have revealed the major features of submarine landslide zones that have proven to be very different from

terrestrial landslides because they can involve the movement of thousands of cubic kilometres of material for hundreds of kilometres. Additionally submarine landslides typically occur on slopes much shallower than with terrestrial landslides and the retrogressive nature of submarine landslides is usually much more extensive in the submarine environment.

Scaled centrifuge modelling has been used for the past several decades to investigate geotechnical engineering problems without the disadvantages of full scale modeling, such as cost, time, and size of testing. This research involves applying this technology to investigating the effect of a stratified profile on the stability of a submarine slope.

1.2 Purpose

The objective of the COSTA-Canada Project is to examine submarine slope failures on continental margins (COSTA-Canada, 2001). COSTA-Canada is seeking to explore six major short-term objectives:

(i)   assessment of historical records of slope instability, slope parameters, seismicity, and tectonic setting;

(ii)   understanding of seafloor failure dynamics through 3-D imaging of sediment architecture and geometry of slope failures;

(iii)   understanding of sediment properties of slip planes and areas prone to slope sliding;

(iv)   determination of presence of gas hydrate and its significance for slope stability;

(v)   modelling of forces and mechanical processes that control the initiation of slope instabilities (release mechanisms), flow dynamics and initiation of tsunamis; and

(vi)   assessment of risk-fields related to slope stability.

The work presented in this thesis is primarily concerned with the fifth item in the above list through the undertaking of a series of centrifuge tests to examine the effect of the presence of impermeable silt layers in various stratigraphic configurations. It was expected that the silt layer would impede the drainage of the sand beneath it contributing to instability. Additionally, the migration of pore pressures towards potential drainage boundaries was expected to cause continued movement of the slope after cessation of the earthquake. The entire COSTA-Canada centrifuge testing program was composed of five tests (A through E) of various configurations. The desire to couple the results of these tests with complimentary Finite Element Method analyses being carried out by COSTA-Canada project collaborators (COSTA-Canada, 2001) led to several compromises in test design, the most significant being the use of a rigid model container. The results of these tests are presented and discussed in this document.

Other objectives that became evident during the development of these centrifuge tests were to investigate the effect of the magnitude of the earthquake applied to the model configuration as three different sizes of model earthquakes were used in this program. In addition, the effect of the application of multiple earthquakes being applied to the model configuration was also investigated. This came about as an examination into the process

3

of "seismic-strengthening" as discussed by Lee et al. (2004), whereby a slope that is exposed to a history of small earthquake events will become strong enough to withstand a more significant earthquake loading.

1.3 Thesis Outline

This thesis is organized into eight chapters that logically follow the sequence of the work performed for this investigation into the initiation of submarine slope failures. The second chapter reviews the available literature on various aspects of submarine slope stability, including: site investigation, triggering mechanisms, cyclic loading of soils, slope stability analysis, and seismic slope analysis. Chapter 3 discusses the intricacies of centrifuge modelling, including the scaling laws and restrictions, as well as the principles of centrifugal earthquake actuation and previous work that has performed in this area. The research facilities and equipment used in this program are presented in Chapter 4 while Chapter 5 describes the experimental testing procedure that was carried out for these tests. Chapter 6 thoroughly presents and discusses the testing results that were gathered. The seventh chapter compares and analyzes these results in the context of various effects and parameters that were examined, including: the effects of the presence of a lower permeability layer, the effects of earthquake magnitude, and the effects of the exposure of the model to multiple earthquakes. Chapter 8 presents the conclusions of the results and analysis with a brief summary of the observations. This final chapter also presents some recommendations for further development of studies in the area of

4

submarine slope instability in the geotechnical centrifuge. Finally, a list of references and an appendix presenting the technical details of model testing instruments is supplied.

2   LITERATURE REVIEW

2.1   Introduction

The stability of submarine slopes is an important consideration in today's world as offshore, in addition to nearshore, exploration and development becomes more prominent and technologically advanced.   Large submarine landslides can have disastrous consequences both economically and socially.   The area of interest for submarine slope stability usually involves the continental shelf, areas which are in close proximity to the world's landmasses.

The COSTA-Canada project is primarily concerned with investigating the stability of the shorelines and continental margins of Canada (Locat et al., 2001).   Poulos (1988) describes how the continental margin, which includes the continental shelf, continental slope, and the continental rise, form approximately 21% of the ocean area.   These areas are of particular interest for offshore oil exploration.

Typically, the continental slope is formed of very shallow gradients of approximately 2° to 6° (Poulos, 1988). Submarine landslides in these areas have been identified frequently in the available literature (Terzaghi, 1956; Bjerrum, 1971; Lee et al., 1981; Piper et al., 1999).   These landslides are common on areas of the seafloor that are inclined environments that are occupied by weak geologic materials including rapidly deposited fine grained material, such as sands and silts (Hampton et al., 1996).

6

Submarine slope stability and its effect on subsequent slope failures can occur on a wide variety of scales, varying in the movement of volumes of sea floor material from hundreds of cubic metres to hundreds of cubic kilometers that can travel downslope for hundreds of kilometres. In addition to a wide variation in magnitudes, there is also a wide range of geologic settings, varying from river dominated to glacial dominated settings (Locat et al., 2001). The majority of known slides have occurred far from land and in prehistoric times. More recently, however slides that have originated nearshore have been noticeable due to their direct impacts on human lives and activities (Hampton et al., 1996).

Engineers have come to realize that these types of submarine failures are so widespread that that they impose many constraints on engineering projects (Prior and Coleman, 1984). The increasing significance of offshore development insists that potentially unstable sloping deposits be identified and analyzed to protect against any type of catastrophic failure that may occur from them (Lee and Edwards, 1986).

When considering the stability of the sea floor several aspects must be considered. Poulos (1988) discusses this and states that any investigation may include some or all of the following considerations:

> (i) investigation and interpretation of the geological history, stratigraphic structure, sedimentology and morphology of the region;
>
> (ii) identification and evaluation of the topographical profile and deformational features of the sea floor;

7

(iii) estimation of the stresses in the seafloor soils due to gravity, wave, earthquake, and additional contributory forces;

(iv) analysis of the stability of the sea floor under the action of these forces;

(v) analysis of the likely movements of the sea floor;

(vi) the effects on these movements on the forces on, and displacements of piles and similar installations in the sea floor.

This literature review will review the aspects of the first five points of the above list as they pertain to submarine slope failures

2.2 Site Investigation and Classification of Soils

A valuable method of learning about submarine slope stability and the possibility of the slope of interest for failure is by looking at case studies of previous slope failures and using the data to interpret unfailed conditions and their ability to fail under various types of loading. Karlsrud and Edgers (1980) point out that case studies of previous slope instabilities can be instructive in several ways. The first of these ways is in the identification of slide prone deposits. The identification of failure prone areas is essentially the primary step in analyzing slope stability. Additionally, case studies provide insight on the mechanism by which submarine slides are initiated and then propagated. Section 2.3 deals specifically with these sources of instability. Finally, if sufficiently documented and analyzed, case studies can provide meaningful data on the input geometries and soil parameters for engineering analysis. This type of input data is

especially valuable for the type of physical modelling studies. These techniques are not directly related to this research but form a basis from which the framework of the COSTA-Canada project has progressed. Karlsrud and Edgers (1980) submit that for maximum benefit, the following information from field investigations is necessary:

(i) the age of the slide;

(ii) the geologic conditions at time of the slide;

(iii) the geotechnical parameters of the slide mass;

(iv) the extent of the slide pit;

(v) the thickness, run out distances, and velocities of the slide material; and

(vi) the geometry of the slide path.

Engineers use the various techniques described here to acquire the above information of previous slides and current slopes that may have the potential to fail and have been used on various locations on the Canadian continental margin (Moran, 1993).

2.2.1 Bathymetry

Echo sounding is a technique used to define the contours of the ocean bottom. It is described by Swan (1979) as a method used in concert with other acoustic data collection methods such sidescan sonar. Echo sounding data can indicate source areas of failure material as well as areas where material has collected, but can only be used as a tool to estimate the volume of material that has been displaced or deposited during submarine slope failure events. Echo sounding data can be valuable as a tool of first reference to

describe the boundaries of the failure and to give future direction for the areas that will provide more valuable data when investigated using more sophisticated sonar equipment (Swan, 1979). This method has several limitations, including a minimum operating water depth and similar results may now be collected by more advanced methods such as sidescan and multibeam sonar.

Mapping of the sea floor can be achieved by using time tested acoustical sonar methods. Sidescan sonar has been used for this purpose for over 20 years. Ryan (1980) explains how a sidescan sonar with a swath width of 5 km was used to explore the continental slope of New England and the mid-Atlantic margin along the east coast of the United States. This investigation clearly showed: submarine canyons, debris flows, longitudinal ridges, faults, scars, faults, areas of detached sediment cover, blocks, pits, and stripping. Sidescan sonar techniques were also used by Swan (1979) to acquire detailed data regarding sea floor features that may indicate areas of instability or give clues as to the mass movement itself. For this study, Swan (1979) likens a well constructed sidescan sonar mosaic to aerial photography for terrestrial studies. Several problems exist with sonar information, as it requires much data correction and can be expensive to obtain.

Sidescan and multibeam sonar was used by Mosher et al. (2001) to map out three submarine slope failures to achieve fine detail imagery that provided important information on the size and the style of mass-wasting. Multibeam sonar has been welcomed into wide use over the last decade to produce near-photograph quality images

of the sea floor (Locat and Lee, 2000). Multibeam sonar surveying provides accurate imagery when it comes to large slope failures, when previously sidescan sonar mosaics had to be developed through interpolation. Locat and Lee (2000) gives several examples of how multibeam sonar has improved interpretations of sea floor behaviours in areas prone to submarine slope failures, including: the Saguenay Fjord in Quebec, the Palos Verdes slide in California, the Eel River Margin in California, and Lake Tahoe in Nevada. With higher and higher resolution becoming the norm, engineers should be able to have more adequate data as it pertains to mapping case studies and investigations, which should lead to improved analysis methods. A further example of a use of these methods is discussed by Piper and McCall (2003) where unpublished multibeam bathymetry and seismic reflection profiles have been synthesized using Geographic Information System software to document the geographic extent of surface and buried submarine mass movements on the eastern Canadian margin.

Underwater photography is not a widely used technique for investigating the stability of sea floor slopes. However, it is a logical technique to investigate depositional areas and to confirm the presence of seafloor instabilities. Jenkins and Keene (1992) use photographic records to point out various areas of sea floor movement along the continental slope off southeast Australia. The photographs clearly showed areas of upturned blocks of lithified sediment, older as well as freshly developed fissures, and water-escape vents. Clearly visible instabilities are indicators of slope stability

11

problems. Photography could be used as a valuable tool to confirm submarine slope analyses for local submarine slopes.

2.2.2 Subsurface Stratigraphy

Seismic reflection data is also a traditionally used technique for gathering data for submarine slope stability analysis. High-resolution two dimensional seismic records were used by Swan (1979) to define the character and genesis of sea floor features. Seismic signals penetrate the sea floor and are reflected back to a receiver. The data can be analyzed to gain an understanding of the stratigraphy and the composition of the sea floor materials. Two-dimensional data involves taking seismic readings along a line to get a profile in section. Seismic data can indicate the presence of a depositional area (Swan, 1979), failure surfaces, sedimentary layers, faults, tensional failures, slumping, or scarps, (Jenkins and Keene, 1982).

A more recent technological advance of seismic reflection methods is the development of three-dimensional seismic surveying. Traditionally used by the petroleum industry to make accurate interpretations of subsurface stratigraphy and rock properties, this technology is being extended to uses in geotechnical engineering, specifically submarine landslide investigations (Hart et al., 2001). Under the COSTA-Canada project Hart et al. (2001) seek to analyze this methodology to be integrated with more traditional geotechnical investigation methods, including borehole logging. When this technology is refined for use by marine geotechnical engineers they will hopefully be able to

experience increased capability when it comes to interpreting bathymetry and stratigraphy as they relate to submarine slope stability analyses.

2.2.3 Geotechnical Properties

Cone penetration testing (CPT) is also a widely used in-situ technique. The data that comes from CPT testing includes cone tip resistance, sleeve friction, friction ratio, and pore pressure measurements (Mosher et al., 2001). Pore pressure measurements are achieved using a piezo-cone type instrument, which contains a piezometer probe. Piezometer probes can measure the excess and absolute pore pressure and can be used with CPT data to determine the in-situ undrained shear strength (of clays) and effective stress levels (Bennett et al., 1980). Mosher et al. (2001) shows how COSTA-Canada researchers have previously used CPT data to estimate the cyclic resistance ratio, of the examined areas in the Strait of Georgia in British Columbia, which is proportional to the peak ground acceleration. This type of data is extremely valuable when assessing earthquake trigger effects of slopes and the slope's ability to reach liquefaction conditions under cyclic seismic loading.

Perhaps the most common investigation method is that of sample coring. Cores are typically retrieved from failure areas or other unfailed submarine slope areas in order to perform subsequent geotechnical tests upon the in-situ sediment. However, there is some problem with current retrieval methods and the degree to which they can be considered undisturbed, particularly with respect to the problems of gases expanding as the sample is

retrieved to the surface. Sample coring techniques can be considered the traditional methodology by which information regarding sea floor sediments can be retrieved but are typically not as easy and much more expensive than current seismic reflection and sonar surveys that may be able to produce the same level of quality (Locat and Lee, 2000). Nevertheless, for large budget projects involving offshore resource development gravity coring is often undertaken to achieve a high level of understanding of the geotechnical properties of the sea floor. Cores can be extracted to a varying degree of depths. The Calypso drill rig, as mentioned by Locat and Lee (2000) and Desgagnes et al. (2000), can consistently drill cores of 60 m in depth. Smaller core depths can also be extracted by various methods, including vibro-cores of less than 3 m in length (Mosher et al., 2001) and other methods mentioned by Locat and Lee (2000) such as Lehigh (up to 3 m), Kastin (up to 3 m), and the box corer, which gives exceptional results but only to a depth of 0.6 m. The development of a remotely operated coring tool, known as PROD, which can reach depths of 100 m in soil or rock is also described by Locat and Lee (2000). The greater the sediment depth the better for geotechnical investigations relating to slope stability, but 100 m would be considered sufficient.

Once cores are retrieved, the samples typically undergo a battery of geotechnical tests that will give engineers a wealth of information for use in analysis. Cores can be obtained and tested with respect to: grain size distribution, water content, saturated unit weight, Atterberg limits, and shear strength. This data could then be used to compute the following characteristics: porosity, liquidity, plasticity, sensitivity, stability and

14

consolidation ratios. More recent testing investigations, such as Desgagnes et al. (2000), have incorporated CATSCAN imaging to obtain information relating to apparent density, macroscopic structure visualization and an overall qualitative evaluation of core quality. Additional tests that may be conducted on core samples include: fall cone testing for shear strength, electron microscopy, specific surface analysis, cation exchange capacity, and organic matter presence (Desgagnes et al., 2000). In addition, consolidation testing and triaxial testing are also very common. However, there remains a challenge of reproducing effective stress conditions to get representative strength & consolidation parameters.

2.2.4 Classification of Marine Soils

The Unified System of soil classification was extended by Noornay (1989) for submarine sediments. In this system, marine sediments are divided into three categories based upon their origin: lithogeneous, hydrogenous, and biogenous. Lithogeneous sediments are those that are of terrestrial, volcanic, or cosmic origins, hydrogenous sediments are precipitates of seawater or interstitial water, and finally biogenous sediments are created from the remains of marine organisms. Noornay (1984) outlines the two major differences that exist between terrestrial and marine soils. The first is that the salinity in the seawater has more dissolved salt and the second is that the higher pressure experienced at great sea depths serves to keep a substantial amount of dissolved gas in the seawater. The consequences of these differences are that the traditional soil

mechanics phase relationships may lead to an error when applying classic water content and void ratio calculations to submarine soils.

2.3 Submarine Slope Failures

Submarine slopes are susceptible to a wide variety of forces that may contribute their instability and subsequent failure. Koning (1980) describes a triggering mechanism as a force that increases shear stresses such that the resisting forces can no longer ensure the stability of the slope and also decrease shear resistance under the presence of increased pore pressure. These mechanisms of instability have been discovered with case study and further data analysis over the past 20 to 30 years. There are a group of major mechanisms of instability, as described by Poulos (1988), which include gravity, hydraulic, and earthquake forces. Presented here are the major groups of triggering mechanisms as well as other minor mechanisms that have been discovered, theorized, and discussed in the available literature.

2.3.1 Earthquake and Tectonic Activity

Earthquake ground motions are caused by the sudden movement of a tectonic fault. At tectonic faults, energy is built up slowly over a long period of time and when the energy is finally released, there are great earth motions that are experienced over great distances. Large earthquakes, as explained by Poulos (1988), generally cause large accelerations, velocities, and displacements over a larger range of frequencies and with greater durations than smaller earthquakes. Geotechnically speaking the main effect of

16

earthquakes is the creation of horizontal waves that travel through the bedrock and soil deposits. In the case of a submarine slope, these waves will cause significant shear stress, both dynamic and cyclic, and may also cause the loss of soil resistance. Earthquake effects are common to both onshore and offshore geotechnical situations but in the case of offshore situations, the risk is increased due to the other forces (hydraulic, gravity, etc.) that may also decrease shear strength or increase shear stress.

Of interest to this project are the submarine failures that have been attributed to liquefaction, either static or cyclic. A comprehensive list of instances of coastal liquefaction is given in Chaney and Fang (1991) with information given pertaining to location, site characteristics, and other observations for almost 100 cases around the globe. Mulder and Cochonat (1996) mention that the 1929 Grand Banks Slide as well as other slide events in the Fraser River Delta can be attributed to cyclic liquefaction caused by the cyclic loading effects that can arise from earthquake exposure.

One approach to analyzing these problems in the case of submarine slope stability is limit equilibrium analysis, where pseudo-static conditions are used to transform the earthquake load into equivalent horizontal and vertical loads. A subset of this approach is to use infinite slope analysis for a total stress undrained analysis for clay slopes. Poulos (1988) also mentions several methods for determining the liquefaction potential of submarine slopes under earthquake loading, which involves estimating the cyclic shear stress caused by the earthquake, estimating the cyclic shear strength of the soil, and a comparison of

17

these two components. Complimentary to this type of potential analysis is an analysis based upon effective stress, which considers the progressive pore pressure increases that can develop during an earthquake event. In an effective stress analysis the resistance to deformation of the slope is dependent upon the effective stress, which is dependent on the pore pressure in the soil sediments.

In case study analysis, earthquake loading is a commonly recognized mechanism of instability. Lykousis (1991) identifies that cyclic loading induced by earthquake activity is the principal cause of the undrained slope failures in the investigated area of the northeastern Mediterranean Sea. This hypothesis is based upon seismic reflection data as well as core sampling that show translational and rotational slides on slopes that are associated with major active fault zones.

Lee et al. (1981) uses the pseudo-static infinite slope analysis methodology to substantiate their hypothesis that a submarine failure off Eureka, California has been earthquake induced. The data for their analysis was taken from geotechnical testing of material taken from core samples retrieved from the failure zone. Another example of Pacific margin earthquake activity is given by Dupperret et al. (1993), who mention in their investigation of submarine slope failures off the coast of Peru that the most likely cause was the tectonic activity generated by the interaction of the Nazca and South American plates.

Behaviour like this on the Eastern Pacific margin has been more actively investigated on Atlantic margins. Embley (1980) identifies earthquakes as the most rational instability trigger for slides on the Atlantic margin off the coast of Africa. It is discussed that earthquake accelerations most likely caused rapid changes in pore water pressure from the sudden introduction of gases or fluids. Additional evidence is given by the fact that some large earthquakes have probably occurred across old lines of weakness such as transform faults that are in close proximity to the region of rifting. However, researchers have paid a great deal of interest to the Western Atlantic margin where in 1929 a large scale submarine slope failure was generated in the Grand Banks off the coast of Newfoundland. The slide was triggered by an earthquake that measured 7.2 on the Richter scale, creating a turbidity current of approximately 200 km^3 of material that extended approximately 1000 km from the epicenter. The landslide event occurred over a period of 12 hours and moved at a speed of approximately 15 m/s. The consequences of this event were considerable as the movement created a tsunami that moved at speeds of up to 500 km/h reaching shore on the Burin Peninsula of Newfoundland, killing 27 people and causing millions of dollars of damage (Batterson et al., 1999; COSTA, 2001). This slide has been investigated by several engineers and researchers, although several assumptions have been made. An example of this is Azizian and Popescu (2001) where conventional limit equilibrium methods and sophisticated finite element analysis software was used to backanalyze the submarine slope failure.

The magnitude and direct effects of the Grand Banks slide has given rise to great concern over the stability of slopes on the western Atlantic margin that are even closer to population centers along the east coat of the United States. Driscoll (2000) discusses the potential for a large scale submarine slope failure along the American mid-Atlantic coast. Fault and slip zones are identified by the authors that place the Virginia-North Carolina coastline and the lower Chesapeake Bay at risk for possible tsunamis that may be created as a consequence of these large failures. There are other notable earthquake-induced landslides including the Humboldt Slide off of Northern California, USA (Gardner et al., 1999), in the Saguenay Fjord in Quebec, Canada (Urgeles et al., 2001), off of Vancouver Island, British Columbia, Canada in 1946 (Mosher et al., 2001), and the slide cause by the 1964 Alaska Earthquake (Lemke, 1967).

A side effect of the exposure of slopes to seismic activity is a mechanism termed "seismic strengthening". This effect is described by Lee et al. (2004) as a process that involves densification of sediment following earthquake events thereby leading to a higher level of stability than what would be expected. Laboratory work to observe this effect was performed by Boulanger et al. (1998), where sediment samples were consolidated in a direct shear device to a predetermined vertical consolidation level. Following this, the samples were exposed to a series of simulated earthquakes. Next, a set of shear stress cycles was applied to the samples under undrained conditions. Pore pressure development was observed and then allowed to dissipate and drain. This was repeated with additional cyclic stress cycles. The induced over consolidation of the

samples was then determined by using a comparison to one-dimensional consolidation tests of comparable samples. It was concluded that the regular occurrence of earthquakes enables sediment to build up shearing resistance against cyclic loading, thus reducing greatly the occurrence of superficial submarine landslides. Lee et al. (2004) summarizes various field observations and states that in the Santa Barbara Channel, off the coast of California, the sediment shear strength is at least twice as large as would be expected for normally consolidated sediment. It is suggested that this is so because of the effect of "seismic strengthening" and that with each passing earthquake the sediment's strength and density is increased. In addition, if the sediment does not fail immediately, the pore pressure will dissipate as pore water drains and the sediment will densify. Over time, the sediment will become strong enough to withstand strong earthquake loading.

2.3.2   Wave Loading

In the case of wave forces, several unique effects are generated on the ocean bottom that affects its stability. These failure effects are discussed at length in Poulos (1988) and consist of wave induced shear and wave induced liquefaction. Wave action causes a bottom pressure that is a function of the wave height, wave length, and water depth. This wave induced bottom pressure acts as a driving force and exerts stress in the bottom sediments, that can be felt horizontally, vertically, and most importantly in the shear direction. These stresses can be calculated using the wave induced pressure and other wave characteristics, as presented as a modification of Bousinesq's solution. In contrast, waves can also create a resisting force in the slope that consists of wave induced pore

pressures. The pore pressure that is experienced by the submarine sediments under wave loading is actually the difference between what is termed the transient and residual pore pressures. Poulos (1988) stares that transient pore pressures result from the coupled response of the soil skeleton and the pore water to wave loads and that residual pore pressures are caused by the cyclic shear stresses generated by the dynamic wave pressures that vary harmonically in space and time. Residual pore pressure can be thought of as excess pore pressure and is calculated as a function of the number of wave loading cycles.

Wave induced liquefaction is a unique process that can be classified into two categories based upon their discrete failure mechanisms, as discussed in Zen and Yamazaki (1991). The first type of wave induced liquefaction acts similarly to earthquake induced liquefaction in that it is caused by cyclic shear stress, which generates the progressive accumulation of excess pore pressure. The second type of liquefaction occurs due to a spatial difference in the pore pressure in the seabed sediment. When the wave induced bottom pressure is applied to the seabed it does not fully propagate into the soil, which causes these spatial differences. This type of failure is the focus of both Zen and Yamakazi (1990) and Zen and Yamakazi (1991). The excess pore pressure difference is created by damping and phase lagging, and accelerated by low saturation, as the bottom pressure oscillates in conjunction with the ocean wave. Liquefaction occurs when the wave-associated vertical effective stress becomes equal to the vertical effective stress during calm (no wave) ocean conditions. It was found that pore pressure can oscillate

between positive and negative values following the passage of the wave and the liquefaction potential can be evaluated knowing initial pore pressure and stress conditions, as well as generated pore pressure conditions. Wave induced liquefaction can also be closely related to the upward seepage flow induced in the seabed by the rapid lowering of the sea level caused by the oscillation of the surface during wave action. It is important to understand the nature of the wave signals as well as their expected duration. The number of cycles is an important factor in determining the cyclic stresses that can develop as a function of the wave induced pressures. These types of wave induced failures are typically limited to shallow water depths.

2.3.3 Gas Hydrate Presence

The theory of the presence of gas hydrates contributing to submarine slope instability is one of the mechanisms that is presently garnering more and more attention. The potential mechanism by which gas hydrate decomposition contributes to submarine slope stability is explained by Paull et al. (2000). The formation and eventual decomposition of gas hydrates in the sea floor appears to have a direct influence upon the mechanical properties of the sediments. When methane hydrates are formed within the sea floor water and methane is extracted from the pore spaces and converted into solid gas hydrate crystals. When the liquid water is removed from the pore space and replaced by the crystal structure a net increase in sediment shear strength is experienced along with a decrease in porosity and permeability. Eventually the gas hydrate will decompose into its ingredient components, water and gas. The change of solid material into a mixture of

liquid and gas phase materials decreases the shear strength of the material. If gas bubbles are released a further strength decrease is experience by the marine sediments. Gas hydrate decomposition also affects pore pressures within the sediments, as when the methane hydrate decomposes in sediments that are already saturated with methane a volume of both water and methane will be released into the pore spaces that were previously occupied by a smaller volume of methane hydrate crystal. This can have several effects that will decrease the soil strength, including: increased pore pressure, sediment dilation, and development of interstitial gas bubbles.

Paull et al. (2000) points towards evidence of gas hydrate decomposition weakening in slides such as the Cape Fear Slide in the United States and the Storegga Slide in Norway. The potential for gas hydrates to alter the mechanical properties of the submarine sediments is not uniformly distributed with depth as proper temperature and pressure as well as the presence of gas are all instrumental in hydrate development. For these reasons it has been difficult to substantiate the effects of gas hydrates on submarine slope stability. However, Locat et al. (2001) discusses future work in this area under the COSTA-Canada project. This work is to focus on the Scotian Shelf and Grand Banks areas of offshore Canada where shallow gas and pockmarks are widespread in areas where failures have occurred. It is also suggested that high-resolution seismic experiments should be able to alert engineers to the presence of gas hydrates in submarine slope areas of interest.

2.3.4 Sedimentation

The results of sedimentation rates and types can affect the shear strength in the submarine soils. Nitzsche (1989) is a comprehensive study of the instability of submarine slopes in the Eastern Banda Sea, which identified several possible mechanisms for slope instability, including the loading and presence of soft sediments. These soft sediments include such soils as calcareous and siliceous sediments as well as volcanic muds that have low shear strength values.

When sediment is deposited rapidly there is a rapid increase and delayed dissipation in pore pressure that reduces the strength of the soil. Kostaschuk and McCann (1989) have shown evidence of how rapid sedimentation in the Bella Coola Fjord in British Columbia may have caused slope failures. The chute areas of the Bella Coola Fjord are pointed out as the most susceptible to this type of instability mechanism, where sandy silt deposits have sufficiently low permeability to restrict the drainage and induce undrained conditions and thus the stability of the soil should be considered using an undrained analysis. For this site, it was shown that the delta fan was prograding at a rate of 8.6 m/year with a nominal thickness of 2.2 m considering a slope gradient of 15 degrees. Kostaschuk and McCann (1989) theorize that the deposition may be rapid enough and the pore pressure dissipation slow enough to cause an undrained failure and shallow mass movements at distributory mouths.

25

A similar study by Dimakis et al. (2000) analyzed the ability of a fan in the Barents Sea of a slope of about 1 degree to fail under sediment loading of a rate of about 0.6 m/year. It was found that these large sedimentation rates may act in concert with periods of peak glaciation to result in very large and frequent slope failures.

2.3.5 *Oversteepening*

Oversteepening is a largely gravity driven mechanism of submarine slope instability. As described by Schwab et al. (1991) the sea floor becomes too steep due to tectonic movement that increases the amount of shear stress experienced by the various soil layers that may be present. When slopes become steep enough, another triggering mechanism, such as seismic activity, may not have to be as strong to initiate a failure. Schwab et al. (1991) explains how this occurred on the northern slope of Puerto Rico, where the northward tilting of the slope from tectonic movement caused an increase in the shear stress of the seabed sediments. Oversteepening has also been observed to occur in several other locations around the world, such as the volcanic slopes of Hawaii (Moore et al., 1989) and the continental slope of Norway (Bugge et al., 1987). The process of oversteepening is not a particularly rapidly progressing one. In the case of the northern slope of Puerto Rico the oversteepening is thought by Schwab et al. (1991) to have occurred in the last 4 million years, so oversteepened areas should be readily identifiable by ocean mapping programs and potential from failure could be further assessed using appropriate sampling to observe in-situ strengths of the submarine soils. Infinite slope analysis is useful when assessing slopes that have become oversteepened. Kostaschuk

and McCann (1989) explain that this type of analysis has shown that drained slope failures will occur only when the bottom slope exceeds the friction angle of the sediments.

2.3.6 Tidal Drawdown and Pore Pressure Gradients

Another mechanism of instability that must be considered in nearshore areas is tidal drawdown in seabed areas with low saturation values. As described by Kostaschuk and McCann (1989) areas that are affected by large tidal ranges (approximately 5 m) excess pore pressures can be produced as the tide falls. If the sea floor soil were to have a low permeability, the movement of the water would be restrained, as the tide lowers, and excess pore pressure would be generated. Evidence of this type of water entrapment is shown as small sand volcanoes that can appear in an intertidal zone. The volcanoes are produced as the pressure is released from the sediment. Tidal drawdown is also mentioned by Johns et al. (1984) where in the Kitimat Fjord of British Columbia unstable conditions were caused by low tides. Undrained failure may have occurred at high tide in soils with an undrained shear strength of less than 52.2 kPa, as compared to the low tide failure when a lower shear strength value of only 47.9 kPa was required.

There are also other instability mechanisms related to pore pressure differences. Orange (1992) discusses how slope instability can occur from excess pore pressure gradients. When sediments are compacted and deformed, fluid expulsion results, creating an elevated pore pressure gradient. When this gradient exceeds a critical value (dependent

upon material strength, porosity, fluid and soil densities, and slope angle) then the slope will have the ability to fail. Additional pore pressure influences can include increased excess pore pressure from aquifers as well as surface run-off.

Failures themselves can in turn cause pore pressure differences that cause subsequent failures. Koning (1980) shows how large volumes of high porosity sand are removed during a shear failure event an overall volume decrease can occur that causes an increase in pore pressure. In situations such as this, the increased pore pressure can lead to liquefaction.

2.3.7 Other Possible Sources of Instability

There are several other instability mechanisms that have been proposed or theorized. Embley (1980) discusses the possibility of erosional undercutting by turbid flow currents as an instability mechanism for slides off the coast of Africa. This phenomenon usually occurs in conjunction with earthquake loading. When a large flow, that is triggered by an earthquake, mobilizes it can transform into turbidity current which can undercut another slope. Toe erosion is also a logical instability mechanism. If the toe of a slope were to be removed by current or wave forces, the slope would become instable and experience a loss in shear strength as gravitational driving forces would then increase. Other triggering mechanisms suggested by Embley (1980) include the migration of freshwater through aquifers that outcrop on the continental slope as well as diapirism.

28

Additional instability mechanisms suggested by Koning (1980) include local slope scouring, construction activities such as dredging, dumping, or pile driving, or other non-naturally driven events such as explosions, ship collisions, or vibrations.

In this same vein as explosions or ship collisions, one of the more novel explanations for submarine slope instability is the possibility that a meteor landing in the ocean caused an unstable environment, as suggested by Norris et al. (2000). Norris et al. (2000) has discussed the possibility of the Chicxulub meteor, which collided with the earth 65 million years ago, causing massive submarine failures around the western North Atlantic, in particular the Gulf of Mexico and Caribbean regions. However, an impact of this magnitude would have caused large seismic events, which would essentially be the triggering mechanism. In this case, the meteor would be the cause for the seismic activity as opposed to tectonic plate movement as experienced with conventional seismic movements.

2.3.8   Retrogressive Nature of Submarine Failures

Mulder and Cochonat (1996) state that a retrogressive pattern is a major feature of many submarine landslides. This is most evident with those slides that have large scars and feature significant run-out distances. On occasion, the landslide can originate nearshore and retrogress back across the shoreline including the Humboldt Slide (Hampton et al., 1996), the 1888 Trondheim Harbor Slide in Norway (Andersen and Bjerrum, 1967) and the 1964 Alaskan Slides (Lemke, 1967).

A retrogressive failure is defined by Hampton et al. (1996) as sliding that occurs serially as numerous adjacent failures progress upslope. Figure 2.1 shows the four significant types of successive landslides highlighted by Mulder and Cochonat (1996). The Type A slide is a successive overlapped slide where the slide leads to instability only on the upper back part of the main scar. Adjacent flows, as shown as Type B, only occur if the main body triggers the instability along the whole perimeter of the scar. A Type C slide occurs when the failure surfaces of the main body are not merged with the main one and a Type D 'domino-like' slide is produced when a topographically high mass of sediments fails and induces mobility in an underlying second material mass. Since retrogression only occurs in the upslope direction according to Hampton et al. (1996) only Types A and B can be termed retrogressive as Types C and D are actually successive failures.

retrogradation

retrogradation

4

3

2

1

plane

channelized
progradation

**A - successive overlapped
slumps**

retrogradation

Failure surfaces

4

3

2

1

progradation

section

retrogradation

retrogradation

3

2

retrogradation

1

retrogradation

channelized progradation

B - successive adjacent flows

Rotational failure surfaces

2

3

1

Translational failure surfaces

1

2

**C - fitted together
slides**

1

2

D - successive "domino-like"

Figure 2.1: Successive Submarine Slides and Slumps.
After Mulder and Cochonat (1996).

31

Retrogressive flow failures in submarine sand, silt, and sensitive clay deposits are commonly described in the literature. Both Terzaghi (1956) and Andersen and Bjerrum (1967) observed retrogressive flow failures in loose sandy and silty deposits in Scandinavia while Hampton et al. (1996) and Piper et al. (1999) described these types of failures on the Pacific and Atlantic margins of North America respectively. A contributory consequence to these retrogressive failures is their coincidence with low tide conditions when excess pore pressure generated at high tide does not have enough time to dissipate. However, retrogression is also a major feature of large earthquake-induced submarine landslides like the 1929 Grand Banks Slide.

2.4 Cyclic Loading of Soils

The major result of earthquake loading of submarine slopes is cyclic loading. Cyclic loading is defined by O'Reilly and Brown (1991) as a system of loading which exhibits a degree of regularity in both its magnitude and its frequency. There are a few fundamental features of soil response that can be reasonably explained, even though their behaviour is also rather complex. There are, as explained by O'Reilly and Brown (1991) three distinct classes of behaviour that are displayed in varying degrees by all soils. These classes are:

      (i)   the effect of stress reversals;

      (ii)   the rate-dependent response of the soil; and

      (iii)   the dynamic effects where static analyses become inapplicable.

These classes are outlined here in this section. Additionally a look is taken at where earthquake motions fit into this spectrum of varied loading patterns.

2.4.1   Stress Reversals

O'Reilly and Brown (1991) explain that the term stress reversal as it applies to cyclic soil loading does not refer to a change in the sign of a stress but instead to a change in the sign of the rate of the stress increase. An example of this behaviour would be a soil that experiences a stress increase followed by a stress reduction. Figure 2.2 shows an idealized version of dry granular drained soil behaviour between two stress states S_1 and S_2. Following each cycle there is a change in shear strain. Some of this strain is recovered during unloading and some is not. As is seen the magnitude of the recoverable strain is somewhat constant with each cycle, but the plastic irrecoverable strain experienced during each cycle reduces with each succession. Eventually, following numerous cycles, the elastic strain will be much greater than the plastic strain. This is what is known as the resilient stiffness of the soil. Resilient stiffness is largely stress-level dependent.

shear stress

S2

S1

shear strain

resilient shear
strain, γ_r
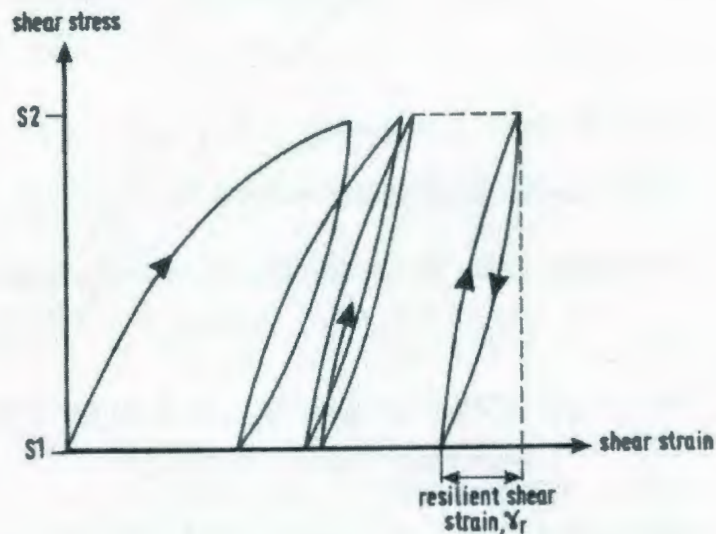
Figure 2.2: Shear Strain Development During Cyclic Loading.
After O'Reilly and Brown (1991).

If saturated soil is considered, changes in pore pressure will occur during rapid cycling where changes in pore pressure are not allowed to dissipate. Laboratory testing shows that in these cases failure can occur in stress states well below those of monotonic loading for the same soil due to the continued generation of additional pore pressure. An example of this behaviour is shown in Figure 2.3 for a loose Niigata sand as shown by Ishihara et al. (1975). This constant amplitude cyclic loading leads to a dramatic change at point 22 on Figure 2.3. At this point large pore pressures are generated and there is a loss in shear stiffness with subsequent cycling. During the cycling at fairly low stress levels an equilibrium condition is reached similar to that shown in Figure 2.2, where both pore and strain pressures are mostly recoverable. For faster rates of cycling the more the situation is similar to undrained conditions, alternatively the slower the cycle rate the

34

more the soil will behave like fully drained soil. This "faster rate" of cycling is dependent upon soil permeability and on the boundary conditions. Seed and Idriss (1982) have shown how pore pressures are constantly accumulating as a result of continued cyclic loading and then dissipating along gradients of excess pore pressure. O'Reilly et al. (1991) have completed tests on a clay in which cyclic loading and drainage are alternated, which may be a possible simulation of earthquake motions that are followed by periods of drainage.
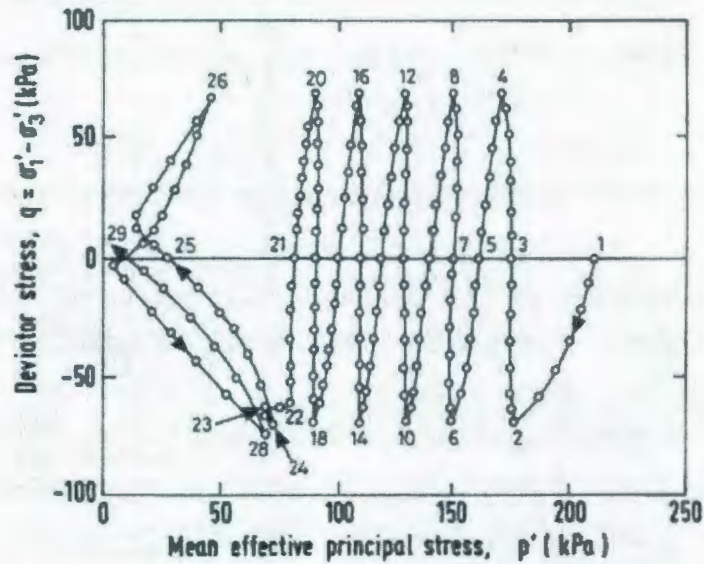
Figure 2.3: Niigata Sand Response to Low Amplitude Cyclic Stress. After Ishihara et al. (1975).

This behaviour can be explained by looking at the soil particles themselves and how they behave with changes in soil stiffness and the dissipation on energy within the soil. Soils experience a certain amount of hysteresis whereby they do not return the energy that has

been exerted upon them during the loading. This hysteresis can be considered as a type of damping under which the soil skeleton suppresses its own vibration by absorbing the cyclic energy. A submarine slope would be an example where a saturated undrained soil matrix would experience some damping. Since the pore water does not have an opportunity to drain, pore pressures will continue to increase as it aids in the damping of the vibration.

2.4.2 Rate Effects

O'Reilly and Brown (1991) define rate dependency as the influence of the rate of loading, or the rate of strain, on the strength and stiffness of the soil. Ishihara (1996) describes how the rapidity of load application is a feature of the dynamic load causing the stress. Figure 2.4 displays events of engineering significance classified according to the time of loading, as shown on the horizontal axis. Higher frequency events, such as water waves or vibration, are considered as events with longer loading times. Events like these where the load being applied lasts for longer than tens of seconds are usually considered as static problems, where events with much shorter times of load application are dealt with as dynamic problems.
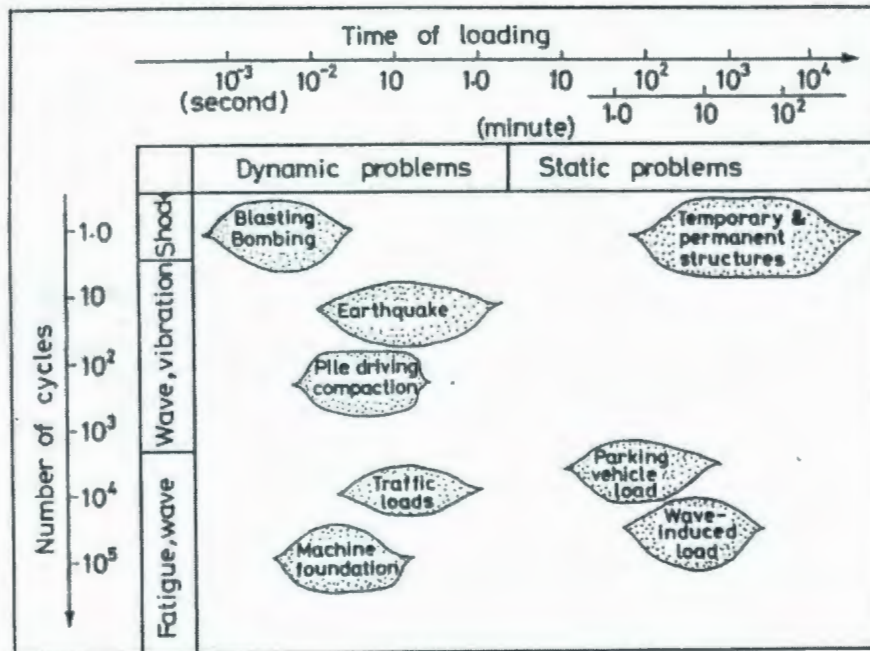
Figure 2.4: Classification of Dynamic Problems.
After Ishihara (1996).

This length of loading can be expressed in terms of speed of loading or rate of straining and can be collectively referred to as the rate effect. This phenomenon is dependent upon two sources: the viscous interparticle action of the soil, and the time-dependent dissipation of excess pore pressures that are generated during cyclic loading.

For clay soils it is apparent that the viscous stress-strain response is dependent upon the rate of strain. However, for granular soils it is apparent that rate dependency has little to do with the response. Generally, soils that are subject to cyclic loading experience higher rates of strain than soils exposed to monotonic loading. O'Reilly and Brown (1991)

37

explain this by stating that traffic, machine, wave, and earthquake induced cyclic loads are typically applied in frequencies between 0.1-20 Hz. This loading can produce rates of stress increase that are many orders of magnitude larger than typical static loading situations.

The time-related response to excess pore pressure is dependent upon permeability and existing hydraulic gradients when the rate of cyclic loading is high, even when the permeability of the soil can be considered "adequately" permeable. This is especially evident in the liquefaction of sands, which are usually considered highly permeable under static conditions, under earthquake loading where the pore pressure will build up faster than it can dissipate.

2.4.3 Dynamic Effects

The dynamic phenomenon is the regime under which the load is repetitively applied many times with some frequency. This type of characteristic is displayed on Figure 2.4 on the vertical axis. As stated by O'Reilly and Brown (1991), when the frequency is high dynamic effects add extra complexity to the problem. This is of particular importance to earthquake engineering. Dynamic problems add extra considerations to an engineer, such as: damping properties, inertial effects, realistic modelling of boundary conditions and the stiffness of the soil at small strain levels.

Different dynamic phenomenon can be of interest in different types of events, as shown by Ishihara (1996). In the instance of blasting, there is a shock type of loading associated with loading that lasts only 10^{-3}-10^{-2} seconds. Irregular seismic loading can involve shaking of 10-20 cycles with varying amplitudes and a period between 0.1 and 3.0 seconds. Pile driving or vibro-compaction can lead to the application of a load in hundreds or thousands of cycles with a frequency of 10-60 Hz. All of these events can be associated with wave propagation. In cases where loads are trivial but the number of cycles is immeasurable, such as traffic loading, it may be required to understand the problem as a consequence of fatigue. When dealing with dynamic problems such as cyclic loading it is important to understand the aspects of the problem that will influence the soil's behaviour. Different frequencies, amplitude, and number of loading cycles can greatly affect the approach that is taken during investigation.

2.5   Slope Stability Analysis

There are numerous developed methods to analyzing the stability of slopes, some simple and some complex. In recent years, the advent of microcomputers and methods that are more complex have allowed for increased reliability in the analysis of the static and dynamic stability of slopes. Traditionally, limit equilibrium and limit analysis methods have been developed but the computational power of today's technology has allowed for the development of more comprehensive methods. However, to understand today's state of practice in slope stability analysis it is important to gain a general understanding of the more traditional methods that were developed and how they may be applied. These

methods do have limitations, but are nonetheless important because they are simple to apply as approximation of the stability of a given slope condition. Additionally, they have been calibrated against field observations and, according to Yu et al. (1998), can provide results that are within ± 5-10% of the actual results for both drained and undrained conditions. This section describes these methods along with more recently developed methods, including numerical and reliability analyses.

2.5.1 *Limit Equilibrium Analysis*

Limit equilibrium is a widely used concept that has been consistently adapted over the past 50 plus years. The primary consideration of the different varieties of these methods is to compare the driving forces to the resisting forces acting on a given an arbitrary linear or curved failure plane. The factor of safety is developed as a ratio of these forces. The global equilibrium along this failure surface is considered and the internal distribution of stresses is not regarded. For submarine slopes, a type of infinite slope analysis is typically used considering the large size that submarine slope failures typically entail (Lee and Edwards, 1986). Poulos (1988) stipulates however that in these analyses it must be considered whether the slope is considered undrained, fully drained, or partially drained.

Most of the prominent limit equilibrium methods focus on the various different methods of slices. If, for instance, we consider the sliding block along an arbitrary slip surface is divided into a number of slices (p), as shown in Figure 2.5, we can consider the forces

that act upon each slice: the shearing forces acting on the sides of each slice (X_1 and X_2), the normal forces acting upon the sides of each slice (E_1 and E_2), the weight of the slice (W), the water force exerted on the base (ul) where u is the pore water pressure and l is the length of the base), and the normal (N') and tangential (T) components of the reactionary forces acting along the slip surface.

$$F = \frac{\tau_f}{\tau_m}$$
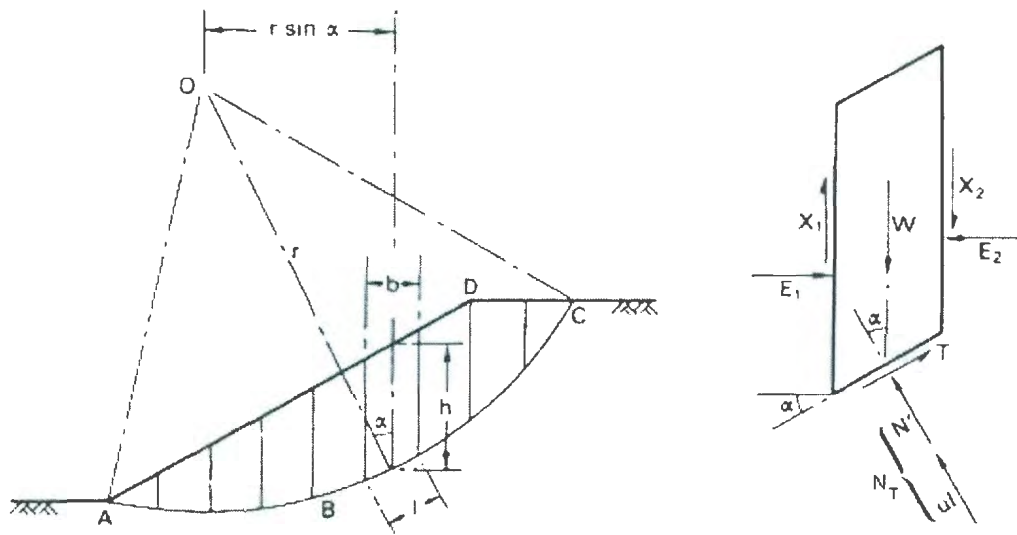
Figure 2.5: Method of Slices.
After Craig (1997).

Comparing the sum moments of the driving forces to the sum of the moments of the resisting forces will give a solution for the factor of safety (F_s) for a given slope taken on an arbitrary failure surface. This process is repeated over several arbitrary slip surfaces

to find the minimum factor of safety. The normal force (N_T), which is the sum of N' and ul, acting on the slice can be defined as:

$$N_T = \frac{W + (X_2 - X_1) - \dfrac{c'l \sin \alpha + ul \sin \alpha \tan \phi'}{F_s}}{\cos \alpha + \dfrac{\sin \alpha \tan \phi'}{F_s}} \tag{2.1}$$

where c' and ϕ' are effective shear stress parameters of the soil, α is the inclination of the base of the slice to the horizontal, and W is the total submerged weight of the sliding block.

The Fellenius (1936) method assumes that for each slice the resultant of the interslice forces is zero. It was proposed that the interslice forces could be neglected because they are parallel to each slice. This also involves resolving the forces on each slice normal to the base. However, this method has one major flaw since it does not satisfy the vertical equilibrium between slices.

Bishop (1955) proposed to neglect the interslice shear forces, thus assuming that a normal force adequately defines the interslice forces. Although Bishop (1955) satisfies the equations of equilibrium with respect to moment, it does not satisfy it with respect to forces. Spencer (1967) provided a method that supplied a factor of safety by taking into account the interslice forces that does satisfy both equilibrium of forces and moment. This lead to the expression of two factors safety for force and moments respectively.

Another advancement of this type of analysis came with the findings of Morgenstern and Price (1965) where a method was proposed to satisfy all boundary and equilibrium conditions, but where the failure surface could be any shape, including: circular, non-circular, or even compound. Much like Spencer (1967) this method produces two factors of safety, again one each for force and moment equilibrium. Unique to this analysis however is the use of an arbitrary function to describe the direction of the interslice forces.

Further extensions to the general method of slices were proposed by Chen and Morgenstern (1983) where it was shown there were restrictions that existed on the assumptions to make it statically determinate.

2.5.2   Limit Analysis

Limit analysis is a method of investigating slope stability first developed by Drucker and Prager (1952). It involves using the upper and lower bound theorems of plasticity to determine the corresponding bounds of collapse load as described by both Chen (1975) and Atkinson (1981).

The lower bound theorem states that collapse will not occur and the external loads on a body are at a lower bound to the true collapse load when a set of external loads acting on the body are in a state of equilibrium in a stress state which does not exceed the failure criterion for the given material at any point.

The upper bound theorem states that collapse must occur and the external loads on a body are at an upper bound to the true collapse load when a mechanism of plastic collapse and set of external loads acting on a body are such that the increment of work done by the external loads in an increment of displacement is equal to the work being done by the internal stresses acting on the body.

Both of these theorems can provide an infinite amount of solutions. This is because in the lower bound analysis compatibility is not satisfied and in the upper bound analysis stress equilibrium is not satisfied. This type of analysis is also based on several assumptions, including: the use of a single convex yield surface, the perfect plastic behaviour of the material with no strain softening or hardening, and the application of the principles of virtual work. When both the upper and lower bound values are equivalent, the solution is said to be exact. In terms of slope stability the lower bound theorem is of more interest to researchers because it provides a safe limit.

2.5.3 Numerical Analysis

Numerous complex methods of numerical analysis have gained prominence over the past 20 years with the advent of more powerful microcomputers to solve numerous equations with many variables. These methods include: Finite Element, Finite Difference, Boundary Element, and Discrete Element Methods. A full examination of these methods is beyond the scope of this thesis but Finite Element Methods (FEM) are by far the most prominent of these methods when considering the deformation and stability of natural

slopes. The major advantage of these methods over the traditional methods previously discussed is that no assumption of soil behaviour mode or failure mechanism is required as they can be assessed from the results of the analysis (Griffiths and Lane, 1999).

Poulos (1988) states that the major advantage of FEM is that they can accurately predict the movements of non-homogeneous and/or anisotropic seabed soil deposits. However, these models typically require accurate input parameters based upon the soil properties of the deposit being studied. In the case of real life soil deposits, these parameters can often be difficult to obtain. FEM consider a finite number of elements in the problem geometry and using developed constitutive laws, such as elasto-plastic behaviour can thus determine solutions for the development of pore pressures and displacements caused by various loading and stress conditions.

FEM are used quite frequently to solve the problems associated with submarine slope stability and Azizian and Popescu (2003) and Leynaud and Mienert (2003) are just a few of the successful examples of the applications of these methods.

2.5.4 Risk & Reliability Analysis

Like most types of geotechnical analyses, slope stability analysis does contain several sources of uncertainty. It is for this reason that risk and reliability analysis has been developed as an additional tool to augment more traditional methods of analysis.

These methods involve applying probabilistic methods to the analysis of slopes, which can include such methods as: Monte Carlo Simulation, Mean Value & Advanced Value First Order Second Moment, or Point Estimation. Numerous different types of analyses have been used to examine different attributes of slope stability analysis. This includes: hazard mapping and analysis (Hansen, 1984), quantifying risk and reliability (Christian et al., 1994), critical slip surface determination (Hassan and Wolff, 2000), failure back analysis (Tang et al., 1999), as well as earthquake effects (Christian and Urzua, 1998).

Reliability methods do however have some noted limitations as they can require some estimation of input parameters. Additionally, they are not as well known or used as other traditional methods that quickly yield a useful factor of safety (Christian, 1996).

2.6 Seismic Slope Analysis

Specific to the cyclic loading assessment of sands we need to examine the following questions as put forth by Poulos (1988):

      (i)   What is the likelihood of liquefaction potential of the sand?

      (ii)   What is the magnitude of the excess pore pressure generated by cyclic loading?

      (iii)   What is the cyclic strain or displacement of the soil?

      (iv)   What is the permanent (residual) displacement of the soil?

This section will look at some of the current methods of determining answers to these questions

2.6.1 Simplified Procedure Assessment of Liquefaction Potential

The liquefaction potential of a sand deposit is typically determined by what has become known as the 'Simplified Procedure' as first proposed by Seed and Idriss (1971) and now currently defined by Youd et al. (2001).

The stability of a saturated slope is affected by the residual excess pore pressure that is developed after N_c cycles. The relationship for the development of this excess pore pressure (u_e) was developed by Seed and Idriss (1971) as:

$$u_e = \sigma'_{v0} \left(\frac{2}{\pi} \arcsin\left(\frac{N_c}{N_l} \right)^{\frac{1}{2\beta}} \right) \tag{2.4}$$

where σ_{v0}' is the initial vertical effective stress, N_l is the number of cycles to liquefaction, and β is the soil parameter, typically 0.9 for loose sands. To solve this equation the number of cycles to liquefaction must be determined and an irregular acceleration-time history for a seismic event must be converted into an equivalent number of uniform cycles as prescribed by Seed et al. (1975). By using this procedure the irregular history can be transformed into an equivalent number of cycles at 0.65 times the maximum acceleration of the seismic event (a_{max}).

The value of N_l can be approximated through a procedure descried in Youd et al. (2001). However, to determine N_l, the cyclic stress ratio (CSR) and the cyclic resistance ratio (CRR) must also be determined.

The CSR can be determined using the following formula as given by Seed and Idriss (1971):

$$CSR = \tau_{av}/\sigma_{v0}'$$ (2.5)

where τ_{av} is the average cyclic shear stress. With some rearrangement and substitution the formula can be expanded to:

$$CSR = 0.65\left(\frac{a_{max}}{g}\right)\left(\frac{\sigma_{v0}}{\sigma_{v0}'}\right)r^d$$ (2.6)

where g is the acceleration due to the earth's gravity, a_{max} is the maximum acceleration from the shaking, σ_{v0} is the initial total stress and r^d is a stress reduction coefficient that can be determined for soil depths equal to or less than 9.5 m using the following formula found in Liao and Whitman (1986):

$$r^d = 1.0 - 0.00765z$$ (2.7)

where z is the depth below soil in metres.

The determination of cyclic resistance ratio is a more complicated and sophisticated procedure than that of determining cyclic stress ratio. The currently most accepted method is proposed by Robertson and Wride (1998) and is based upon the acquisition of

48

CPT data for the deposit being investigated. This procedure involves several calculations using a prescribed flow chart. It is important to note that this method solves for a CRR normalized to an earthquake with a magnitude equal to 7.5, which must be corrected for later in the procedure.

Once CSR and CRR are determined, N_l can be approximated. When liquefaction occurs we can assume that at the location where liquefaction is taking place, the factor of safety is approximately equal to one. Therefore, if a spatially variable local safety factor (F_{ls}) equal to one is assumed then Seed and Idriss (1982) shows that the magnitude scaling factor (MSF) and subsequently the earthquake magnitude (M) can determined using the following formulae:

$$MSF = \frac{CSR}{CRR_{7.5}} \qquad (2.8)$$

$$M = 10^{[(2.24 - \log MSF)/2.56]} \qquad (2.9)$$

Once M is calculated, N_l can be approximated using Figure 2.6 as shown in Seed and Idriss (1982).
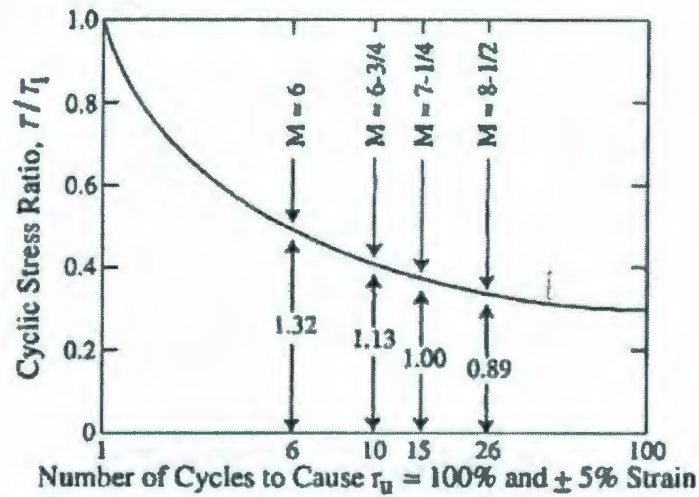
Figure 2.6: Relationship between CSR, M, and N_1.
After Seed and Idriss (1982).

Following this procedure, the derived excess pore pressure can be used in more traditional slope stability analysis methods to assess the potential of liquefaction under the given earthquake loading. However, additionally, sloping ground does not generally liquefy due to static shear stress.

Additionally, Youd et al. (2001) define F_{sl} against liquefaction for depths shallower than 15 m as:

$$F_{ls} = \left(CRR_{7.5} \middle/ CSR \right) \bullet MSF \bullet K_\sigma \bullet K_\alpha \tag{2.10}$$

where K_σ and K_α are correction factors that account for the effects of overburden pressure and static shear stress that affect the susceptibility to liquefaction. Youd et al. (2001)

50

supplies a relationship for the use of K_σ values but the use of values for K_α are discussed by various sources, including Seed and Harder (1990) and Harder and Boulanger (1997).

This analysis usually requires CPT data from the field area under investigation as discussed by Stark and Olson (1995) and Robertson and Wride (1998). An example of the extrapolation of this data for the examination of submarine slopes is the investigation by Mosher et al. (2001) into the stability of the Strait of Georgia in British Columbia during an earthquake in 1946.

2.6.2 Steady State Line Assessment of Liquefaction Potential

Poulos (1981) introduced the steady state line approach to evaluate liquefaction potential. The major ideal of this method is that at a constant volume a liquefied soil is still capable of sustaining a shear stress, described as the steady state strength by Poulos (1981). The steady state line, as shown below in Figure 2.7, is defined as a straight line upon which the points representing the steady state condition of soil fall on a semi-log plot of void ratio against effective confining pressure.
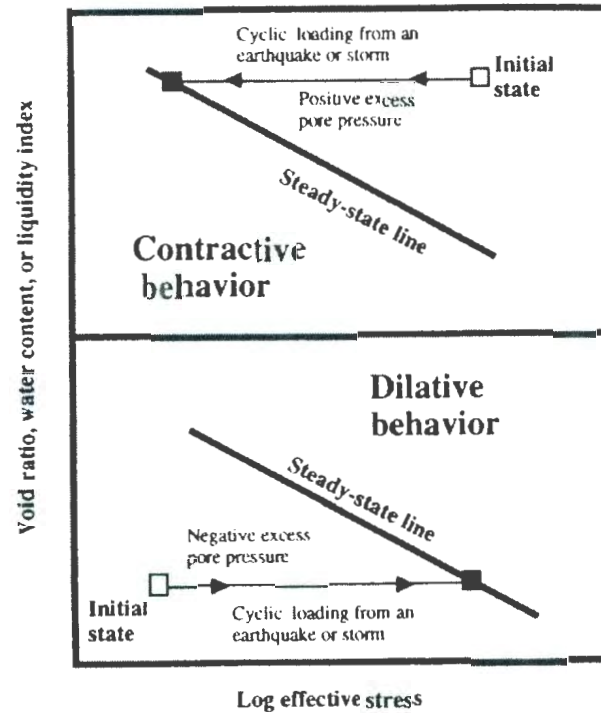
Figure 2.7: State Change During Undrained Failure.
After Hampton and Lee (1996).

Considering a cyclic stress, such as an earthquake, different behaviours can be explained using this analysis. In materials that dilate after yielding, such as dense sands, the effective stress and undrained shear strength will increase leading to the termination of deformation. In other materials, where the initial state lies above the steady state line the pore pressure and effective stress will decrease during undrained shearing. The transformation to this state will allow the soil to liquefy as the shear stress approaches zero, as is experienced at Point 29, shown in Figure 2.3 for Niigata Sand.

An example of the use of this approach in the analysis of submarine slopes is the work presented by Chillarige et al. (1987) to examine flow liquefaction in the Fraser River delta in British Columbia.

The state parameter (ψ) measures how far the soil state is from the steady state line and when it is equal to zero, the state lies on this line, but is not necessarily liquefied unless shear stress is also zero. This approach, as developed by Been and Jefferies (1985), can be considered an extension of this method and has also been used in liquefaction analysis, including Been et al. (1987) where it was applied to the failure of the Nerlerk Berm in the Beaufort Sea.

2.6.3 Newmark Displacement Analysis

A simple procedure to calculate the permanent slope displacement of due to earthquake shaking was first introduced by Newmark (1965). The Newmark method of displacement analysis consists of two major steps. The first step is to obtain a critical acceleration that is a threshold value of acceleration that causes pseudo-static instability of the slope in question. Following this, the second step of the analysis involves taking the portion of the acceleration time history of the earthquake event that exceeds the critical acceleration and double integrating it. The idea behind this type of analysis is that the pseudo-static factor of safety for the slope can become less than one, typically corresponding to a Newmark displacement of a few centimeters, during the earthquake without necessarily causing the collapse of the slope.

Newmark analysis has been used many times to investigate slopes and earthquakes, Urgeles et al. (2001) for example. Nevertheless, there have been some identified limitations to Newmark analysis related to the analysis of submarine slopes, as discussed by Azizian and Popescu (2001). Essentially, the presence of water leads to a vulnerability to liquefaction, which contains some effects that cannot be fully considered in Newmark displacement analysis.

3 CENTRIFUGE MODELLING

3.1 Introduction

Over the past several decades small scale centrifuge modelling has been used to investigate various gravity dependent phenomenon (Schofield, 1980). In the study of materials, shear failure is dependent upon the applied stress level. The use of geotechnical centrifuges has been cited as a proven technique to properly simulate stress dependent behaviour of soils (Schofield, 1980; Cheney and Fragaszy 1984; Phillips, 1993; Murff, 1996).

The wide acceptance of centrifuge modelling in all parts of the world is based upon the fact that the underlying principles are widely understood. These two principles are: the increase of self-weight by the increase of acceleration is equal to the reduction of the model scale; and the reduction of time for model tests as the scale is reduced can be explained by time scaling laws (Schofield, 1988).

Centrifuge modelling involves placing a model upon a rotating centrifuge arm. As the centrifuge begins to rotate it generates an inertial radial acceleration that simulates an increased level of gravity. This increased gravitational field allows for the similarity of stresses between the reduced-scale model being tested and the full-scale prototype. Materials within the soil model being tested is subjected to an increasing stress level that

increases with radius (depth) at a rate that is dependent upon material density and the magnitude of the speed of rotation of the centrifuge and thus the accelerated gravitational field.

Centrifuge modelling is indeed a useful tool for providing results for geotechnical investigations in comparison to full-scale modelling. Model construction costs can be significantly lower and with shorter observation time involved to monitor the phenomenon in question.

However, it is important to note that a centrifuge model is a simplified replica of the larger full-scale prototype situation and provides unique solutions to a unique situation. Additionally, centrifuge modelling features several limitations due to this simplification. The purpose of this section is to review the model scaling laws that govern centrifuge operations, the errors that are inherent in centrifuge modelling and how they can be minimized, the development of earthquake actuation in the centrifuge, and finally a review of previous centrifuge testing in the vein of seismic testing of submerged slopes.

3.2 Modelling Scaling Laws

When considering the different types of scaling laws that govern the modelling of materials it is important to consider the following fundamentals put forth by Fugslang and Ovesen (1988):

>   (i)   all significant influences should be modeled in similarity;

(ii)   all phenomena not modelled in similarity should be established secondarily by experimental evidence; and

(iii)   any phenomenon that is unknown should be disclosed or confirmed as insignificant by utilizing the test results.

3.2.1 General Scaling

Soil stresses between the model and prototype may be directly compared if the same soil with the same stress history is used in both the prototype and model. The basis of centrifuge modelling is that when a model is exposed to an increased acceleration field of n times the Earth's gravity, the vertical stress at depth h_m in the model will be equal to the prototype vertical stress at depth h_p where $nh_m = h_p$. Therefore, stresses will be equal at homologous points in a model of scale $1:n$ that is accelerated to a simulated gravitational field to n times the earth gravity (g).

When developing a properly scaled centrifuge model that is to be an accurate representation of a given prototype condition the correct acceleration level and geometric scale (n) must be chosen to correspond the appropriate prototype conditions (Taylor, 1995). If the stress levels are to be equal between the model and the prototype at homologous points then the linear dimension in the prototype (h_p) must be equal to the linear dimension in the model multiplied by the geometric scale (nh_m). Considering that the model is also a geometric representation of the prototype, any displacements observed in the model will also be at the model to prototype scale of $1:n$. Consequently, since

strain is defined as a ratio of displacement to length, which are both modeled at *1:n*, strain is also measured in a 1:1 relationship between the prototype and model.

3.2.2 Static & Dynamic Time Scaling

There exist different time scales for different phenomenon, including dynamic and static events, both of which are experienced in dynamic earthquake tests. As a result, time scaling conflicts can occur and an experimenter must consider the scaling limitations that are placed upon their test.

Dimensional analysis has been used to characterize the centrifuge scaling factors of various types of phenomenon and are presented in various sources (Prevost and Scanlan, 1983; Cheney and Fragaszy, 1984; Fugslang and Ovesen, 1988), as well as in Table 3.1. For the parameters listed dimensionless numbers are given and the similarity conditions given are expressed in *N*-values, assuming that the acceleration is scaled at *n* and model lengths are scaled at *1/n* and that the prototype material is used in the model. The major observation of these relationships is that for inertia (dynamic) events and laminar flow (static) events there exist different time scales of *1/n* and $1/n^2$. This relationship is also discussed comprehensively by Goodings (1985). In order to provide a valid model testing condition the time scales for motion and fluid flow must be matched. It is important to consider this difference in time scaling and provide a possible solution when undertaking seismic tests in the centrifuge. Other parameters involved in earthquake

testing, such as model length, soil density, acceleration, stress, and strain remain the same

for dynamic and static centrifuge modelling.

Table 3.1: Scaling Factors in Centrifuge Tests.
After Fugslang & Ovesen (1988).

Parameter	Symbol	Dimensionless Number	Similarity Requirement	Scaling Factor
acceleration	a		$N_a =$	n
model length	l		$N_l =$	$1/n$
soil density	ρ		$N_\rho =$	1
particle size	d	d/l	$N_d =$	1
void ratio	e	e	$N_c =$	1
saturation	S_r	S_r	$N_S =$	1
liquid density	ρ_l	ρ_l/ρ	$N_{\rho_l} = N_\rho =$	1
surface tension	σ_t	$\dfrac{\sigma_t}{\rho_l a d l}$	$N_\sigma = N_\rho N_a N_d N_l =$	1
capillarity	h_c	$\dfrac{h_c \rho_l a d}{\sigma_t}$	$N_h = N_d N_\rho^{-1} N_a^{-1} N_d^{-1} =$	$1/n$
viscosity	η	$\dfrac{\eta}{\rho_l d \sqrt{al}}$	$N_\eta = N_\rho N_d N_a^{1/2} N_l^{1/2} =$	1
permeability	k	$\dfrac{k\eta}{d^2 \rho_l a}$	$N_k = N_d^2 N_\rho N_a N_\eta^{-1} =$	n
particle friction	φ	φ	$N_\varphi =$	1
particle strength	σ_c	$\dfrac{\sigma_c}{\rho a l}$	$N_\sigma = N_\rho N_a N_l =$	1
cohesion	c	$\dfrac{c}{\rho a l}$	$N_c = N_\rho N_a N_l =$	1
compressibility time	E	$\dfrac{E}{\rho a l}$	$N_E = N_\rho N_a N_l =$	1
inertia	t_1	$t\sqrt{a/l}$	$N_t = N_l^{1/2} N_a^{-1/2} =$	$1/n$
laminate flow	t_2	tk/l	$N_t = N_l N_k^{-1} =$	$1/n^2$
creep	t_3			1

As discussed by Dewoolkar et al. (1999a) the conflict between dynamic and static scales can be resolved by slowing the static event. This can primarily be achieved by reducing

the permeability of the model soil by one of two means, either by reducing the size of the soil particles and maintaining the same pore fluid (water) or by maintaining the same soil structure and employing a substitute pore fluid which is *n* times more viscous that water.

It is not normally a viable option to change the grain size of the soil material in the model since in order to maintain similar stresses and strains in the model and prototype there must not be a significant change in grain size. Therefore, the only reasonable option is to use a substitute viscous pore fluid to reconcile the differences in time scaling. Using this method, Darcy's law of seepage would dictate that the time scale for static events like diffusion then be *1:N* and thus equivalent to the time scale for dynamic events.

A fluid that is much more viscous than water but has similar density and shear properties to water is the most desired. There are also other considerations, including: environmental friendliness, safety, and cleanliness in laboratory conditions and equipment (Ko, 1994; Dewoolkar et al., 1999a). Some of the possibilities for this substitute pore fluid have been explored in the past 10 years. These have included silicone oil, which is expensive and hard to dispose of, and a water-glycerin mixture. However, a more effective and inexpensive pore fluid has become more prevalent in the geotechnical testing community in North America over the past several years. This substance is hydroxypropyl methylcellulose (HPMC), a readily available powder. This HPMC powder can be mixed readily to achieve a wide range of viscosities as compared to water with easily repeatable results. Additional benefits include the HPMC solution's

61

ease of cleaning, ease of disposal, and resemblance to water with respect to many physical properties (Stewart, 1998; Dewoolkar et al., 1999b).

3.3 Modelling Restrictions

3.3.1 Acceleration and Stress Variation

In centrifuge modeling a high acceleration field is used to achieve a representative scale model of a full-scale geotechnical condition. However, the acceleration field felt inside the model is not uniform. Acceleration increases as the distance from the centre of rotation increases, this is determined by the fact that the magnitude of acceleration field is equal to $r^2\omega$, where ω is the angular rotational speed of the centrifuge and r is the radius from the centre of rotation to the element of interest. If it is assumed that during operation the top of the model is closest to the centre of rotation and the bottom of the model is furthest away from the centre of rotation, then the acceleration field experienced in the model will become greater from the top of the model to the bottom of the model in a nonlinear fashion, due to the influence of r. This variation of acceleration dictates expressly the magnitude of the stress profile inside the model. Ordinarily, the prototype would experience a linear increase in stress as depth into the soil increases due to the constant gravity put upon it by the Earth's rotation. However, the model experiences a nonlinear stress profile that increases with depth proportional to the variation of the induced acceleration field.

It turns out that the error experienced from this effect is minor and can be minimized. This can be achieved by considering the relative magnitudes of over- and under-stress to define a region of exact association in the stress experienced in the model and the prototype at two-thirds of the model depth (Taylor, 1995; Schofield, 1980). The region of maximum under-stress dictates the effective radius as being the distance measured from the centre of rotation to one-third the model depth. This relationship can be seen in Figure 3.1, where R_e is the effective centrifuge radius and R_t is the radius to the top of the model. Typically, this stress profile error has been found to be less than 3% of the stress experienced in the prototype, which is not overly significant but should nonetheless be considered when performing tests of this nature. Schofield (1980) also suggests that as long as the overall soil model depth is less than 10% of the effective centrifuge radius, the acceleration level may be assumed constant with model depth without excessive error.
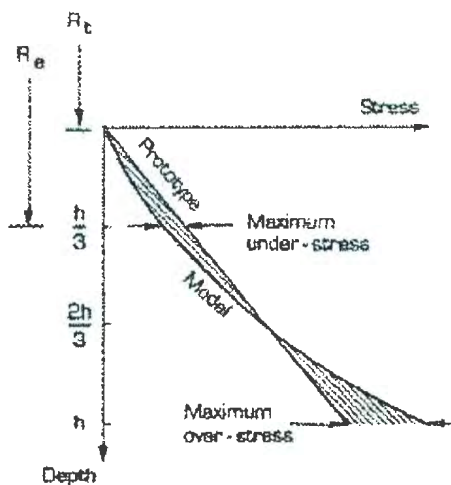
Figure 3.1: Stress Variation With Depth In Centrifuge Model & Corresponding Prototype.
After Taylor (1980).

An effect closely related to the variation in acceleration with depth is the direction of the acceleration. The spinning motion of the centrifuge directs the acceleration radially away the centre of rotation in the horizontal plane. This leads to a change in direction, relative to the normal, across the width of the model from the centre of the model to the sidewalls. At the centre of the model the direction of the acceleration is completely in the normal direction, but considering elements closer to the sidewalls the direction of the acceleration becomes more inclined from this normal and away from the centre of rotation. This effect can cause a significant error if the testing involves considerable activity in the regions close to the sidewalls of the container. However, there are methods of attenuating for this error. For smaller centrifuges operators have discovered that various shapes of models can be used that compensate for this radial variation of the acceleration field. In most tests, it is considered advisable to ensure that any major events occur in the centre of the model where the direction of acceleration is closer to vertical, and thus closer to the vertical nature of the direction of acceleration experienced in the prototype.

An additional error is the fact that any model subjected to an increased acceleration field in the centrifuge also experiences the Earth's natural acceleration field. In a beam centrifuge the induced acceleration field acts parallel to the plane created by the arc of travel of the arm in a direction away from the center of the arc. As the centrifuge increases speed the basket swivels upward so that this induced acceleration field acts in the same direction in the model as it does in the prototype and the vertical plane in the

model is now parallel to the horizontal plane in "our observed space". However, it is impossible to remove the constant acceleration effect of the Earth's rotation and when the model swivels into its final position it experiences this natural field perpendicular to the induced effect caused by the centrifuge rotation and in the horizontal plane of the model. For the most part this effect is rectified by the articulated upward swiveled position of the basket. However, there is a certain amount of friction that is developed in this swing connection that prevents it from achieving a position that alleviates this effect fully. The result of this frictional force is that the model does not experience an acceleration field that acts truly parallel to the vertical axis of the model as the prototype does in its vertical plane as caused by the Earth's gravity. The model does experience a resultant acceleration field that is very close to vertical by virtue of the fact that the induced acceleration field acting away from the center of the rotation (ng) is typically many times larger the horizontal acceleration acting towards the Earth's centre (1 g). The magnitude is this error is typically insignificant. Considering a test at a test acceleration of 100 g, this resultant acceleration will act less than 0.6 degrees from vertical. Another possible solution is to place a wedge underneath the model to ensure that the acceleration field is more directly perpendicular in the model.

3.3.2 Coriolis Effect

The modelling of dynamic events in a centrifuge can experience the problem of Coriolis effect (Schofield, 1980). This acceleration effect develops in the rotational acceleration field when there is movement inside the model in the plane of the rotation. An example

of this type of movement would be earthquake shaking or seepage movement. This type of error can be combated by orienting the major vertical plane of the model perpendicular, instead of parallel, to the plane of rotation. Nevertheless, this type of adjustment does not eliminate all Coriolis acceleration, as vertical movements in the plane of rotation may still exist, although they may not be the major movements of interest to the researcher. Taylor (1995) has concluded that there is a range of velocities for movements of a mass inside the model (v) that do not give rise to significant Coriolis accelerations. This range is stated as: $0.05V > v > 2V$, where V is the velocity of the centrifuge model.

3.3.3 Data Interpolation

All model tests have the need to have their test results calibrated in order to make comparisons to the prototype. One technique that may be employed to apply this philosophy to centrifuge modelling is the technique known as "modelling of models" (Schofield, 1980; Taylor, 1995).

Modelling of models requires the modelling of a given prototype in a variety of acceleration fields with the correspondingly appropriate geometric sizes. If it is considered that the ratio of stresses and strains between the model and prototype is constantly 1:1, as previously established, regardless of g-level as long as the geometry is appropriately scaled for that acceleration, then the resultant stresses should be constant at each g-level investigated.

By investigating various model sizes at their corresponding *g*-levels, a confirmation of modelling procedures should be accomplished, assuming there are no other observed errors.

3.3.4 Grain Size Effects

Arguments have been made that in a model test scaled down to *1:n* the grain size of the soil being investigated should be scaled down *n* times to accurately reflect the soil in the prototype. This sort of argument would require a prototype condition featuring a fine sand would be best approximated by a clay or silt in a centrifuge model. However, since clays or silts do not behave in the same fashion of sands when exposed to stress, this sort of replacement cannot be made. Grain size characteristics are an important quality with respect to the behaviour of soils and the soil material used in the model should not differ from the prototype or behaviour will not be accurately replicated.

To combat this argument, modelers have given this type of error much attention. It has been found that it is important to develop guidelines on the critical ratio between a major dimension in the model to the average grain size diameter. An example of this is Ovesen (1979) where in research into the performance of circular foundations on sand it was found using modelling of models that centrifuge modelling scaling laws were valid until a point where the ratio of the foundation diameter to the grain size was less than about 15. In terms of instability of slopes constructed of granular materials, such as sands, Goodings and Gillette (1996) concluded with the analysis of 61 centrifuge models that

full and unimpeded development of failure may occur only when the distance between the soil surface and failure surface is at least 30 grain diameters in fully drained, dilatant soils. This type of data displays why, when a centrifuge experiment is being designed, it is important to recognize that in some tests the relationship of the size of the model to the soil particle size may have an effect on the results.

3.3.5 Boundary Effects

In beam centrifuges models are typically contained by some sort of container or reinforced strongbox to manage the high stresses that arise from increased gravitational acceleration. The walls of the container must be rigid in order to provide a lateral stiffness to prevent lateral soil movement. However, the use of a model container introduces boundary conditions different from that seem in the prototype. Santamarina and Goodings (1989) state that danger exists in extrapolating the behaviour of small physical models with relatively close boundaries to that of full-scale configurations in which the boundaries exist at geometrically greater distances.

The size of the model container is mostly dependent upon the limitations of the centrifuge upon which it is being placed. The smallest geometric scale that is allowed by any centrifuge is correlated to the maximum g level that may be obtained in that machine. Additionally, the dimensions of the centrifuge platform dictate the maximum dimensions of the container being loaded. In the case of an arm fitted with a shake table, dimensions are further limited.

Processes such as soil consolidation, settlement, and displacement occur during a dynamic centrifuge test. This typically involves soil shearing along the container walls and the friction from the soil shearing along the container walls must be minimized. In models with sand this can be accomplished with the installation of a material such as glass or highly polished stainless steel between the model material and the container wall. This type of treatment could also be augmented with the application of grease to the container walls or even applying a latex membrane to accommodate any vertical soil displacements. Santamarina and Goodings (1989) also suggest that the model soil width to depth ratio should be greater than four to eliminate boundary influences.

Dynamic centrifuge modellers have also developed a unique type of model container to deal with boundary conditions. Ko (1994) explains that this container should maintain a constant horizontal cross-section during shaking, and have zero mass and zero stiffness to horizontal shear. The solution to this problem has been to develop a stacked ring type container that will deform laterally in a method complimentary to the soil that is being tested. Thus, the container will behave similarly under shaking at the soil container boundary to the prototype condition where soil would be surrounding the test area. Two types of these containers have been developed to meet some, but not all of the conditions mentioned by Ko (1994); the laminar container (Hushmand et al., 1988; Law et al., 1991; Van Laak et al., 1994a), and the equivalent shear beam container (Zeng and Schofield, 1996; Madabhushi et al., 1998; Brennan and Madabhushi, 2002). The former uses roller bearings between the stacked rings to allow movement, and the latter features a

deformable material, typically rubber, between the rings. Comparisons of the behaviour of these types of stacked ring containers have been made in such studies as Whitman and Lambe (1986) and they have been compared to each other by Fiegel et al. (1994). It was found that each of the containers has its own dynamic properties and characteristics in terms of stiffness, mass and damping. When evaluating the results of centrifuge tests, by numerical modelling or otherwise, these properties must be fully understood and incorporated.

In dynamic centrifuge tests there also exists a unique boundary effect with the reflection of waves from this interface. Some work had gone into finding materials than can be placed between the model soil and the boundary walls. One of these materials is known as "duxseal" and has been investigated by Campbell et al. (1991) and Madabhushi et al. (1994). It was found that at least 65% of the incident stress waves are absorbed by a duxseal boundary.

3.4 Earthquake Actuation

The most widely modelled problems in relation to slope stability in the centrifuge, both onshore and offshore, are those of a seismic nature. By using an earthquake actuator on board the centrifuge arm, a modeler can use a scaled earthquake signal to deliver controlled, simulated, and properly scaled earthquake movements to the scaled soil model. Earthquake mitigation is an especially major challenge given the low predictability of both the location and magnitude of earthquake movements. Much of the

research with seismic slope failure triggering has dealt with liquefaction and liquefaction potential.

One such technique to deliver earthquake motion was the concept of releasing a cocked spring to produce free, damped vibrations (Morris, 1983). The problems related to this method are that the motion of the spring is dependent upon the mass of the model and the stiffness of the spring, variables that cannot be easily altered to meet the requirements of a particular test (Ko, 1994). Another technique that was developed to deliver earthquake motion was the bumpy road method as described by Schofield (1981). This method involved the test package making contact with a wavy track mounted on the wall of the centrifuge chamber. However, several problems were identified with this method. Often the motion was contaminated by other frequencies than those desired due to the dynamics of the motion transfer mechanism and also the input frequency is dependent upon the speed of the machine (Ko, 1994). Several other methods used by others include the process used by Arulananadan et al. (1982) to use piezoelectric effects to produce motion, the detonation of explosives at the container boundary by Zelikson et al. (1981), and the use of electromagnet excitation by Fujii (1991).

Despite this plethora of available systems, one method has emerged as the most versatile, which is an electro-hydraulic method that uses servo-controls to deliver most desired motions to the test package (Ko, 1994). This method is an extension of technology that has been used for many years in structural and laboratory testing to great success. These

types of simulators involve the use of a hydraulic ram controlled by servo valves. The position of the shaker is typically monitored by a Linear Variable Differential Transformer (LVDT) and controlled by a closed loop feedback system. The advantages of this system are that they are commercially produced, capable of generating large forces, and lightweight (Arulanandan et al., 1982). Examples of these types of earthquake simulators (EQS) exist in various parts of the world, including Japan (Inatomi et al., 1988; Nagura et al., 1994; Matsuo et al., 1998) and the United States (Kutter et al., 1994; Van Laak et al., 1994b; Figueroa et al., 1998). Recently this technology was developed and commissioned for use with the C-CORE centrifuge in St. John's, Canada. This EQS is the device upon which the tests for this research were performed. A full description of this system is given in Chapter 4.

3.5 Previous Work

There have numerous previous centrifuge studies related to saturated slopes. These studies have had various different purposes, from investigating the stability of sand embankments to investigating the repeatability of testing results at different testing centres to studying specific phenomenon that take place during slope failure. This section will review some of these tests in order to give an overview of the types of projects that have been completed to date.

3.5.1 Submerged Slopes

Lee and Schofield (1988) used a bumpy road shaking table at the Cambridge geotechnical centrifuge centre to conduct a study the effects of earthquakes on sand embankments and islands. Several two-sided embankment models and circular half-island models were both constructed and subjected to earthquake movements. The tests showed that during earthquake actuation positive pore pressures are generated at the crest of a loose or medium dense embankment. Additionally, it was found that when dense embankments are exposed to strong earthquakes, spiky accelerations are observed at the shoulders of the embankment. This testing program utilized silicone oil as its viscous pore fluid. The likelihood of liquefaction was also found to be greatly diminished when the relative density of the embankment exceeded 80%.

Similarly to the tests discussed above, Arulanandan et al. (1988) presents results of a centrifuge test of similar geometry except that a clay layer was situated over the sand embankment. Water was used instead of a replacement pore fluid because alternate pore fluids have been found to adversely effect the mechanical properties of clayey soils. Therefore, the model does not represent any specific prototype condition. The results showed that soils that prevent the escape of pore pressures, such as clay, are potentially more susceptible to flow failure than a uniform deposit of liquefiable sand.

The idea of adding countermeasures against soil liquefaction to constructed embankments was investigated by Koga et al. (1991). A model was tested that featured an embankment

constructed upon horizontal liquefiable soil. Test results from a model where no countermeasures were placed at the toe of the embankment in the horizontal soil were compared with test results from a model where countermeasures were placed at the toe. In this test, the countermeasures were 6 mm thick steel plates.

Nagase et al. (1994) discovered an important relationship between permanent ground displacement and the thickness of the liquefied layer in sloping ground. An infinite slope type of setup was employed at a combination of base angles of 5 and 10% and centrifugal accelerations of 80 or 20 g. A linear relationship on a log-log plot of ground displacement against the thickness of the liquefied layer if the slope angle and relative density are kept constant was discovered. In addition, the permanent displacement was found to occur in the whole liquefied layer.

A rather comprehensive investigation into earthquake induced later spreading in sand was undertaken by Taboada-Urtuzuastegui and Dobry (1998) where 11 dynamic centrifuge tests were performed in a laminar box. The slope angle, input acceleration, and input frequency were all varied to observe their effects on the response of a sloping liquefiable sand. It was determined that as the slope angle increases the pore pressure and the thickness of the liquefied soil either decrease of stay constant; the soil acceleration increases and becomes asymmetric in the liquefied soil, the settlement decreases; and the permanent lateral displacement and shear strain increases. It was also concluded that as the input acceleration was increased the permanent shear strain and settlement stay

constant or and increase and the pore pressure, thickness of liquefied soil, soil acceleration, and permanent lateral displacement definitely increase. In terms of varying the input frequency it was found that as it increased the pore pressure, thickness of liquefied soil, soil acceleration, permanent lateral displacement and shear strain, and settlement all decrease.

Lateral movements were also studied by Imamura et al. (2002). However, in this case the lateral flow of two-layered slopes during earthquake shaking was examined. A model consisting of a uniform single layer of sand and a model consisting of a layer of sand overlaid by a silt layer were both tested in increased centrifuge gravity. The influence of soil layering was that the displacement fields and velocities of lateral flow in the single layer model seemed to follow a sinusoidal shape while in the double layer model the upper impermeable silt layer was found to move as a solid block and was found to be subjected to larger lateral displacements than the model with uniform conditions. It was also concluded that soil density significantly affects the generation and dissipation of pore pressures, lateral displacement, and velocity of lateral flow. This study also managed to quantify that 80% of lateral flow occurs during seismic excitation and the rest continues after shaking, regardless of soil layering and density.

Also investigating the effects of silt layers on lateral spreading was Haigh and Madabhushi (2002). This investigation involved observing the behaviours of buildings constructed on slopes that consisted of alternate layers of liquefiable sand and silt. The

centrifuge tests revealed that during earthquake motion the retention of pore-pressures for sufficiently long periods that large lateral spreads might be expected to occur. This retention of pore pressures causes the formation of extremely low shear strength water films at the boundaries between the layers. This phenomenon is further discussed in section 3.5.4.

Building upon these types of tests, centrifuge studies were undertaken on the stability of underwater slopes by Zhou et al. (2002) and Taboada-Urtuzuastegui et al. (2002). Zhou et al. (2002) states that up to the date of publication there was no well-accepted method to estimate the stability of underwater slopes. Thirteen groups of centrifugal model tests were undertaken to determine the critical gradient for slopes consisting of loam and fine sand. It was found that critical slope gradient of fine sand is smaller than it is for loam. However, this series of tests was under static conditions. Taboada-Urtuzuastegui et al. (2002) takes a similar geometry to Zhou et al. (2002) and subjects it to seismic motion to understand the response of liquefied soil beyond initial liquefaction. It was found that a dilative behaviour of the soil existed near the slope where static shear stresses were present. Correspondingly, it was found that there were drops in pore pressure and simultaneous negative upslope spikes in the acceleration records. When the input acceleration was increased, it was found that this dilative response became stronger thus limiting downslope accumulation and reducing permanent lateral acceleration. These results indicate that larger input motions produce smaller permanent displacements. Dilative responses were not observed away from the slope where no static shear stress was present.

3.5.2 Embankment Dams

An extension of the work performed by Arulanandan et al. (1988) is the centrifuge modelling of underwater slopes with respect to embankment dams. This type of work was continued by Muraleetharan and Arulanandan (1991) where a model earth dam containing alternating layers of clay and sand was subjected to simulated earthquake shaking in the centrifuge. The model featured three sand layers, a central clay core, an upstream clay blanket, and a downstream berm. The results of these tests showed there was loosening and weakening of sand close to the bottom of the clay/sand interfaces and that the model dam failed with layers moving downward and outward from the centerline. At the crest of the embankment, measured accelerations indicated evidence of yielding and reduction in shear strength during shaking.

An example of an actual prototype situation modelled in a centrifuge is that of the O'Neill Forebay Dam in California as presented by Law et. al. (1994). In 1989, the Loma Prieta magnitude 7.1 earthquake occurred in northern California triggering responses in transducers of nearby embankment dams. The researchers saw this as a good opportunity to correlate field data with centrifuge modelling data. Four model embankment dams were tested in the centrifuge to simulate the field event at the given location. The tests were conducted under three different g levels and model sizes. Using the principle of modelling of models it was found that the centrifuge data yielded satisfactory data in correlation to the measured field values for the earthquake event.

This important test verified the use of centrifuge of modelling to predict responses of submerged slopes during earthquakes.

A study of the effects of earthquakes on saturated soil embankments is offered by Astaneh (1993) and Astaneh et al. (1994). In these experiments, saturated models of homogeneous and zoned soil embankments were subjected to earthquake motion in the centrifuge. Different relative soil densities of 40% and 60% were used. It was observed that the rise in excess pore pressure at some locations in the models was high enough to cause liquefaction, which in some cases lead to observed structural degradation and localized slope failure of the embankment. These sudden movements were observed through embedded accelerometers that indicated liquefaction when they lost the ability to transmit motion. In addition, it was concluded that the denser sand areas exhibited a much higher resistance to liquefaction than the areas that contained the looser sand and that homogeneous embankments showed much better stability against dynamically induced liquefaction. The silt used in any of the models did not experience any significant pore pressure and the cores of the model were never observed to suffer any damage due to liquefaction.

3.5.3 VELACS

The Verification of Liquefaction Analysis using Centrifuge Studies (VELACS) project as described by Arluanandan et al. (1994) is yet another example of how seismic centrifuge modelling techniques have been used to explore the behaviour of submarine slopes.

Although the VELACS project was conducted to improve existing methods for the analysis of the consequences of soil liquefaction and not specifically for research into submarine slope stability it showed that centrifuge studies are repeatable under carefully controlled conditions. The VELACS project was a collaborative project that sought to provide experimental data from centrifuge tests to determine the efficiency of various computer codes. Nine centrifuge models were explored, and three of those directly resemble slope stability problems. These centrifuge test configurations are shown in Figure 3.2. Models number 2 (Aubry et al., 1993; Dobry & Taboada, 1993; Lacy et al. 1993), number 6 (Arulanandan and Zeng, 1993; Elgamal et al., 1993, Manzari and Yogachandran, 1993), and number 7 (Anandarajah and Bardet, 1993; Ko and Astaneh, 1993; Wilson et al., 1993) are those that are of most interest to slope stability analysis. A portion of the work presented by Astaneh (1993) is also considered as part model number 7 of the VELACS project.
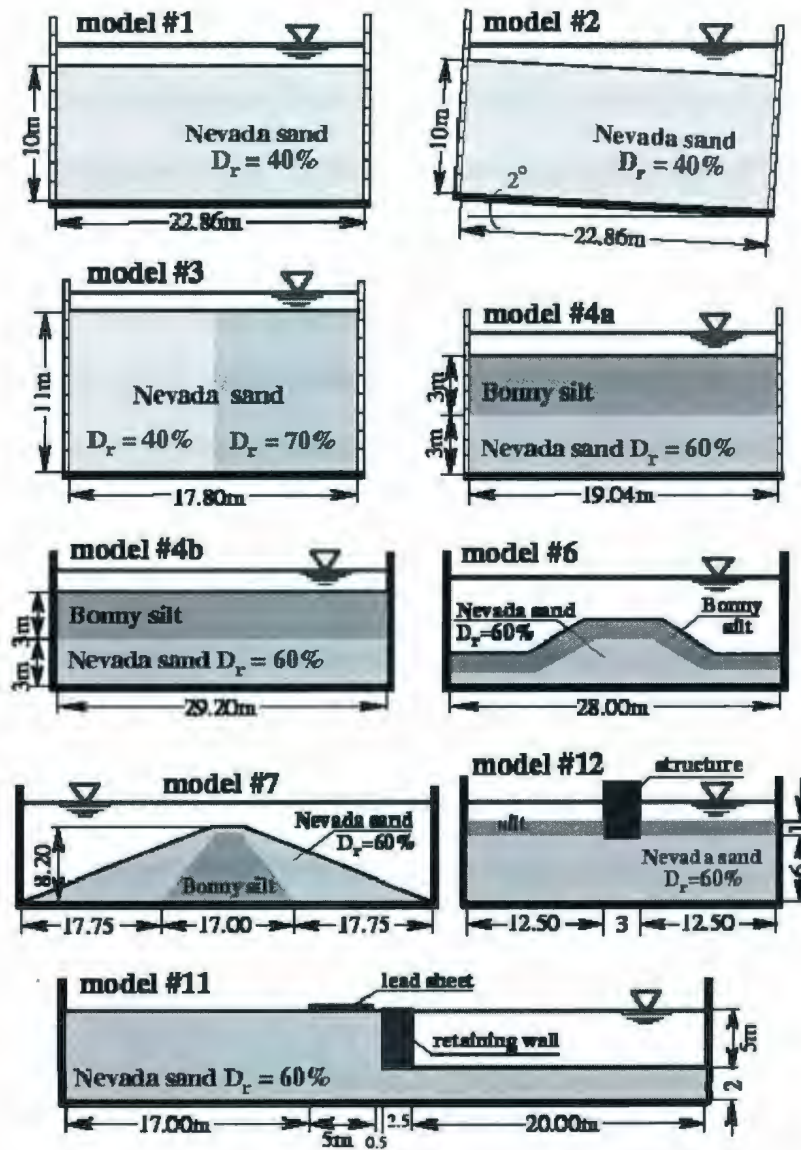
Figure 3.2: VELACS Centrifuge Test Configurations.
After Arulanandan et al. (1994).

The repeatability of the centrifuge experiments was shown only if the shakers used are capable of reproducing the frequency components of the input base motion and care is taken during model preparation (Scott, 1993; Arulanandan et al, 1994). The difficulties

encountered during the VELACS project with regard to repeatability are important to understand and consider when undertaking this type of modelling.

3.5.4 Void Redistribution & Water Film Generation

There has been some centrifuge testing undertaken to examine slope failure mechanisms specific to layered sand deposits. Most notable of these mechanisms is void redistribution or as it is sometimes known, water film generation.

This effect was first discussed in this context by Dobry and Liu (1992) where it was theorized that during a dynamic centrifuge test there was a formation of a water film between an underlying sand overlain by lower permeability silt. Following this, Fiegel and Kutter (1994) performed centrifuge tests on shallow slopes that showed localized deformations near the interface of a liquefiable sand layer and an overlying lower permeability layer. Kokusho (1999) showed in shake table tests on slopes of homogeneous sand with thin silt layers, that a water film beneath was produced underneath the silt layer and after shaking had stopped flow failures continued. These studies showed the interest of permeability contrast that was also discussed in section 3.5.1 by Imamura et al. (2002) and Haigh and Madabhushi (2002).

Further shake table tests, one-dimensional liquefaction tests, torsional simple shear tests, in-situ soil investigations, and case history studies by Kokusho (2001), Kokusho and Kojima (2002), and Kokusho (2003) have investigated why lateral flow movement is

sometimes immensely larger than the free surface settlement and can exceed several meters even in slopes than can be considered gentle. It was found that water films can very easily be formed in very short time beneath sublayers and can serve as a sliding surface even after the conclusion of earthquake shaking. Additionally, large flow displacements can be facilitated by this void redistribution mechanism without the mobility of any dilatancy effect because the developed water film can serve as a shear stress isolator.

These effects have been further studied in centrifuge tests presented by Malvick et al. (2002) and Kulasingam et al. (2004). These experiments showed evidence of flow failures in localized shear zones, without the presence of a generated water film beneath a silt layer of silt planes that were embedded in sand slopes. Malvick et al. (2002) used centrifuge testing to characterize the void redistribution of saturated sand (with embedded silt) due to pore pressure gradients with respect to its ability to affect the shear resistance. It was found that certain factors; such as initial relative density, thickness of confined sand layer, and earthquake amplitude and duration; could give rise to localized shear strains and large slope movements. Furthermore, it was concluded that localized shear strains were more likely to be caused by longer duration earthquake motions in sand deposits of an initial relative density of 20-50%.

This phenomenon has also been replicated through undrained cyclic triaxial tests. Konrad and Dubeau (2002) used these types of laboratory tests to examine the effect of layering

sand and silt on cyclic resistance. It was concluded that this type of layering induced a much lower cyclic resistance to failure than either of the materials on their own. The differential pore pressures observed in each soil unit suggested that strength reduction, through the creation of small expansive volumetric deformations, was caused when water migrated from the sand layer to the silt layer, thus accelerating the process of liquefaction.

3.5.5 Calibration Of Numerical Methods To Centrifuge Model Tests

As stated, another purpose of this research is to provide information to researchers performing numerical model analysis to situations similar to those being tested in the centrifuge. An example of this methodology was studied by Mehrabadi (2006), where finite element analysis methods utilized previously performed centrifuge tests in the following manner:

  i)   to calibrate and validate the numerical model to be used for liquefaction
         analysis in the Fraser River Delta in British Columbia;

  ii)   to study the boundary effects caused by a rigid centrifuge container used in
         a series of tests evaluating the seismic behaviour of waterfront slopes; and

  iii)   to study the effects of incomplete saturation on the sand seismic behaviour
         within the process of numerical model calibration.

The most important element of this is the comparison of centrifuge results to the results of finite element analyses for underwater slopes. This work was completed as part of the Earthquake Induced Damage Mitigation from Soil Liquefaction Project.

4 RESEARCH FACILITIES

4.1 C-CORE Centrifuge Centre

The C-CORE Centrifuge Centre research facility is located on the campus of the Memorial University of Newfoundland as introduced by Phillips et al. (1994). The centrifuge centre was established through funding by the Canada/Newfoundland Offshore Development Fund, the Technology Outreach Program of Industry, Science and Technology Canada and the Natural Sciences and Engineering Research Council of Canada.

The major feature of the Centrifuge at its inception in 1993 was the ability to model cold regions with a refrigeration system that can deliver temperatures reaching $-30^{\circ}C$. The centrifuge centre is a two-story building that contains offices on the second level. The lower level of the building houses the test preparation area and the Acutronic 680-2 geotechnical centrifuge structure. The test preparation area also includes several other facilities, including a machine shop, a sand raining room, an electronics laboratory, a refrigerated cold room, an x-ray facility, and a darkroom.

The centrifuge structure is comprised of three levels. The lower level of the structure is underground and contains the centrifuge drive unit, refrigeration unit, hydraulic controls, and an exhaust fan to manage the temperature of the area. The central level contains the main centrifuge chamber, which is accessible through large doors that can facilitate the

passage of a forklift for model package handling. The dimensions of this main chamber are 4.2 m in height and 13.5 m in diameter. The walls of the chamber are constructed of 300 mm thick reinforced concrete surrounded on the exterior of the building by a sloping rock berm. The upper level is a stiff concrete ceiling structure that resists the aerodynamic excitation created by the centrifuge during rotation. This upper level additionally houses the electrical slipring capsule and is also used for document storage.

4.2 Acutronic 680-2 Centrifuge

The Acutronic 680-2 Centrifuge at C-CORE is shown below in Figure 4.1. It is capable of testing models up to an acceleration of 200 g, which translates to a speed of 189 RPM. The centrifuge has a radius of 5.5 m from the axis of rotation to the floor of the platform. Typically, the centroid of a model is at a nominal working radius of 5 m during operation. The maximum payload of the 680-2 is 100 g x 2.2 tonnes = 220 g-tonnes at the 5 m working radius. When the centrifuge is operating at the maximum rotational speed, producing 200 g of force, the platform's self weight is significantly increased. This reduces the maximum payload to 130 g-tonnes. The specifications and capacity envelope of the Acutronic 680-2 centrifuge are provided in Figure 4.2. The maximum size of the payload is about 1.1 m high by 1.4 m long by 1.1 m wide.

Figure 4.1: C-CORE Acutronic 680-2 Geotechnical Centrifuge.

Centrifuge Specifications

Machine:	Acutronic 680-2
Platform Radius:	5.5 m
Platform Width:	1.1 m
Platform Depth:	1.4 m
Maximum Usable Height:	1.5 m
Acceleration Range:	10 - 200 g
Acceleration Accuracy:	0.5 %
Maximum Operating Imbalance:	100 kN
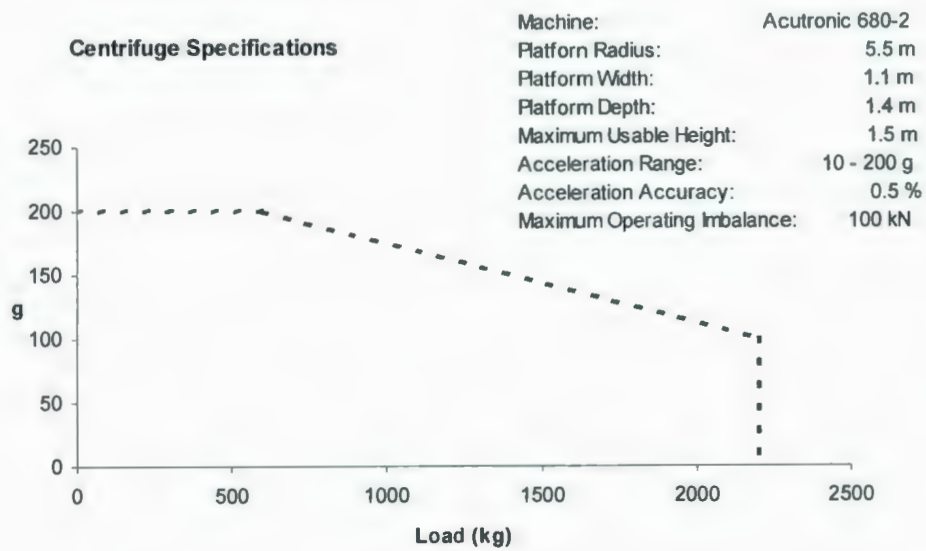
Figure 4.2: C-CORE Centrifuge Specifications.

The centrifuge arm consists of two parallel steel tubes that are held apart by a central drive box and spacers, as shown in Figure 4.3. The swing platform is suspended on pivot bushings from the ends of the load carrying beams and is covered by a shroud used to decrease aerodynamic drag. A counterweight of a mass of 20.2 tonnes balances both the payload and the platform. The position of the counterweight can be adjusted by driving a series of gearwheels along screwheads on the outside of the steel arm tubes using an electric motor. The arm of the centrifuge rotates on a set of tapered roller bearings inside the central drive box, which is mounted on a central shaft. This central shaft is attached to a concrete base by a four branch star support that is suspended on four springs. Each of these springs is strain-gauged in order to observe any imbalance within the centrifuge arm to within ± 10 kN.
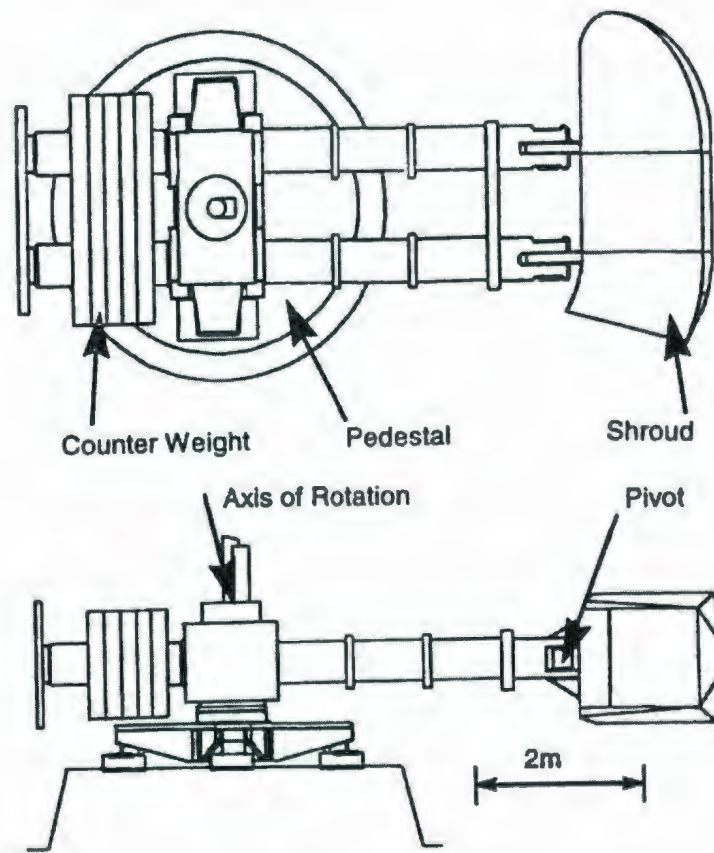
Figure 4.3: Acutronic 680-2 Centrifuge.

The drive unit of the centrifuge includes a 450 kW AC variable speed motor connected directly to a 9:1 gear reducer while two 250 kW invertors energize the variable speed motor.

Two rotary joints mounted beneath the central shaft allow fluids to flow through the central axis of the machine to the swiveling platform. Fluids that are commonly delivered through these rotary joints include: high pressure hydraulic fluid (for the

operation of the earthquake simulator or other hydraulically driven actuators), air or water (for specific uses in model tests), and refrigeration fluid (related to the cold regions capacity of the system).

4.3 Actidyn QS 67-2 Earthquake Simulator

4.3.1 Introduction

In 1997 it was decided to increase the capacity of the Centrifuge to include earthquake testing and studies of liquefaction and its effects. When considering how to achieve this ability there are several objectives that must be considered, as partially discussed by Van Laak et al. (1994b):

(i)   capability for producing input motions having arbitrary shape;

(ii)   base excitation in one direction only, with constraints to prevent uncontrollable vertical and transverse horizontal motions;

(iii)   easy installation and removal;

(iv)   low maintenance and high reliability; and

(v)   capability for multiple successive shakings without stopping the centrifuge.

In addition to these general objectives there were other objectives that were unique to C-CORE's centrifuge, including:

(i)   platform size constraints;

(ii)   mass constraints;

(iii)   capability of operation at up to 80g centrifugal acceleration;

(iv)   capability to run the earthquake shaker and acquire data simultaneously;

(v)   elimination of rocking moment generated in the slip plane typically caused by classical earthquake actuators;

(vi)   attenuation of undesirable centrifuge mode shapes; and

(vii)   maintaining centrifuge versatility and quick test turn around.

With these objectives in mind the original manufacturers of the C-CORE Centrifuge, Actidyn Systemes (formerly Acutronic) of France, developed the Model QS 67-2 Electro-hydraulic Earthquake Shaker (EQS). Funding for the EQS was provided by the Natural Sciences and Engineering Research Council of Canada, the Canadian Foundation for Innovation, and C-CORE.

4.3.2   Classical Electro-hydraulic Earthquake Actuation

Classical electro-hydraulic earthquake shakers feature a model container attached to a slip table carried by the centrifuge platform at the end of the centrifuge arm. When an actuation force is applied to the soil model of mass (M_a) a moment or torque $(T = M_a * d)$ is applied to the centrifuge platform, where d is distance. This moment is then offset by the inertia of the spinning platform and the overall centrifuge structure itself.

As described by Perdriat et al. (2002) when a dynamic force (F_m) is applied to a soil model mounted on a classical unbalanced earthquake simulator on a functioning

centrifuge the mass of the soil and its container generates a dynamic moment (T_m) that is counteracted by the platform inertia and stiffness as shown in Figure 4.4.
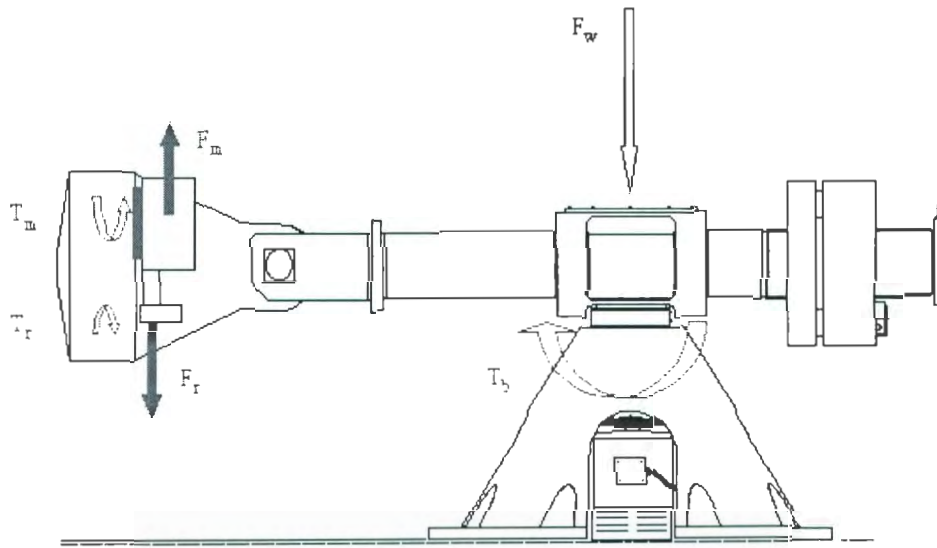
Figure 4.4: Centrifuge Reaction Forces.
After Perdriat et al. (2002).

Since the earthquake actuator is attached to the centrifuge platform a reaction force (F_r) and reaction moment (T_r) is transmitted to the platform. This configuration typically allows the platform to experience some sort of distortion since T_m and T_r are counteracting moments that do not equal each other due to their geometry. This type of action is then transmitted to the centrifuge bearings through the rotating arm. F_r acts to add or subtract from the self weight of the centrifuge (F_w) and creates a large bending moment (T_b) to be developed in the centrifuge arm.

These dynamic forces and moments when applied to the structure of the centrifuge create significant stress and strain in addition to motions that inhibit the desired motion to be applied to the soil model.

The most significant observed detrimental effect in these classical types of actuation systems is that the centrifuge acts like a spring. The reaction forces drive the platform to rock back and forth with the same frequency of the intended actuation force. This is complicated by the fact that the centrifuge structure is a complex mass spring system that has several resonant frequencies that may be excited by these reaction forces.

4.3.3 EQS Dynamic Balancing

To overcome the rocking motion described in Section 4.3.2 a new concept was developed by Actidyn for the EQS to be installed on the C-CORE Centrifuge. This concept involves dynamically balancing the shake table through the reciprocal actuation of both the model and a new component – the balancing counterweights (CW). Perdriat et al. (2002) describes the soil model CW with masses, M_m and M_{cw} respectively, as having centre of masses located at distances d_m and d_{cw} from the platform surface. This setup is shown in Figure 4.5. If during actuation $F_{cw} * d_{cw} = F_m * d_m$ the torque applied to the centrifuge platform becomes minimal. The two forces, F_{cw} (counterweight force) and F_m become balanced when the centres of mass of the CW and the model are the same height above the centrifuge platform. This setup requires complete symmetry along the X and Y

92

axes, which is achieved by balancing the applied force through a close loop control of parallel pairs of actuators for each degree of freedom.
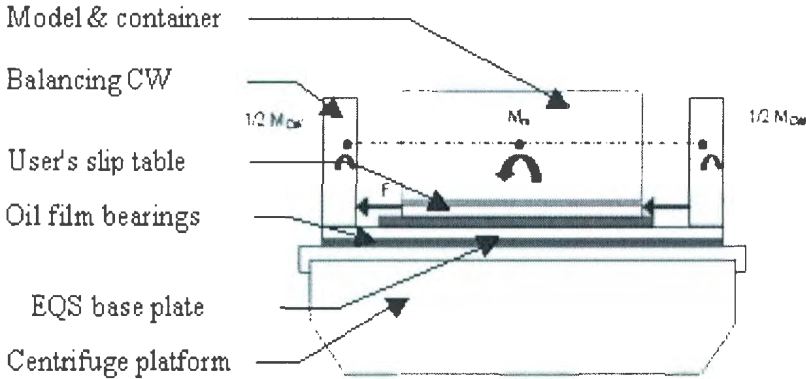
Figure 4.5: Dynamically Balanced Earthquake Simulator.
After Perdriat et al. (2002).

A distributed hydraulic bearing system was used across the moving and stationary platform surfaces to eliminate any local surface distortion of the base caused by moment distribution.

Overall the EQS was intended to be free of any resonance from 30 to 350 Hz, which was the frequency range of interest for possible scaled earthquake input motions. The proposed performance envelope of the C-CORE EQS is given in Figure 4.6.
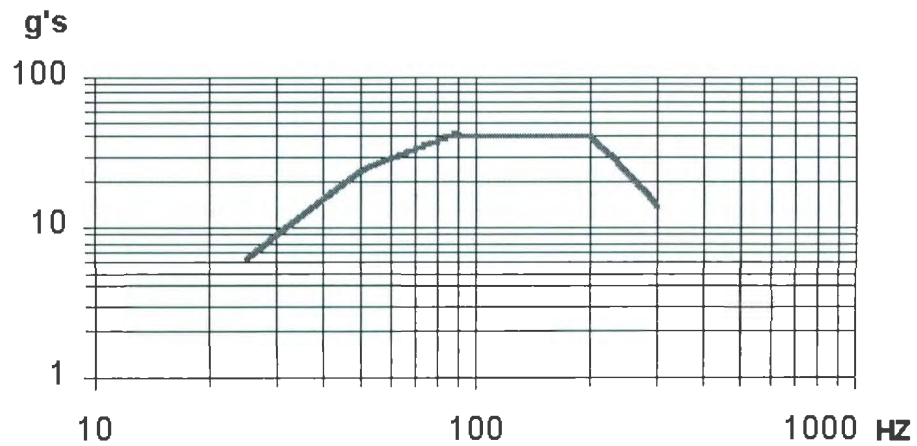
Figure 4.6: C-CORE EQS Performance Envelope.
After Phillips et al. (2004).

4.3.4   EQS Assembly

The configuration of the EQS system is shown in Figure 4.7 and is described in detail by Perdriat et al. (2002). The major components are a flat base that supports the dual hydrostatic bearing, the reciprocal hydraulic actuators, the shaking platform, and the balancing platform. The balancing platform and the slip table are the two moving components that reciprocate one another.

Oil accumulators

Model

Balancing CW

Model on
Slip table

Return tank

Centrifuge platform
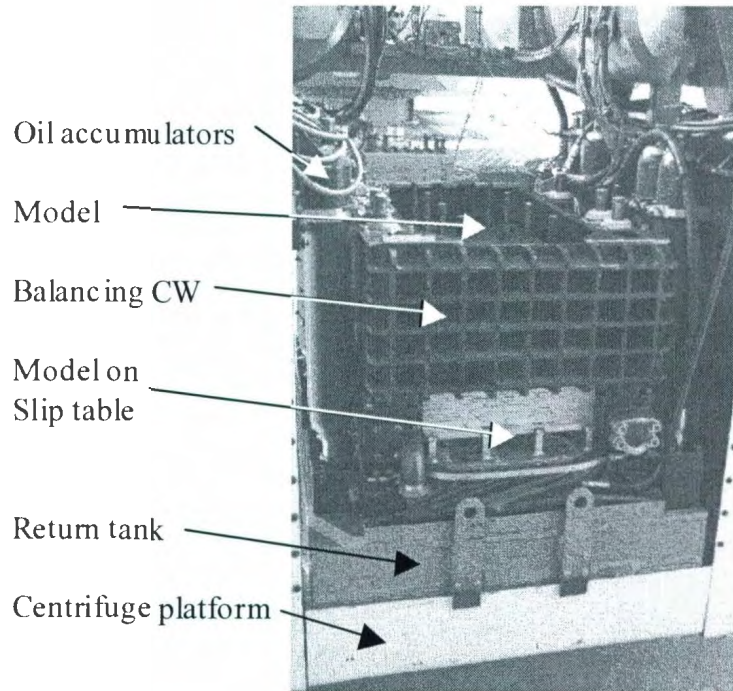
Figure 4.7: C-CORE EQS Assembly.
After Phillips et al. (2004).

The balancing platform is supported by two back-to-back oil film bearings and slides in a

sandwich between the slip table and the EQS base that is attached the basket supporting

face. The geometrical integrity of the system is supported by a large number of parallel

rows of hydraulic bearings. The intermediate platform carries a pair of hydraulic

actuators, local accumulators, servo-valves, bracing interfaces, and the load balancing

counterweights. Some of the highlighted features of the EQS are: the large bandwidth

high-g servo-valves to control the axial motion of the shaking platform; the position of

the 100 g-rated accumulators to minimise piping and maximise compaction; and the

inclusion of manifolds to eliminate piping and minimise hydraulic resonances between the servo valves and the actuators.

The EQS is designed to operate several times during the same centrifuge flight. The soil model payload is mounted securely to the slip table and the counterweights are removable to allow easy access to the soil model container. In addition, the counterweights are adjustable to permit centre of mass alignment. The overall structure of the EQS was designed so that all mechanical resonances should be out of the frequency range of interest.

The maximum size of the model payload is 1 m by 0.5 m by 0.6 m with a maximum mass of 400 kg up to an 80 g vertical acceleration. This maximum payload can be excited with frequencies of 40 to 200 Hz with a maximum dynamic force of 160 kN. The maximum available payload displacement is 2.5 mm and the maximum velocity is 0.5 m/s.

4.3.5 EQS Control System

The EQS control system is made up of three major parts: a logic controller; a set of hydraulic loop controllers; and a dual axis digital controller and generator. This system is discussed in more detail by Perdriat et al. (2002) and Hutin et al. (2002). Figure 4.8 illustrates the control system for a single axis. A second axis controller is identical to this setup using two additional hydraulic loop controllers.
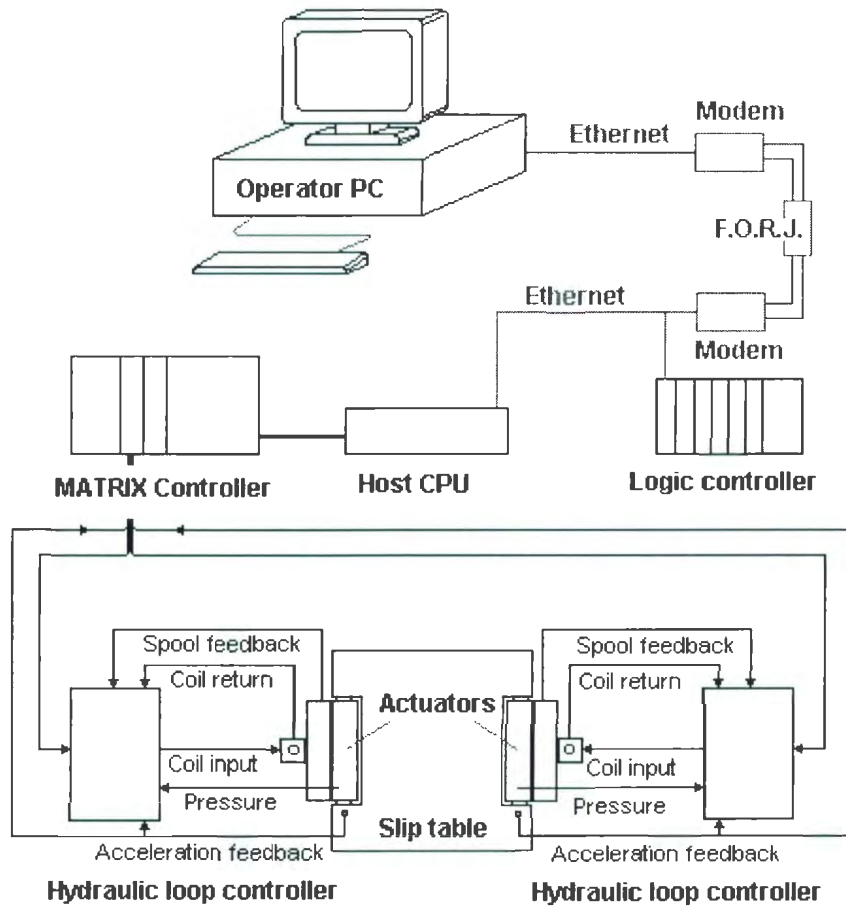
Figure 4.8: C-CORE EQS Control System.
After Perdriat et al. (2002).

The logic controller is used to perform all logic functions used for proper operation of the hydraulic power supplies, the oil pressure, flow control, safety interlocks, as well as fault detection. This controller interfaces directly with the Matrix multi-axis digital controller and signal generator, which is a dedicated digital control system that can provide the application of sine, random, and shock signals. The Matrix controller continuously

controls to adapt to the dynamics of the system during the test. Control accuracy is kept high through the compensation of the cross-coupled dynamic responses in the multiple inputs simultaneously.

Hydraulic loop controllers are used to provide the servo valves with control power. They operate as cascade closed loops that give feedback signals based upon actuator acceleration, actuator differential pressure, and servo valve spool position. These loop controllers also compensate for the hydraulic circuit resonance frequency. Acceleration feedback is observed through piezo-electric accelerometers located on either side of the shaking table. Position feedback signals are gathered through the use of an LVDT sensor.

4.3.6 Data Acquisition System

The data acquisition system acquired data simultaneously with the operation of the EQS. The matrix system includes eight analogue data inputs filtered at 1 kHz and sampled at 2.56 kHz per channel using VXI hardware. This hardware has a further 24 channels of analogue inputs controlled by Data Physics 620 data acquisition software. These 24 inputs are typically filtered at 2 kHz and sampled at 5.12 kHz/channel for a 16 second period before, during, and after the earthquake event.

4.3.7   EQS Operation

The EQS is tuned over a two hour period prior to each geotechnical model test. A dummy payload similar in mass and centre of mass to the geotechnical model is mounted on the EQS. At the desired centrifugal acceleration level, the dummy payload is subjected to a pre-test comprising about 8 random bursts of uncorrelated accelerations in the range 40 to 400 Hz to each actuator. The pre-test acceleration magnitude is set to a similar Root Mean Square (RMS) value to that of the target earthquake. The actuators gain and phase transfer functions are assessed from the average system response to these bursts as shown in Figure 4.9.
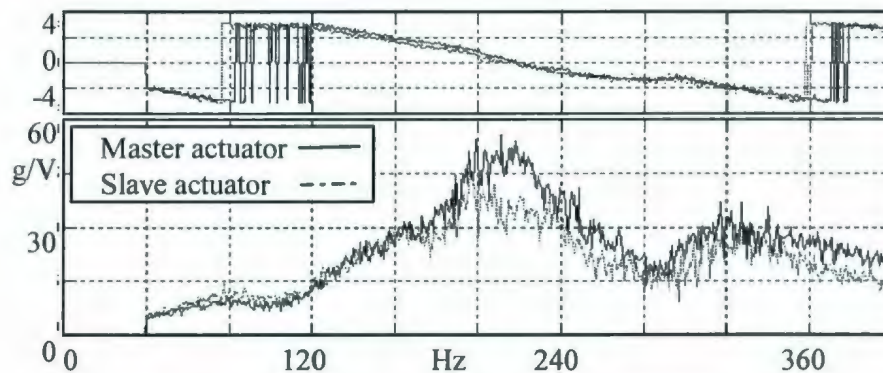
Figure 4.9: Typical Actuator Transfer Functions.
After Phillips et al. (2004).

The target earthquake motion is assessed from the prescribed earthquake motion defined in prototype terms. The prescribed motion is scaled in amplitude and time according to centrifuge similitude laws. The scaled motion is passed through a 40-200 Hz band pass filter to fit the EQS frequency and amplitude specification. The filtered motion is base

line corrected to remove any residual displacement or velocity at the end of the record to give the target earthquake.

The target earthquake is imposed on the dummy payload. The actuator drive signals are improved over about five iterations to reproduce the target frequency content and phase relationships. The geotechnical model then replaces the dummy payload. The saved drive signals are replayed to conduct the geotechnical earthquake test.

5   EXPERIMENTAL TESTING PROCEDURE

5.1   Introduction

As previously mentioned the objective of this research is to examine the dynamic response of submarine slopes exposed to earthquake loadings. Specifically, this work pertains to the earthquake effects of a sloping soil formation that contains naturally stratified soils. These types of stratifications are not unusual in field conditions where sand deposits can consist of sublayers with different particle sizes and permeability which are continuous in the horizontal direction, as explained by Kokusho (2003).

To fully understand the effect of earthquakes on submerged soil, one of the centrifuge model tests undertaken was a homogenous sand control test. This allowed for comparison of the effects of layering to be fully realized. In comparison to this homogeneous test, two different layered silt geometries were examined.

The first type of layering geometry that was utilized was a 2:1 sand slope with a buried silt layer following a simulated draped depositional profile. The second type of layered geometry involved the construction and testing of a 2:1 sand slope with a buried silt layer following a linear 5.5:1 slope, that allowed for more kinematic freedom to develop upon earthquake actuation. In total five different models were constructed, instrumented and subjected to various sequences of earthquake signals, in order to also examine other

effects, such as seismic strengthening of deposits exposed to a series of earthquake events.

In a larger framework, these experiments were carried out as part of a larger COSTA-Canada project to easily compare the result of physical modelling to the finite element analysis of similar geometries exposed to earthquake motions. Therefore, there is a need to understand the known boundary conditions on the model area within such a centrifuge model. These known testing limitations include any possible reflection of seismic waves from the rigid end and sidewalls of the model container as well as the contained nature of the toe of the model slope, which limits run out distance of any mobilized failure materials. Both of these effects would not be present in naturally occurring situations.

This chapter presents the characteristics of the construction techniques and testing configurations used in these experiments. The testing program discussed herein constituted the first series of dynamic centrifuge model tests completed at the C-CORE centrifuge. Therefore, it is important to note that many of the experimental procedures presented here were developed as part of this work in order to allow for this type of testing.

5.2 Centrifuge Model Preparation

5.2.1 Model Geometries

The five tests undertaken were given different names to identify them; they were identified as "COSTA" tests and given an alphabetical suffix based on the sequence in which they were performed. In the cases of all tests the model materials, both sand and silt were air pluviated into the model container within a few millimeters of the intended geometry. Air pluviation involves filling the test container with the model sand through a device, such as a funnel or flexible tube, with a known opening, typically drilled holes or a screen mesh, from a constant drop height. The density at which the sand is deposited is controlled by varying these two variables, funnel opening size and drop height. The size of opening controls the degree of separation of the individual sand particles, and thus the size of the object falling though the air. The drop height controls the speed at which the particles, or groups of particles, are deposited in the container. Typically, the higher the drop height, the more dense the model. This occurs until the drop height is increased to the point where the falling sand particles will achieve their terminal velocity before being deposited. The terminal velocity is in turn variable upon how separated the sand particles are from each other when dropped, and thus the opening size.

Loose sand portions of the models were pluviated for an intended relative density at test conditions of 40%, where the dense sand portions were targeted for 80%. Based on previous experience and trials it was estimated that from the time of the air pluviation of the model to the actual testing of the model at 70 g an increase of approximately 8-10%

103

in the relative density would be experienced. Following air pluviation the model undergoes several activities that result in some densification of the model. These include vacuum saturation, the transportation of the model to the centrifuge arm, and the swing-up of the centrifuge to test speed that causes the aforementioned compression due to self-weight. Considering these effects the loose sand is air pluviated into the model at a target relative density of 30-32% to accommodate the resulting densification that occurs later. The drop height to achieve these relative densities was calibrated for the pluviation equipment used at C-CORE. Drainage gravel was placed at the bottom of the model in order to aid in the saturation process.

The COSTA-A test features a draped silt layer that has a profile that matches the overlying sand surface. This configuration is shown in Figure 5.1 and all measurements shown in this chapter are given in millimeters.
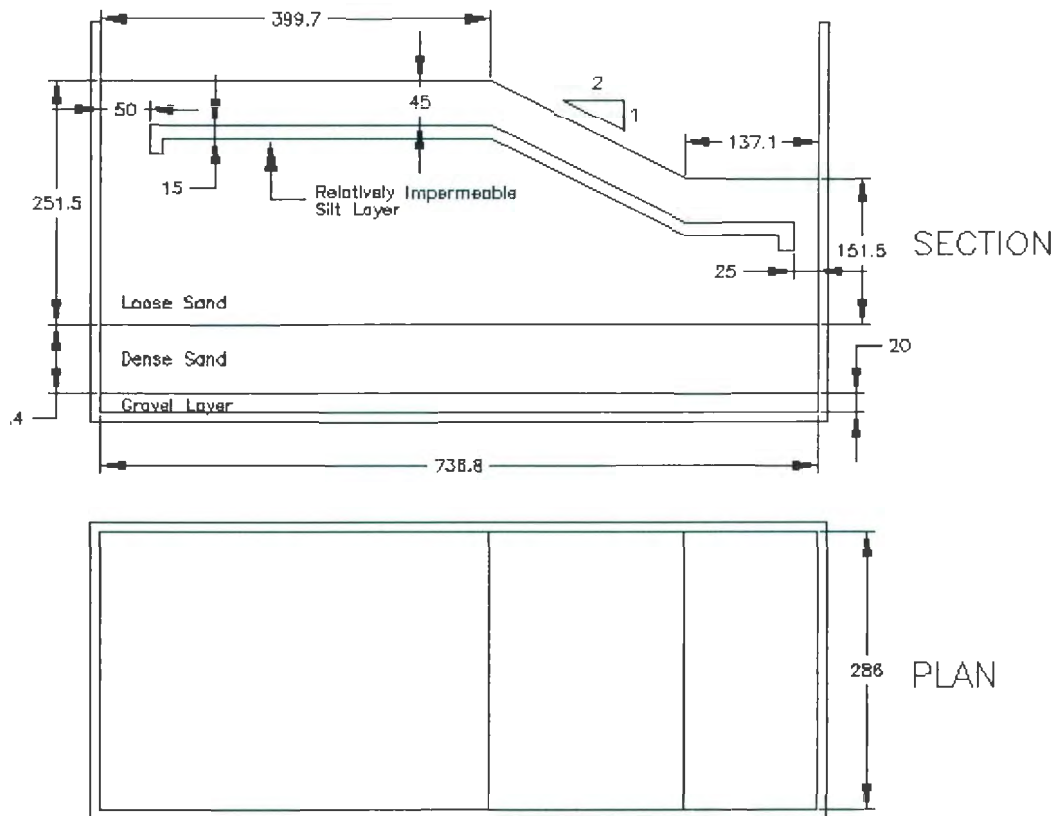
Figure 5.1: COSTA-A Model Geometry.

The COSTA-B, C, & E models, as shown in Figure 5.2, featured a silt layer that bisects the sand surface with a profile of a 5.5:1 slope. In these tests and a layer of filter paper was placed at the gravel/sand interface to prevent any mixing. Additionally, fine sand was placed on an inclined position between the silt and the sidewalls of the model container in order to minimize any friction that may be experienced. Figure 5.3 shows a typical cross-section of how this fine sand was situated. Petroleum jelly was smeared on the sidewalls starting at the depths of the silt and upward to further minimize any friction that may occur.
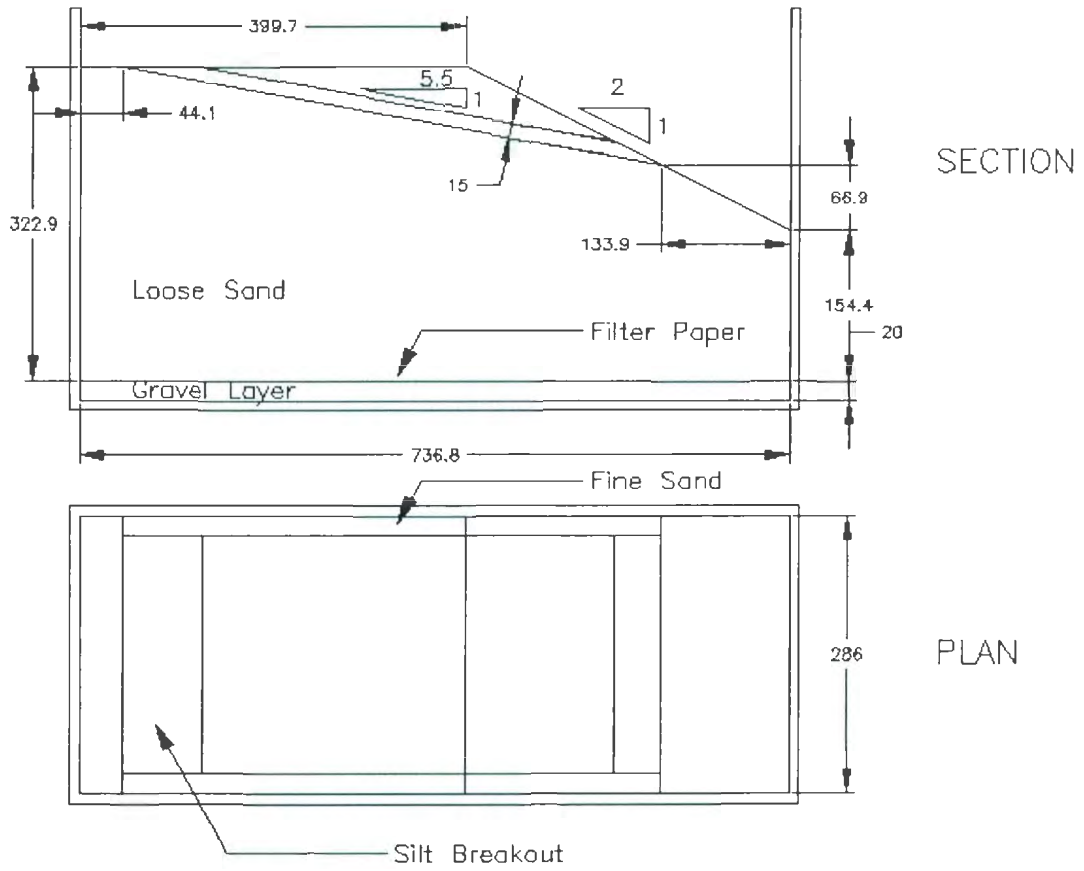
Figure 5.2: COSTA-B, C, & E Model Geometry.
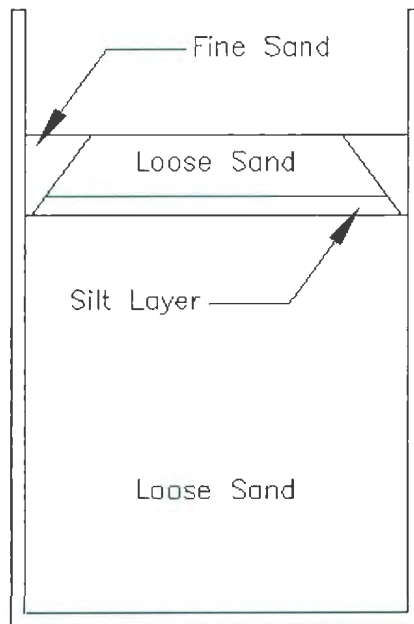
Figure 5.3: COSTA-B, C, & E Typical Model Cross-Section.

The final model configuration used, as shown in Figure 5.4, was constructed for the COSTA-D test. It features the same slope geometry that was used for the COSTA-B, C, & E models but does not feature a buried silt layer.

Following pluviation, small white pieces of gravel were placed on the model slope face prior to saturation in a square grid measuring approximately 25 mm by 25 mm. This was done to make qualitative comparisons of the movement of the slope face during the test.
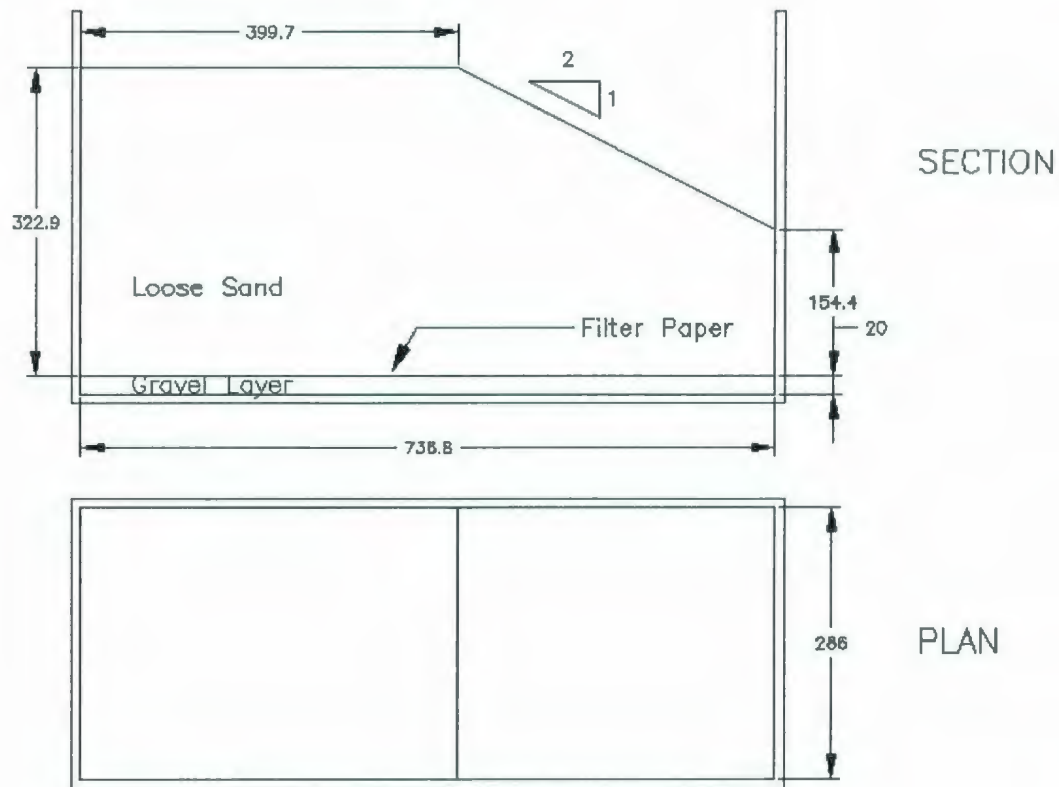
Figure 5.4: COSTA-D Model Geometry.

5.2.2 *Model Container*

The model container that was used for this test is of rigid construction. This container is a modified version of the equivalent shear beam container that was designed for C-CORE and this testing program and shown in Figure 5.5. This container is advantageous because it has been designed to fit onto the centrifuge basket that has been equipped with the earthquake simulator shake table. The container was modified for these experiments into a rigid container by fitting 14 threaded steel rods through the aluminum rings and anchored to the base plate. These rods serve to prevent any lateral movement that may be

induced by earthquake shaking. The interior walls of the model container have been fitted with smooth stainless steel sheets to minimize friction at the boundary of the slope model. The model top lid is only affixed to the model container, via the rigid threaded rods, to create vacuum conditions in the model during the saturation phase and is removed prior to earthquake testing. Following saturation the model container is then loaded onto the centrifuge arm. Coupling of the model container with the shake table is achieved by placing a high friction paper sheet between the container and the shake table. The model container is secured using four M20 bolts through the base plate into a threaded hole on the shake table itself. Two of these bolt holes are located on either side of the base plate where it extends out from the set of stacked aluminum rings.
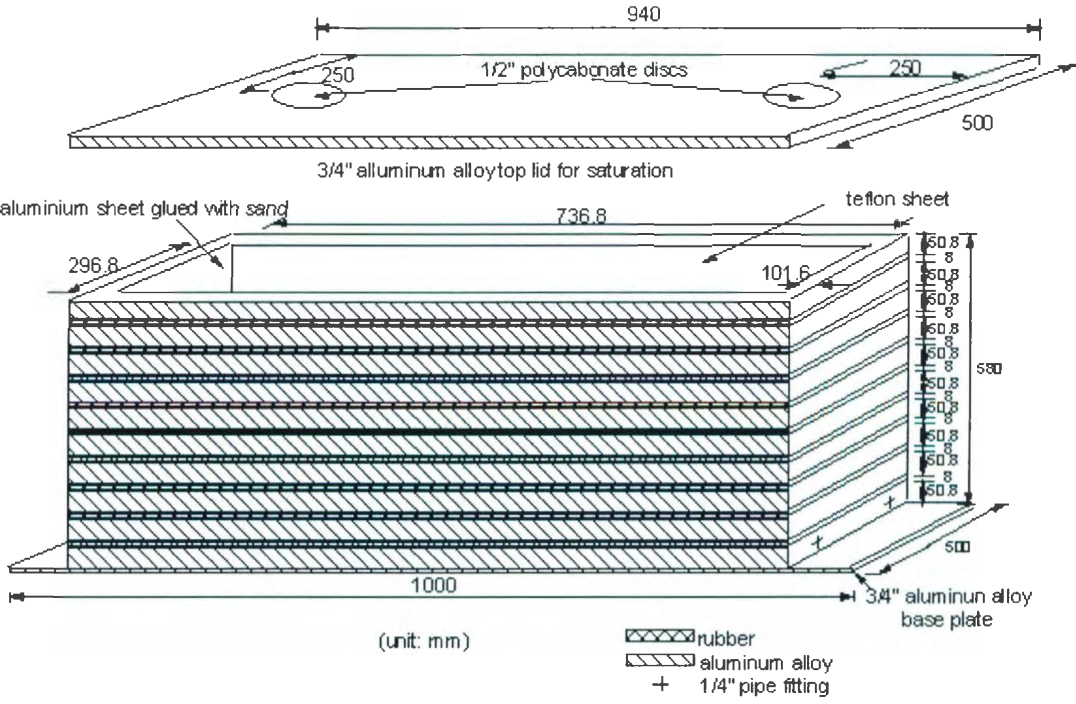
Figure 5.5: C-CORE Earthquake Strongbox.

109

5.2.3 Model Materials

The major constituent of the COSTA-Canada models is Fraser River sand. This sand has been imported from the Fraser River delta in British Columbia on the west coast of Canada. This sand is uniform, grey coloured, and medium grained with subangular to subrounded particles. Fraser River sand features an average mineral composition of 40% quartz, 11% feldspar, 45% unaltered rock fragments, and 4% other minerals (Vaid and Sivathayalan, 1996). Before pluviating Fraser River sand into the model, it is passed through a 2 mm sieve to remove any large particles that may be uncharacteristic of its overall uniformity. The void ratio of Fraser River sand can range between minimum and maximum 0.62 and 0.94, respectively. This sand has a D_{50} of 0.26 mm with a fines content of 0.4%. The specific gravity is 2.71 and the maximum and minimum dry densities are 1.40 and 1.67 grams/cm^3, respectively (Liquefaction Remediation Project, 2004).

The fine sand used between the silt and the container sidewalls was the portion of the Fraser River sand corresponding to less than the D_{10} fraction. For practical purposes, a sieve with an opening size of 0.18 mm was used to acquire this material.

The silt that was used for the barrier layer consisted of U.S. Silica Sil-Co-Sil 52 Fine Ground Silica silt. This material is uniform, white in colour, and consists of a mineral composition of primarily silicon dioxide quartz. Some basic tests have been performed on a silt/stainless steel interaction. For this condition, an angle of internal friction was

110

found to be approximately 24.5 degrees, but this can be reduced by approximately 5 degrees if petroleum jelly is added to the interface to provide a more slippery sliding surface. The specific gravity of this material is 2.65 (U.S. Silica, 2004).

The gravel material used for the base of the model is installed to aid in the saturation of the model under vacuum conditions as the pore fluid is introduced from the bottom of the model. It is a gravel material consisting of particles between 1 and 5 mm in diameter that is sieved out of a readily available sand/gravel mixture. The grain size distribution of all three materials is shown in Figure 5.6.

Particle Size Distribution Curve
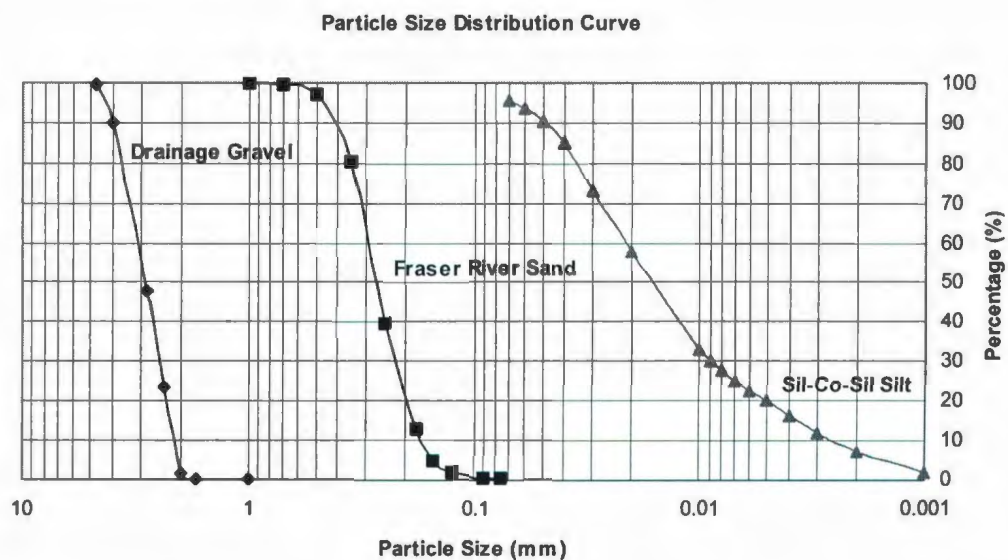
Figure 5.6: Model Materials Grain Size Distribution.

5.2.4 Relative Density Estimation

Following air pluviation an estimate of the relative density of the dry sand could be made. This was done for the COSTA-B through COSTA-E tests and is presented in Table 5.1. For tests with a silt layer, COSTA-B, C, & E this estimation was only performed for the sand placed beneath the sand layer. After the placement of the silt layer, the fine sand on the sidewall margins, and the loose sand on top of the silt layer estimating the relative density of the model becomes much more complex. This problem only becomes more difficult once pore fluid is introduced, so no certain data can be presented for the actual pre-test relative density. Conversely, for the COSTA-D test an estimate of the relative density could be performed for the entire homogeneous loose sand model. This estimate was calculated by considering the mass and volume of sand added to the model container. However, it should be noted that this observed mass is +/- 2 kg as measured with the overhead lab crane. This margin of error can significantly affect this calculated relative density by as much as +/- 15%.

Table 5.1: Estimated Post-Pluviation Relative Densities.

Test Label	Estimated Post-Pluviation Relative Density
COSTA-A	Unknown
COSTA-B	34%
COSTA-C	34%
COSTA-D	28%
COSTA-E	34%

5.2.5 Substitute Pore Fluid

As discussed in Chapter 3 a substitute pore fluid was required to be used to saturate the model in order to satisfy the scaling differences between static and dynamic events in the centrifuge. Hydroxypropyl methylcellulose (HPMC) was selected for this task because it possesses several advantageous characteristics, including: its ability to be mixed into a wide range of viscosities, its similarity to water in unit weight, surface tension, and Newtonian behaviour, its physical consistency from batch to batch, its benign impact on the environment, its ready availability, and its lack of expense (Stewart et al, 1998; Dewoolkar et al, 1999a; Dewoolkar et al, 1999b). The HPMC fluid that was used in this test was prepared by mixing Methocel F50 Powder manufactured by Dow Chemical Company. As part of this project and the development of procedures for dynamic testing at C-CORE numerous trials were performed on the mixing of this material with deionised water at various concentrations and at different temperatures, as its viscous behaviour is temperature dependent. Originally, it was assumed that the tests would occur at a nominal temperature of $20^{\circ}C$, however following the completion of COSTA-A it had been observed that the model could reach a temperature of approximately $25^{\circ}C$. Figure 5.7 shows the results of the trials for $25^{\circ}C$. Therefore, a relationship between concentration of HPMC powder and viscosity was developed and used for the tests to acquire the desired conditions.
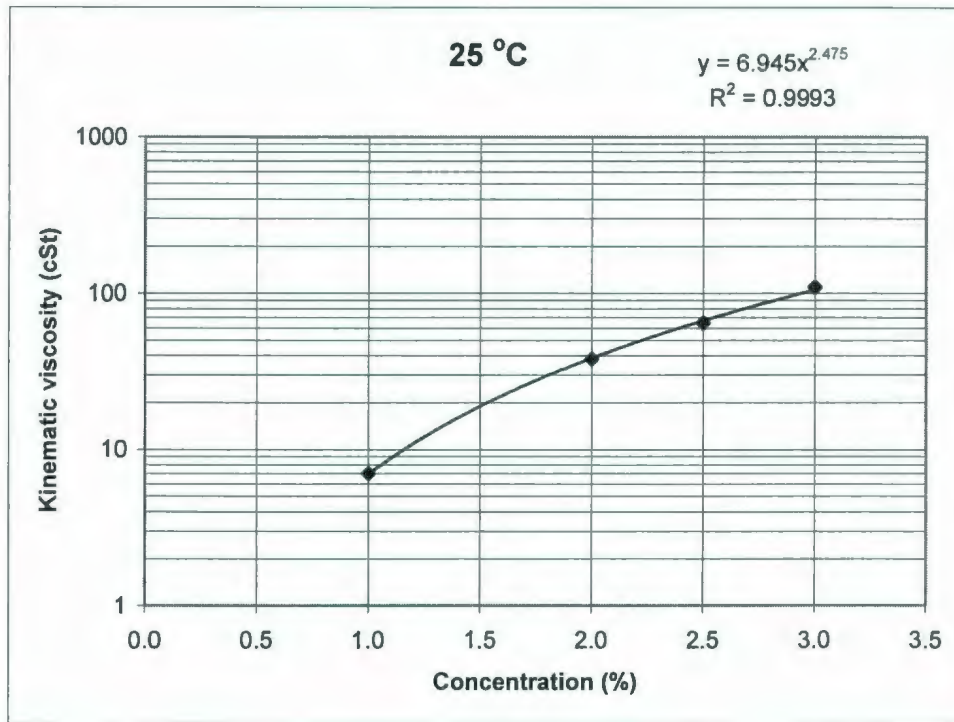
Figure 5.7: Developed Relationship for Methocel F50 at 25°C.

The target centrifugal testing level for this experiment was to be 70 *g*, which for absolute agreement of scaling properties requires a pore fluid of a kinematic viscosity of 70 cSt. However, a pore fluid of this high viscosity is quite difficult to saturate a sand model with due to its flow properties. It was decided to use a pore fluid with a target kinematic viscosity of 35 cSt, half the ideal value. This allowed easier and timelier saturation to occur. Therefore, it was imperative to design the fluid so that it was about 35 cSt at this operating temperature.

For a 35 cSt HPMC mixture at 25°C a mass of HPMC powder of 1.922% of the entire solution volume is required. Additionally, a mass of Benzoic Acid USP powder equal to approximately 1% of the mass of the HPMC powder is added to the mixture to prevent any bacterial growth that may occur in the completed fluid batch.

The HPMC fluid is prepared by mixing the required mass of HPMC powder with the required amount of deionised water at room temperature over several hours in a large plastic barrel fitted with a simple electric motor that rotates a mixing paddle at a vigorous speed. Typically, batches are prepared in 100 L volumes, which provides enough fluid for two different centrifuge tests. Once prepared the fluid is tested for viscosity and transferred into a vacuum reservoir where it is de-aired for at least 48 hours before introducing it to the sand model under vacuum conditions.

The viscosity of the pore fluid was measured with a reverse flow viscometer both before and after saturation, except for in the case of COSTA-A where it was only measured before the saturation stage. These measured viscosities are shown in Table 5.2. The obtained values indicate good agreement with expected values. At the various temperatures, the observed viscosity is within the design limits for a 35 cSt fluid at 25 °C.

Table 5.2: Measured Pore Fluid Viscosity.

Test Label	Pre-Saturation		Post-Saturation	
	Viscosity (cSt)	Temperature (°C)	Viscosity (cSt)	Temperature (°C)
COSTA-A	33.0	20.0	Unknown	Unknown
COSTA-B	37.9	20.0	38.2	21.5
COSTA-C	34.5	24.5	37.5	19.5
COSTA-D	37.2	20.0	37.0	19.7
COSTA-E	37.2	20.0	40.1	18.9

5.2.6 Vacuum Saturation

The COSTA-Canada centrifuge tests require a high level of saturation to ensure the proper stability of the slope model. The stability of saturated sand slopes is extremely sensitive to saturation levels that are even marginally below 99%. As part of these model tests, a vacuum saturation method has been developed and employed to ensure the adequate saturation of the model, similar to that presented by Ueno (1998). After the sand model is pluviated into the model container and vacuumed to achieve the proper slope profile, the slope is fitted with a light aluminum mould to prevent the slope from failing during saturation and transportation. Then the container is fitted with a vacuum lid and placed under the available vacuum of approximately 60 kPa for at least 12 hours to remove most of the air that may be present.

Following this initial vacuum stage the vacuum pump to the container is shut off as the sealed model container has the ability to hold the vacuum condition. Carbon dioxide is then used to displace the less soluble air that may be present in the voids of the sand model. Carbon dioxide gas is introduced into the bottom of the model at virtually atmospheric pressure from a depressurization chamber that serves to regulate the high-pressure carbon dioxide gas from the compressed gas supply bottle. Gradually over the period of 45 minutes to one hour the pressure inside the sealed model container is brought back to atmospheric pressure using the carbon dioxide gas. Following this, it is again placed under vacuum for approximately 20 minutes to bring it back to the 60 kPa vacuum level. After reaching the original level of vacuum the carbon dioxide introduction process is repeated again for the second time. Following this it is repeated a third time to further decrease the amount of air inside the model. The majority of gas inside the container should be carbon dioxide which is much more soluble and allows for more complete saturation. The entire saturation setup developed and used in this test is shown in Figure 5.8.
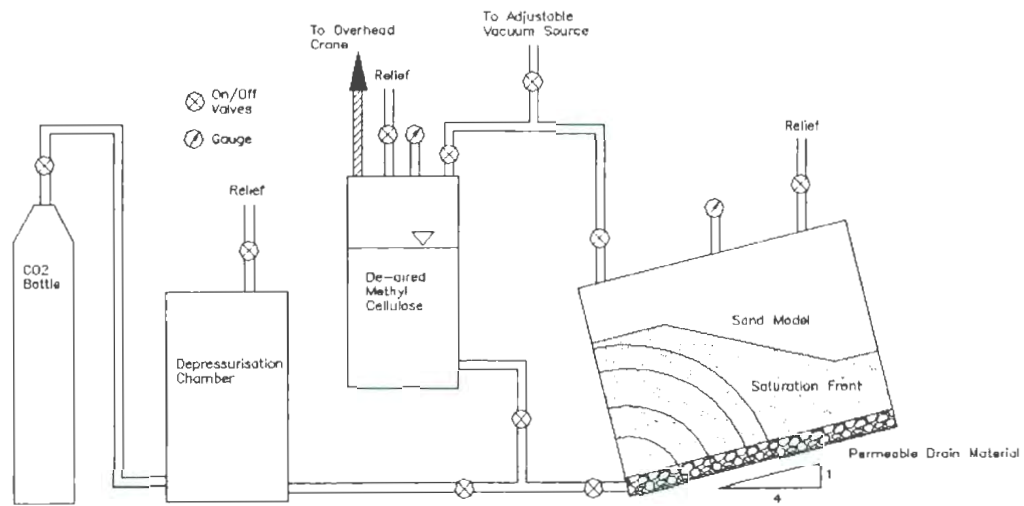
Figure 5.8: Vacuum Saturation Setup.

The next step of the process is to open the vacuum to both the deaired pore fluid reservoir and the model container to ensure equal vacuum to both containers so that when fluid is introduced it is not moving by differential pressure that can cause disturbance to the model. After equalizing the vacuum between the two containers, a valve is opened to allow the pore fluid to saturate the model from the bottom up over a period of approximately 2 days. The model container is slightly inclined to provide a more uniform saturation front and to prevent seepage-induced slope failure. The pore fluid is only ever driven into the model container from the fluid reservoir using differential head that is achieved by lifting the container off the laboratory floor. The level to which it is lifted has been calculated so as not to cause quick condition inside the model from the head pressure that the elevated container creates.

Following the full introduction of fluid into the model the vacuum is released slowly and the vacuum cover is removed. Once the model is transported onto the centrifuge arm the slope mould that was placed on it prior to saturation is removed.

In the case of the COSTA-B, C, & E tests, this saturation was done twice. The sand model below the silt layer was prepared and saturated. Then the vacuum was released and the silt layer and the remaining sand was pluivated and further saturation was accomplished by using a tube that introduced the pore fluid at a level equal to the silt layer. The saturation time, as well as the mass of fluid added was recorded for all tests except COSTA-A and is presented in Table 5.3. In the case of the first stage of saturation for the COSTA-E test, more fluid was added than in previous two-stage tests (46 kg as compared to 25-27 kg) due to the fact that it was left to saturate longer and more fluid was pushed through the model. This resulted in a greater amount of free fluid on top of the model, which was subsequently removed before construction of the model continued. Following saturation the fluid was at a height of 373 mm above the bottom of the model container for all tests.

Table 5.3: Model Saturation Progress.

Test Label	Time Required for Saturation		Mass of Fluid Added	
	First Stage	Second Stage	First Stage	Second Stage
COSTA-A	~ 48 Hours	Unknown	Unknown	Unknown
COSTA-B	46 Hours	27 Hours	25 kg	15 kg
COSTA-C	60 Hours	30 Hours	27 kg	15 kg
COSTA-D	62 Hours	N/A	43 kg	N/A
COSTA-E	89 Hours	48 Hours	46 kg	15 kg

Following the full introduction of fluid into the model the vacuum is released slowly and the vacuum cover is removed. Once the model was transported onto the centrifuge arm the slope mould that was placed on it prior to saturation was removed. Chapter 6 will discuss the measurement of the model profile following saturation and following transportation to and placement on the centrifuge arm. This profiling can also give an estimate of the relative density at the various stages.

5.3 Model Testing Procedure

5.3.1 Testing Instruments

There are five types of instruments employed on this test: 9 miniature pore pressure transducers (PPT), 10 miniature accelerometers, 4 linear variable differential transformers (LVDT), 1 laser distance sensor, and 1 triaxial accelerometer. Details regarding the specifications of these instruments can be found in Appendix A.

The miniature pore pressure transducers were used inside the model to monitor the generation and dissipation of pore pressures at various locations. The ones used in this test are Druck PDCR 81 and featured a range of either 200 or 100 PSI, with the larger capacity instruments being used at larger depths. The miniature accelerometers were used inside the model to observe the experienced acceleration in the direction of shaking and were PCB Piezotronics 353B18 ICP Accelerometers. These accelerometers have been encased in shrink-wrap to eliminate contact with the electrically conductive pore fluid. The LVDTs used are Trans-Tek Series 240 DC LVDTs. They were used to measure the surface deformations of the slope model. A Baumer OADM 2014460/S14C laser distance sensor was used to measure the lateral displacements of the model container in the direction of shaking during the earthquake event. Finally, a triaxial accelerometer, which is permanently mounted on the earthquake shaker, is used to monitor the acceleration of the shake table in the direction of shaking as well as the other two axes.

The different instruments used feature different frequency responses. The miniature PPTs have a normal frequency response of 2 kHz with no filter present, however when placed in high viscosity fluid they must be fitted with a sintered bronze stone. Using the work provided by Lee (1990) it was determined that this frequency response should not significantly diminish below 2 kHz for a 35 cSt pore fluid for the type of bronze used at C-CORE. Calculations indicate that there is virtually a one to one ratio of the actual and observed pore pressures for these conditions. The miniature accelerometers have a

frequency response of 1 Hz to 10 kHz. The LVDTs have a rather limited frequency response of 100 Hz. The laser distance sensor averages data over a 10 ms increment. Finally, the triaxial accelerometer has a frequency response of 500 Hz in the z-axis, 100 Hz in the x-axis, and 1000 Hz in the y-axis.

The position of the instruments was planned prior to the tests. The miniature PPTs and accelerometers were placed in the sand model during air pluviation in the vicinity of these planned locations. Following the tests, the model was off-loaded and excavated to determine the exact resting position of these instruments. Tables 5.4 through 5.8 summarize this information for each individual model. Figures 5.9 through 5.13 are also provided to illustrate the position of these instruments. Accelerometers are identified as "A" instruments and PPTs are identified as "P" instruments. All positions are given in model scale in millimeters.

Table 5.4: COSTA-A Miniature Accelerometer & PPT Positions.

| Instrument #	Post-Test Position			Planned Position		
	X (mm)	Y (mm)	Z (mm)	X (mm)	Y (mm)	Z (mm)
A1	147	141	143	157	143	151
A2	164	198	257	157	186	273
A3	152	88	288	157	100	308
A4	367	168	53	367	186	53
A5	487	150	205	476	143	223
A6	526	167	229	504	186	258
A7	297	144	146	307	143	151
A8	648	107	157	657	100	173
A9	644	155	194	657	143	208
A10	387	152	318	390	143	333
P1	145	132	139	143	143	151
P2	145	190	253	143	186	273
P3	142	74	288	143	100	308
P4	405	100	258	400	100	273
P5	497	140	205	490	143	223
P6	512	185	231	490	186	258
P7	603	195	161	600	186	173
P8	658	96	155	671	100	173
P9	653	164	197	671	143	208
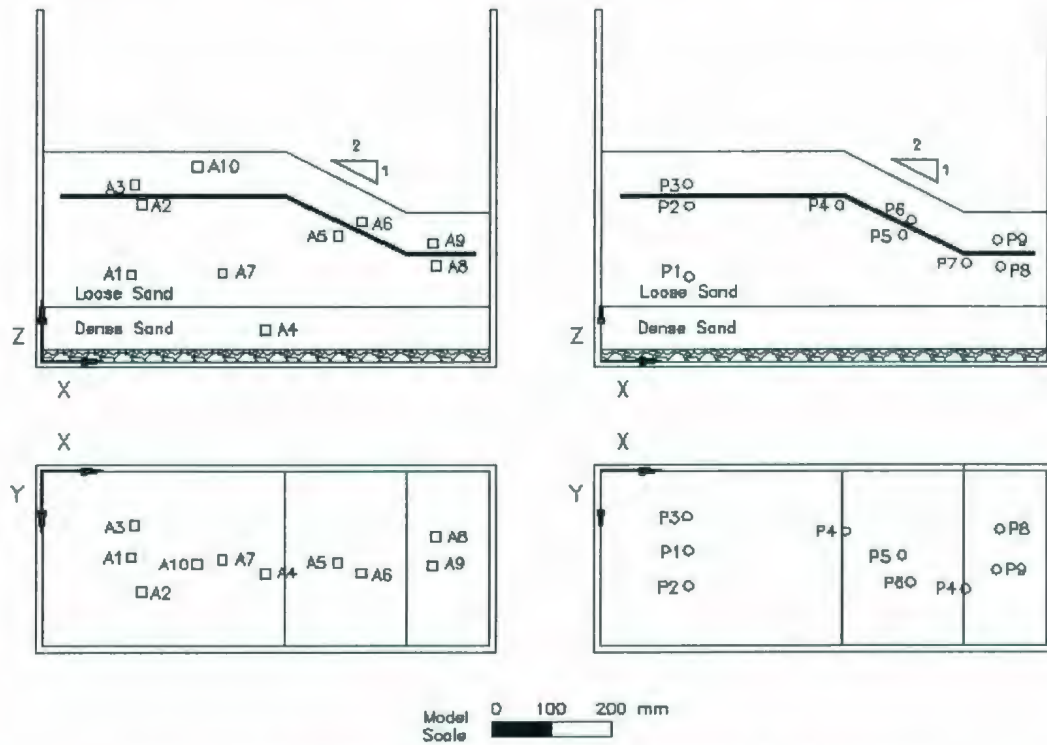
Figure 5.9: COSTA-A Miniature Accelerometer & PPT Positions.

Table 5.5: COSTA-B Miniature Accelerometer & PPT Positions.

Instrument #	Post-Test Position			Planned Position		
	X (mm)	Y (mm)	Z (mm)	X (mm)	Y (mm)	Z (mm)
A1	380	179	61	367	186	53
A2	163	140	147	157	143	151
A3	315	146	151	307	143	151
A4	514	105	152	512	100	151
A5	150	111	297	140	100	311
A6	248	162	257	268	143	265
A7	590	183	218	583	186	223
A8	310	210	298	245	186	331
A9	495	99	261	358	100	308
A10	623	77	253	465	100	285
P1	160	190	148	143	186	151
P2	333	140	151	321	143	151
P3	528	98	152	526	100	151
P4	57	89	325	63	100	326
P5	207	141	288	203	143	298
P6	355	180	242	343	186	250
P7	486	136	232	483	143	243
P8	627	194	212	623	186	214
P9	408	200	285	343	186	316
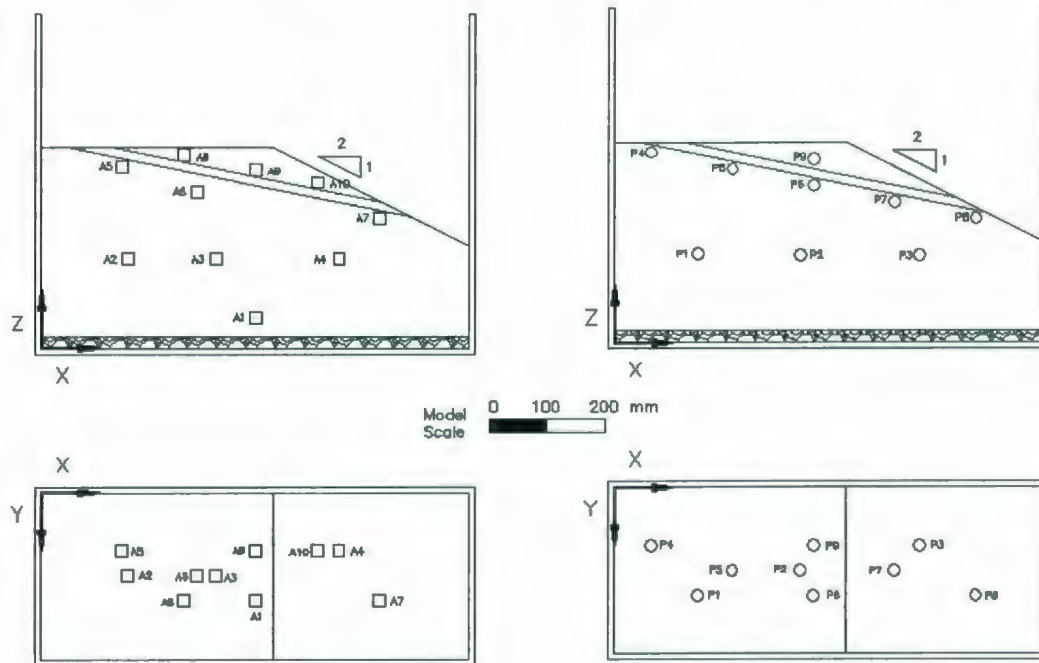
Figure 5.10: COSTA-B Miniature Accelerometer & PPT Positions.

Table 5.6: COSTA-C Miniature Accelerometer & PPT Positions.

| Instrument #	Post-Test Position			Planned Position		
	X (mm)	Y (mm)	Z (mm)	X (mm)	Y (mm)	Z (mm)
A1	362	170	51	367	186	53
A2	157	140	150	157	143	151
A3	50	145	157	56	143	151
A4	410	95	154	410	100	151
A5	144	115	311	140	100	311
A6	377	142	263	368	143	265
A7	605	192	222	583	186	223
A8	277	105	319	245	100	331
A9	399	185	300	358	186	308
A10	520	70	276	465	100	285
P1	142	190	148	143	186	151
P2	327	130	157	321	143	151
P3	525	95	157	526	100	151
P4	72	115	320	63	100	326
P5	204	135	290	203	143	298
P6	343	205	248	343	186	250
P7	497	142	240	483	143	243
P8	625	197	217	623	186	214
P9	389	115	299	343	100	316
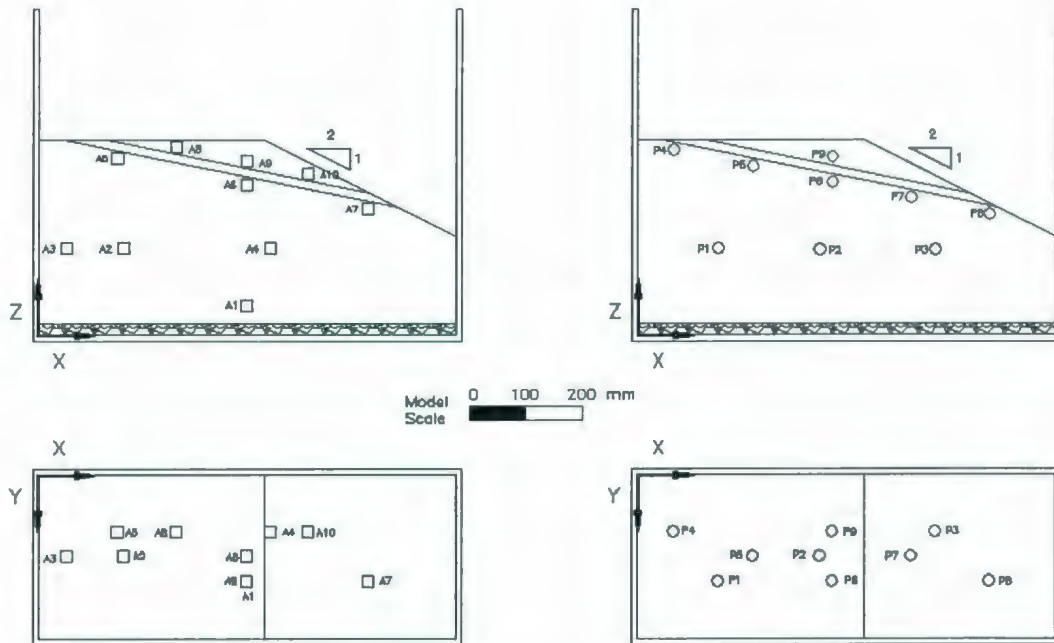
Figure 5.11: COSTA-C Miniature Accelerometer & PPT Positions.

125

Table 5.7: COSTA-D Miniature Accelerometer & PPT Positions.

Instrument #	Post-Test Position			Planned Position		
	X (mm)	Y (mm)	Z (mm)	X (mm)	Y (mm)	Z (mm)
A1	365	170	53	367	186	53
A2	177	146	150	157	143	151
A3	70	146	149	50	143	151
A4	403	102	150	410	100	151
A5	150	112	306	140	100	311
A6	282	145	270	268	143	265
A7	593	192	222	583	186	223
A8	251	203	317	245	186	331
A9	359	104	301	358	100	308
A10	486	106	282	465	100	285
P1	142	185	153	143	186	151
P2	326	145	155	321	143	151
P3	513	99	153	526	100	151
P4	57	108	332	63	100	326
P5	216	146	286	203	143	298
P6	354	191	248	343	186	250
P7	498	142	239	483	143	243
P8	620	184	216	623	186	214
P9	345	202	307	343	186	316
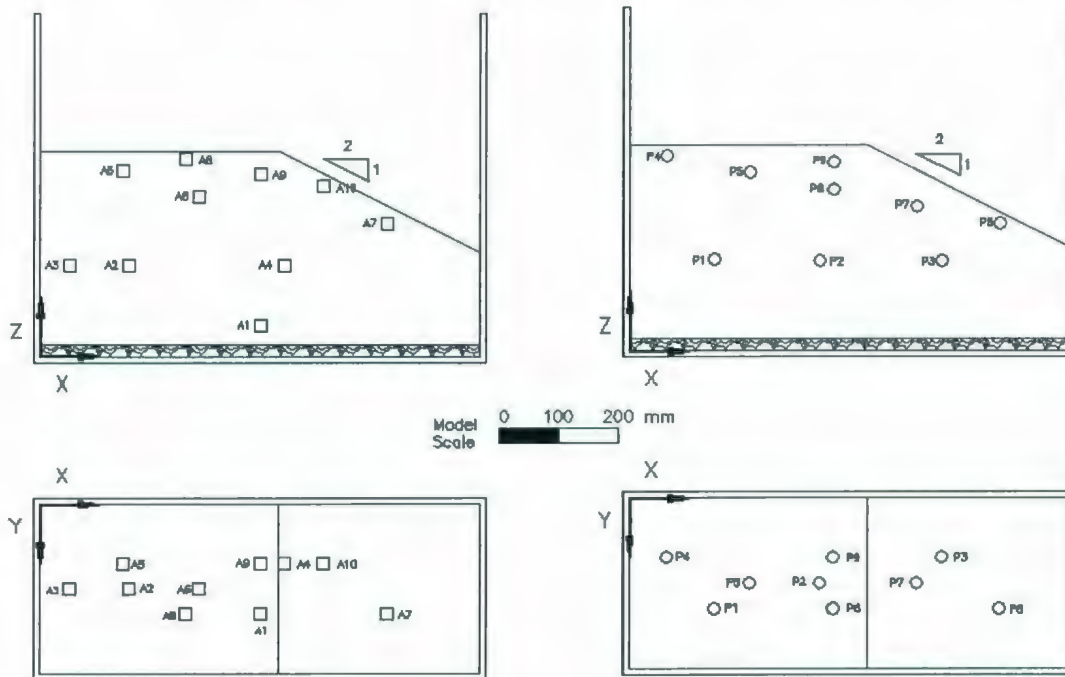
Figure 5.12: COSTA-D Miniature Accelerometer & PPT Positions.

126

**Table 5.8:** COSTA-E Miniature Accelerometer & PPT Positions.

Instrument #	Post-Test Position			Planned Position		
	X (mm)	Y (mm)	Z (mm)	X (mm)	Y (mm)	Z (mm)
A1	368	187	54	367	186	53
A2	162	142	150	157	143	151
A3	59	142	149	50	143	151
A4	410	110	151	410	100	151
A5	158	105	306	140	100	311
A6	284	143	262	268	143	265
A7	597	184	216	583	186	223
A8	261	189	319	245	186	331
A9	373	100	299	358	100	308
A10	485	111	276	465	100	285
P1	137	189	152	143	186	151
P2	328	149	148	321	143	151
P3	515	113	150	526	100	151
P4	61	115	314	63	100	326
P5	269	141	288	268	143	298
P6	348	176	245	343	186	250
P7	499	146	236	483	143	243
P8	626	175	207	623	186	214
P9	353	206	306	343	186	316
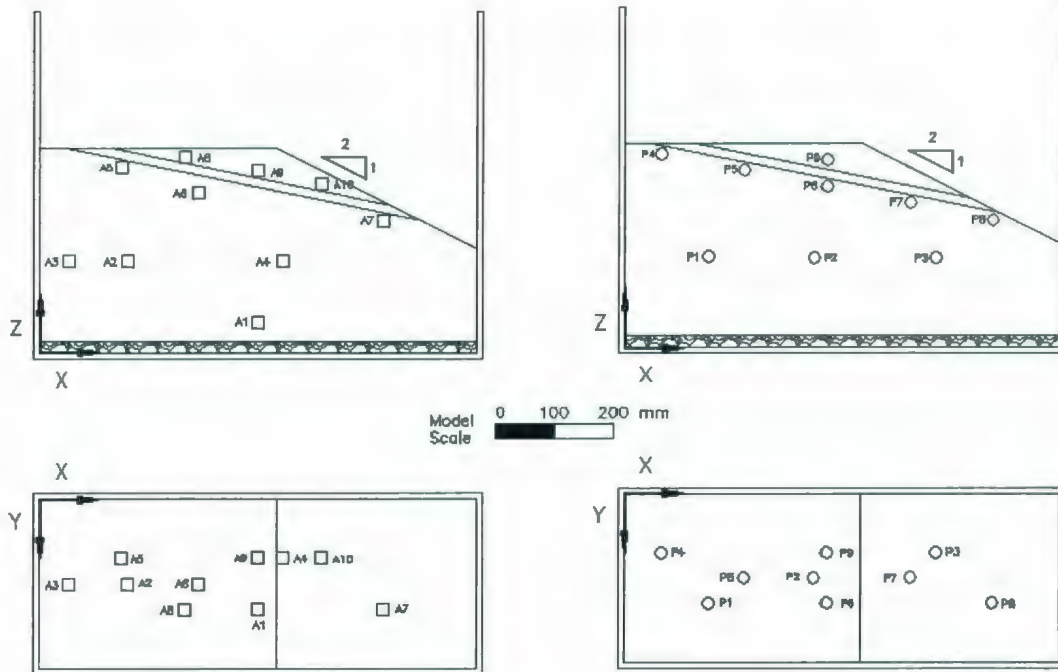
Figure 5.13: COSTA-E Miniature Accelerometer & PPT Positions.

The final three types of instruments were all mounted externally to the pluviated sand models. Their positions are shown in Figure 5.14 for COSTA-A and Figure 5.15 for COSTA-B, C, D, & E. In the COSTA-A test L1 through L4 were the LVDTs used to measure the surface deformation and were in contact with the surface via a small plexi-glass pad of approximately 25 by 12 mm that was glued to the LVDT spindle. In the other four tests L1, L3, and L4 are the LVDTs used to measure the surface deformation. In these tests, the LVDT spindles were in contact with the surface via a small plastic pad of approximately 30 mm x 30 mm but were not attached to the pads in any way so as not to restrict their movement horizontally. L2 is an LVDT used to measure the movement of the sand on top of the silt layer in a direction parallel to the inclined silt layer surface. It featured a buried plexi-glass anchor bar measuring 195 mm in length and a square cross-section of 6 mm x 6 mm. The anchor was attached to a string that ran through a greased plastic tube to the surface of the model and then traveled through a pulley system to an LVDT spindle that measured its movement as the anchor traveled down the silt slope during and after shaking. The actual locations of the LVDT instruments are also given in Table 5.9 for COSTA-A and Table 5.10 for COSTA-B, C, D, & E. The position of the displacement laser is denoted as L5 and the position of the triaxial accelerometer is noted as Tx, Ty, and Tz. However, in the COSTA-E test a change was made in the configuration of this triaxial accelerometer and it was no longer compatible with the data acquisition system causing data for its response to be unavailable. All positions are given in model scale in millimeters.
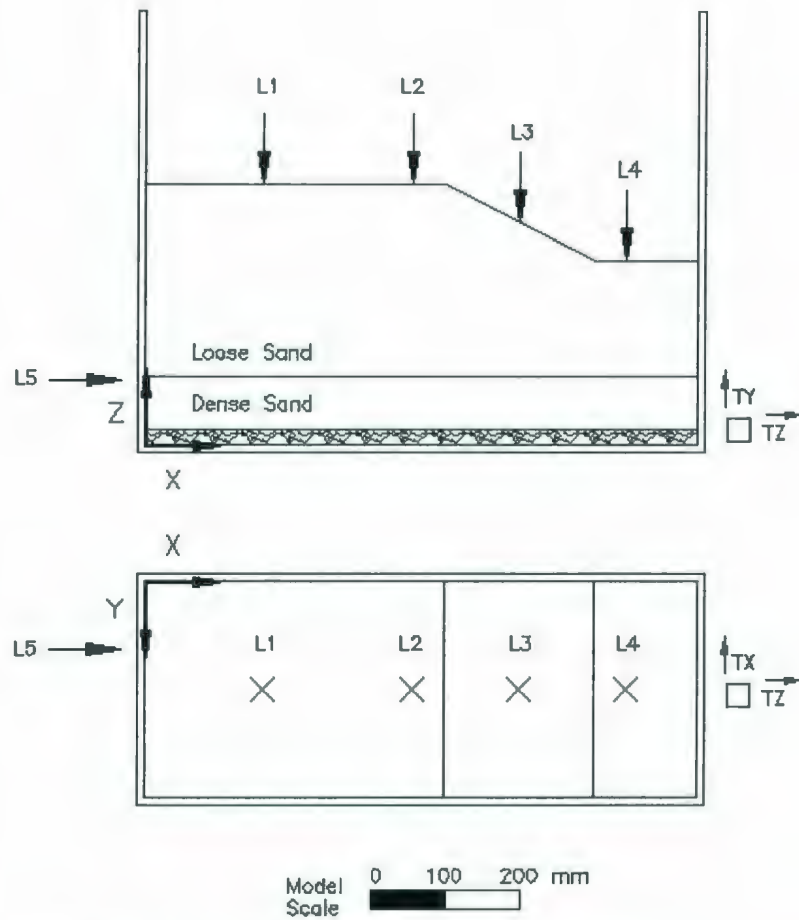
Figure 5.14: COSTA-A External Instrument Positions.

Table 5.9: COSTA-A External Instrument Positions.

Instrument #	X Position (mm)	Y Position (mm)	Z Position (mm)
L1	157	143	N/A
L2	357	143	N/A
L3	500	143	N/A
L4	643	143	N/A
L5	N/A	70	145
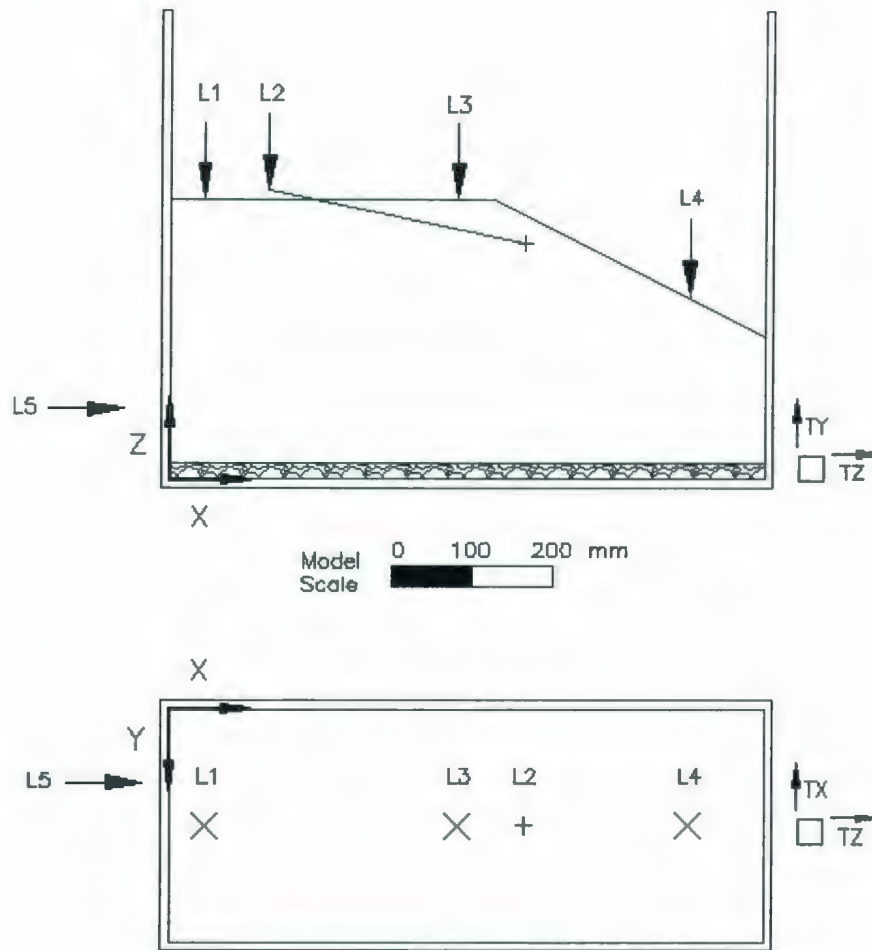
Figure 5.15: COSTA-B, C, D, & E External Instrument Positions.

Table 5.10: COSTA-B, C, D, & E External Instrument Positions.

Instrument #	X Position (mm)	Y Position (mm)	Z Position (mm)
L1	43	214	N/A
L2	440	N/A	288
L3	357	143	N/A
L4	643	143	N/A
L5	N/A	70	145

5.3.2 Test G-Level

The targeted g-level for this experiment was 70 *g* at a depth in the model equal to two-thirds the slope height of the COSTA-A test geometry. This is a level corresponding to 66.67 mm below the upslope surface in model scale. Figure 5.16 illustrates this position.
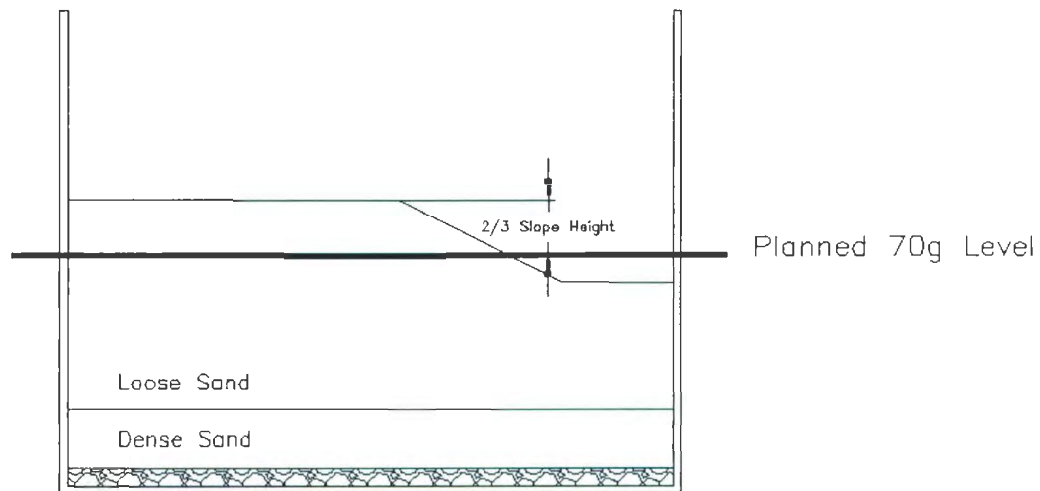
Figure 5.16: Location of Targeted G-Level.

In model scale the target g-level location corresponds to a location 590 mm above the centrifuge platform, which is 5.5 m away from the centre of the centrifuge itself. This target g-level location was then spinning in the centrifuge at a radius of 4.91 m. At the time of testing for the COSTA-A test the centrifuge was spinning at 112 RPM, which corresponds to a rotational speed of 11.73 rads/sec. At a radius of 4.91 m, this translated to an achieved g-level of 68.87 *g* at the target location.

In the remaining tests, at the time of testing the centrifuge was spinning at 113 RPM, which corresponds to a rotational speed of 11.83 rads/sec. At a radius of 4.91 m, this translated to an achieved g-level of 70.09 g at the target location.

5.3.3   Acoustic Wave Response

The saturation of this model was to be checked by observing the travel time of acoustic waves through the model. The intention was to observe these acoustic wave responses at test speed a few moments before the initiation of the model earthquake.

The generation of acoustic waves was achieved by tapping the upslope end of the model container with a small solenoid operated hammer that was constructed and developed for these tests. This generated signal is then observed by two accelerometers (A1 and A7 in COSTA-A and A2 and A3 in all other tests) placed in-line along the centre axis of the model at a known distance apart. In all tests they were placed in opposite orientations so that no wave signal could travel down any of the connecting wires. This setup ensures that the signals that are being observed by both accelerometers are independent of each other. After COSTA-A it was determined the signal may have been traveling faster around the walls of the box and then perpendicularly through the soil to the second receiver before it could travel directly from the endwall and then through the soil. Following, this an insulated metal shaft was installed through the endwall of the model container at the location of the solenoid hammer. This allowed the transmittal of the

hammer signal through the endwall of the box directly to the soil without transmittal of the signal into the walls of the container.

The arrival signals are observed in the centrifuge control room in-flight using an electronic oscilloscope software program called GageScope. According to previously published results, (Ishihara et al, 2001) a P-wave speed of 750 m/s corresponds to a degree of saturation of at least 99%. This speed was the target observed speed to ensure that the model was properly saturated.

The response of the accelerometers to the generated acoustic waves for each test is presented and discussed further in Chapter 6.

5.3.4 Earthquake Actuation

At test speed, the models were exposed to three different earthquake motions in a variety of regimes. The basis for these earthquake motions are the acceleration time histories known as A475 and A2475, which are shown in Figure 5.17 and Figure 5.18 respectively. The final earthquake motion used was known as 2A2475, which is shown in Figure 5.19 and is an earthquake with twice the acceleration and the same frequency as A2475.
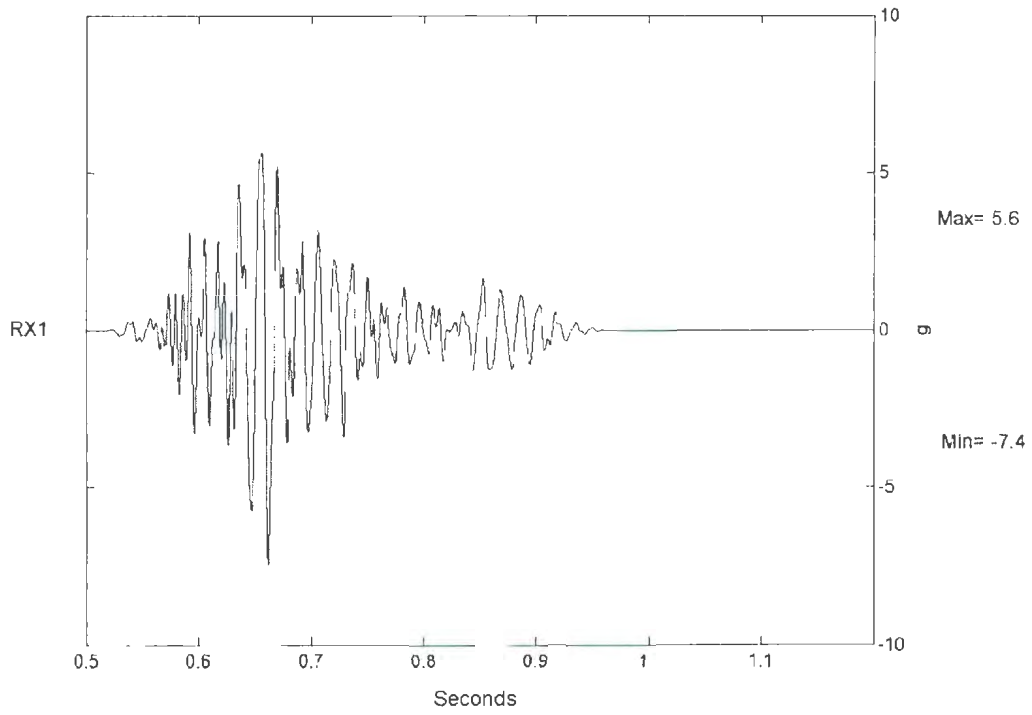
Figure 5.17: Prescribed A475 Earthquake Motion.
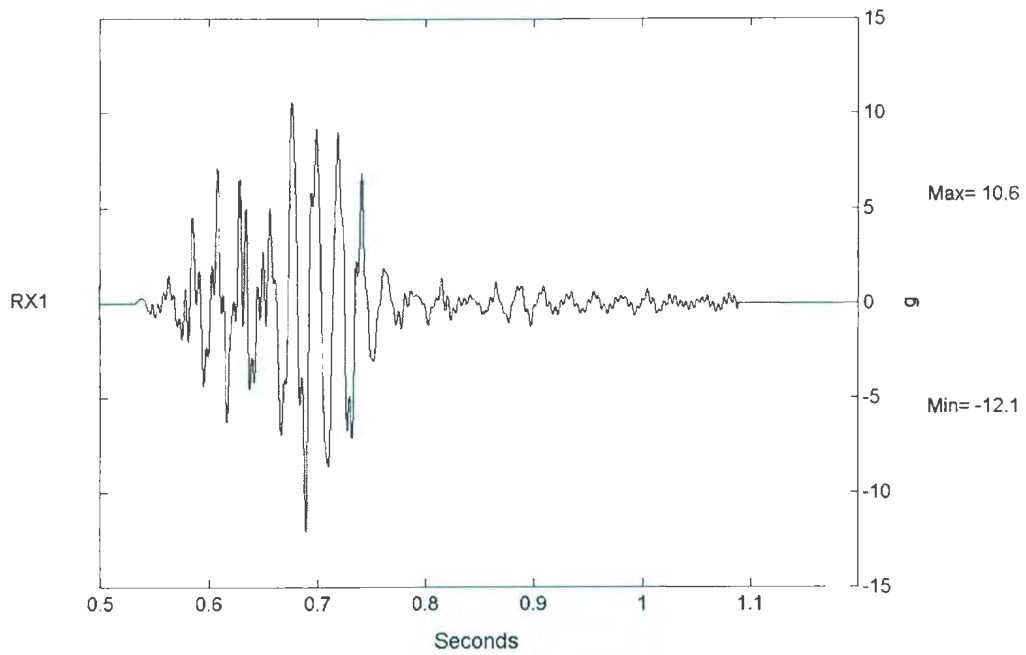
Figure 5.18: Prescribed A2475 Earthquake Motion.

134
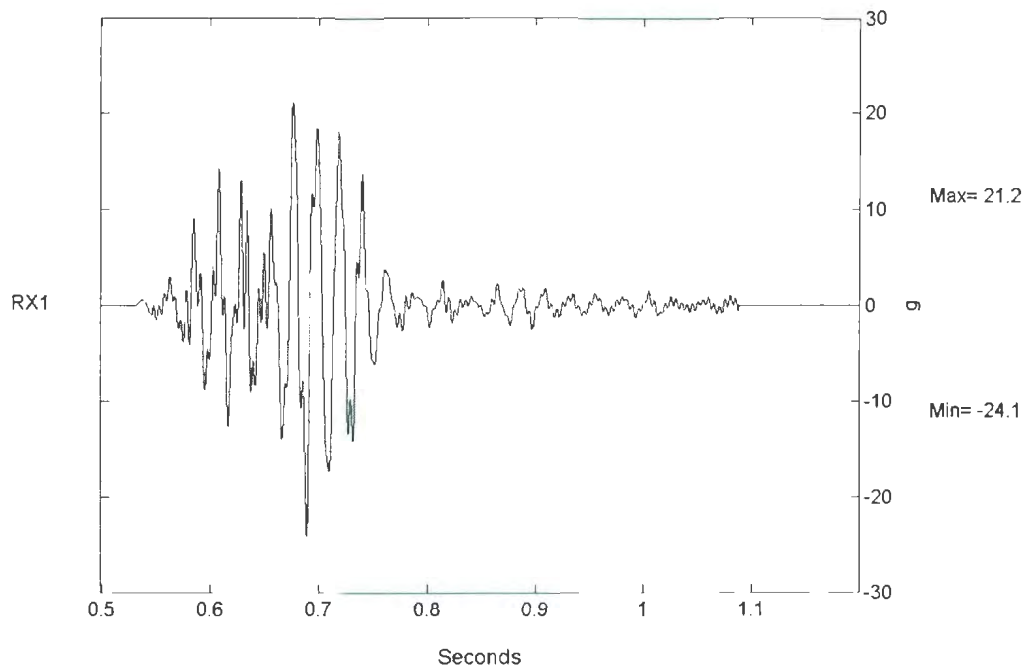
Figure 5.19: Prescribed 2A2475 Earthquake Motion.

The frequency of the A475 and A2475 records are based upon real world earthquake events. The A475 earthquake event is an acceleration record matching the firm ground target spectrum for the current building code for Vancouver, British Columbia, Canada, which has 10% possibility of exceedence in a 10 year period. Whereas, the A2475 acceleration time record has been altered to match the target spectrum for the proposed new building code earthquake for the same location, which has a 2% possibility of exceedence in a 50 year period (Liquefaction Remediation Project, 2004).

The earthquake regimes applied to each model are presented in Table 5.11. In the COSTA-B and COSTA-E tests where there were multiple earthquakes applied, a period of approximately one minute was allowed to pass between applying earthquake events. This was done to allow any generated pore pressures to dissipate, ensuring the independence of each of the earthquake events.

Table 5.11: Applied Earthquake Actuation Motions.

Test Label	Applied Earthquake Motion(s)
COSTA-A	A2475
COSTA-B	A2475 followed by 2A2475
COSTA-C	2A2475
COSTA-D	2A2475
COSTA-E	5 x A475 followed by 2A2475

The performance of the EQS for each test in terms of reproducing these earthquake motions is presented further in Chapter 6. This is primarily done by comparing the prescribed earthquake motion with the response of the Tz accelerometer mounted external to the soil model.

5.3.5 Instrument Observation

As mentioned before the responses of the instruments described in 5.3.1 were monitored using the integrated data acquisition system for 16 seconds during a period before,

136

during, and after the earthquake. In Chapter 6 these responses are presented in a short-term (0.5 seconds) and long-term (6 seconds) context for comparison and analysis purposes.

5.4 Post-Test Investigations

Following the completion of the centrifuge test several different observations were made, including: the temperature of the model during the test, the post-test surface profile, the movement of the gravel marker grid placed on the surface of the slope, embedment of LVDT contact pads, and the excavation of the model revealing silt layer thickness and instrument position if applicable.

5.5 Experimental Test Program Summary

A total of five centrifuge tests were conducted. Table 5.12 summarizes the conditions and characteristics for each model in the testing program.

Table 5.12: Summary of Centrifuge Experiment Specifications.

Test Label	Description	Applied EQ Motion	Centrifuge g-Level	Pre-Sat. Rel. Dens (%)	Pore Fluid	
					Visc. (cSt)	Temp (°C)
COSTA-A	Draped Silt Layer	A2475	68.87	Unknown	33.0	20.0
COSTA-B	5.5:1 Silt Layer	A2475 + 2A2475	70.09	34%	37.9	20.0
COSTA-C	5.5:1 Silt Layer	2A2475	70.09	34%	34.5	24.5
COSTA-D	No Silt Layer	2A2475	70.09	28%	37.2	20.0
COSTA-E	5.5:1 Silt Layer	5 x A475 + 2A2475	70.09	34%	37.2	20.0

6 EXPERIMENTAL TESTING RESULTS

6.1 COSTA-A

6.1.1 Pre-Test Observations

As mentioned in Chapter 5 the surface profiles of the models were measured following saturation and then following transportation to and loading on the centrifuge arm. For the COSTA-A test the surface profile was only measured following installation of the model on the centrifuge arm, which is shown in both Table 6.1 and Figure 6.2. A moderate amount of settlement, on the order of 10 mm was observed in the farfield upslope area. In future tests this was to be decreased with increased care and refinement of saturation and refinement techniques.

Table 6.1: COSTA-A Pre-Test Surface Profile.

Distance from Upslope End (mm)	Post Construction Profile	Pre Test Profile
0	343	334
50	343	335
100	343	334
150	343	337
200	343	335
250	343	336
300	343	334
350	343	329
400	343	325
450	318	309
500	293	286
550	268	258
600	243	245
650	243	244
700	243	242
737	243	240
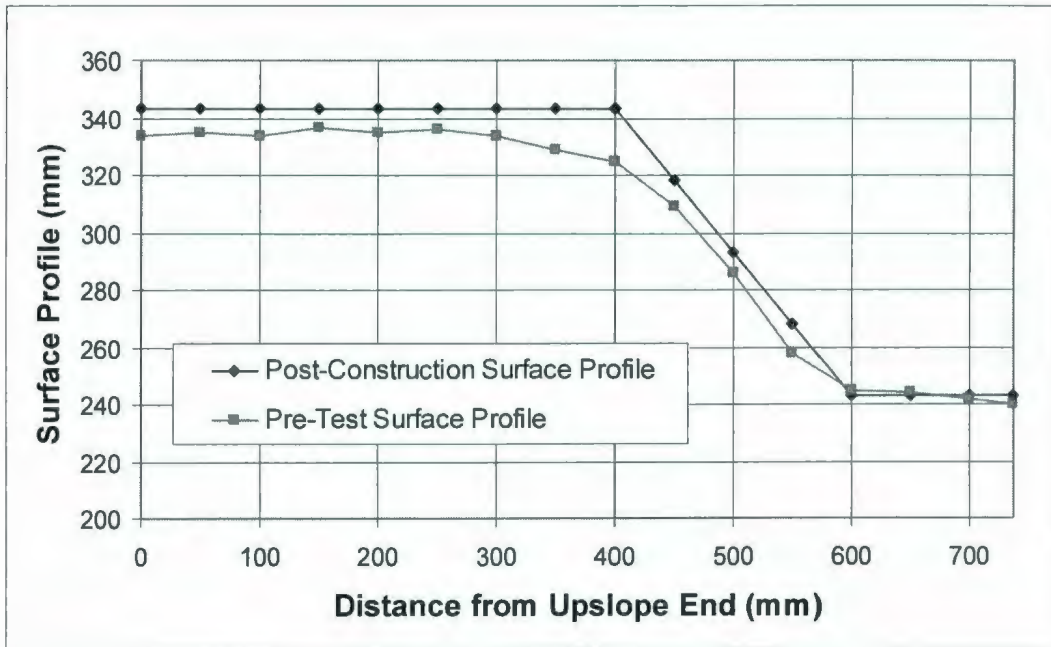
Figure 6.1: COSTA-A Pre-Test Surface Profile.

During the swing-up of the centrifuge to test speed the PPTs and LVDTs and were monitored for any irregular changes as well as the integrity of the slope and for the settlement of the model due to self-weight. For illustrative purposes, the responses of these instruments during swing-up for COSTA-A are shown in Figures 6.2 through 6.4. For subsequent tests, this data is not illustrated. During swing-up P6 was discovered to be damaged in some way prior to the test, so therefore no data for that instrument was available at any point in the test. Time is shown in these figures, as well as in all future figures, in model scale. In this chapter, changes in pore pressure and deformation response are tracked from a value of zero at the start of the swing-up of the centrifuge.
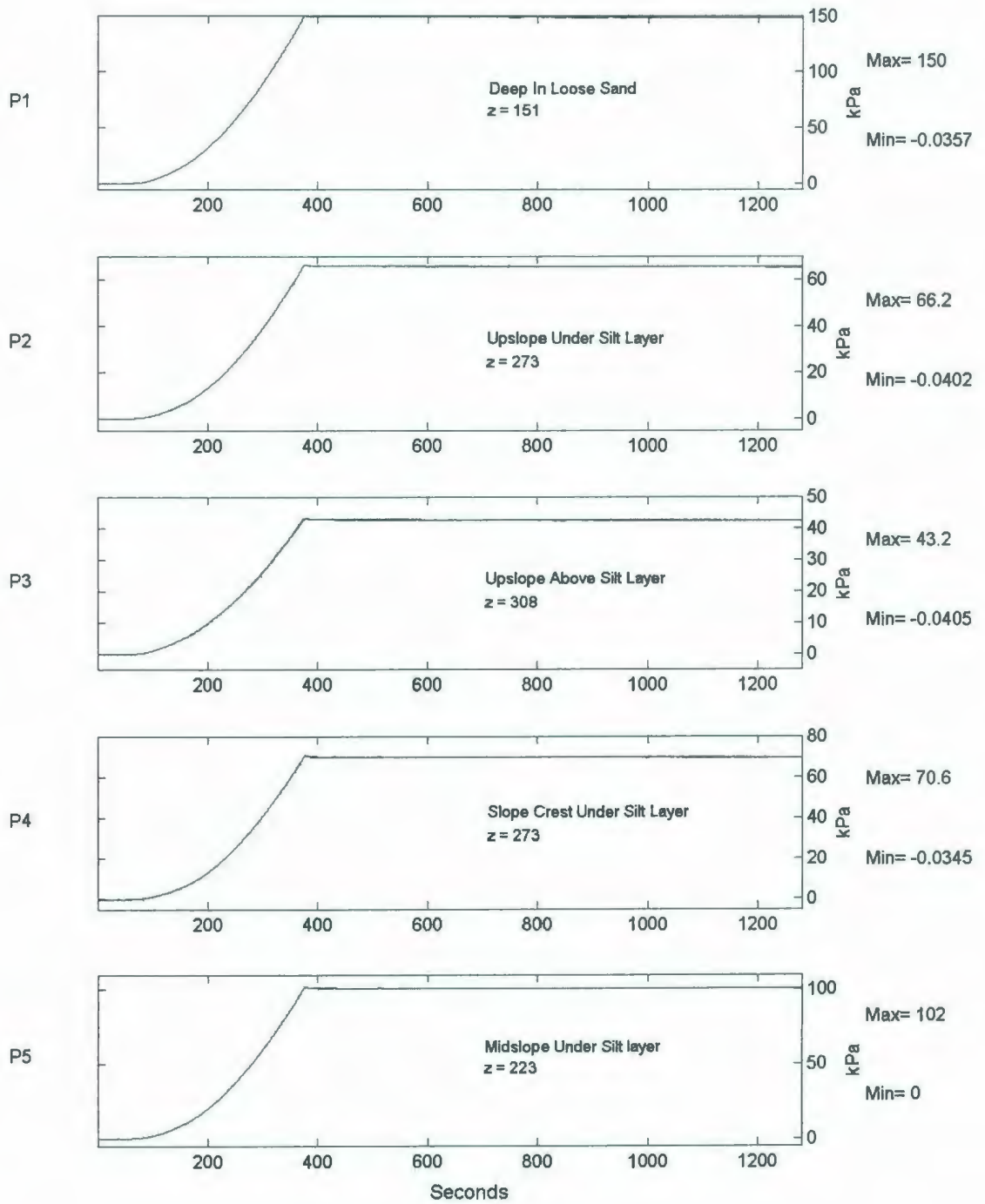
Figure 6.2: COSTA-A PPT Response During Swing-Up for P1-P5.
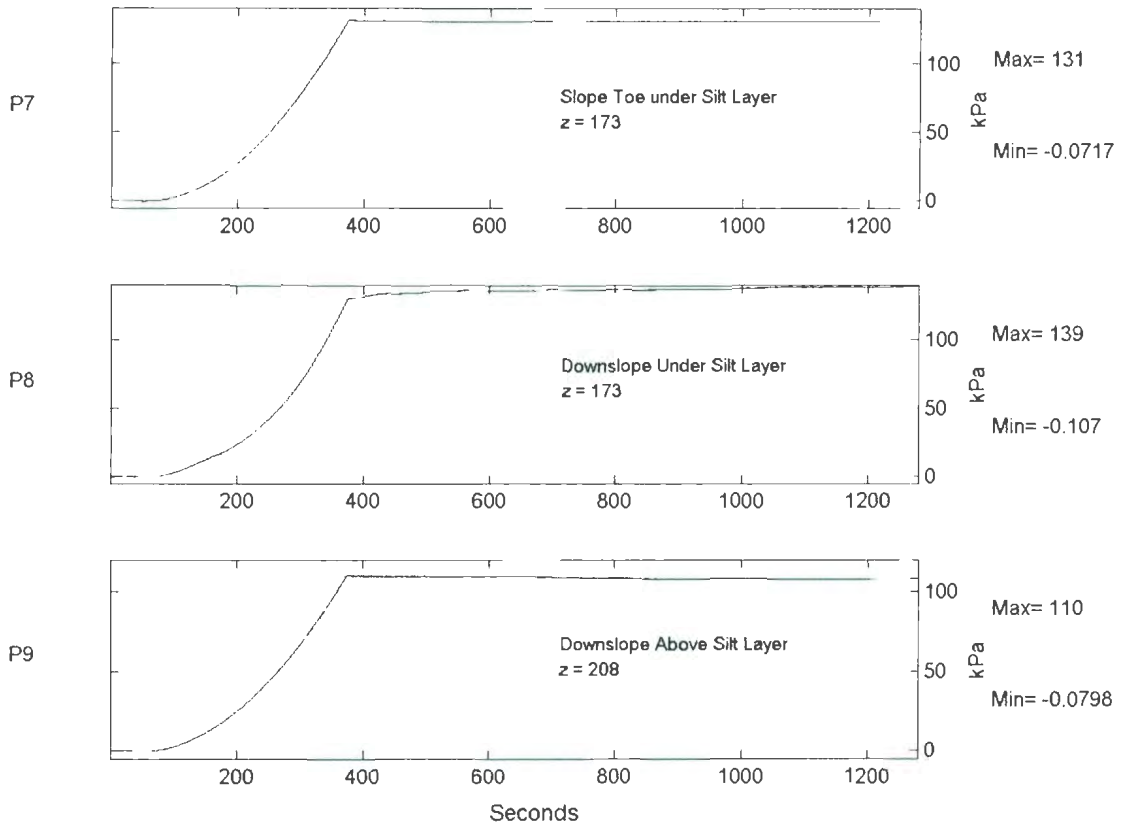
Figure 6.3: COSTA-A PPT Response During Swing-Up for P7-P9.
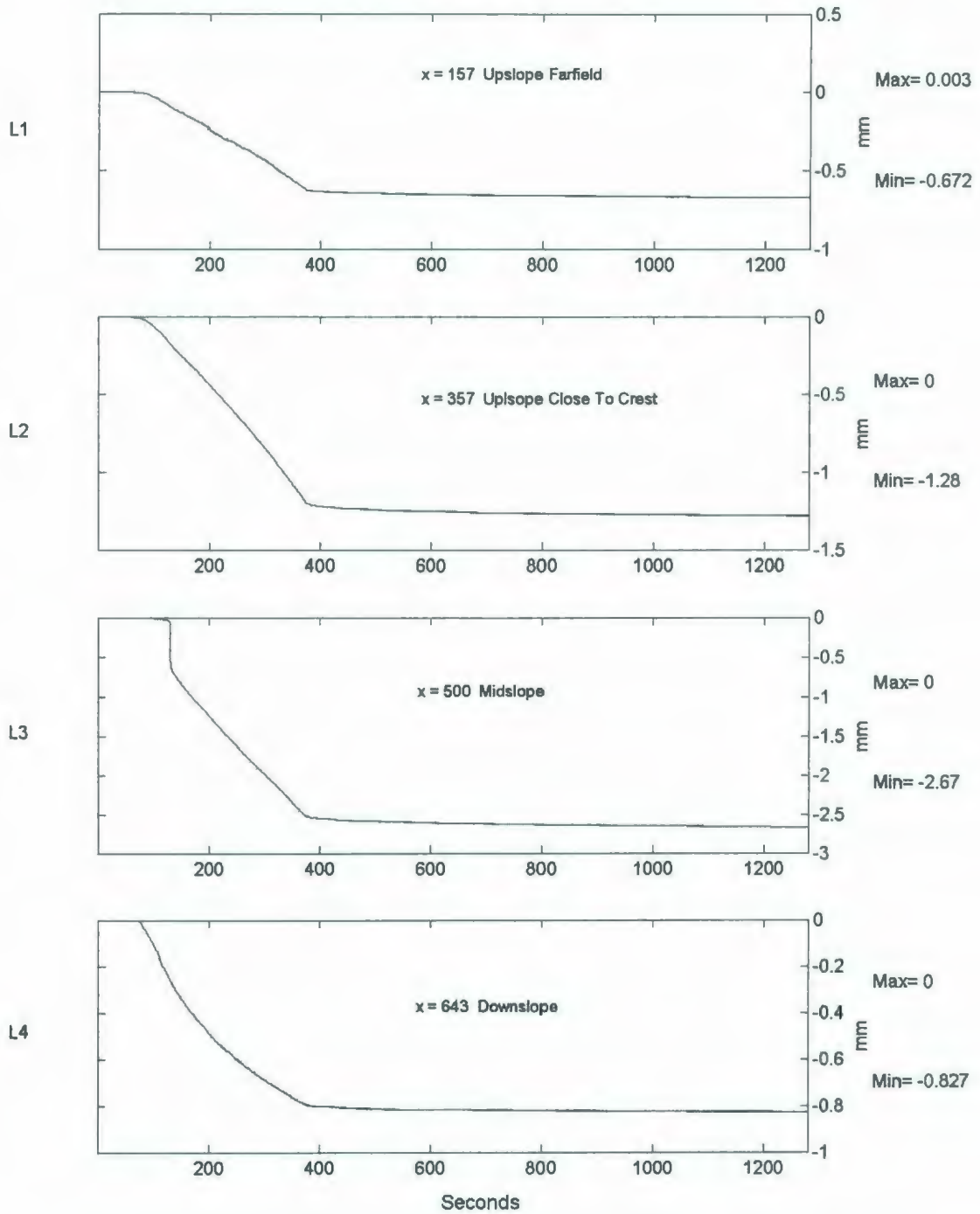
Figure 6.4: COSTA-A LVDT Deformation Response During Swing-Up for L1-L4.

All PPTs increased at the correct rate during the increase to g-level and to the proper levels considering their locations in the model. This indicates that the PPT instruments were operating correctly.

The LVDT responses, as show in Figure 6.4, indicate that the compression due to self-weight is on the order of 1 mm, except in the case of L3, which is situated on the slope face. Note that at approximately 120 seconds L3 experiences an instantaneous settlement of just less than 1 mm. This may be attributed to the spindle of the LVDT becoming stuck in the LVDT housing due to friction. It is possible that at 120 seconds the downward g-force in the model overcame the frictional force in the LVDT housing, thus releasing the LVDT spindle and pad onto the model surface. A compression of 1 mm does not have a significant effect on the relative density of the model. In future tests it was determined to estimate the relative density of the model at the crest using the pre-test profiling data as well as the settlement observed at from L1 during the swing-up.

As mentioned previously in Chapter 5 the saturation of this model was checked by observing the travel time of acoustic waves through the model. The intention was to observe these acoustic responses at test speed a few moments before the initiation of the model earthquake. However, the hammer device ceased to operate after an acceleration level of approximately 30 to 40 g. Data is available for an acceleration level of 30 g. The generation of these waves was achieved by tapping the upslope end of the model container with a small solenoid operated hammer. This generated signal is then observed

144

by two accelerometers (in this case A1 and A7) placed in-line along the centre axis of the model at a known distance apart (150 mm). The captured signal in these two accelerometers at 30 g is shown in Figure 6.5. The accelerometer data shown in this figure has not been corrected for their opposite orientations. The speed of this wave can be estimated by comparing the time difference of the first major peak in Channel 1 and major trough in Channel 2. This time difference was observed to be 0.000181 seconds. If an accelerometer separation of 107 mm is considered a wave speed of 828.73 m/s. This value is greater than the required P-wave speed of 750 m/s as mentioned in Chapter 5 to ensure that the model was saturated to a level greater than 99%. However, following the COSTA-A test it was considered that the Channel 2 accelerometer could be experiencing a faster response due to the preferential travel of a wave signal through the sidewalls of the model container. Additionally, the signals were somewhat irregular in their mode making them more difficult to interpret. For future tests the Channel 1 accelerometer was moved closer to the wave source and Channel 2 was also correspondingly moved closer to the source in order minimize these effects.
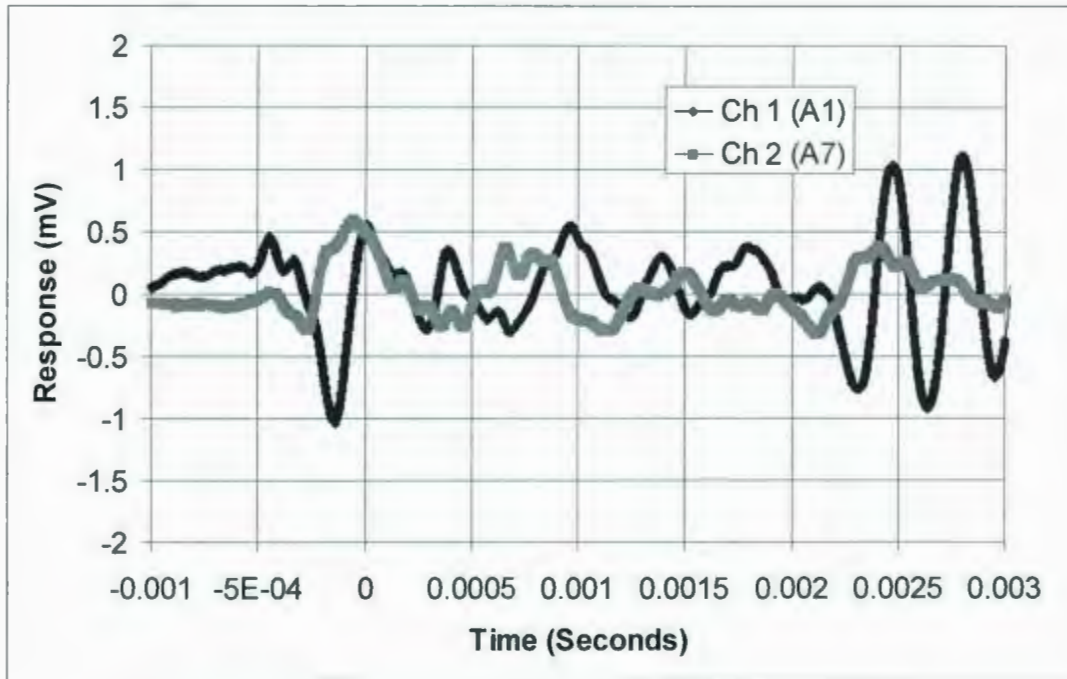
Figure 6.5: COSTA-A Acoustic Wave Response at 30g.

6.1.2 *A2475 Earthquake Actuation*

The top portion of Figure 6.6 illustrates the desired A2475 acceleration-time history in model scale. The bottom portion of Figure 6.6 shows the observed earthquake signal in Tz, which is in the direction of shaking. As described in Chapter 5, Tz is mounted exterior to the model, close to the shaking table and therefore gives a relatively good indication of the acceleration at the base of the model. Additionally, Figure 6.7 shows the fast Fourier transforms (FFT) of these two signals. The two signals compare relatively well with respect to frequency as well as magnitude. The actual observed earthquake being slightly larger in magnitude. With respect to the amount of energy

146

delivered, less energy was observed than prescribed. This can be found by comparing the areas under the curves shown in Figure 6.7, which can be used to calculate the amount of energy delivered by the actuation. This comparison shows how less energy was observed than prescribed. In terms of frequency content, as observed in the FFT signals, it is observed that the EQS delivered an earthquake with larger content in the 40 to 50 Hz range and lower content in the 50 to 60 Hz range. However, this can still be considered good agreement between the observed and desired earthquake motion. Figure 6.8 shows the response of the triaxial accelerometer in the vertical direction. This response was captured by Ty and shows that there is a spurious vertical motion that is experienced during the earthquake event. The range of this acceleration ranges between +3 to –4.5 g and is significant enough to be a concern. It was considered that this motion was caused by the rocking of the model on the shake table. Throughout the duration of the COSTA earthquake tests, modifications and adjustments to the EQS were undertaken in an attempt to alleviate or minimize these effects.
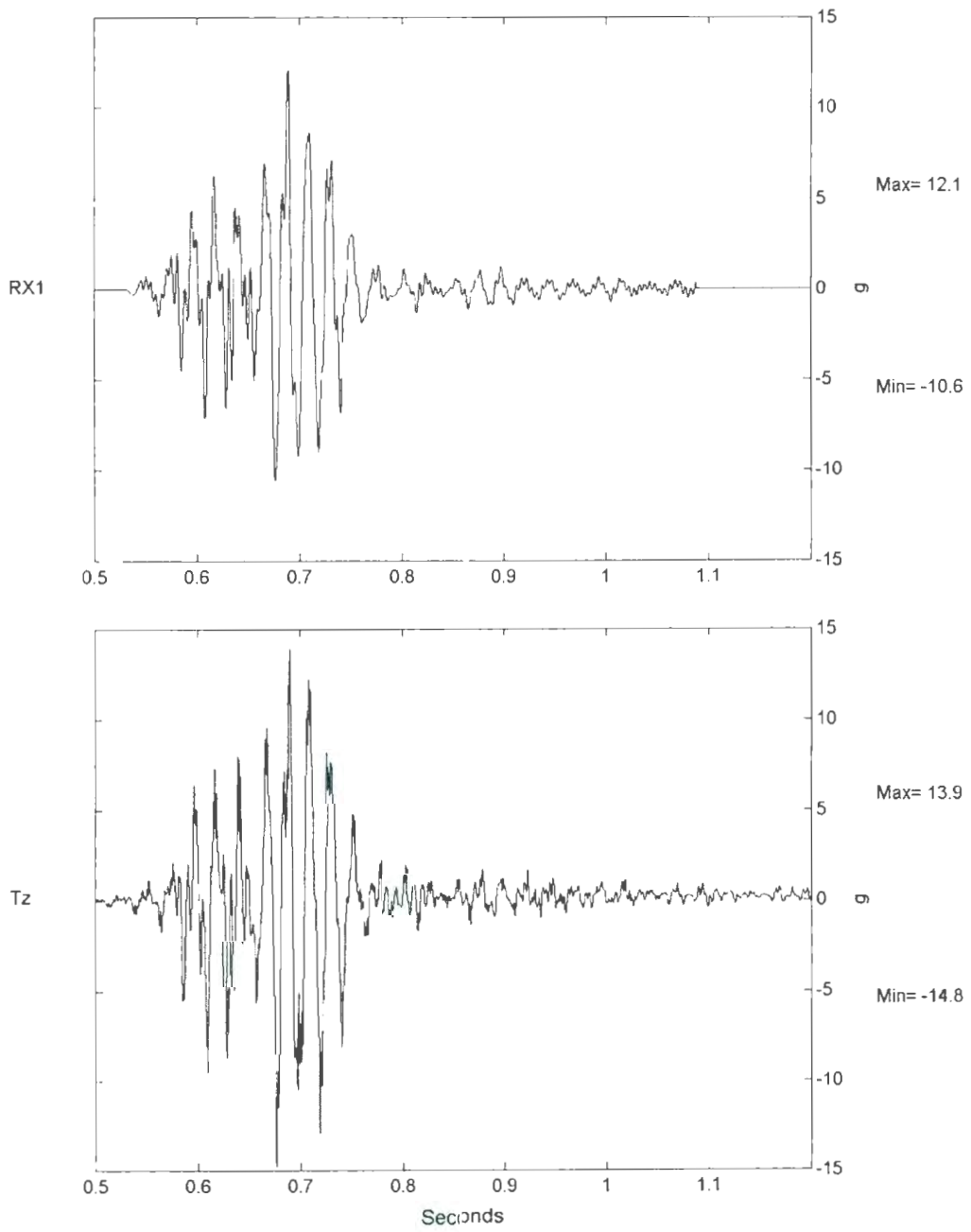
Figure 6.6: Comparison of A2475 Earthquake Record & Observed COSTA-A Tz Acceleration.

148
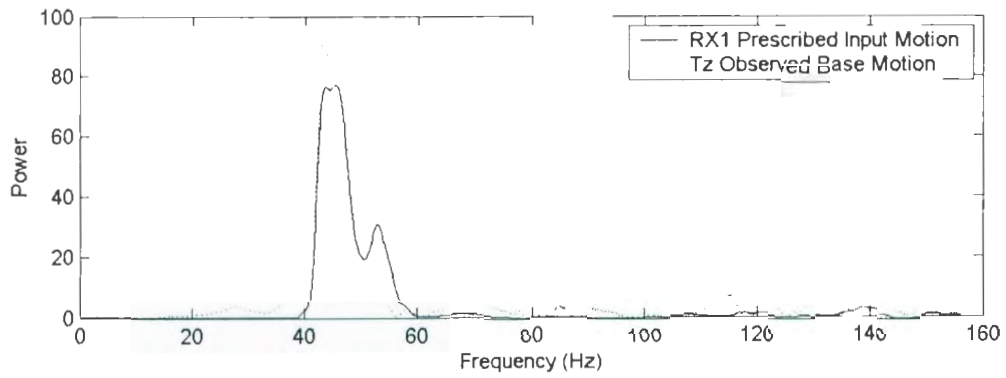
Figure 6.7: FFT Comparison of A2475 Earthquake Record & Observed COSTA-A Tz Acceleration
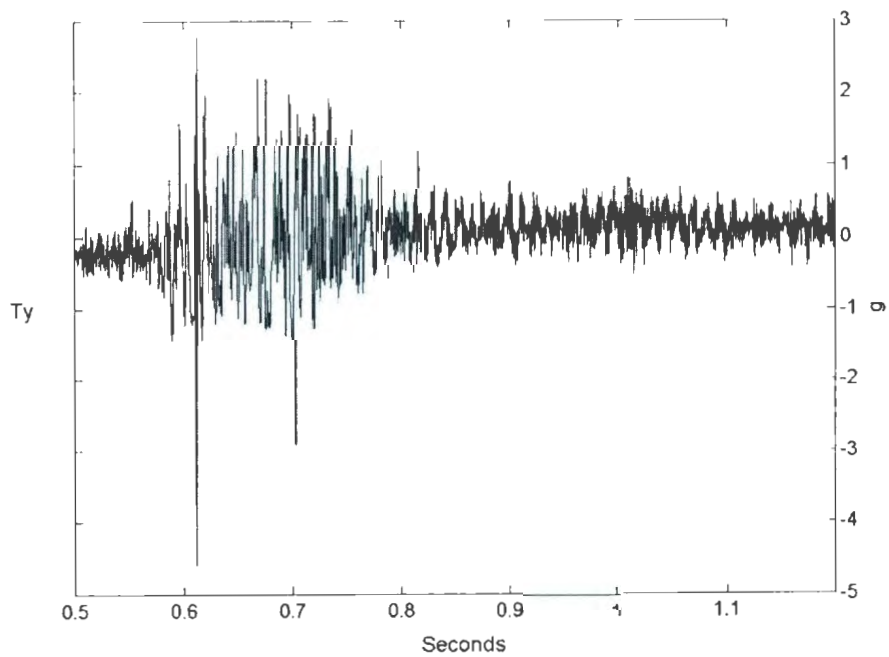
Figure 6.8: COSTA-A A2475 Observed Ty Vertical Acceleration.

6.1.3 A2475 Short-Term Testing Instrument Responses

As mentioned in Chapter 5 all operating instruments were monitored during and shortly after the A2475 earthquake event. Figures 6.9 through 6.13 illustrate the observed responses in the various instruments. In these figures, as well as all future figures, positive acceleration is measured in the upslope direction. Additionally, in PPTs where the observed pore pressure value approached the value where the pore pressure ratio (r_u) was equal to one a line is drawn on the figure to denote this value. The pore pressure ratio is defined as:

$$r_u = {u_c}\big/{\sigma'_{v0}} \tag{6.1}$$

where u_c is the excess generated pore pressure and σ'_{v0} is the initial effective vertical stress as calculated from the instruments' originally planned position in the model considering the buoyant unit weight of Fraser River sand is 9.4 kN/m^3 (Tu, 2004) and the centrifugal acceleration field of 70 g. When the r_u is equal to one the condition of liquefaction is satisfied.

It should also be noted that the responses of A1 and A7 are clipped at a level of ± 5 g. This is due to electronic gaining that was applied to these instruments in an attempt to observe the acoustic wave responses of these instruments during the application of a signal from a solenoid hammer to verify the saturation level of the model. This clipping effect was rectified in future tests.

150
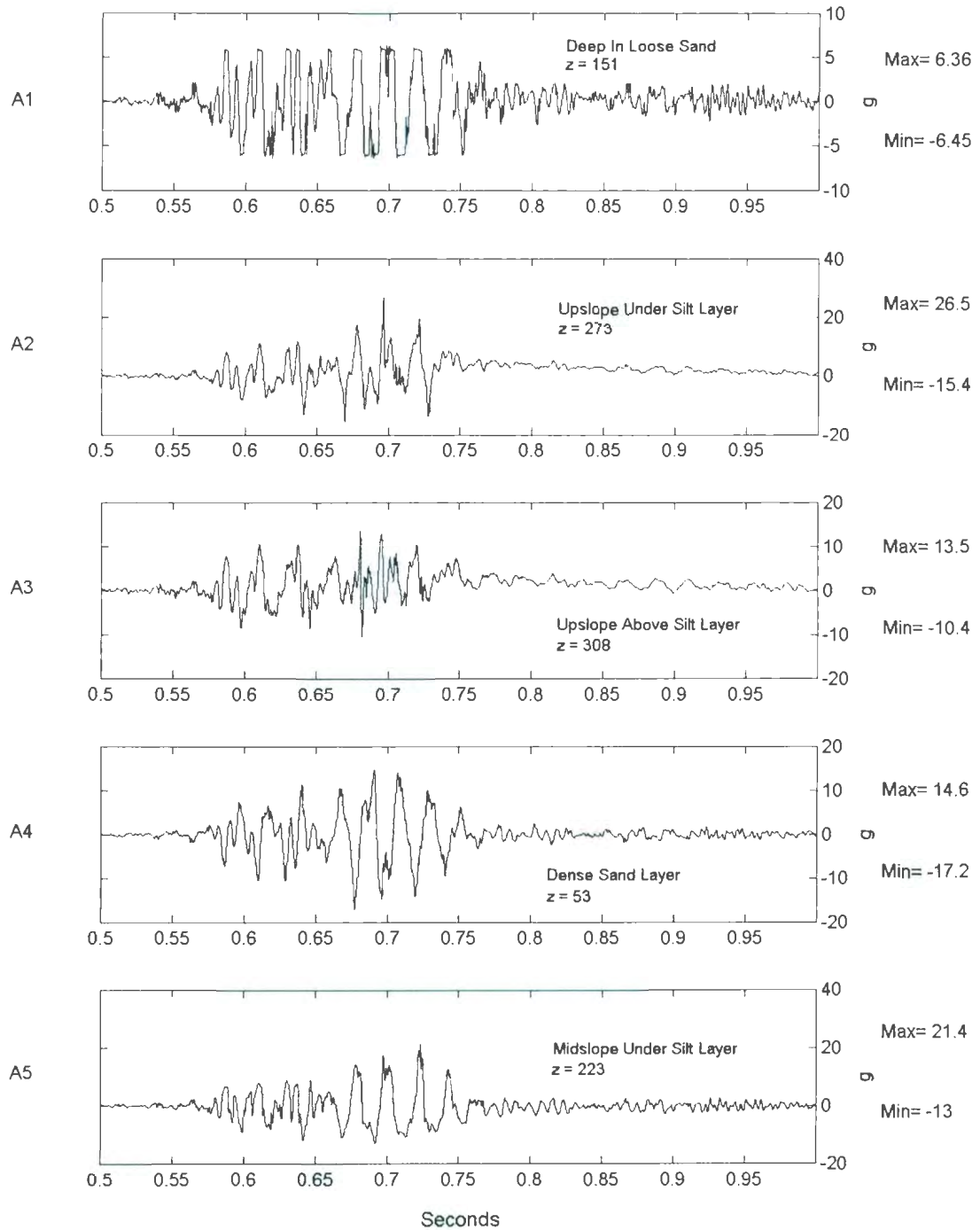
Figure 6.9: COSTA-A A2475 Short-Term Accelerometer Response for A1-A5.
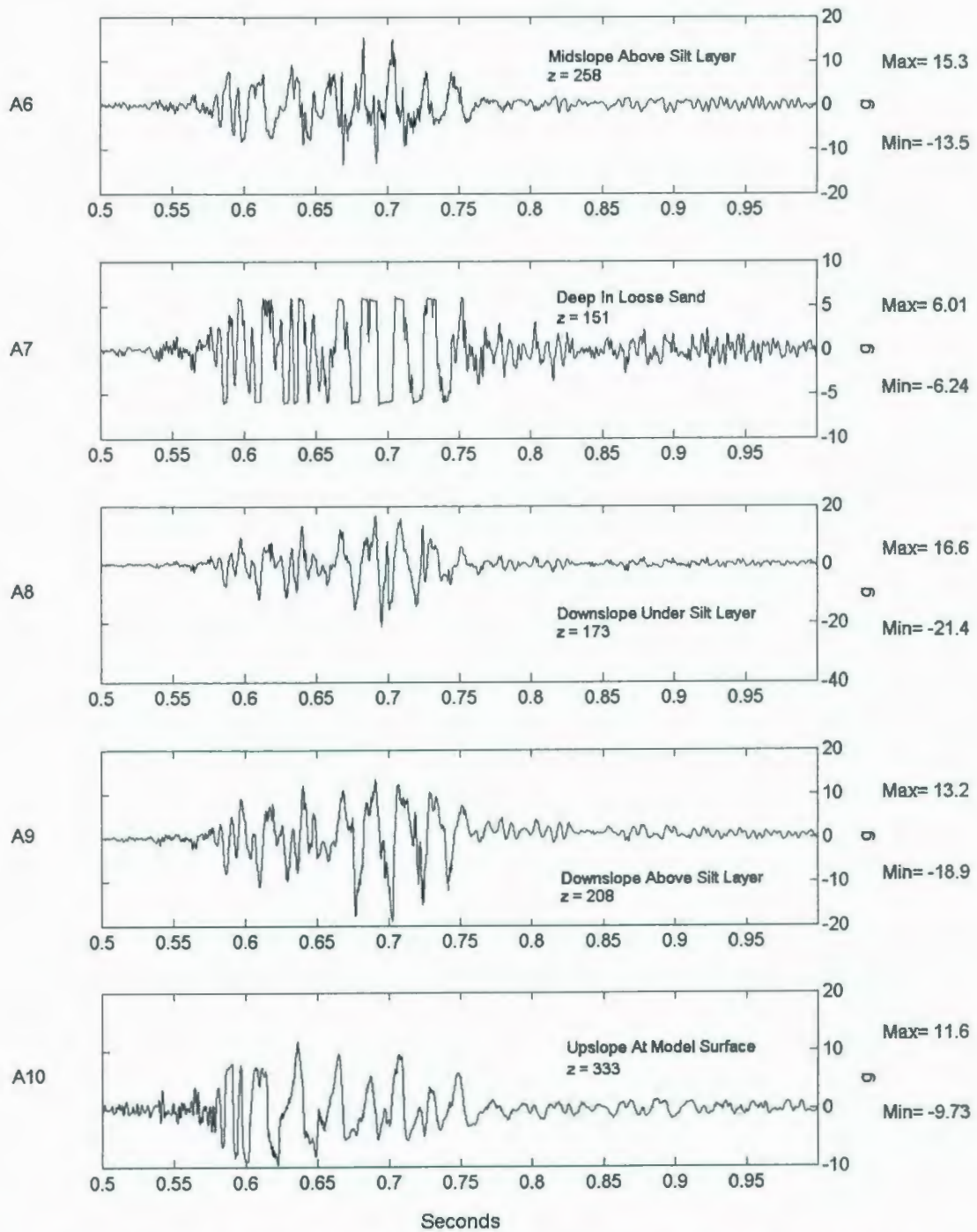
Figure 6.10: COSTA-A A2475 Short-Term Accelerometer Response for A6-A10.
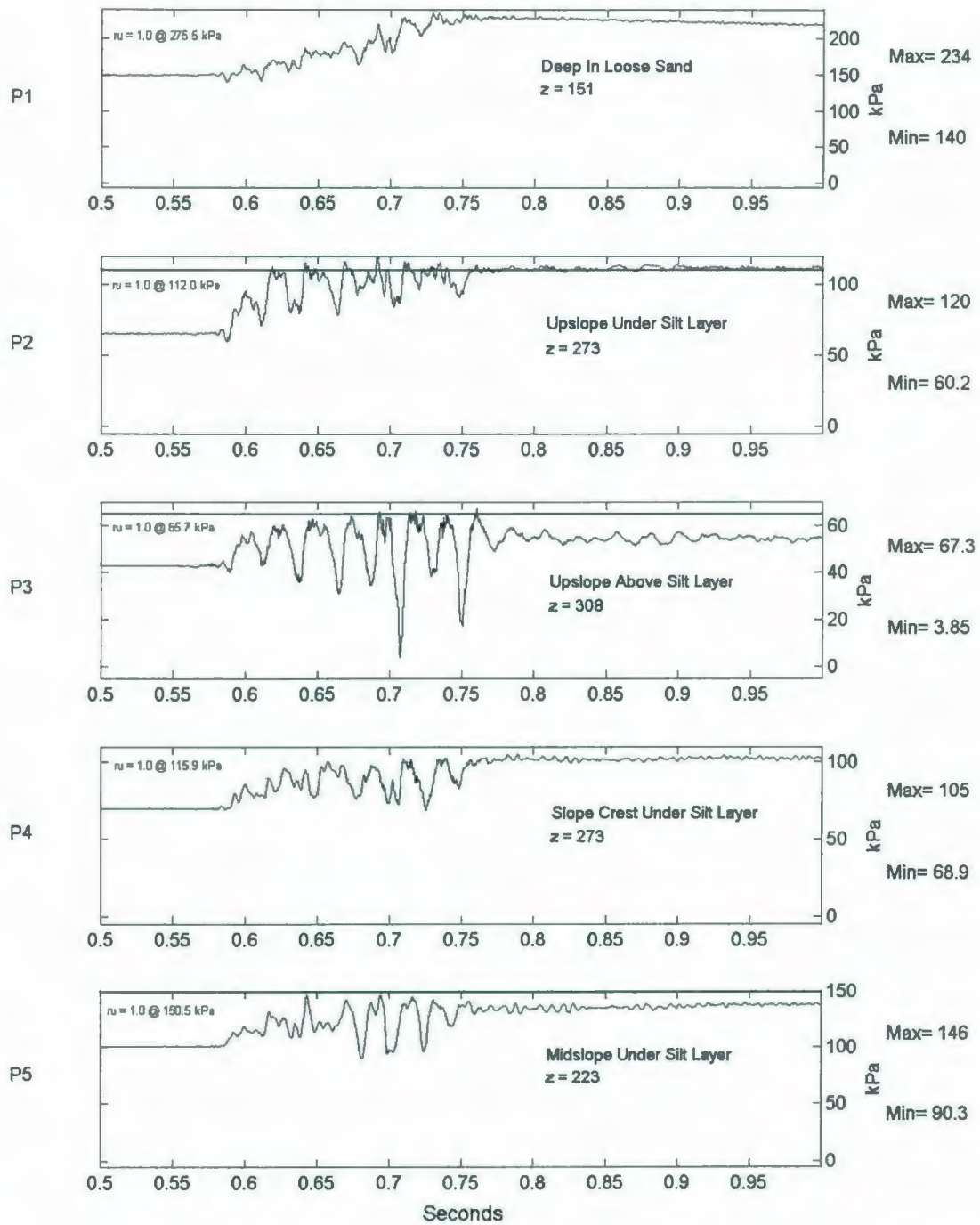
Figure 6.11: COSTA-A A2475 Short-Term PPT Response for P1-P5.

153
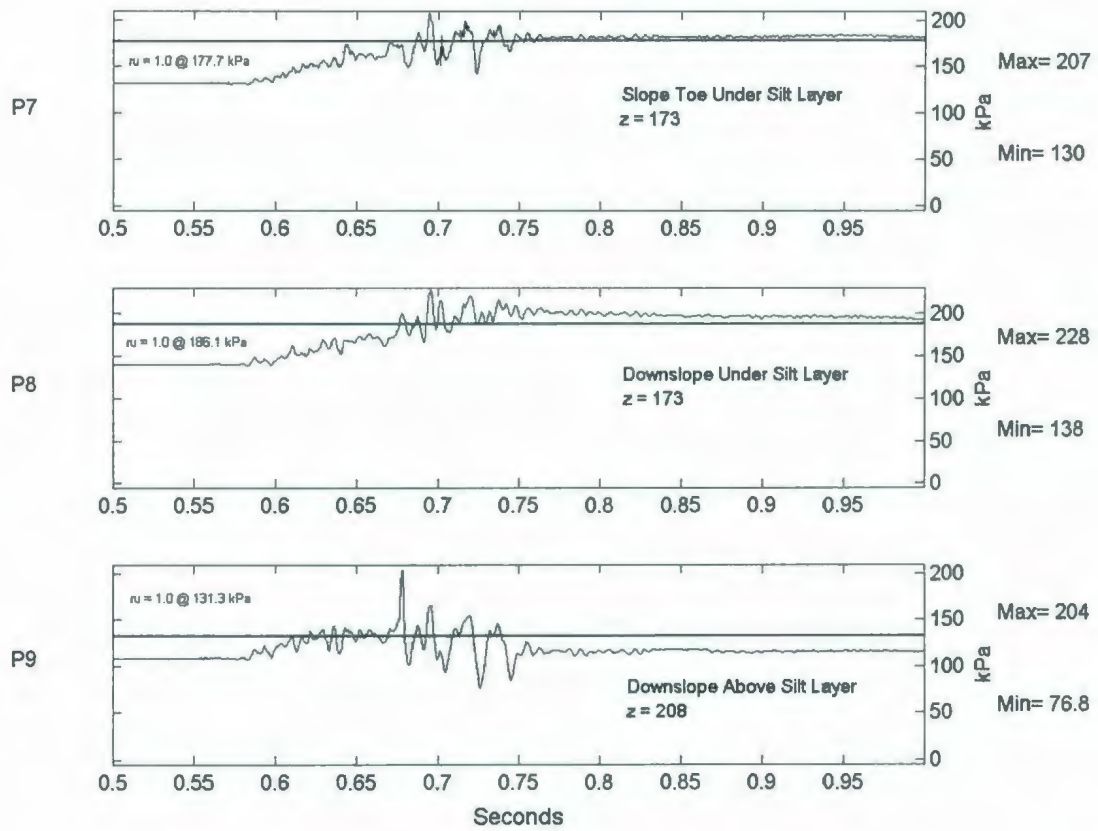
Figure 6.12: COSTA-A A2475 Short-Term PPT Response for P7-P9.
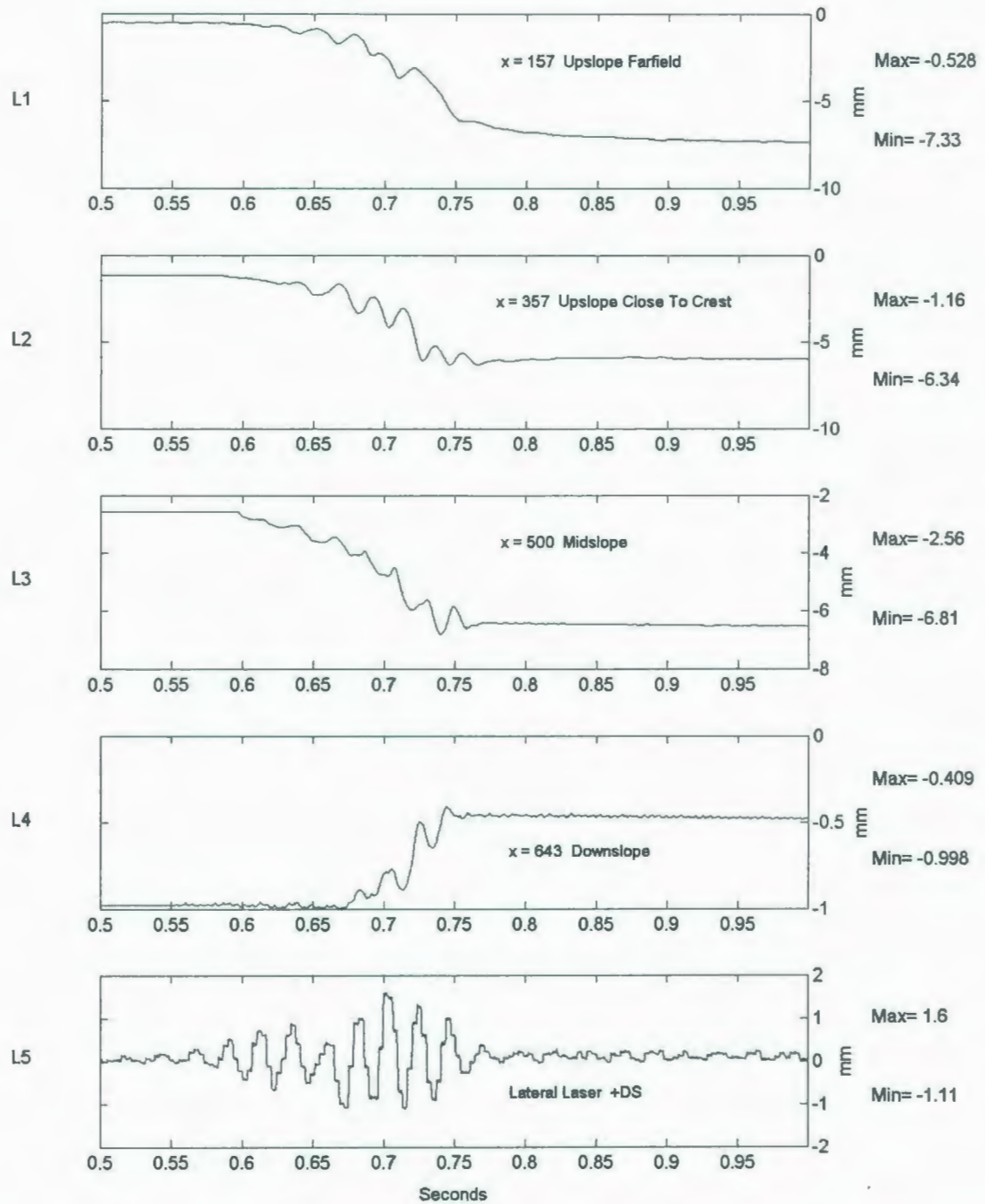
Figure 6.13: COSTA-A A2475 Short-Term LVDT Deformation & Lateral Laser Displacement Responses.

There are several initial observations that can be made from the short-term data. First, it seems that the deeper accelerometers experienced higher levels of acceleration, as with A4 and A8, which are two of the deepest accelerometers. These results do not illustrate the dilation spikes that were observed in accelerometers in tests with similar geometries, such as Taboada-Urtuzuastegui et al. (2002), as might be expected in A3 from the large negative spiking response of P3 at 0.71 and 0.75 seconds

The PPTs under the silt layer can be seen to be gaining pore pressure at a greater rate with time than those located above the silt layer. In the observed PPT responses above the silt layer there were fluctuations but after cessation of the earthquake they quickly returned to their pre-shake levels. Deeper PPTs, such as P1, measured larger generated pore pressures.

The condition of liquefaction was observed at several positions in the model. Beneath the silt layer at P2 liquefaction was observed intermittently before reaching a stable condition of liquefaction at 0.76 seconds. Other PPTs situated beneath the silt layer that achieved liquefaction were P7 and P8, which both achieved a sustained liquefaction condition at approximately 0.7 seconds. This seems to indicate that liquefaction was achieved in the downslope areas of the model before it was achieved in the upslope portion. Liquefaction was also observed only intermittently above the silt layer, in both P3 and P9, which are in the upslope and downslope positions respectively. However, they did not sustain these levels following the cessation of shaking.

156

As for surface deformations monitored by the LVDTs, it is apparent that the top of the slope settled about 5-6 mm while the midslope noticed a slump of just over 4 mm. At the toe of the slope, as monitored by L4, heave was observed on the order of 0.6 mm. It was observed that the pad for L3 was embedded approximately 2 mm more into the soil than the other comparable LVDT pads. This most likely accounts for the sudden downward displacement observed on spinup at approximately 150 seconds, as shown in Figure 6.4.

6.1.4   A2475 Long-Term Testing Instrument Responses

In addition to monitoring the short-term responses for the testing instruments, the long-term responses were also collected to examine the behaviour of the model for several seconds after the A2475 earthquake event. Figures 6.14 through 6.18 illustrate these responses.
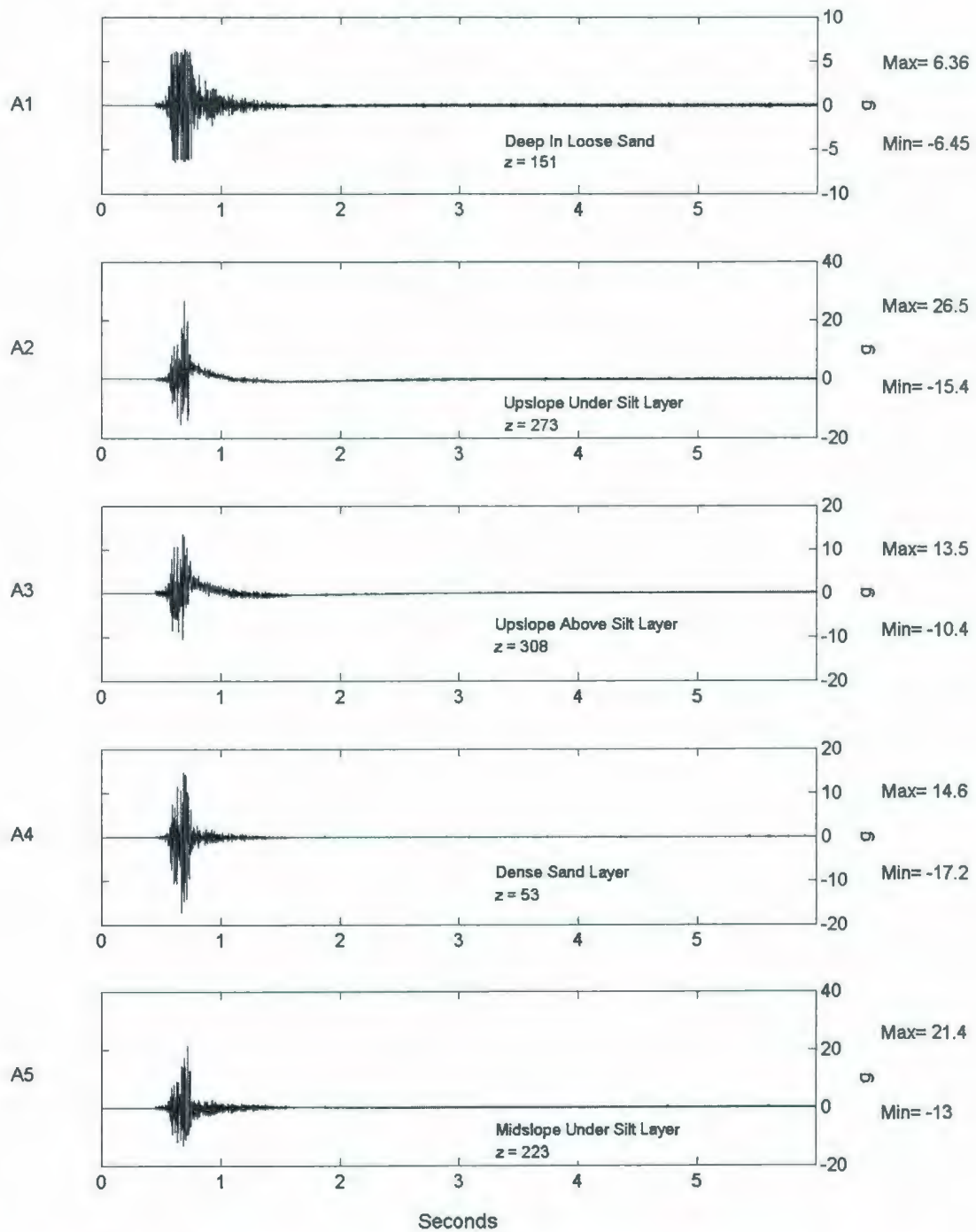
Figure 6.14: COSTA-A A2475 Long-Term Accelerometer Response for A1-A5.
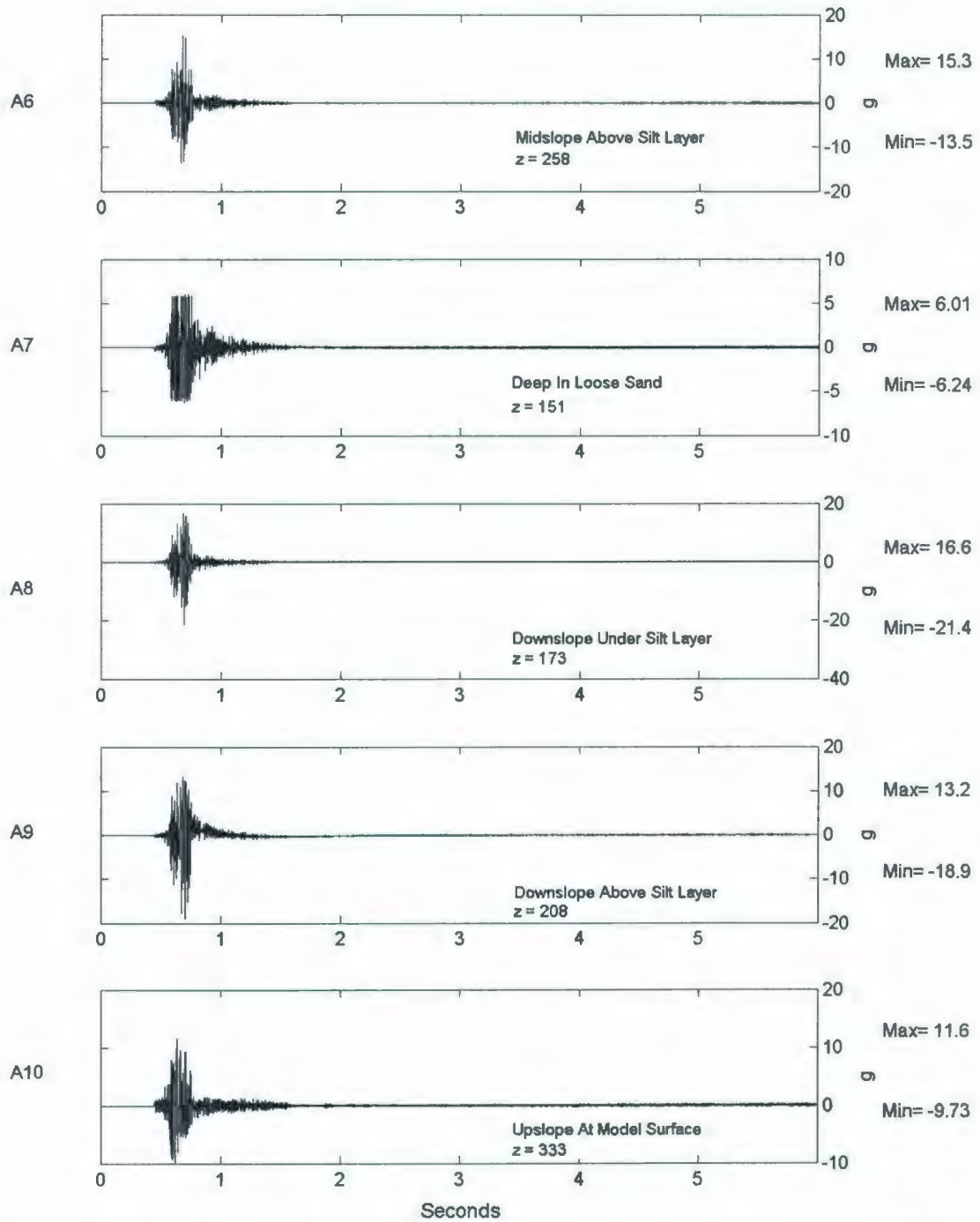
Figure 6.15: COSTA-A A2475 Long-Term Accelerometer Response for A6-A10.

P1

Max= 234

Min= 140

Deep In Loose Sand
z = 151

ru = 1.0 @ 275.5 kPa

P2

Max= 120

Min= 60.2

Upslope Under Silt Layer
z = 273

ru = 1.0 @ 112.0 kPa

P3

Max= 67.3

Min= 3.85

Upslope Above Silt Layer
z = 308

ru = 1.0 @ 65.7 kPa

P4

Max= 105

Min= 68.9

Slope Crest Under Silt Layer
z = 273

ru = 1.0 @ 115.9 kPa

P5

Max= 146

Min= 90.3

Midslope Under Silt Layer
z = 223

ru = 1.0 @ 150.5 kPa

Seconds
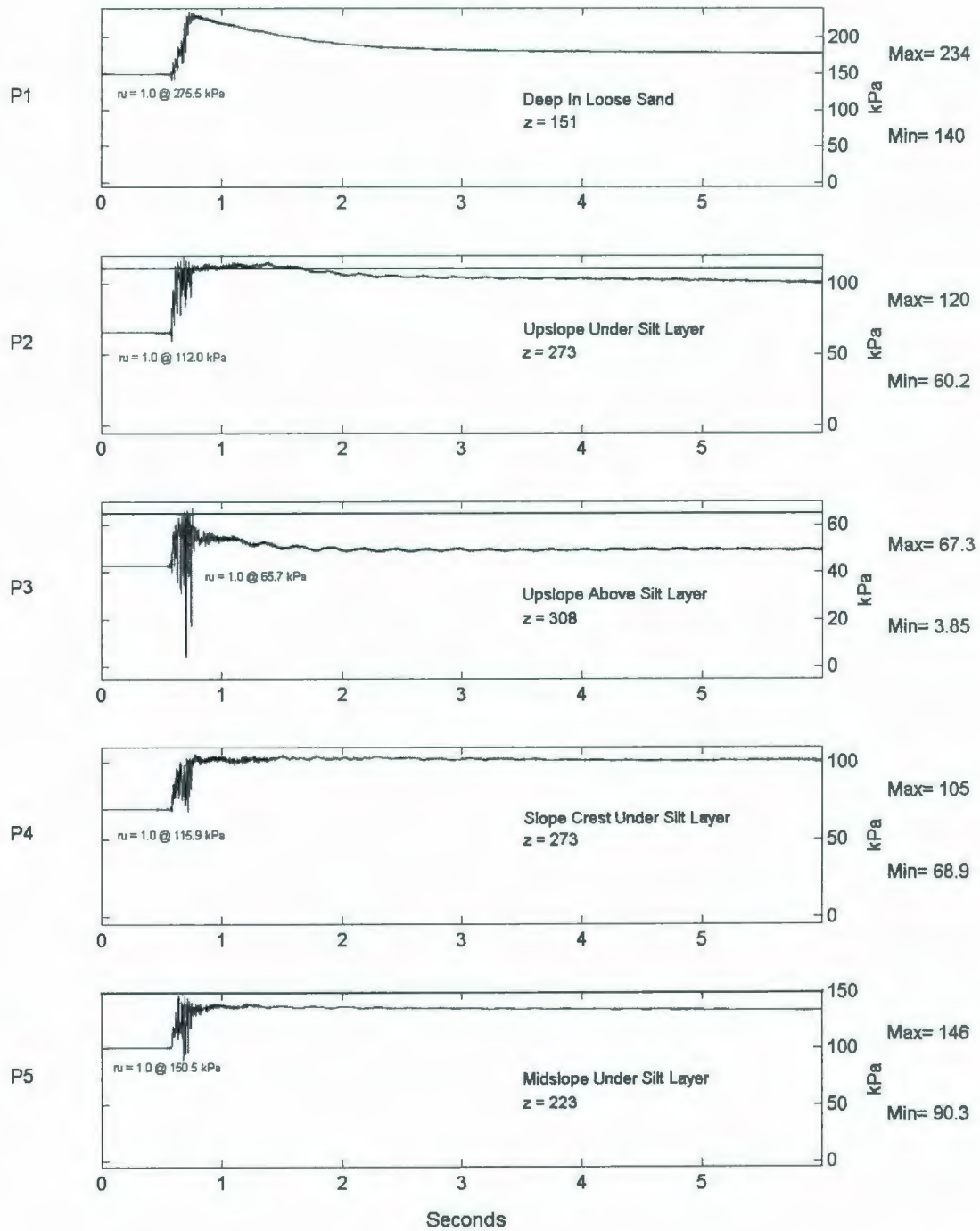
Figure 6.16: COSTA-A A2475 Long-Term PPT Response for P1-P5.
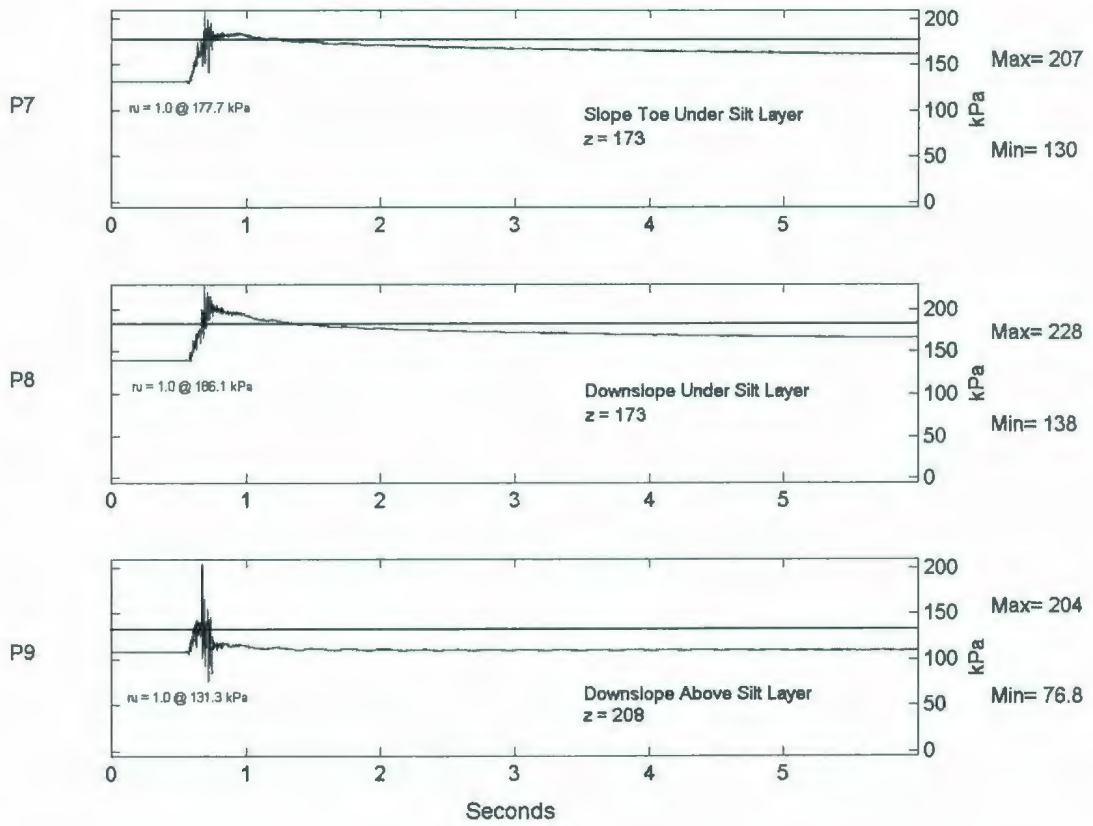
Figure 6.17: COSTA-A A2475 Long-Term PPT Response for P7-P9.
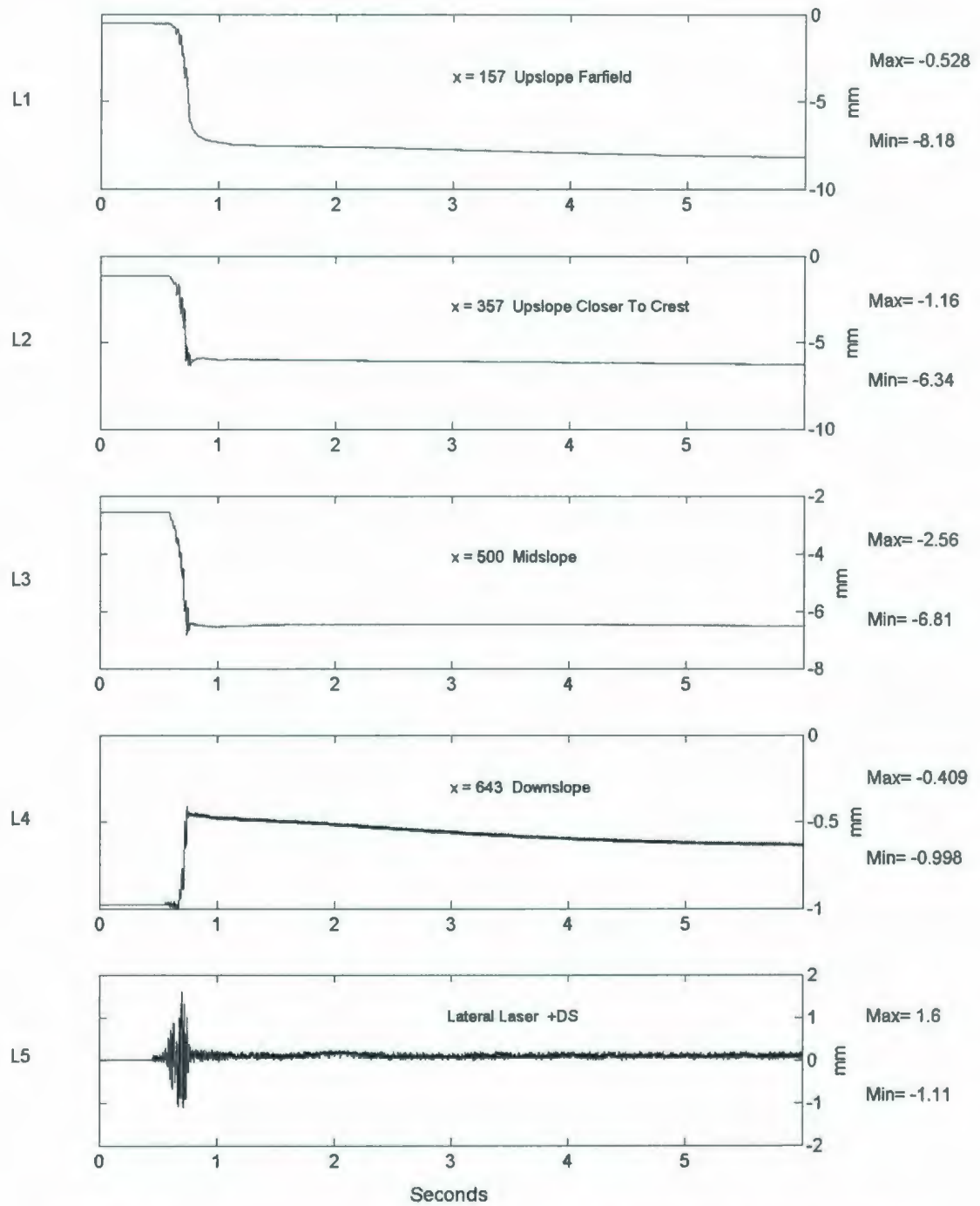
Figure 6.18: COSTA-A A2475 Long-Term LVDT Deformation & Lateral Laser
Displacement Responses.

162

In the long-term conditions after the earthquake event a noticeable trend can be detected in the upslope accelerometers A2 and A3 where they experienced some residual positive acceleration in the upslope direction for approximately 0.5 seconds before it returned to pre-shake levels. Most of the movement of the model ceased after less than 2 seconds, corresponding to the values observed at Tz.

With respect to pore pressure measurements in the long-term condition, there is one major trend. This is that the PPTs situated directly beneath the silt layer (P2, P4, P5, P7, and P8) measured increased levels of excess pore pressure for several seconds after the earthquake event as compared to the PPTs directly above the silt layer (P3 and P9).

Surface deformations stayed constant immediately after the earthquake, with the exception of L4, which experienced heave during the earthquake. Over the next five seconds, the toe is observed to have compressed slightly. An explanation for this is that the loose material that is collecting at the toe from the slope failure is becoming compressed by the centrifugal action.

P2 shows continued liquefaction during the period in which generated excess pore pressure is dissipating, at approximately 1 to 2 seconds, as shown in Figure 6.16. Both P2 and P3 should be affected by the actuation energy from the endwall, but this does not explain why liquefaction continues. Correspondingly, the response of L1 shows that the surface is settling in this area during the earthquake and continues to settle during the

post-earthquake period where generated excess pore pressure is migrating upward from lower depths, causing the post-shake liquefaction behaviour observed in the response of P2.

6.1.5 Post-Test Observations

Similarly to swing-up, the PPTs and LVDTs were monitored during swing-down for their response. This is done to observe any slope movements that may occur due to the release of centrifugal force and to observe the response of the PPTs as the g-level is decreased. The observed pore pressure level should return to a value of zero following the swing-down of the centrifuge. For illustrative purposes, the swing-down responses for COSTA-A are included in Figures 6.19 through 6.21, but for subsequent tests these figures will not be included.

P1 — Deep In Loose Sand, z = 151 — Max= 148, Min= -0.143
P2 — Upslope Under Silt Layer, z = 273 — Max= 70.4, Min= -0.0402
P3 — Upslope Above Silt Layer, z = 308 — Max= 47.4, Min= -0.203
P4 — Slope Crest Under Silt Layer, z = 273 — Max= 70.3, Min= 0.0827
P5 — Midslope Under Silt Layer, z = 223 — Max= 101, Min= 0.201

Seconds
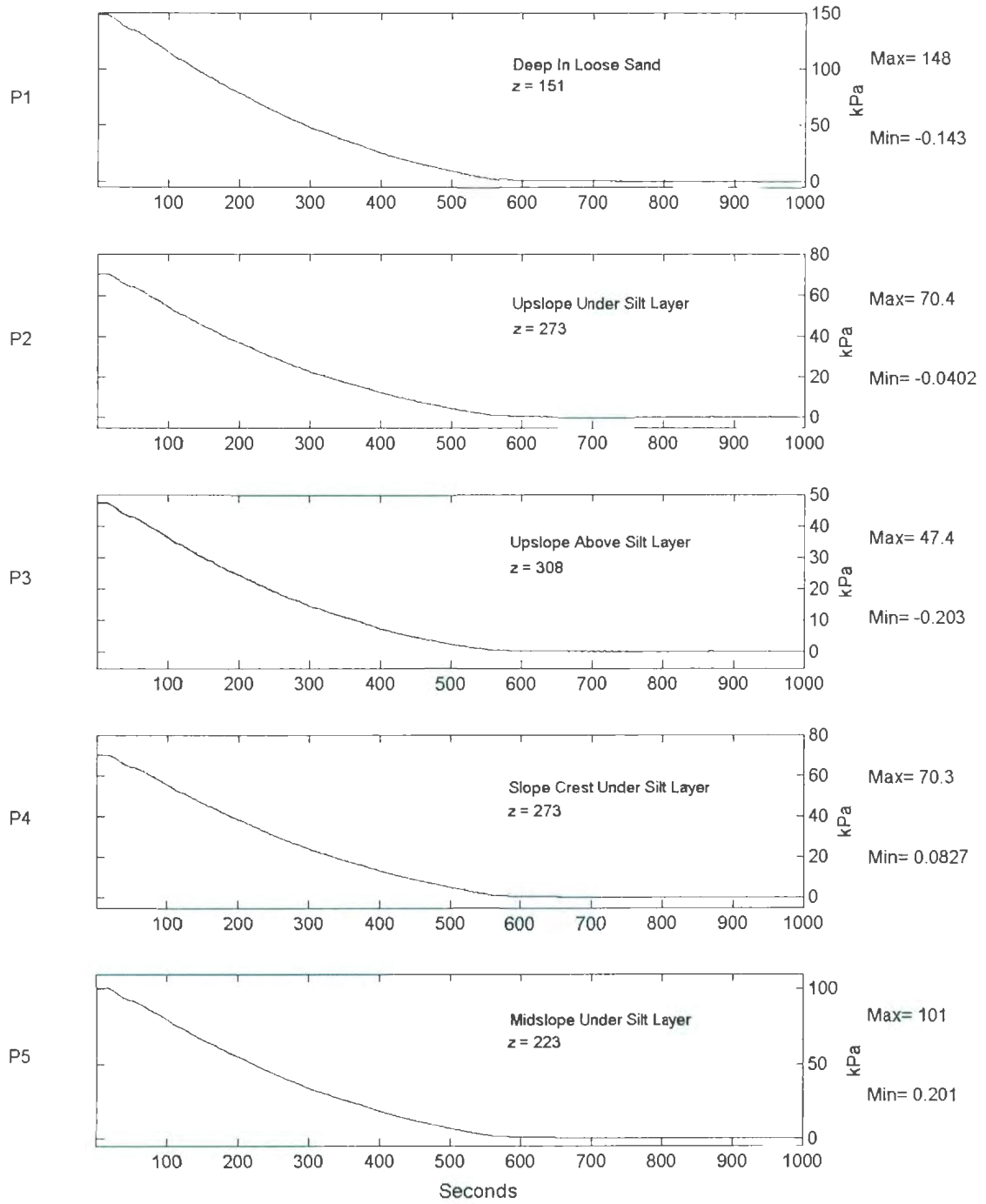
Figure 6.19: COSTA-A PPT Response During Swing-Down for P1-P5.
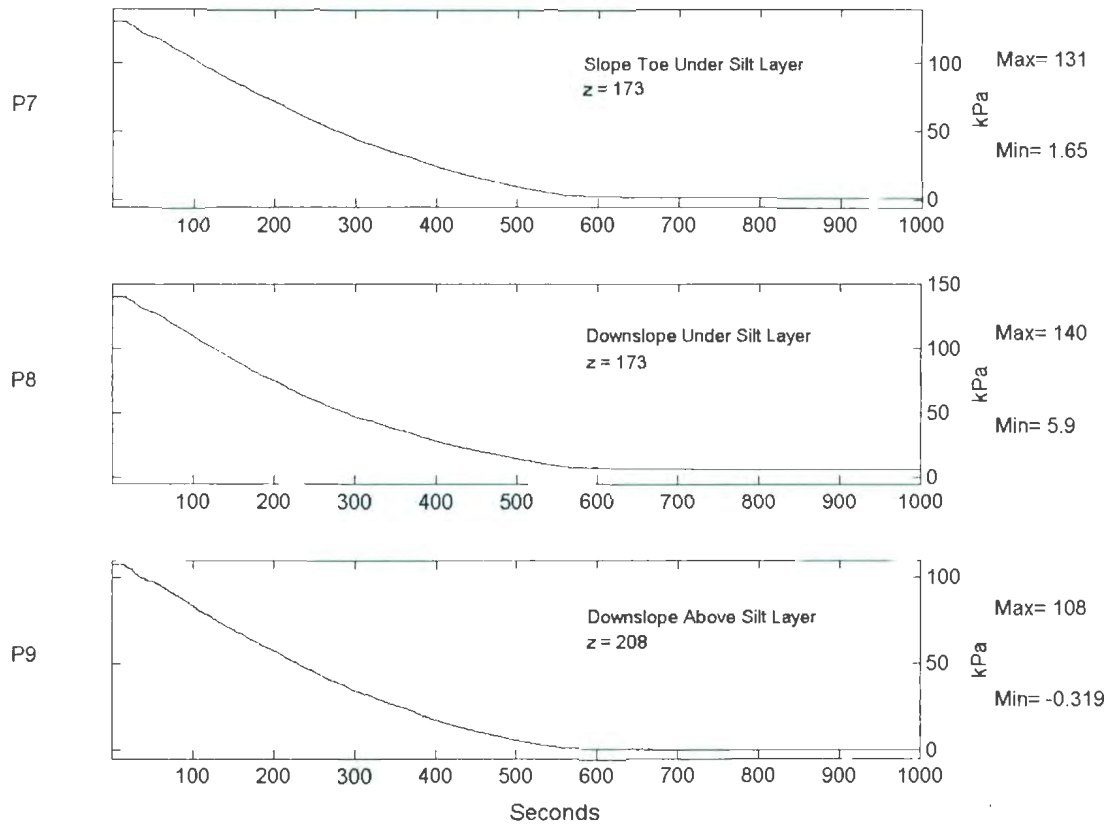
Figure 6.20: COSTA-A PPT Response During Swing-Down for P7-P9.
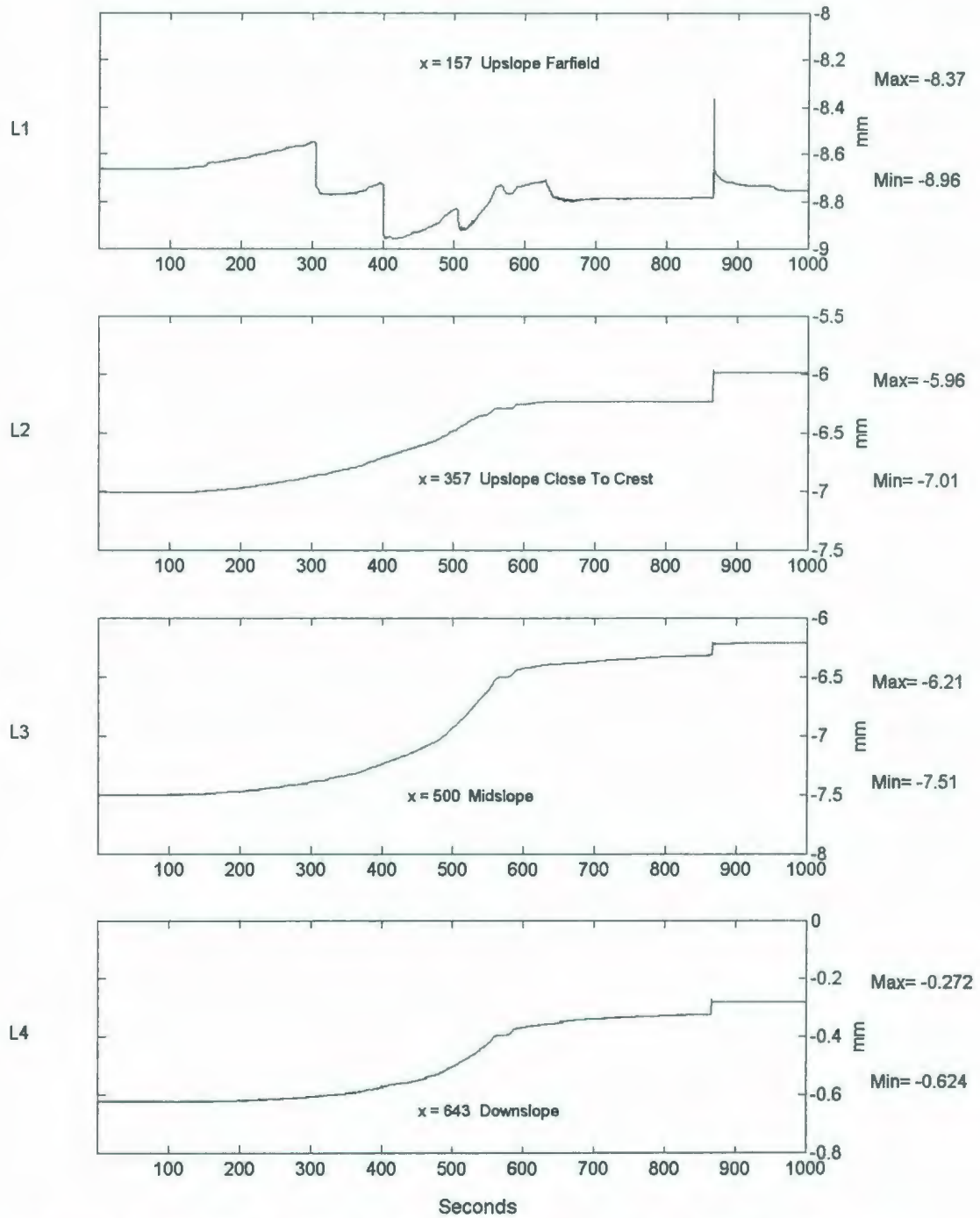
Figure 6.21: COSTA-A LVDT Deformation Response During Swing-Up for L1-L4.

All PPTs seem to experience the correct rate of reduction of pore pressure as the g-level decreases indicating that there were no large changes in pore pressure during swing-down. All PPTs return to a value of approximately zero, with the exception of P8, which returns to 5.9 kPa. This PPT seems to be retaining some of the pressure that was applied during the test.

Looking at the response of the LVDTs there is some strange behaviour observed at about 875 seconds, which is most likely due to some change in the electrical system that acquires the data or by someone bumping the centrifuge basket after it had stopped. Just as in Section 11.2, the observed responses of LVDTs are opposite to what is being experienced by the models. Considering this, it is apparent that L2, L3, and L4 indicate that the model decompresses as the model swings down. Some of this behaviour can also be attributed to the elastic recovery of the support beam to which the LVDT instruments were attached. L1 experiences some very strange behaviour which might be possibly explained by the foot pad of the LVDT somehow moving around on the surface of the model or possibly the LVDT housing moving around or becoming loose from its mount. This type of response was to be alleviated with the reconfiguration of the LVDT spindles as discussed in Chapter 5.

During COSTA-A it was observed that the temperature of the model was increased beyond the planned 20°C due to the operation of the EQS hydraulic system. However, no

definitive temperature observations were undertaken. In future tests, this temperature was monitored at various stages of model preparation on the day of the test.

After the centrifuge flight was completed, the profile of the model surface was measured while model was still situated on the arm. The results shown in Table 6.2 and Figure 6.22 showed little change in the profile of the model compared to the measurements taken prior to the test. Most of the settlement occurred in the farfield location where the model settled less than 10 mm. A small amount of heave, on the order of 3 mm, was observed at the toe of the model. No other signs of failure were observed from this process.

Table 6.2: COSTA-A Post-Test Surface Profile.

Distance from Upslope End (mm)	Pre-Test Surface Height (mm)	Post-Test Surface Height (mm)
0	334	328
50	335	325
100	334	327
150	337	327
200	335	327
250	336	327
300	334	326
350	329	320
400	325	317
450	309	307
500	286	282
550	258	259
600	245	246
650	244	242
700	242	245
737	240	243
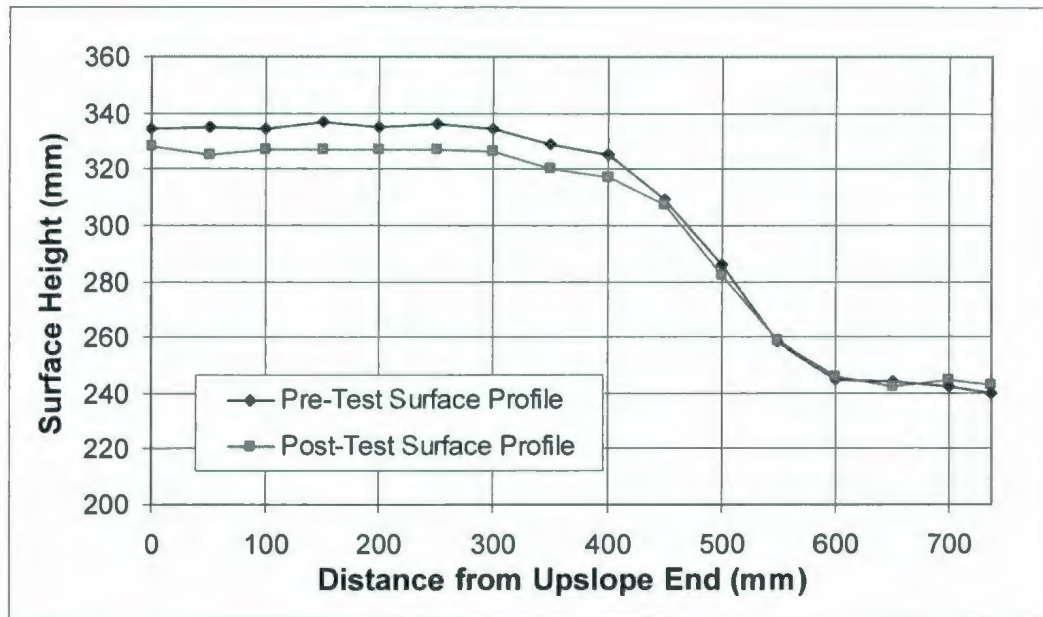
Figure 6.22: COSTA-A Post-Test Surface Profile.

As discussed in Chapter 5, no surface markers were used in this experiment. However, in subsequent tests small white pieces of gravel were placed on the slope face prior to saturation in a square grid measuring approximately 25 mm by 25 mm grid. Photographs of this grid taken prior to saturation and then again after the test after draining the free fluid will enable qualitative comparisons of the before and after marker grid. This should yield insight into the movement of the slope face during the test. In addition, if it is noticed that the grid deforms in any way during movement observations can be made regarding the amount of friction that the model is experiencing with the interface of the walls of the model container.

Following the test the model was transported off the centrifuge arm to the lab floor where it was drained and excavated. During excavation, the position of the internal instruments was noted as shown in Chapter 6. Additionally, the location of the installed silt layer was measured and the height of this layer as well of a comparison with its intended position is given in Table 6.3 and Figure 6.23. The values presented are for the top of the silt layer. It was also observed that the silt layer had compressed by approximately one-third, leaving it approximately 10 mm thickness in model scale. No significant mixing of the Fraser River sand and the Sil-Co-Sil silt was observed, except a small amount of silt that seemed to have made its way to the surface of the model either during saturation or possibly during the liquefaction observed during the test that was observed in P3. No horizontal movement of the silt layer was observed, indicating that no sliding had occurred. The vertical location of the silt layer decreased more in the farfield than on the slope. This observation mirrors the observations of the model surface profile. The change in silt layer position can be contributed to the compression of the installed silt material as well as the densification of the model below the silt layer due to earthquake shaking.

Table 6.3: COSTA-A Silt Layer Profile.

Distance from Upslope End (mm)	Pre-Test Silt Profile	Post-Test Silt Profile
100	298	273
200	298	274
300	298	273
400	298	269
500	248	238
600	198	188
700	198	186
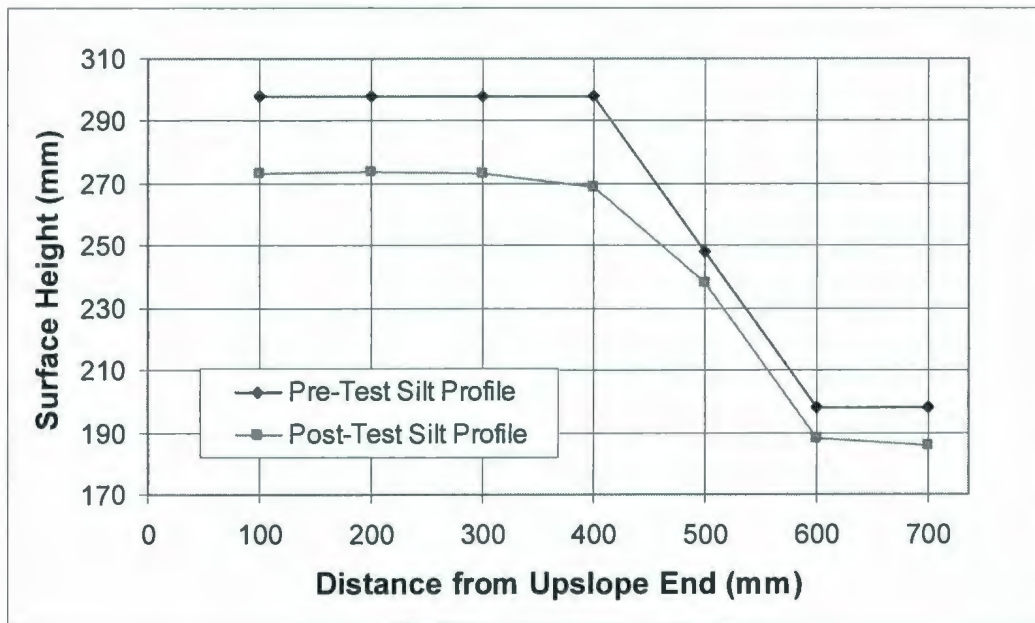
Figure 6.23: COSTA-A Silt Layer Profile.

6.2   COSTA-B

6.2.1   Pre-Test Observations

The pre–test surface profiles are shown in Table 6.4 and Figure 6.24. There is little change between the post-saturation and post-test profile. However, it appears that the crest of the slope has decreased by 26 mm between construction and pre-test conditions, showing some slumping of the model. The farfield pre-test settlement although is less than what was experienced in COSTA-A as discussed in Section 6.1.1.

Table 6.4: COSTA-B Pre-Test Surface Profile.

Distance from Upslope End (mm)	Post Construction Profile	Post Saturation Profile	Pre Test Profile
0	343	338	338
50	343	337	336
100	343	336	336
150	343	334	334
200	343	332	331
250	343	332	330
300	343	330	327
350	343	--	322
400	343	--	317
450	319	--	304
500	295	--	278
550	271	--	262
600	247	--	236
650	223	--	207
700	199	--	192
737	175	--	178
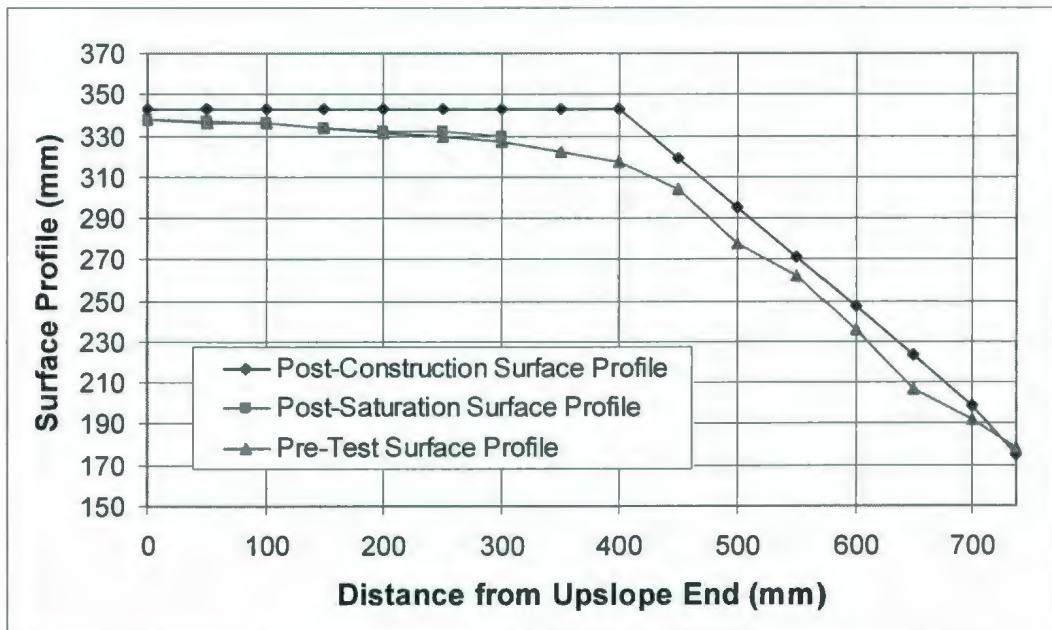
Figure 6.24: COSTA-B Pre-Test Surface Profile.

173

Monitoring of the PPTs during swing-up of the centrifuge showed that all PPTs were operating correctly and that their results showed increased pore pressure at the correct rate considering their position in the model. Observation of the LVDTs at the same time showed that the model experienced a settlement due to self-weight in the order of 2-3 mm, which should not significantly affect the intended relative density of the model. L2, which is used to measure horizontal displacements of the slope above the silt layer, experienced a large response that can be attributed to the tightening of slack in the string and pulley mechanism. It is important to note that in future figures downslope movement is recorded in the negative direction. Table 6.5 shows the estimated relative density based upon the pre-test observations. The calculated relative density directly before the earthquake is 48%, which is greater than the target relative density of 40%. In subsequent tests more care was taken to ensure minimal settlement during all pre-test activities.

Table 6.5: COSTA-B Pre-Shake Observed Relative Density at Farfield.

Condition	Settlement (mm)	Relative Density (%)
Post-Construction	N/A	34
Post-Saturation	5.0	43
Post-Loading	0.0	43
After Spin-Up	2.5	48

Like the COSTA-A test the saturation of this model was to be checked by observing the travel time of acoustic waves through the model. However, the acoustic wave hammer device failed to operate shortly after the start of the centrifuge flight and no data was acquired.

6.2.2 A2475 Earthquake Actuation

The testing regime for the COSTA-B test was comprised of two separate earthquake events, the A2475 event then after a period of several minutes to allow the generated pore pressures to dissipate, the application of the 2A2475 event. The top portion of Figure 6.25 illustrates the desired A2475 acceleration-time history in model scale. The bottom portion of Figure 6.25 shows the observed earthquake signal in Tz, which is in the direction of shaking. Figure 6.26 shows the fast Fourier transforms (FFT) of these two signals. The two signals compare relatively well with respect to frequency as well as magnitude. The actual observed earthquake being slightly larger in magnitude. In terms of frequency content, as observed in the FFT signals, it is observed that the EQS delivered an earthquake with larger content in the 40 to 50 Hz range and almost identically matching it in the 50 to 60 Hz range, which is an improvement over the COSTA-A observations. These results can be considered as a good agreement between the prescribed and observed earthquake motions. Figure 6.27 illustrates the response of the triaxial accelerometer in the vertical direction. This response was captured by Ty and shows that there is a spurious vertical motion that is experienced during the earthquake event. The range of this acceleration ranges between +2 to −8 g and is mostly characterized by spikes in the negative direction. These spikes are probably unreal as this accelerometer failed completely shortly after this centrifuge test.
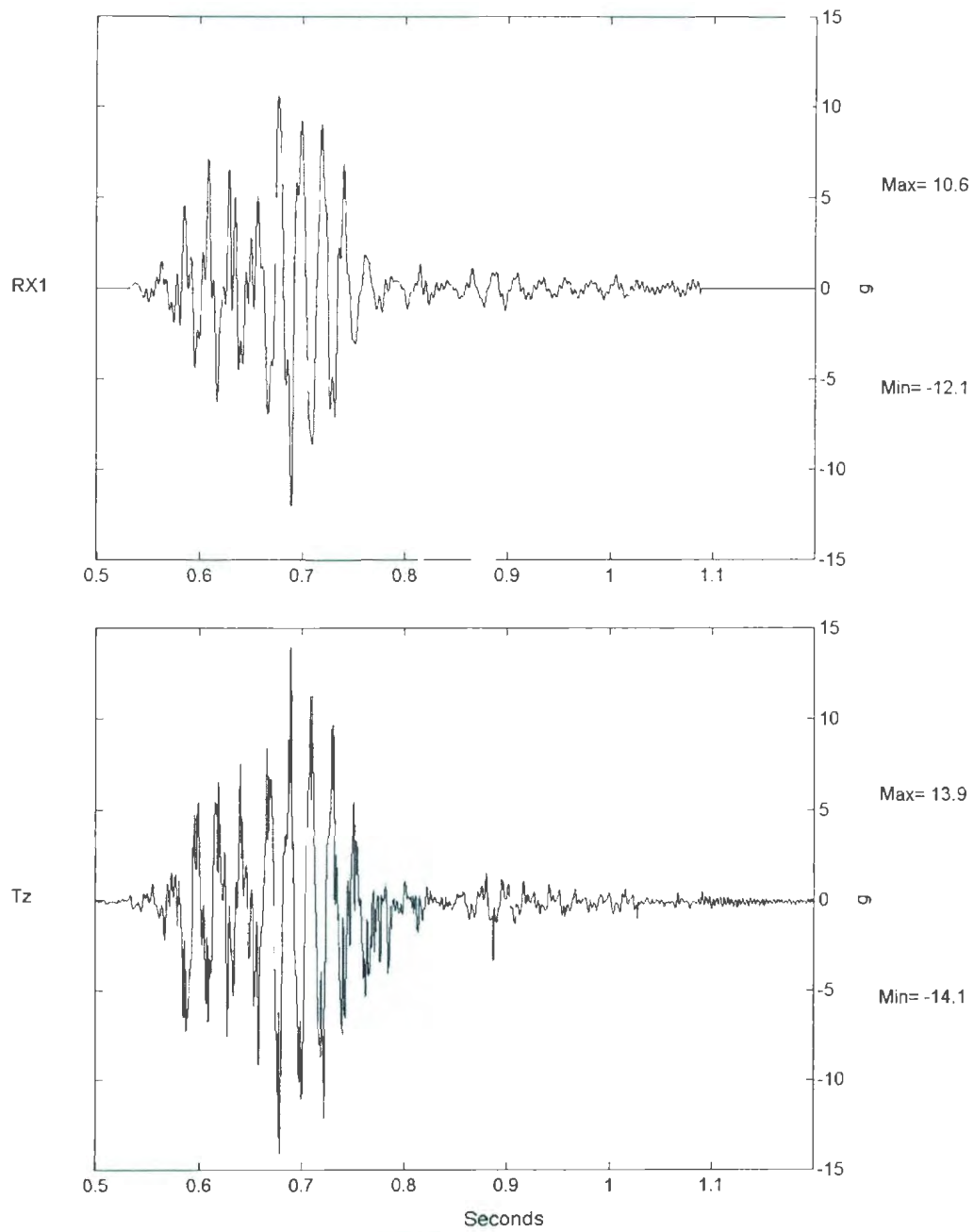
Figure 6.25: Comparison of A2475 Earthquake Record & Observed COSTA-B Tz
Acceleration.

176
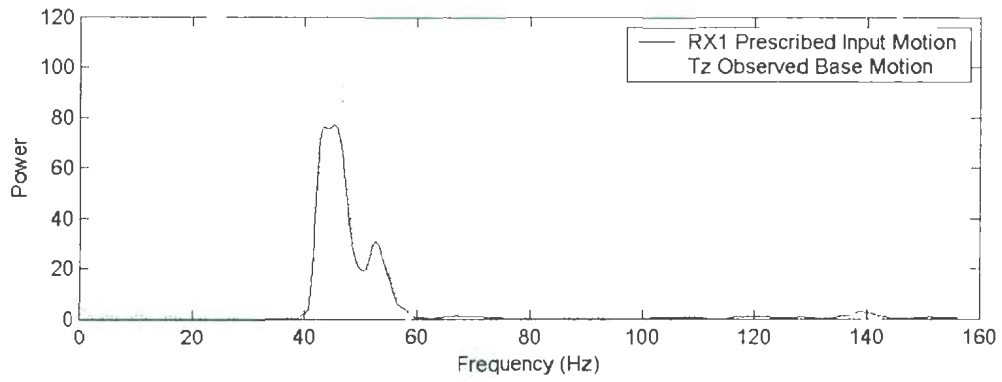
Figure 6.26: FFT Comparison of A2475 Earthquake Record & Observed COSTA-B Tz Acceleration.
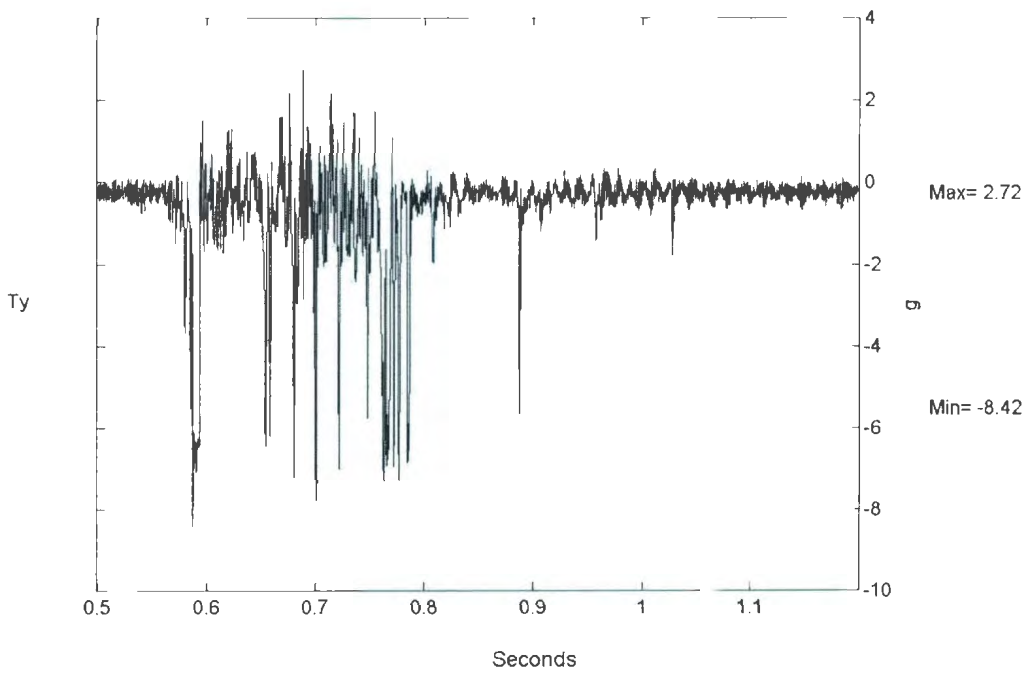
Figure 6.27: COSTA-B A2475 Observed Ty Vertical Acceleration Response.

6.2.3 *A2475 Short-Term Testing Instrument Responses*

All instruments were monitored during and shortly after the A2475 earthquake event. Figures 6.28 through 6.32 illustrate the observed responses in the various instruments during a 0.5 second period.
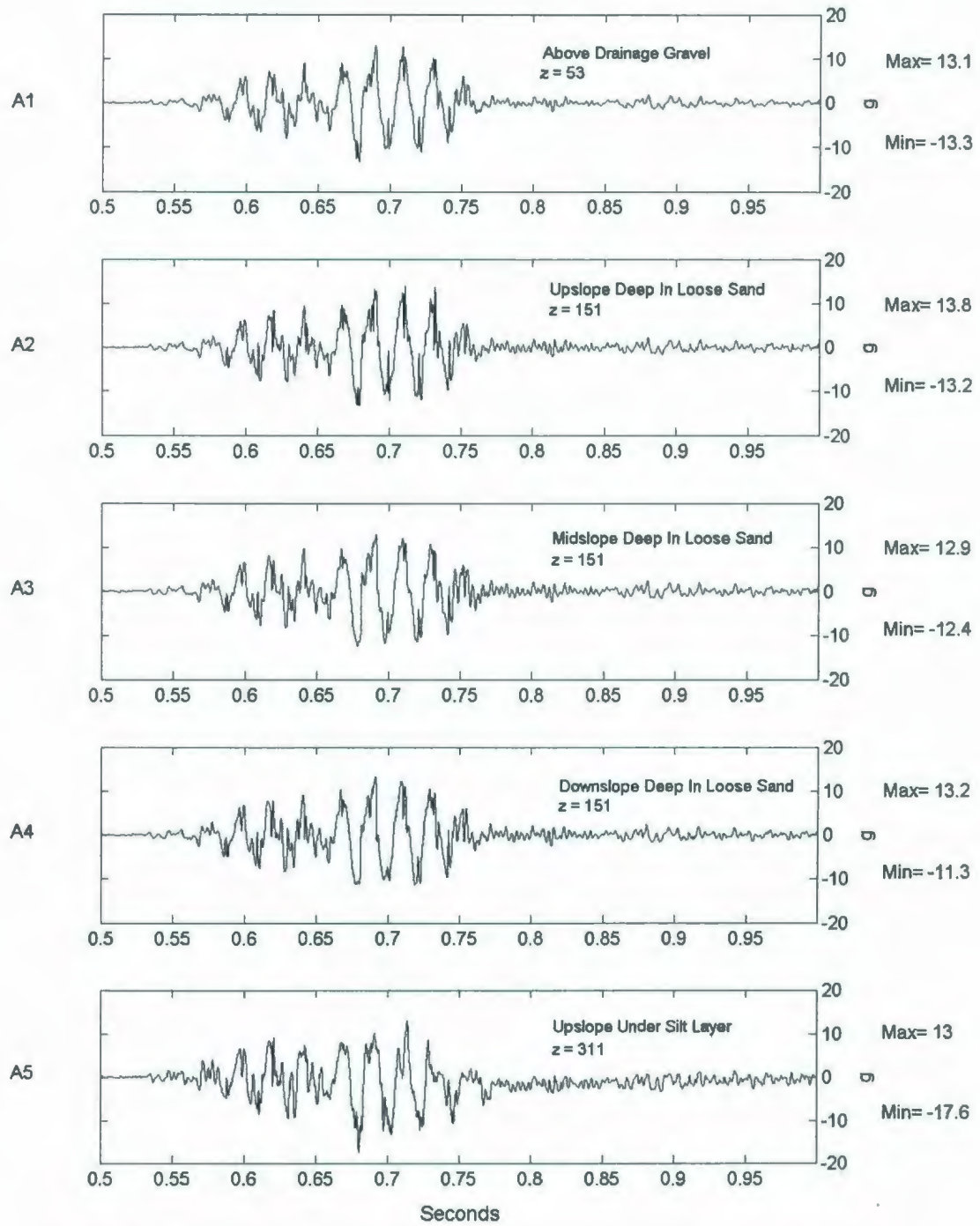
Figure 6.28: COSTA-B A2475 Short-Term Accelerometer Response for A1-A5.
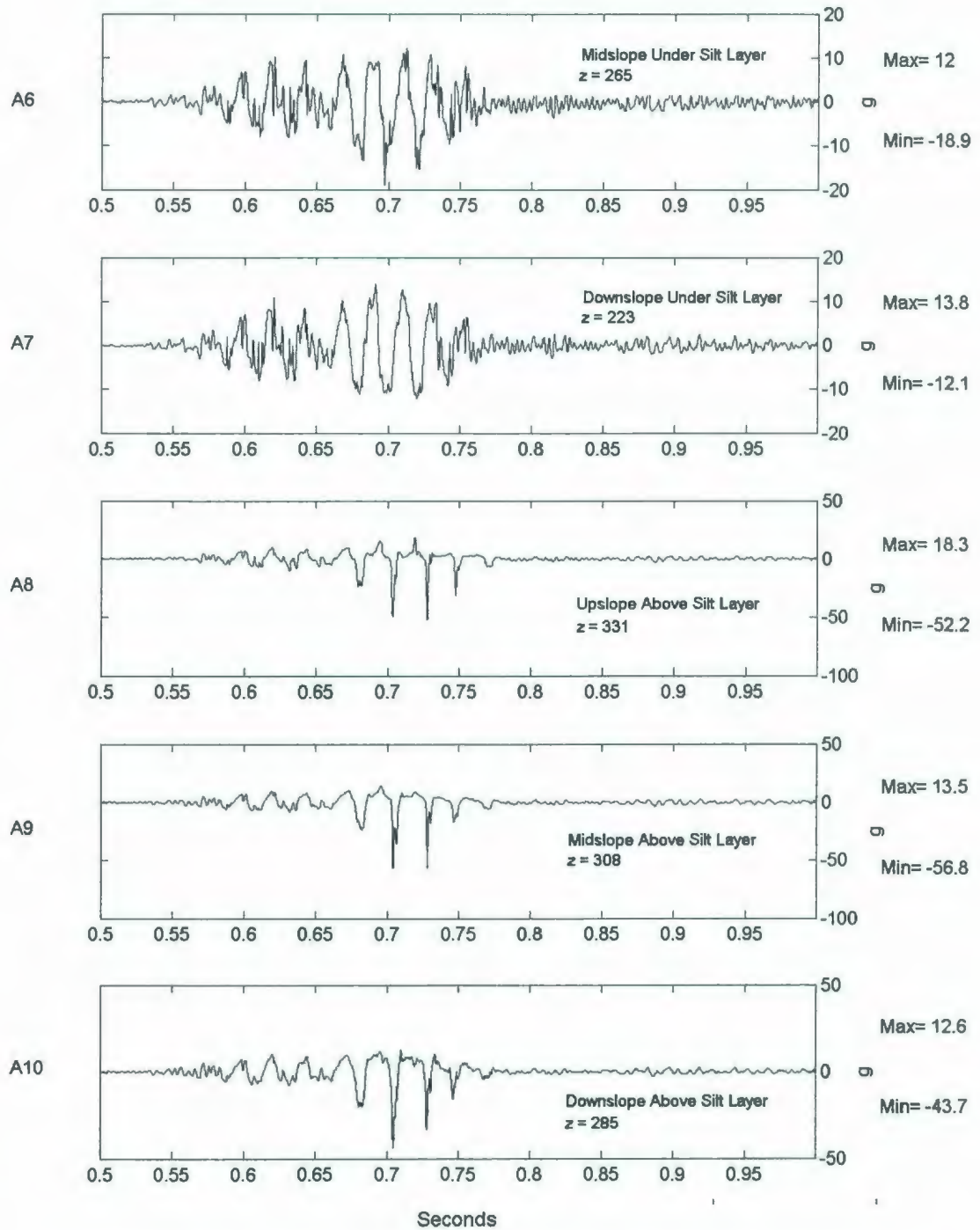
Figure 6.29: COSTA-B A2475 Short-Term Accelerometer Response for A6-A10.

P1

ru = 1 0 @ 301.6 kPa

r_u line is outside vertical axis scale

Upslope Deep In Loose Sand
z = 151

Max= 216

Min= 174

P2

ru = 1.0 @ 270 1 kPa

r_u line is outside vertical axis scale

Midslope Deep In Loose Sand
z = 151

Max= 192

Min= 143

P3

ru = 1 0 @ 228 2 kPa

r_u line is outside vertical axis scale

Downslope Deep In Loose Sand
z = 151

Max= 190

Min= 142

P4

ru = 1.0 @ 47.0 kPa

Upslope Under Silt Layer
z = 326

Max= 51.4

Min= 21.5

P5

ru = 1 0 @ 76 7 kPa

Upslope of Midslope Under Silt Layer
z = 298

Max= 73

Min= 26.5

Seconds

Figure 6.30: COSTA-B A2475 Short-Term PPT Response for P1-P5.

181
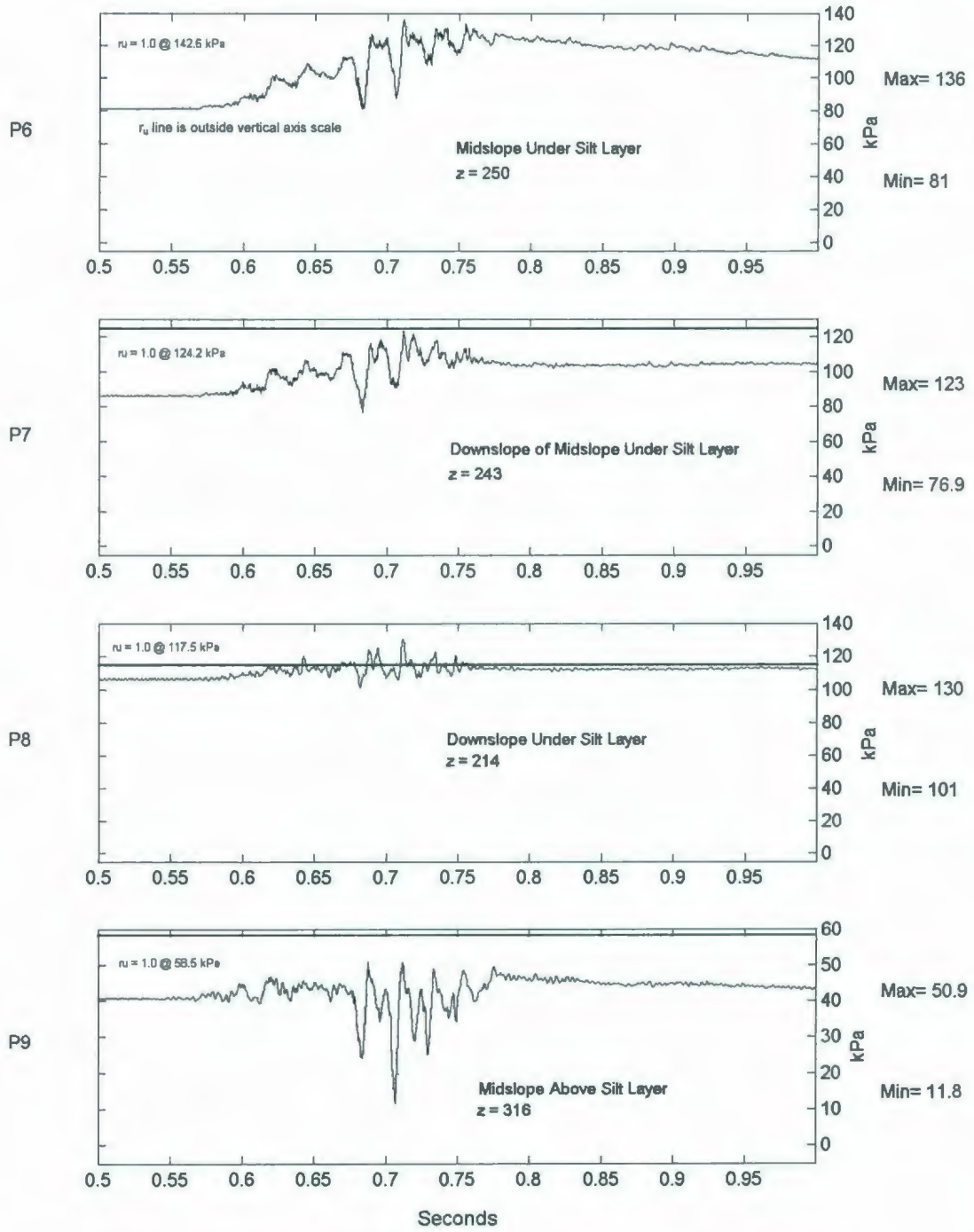
Figure 6.31: COSTA-B A2475 Short-Term PPT Response for P6-P9.
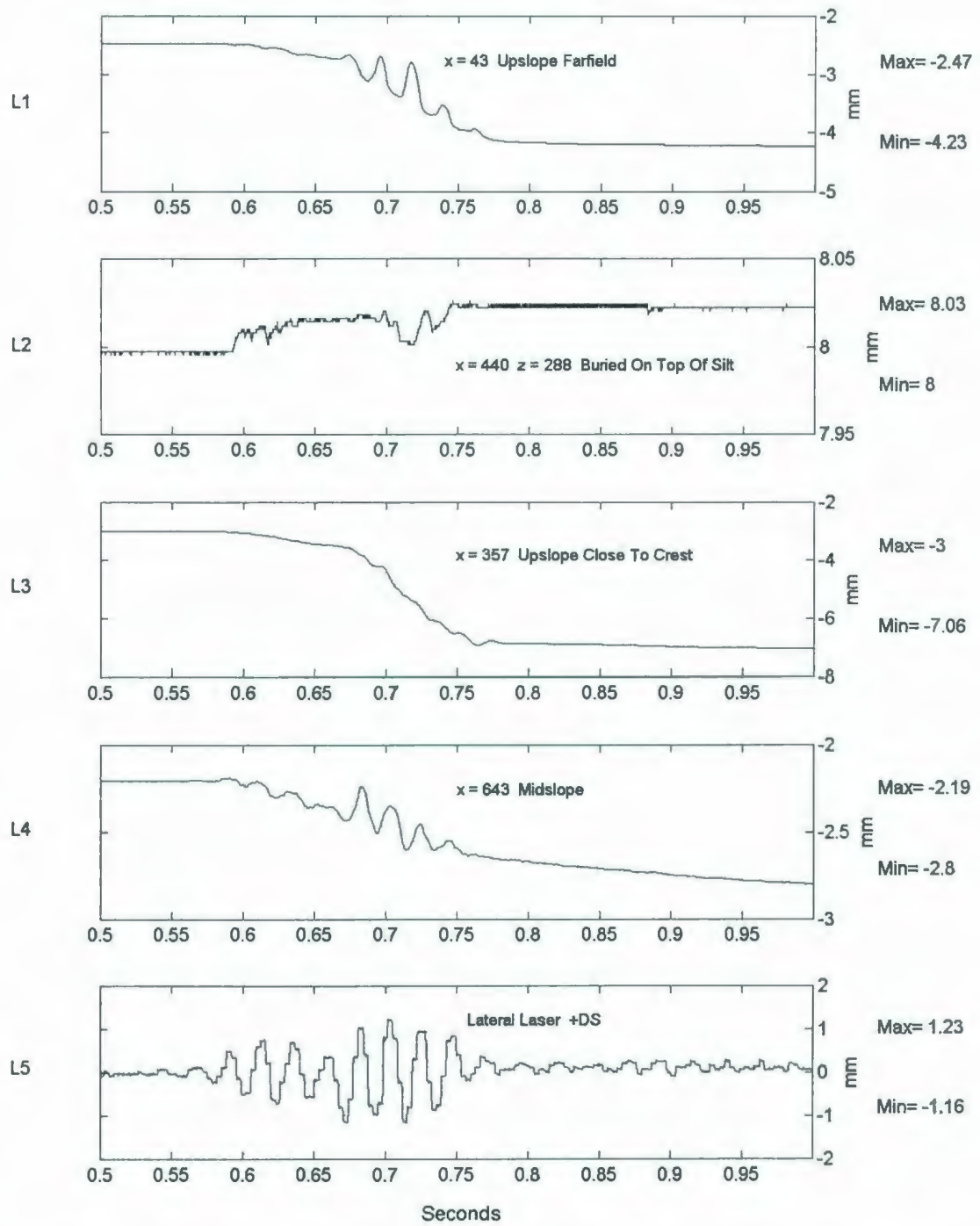
Figure 6.32: COSTA-B A2475 Short-Term LVDT Deformation & Lateral Laser Displacement Responses.

183

In the short-term, it is evident that there is a large increase in the tendency of the accelerometers to measure negative dilation spikes with increased elevation in the model. This is especially evident in the accelerometers that are above the silt layer (A8, A9, & A10). These spikes disappear at the end of shaking after 0.75 seconds. The accelerometers below the silt layer do not experience any such exaggerated negative response. As is mentioned by Taboada-Urtuzuastegui et al. (2002) these upslope spikes, coupled with simultaneous drops in the piezometric responses, tend to limit the downslope accumulation.

There is also evidence to show that there is quicker dissipation of generated pore pressures above the silt layer than below it. PPTs placed above the silt layer (P4, P5, P6, & P7) show an elevated pore pressure level following the majority of the shaking. The PPT placed above the silt layer (P9) did not exhibit this type of behaviour, but did show spikes associated with dilation. This spiking corresponds to the spiking also observed in accelerometers in corresponding locations, P4 and P5. Liquefaction was only observed under the silt layer at the upslope farfield location (P4) and the downslope location (P8).

In terms of surface effects, there is relatively little movement because of the shaking. L1, L3, & L4 show that the surface of the model only settles 1-4 mm and L2 only shows a small amount of movement in the downslope direction. L5 shows no net payload displacement from the earthquake actuation.

184

6.2.4 A2475 Long-Term Testing Instrument Responses

In addition to monitoring the short-term responses for the testing instruments, the long-term responses were also collected to examine the behaviour of the model for several seconds after the A2475 earthquake event. Figures 6.33 through 6.37 illustrate these responses.
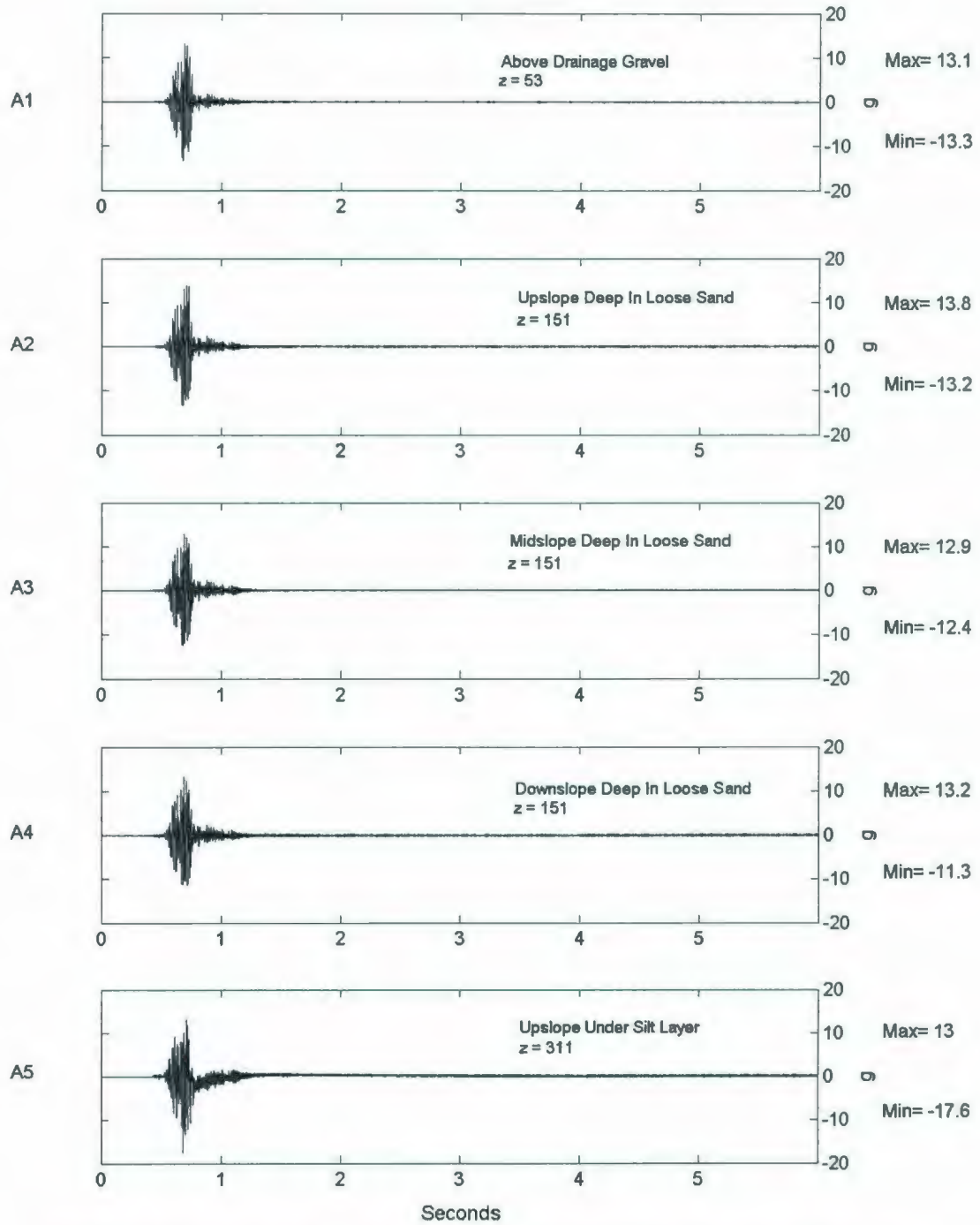
Figure 6.33: COSTA-B A2475 Long-Term Accelerometer Response for A1-A5.
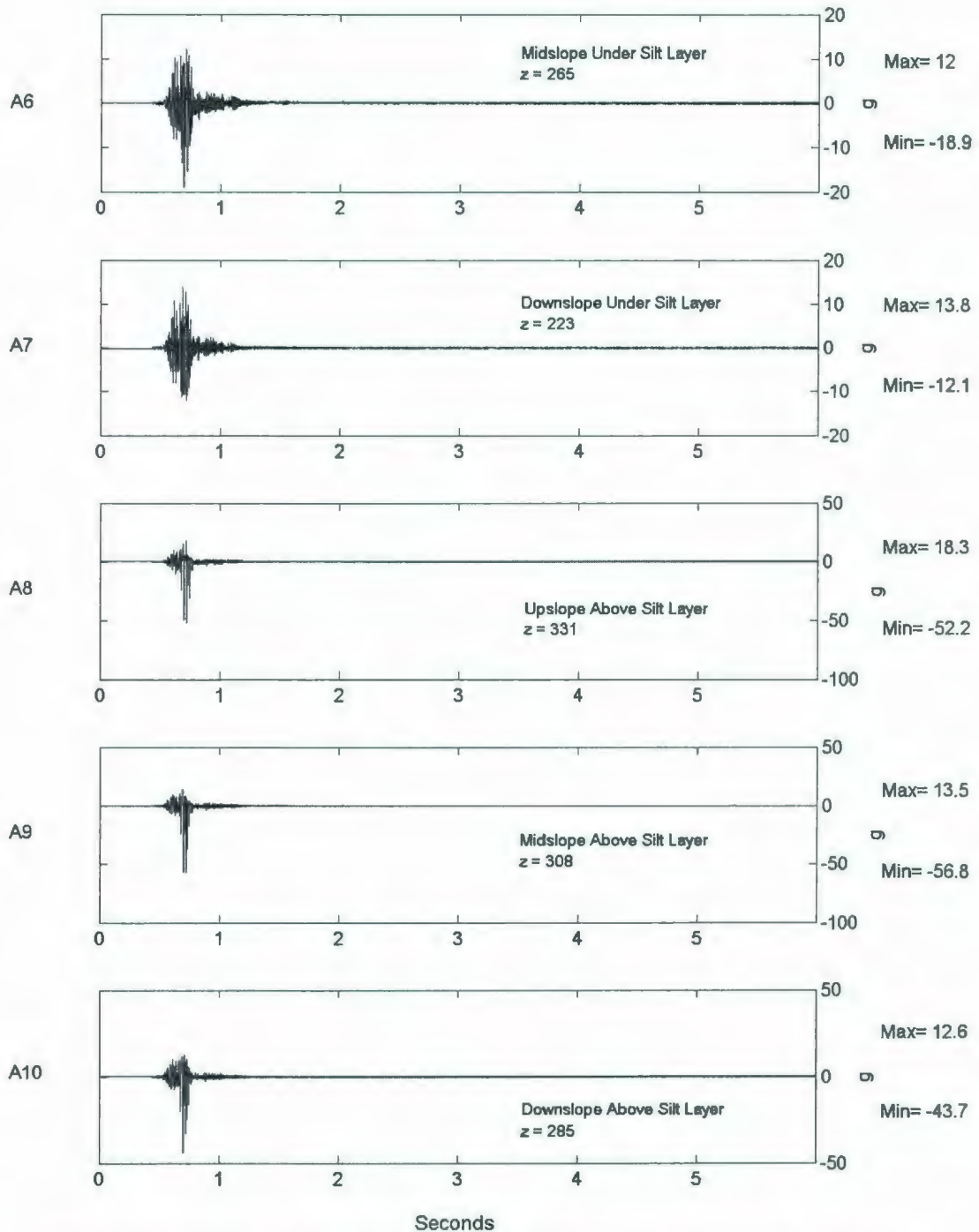
Figure 6.34: COSTA-B A2475 Long-Term Accelerometer Response for A6-A10.

P1

ru = 1.0 @ 301.6 kPa

rᵤ line is outside vertical axis scale

Upslope Deep In Loose Sand
z = 151

Max= 216

Min= 174

kPa

P2

rᵤ = 1.0 @ 270.1 kPa

rᵤ line is outside vertical axis scale

Midslope Deep In Loose Sand
z = 151

Max= 192

Min= 143

kPa

P3

ru = 1.0 @ 228.2 kPa

rᵤ line is outside vertical axis scale

Downslope Deep In Loose Sand
z = 151

Max= 190

Min= 142

kPa

P4

ru = 1.0 @ 47.0 kPa

Upslope Under Silt Layer
z = 326

Max= 51.4

Min= 21.5

kPa

P5

ru = 1.0 @ 76.7 kPa

Upslope of Midslope Under Silt Layer
z = 298

Max= 73

Min= 26.5

kPa

Seconds

Figure 6.35: COSTA-B A2475 Long-Term PPT Response for P1-P5.

188
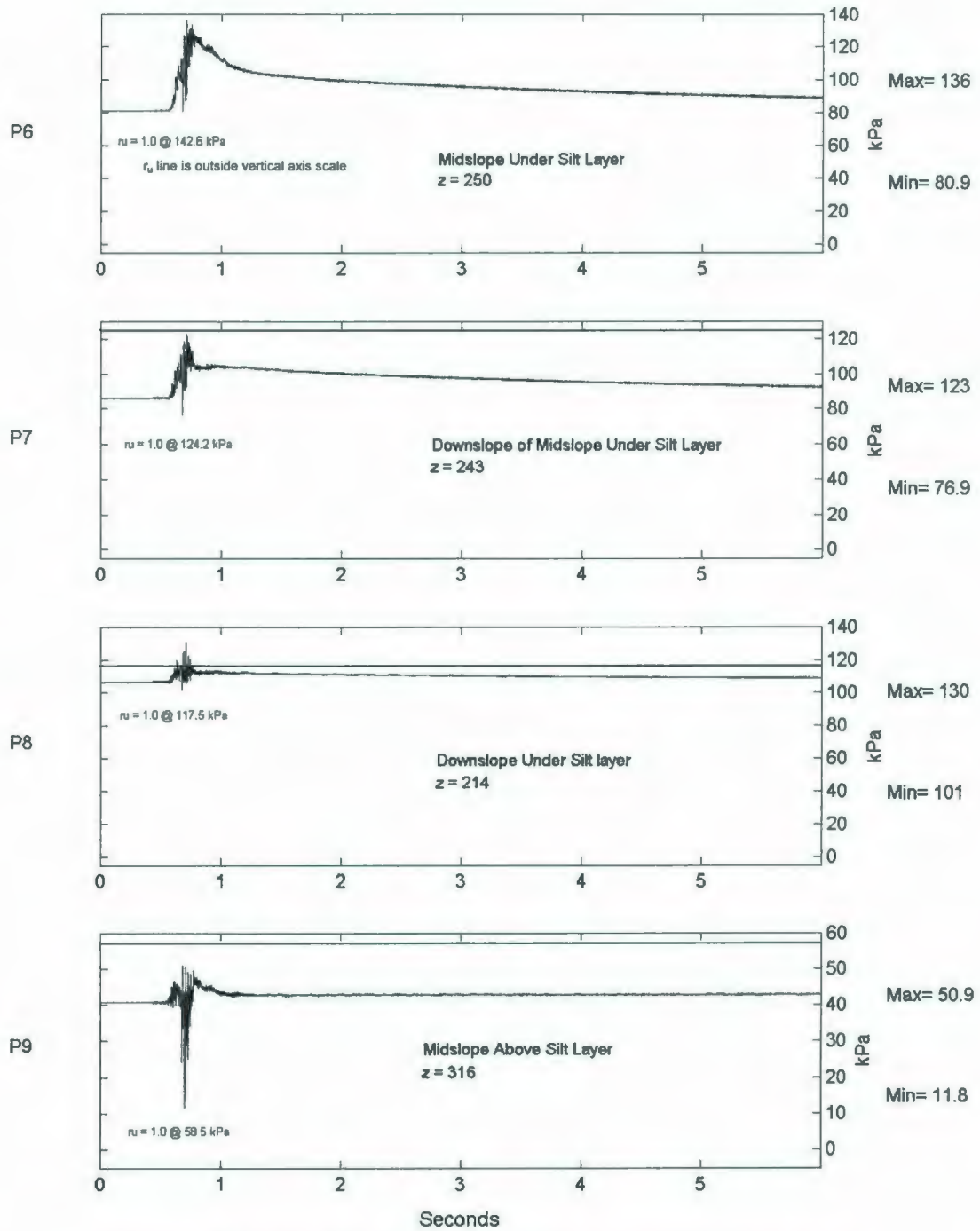
Figure 6.36: COSTA-B A2475 Long-Term PPT Response for P6-P9.
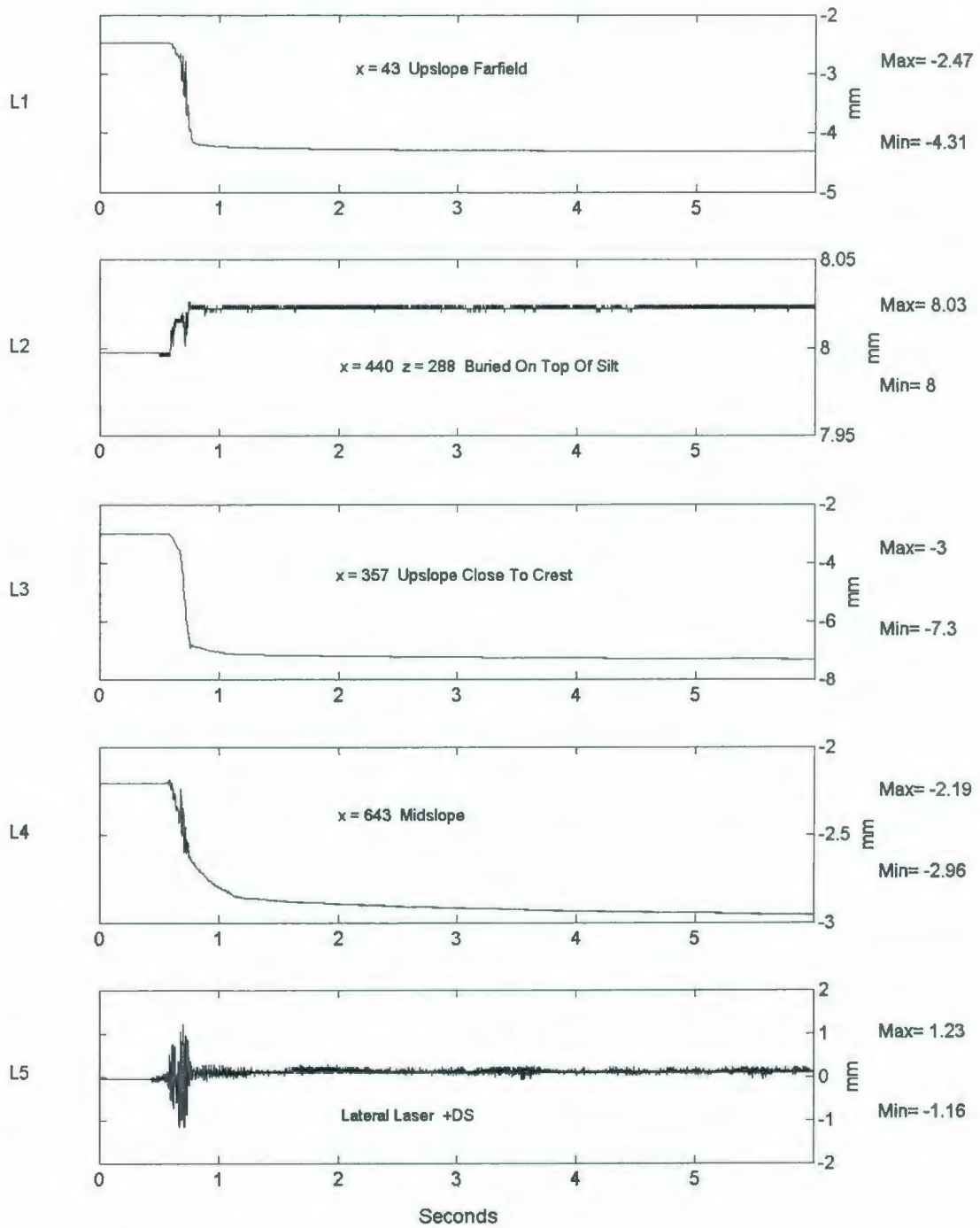
Figure 6.37: COSTA-B A2475 Long-Term LVDT Deformation & Lateral Laser
Displacement Responses.

190

Long-term accelerometer results show that the accelerometers recover to pre-shake levels fairly uniformly after the shaking, with the exception of A5 where the response indicates a negative tendency in observed acceleration that recovers during the cessation of shaking. The long-term results also serve to highlight the importance of the negative spikes in observed acceleration above the silt layer.

The long-term results show that there is indeed a great deal of slower pore pressure dissipation below the silt layer than above it. The response of P7 compared to P9 is a good example of this where it takes several seconds for the pore generated pore pressure underneath the silt layer to return close to its pre-shake levels. Additionally, several PPTs, including P1, P2, P3 & P4, do not return to their hydrostatic pre-shake levels during the long-term observation period. This delayed dissipation is the major trend of all of the PPTs that are directly below the silt layer. This is in contrast to P9 where the pore pressure returns to its pre-shake level shortly after the cessation of the quake. The liquefaction experienced in P4 ceases at about 1 second. The large negative spike in P9 is also evident in the long-term records. This is a corresponding effect to the negative spikes experienced in the same location with the accelerometers.

Surface settlement in L1, L3 & L4 occurred only during the short-term observation period with only a small amount of movement occurring following the earthquake. L4, placed on the midslope, does experience a small amount of continued movement on the

order of 0.1 mm between 1 and 6 seconds. There is no observed long-term horizontal slope movement observed in L2.

6.2.5 2A2475 Earthquake Actuation

Much like, the behaviour observed in the COSTA-A test, as discussed in Section 6.1.4, P4 shows continued liquefaction and increased pore pressure during the period in which generated excess pore pressure is dissipating. In addition, L1 shows a small amount of surface settlement during this post-earthquake period from the compression of liquefied material. The continued liquefaction, then, is most likely due to the continued migration of excess generated pore pressure from deeper down in the model.2A2475 Earthquake Actuation.

As mentioned in Section 1.2.2 the second part of the COSTA-B test involved applying the 2A2475 earthquake. The top portion of Figure 6.38 illustrates the desired 2A2475 acceleration-time history in model scale and the bottom portion of Figure 6.38 shows the observed earthquake signal in Tz, which is in the direction of shaking. Figure 6.39 displays the fast Fourier transforms (FFT) of these two signals. The two signals compare relatively well with respect to frequency as well as magnitude. The actual observed earthquake being slightly larger in magnitude, especially in the negative direction. In terms of frequency content, as observed in the FFT signals, it is observed that the EQS delivered an earthquake with larger content in the 40 to 50 Hz and 50 to 60 Hz ranges. These results can still be considered as a good agreement between the prescribed and

observed earthquake motions. Figure 6.40 illustrates the response of the triaxial accelerometer in the vertical direction. This response was captured by Ty and shows that there is a spurious vertical motion that is experienced during the earthquake event. The range of this acceleration ranges between +4 to -10 g and is mostly characterized by a large drop to -6 g shortly before 0.8 seconds. This again is evidence of the eventual failure of this instrument, as previously discussed in Section 6.2.2.
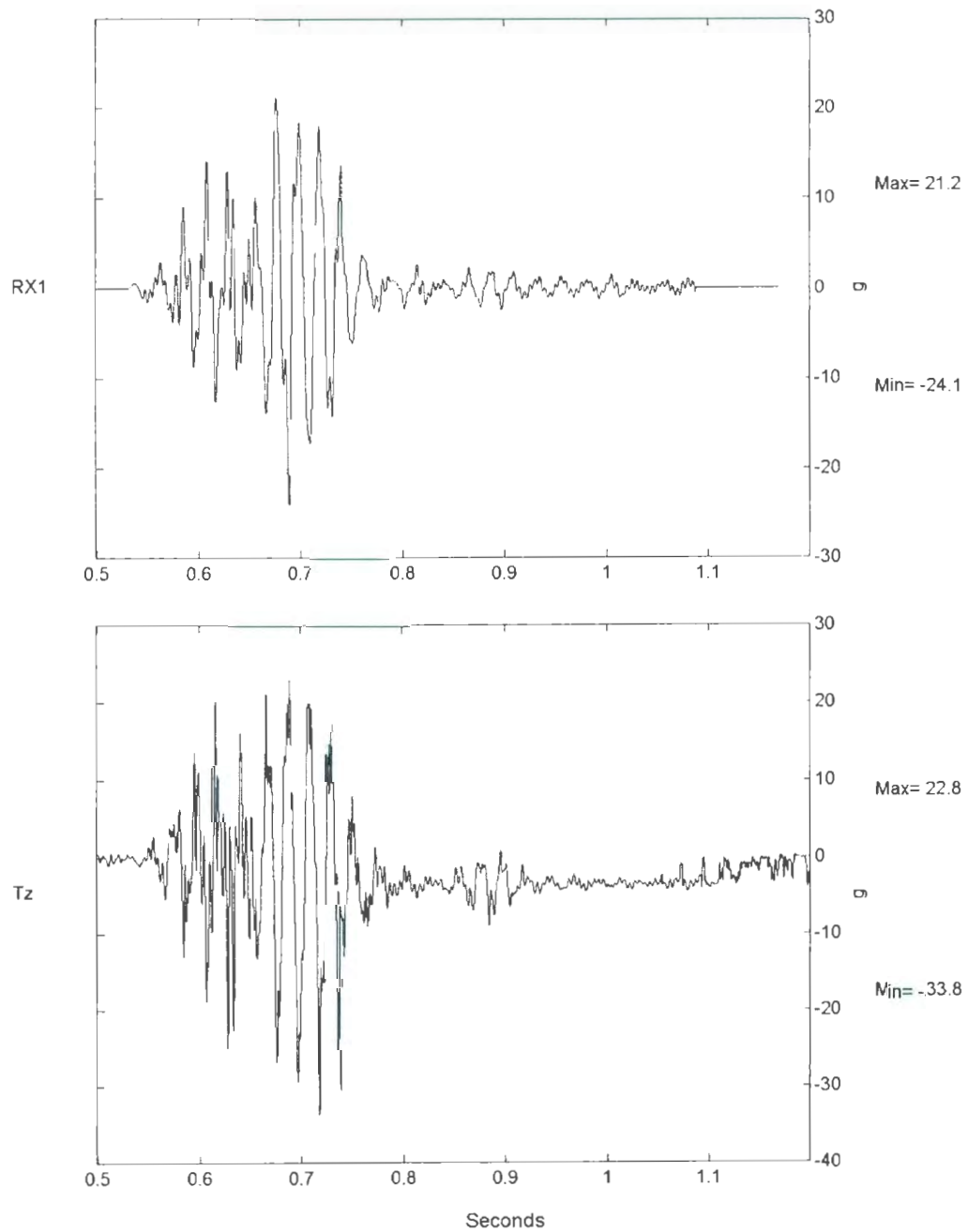
Figure 6.38: Comparison of 2A2475 Earthquake Record & Observed COSTA-B Tz Acceleration.
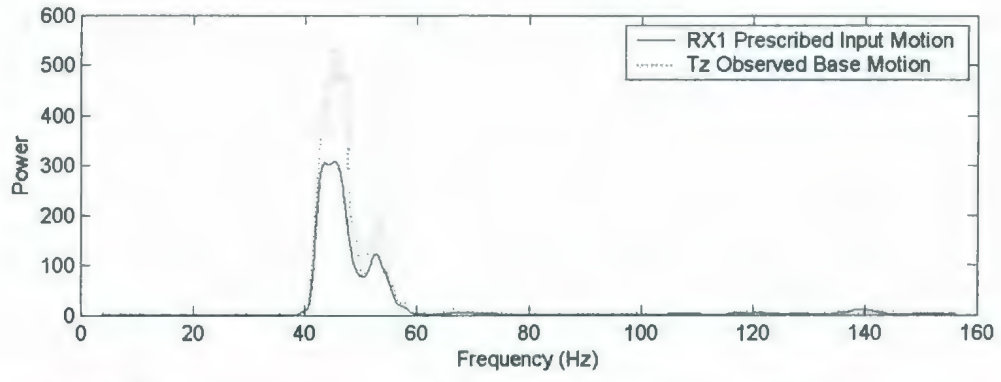
Figure 6.39: FFT Comparison of 2A2475 Earthquake Record & Observed COSTA-B Tz Acceleration.
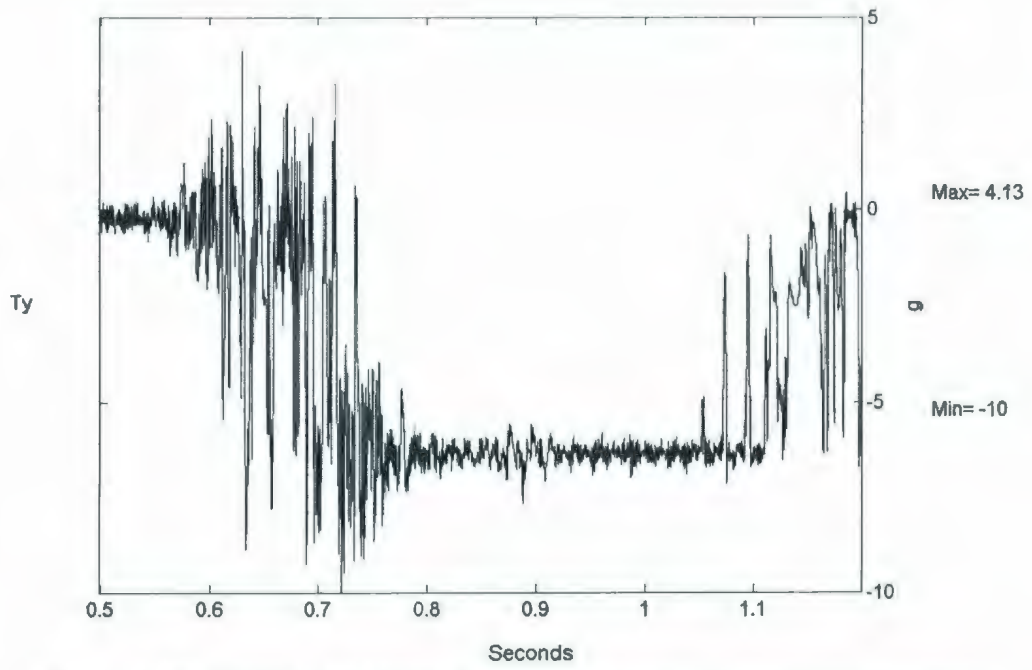
Figure 6.40: COSTA-B 2A2475 Observed Ty Vertical Acceleration Response.

195

6.2.6 2A2475 Short-Term Testing Instrument Responses

Likewise to the COSTA-B A2475 event, all instruments were monitored during and shortly after the 2A2475 earthquake event. Figures 6.41 through 6.45 present the observed responses in the various instruments during a 0.5 second period.
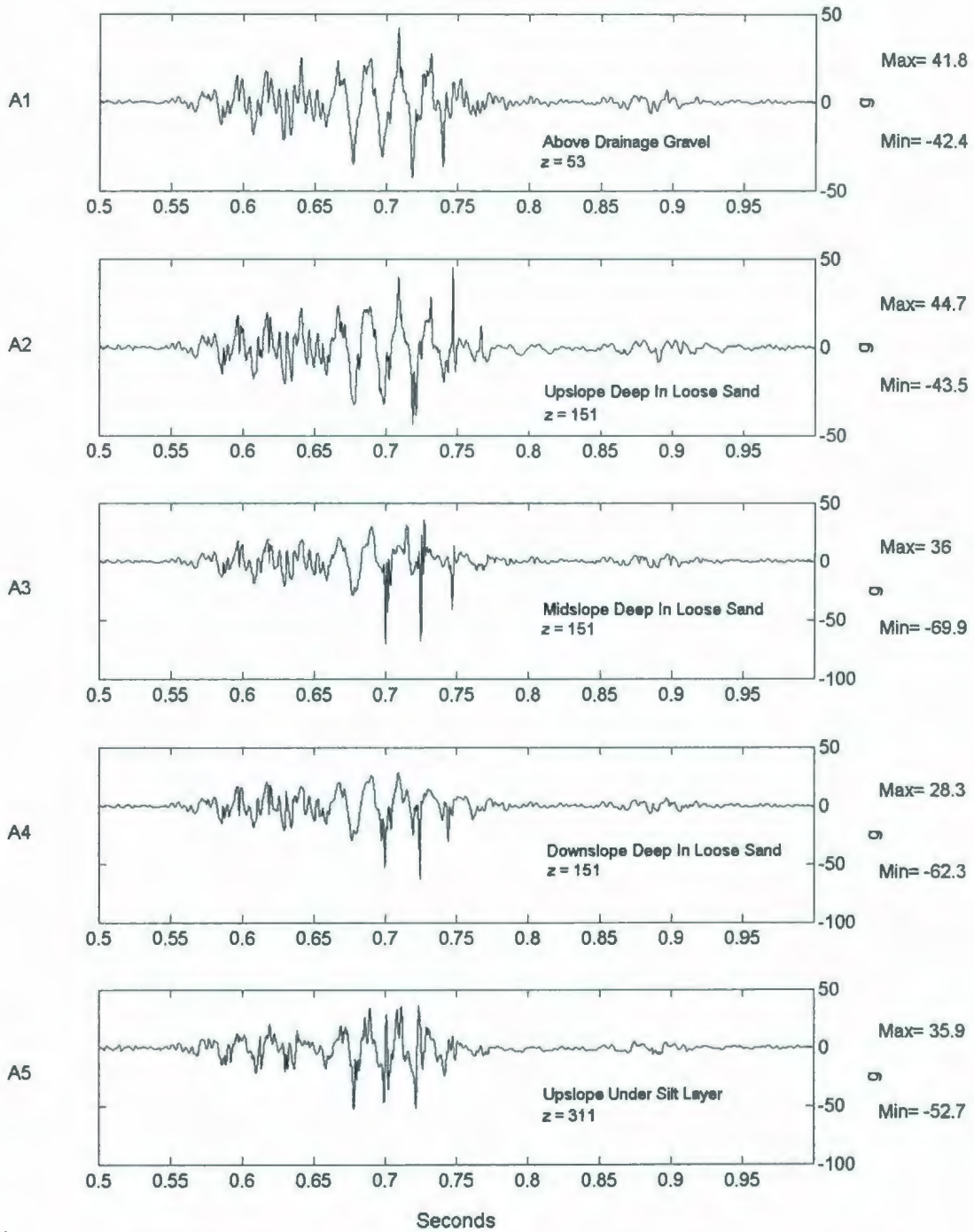
Figure 6.41: COSTA-B 2A2475 Short-Term Accelerometer Response for A1-A5.
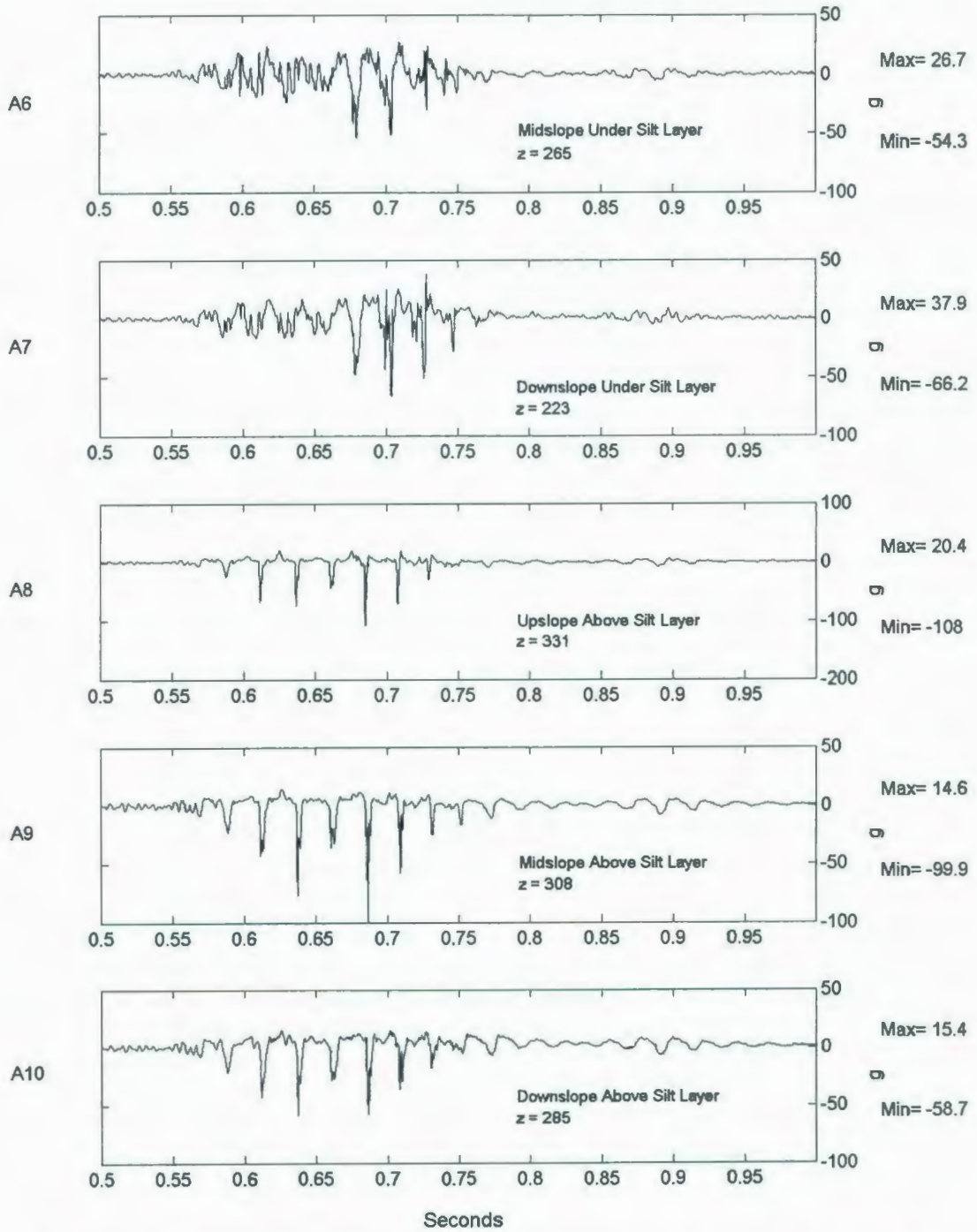
Figure 6.42: COSTA-B 2A2475 Short-Term Accelerometer Response for A6-A10.
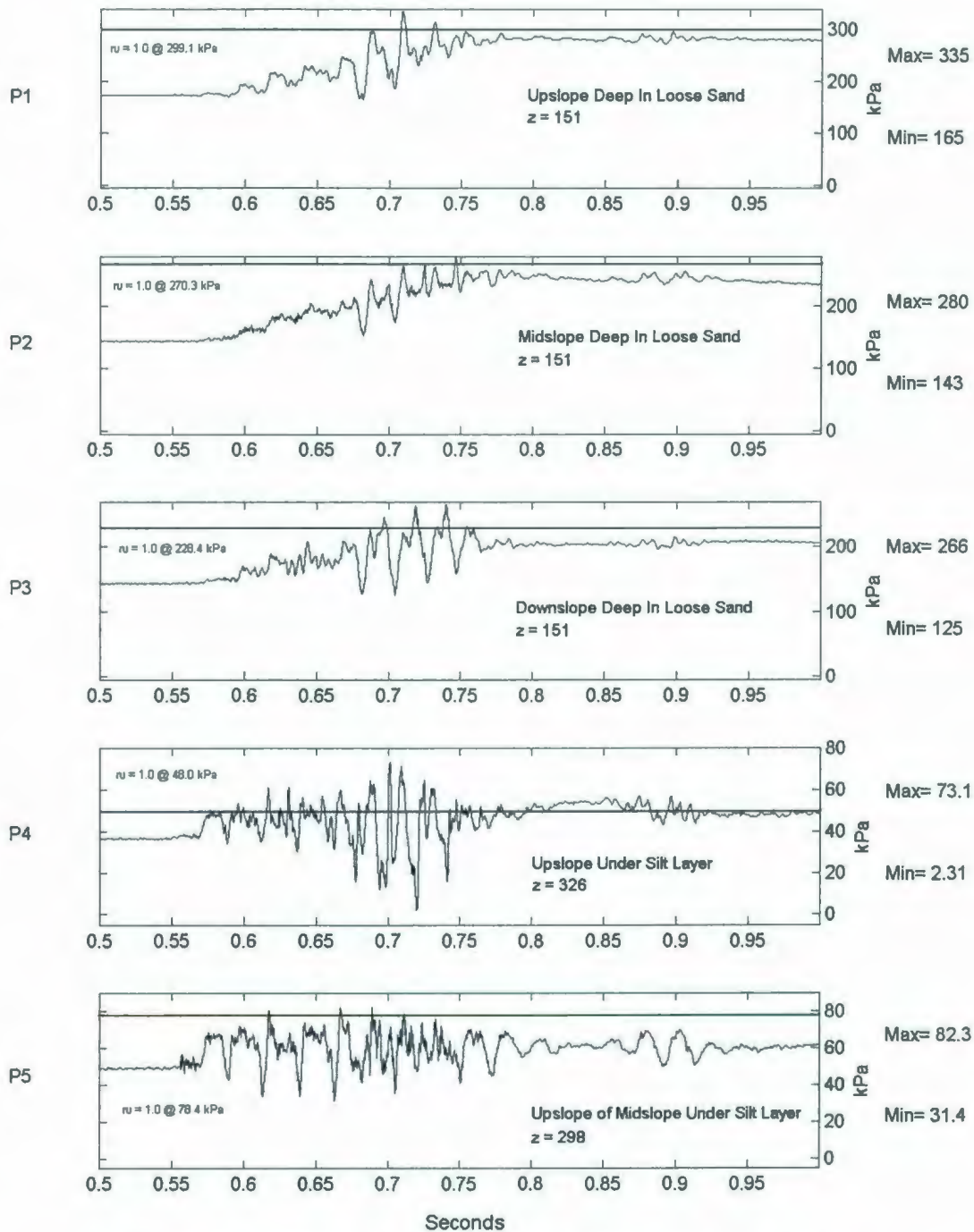
Figure 6.43: COSTA-B 2A2475 Short-Term PPT Response for P1-P5.
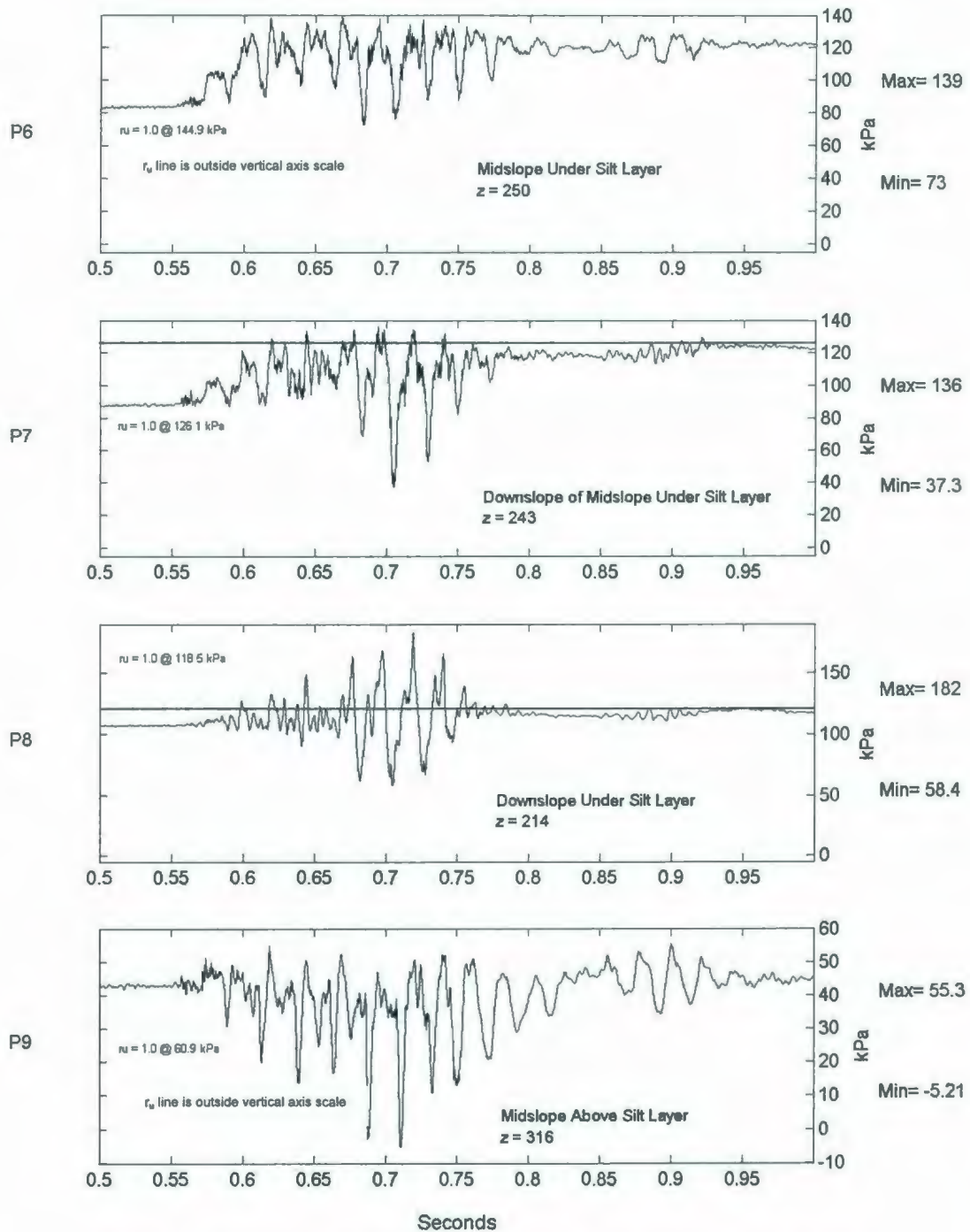
Figure 6.44: COSTA-B 2A2475 Short-Term PPT Response for P6-P9.
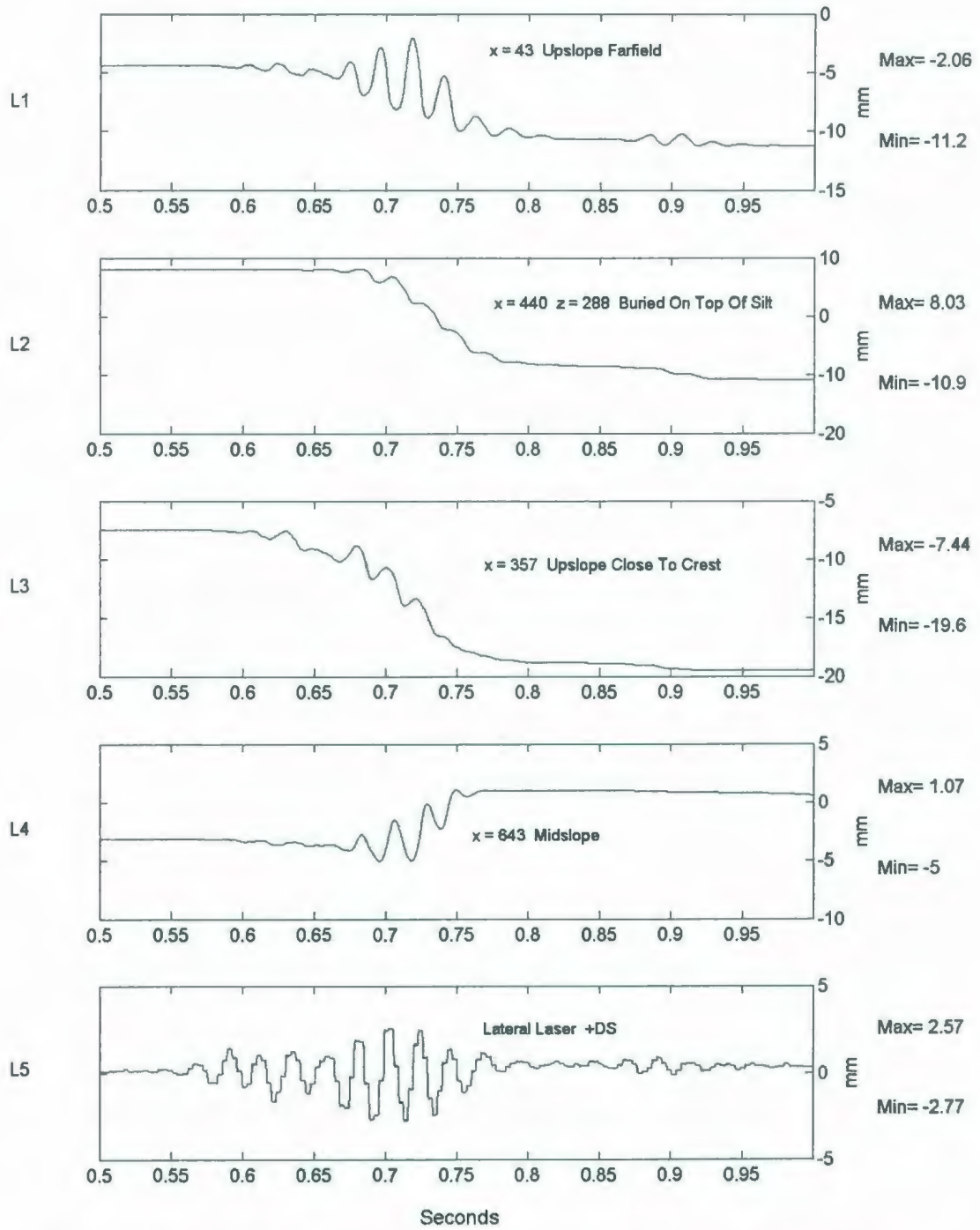
Figure 6.45: COSTA-B 2A2475 Short-Term LVDT Deformation & Lateral Laser Displacement Responses.

201

Some of the trends observed following the first smaller earthquake event are also evident in this larger shaking event. There is a more pronounced increase in negative acceleration spikes as elevation increases in the model. Most noticeably is this behaviour in the accelerometers above the silt layer (A8, A9 & A10) where there are clear large negative spikes between −50 and −100 gravities, which is far beyond the magnitude of the maximum input acceleration of approximately 30 gravities. This negative behaviour is also more pronounced in all accelerometers below the silt layer. Where in the smaller A2475 event the acceleration was fairly balanced in the positive and negative directions for these accelerometers (A1 through A6), in this larger 2A2475 event there is a much clearer tendency to experience larger accelerations in the negative (or upslope) direction. This is especially evident in such instruments as A3, A4, A6 and A7 where the negative peak acceleration is almost 100% greater than the peak positive acceleration. This behaviour is not as pronounced in upslope accelerometers under the silt layer (A2 & A5) where the acceleration response is more balanced.

Expectedly the generated excess pore pressures and accelerations are larger than in the smaller first earthquake. The behaviours of PPTs below the silt layer, P6 & P7 for example, also display the delayed dissipation of generated pore pressures as seen in the previous A2475 event. In addition, above the silt layer there is a distinct drop of pore pressure to below zero during the shaking event when the model slope is moving upslope. These negative spikes are also more frequent in this larger event as evidenced in the

response of such instruments as P9 above the silt layer and P6 through P8 below the silt layer.

Liquefaction occurs in a wider range of PPT locations during this larger earthquake (all instruments except P6 and P9) than in the previous smaller earthquake. Liquefaction is first observed in instruments beneath the silt layer, such as P4 and P8 at about 0.6 seconds. Liquefaction does not occur in the deeper sand, such as in P3, until approximately 0.7 seconds. Comparing the response of P3, which is deeper in the model, to that that of P4, which is shallow in the model beneath the silt layer, it is observed that there is some immediate dissipation of excess pore pressure at the deep location at about 0.75 to 0.80 seconds. Alternatively, the shallower instrument, P4, shows increased or increasing excess pore pressure throughout this period, indicating that excess pore pressure is migrating upwards from deeper locations.

The LVDTs showed considerable response in both surface settlement and downslope movement. L1 showed that the farfield settled approximately 9 mm while the crest of the slope, as measured by L3, settled approximately 12 mm. In the short-term L4, on the slope face, showed that there was a small amount of heaving on the order of 6 mm. Downslope movement was much more significant in this 2A2475 earthquake event, about 19 mm, than in the smaller earthquake event. This downslope movement does not commence until approximately 0.69 seconds, which is 0.14 seconds after the start of shaking. In contrast, the upslope LVDTs (L1 & L3) experience a quicker response, with

settlement being experienced only 0.05 seconds after the start of the earthquake event at approximately 0.55 seconds. The midslope vertical response, observed in L3, is also delayed until approximately 0.68 seconds.

6.2.7 2A2475 Long-Term Testing Instrument Responses

The long-term responses were collected to examine the behaviour of the model for several seconds after the 2A2475 earthquake event. Figures 6.46 through 6.50 illustrate these responses.
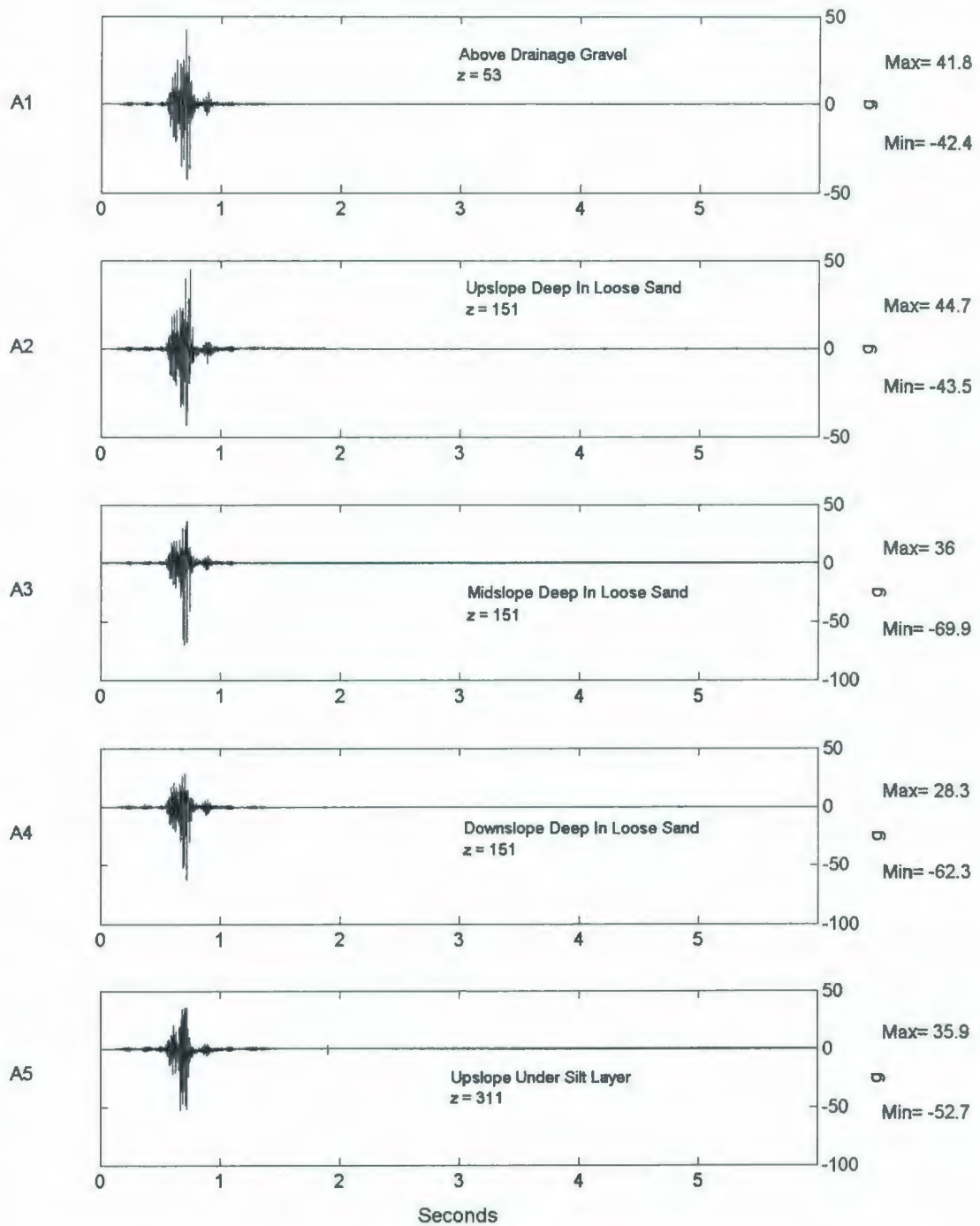
Figure 6.46: COSTA-B 2A2475 Long-Term Accelerometer Response for A1-A5.
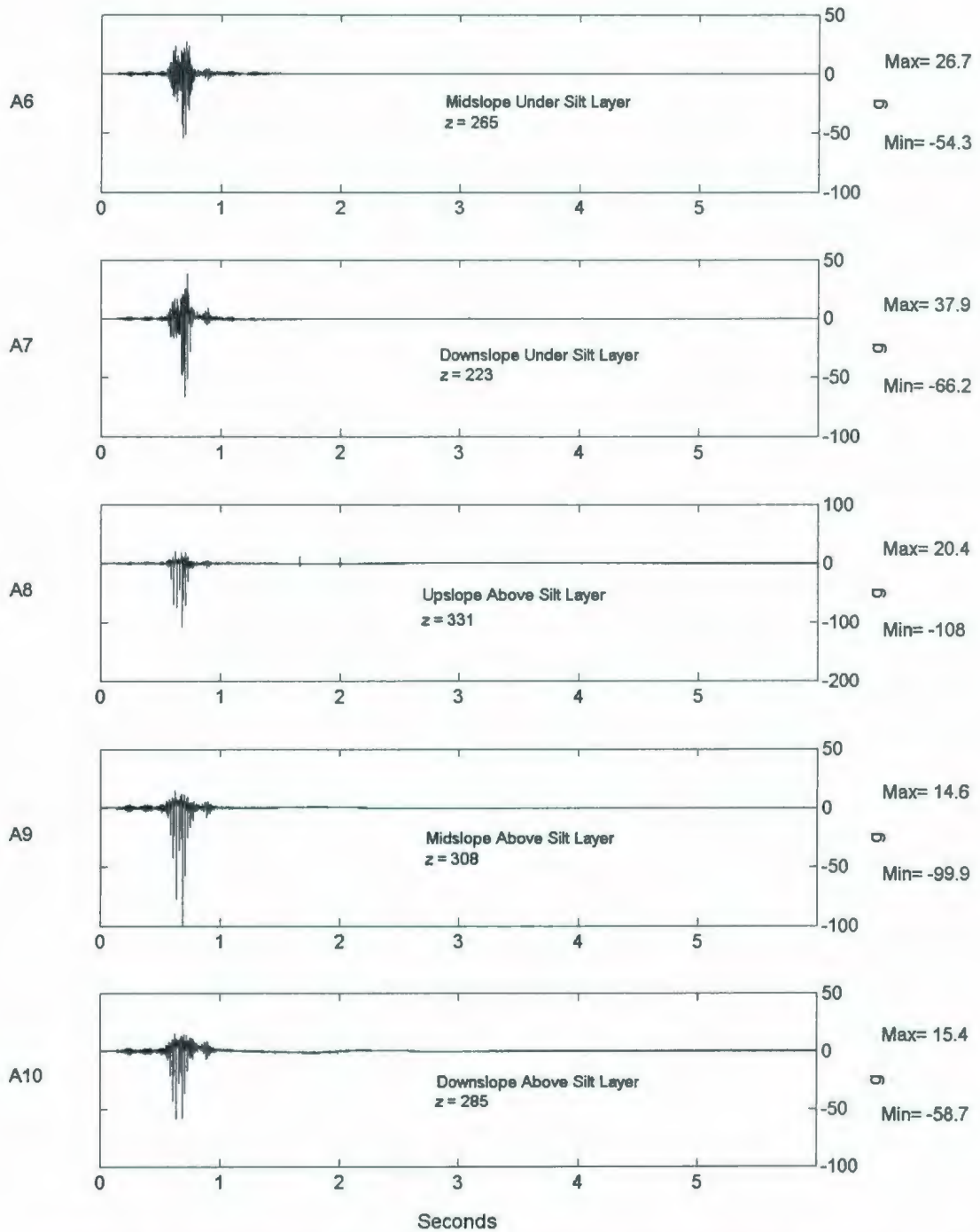
**Figure 6.47:** COSTA-B 2A2475 Long-Term Accelerometer Response for A6-A10.
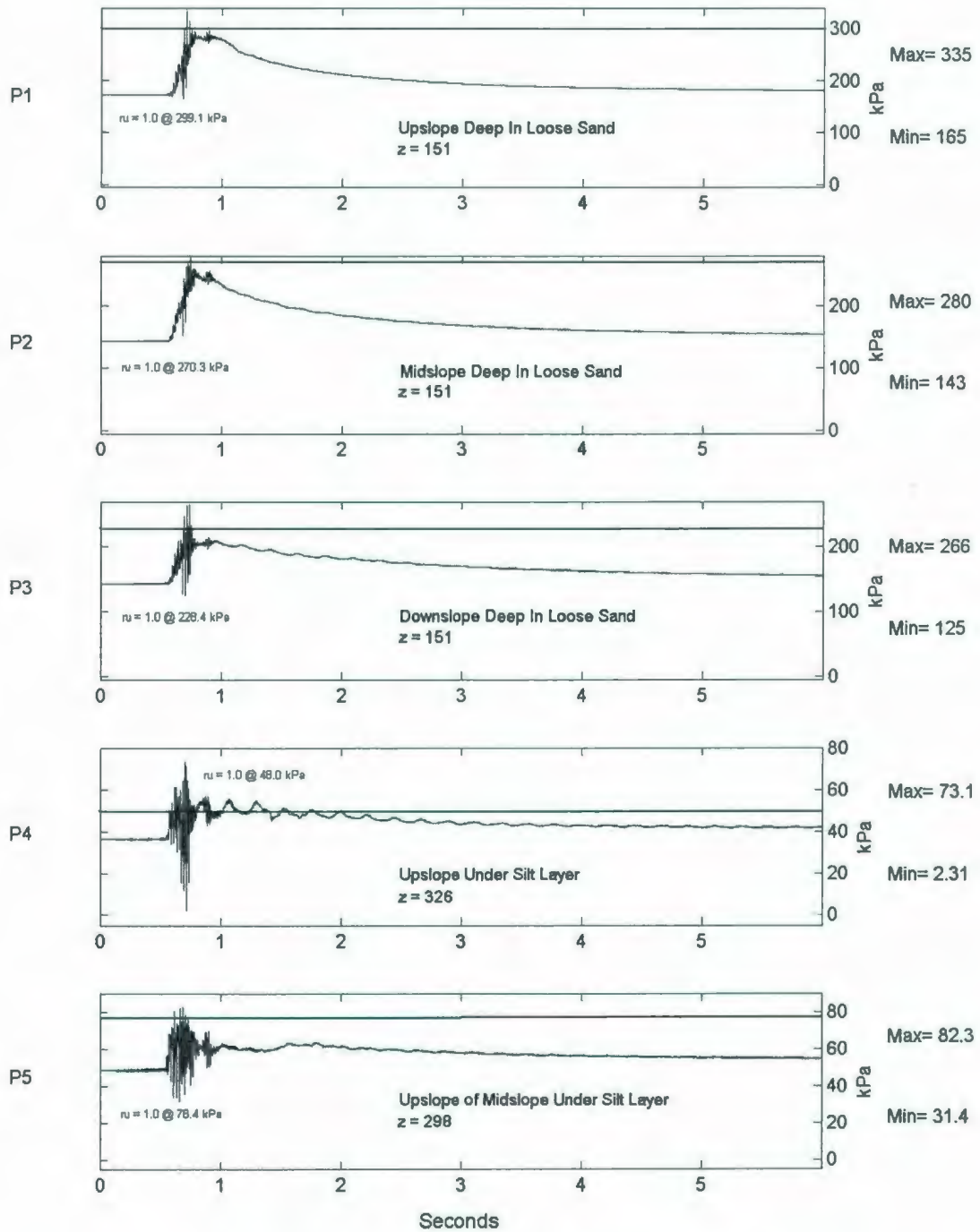
Figure 6.48: COSTA-B 2A2475 Long-Term PPT Response for P1-P5.

207
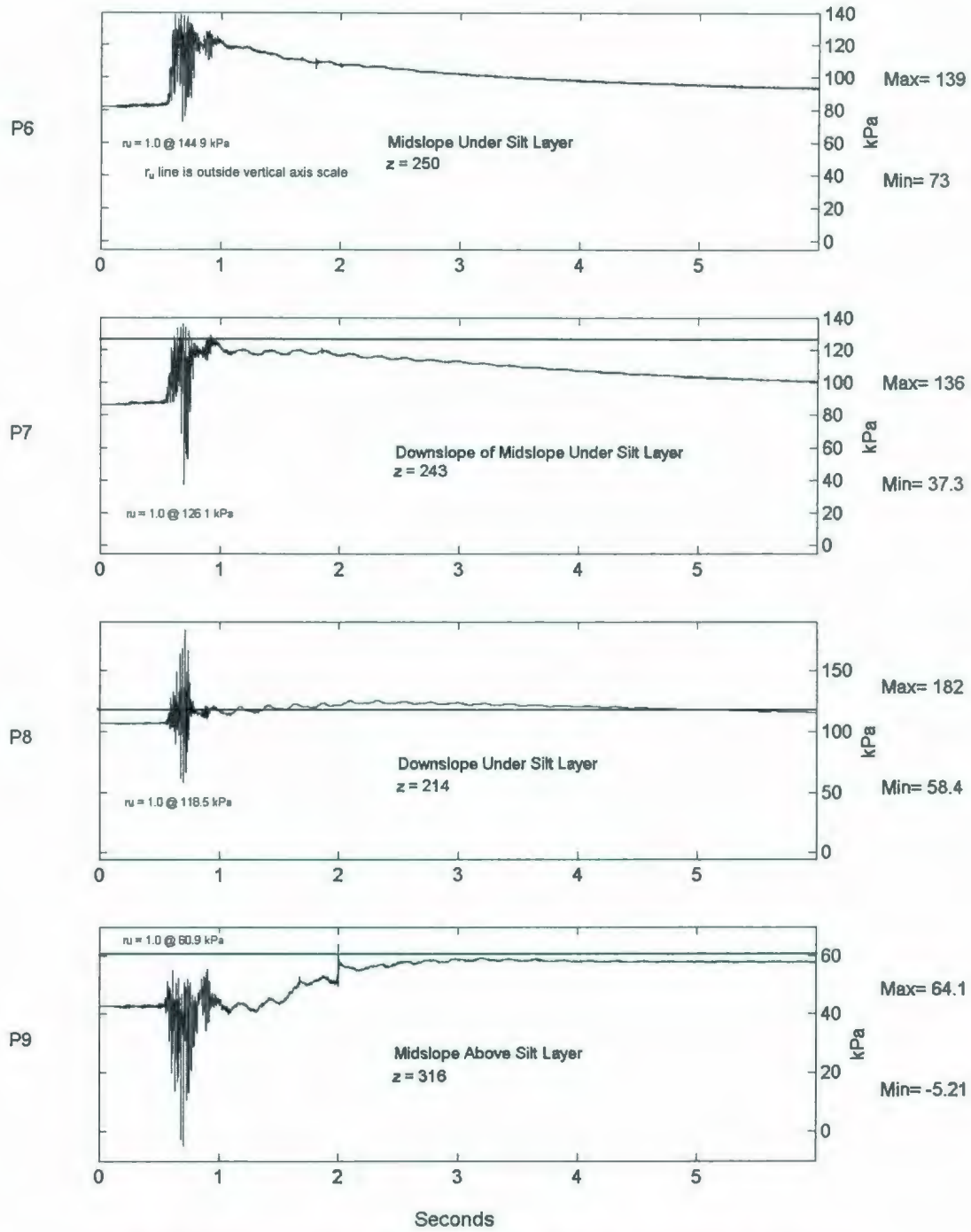
Figure 6.49: COSTA-B 2A2475 Long-Term PPT Response for P6-P9.
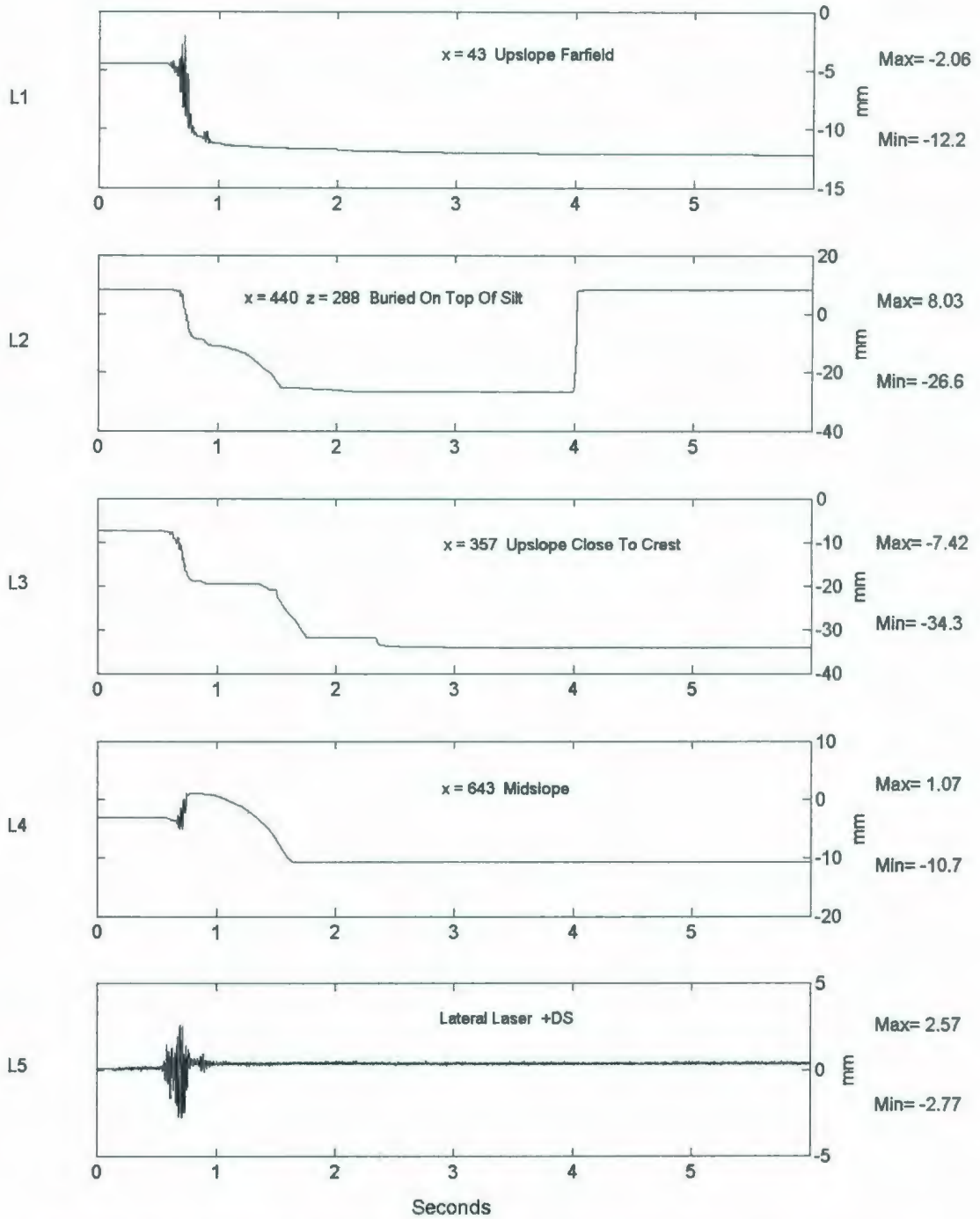
Figure 6.50: COSTA-B 2A2475 Long-Term LVDT Deformation & Lateral Laser Displacement Responses.

209

Long-term accelerometer responses indicate the stoppage of acceleration quickly after the quake and show the increased negative response as compared to the previous smaller earthquake. However, there is some evidence of movement following the earthquake. This can be seen in the fluctuating response of the response of A9 and A10 from the period of approximately 1 to 3 seconds.

The long-term trends also show that there is prolonged dissipation of generated pore pressures. Nevertheless, the most notable PPT response in the long term is the significant gain in pore pressure observed in P9 after the earthquake event by approximately 20%. This could be caused by the movement of the slope and the subsequent movement of the P9 instrument itself at a deeper position thus experiencing and increased static pore pressure level. Liquefaction conditions continue following shaking under the silt layer in the upslope farfield as well as downslope under the silt layer as shown by the responses of P4, P7, and P8 respectively. This post-earthquake activity indicates that there is downslope movement after the earthquake event. Nevertheless, liquefaction conditions observed deeper in the model in the short-term results in P1, P2 & P3 ceases shortly after the earthquake has stopped, indicating that there is upward migration of excess pore pressure from deep in the model to up under the silt layer

There is prolonged movement observed in L2 indicating that there is movement of the slope after the shaking has stopped. This movement is approximately 17 mm from 1 to 4 seconds of the record. L2 ceased to operate correctly at about 1.6 seconds. After the test,

it was observed that the string had broken. The short-term heave observed in the downslope area by L4 was negated in the long-term by observed settlement. The linearly plateaued response of L4 after approximately 1.7 seconds seems to indicate that this instrument failed to operate after this period, as absolutely no response was observed. L1, which observed settlement in the upslope farfield revealed little settlement following the shaking period. However in contrast, L3, at the crest of the slope showed two successive periods of settlement occurring between 1.5 and 2.5 seconds. This indicates some surface settlement and slope movement taking place following shaking. The horizontal response of L2 in combination with the vertical response of L3 shows that there was observed slope movement that occurs following the end of the shaking event that ceases the majority of its effects at approximately 0.8 seconds.

6.2.8 Post-Test Observations

During the monitoring of the transducers during swing-down all PPTs seemed to experience the correct rate of reduction of pore pressure as the g-level decreased and most of the PPTs returned to a value close to zero indicating that there were no large changes in pore pressure during swing-down. However, it should be noted that the response of P1 did not completely return to a zero level indicating that there may have been some sort of electrical problem with that instrument. All LVDTs show little change during the swing-down period. The only noticeable change is in L1 in the farfield where the model seems to decompress by about 2 mm during the unloading of increased gravity.

211

Temperature measurements of the model were taken periodically before and after the loading of the model on to the centrifuge arm, as well as after the test. In previous tests warm oil circulating in the hydraulic mechanisms of the shaker have been observed to significantly effect the temperature of the model. A temperature probe was installed during pluviation deep in the loose sand. Table 6.6 displays these observed temperatures.

Table 6.6: COSTA-B Observed Model Temperature Response.

Time	Location	Comments	Temperature (^{o}C)
8:00 AM	On Lab Floor	Pre Loading	21.5
9:00 AM	On Arm	After Loading	21.5
10:00 AM	On Arm	Test Preparation	22.3
11:00 AM	On Arm	Test Preparation	23.6
12:00 PM	On Arm	Test Preparation	26.7
2:45 PM	On Arm	Pre-Test	30.4
4:00 PM	On Arm	Post-Test	31.5

It was observed from the centrifuge control instrument panel that the temperature in the chamber at the time of shaking was somewhere between 30.4 to 31.5^{o}C. This is greater than the anticipated 25°C for the test. This elevated model temperature was created because there were some difficulties encountered when setting up the data acquisition system and testing instruments. Because of these difficulties, the model sat on the shaker for approximately 6 hours before testing, which is atypical. The elevated temperature most likely had an effect of the viscosity of a pore fluid decreasing it to approximately 30 cSt at the time of the shaking.

212

After the centrifuge flight was completed, the profile of the model surface was measured while the model was still situated on arm. The results showed reduction in height on the farfield upslope surface as well as some collection of material at the toe. In addition, it appears that the crest of the slope has failed and moved considerably. Table 6.7 and Figure 6.51 give a comparison of the pre- and post-test slope heights. These measurements correspond well to the measurements collected by the vertical LVDTs, L1 and L3 at their respective positions. At L4, this correspondence does not hold true. Looking at the long-term behaviour, in Figure 6.50, of this instrument, initial accumulation at the toe is shown during the earthquake, but then in the long term showed a negative response, which does not correlate with accumulation. Upon model excavation, the pad for this instrument was shown to be imbedded below the surface of the accumulated material, explaining this discrepancy.

Table 6.7: COSTA-B Post-Test Surface Profile.

Distance from Upslope End (mm)	Pre-Test Surface Height (mm)	Post-Test Surface Height (mm)
0	338	323
50	336	328
100	336	326
150	334	313
200	331	306
250	330	304
300	327	303
350	322	296
400	317	291
450	304	287
500	278	284
550	262	281
600	236	273
650	207	254
700	192	236
737	178	236
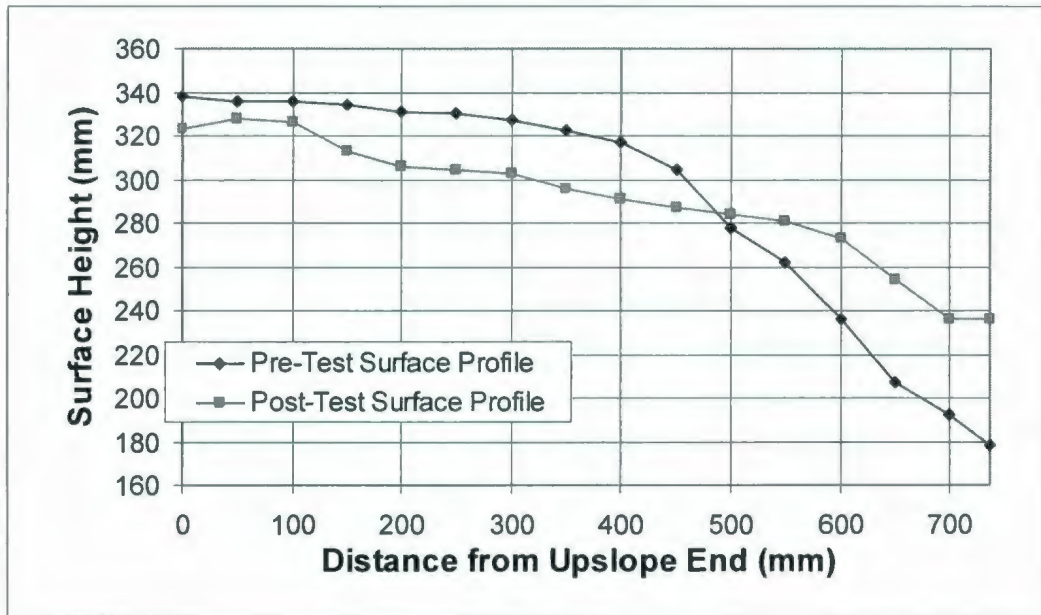
Figure 6.51: COSTA-B Post-Test Surface Profile.

Small white pieces of gravel were placed on the model slope face prior to saturation in a square grid measuring approximately 25 mm by 25 mm grid. A photograph of this grid as placed pre-test is shown in Figure 6.52. As previously mentioned this was done to make qualitative comparisons of the movement of the slope face during the test.
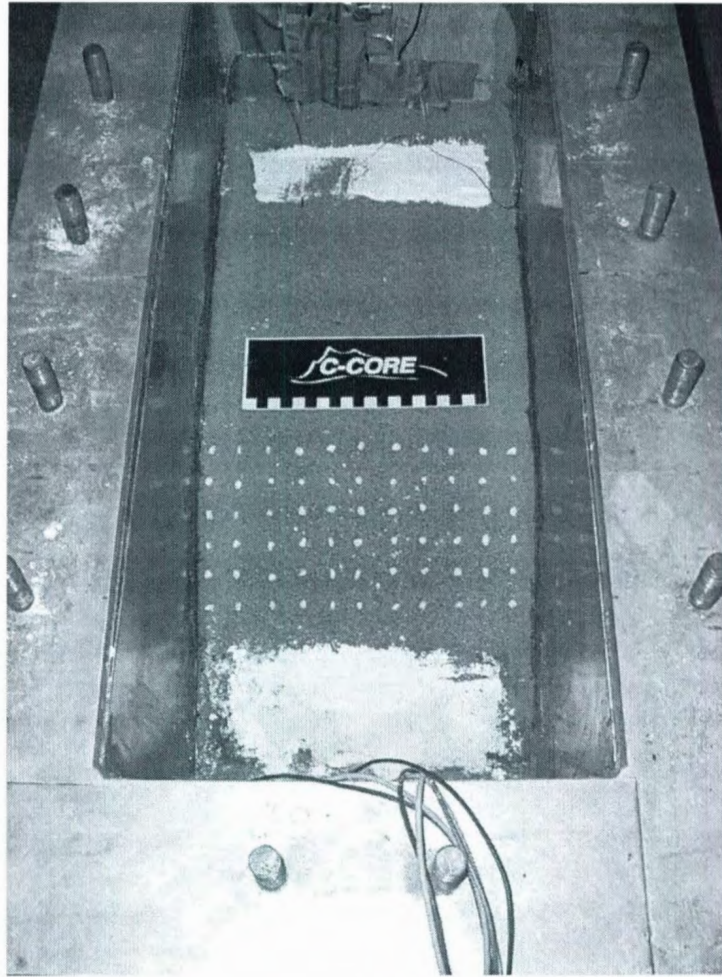
Figure 6.52: COSTA-B Pre-Test Slope Marker Grid.

Following the test a photograph of the model slope, similar to that shown in Figure 6.52 was also taken. The post-test marker grid conditions are shown in Figure 6.53. It is shown that no significant horizontal deformation of the marker grid occurred during slope failure. This indicates that no significant friction was observed between the sand and the interface of the walls of the model container. Additionally it was observed that the

markers at the crest of the slope moved approximately 100 mm towards the downslope end of the model.

Figure 6.53: COSTA-B Post-Test Slope Marker Grid.

Following the test the model was transported off the centrifuge arm to the lab floor where it was drained and excavated. During excavation, the positions of the internal instruments were noted as shown in Chapter 5. Additionally, the location of the installed silt layer was measured and the height of this layer as well of a comparison with its

intended position is given in Table 6.8 and Figure 6.54. The values presented are for the top of the silt layer. It was also observed that the silt layer had compressed slightly leaving it approximately 12-15 mm thickness in model scale. No significant mixing of the Fraser River sand and the Sil-Co-Sil silt was observed. It appeared that the silt layer had acted as a single element and had slid down the underlying sand slope until it came to rest against the downslope end wall of the model container. The silt layer was not observed to have broken in any major way.

Table 6.8: COSTA-B Silt Layer Profile.

Distance from Upslope End (mm)	Pre-Test Silt Profile	Post-Test Silt Profile
100	343	--
120	343	318
200	330	306
300	312	292
400	294	279
500	275	262
550	265	257
600	242	252
637	--	244
675	--	238
700	--	232
737	--	236
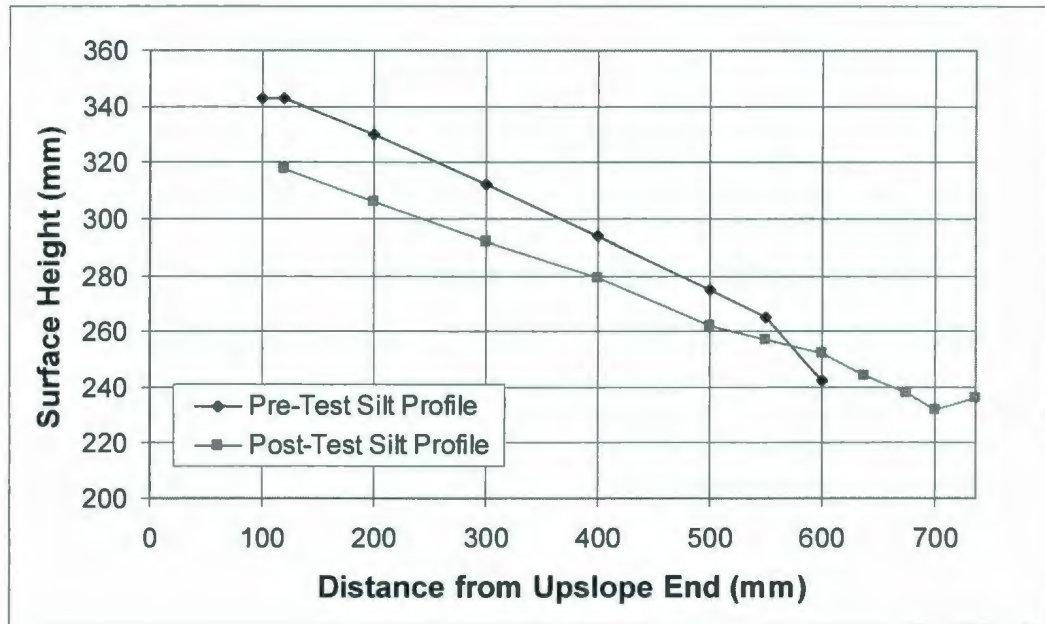
Figure 6.54: COSTA-B Silt Layer Profile.

6.3 COSTA-C

6.3.1 Pre-Test Observations

The pre–test surface profiles are shown in Table 6.9 and Figure 6.55. There is little change between the post-saturation and post-test profile, with the model staying fairly true to the construction geometry. The crest of the slope had only settled 4 mm during saturation and transportation, which does not represent a significant change. This improvement was due to the used of a aluminum surface template that was installed on the model slope in order to preserve its shape following construction and during saturation, transportation, and handling.

Table 6.9: COSTA-C Pre-Test Surface Profile.

Distance from Upslope End (mm)	Post-Construction Profile	Post-Saturation Profile	Pre-Test Profile
0	343	343	343
50	343	343	343
100	343	343	342
150	343	343	343
200	343	341	341
250	343	341	340
300	343	341	340
350	343	--	339
400	343	--	339
450	319	--	319
500	295	--	294
550	271	--	273
600	247	--	248
650	223	--	223
700	199	--	195
737	175	--	179
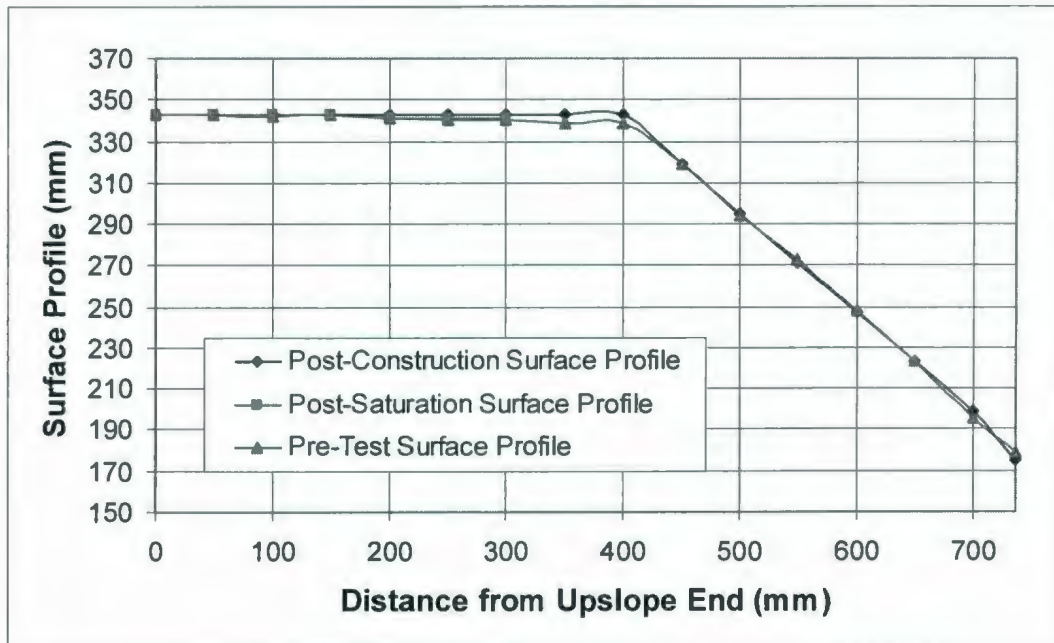
Figure 6.55: COSTA-C Pre-Test Surface Profile.

Monitoring of the PPTs during swing-up of the centrifuge showed that all PPTs were operating correctly and that their results showed increased pore pressure at the correct rate considering their position in the model. Observation of the LVDTs at the same time showed that the model experienced a settlement due to self-weight in the order of 1-2 mm, which should not significantly affect the intended relative density of the model. L2, which is used to measure horizontal displacements of the slope above the silt layer, experienced a large response that can be attributed to the tightening of slack in the string and pulley mechanism. Table 6.10 shows the estimated relative density based upon the pre-test observations. The calculated relative density directly before the earthquake is 38%, which is closer to the target relative density of 40% than in the COSTA-B test.

Table 6.10: COSTA-C Pre-Shake Observed Relative Density at Farfield.

Condition	Settlement (mm)	Relative Density (%)
Post-Construction	N/A	34
Post-Saturation	0.0	34
Post-Loading	0.0	34
After Spin-Up	1.8	38

As was attempted in COSTA-A and COSTA-B the saturation of this model was to be checked by observing the travel time of acoustic waves through the model. The intention was to observe these acoustic wave responses at test speed a few moments before the initiation of the model earthquake. The generation of these waves was achieved by tapping the upslope end of the model container with a small solenoid operated hammer. This generated signal is then observed by two accelerometers (in this case A3 and A2) placed in-line along the centre axis of the model at a known distance apart (101 mm).

220

The captured signal in these two accelerometers at 70 g is shown in Figure 6.56. The accelerometer data shown in this figure has not been corrected for their opposite orientations. The speed of this wave can be estimated by comparing the time difference of the first major trough in Channel 1 and major peak in Channel 2. The acoustic wave data from this test is much more clearly interpreted from the data acquired in COSTA-A. The modes of the responses are much more clearly defined. This configuration seemed to work fairly well at capturing the acoustic waves and was utilized for all subsequent COSTA tests.
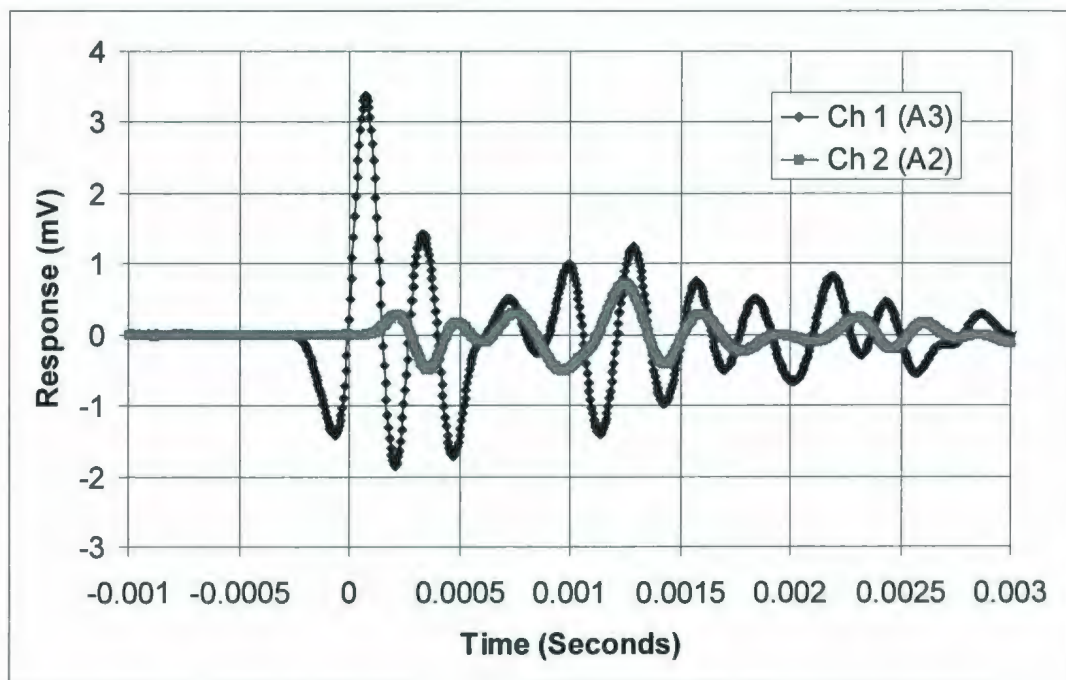
Figure 6.56: COSTA-C Acoustic Wave Response at 70g.

Acoustic wave speeds were calculated at various centrifugal accelerations using the same process described for COSTA-A in section 6.1. Table 6.11 summarizes the analysis of the calculated wave speeds for all g-levels at which acoustic wave response data was collected, both during swing-up and swing-down. The maximum calculated wave speed of 388.36 m/s occurred at 70 g following the earthquake actuation. Wave speeds typically get larger as centrifugal acceleration increases. This is most likely due to increased coupling between the soil skeleton and the accelerometer device. If this setup was indeed measuring P-waves, it does seem to indicate that the model was poorly saturated, as described by Ishihara et al. (2004). However, at the time of this test and throughout the completion of the five COSTA tests work was ongoing by project collaborators to characterize the nature of the waves that this hammer device was creating. Unfortunately, at the conclusion of this research this work was ongoing and inconclusive. It is however, possible that this model was inadequately saturated thus increasing the sensitivity of this model to failure. Another possibility is that this experiment captured complimentary shear waves that are produced by the hammer.

Table 6.11: COSTA-C Acoustic Wave Response Summary.

G-Level	Condition	Wave Velocity (m/s)
1	Pre-Test	93.52
10	Spinup	114.12
25	Spinup	174.14
35	Spinup	196.12
45	Spinup	217.20
60	Spinup	272.97
70	Pre-Shake	360.71
70	Post-Shake	388.46
60	Spindown	374.07
50	Spindown	348.28
40	Spindown	336.67
30	Spindown	315.63
20	Spindown	292.75
10	Spindown	243.37

Acoustic wave, or in this case primary wave (P-wave), velocity can be more accurately measured from the differential time of the first breaks of the P-wave on the two receiving accelerometers rather than from the first peaks, as calculated here. Additionally, Biot theory may be needed t predict P-wave velocity in saturated porous media where the pore fluid is not water and has both scaled density and viscosity. However, dramatic increase in P-wave velocity with increased saturation can only be used as a 'relative indicator', so more complex assessment of quantitative P-wave velocity is not required in these types of tests.

6.3.2   2A2475 Earthquake Actuation

The testing regime for the COSTA-C test was comprised of only one 2A2475 event. The top portion of Figure 6.57 illustrates the desired 2A2475 acceleration-time history in

model scale. The bottom portion of Figure 6.57 shows the observed earthquake signal in Tz, which is in the direction of shaking. Figure 6.58 shows the fast Fourier transforms (FFT) of these two signals. The two signals compare relatively well with respect to frequency as well as magnitude. The actual observed earthquake being marginally larger in magnitude in both the negative and positive directions. In terms of frequency content, as observed in the FFT signals, it is observed that the EQS delivered an earthquake with almost identical content in the 40 to 50 Hz and 50 to 60 Hz ranges. These results can be considered as a very good agreement between the prescribed and observed earthquake motions. Figure 6.59 illustrates the response of the triaxial accelerometer in the vertical direction. This response was captured by Ty and shows that there is a spurious vertical motion that is experienced during the earthquake event. The range of this acceleration ranges between +6 to −3.5 g and is characterized by a more regular motion that closely resembles the horizontal motion, as compared to the observations from the applied earthquakes in COSTA-A and COSTA-B, which as previously mentioned had trouble with the Ty accelerometer.
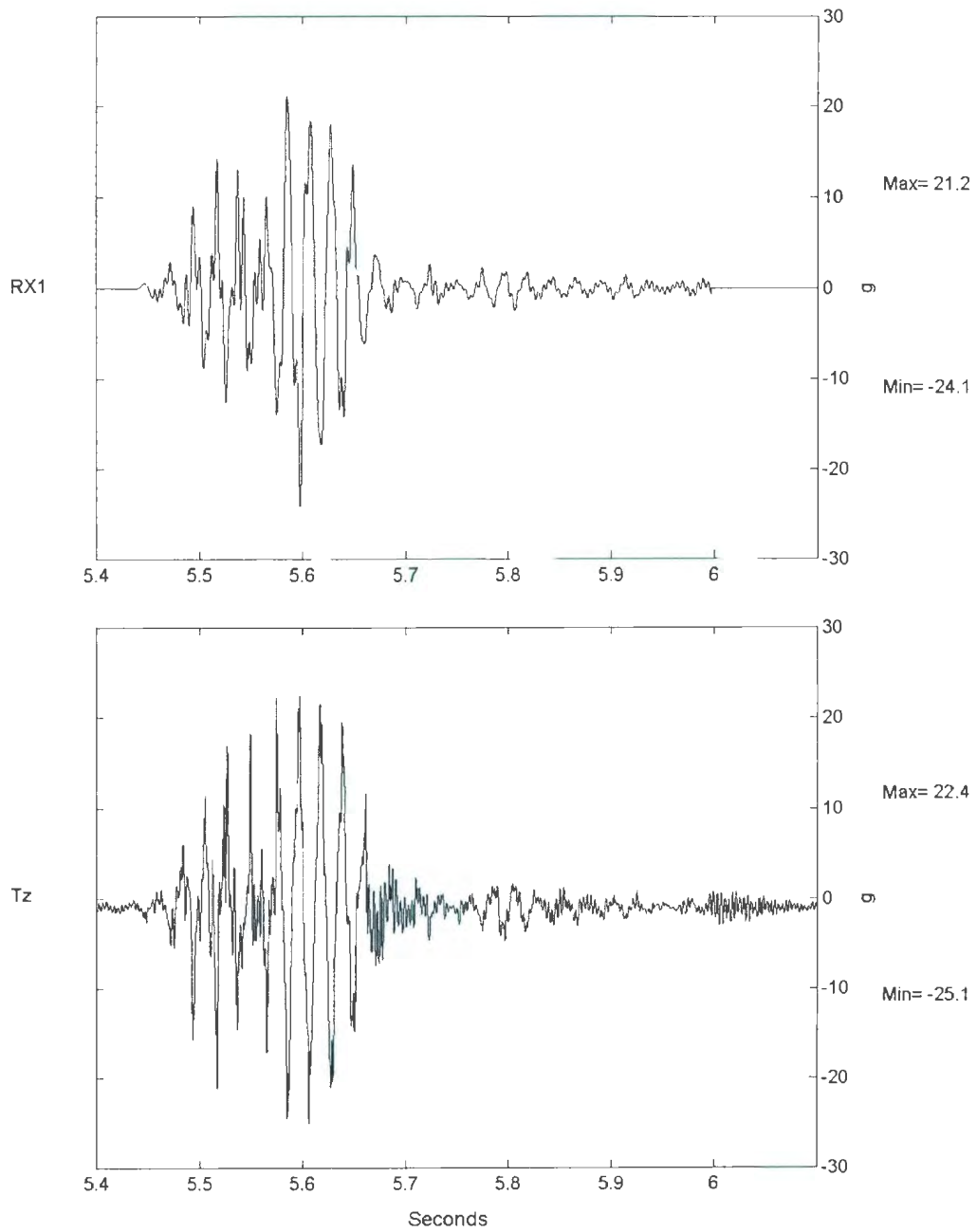
Figure 6.57: Comparison of 2A2475 Earthquake Record & Observed COSTA-C Tz Acceleration.
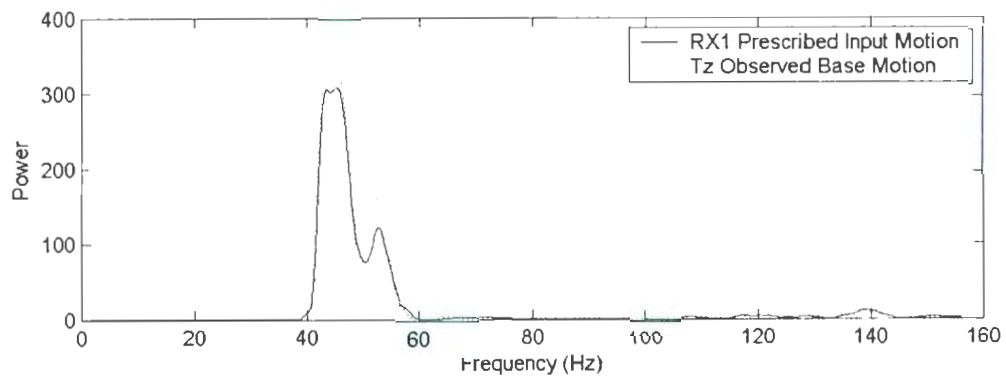
Figure 6.58: Comparison of 2A2475 Earthquake Record & Observed COSTA-C Tz Acceleration.
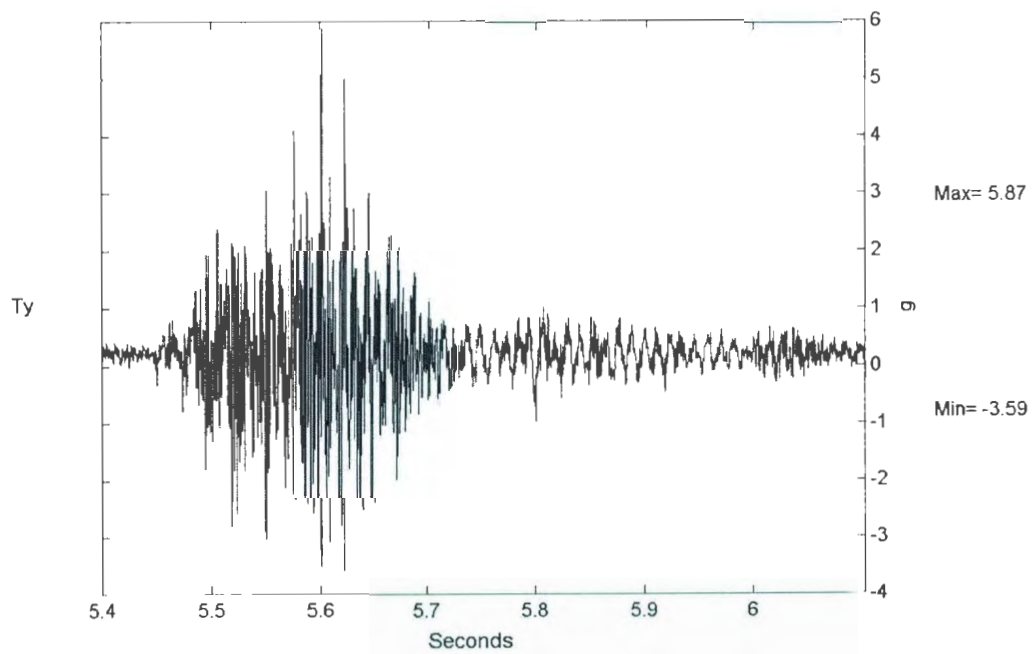
Figure 6.59: COSTA-C 2A2475 Observed Ty Vertical Acceleration Response.

226

6.3.3 2A2475 Short-Term Testing Instrument Responses

All instruments were monitored during and shortly after the 2A2475 earthquake event.

Figures 6.60 through 6.64 illustrate the observed responses in the various instruments

during a 0.5 second period.
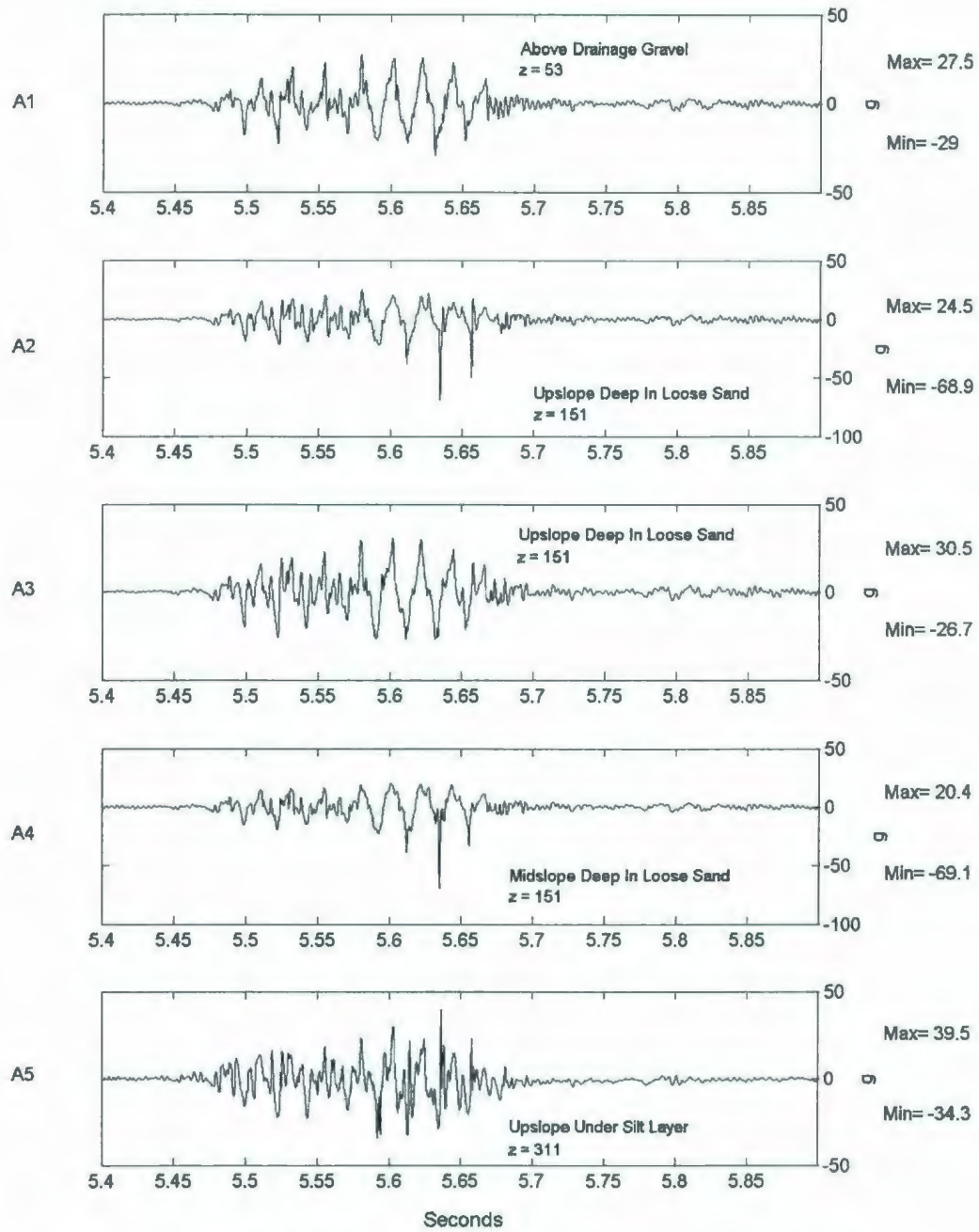
Figure 6.60: COSTA-C 2A2475 Short-Term Accelerometer Response for A1-A5.
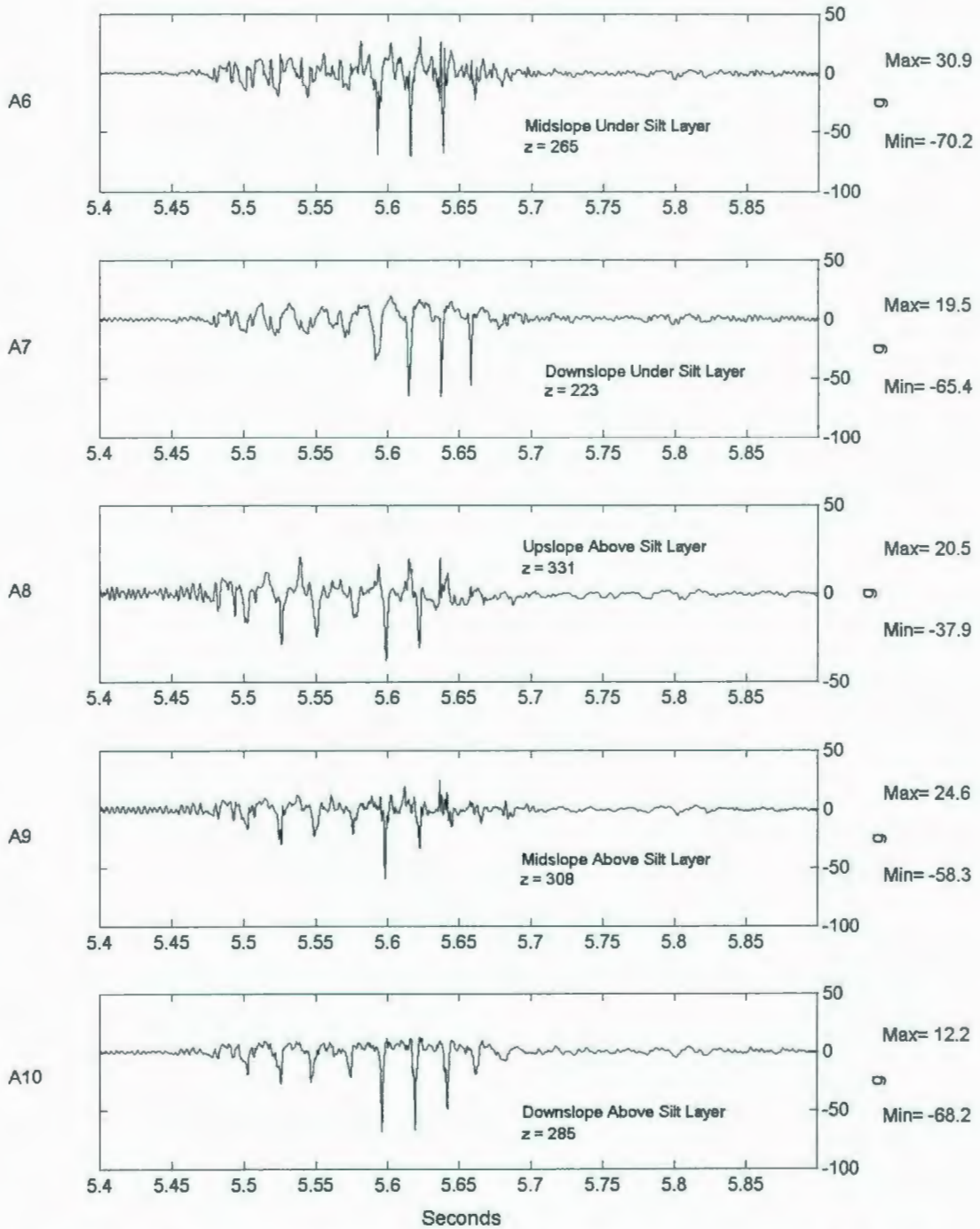
Figure 6.61: COSTA-C 2A2475 Short-Term Accelerometer Response for A5-A10.
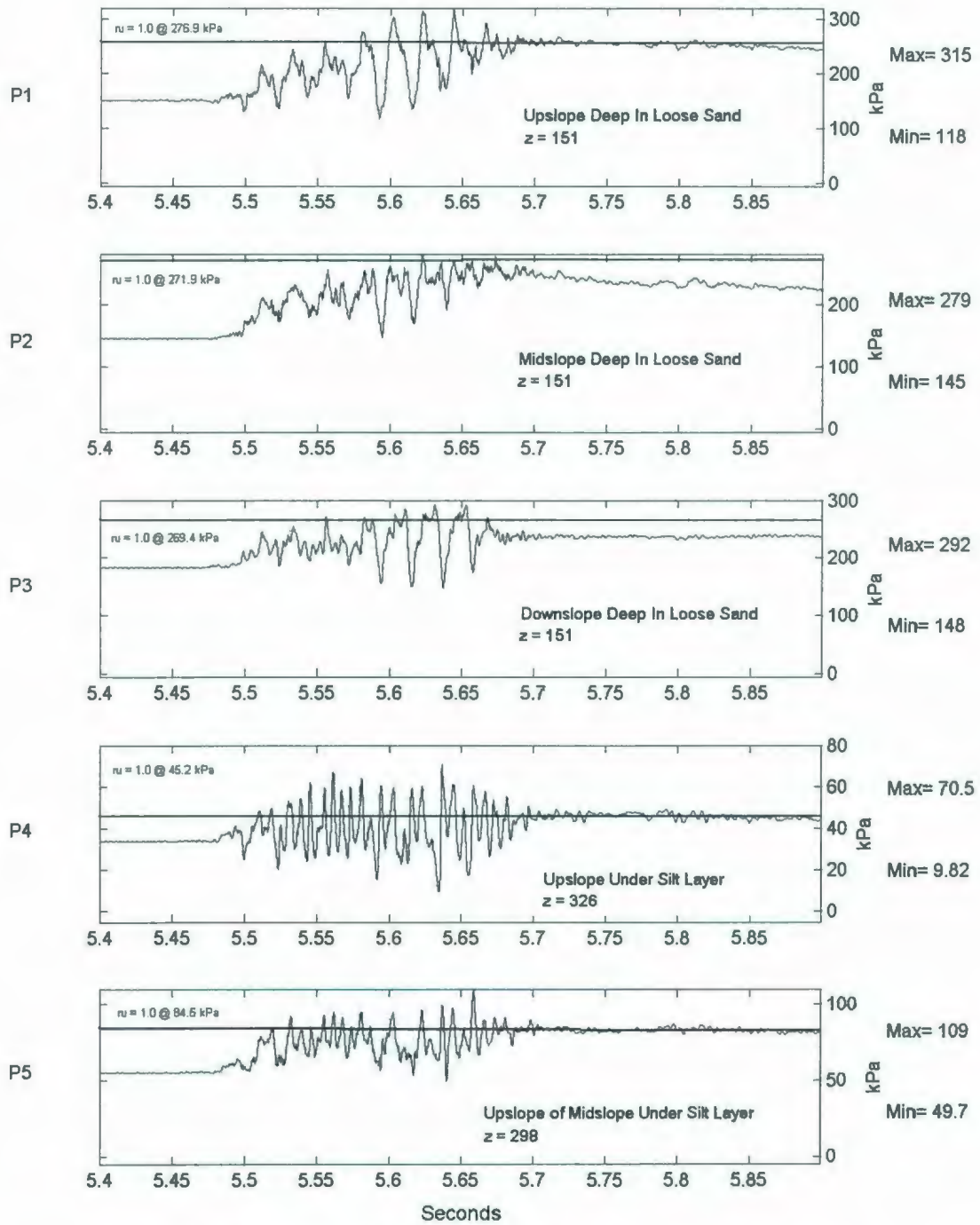
Figure 6.62: COSTA-C 2A2475 Short-Term PPT Response for P1-P5.
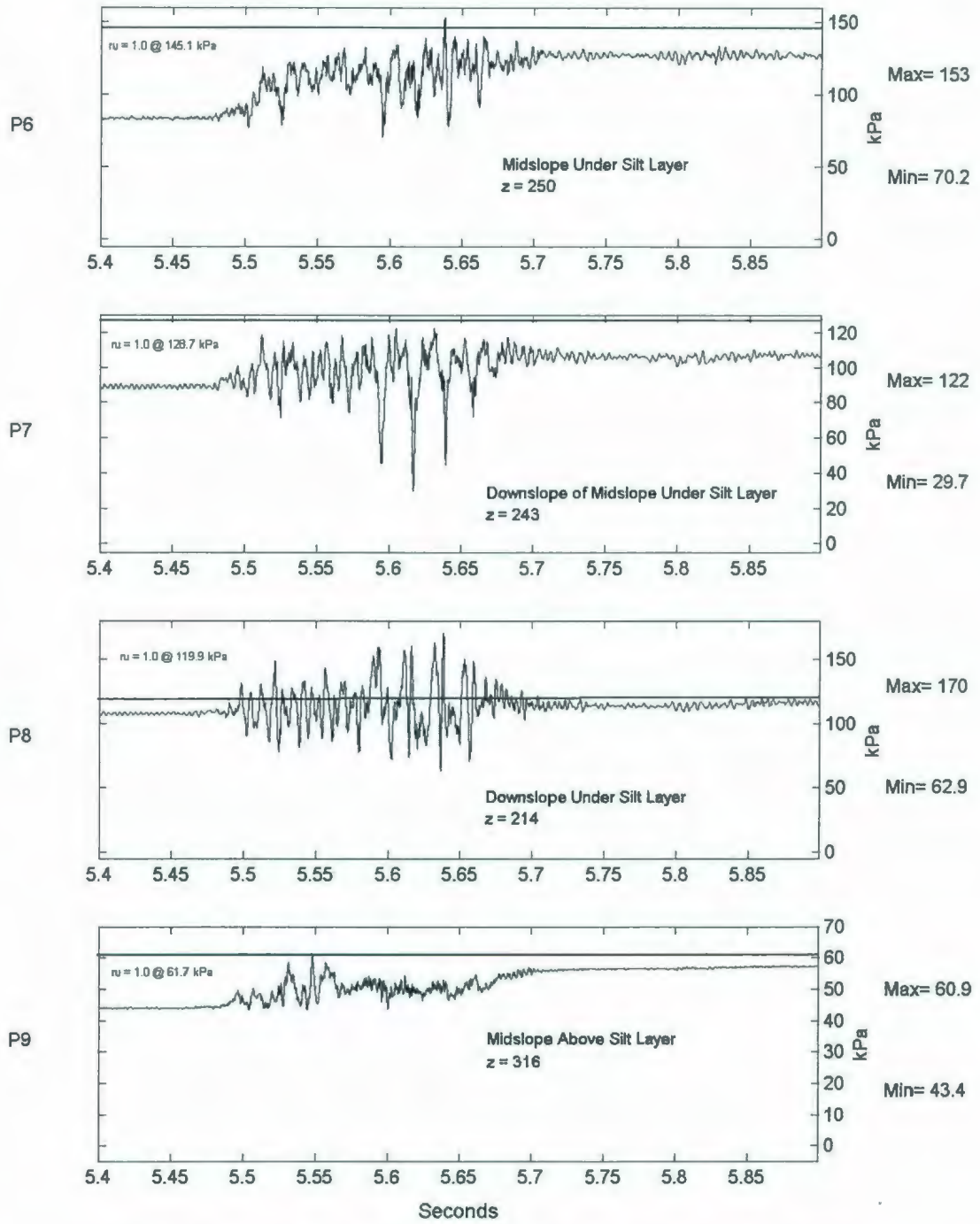
Figure 6.63: COSTA-C 2A2475 Short-Term PPT Response for P6-P9.
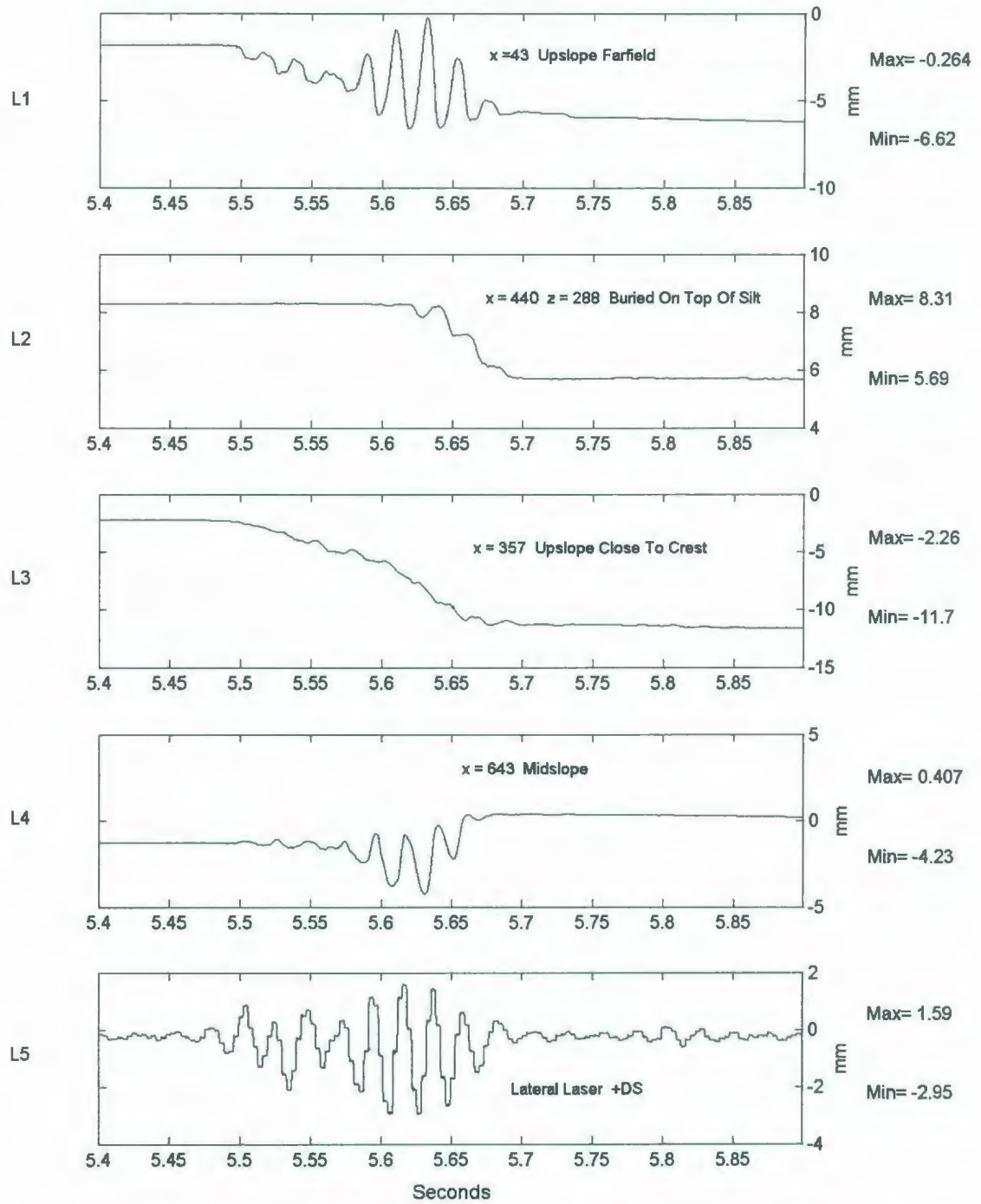
Figure 6.64: COSTA-C 2A2475 Short-Term LVDT Deformation & Lateral Laser Displacement Responses.

232

In the short-term, it is evident that there is a large increase in the tendency of the accelerometers to measure negative spikes with increased elevation in the model. This is especially evident in the accelerometers that are above the silt layer (A8, A9, & A10).

There is also evidence to show that there is quicker dissipation of generated pore pressures above the silt layer than below it. Upon zooming in on the response of the accelerometers above the silt layer there is evidence of small downslope acceleration following the earthquake event, indicating slope movement. Liquefaction occurs in all PPTs except P7 and P9, although, it comes very close to happening in P9 above the silt layer. Evidence of liquefaction is evident quicker directly beneath the silt layer in PPTs such as P4 and P5 at approximately 5.52 seconds. Liquefaction is also apparent in the deeper sections of model, as shown in the responses of P1, P2 & P3. This liquefaction response does not however occur until approximately 5.58 seconds or later.

In terms of surface effects, there is a noticeable change during the shaking. Both L1 and L3 show that the model settles at their locations, 6.4 mm and 9.5 mm respectively. Near the toe of the slope L4 shows that there is a small amount of heave in the short-term, approximately 4.6 mm. Given that P8 does show liquefaction in this zone, it is likely that the pad that the LVDT rod for L4 sits on became embedded under the surface as movement occurred and material collected downslope. The response of L2, which measures downslope movement, indicates that the movement of the slope does not commence until approximately 0.15 seconds after the start of shaking, resulting in

approximately 2.6 mm of downslope movement. Similar to the second larger earthquake event applied in the COSTA-B test the responses in the upslope LVDTs (L1 & L3) are delayed from the start of shaking by approximately 0.05 seconds where the midslope heave, shown in L4, took longer to appear in the instrument.

6.3.4   2A2475 Long-Term Testing Instrument Responses

The long-term responses were collected to examine the behaviour of the model for several seconds after the 2A2475 earthquake event. Figures 6.65 through 6.69 illustrate these responses.
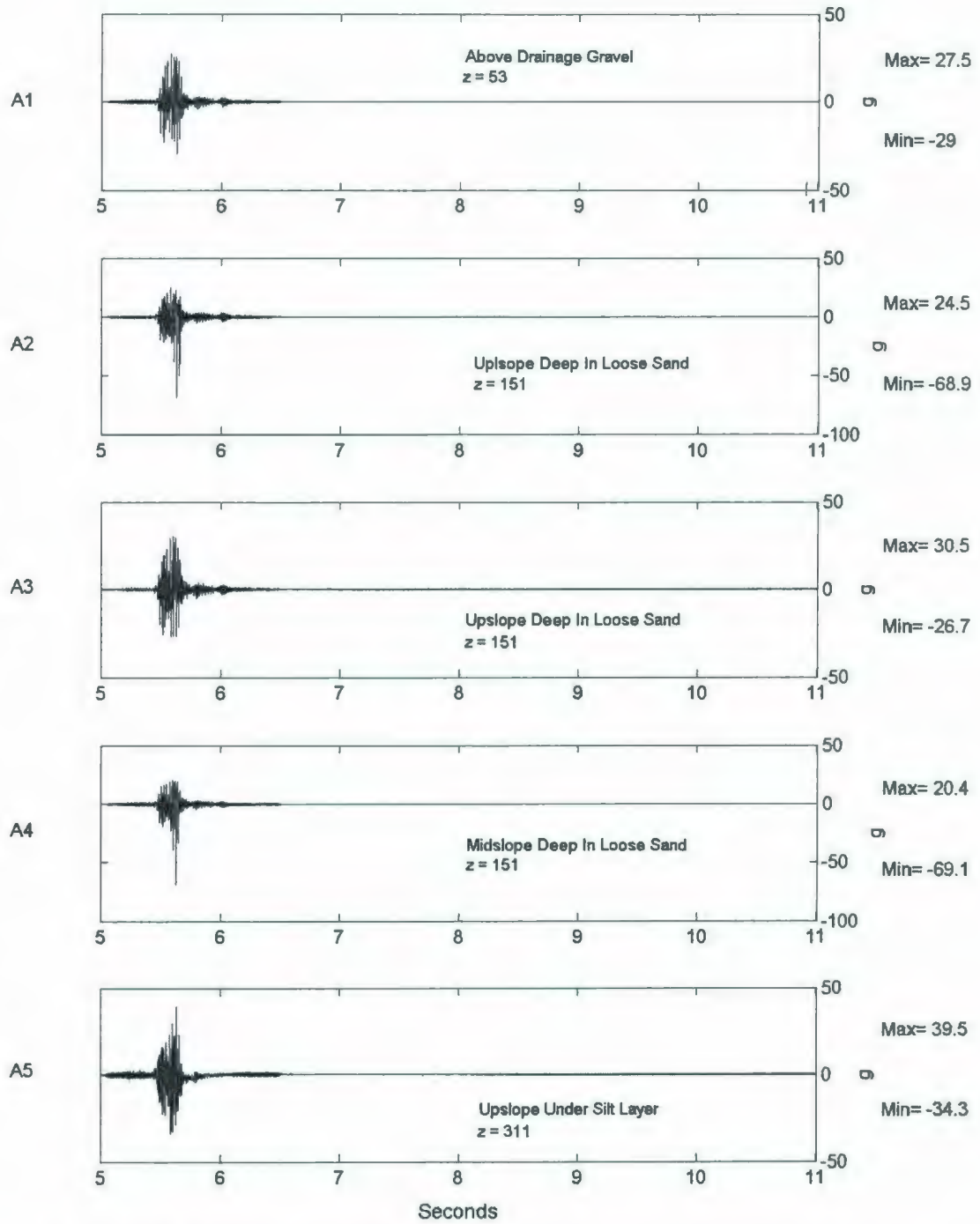
Figure 6.65: COSTA-C 2A2475 Long-Term Accelerometer Response for A1-A5.
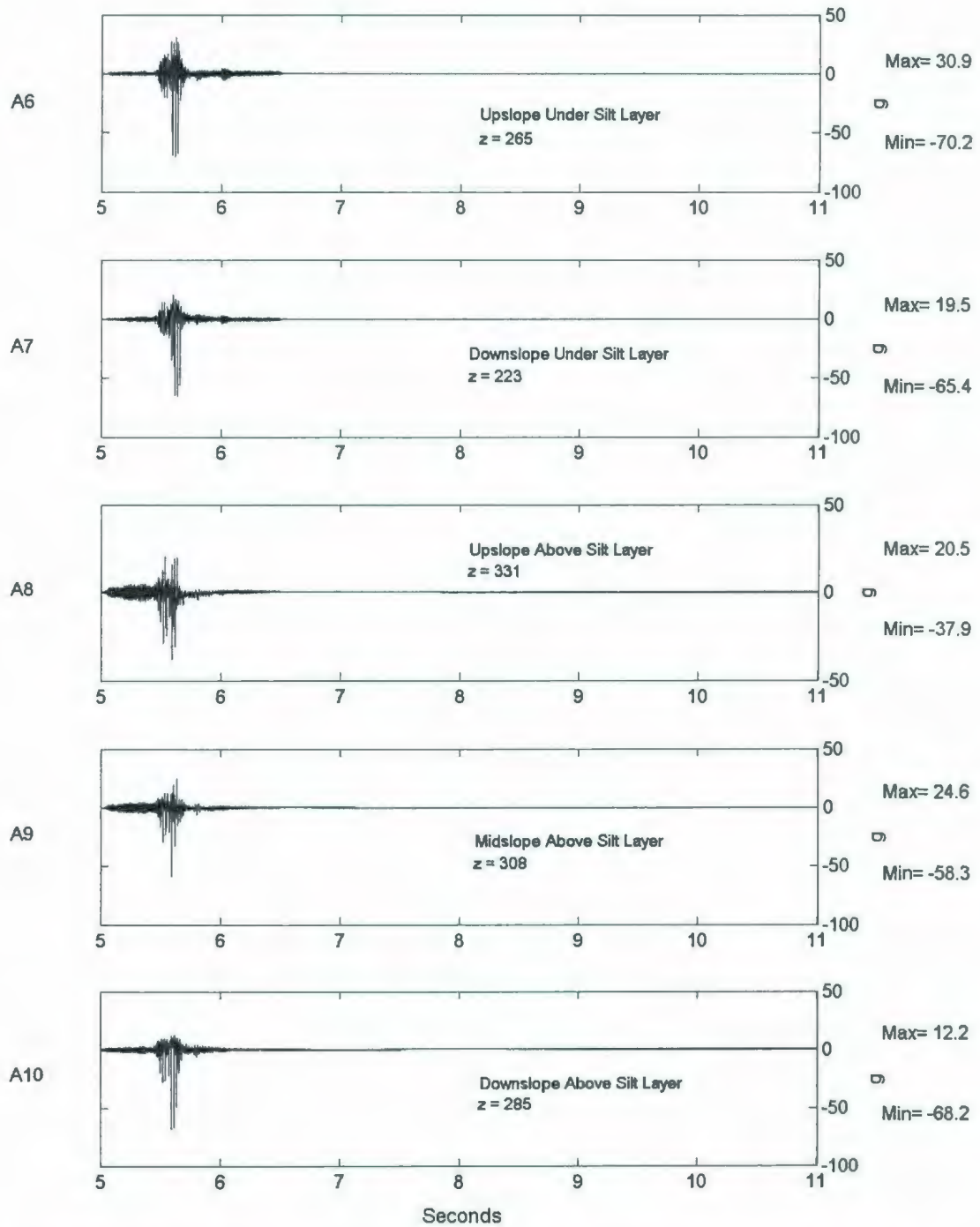
Figure 6.66: COSTA-C 2A2475 Long-Term Accelerometer Response for A6-A10.
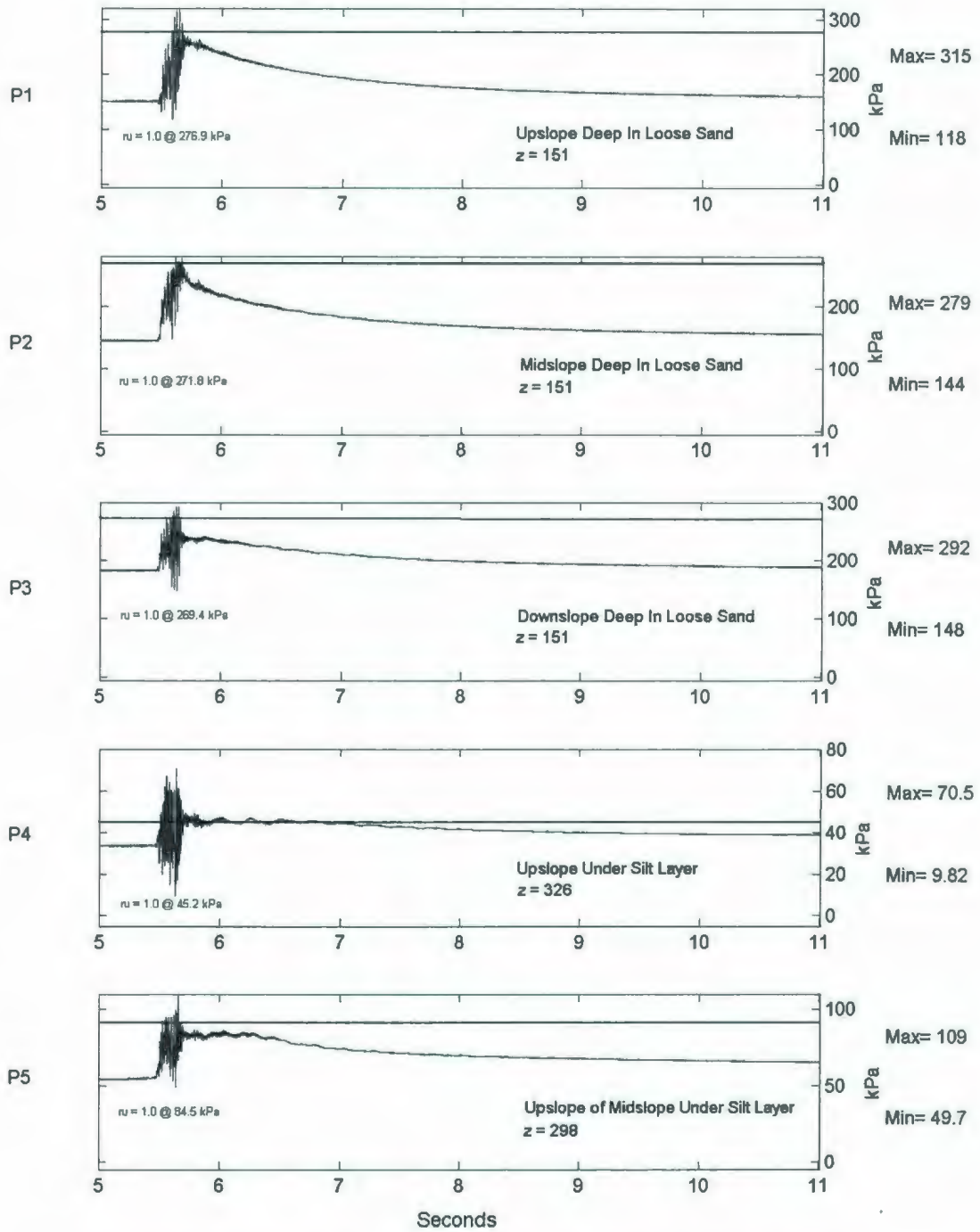
Figure 6.67: COSTA-C 2A2475 Long-Term PPT Response for P1-P5.
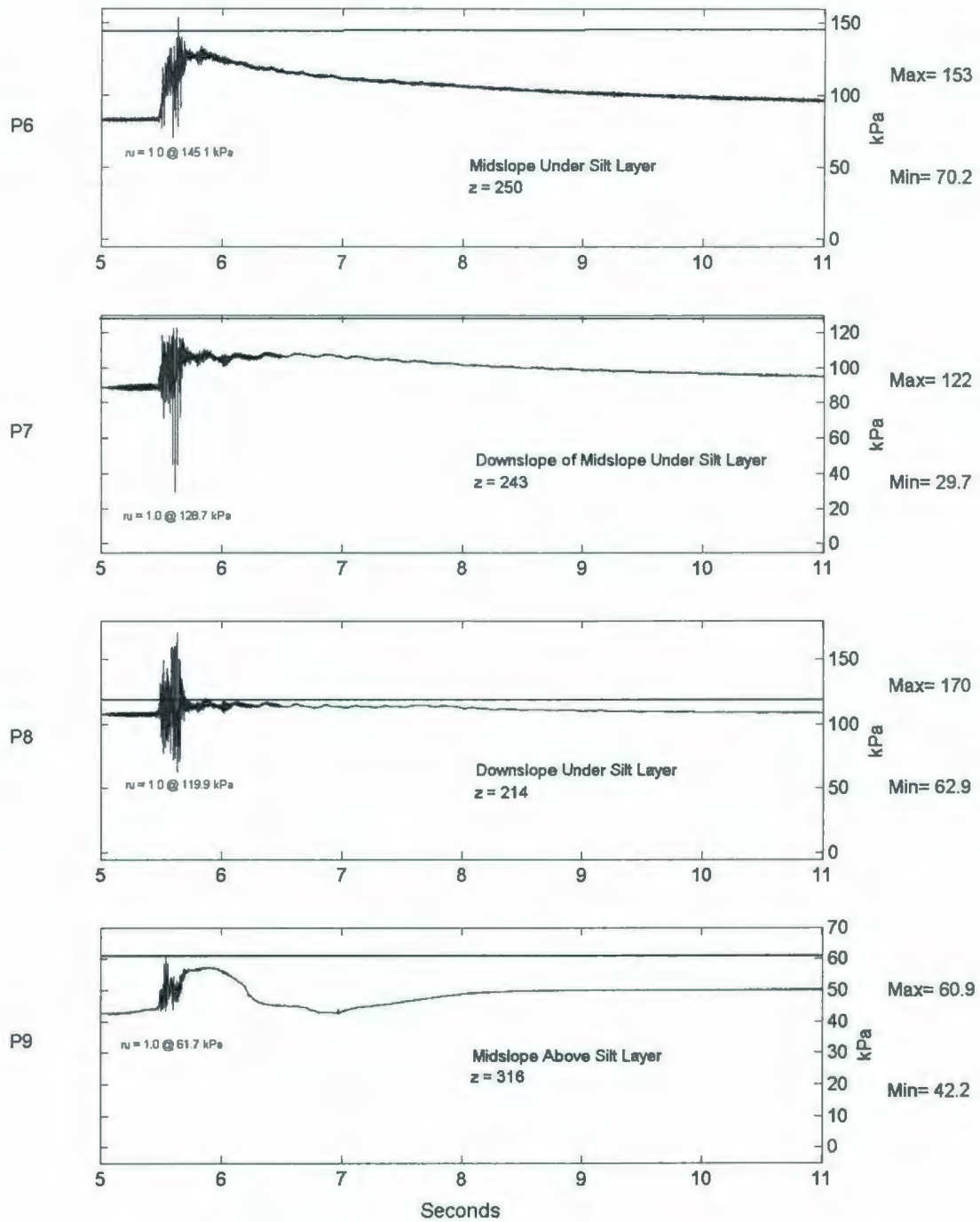
Figure 6.68: COSTA-C 2A2475 Long-Term PPT Response for P6-P9.

238
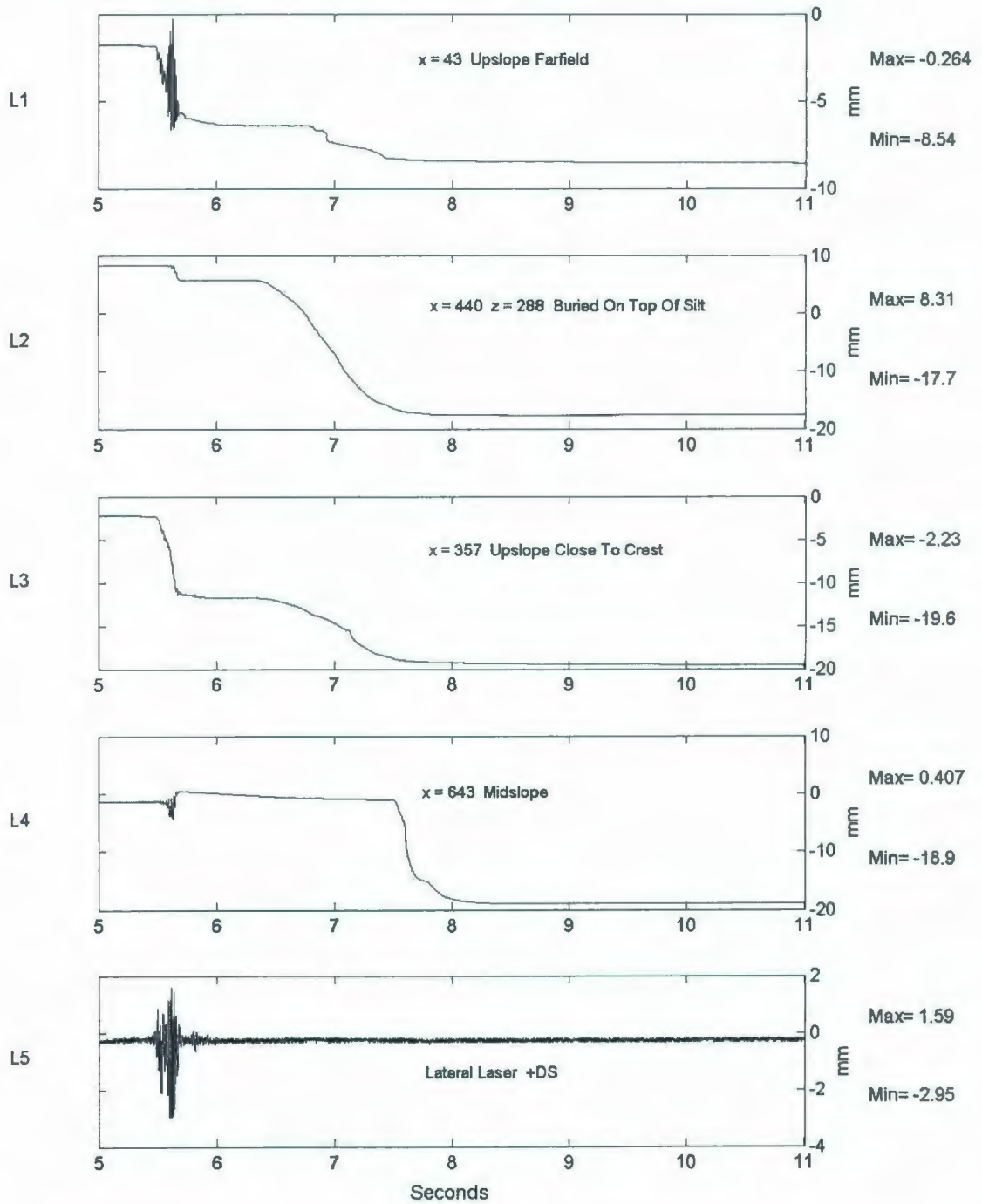
Figure 6.69: COSTA-C 2A2475 Long-Term LVDT Deformation & Lateral Laser Displacement Responses.

239

The long-term results show that there is indeed a great deal of slower pore pressure dissipation below the silt layer than above it. P5, P6, and P7 are good examples of this where it takes several seconds for the pore pressure to return to its pre-shake levels. This delayed dissipation is the major trend of all of the PPTs that are directly below the silt layer. This is in contrast to P9 where the pore pressure returns to its pre-shake level shortly after the cessation of the quake, but where some unique behaviour is observed near the end of the shaking event and for the period of about one second following it, due to the elevation change of this instrument as the slope fails. The positive behaviour of P9 from the period of 7 to 9 seconds indicates that there is downslope movement following the earthquake. There is also some evidence of excess pore pressure migrating in an upslope direction for several seconds after the shaking has ceased. The excess pore pressure in the most downslope PPT, P8, dissipates quite quickly as compared to the most upslope PPT, P4, where at the conclusion of the long-term observation period the instrument is still experiencing some excess pore pressure beyond its pre-shake level. Long-term liquefaction occurs only in P4, which is upslope under the silt layer, where it continues until about 7 seconds in the record, which is 1.3 seconds after the majority of the shaking stops at 5.7 seconds.

The responses of L1 and L3 seem to indicate that there is continued settlement or failure of the model in the upslope area after the cessation of shaking with 2 and 8 mm of settlement occurring at these locations after the short-term observation period respectively. The behaviour of L4 at approximately 7.8 seconds, where there is a large

change in displacement, indicates that this is likely where the spindle of the LVDT slipped off the pad due to the movement of the slope. Interestingly, the response of L2 indicates a approximately 10 mm of downslope movement continues in the model for the 2 seconds following the cessation of shaking, indicating a delay before a second downslope movement event, caused by upward migrating excess pore pressure from lower depths in the model. A total of 26 mm of downslope was observed during and directly after the earthquake simulation.

6.3.5 *Post-Test Observations*

During the monitoring of the transducers during swing-down all PPTs seemed to experience the correct rate of reduction of pore pressure as the g-level decreased and most of the PPTs returned to a value close to zero indicating that there were no large changes in pore pressure during swing-down. However, it should be noted that the response of P3 did not completely return to a zero level indicating that there may have been some sort of electrical problem with that instrument. L3 and L4 show little change during the swing-down period. L1 seems to experience a large displacement, of approximately 7 mm, at approximately 325 seconds. This is most likely caused by the LVDT spindle slipping off the contact pad. After the spindle slid off the pad, it became embedded into the soil, which was observed following the test. There is also a large downslope movement of approximately 11 mm observed from the response of L2, which is likely due to the slacking of the string mechanism also experienced during swing-up.

Temperature measurements of the model were taken periodically before and after the loading of the model on to the centrifuge arm, as well as after the test. In previous tests warm oil circulating in the hydraulic mechanisms of the shaker have been observed to significantly effect the temperature of the model. A temperature probe was installed during pluviation deep in the loose sand. Table 6.12 displays these observed temperatures.

Table 6.12: COSTA-C Observed Model Temperature Response.

Time	Location	Comments	Temperature ($^{\circ}$C)
10:30 AM	On Lab Floor	Pre Loading	19.2
11:30 AM	On Arm	After Loading	19.7
1:15 PM	On Arm	Test Preparation	22.1
1:30 PM	On Arm	Pre-Test	22.4
2:30 PM	On Arm	Post-Test	24.9

It was observed that the temperature at the time of shaking was approximately 25°C. Therefore, the design of the pore fluid was valid in this experiment.

After the centrifuge flight was completed, the profile of the model surface was measured while the model was still situated on arm. The results showed reduction in height on the farfield upslope surface as well as some collection of material at the toe. In addition, it appears that the crest of the slope has failed and moved about 50 mm horizontally. There is also the collection of a significant amount of material at the toe of the slope. Table 6.13 and Figure 6.70 give a comparison of the pre- and post-test slope heights.

242

Table 6.13: COSTA-C Post-Test Surface Profile.

Distance from Upslope End (mm)	Pre-Test Surface Height (mm)	Post-Test Surface Height (mm)
0	343	335
50	343	335
100	342	329
150	343	329
200	341	326
250	340	326
300	340	322
350	339	323
400	339	324
450	319	316
500	294	300
550	273	277
600	248	251
650	223	231
700	189	216
737	184	213
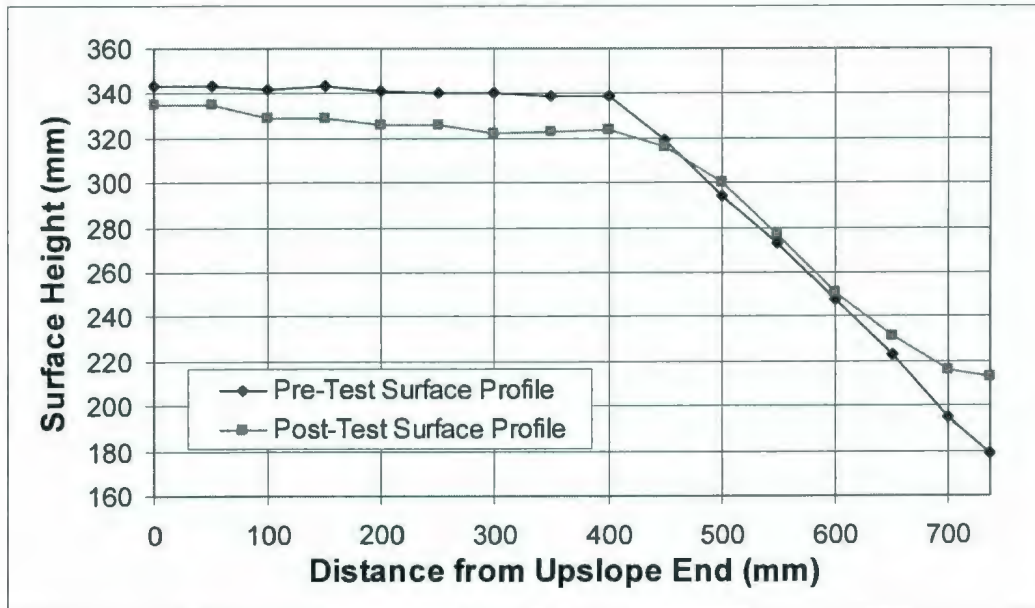
Figure 6.70: COSTA-C Post-Test Surface Profile.

243

Small white pieces of gravel were placed on the model slope face prior to saturation in a square grid measuring approximately 25 mm by 25 mm grid to make qualitative comparisons of the movement of the slope face during the test. However, no photographs of the pre- and post-test conditions of this marker grid were collected for the COSTA-C test.

Following the test the model was transported off the centrifuge arm to the lab floor where it was drained and excavated. During excavation, the positions of the internal instruments were noted as shown in Chapter 5. Additionally, the location of the installed silt layer was measured and the height of this layer as well of a comparison with its intended position is given in Table 6.14 and Figure 6.71. The values presented are for the top of the silt layer. It was also observed that the silt layer had compressed slightly leaving it approximately 10-15 mm thickness in model scale. No significant mixing of the Fraser River sand and the Sil-Co-Sil silt was observed. It appeared that the silt layer had acted as a single element and had slid down the underlying sand slope until it came to rest against the downslope end wall of the model container. The silt layer was not observed to have broken in any major way.

Table 6.14: COSTA-C Silt Layer Profile.

Distance from Upslope End (mm)	Pre-Test Silt Profile	Post-Test Silt Profile
100	343	--
120	343	--
150	339	329
200	330	318
250	321	311
300	312	299
350	303	290
400	294	282
450	284	276
500	275	266
550	265	255
600	242	243
650	--	231
700	--	216
737	--	213
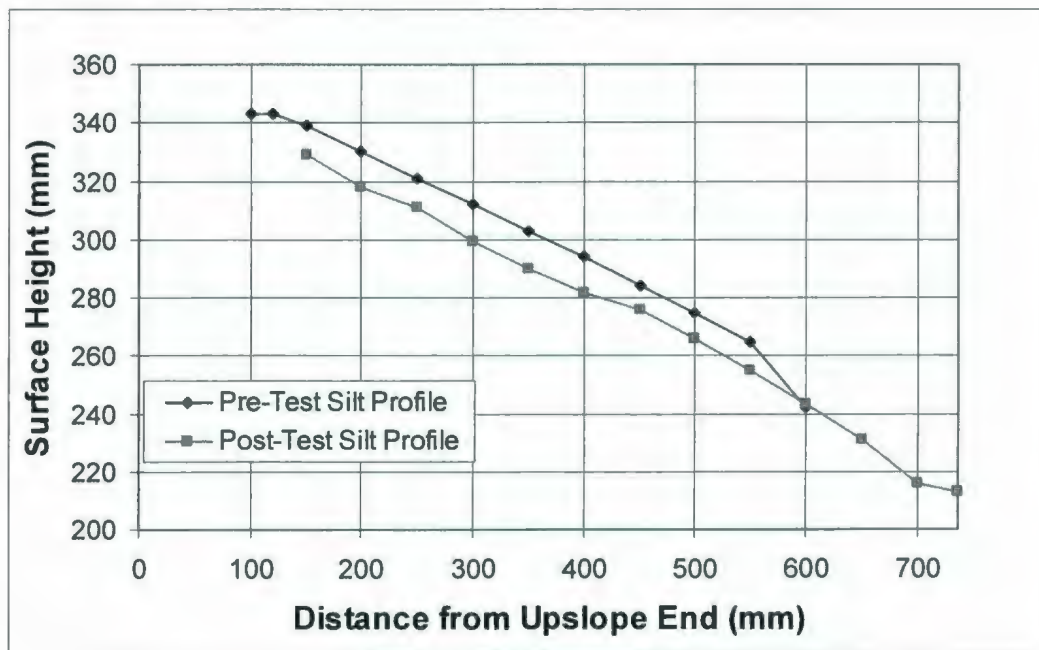
Figure 6.71: COSTA-C Silt Layer Profile.

6.4 COSTA-D

6.4.1 Pre-Test Observations

The pre–test surface profiles are shown in Table 6.15 and Figure 6.72. There is little change between the post-saturation and post-test profile, with the model staying fairly true to the construction geometry. The crest of the slope had only settled at most 5 mm during saturation and transportation, which does not represent a significant change.

Table 6.15: COSTA-D Pre-Test Surface Profile.

Distance from Upslope End (mm)	Post Construction Profile	Post Saturation Profile	Pre Test Profile
0	343	343	343
50	343	342	342
100	343	342	342
150	343	341	341
200	343	341	340
250	343	341	341
300	343	341	341
350	343	--	339
400	343	--	338
450	319	--	317
500	295	--	293
550	271	--	269
600	247	--	242
650	223	--	216
700	199	--	191
737	175	--	174
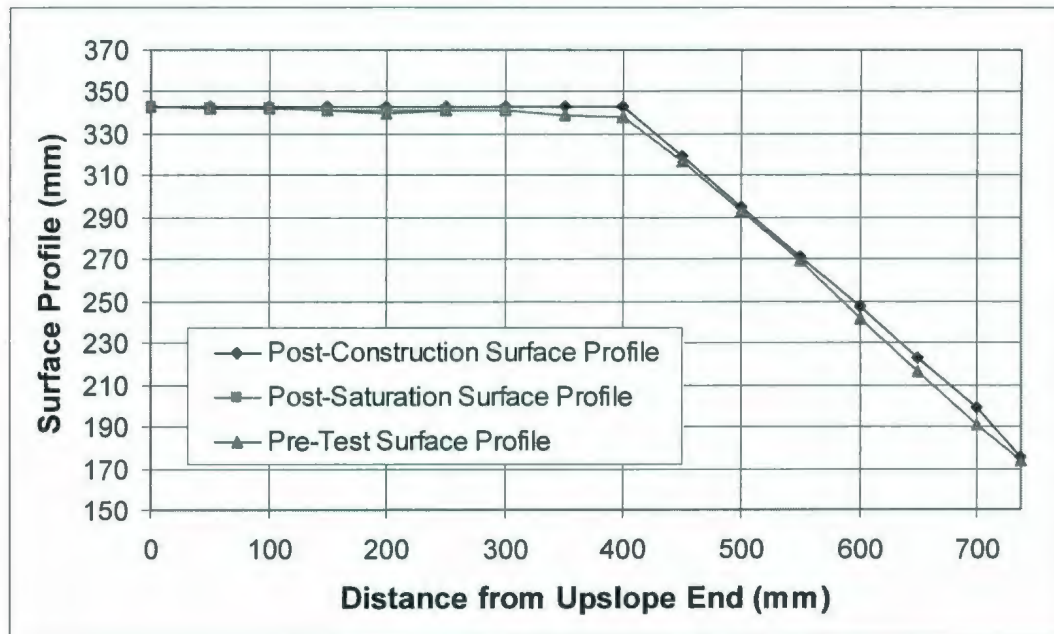
Figure 6.72: COSTA-D Pre-Test Surface Profile.

During the swing-up of the centrifuge to test speed the pore pressure transducers were monitored for any irregular changes. P1-P8 seemed to increase at the correct rates during the increase in g-level and to the proper levels considering their locations in the model. This indicates that these instruments were operating correctly. However, the response of P9 seemed to indicate there was some problem with the response of that instrument. This is likely due to the poor saturation of the instrument, which tends to delay the response of these types of PPTs. L1 & L3 were found to be malfunctioning during swing-up, so their responses are not included in this report. The response of L4 showed that the compression due to self-weight is on the order of 2 mm. L4 did however experience some electrical problems during swing-up, most likely caused by an intermittent loss of

power to the instrument. A noticeable positive response in L2 was observed and again it can most likely be attributed to the tightening of any slack in the horizontal LVDT string and pulley system that was used for this instrument. Table 6.16 shows the estimated relative density based upon the pre-test observations. The calculated relative density directly leading up to the earthquake is 34%, but this calculation is unreliable due to the loss of instruments L1 & L3, as described in the following sections. However, no further calculations were available at this location due to the malfunction of L1.

Table 6.16: COSTA-D Pre-Shake Observed Relative Density at Farfield.

Condition	Settlement (mm)	Relative Density (%)
Post-Construction	N/A	34
Post-Saturation	0.0	34
Post-Loading	0.0	34
After Spin-Up	N/A	N/A

As was done in COSTA-C the saturation of this model was to be checked by observing the travel time of acoustic waves through the model. The intention was to observe these acoustic wave responses at test speed a few moments before the initiation of the model earthquake. The generation of these waves was achieved by tapping the upslope end of the model container with a small solenoid operated hammer. This generated signal is then observed by two accelerometers (in this case A3 and A2) placed in-line along the centre axis of the model at a known distance apart (107 mm). The captured signal in these two accelerometers at 70 g is shown in Figure 6.73. The accelerometer data shown in this figure has not been corrected for their opposite orientations. The speed of this

wave can be estimated by comparing the time difference of the first major trough in Channel 1 and major peak in Channel 2.
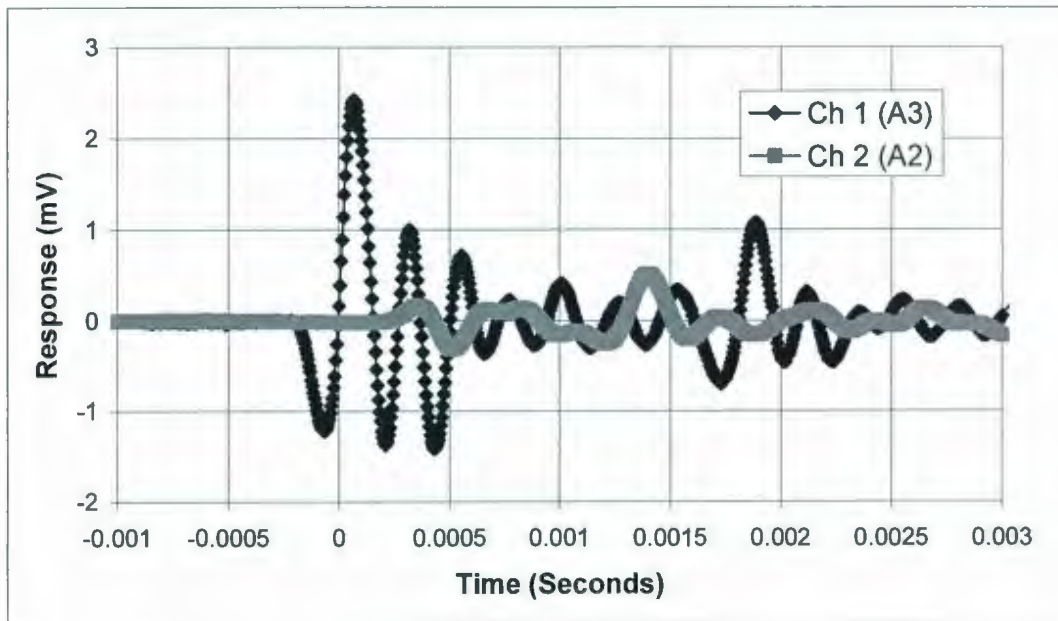
Figure 6.73: COSTA-D Acoustic Wave Response at 70g.

Acoustic wave speeds were calculated at various centrifugal accelerations using the same process described for COSTA-A in section 6.1. Table 6.17 summarizes the analysis of the calculated wave speeds for all g-levels at which acoustic wave response data was collected, both during swing-up and swing-down. The maximum calculated wave speed of 289.19 m/s occurred at 70 g previous to the earthquake actuation. The trend of wave speeds getting larger as centrifugal acceleration increases that was observed in COSTA-C is also observed here. If this setup was indeed measuring P-waves, it does seem to indicate that the model was poorly saturated, as described by Ishihara et al. (2004). As

mentioned in section 6.3 work was ongoing by project collaborators to characterize the nature of the waves that this hammer device was creating. Unfortunately, at the conclusion of this research this work was ongoing and inconclusive. It is however, possible that this model was inadequately saturated thus increasing the sensitivity of this model to failure.

Table 6.17: COSTA-D Acoustic Wave Response Summary.

G-Level	Condition	Wave Velocity (m/s)
1	Pre-Test	82.95
10	Spinup	117.58
20	Spinup	156.20
30	Spinup	181.36
40	Spinup	225.02
70	Pre-Shake	289.19
70	Post-Shake	285.33
60	Spindown	274.36
50	Spindown	257.83
40	Spindown	237.78
30	Spindown	218.37
10	Spindown	147.59
1	Post-Test	148.61

6.4.2   2A2475 Earthquake Actuation

The testing regime for the COSTA-D test was comprised of only one 2A2475 event. The top portion of Figure 6.74 illustrates the desired 2A2475 acceleration-time history in model scale. The bottom portion of Figure 6.74 shows the observed earthquake signal in Tz, which is in the direction of shaking. Figure 6.75 shows the fast Fourier transforms (FFT) of these two signals. The two signals compare relatively well with respect to frequency as well as magnitude. The actual observed earthquake being marginally larger

250

in magnitude in both the negative and positive directions. In terms of frequency content, as observed in the FFT signals, it is observed that the EQS delivered an earthquake with almost identical content in the 40 to 50 Hz and 50 to 60 Hz ranges. These results can be considered as a very good agreement between the prescribed and observed earthquake motions. Figure 6.76 illustrates the response of the triaxial accelerometer in the vertical direction. This response was captured by Ty and shows that there is a spurious vertical motion that is experienced during the earthquake event. The range of this acceleration ranges between +4 to −4 g and like this instrument's response in COSTA-C is characterized by a more regular motion that closely resembles the horizontal motion, as compared to the observations from the applied earthquakes in COSTA-A and COSTA-B.
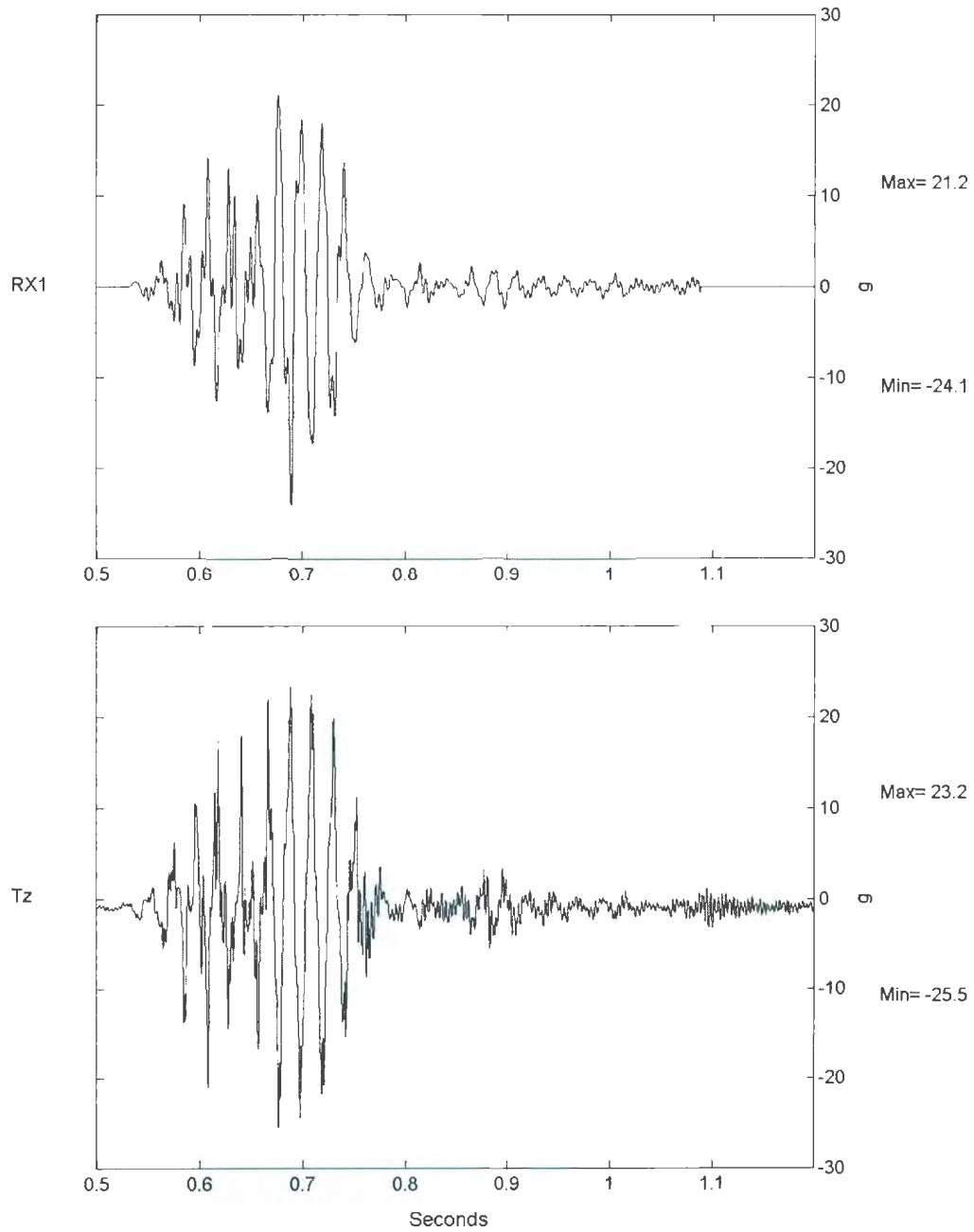
Figure 6.74: Comparison of 2A2475 Earthquake Record & Observed COSTA-D Tz Acceleration.
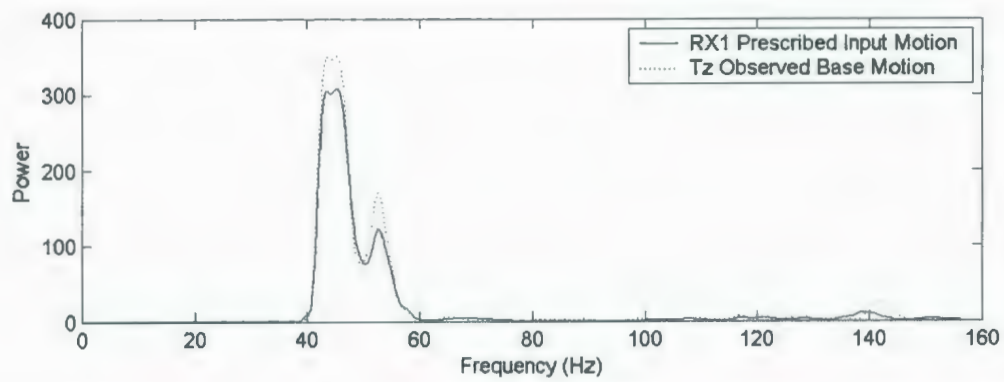
Figure 6.75: FFT Comparison of 2A2475 Earthquake Record & Observed COSTA-D Tz Acceleration.
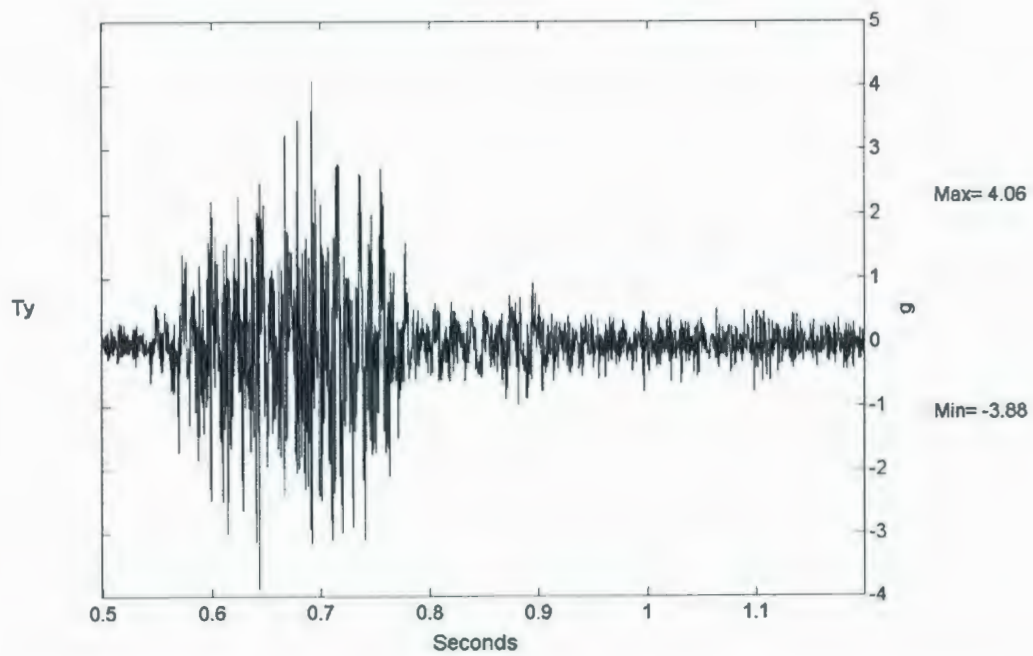
Figure 6.76: COSTA-D 2A2475 Observed Ty Vertical Acceleration Response.

253

6.4.3 *2A2475 Short-Term Testing Instrument Responses*

All instruments were monitored during and shortly after the 2A2475 earthquake event. Figures 6.77 through 6.81 illustrate the observed responses in the various instruments during a 0.5 second period. Although no silt layer is used in this model, the locations of the instruments are described in the figures relative to the location of the silt layer in the previous COSTA-B & COSTA-C tests for comparison purposes.
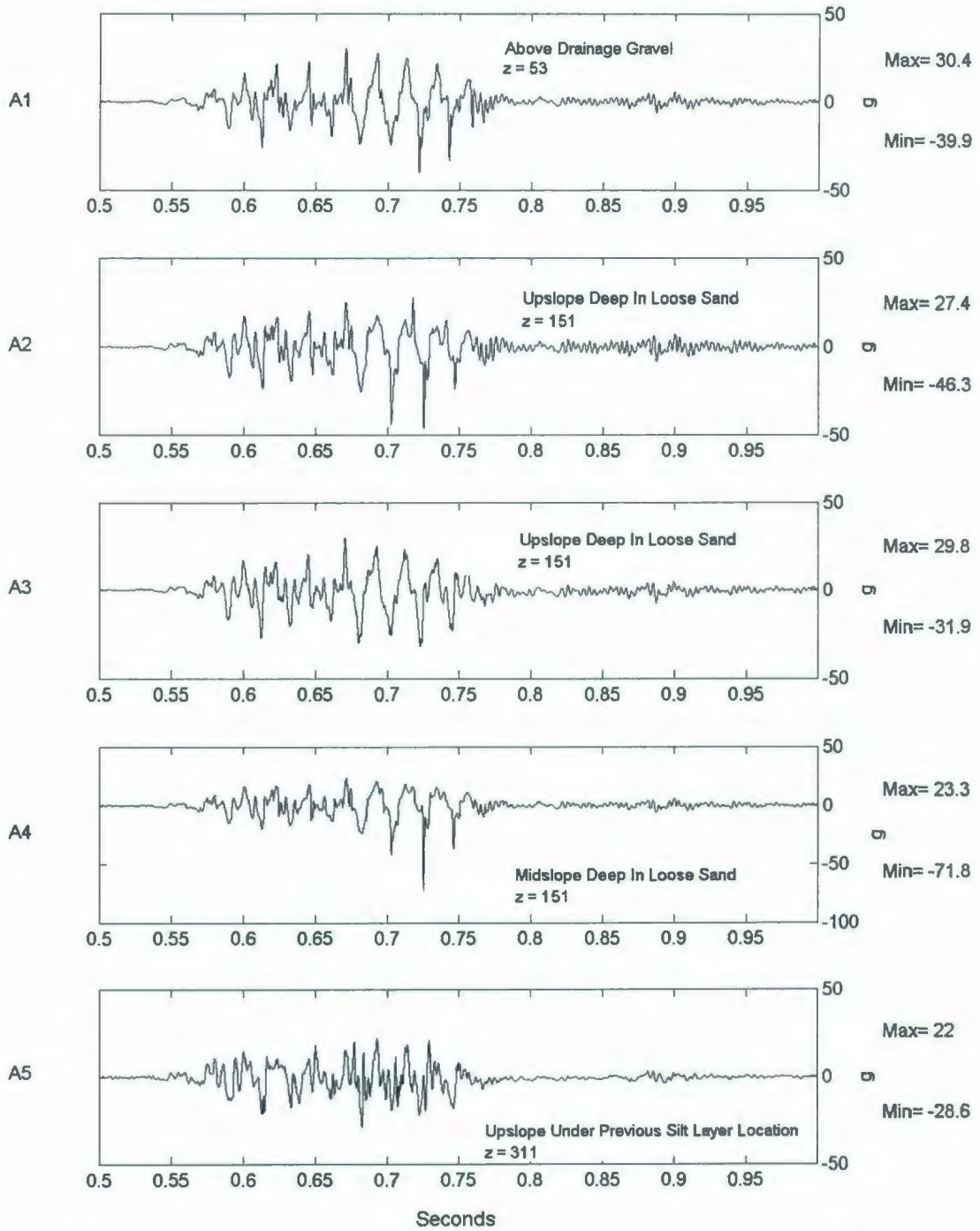
Figure 6.77: COSTA-D 2A2475 Short-Term Accelerometer Response A1-A5.
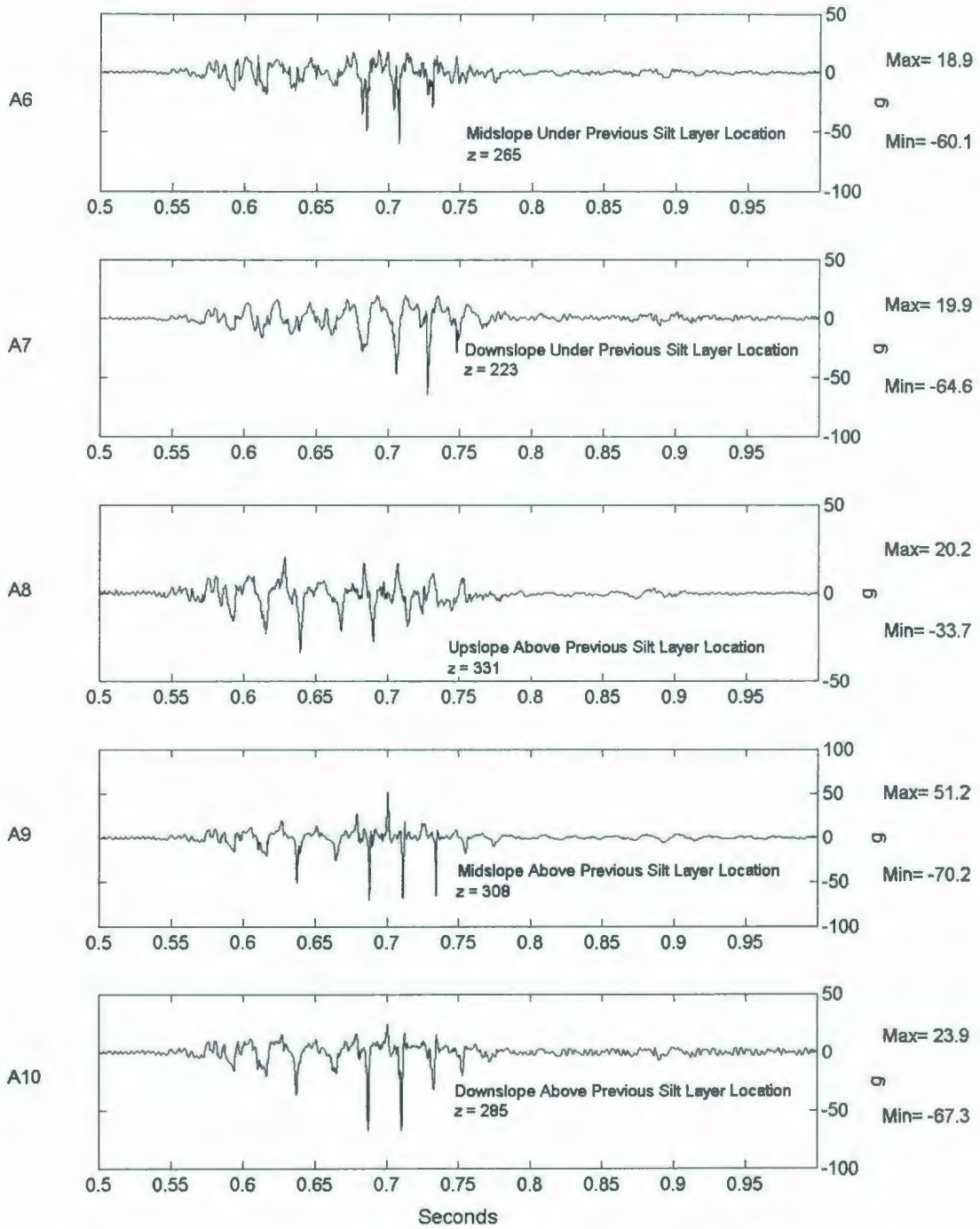
Figure 6.78: COSTA-D 2A2475 Short-Term Accelerometer Response A6-A10.

256
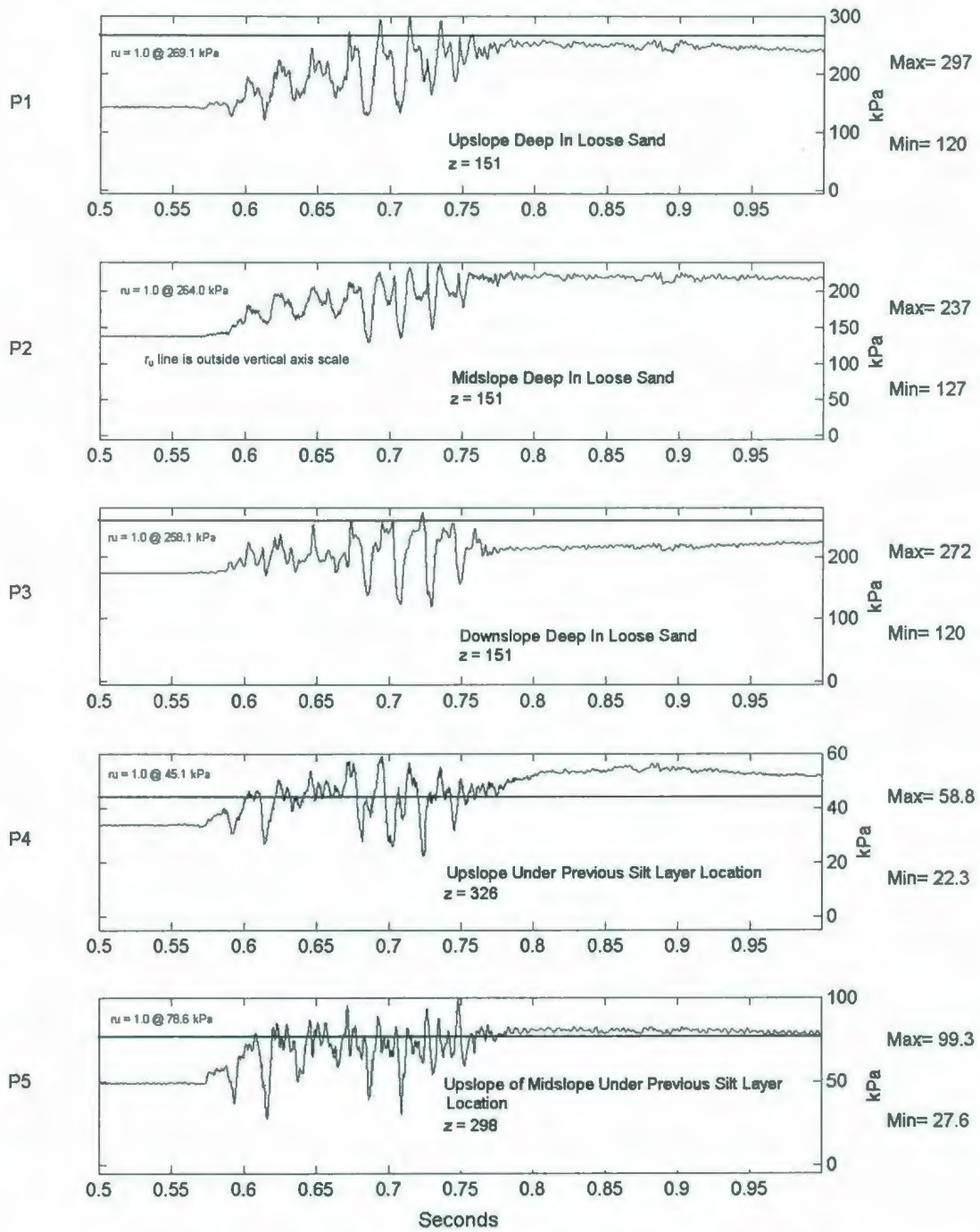
Figure 6.79: COSTA-D 2A2475 Short-Term PPT Response P1-P5.

P6   ru = 1.0 @ 140.0 kPa   Midslope Under Previous Silt Layer Location
z = 250   Max= 144   Min= 77.1

P7   ru = 1.0 @ 122.0 kPa   r$_u$ line is outside vertical axis scale   Downslope of Midslope Under Previous Silt Layer Location
z = 243   Max= 119   Min= 27.4

P8   ru = 1.0 @ 115.3 kPa   Downslope Under Previous Silt Layer Location
z = 214   Max= 162   Min= 51.3

P9   ru = 1.0 @ 49.6 kPa   r$_u$ line is outside vertical axis scale   Midslope Above Previous Silt Layer Location
z= 316   Max= 34.5   Min= 23.7

Seconds

Figure 6.80: COSTA-D 2A2475 Short-Term PPT Response P6-P9.

258
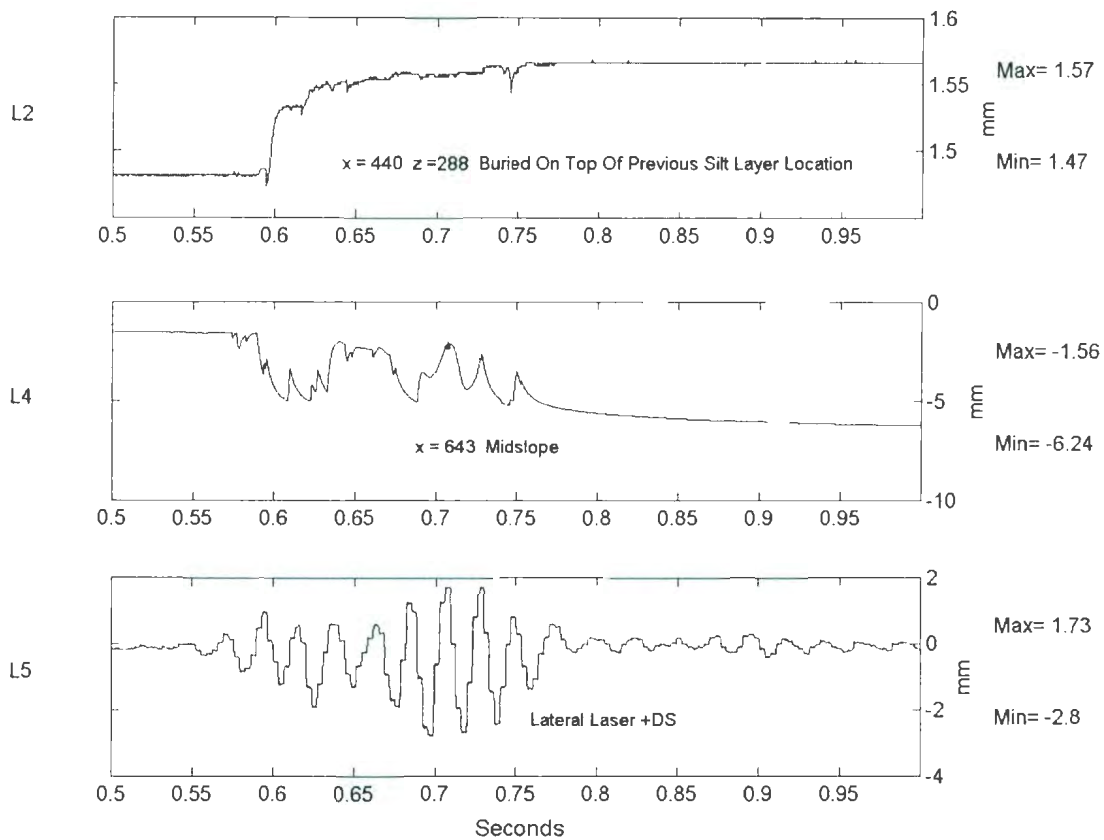
Figure 6.81: COSTA-D 2A2475 Short-Term LVDT Deformation & Lateral Laser Displacement Responses.

In the short-term, it is evident that there is a large increase in the tendency of the accelerometers to measure negative spikes with increased elevation in the model. This is especially evident in the accelerometers that are above the location of the silt layer in COSTA-C (A8, A9, & A10). However, these spikes are not as pronounced as they were in the 2A2475 event in the COSTA-C test. The accelerometers above the silt layer location in previous tests have a more significant positive component than in COSTA-C where measured acceleration was almost exclusively in the negative direction.

259

The PPTs below the previous silt layer location (P4-P8) displayed larger peak pore pressures than when there was a silt layer present. Above the silt layer location, as is shown by the response of P9, the pore pressure is more stable than when a silt layer was present. This behaviour was also probably attenuated by the poor instrument saturation that was previously discussed. Although, two of the PPTs above the silt layer (P7 & P8) displayed negative spikes that correspond to the negative pikes in the accelerometers in similar positions.

Liquefaction occurs in a variety of instruments but is first evident about 0.05 seconds after the start of the 2A2475 earthquake in P8 at the most downslope location. Liquefaction conditions appear to move progressively upslope occurring in P5 and P4 shortly after P8. These liquefaction conditions in the upslope portion were more prolonged that what was experienced deeper in the model. As was seen in previous tests some liquefaction occurred in the deeper portions in the model after it had occurred shallower in the model. This can be seen by the liquefaction occurring in P1 and P3, that does not take place until 0.1 seconds after it had appeared in P3 and P5.

The surface settlement changes on the slope face, provided by the response of L4, shows that there was 4.7 mm of settlement in the short-term. In terms of downslope movement, there was no discernable movement from the observation of the response of L2, with only a slight heave of approximately 0.1 mm taking place.

6.4.4 *2A2475 Long-Term Testing Instrument Responses*

The long-term responses were collected to examine the behaviour of the model for several seconds after the 2A2475 earthquake event. Figures 6.82 through 6.86 illustrate these responses.
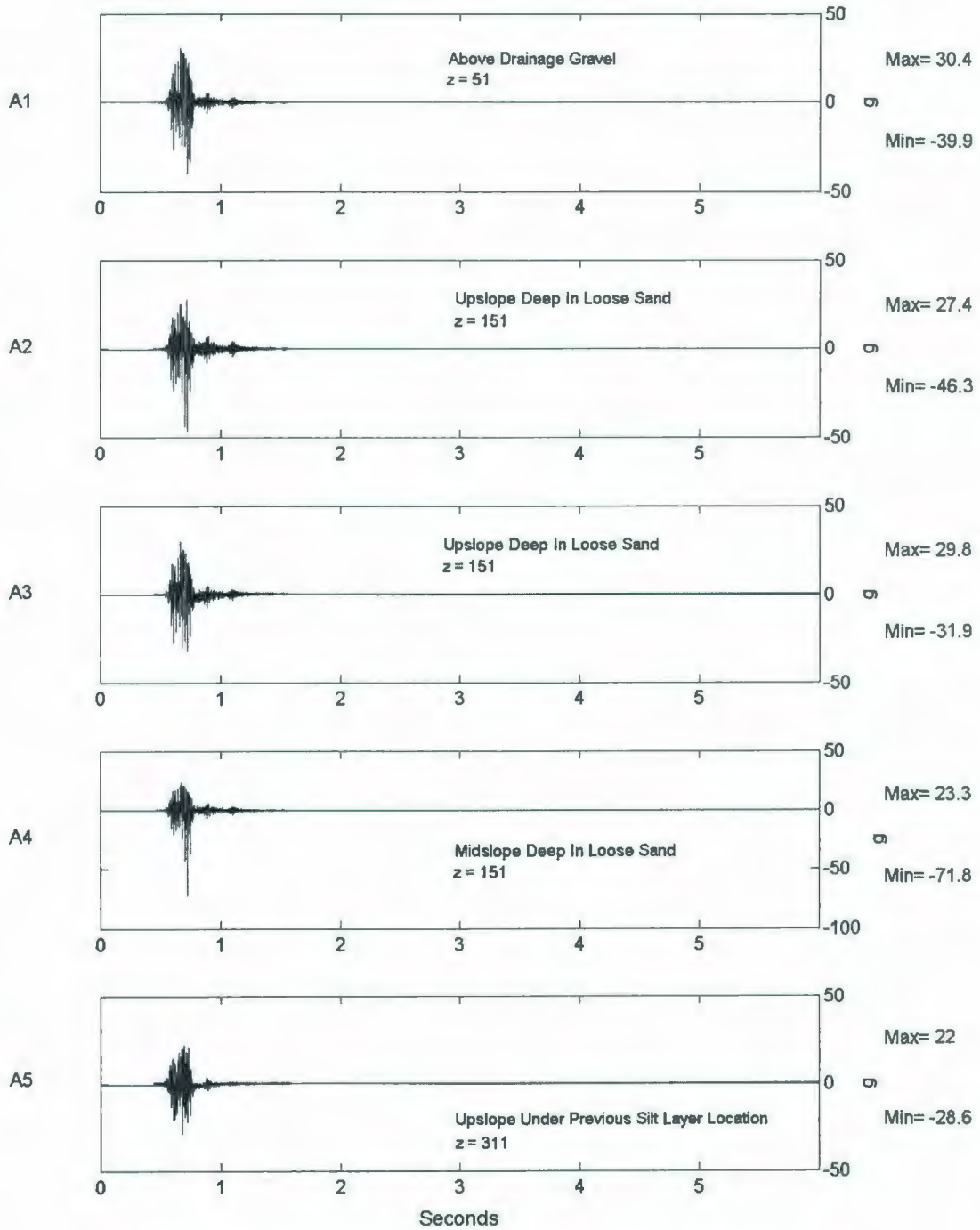
Figure 6.82: COSTA-D 2A2475 Long-Term Accelerometer Response A1-A5.
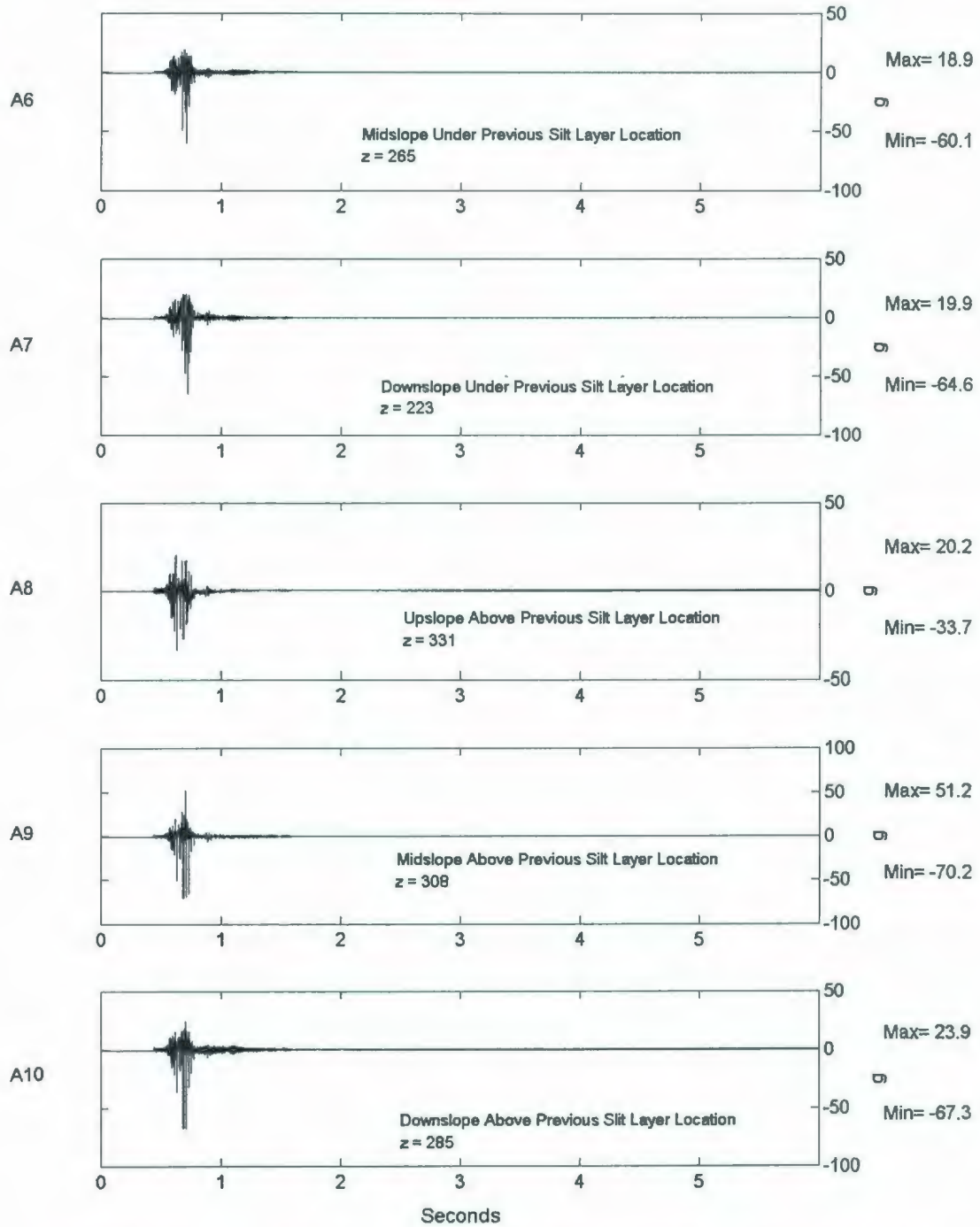
Figure 6.83: COSTA-D 2A2475 Long-Term Accelerometer Response A6-A10.
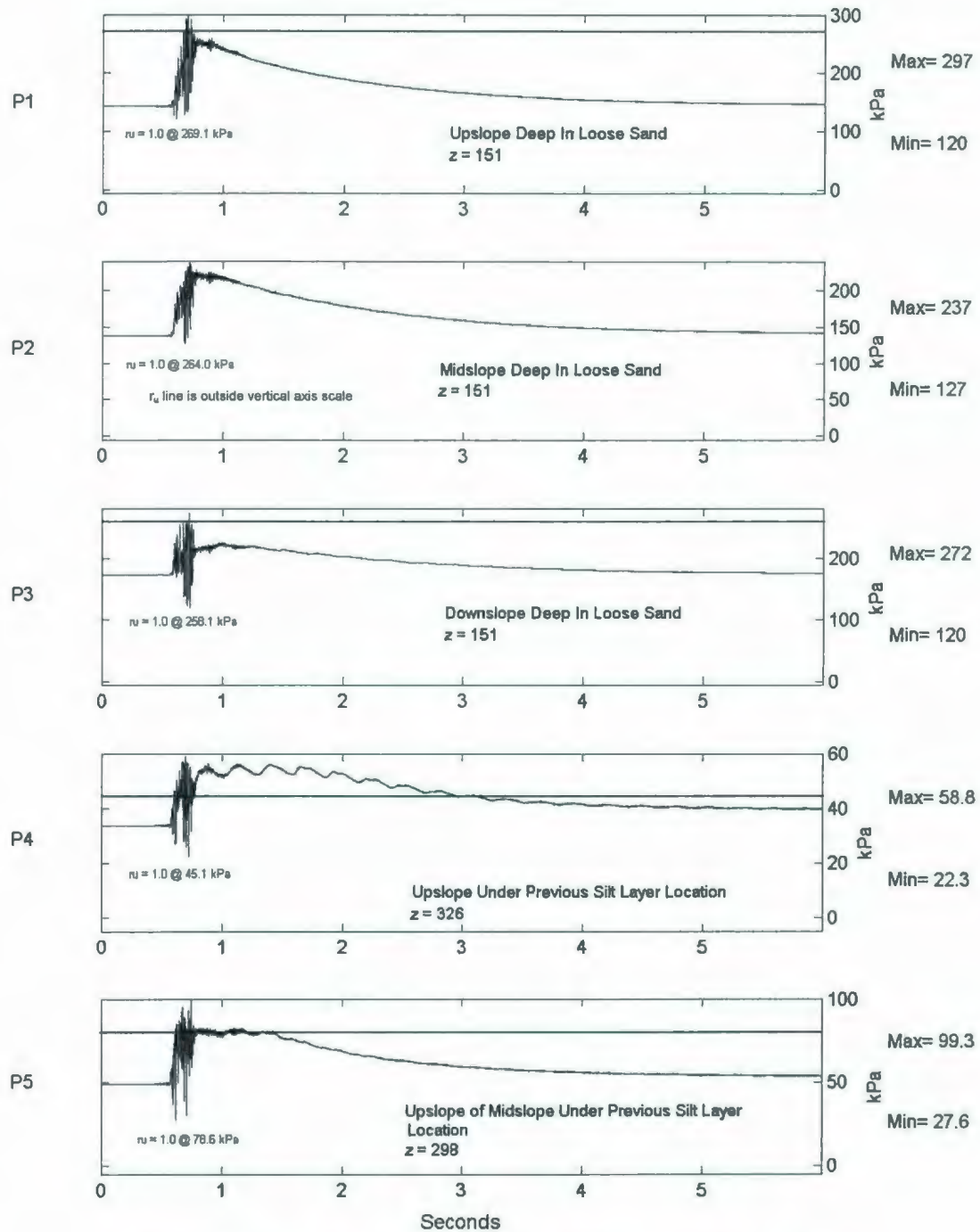
Figure 6.84: COSTA-D 2A2475 Long-Term PPT Response P1-P5.
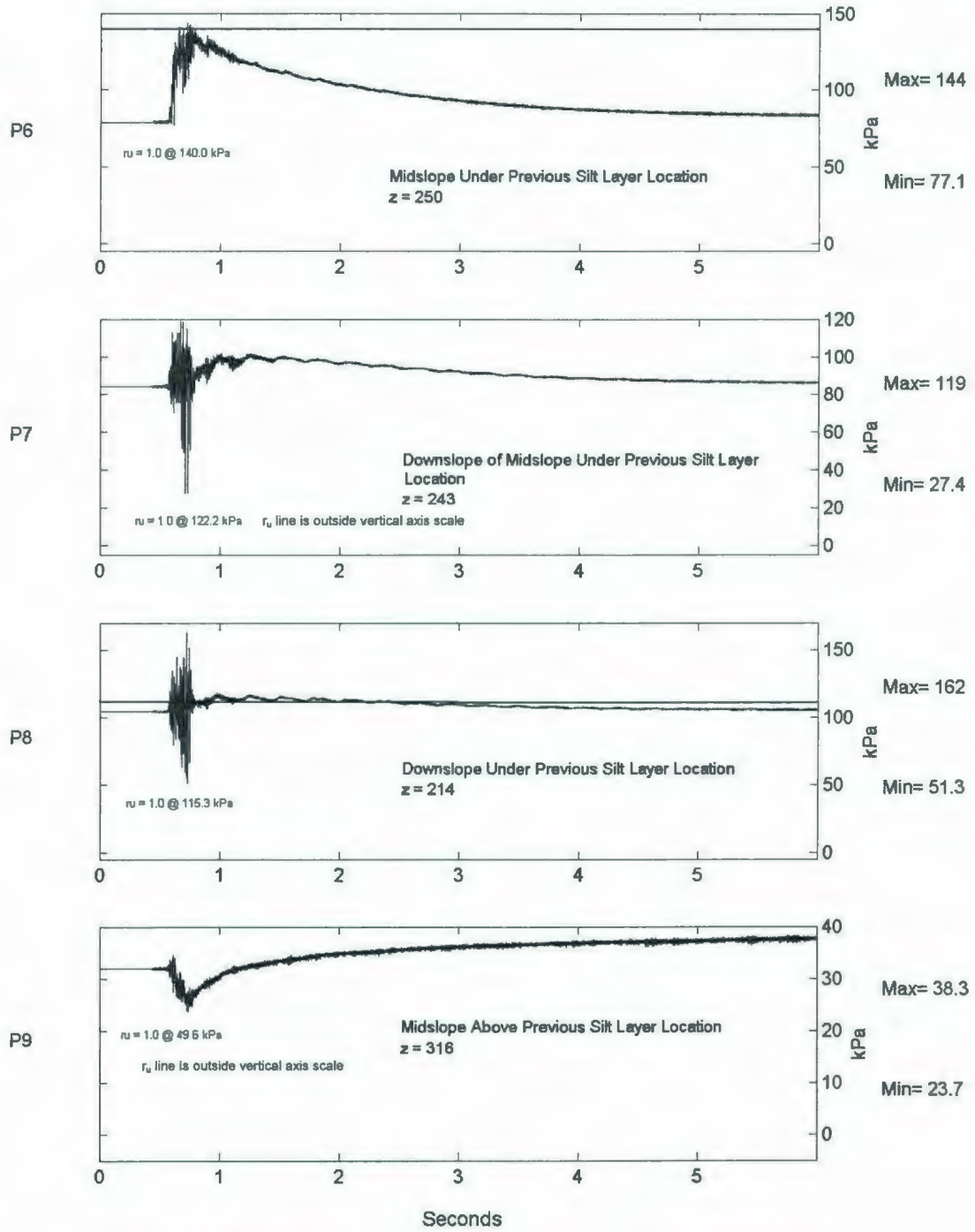
Figure 6.85: COSTA-D 2A2475 Long-Term PPT Response P6-P9.
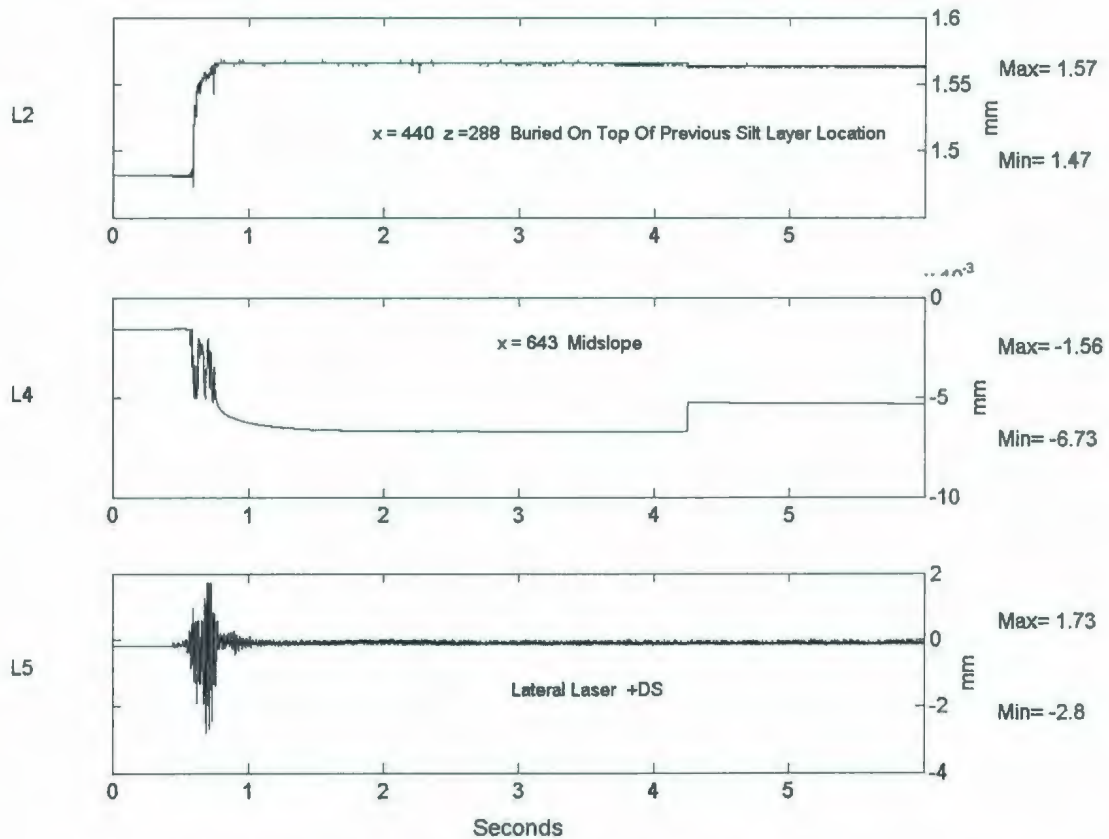
Figure 6.86: COSTA-D 2A2475 Long-Term LVDT Deformation & Lateral Laser Displacement Responses.

The long-term accelerometer results exemplify the negative spikes that were previously discussed with much of the acceleration in the model ceasing after the completion of the majority of shaking at 0.8 seconds. There is some evidence of post-earthquake movement, in such instruments as A5, where there is some observed movement up to approximately 0.5 seconds following shake cessation.

The long-term results show that the deep in the model, as observed by P1-3, pore pressure generation behaviour is similar to COSTA-C where a silt layer was present taking several seconds to dissipate. With respect to the pore pressure generation underneath the silt layer location, P5 and P6 both showed that the generated pore pressure dissipated faster to pre-shake levels than in COSTA-C. P9 showed that in this case there was a sharp decrease in pore pressure during the shaking followed by an overall increase, where when a silt layer was present this decrease was not observed, but again this was most likely an attenuated response due to pore saturation of the instrument.

P4 experienced liquefaction for a prolonged period, for approximately 2 seconds after the earthquake event. This is in contrast to a similarly positioned PPT (P5) where a condition of liquefaction is only sustained for approximately 0.5 seconds after shaking. P8, which is the most downslope PPT, also experiences prolonged liquefaction conditions as the excess pore pressure dissipates. This would indicate that generated excess pore pressure is persistently migrating upward from deeper in the model in these areas.

The LVDTs did not show any significant response during in the long-term response, with no downslope movement observed. The sharp heave of just over 1 mm observed in L4 at 4.25 seconds can most likely be attributed to the instrument housing slipping slightly in its bracket, which would be interpreted as a heaving response.

6.4.5 Post-Test Observations

Similarly to swing-up, the PPT and LVDT responses were monitored during swing-down to ensure integrity of the model and to observe any radical changes that may occur. All PPTs seem to experience the correct rate in reduction of pore pressure as the g-level decreases indicating that there were no large changes in pore pressure during swing-down. Most of the PPTs return to a value close to zero. The change from their original value could be caused by the movement of the PPT in the sand during shaking. However, it should be noted that the response of P3 did not completely return to a zero level. This most likely indicates that there is some electrical problem with the response of this instrument. L4 continued to show the electrical problems experienced during swing-up and the observed relatively large displacement of L2 is likely due to the slacking of the string mechanism also experienced during swing-up.

Temperature measurements of the model were taken periodically before and after the loading of the model on to the centrifuge arm, as well as after the test. In previous tests warm oil circulating in the hydraulic mechanisms of the shaker have been observed to significantly effect the temperature of the model. A temperature probe was installed during pluviation deep in the loose sand. Table 6.18 displays these observed temperatures.

Table 6.18: COSTA-D Observed Model Temperature.

Time	Location	Comments	Temperature (°C)
9:30 AM	On Lab Floor	Pre Loading	19.7
11:30 AM	On Arm	After Loading	19.6
2:30 PM	On Arm	Pre-Test	23.2
3:45 PM	On Arm	Post-Test	24.3

After the centrifuge flight was completed, the profile of the model surface was measured while the model was still situated on arm. The results showed reduction in height on the upslope surface as well as some collection of material at the toe. Table 6.19 and Figure 6.87 illustrate these pre- and post- test conditions. No significant movement of the slope crest in the downslope direction was observed. Much like the response during COSTA-A, only surface settlement, of approximately 10 mm, in the upslope farfield was observed with very little accumulation of material occurring at the toe.

Table 6.19: COSTA-D Post-Test Surface Profile.

Distance from Upslope End (mm)	Pre-Test Surface Height (mm)	Post-Test Surface Height (mm)
0	343	331
50	342	330
100	342	329
150	341	329
200	340	327
250	341	327
300	341	327
350	339	326
400	338	324
450	317	315
500	293	294
550	269	272
600	242	242
650	216	220
700	191	194
737	174	188

269
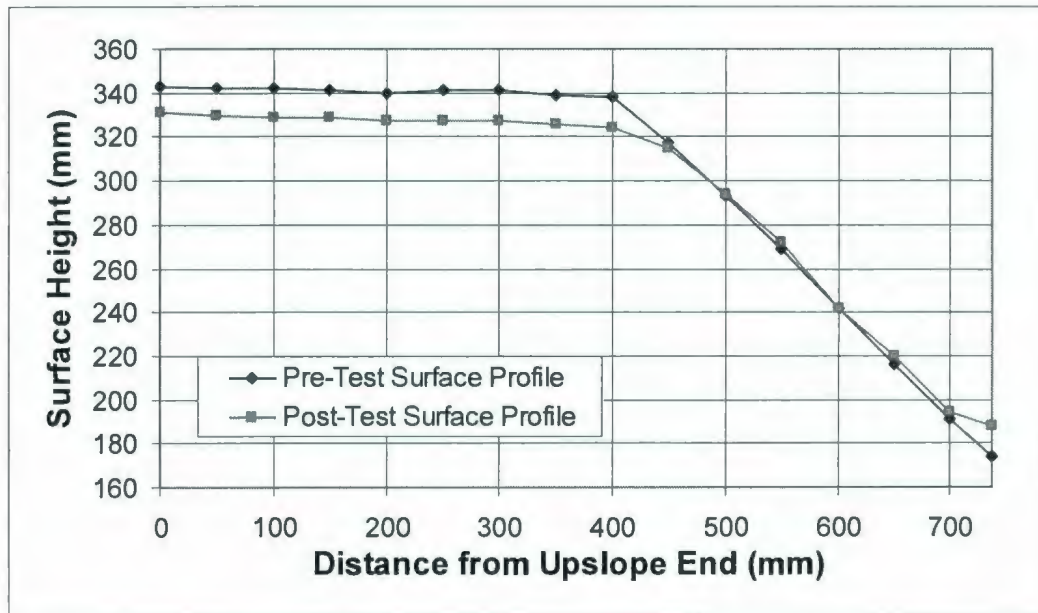
Figure 6.87: COSTA-D Post-Test Surface Profile.

Small white pieces of gravel were placed on the model slope face prior to saturation in a square grid measuring approximately 25 mm by 25 mm grid. A photograph of this grid as placed pre-test is shown in Figure 6.88. This was done to make qualitative comparisons of the movement of the slope face during the test.
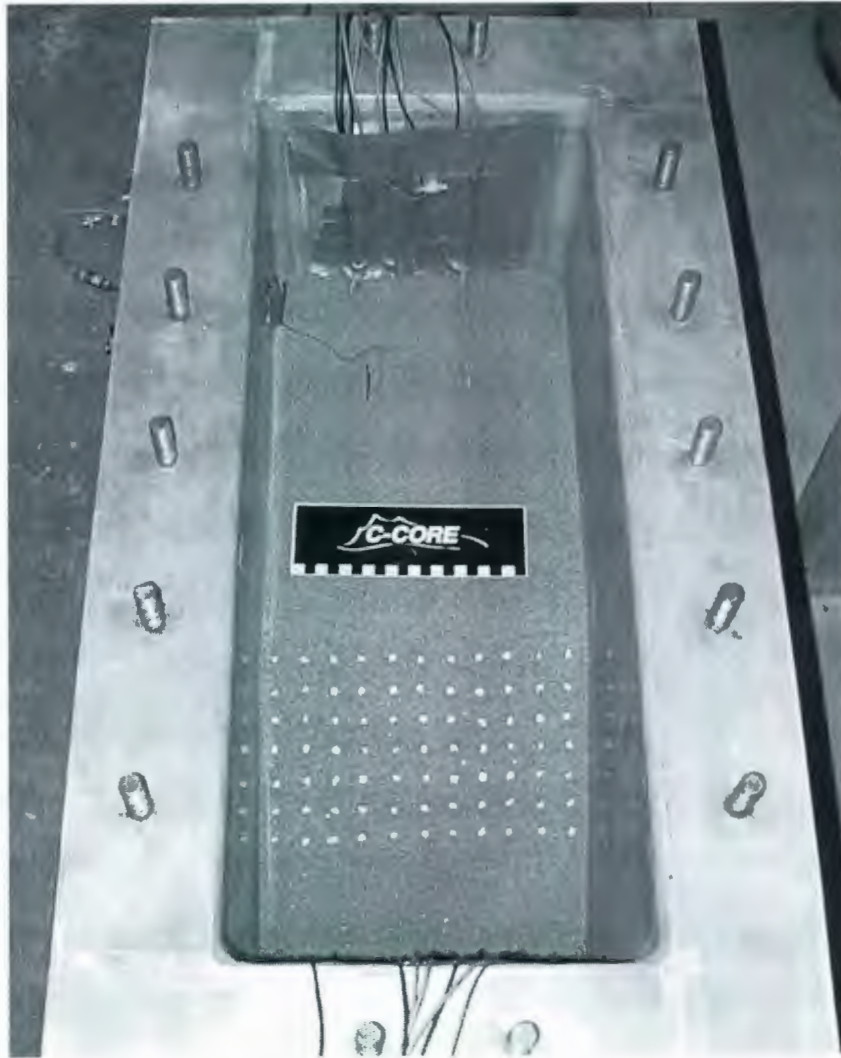
Figure 6.88: COSTA-D Pre-Test Slope Marker Grid.

Following the test a photograph of the model slope, similar to that shown in Figure 6.88 was also taken. The post-test marker grid conditions are shown in Figure 6.89. It is shown that no significant horizontal deformation of the marker grid occurred during slope failure. This indicates that no significant friction was observed between the sand and the

interface of the walls of the model container. This figure also shows hat there was no significant movement or failure of the slope during the application of the earthquake event, much like what is observed by Taboada-Urtuzuastegui et al. (2002)

Figure 6.89: COSTA-D Post-Test Slope Marker Grid.

6.5 COSTA-E

6.5.1 Pre-Test Observations

The pre–test surface profiles are shown in Table 6.20 and Figure 6.90. There is little change between the post-saturation and post-test profile, with the model staying fairly true to the construction geometry. The crest of the slope had settled at most 7 mm during saturation and transportation, which does not represent a significant change.

Table 6.20: COSTA-E Pre-Test Surface Profile.

Distance from Upslope End (mm)	Post Construction Profile	Post Saturation Profile	Pre Test Profile
0	343	342	342
50	343	342	342
100	343	342	341
150	343	341	341
200	343	341	341
250	343	341	340
300	343	340	339
350	343	--	338
400	343	--	336
450	319	--	311
500	295	--	285
550	271	--	263
600	247	--	237
650	223	--	211
700	199	--	185
737	175	--	174
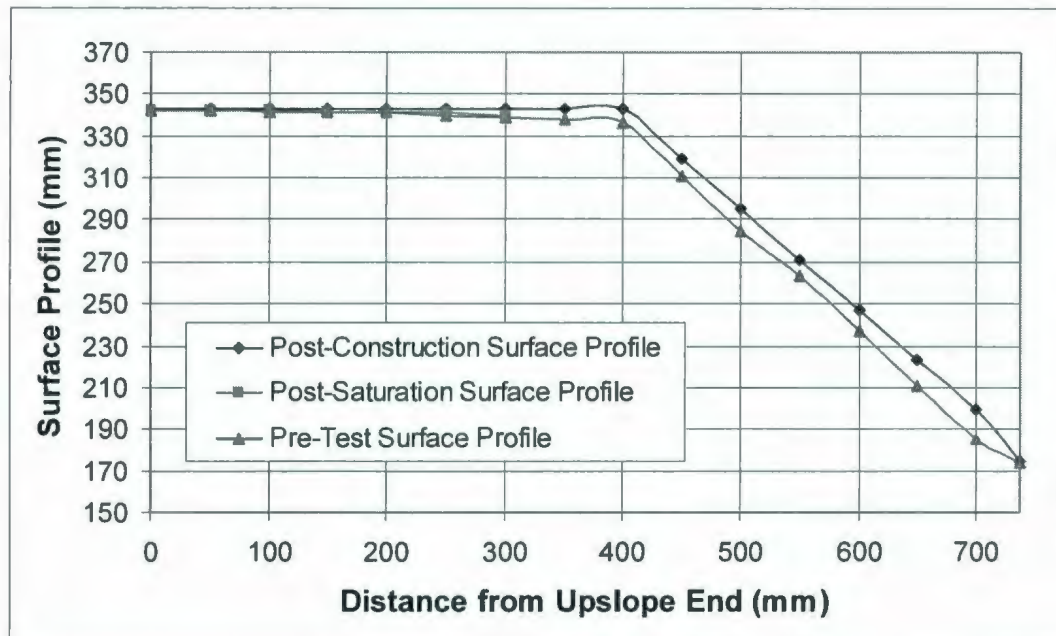
Figure 6.90: COSTA-E Pre-Test Surface Profile.

During the swing-up of the centrifuge to test speed the pore pressure transducers were monitored for any irregular changes. P1 through P7 and P9 seemed to increase at the correct rates during the increase in g-level and to the proper levels considering their locations in the model. This indicates that these instruments were operating correctly. However, the response of P8 showed that there was a problem regarding the proper functioning of that instrument. Therefore, its response in not included in this section. The response of P3 seemed to indicate there was some problem with the response of that instrument. This is likely due to the poor saturation of the instrument, which tends to delay the response of these types of PPTs. L1 & L2 were found to be malfunctioning during swing-up, so their responses are not included in this report. The response of L4

274

showed that the compression due to self-weight is on the order of 1.5-3 mm. Table 6.21 shows the estimated relative density based upon the pre-test observations. The calculated relative density directly leading up to the earthquake is 36%. However, no further calculations were available at this location due to the malfunction of L1.

Table 6.21: COSTA-E Pre-Shake Observed Relative Density at Farfield.

Condition	Settlement (mm)	Relative Density (%)
Post-Construction	N/A	28
Post-Saturation	0.0	28
Post-Loading	0.0	28
After Spin-Up	N/A	N/A

As was attempted in the previous two tests the saturation of this model was to be checked by observing the travel time of acoustic waves through the model. The intention was to observe these acoustic wave responses at test speed a few moments before the initiation of the model earthquake. The generation of these waves was achieved by tapping the upslope end of the model container with a small solenoid operated hammer. This generated signal is then observed by two accelerometers (in this case A3 and A2) placed in-line along the centre axis of the model at a known distance apart (107 mm). The captured signal in these two accelerometers at 70 g is shown in Figure 6.91. The accelerometer data shown in this figure has not been corrected for their opposite orientations. The speed of this wave can be estimated by comparing the time difference of the first major trough in Channel 1 and major peak in Channel 2. It should be also noted that there is some clipping of data in Channel 1. This clipping is inconsequential since the first response trough of Channel 1 was adequately captured.
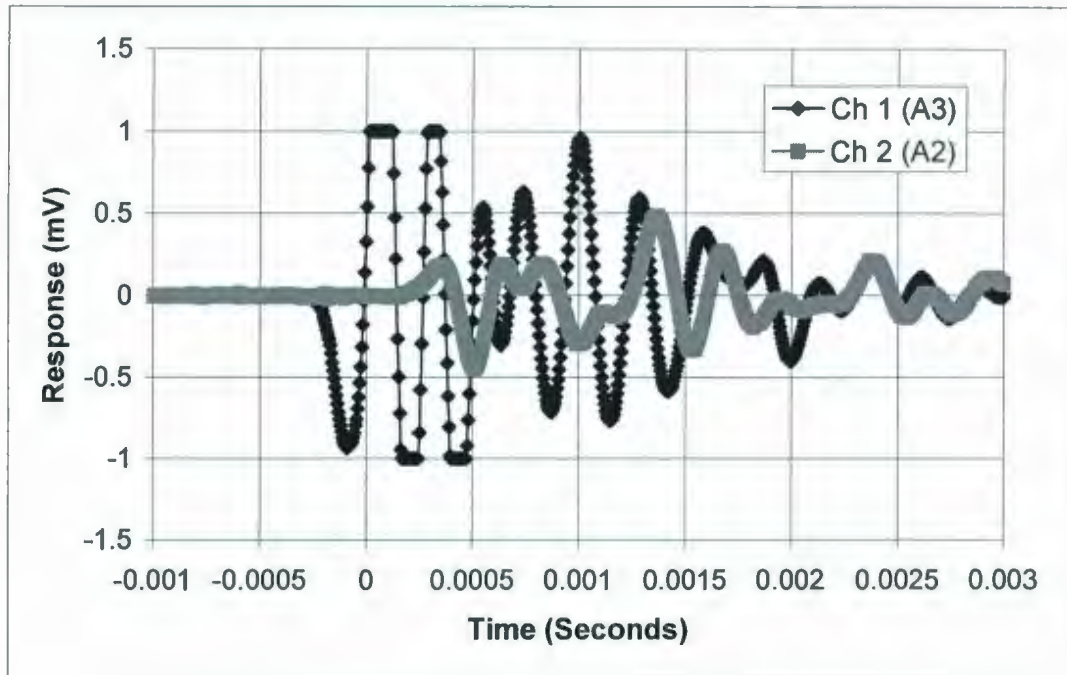
Figure 6.91: COSTA-E Acoustic Wave Response at 70g.

Acoustic wave speeds were calculated at various centrifugal accelerations using the same process described for COSTA-A in section 6.1. Table 6.22 summarizes the analysis of the calculated wave speeds for all *g*-levels at which acoustic wave response data was collected, both during swing-up and swing-down. The maximum calculated wave speed of 298.55 m/s occurred at 70 *g* following earthquake actuation. The trend of wave speeds getting larger as centrifugal acceleration increases that was observed in COSTA-C and COSTA-D is also observed here. If this setup was indeed measuring P-waves, it does seem to indicate that the model was poorly saturated, as described by Ishihara et al. (2004). As mentioned in section 6.3 work was ongoing by project collaborators to

characterize the nature of the waves that this hammer device was creating. Unfortunately, at the conclusion of this research this work was ongoing and inconclusive. It is however, possible that this model was inadequately saturated thus increasing the sensitivity of this model to failure.

Table 6.22: COSTA-E Acoustic Wave Response Summary.

G-Level	Condition	Wave Velocity (m/s)
1	Pre-Test	61.13
10	Spinup	106.74
20	Spinup	150.37
40	Spinup	170.25
50	Spinup	190.74
60	Spinup	200.00
70	Pre-Shake	221.50
70	Post-Shake	298.55
60	Spindown	267.53
50	Spindown	254.32
40	Spindown	242.35
20	Spindown	188.99
10	Spindown	173.11
1	Post-Test	144.06

6.5.2   COSTA-E Earthquake Actuation

This test comprised of the application of six earthquake signals to the model geometry. First, the A475 earthquake signal was applied to the model at test speed. Following this event, generated pore pressures were allowed to dissipate for several minutes. The A475 earthquake event was applied four more times, allowing for pore pressure dissipation following each event. The final earthquake applied to the model was the larger 2A2475 event. However, for the COSTA-E test a change was made in the configuration of the triaxial accelerometer that was used to observe the base acceleration response of the

277

model. This change resulted in this instrument being no longer compatible with the data acquisition system. Therefore, data for its response was unavailable. Based on the results for previous earthquake tests, COSTA-A through COSTA-E, it has been shown that the EQS can reliably reproduce these given signals.

6.5.3 A475-1 Short-Term Testing Instrument Responses

All operating instruments were monitored during and shortly after the first A475 earthquake event. Figures 6.92 through 6.96 illustrate the observed responses in the various instruments during a 0.5 second period.
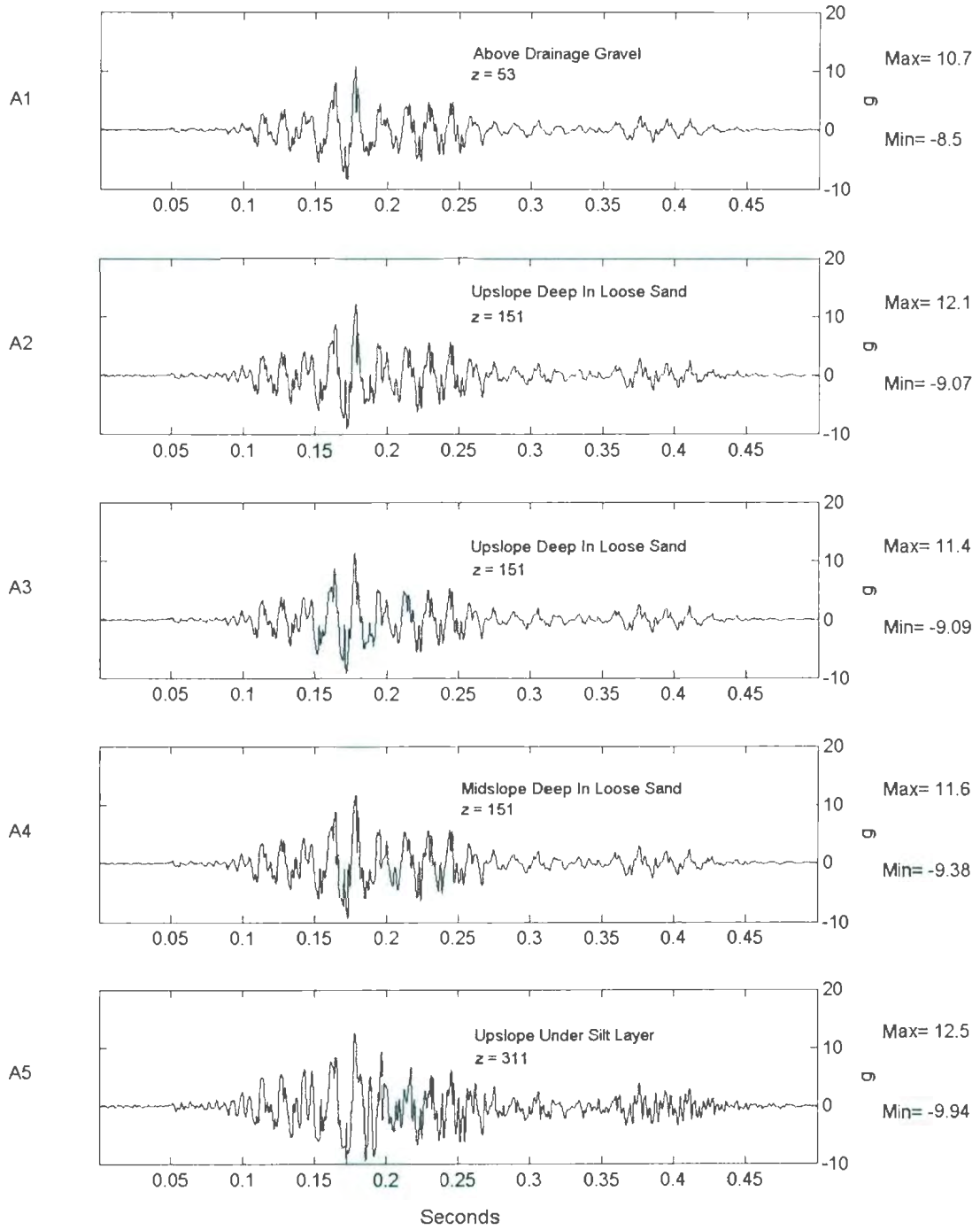
Figure 6.92: COSTA-E A475-1 Short-Term Accelerometer Response for A1-A5.
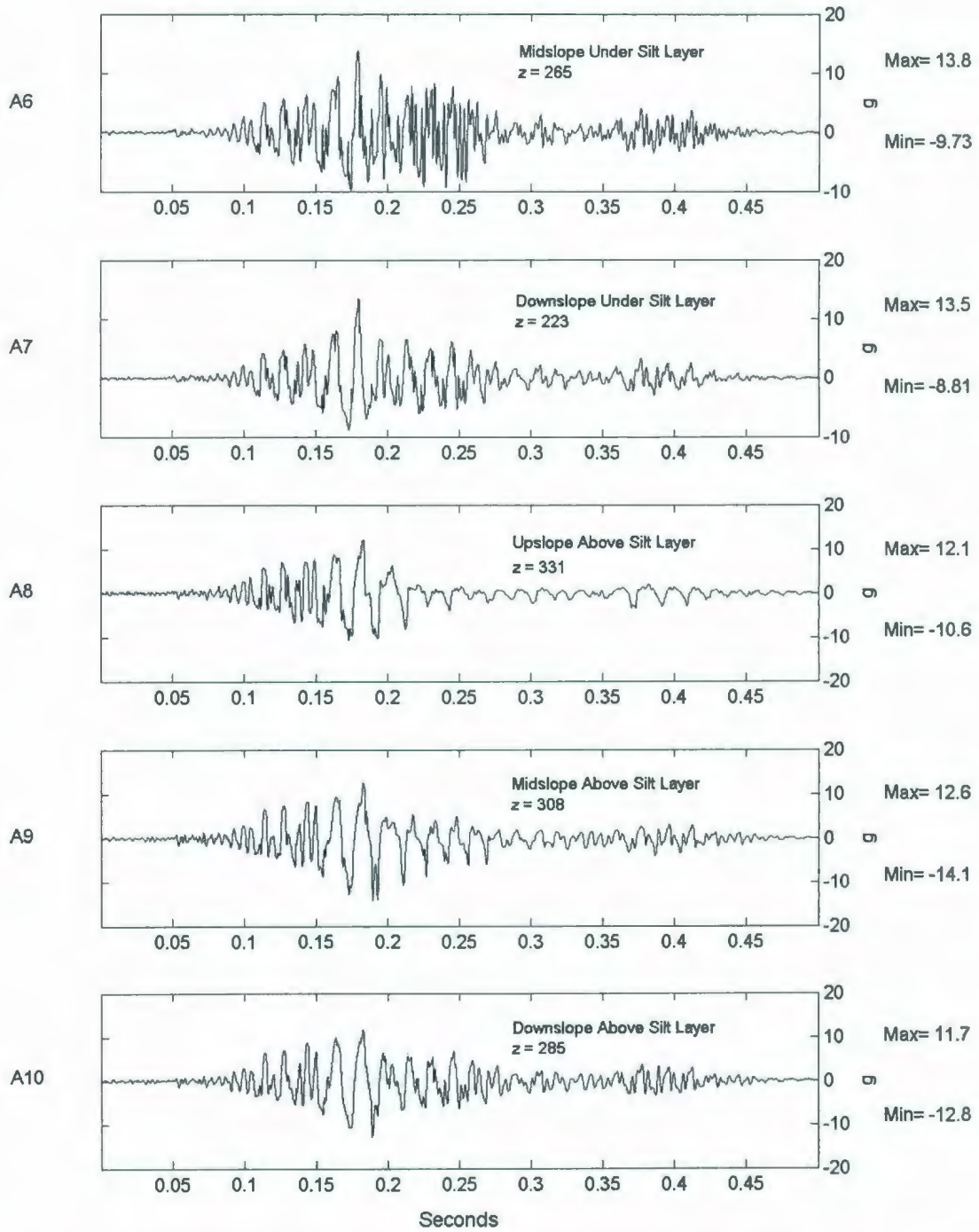
Figure 6.93: COSTA-E A475-1 Short-Term Accelerometer Response for A6-A10.
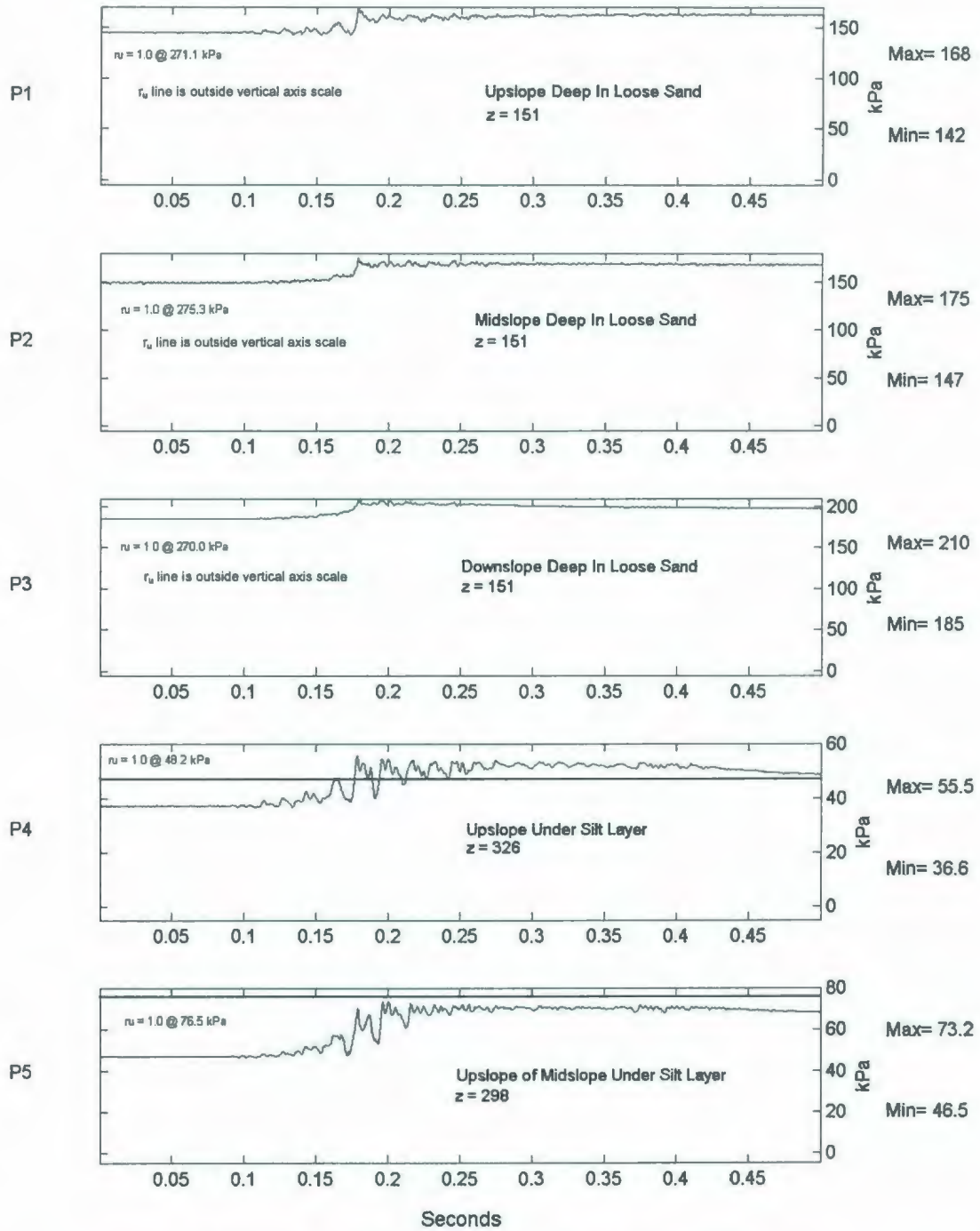
Figure 6.94: COSTA-E A475-1 Short-Term PPT Response for P1-P5.
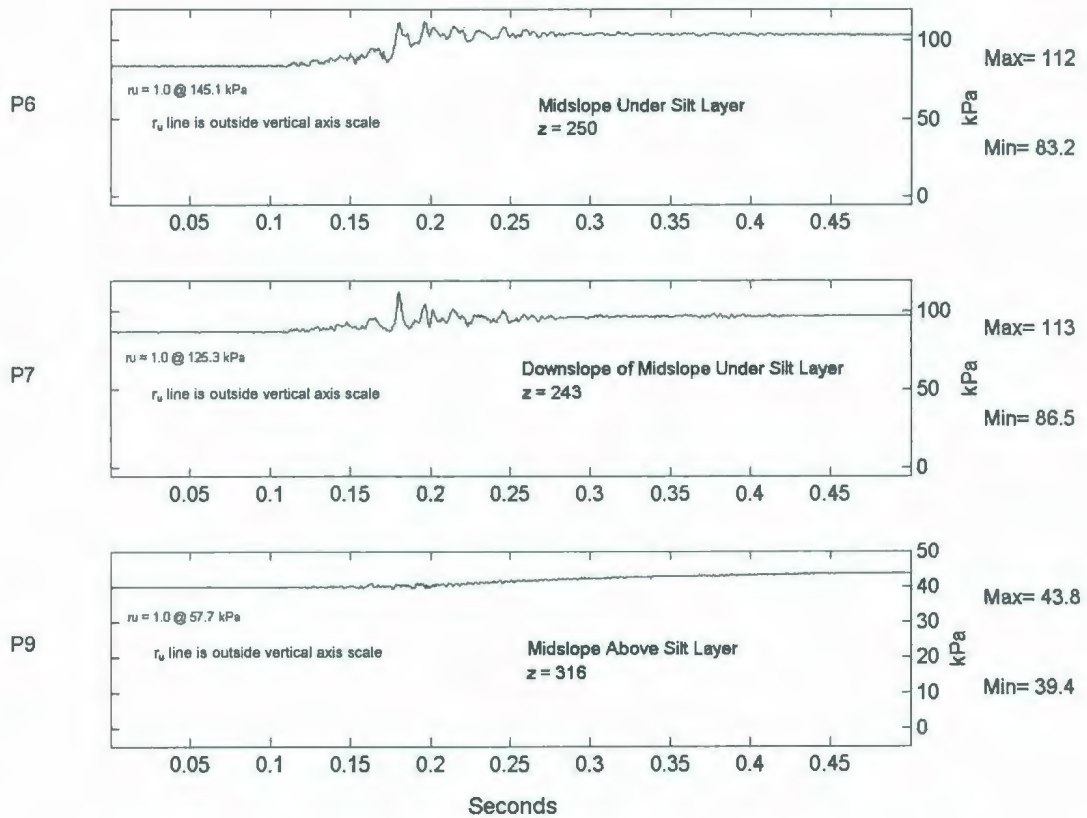
Figure 6.95: COSTA-E A475-1 Short-Term PPT Response for P6-P9.
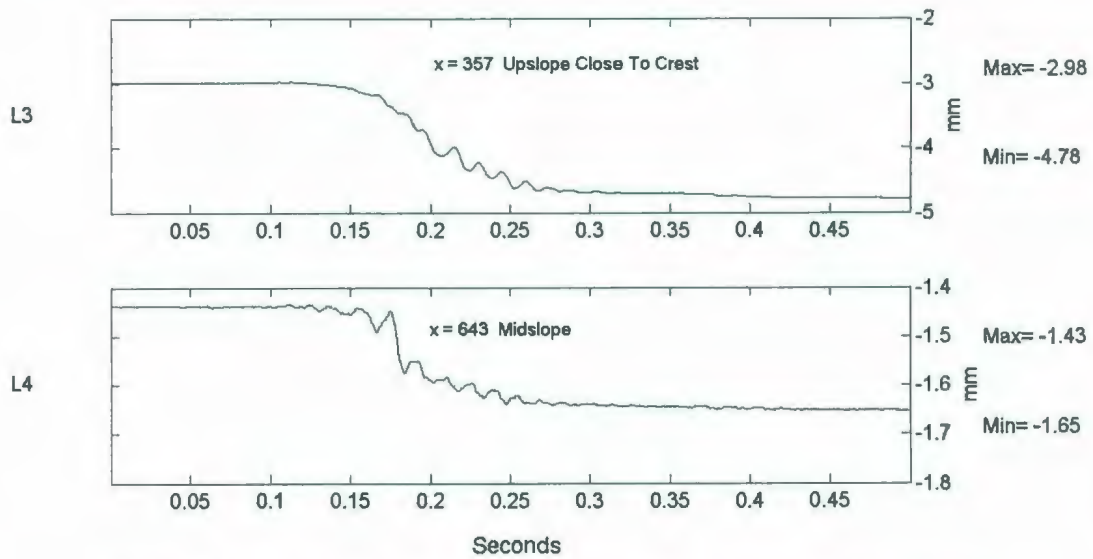
Figure 6.96: COSTA-E A475-1 Short-Term LVDT Deformation Response.

Noting the responses of the accelerometers it is evident that the responses throughout the model at different elevation that the magnitudes of the acceleration in both directions is relatively constant. Additionally, no large negative spikes are present in those responses.

There is a noticeable amount of pore pressure generation under the silt layer but very little pore pressure generation above the silt layer. Liquefaction occurred only in P4 at approximately 0.175 seconds in the short-term record. This condition continued throughout the short-term time period.

The model featured settlement both at the crest, less than 2 mm, and on the slope, even though it was very small being approximately 0.2 mm.

6.5.4 *A475-1 Long-Term Testing Instrument Responses*

The long-term responses were collected to examine the behaviour of the model for several seconds after the first A475 earthquake event. Figures 6.97 through 6.101 illustrate these responses.
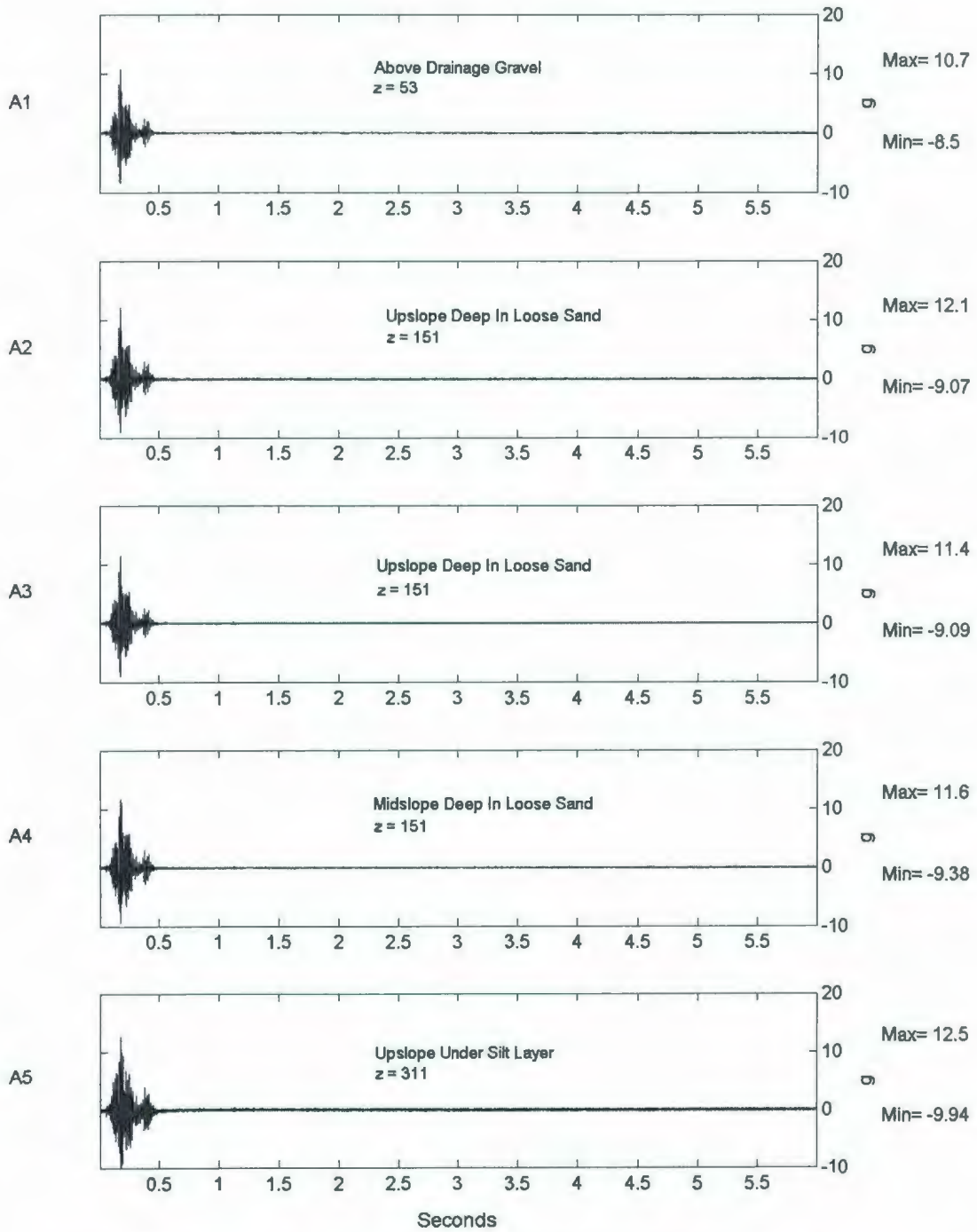
Figure 6.97: COSTA-E A475-1 Long-Term Accelerometer Response for A1-A5.
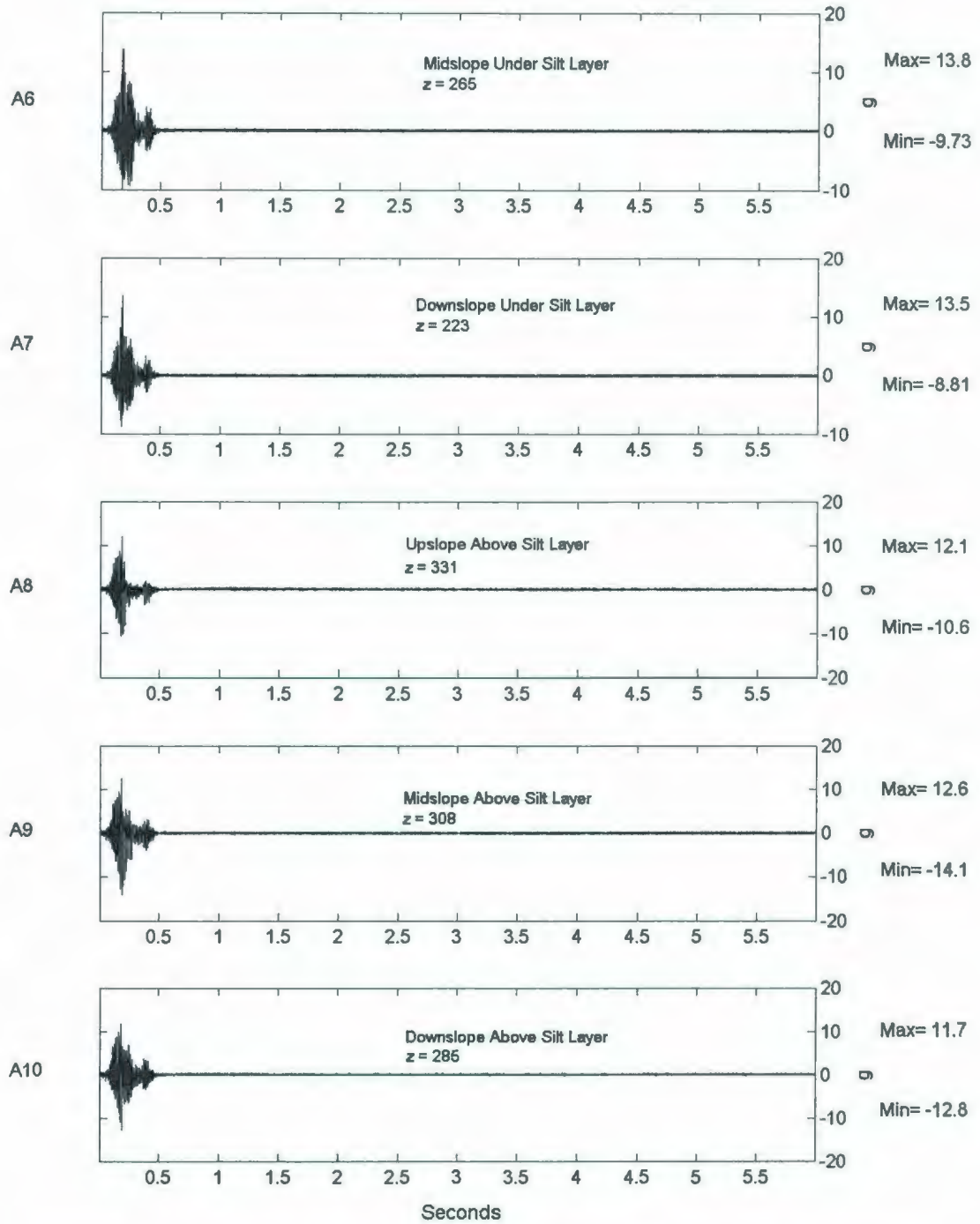
Figure 6.98: COSTA-E A475-1 Long-Term Accelerometer Response for A6-A10.
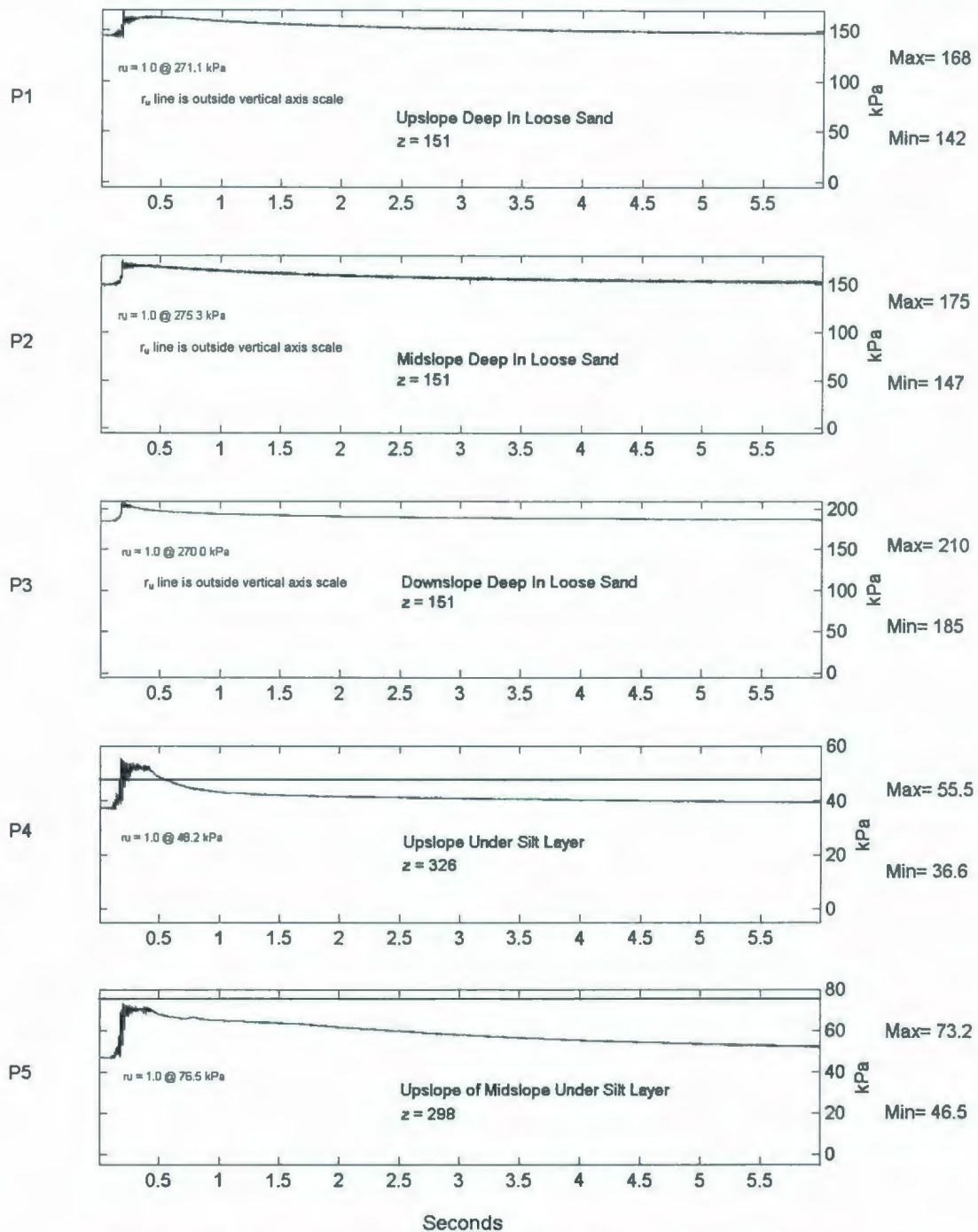
Figure 6.99: COSTA-E A475-1 Long-Term PPT Response for P1-P5.

286

P6

ru = 1.0 @ 145.1 kPa

Midslope Under Silt Layer
z = 250

r_u line is outside vertical axis scale

100
50
0

Max= 112

kPa

Min= 83.2

P7

ru = 1.0 @ 125.3 kPa

Downslope of Midslope Under Silt Layer
z = 243

r_u line is outside vertical axis scale

100
50
0

Max= 113

kPa

Min= 86.5

P9

ru = 1.0 @ 57.7 kPa

Midslope Above Silt Layer
z = 316

r_u line is outside vertical axis scale

50
40
30
20
10
0

Max= 43.8

kPa

Min= 39.4

Seconds
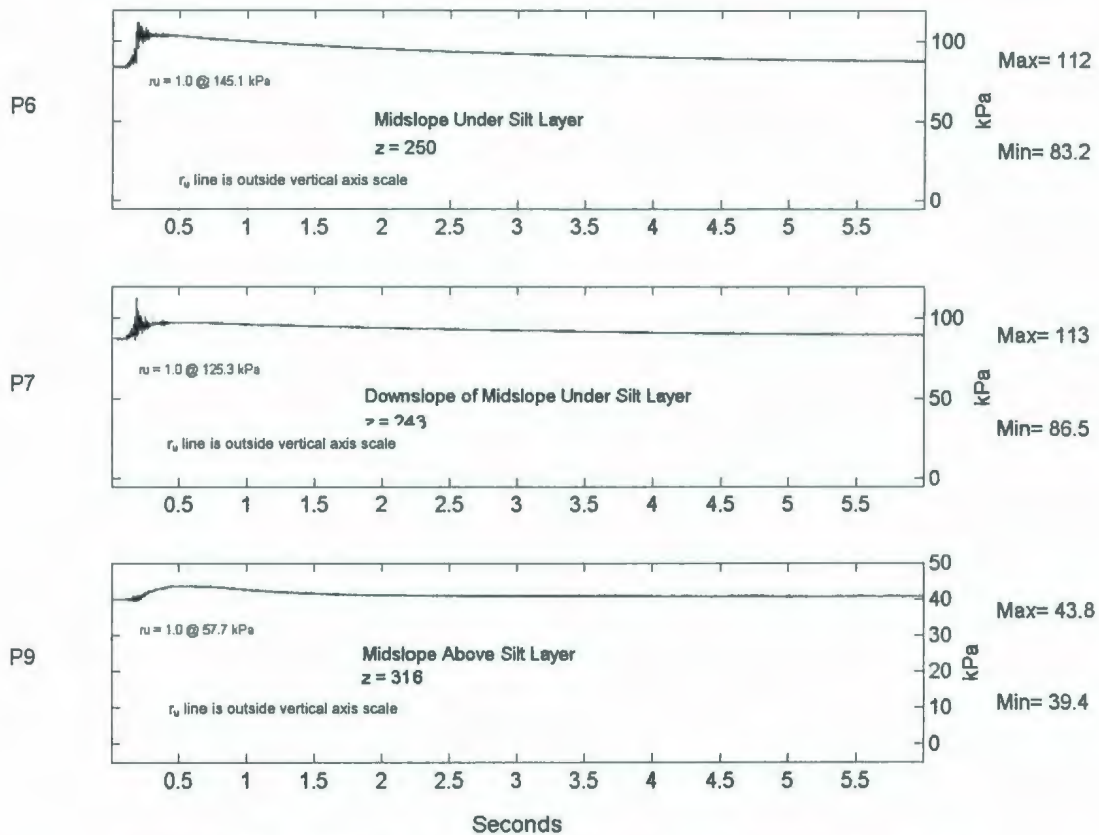
Figure 6.100: COSTA-E A475-1 Long-Term PPT Response for P6-P9.

L3

x = 357 Upslope Close To Crest

-2
-3
-4
-5

Max= -2.98

mm

Min= -4.89

L4

x = 643 Midslope

-1.4
-1.5
-1.6
-1.7
-1.8

Max= -1.43

mm

Min= -1.68

Seconds
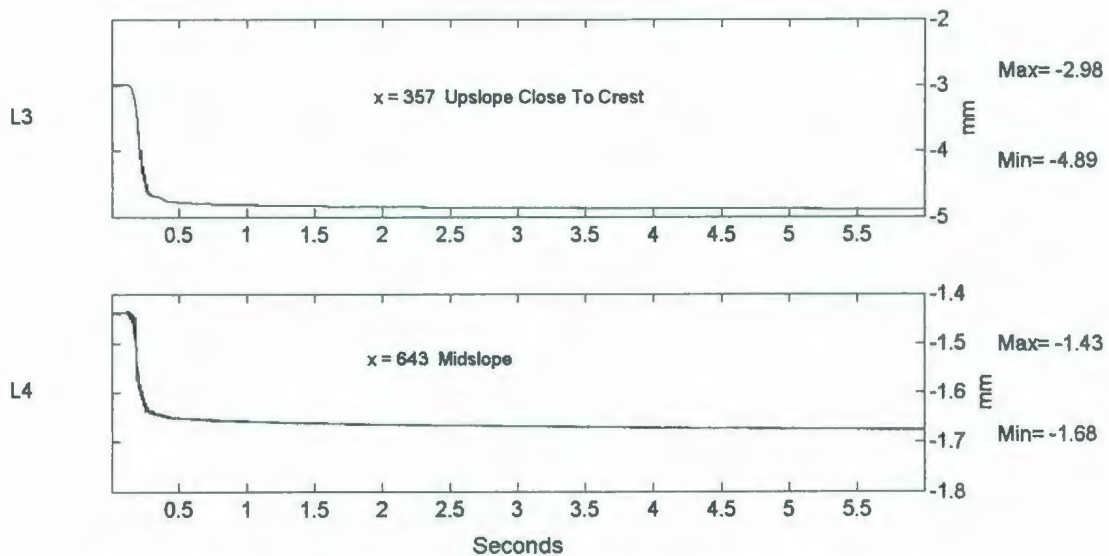
Figure 6.101: COSTA-E A475-1 Long-Term LVDT Deformation Response.

287

The accelerometer responses during the long-term observation period all show a mode shape similar to the A475 earthquake record. None of the negative acceleration spikes that were captured in the previous COSTA tests appears here.

The long-term responses show that for the most part the generated pore pressures dissipate by the conclusion of the specified long-term observation period of six seconds. This pore pressure dissipation occurs in all PPTs at a similarly shaped rate, indicating that elevation in the model did not have an effect on this dissipation. The liquefaction that was observed in P4 in the short term concluded shortly after the cessation of the A475 shaking event.

No significant surface movement was detected in L3 or L4 following the conclusion of the shaking event and the short-term observation period.

6.5.5   *A475-2 Short-Term Testing Instrument Responses*

All operating instruments were monitored during and shortly after the second A475 earthquake event. Figures 6.102 through 6.106 illustrate the observed responses in the various instruments during a 0.5 second period.
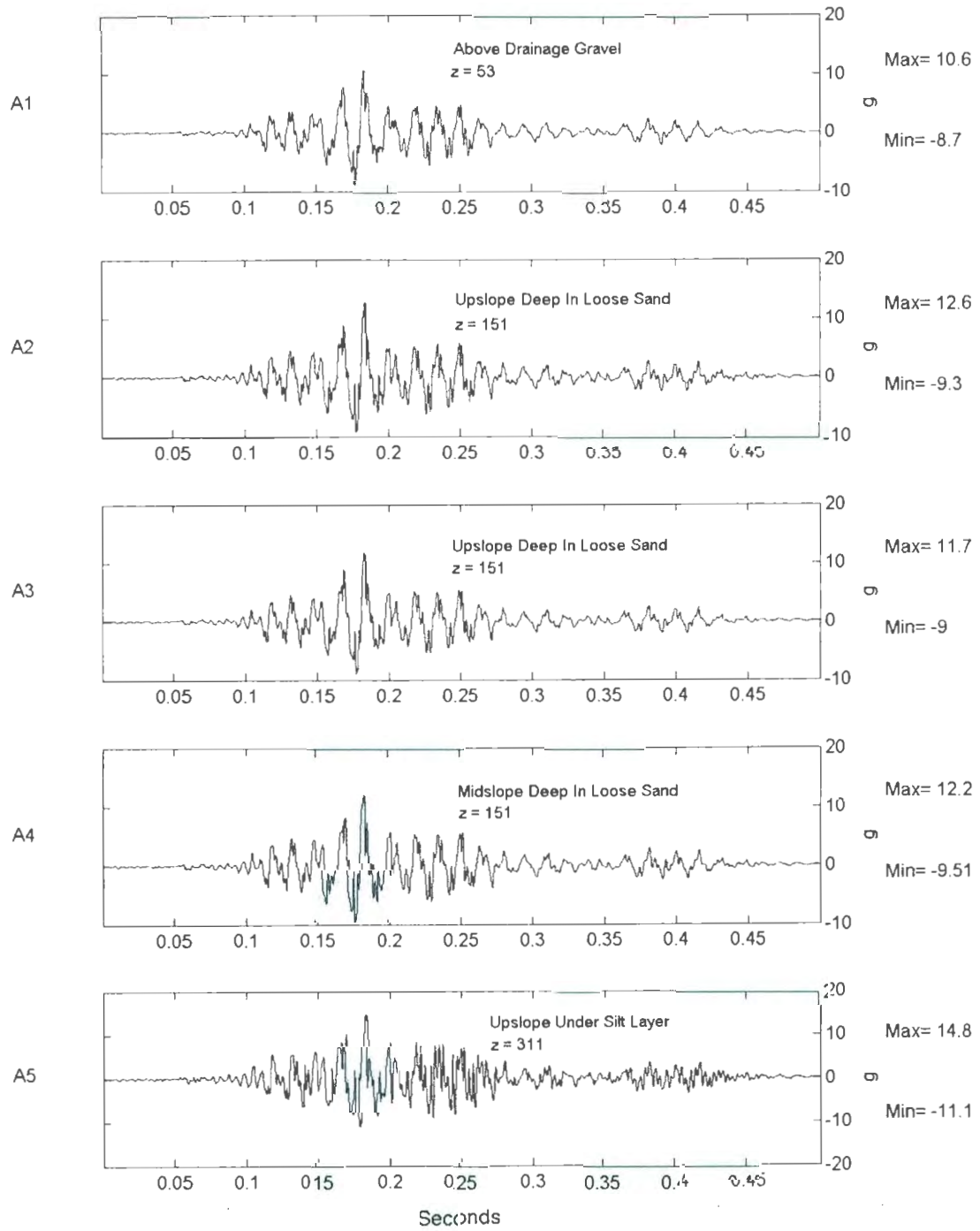
Figure 6.102: COSTA-E A475-2 Short-Term Accelerometer Response for A1-A5.

289
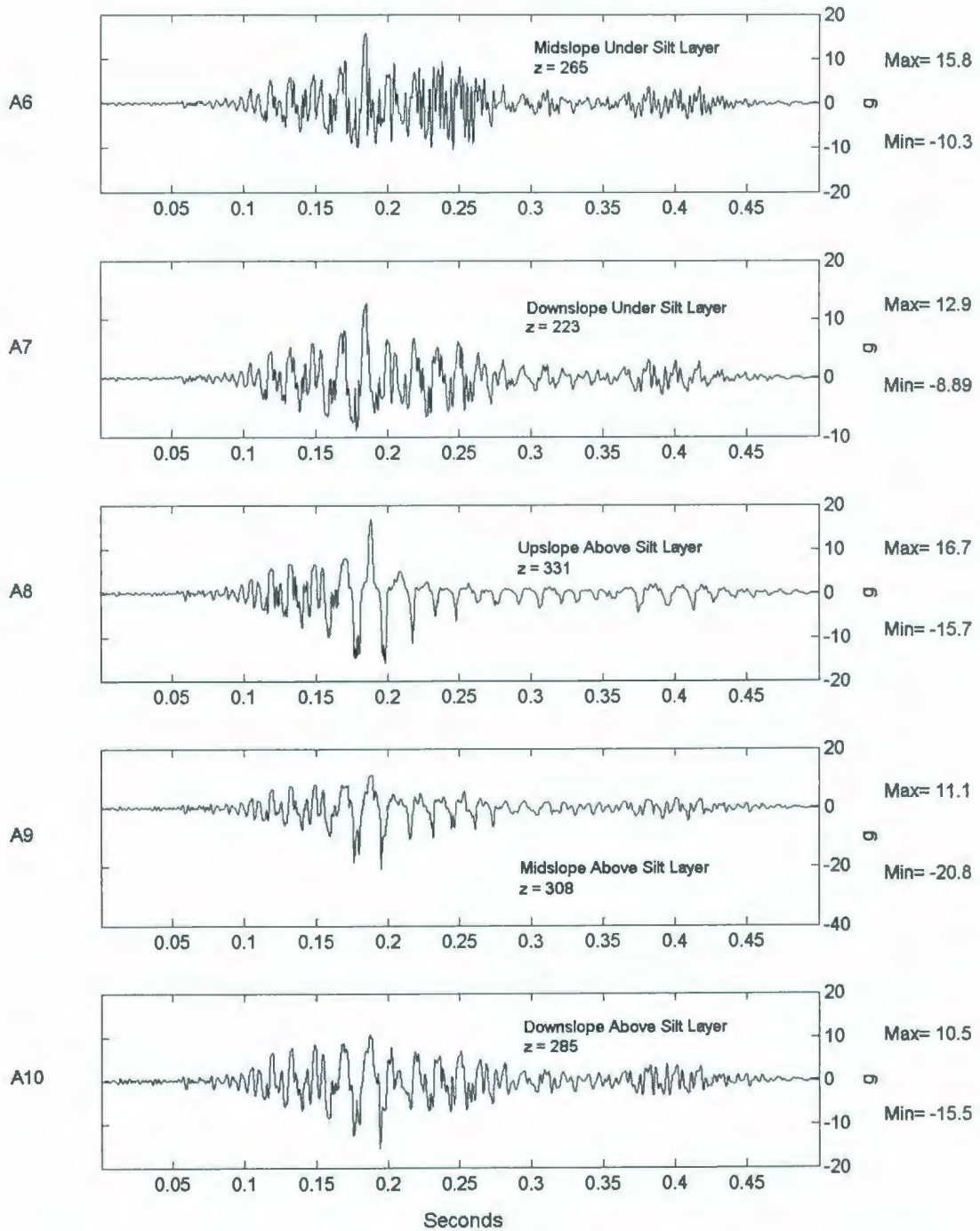
Figure 6.103: COSTA-E A475-2 Short-Term Accelerometer Response for A6-A10.
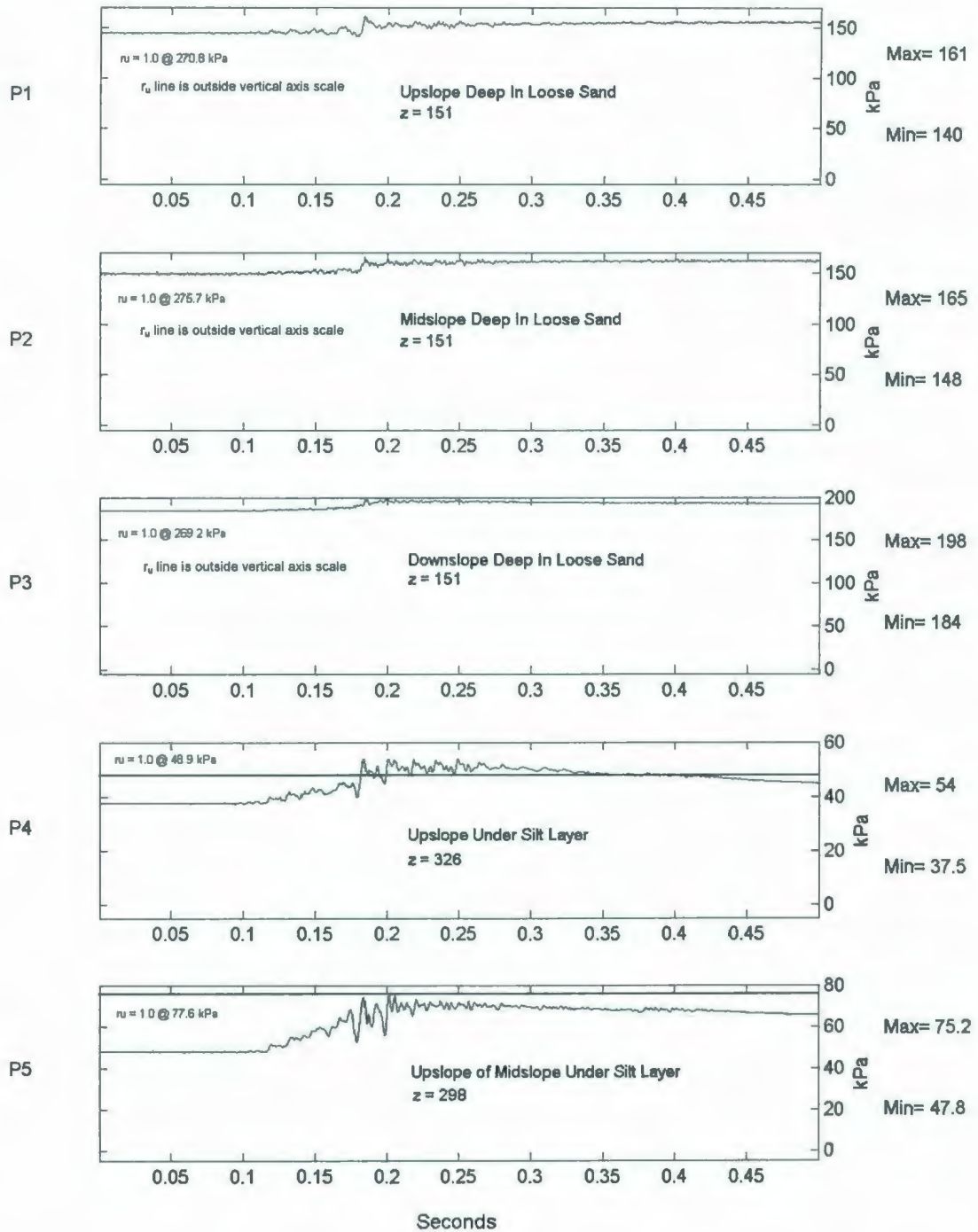
Figure 6.104: COSTA-E A475-2 Short-Term PPT Response for P1-P5.

291

P6 — ru – 1 0 @ 145 2 kPa / ru line is outside vertical axis scale / Midslope Under Silt Layer / z = 250 / Max= 104 / Min= 83.8

P7 — ru – 1 0 @ 125 6 kPa / ru line is outside vertical axis scale / Downslope of Midslope Under Silt Layer / z = 243 / Max= 111 / Min= 86.8

P9 — ru = 1 0 @ 58 3 kPa / ru line is outside vertical axis scale / Midslope Above Silt Layer / z = 316 / Max= 45.8 / Min= 40.4
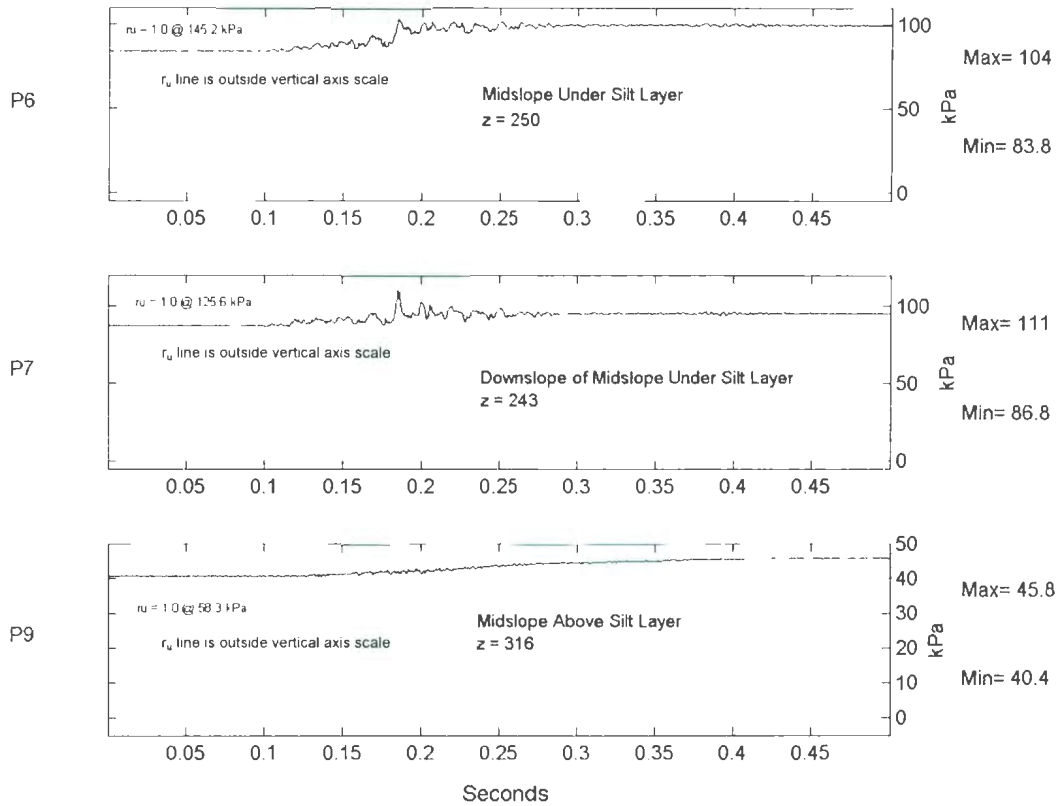
Figure 6.105: COSTA-E A475-2 Short-Term Accelerometer Response for P6-P9.

L3 — x = 357 Upslope Close To Crest / Max= -4.96 / Min= -6.16

L4 — x = 643 Midslope / Max= -1.7 / Min= -1.82
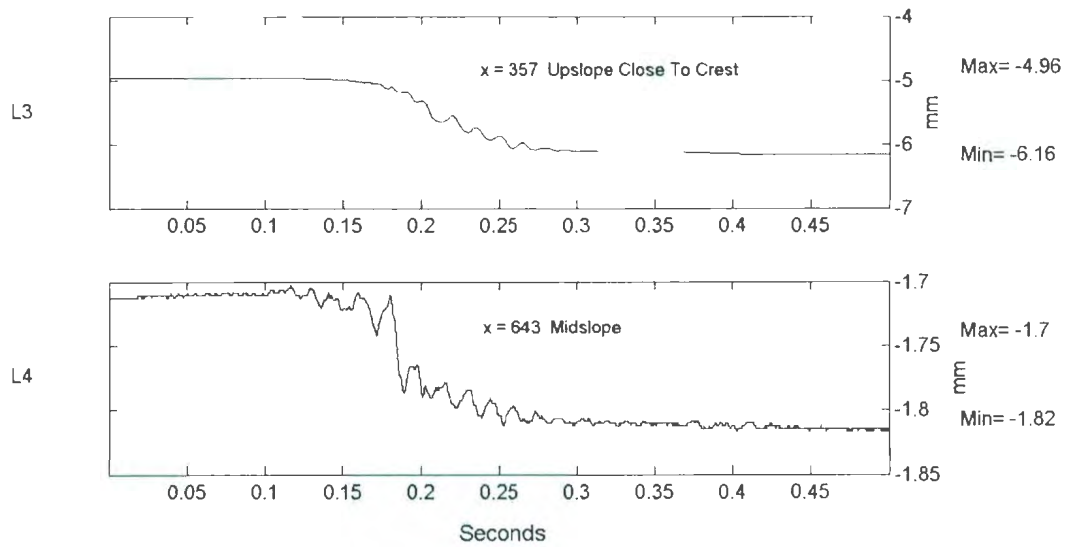
Figure 6.106: COSTA-E A475-2 Short-Term LVDT Deformation Response.

292

The responses in the instruments in the A475-2 event were very similar to the responses for the A475-1 event discussed in section 6.5.3. Pore pressure generation decreased for the most part in all instruments. Model settlement at the crest was observed to be 1.2 mm and the midslope settlement was found to be relatively small at 0.12 mm.

6.5.6 A475-2 Long-Term Testing Instrument Responses

The long-term responses were collected to examine the behaviour of the model for several seconds after the second A475 earthquake event. Figures 6.107 through 6.111 illustrate these responses.
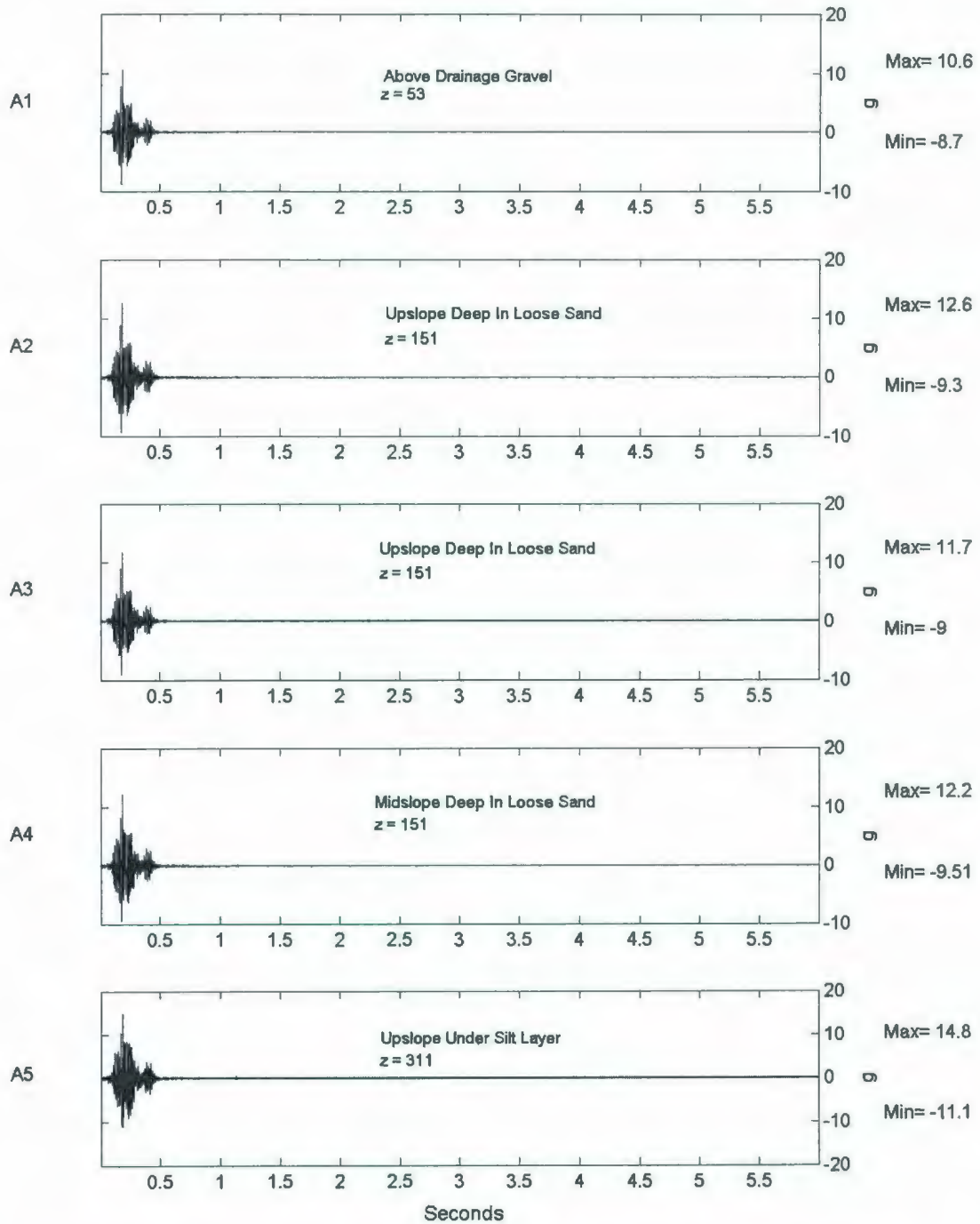
Figure 6.107: COSTA-E A475-2 Long-Term Accelerometer Response for A1-A5.
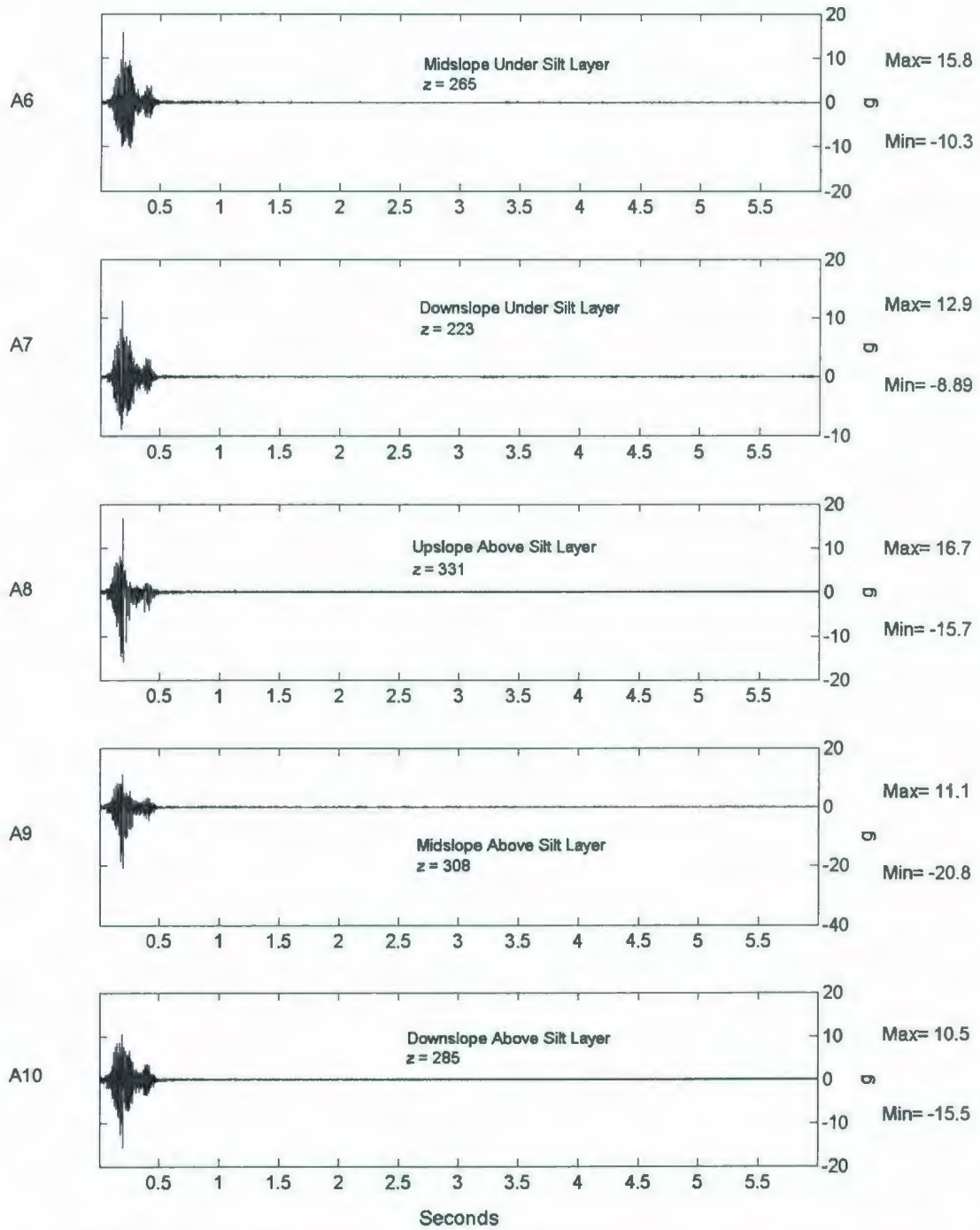
Figure 6.108: COSTA-E A475-2 Long-Term Accelerometer Response for A6-A10.
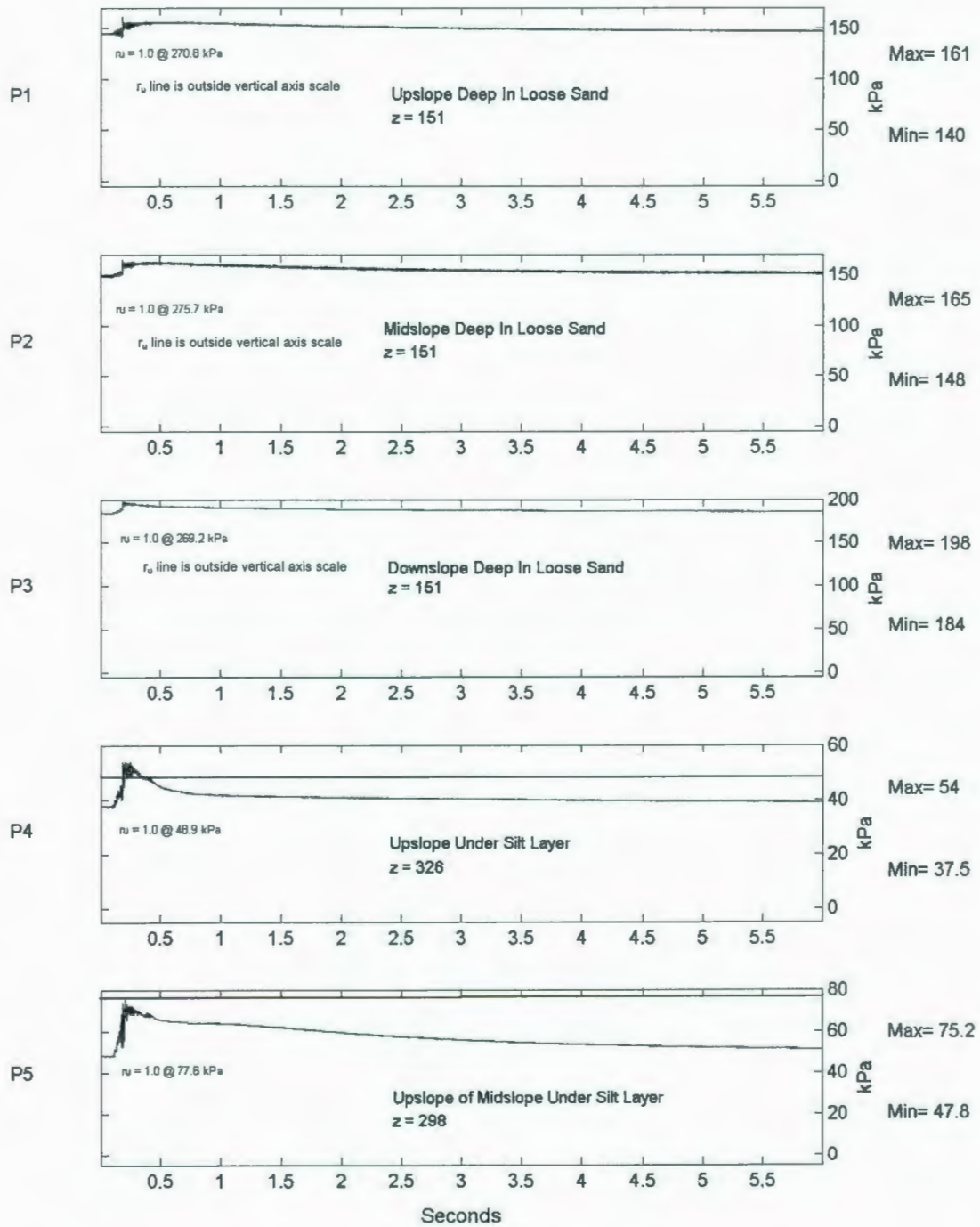
Figure 6.109: COSTA-E A475-2 Long-Term PPT Response for P1-P5.
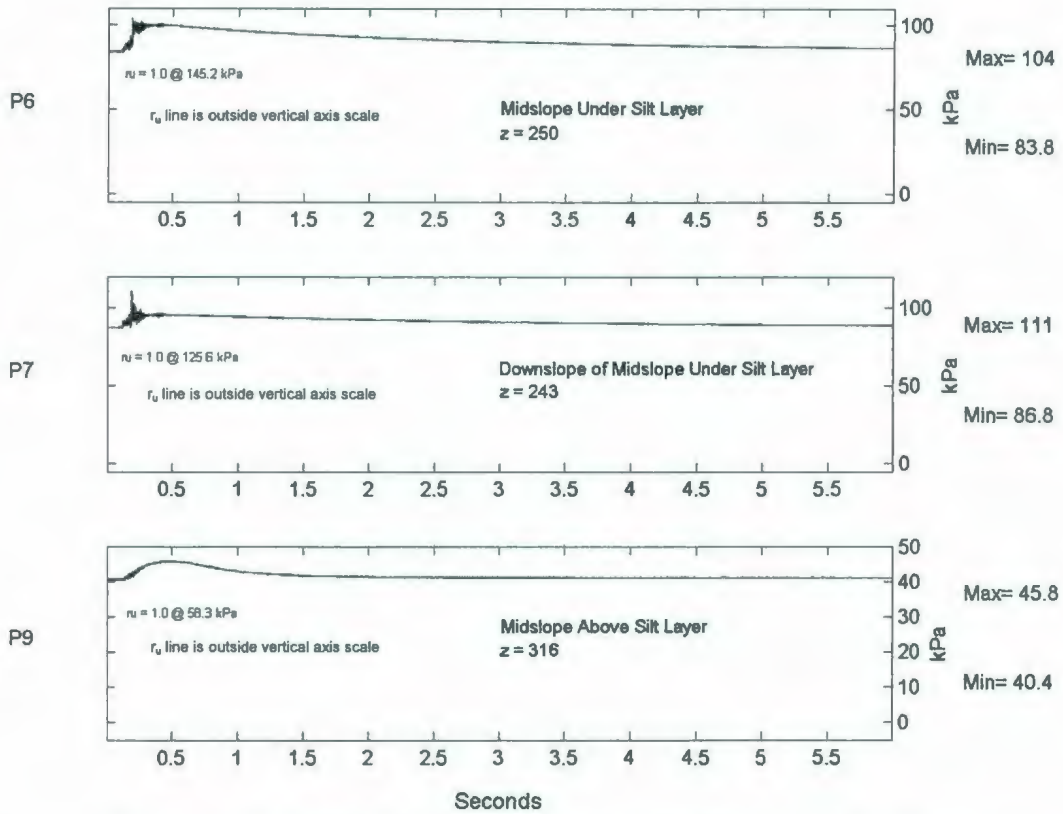
Figure 6.110: COSTA-E A475-2 Long-Term PPT Response for P6-P9.
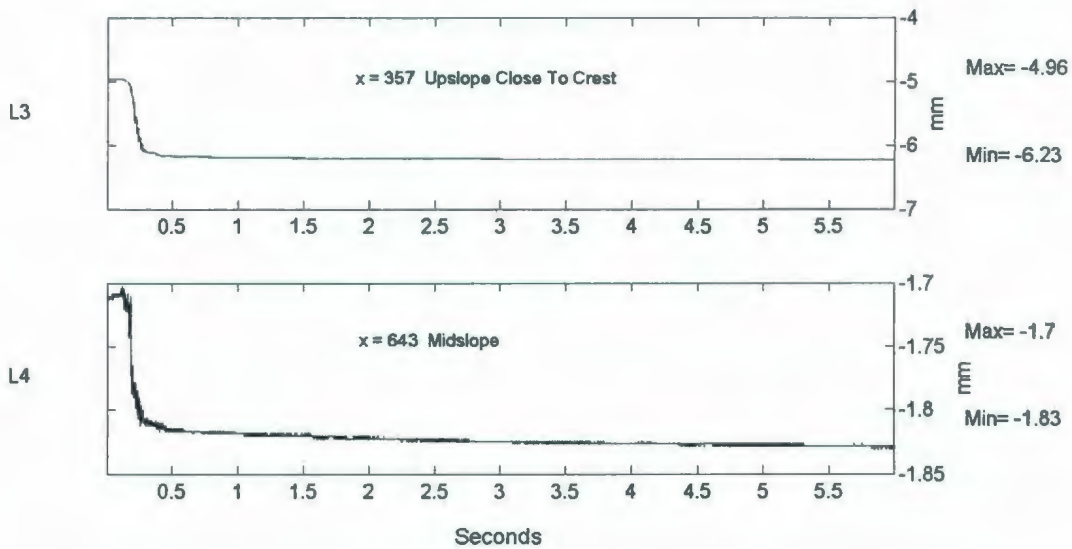
Figure 6.111: COSTA-E A475-2 Long-Term LVDT Deformation Response.

The long-term behaviour of the model during this second event was very similar to the previous event, as discussed in section 6.5.4. However, it was observed that in A8-10 the magnitude of the negative acceleration in the short-term responses was slightly larger.

6.5.7 *A475-3 Short-Term Testing Instrument Responses*

All operating instruments were monitored during and shortly after the third A475 earthquake event. Figures 6.112 through 6.116 illustrate the observed responses in the various instruments during a 0.5 second period.
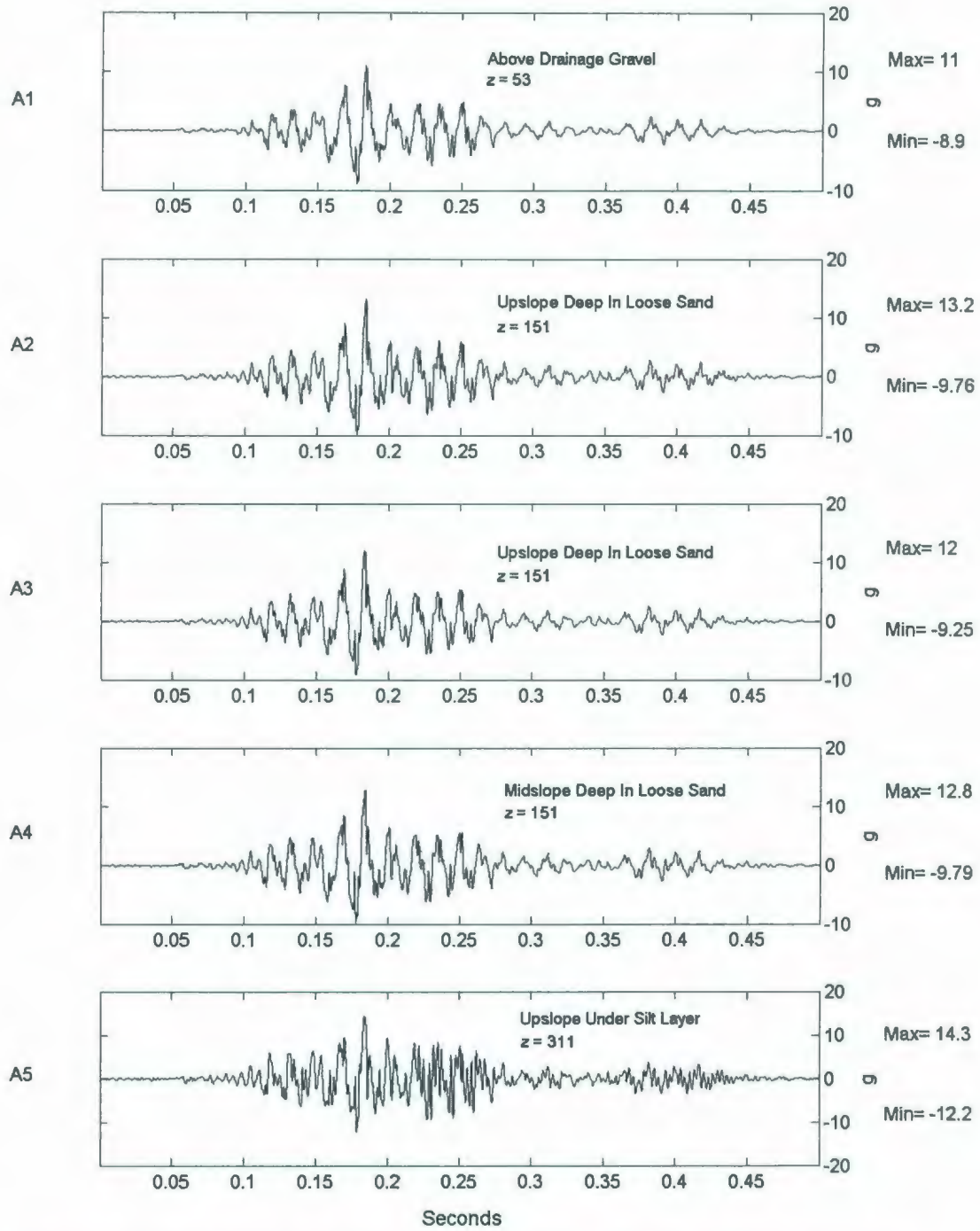
Figure 6.112: COSTA-E A475-3 Short-Term Accelerometer Response for A1-A5.
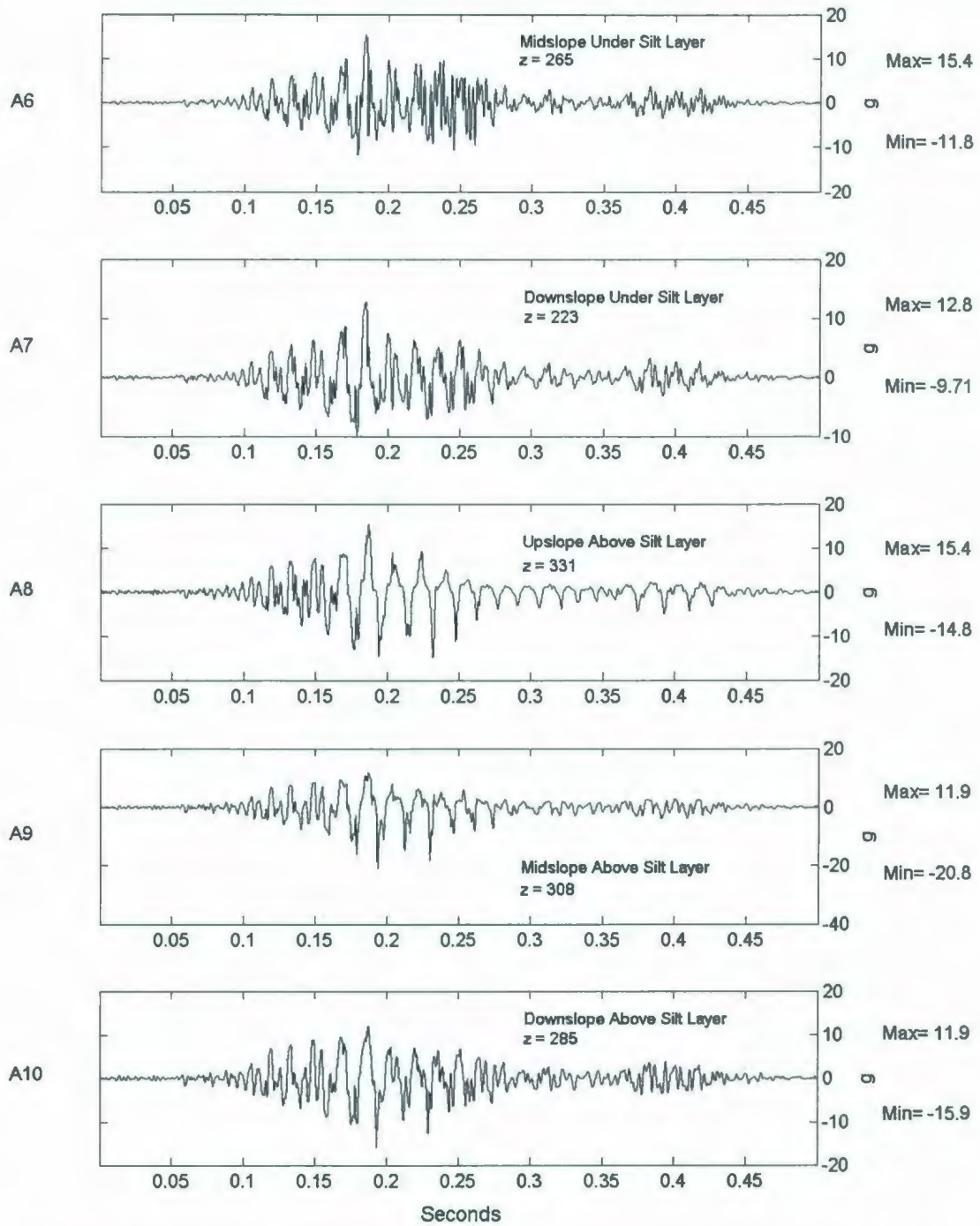
Figure 6.113: COSTA-E A475-3 Short-Term Accelerometer Response for A6-A10.
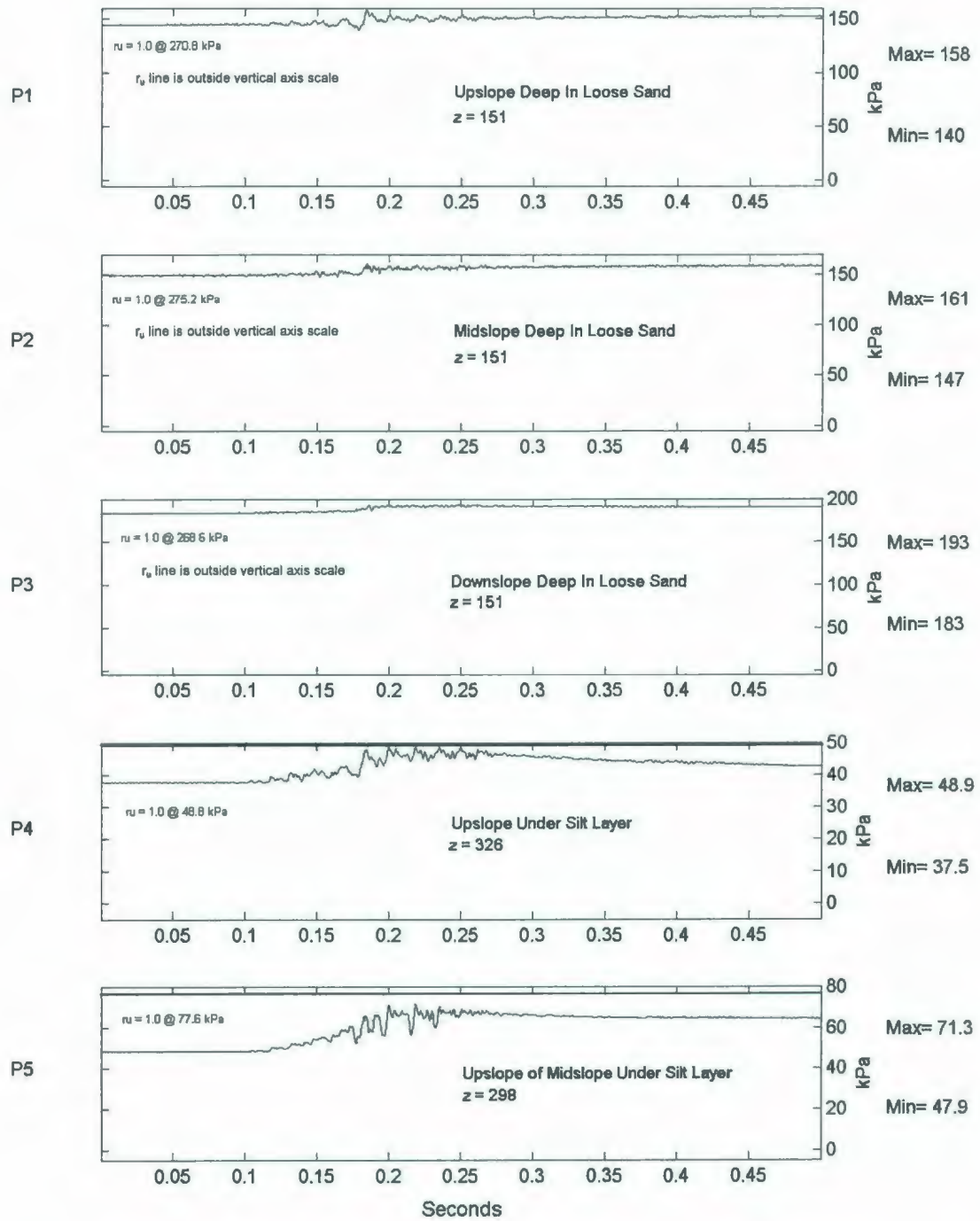
Figure 6.114: COSTA-E A475-3 Short-Term PPT Response for P1-P5.
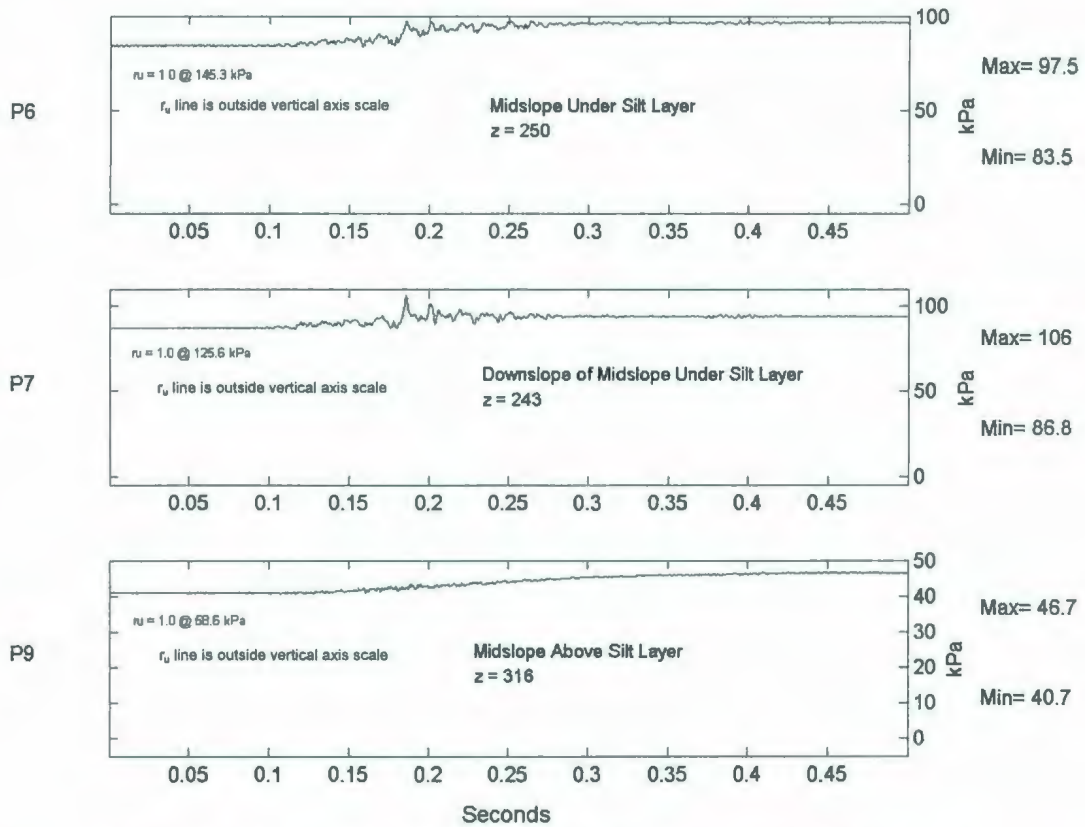
Figure 6.115: COSTA-E A475-3 Short-Term PPT Response for P6-P9.
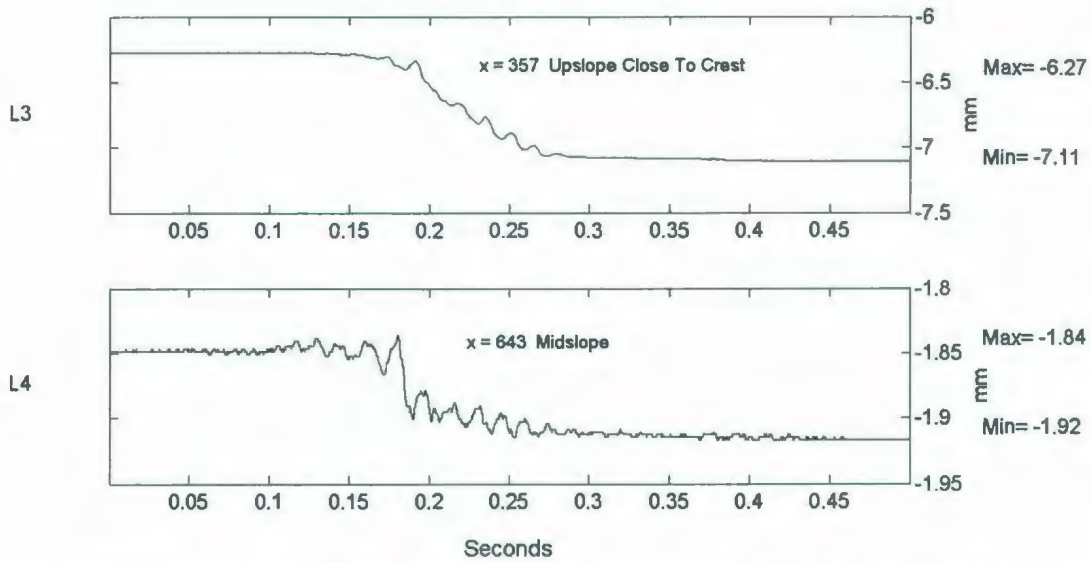
Figure 6.116: COSTA-E A475-3 Short-Term LVDT Deformation Response.

The responses in the instruments in the A475-3 event were very similar to the responses for the A475-2 event. The trend of decreased pore pressure as compared to previous earthquakes in this test continued and as a result, no liquefaction was detected in P4. Settlement at the crest of the slope and on the midslope was further limited to 0.84 an 0.08 mm respectively.

6.5.8   A475-3 Long-Term Testing Instrument Responses

The long-term responses were collected to examine the behaviour of the model for several seconds after the third A475 earthquake event. Figures 6.117 through 6.121 illustrate these responses.
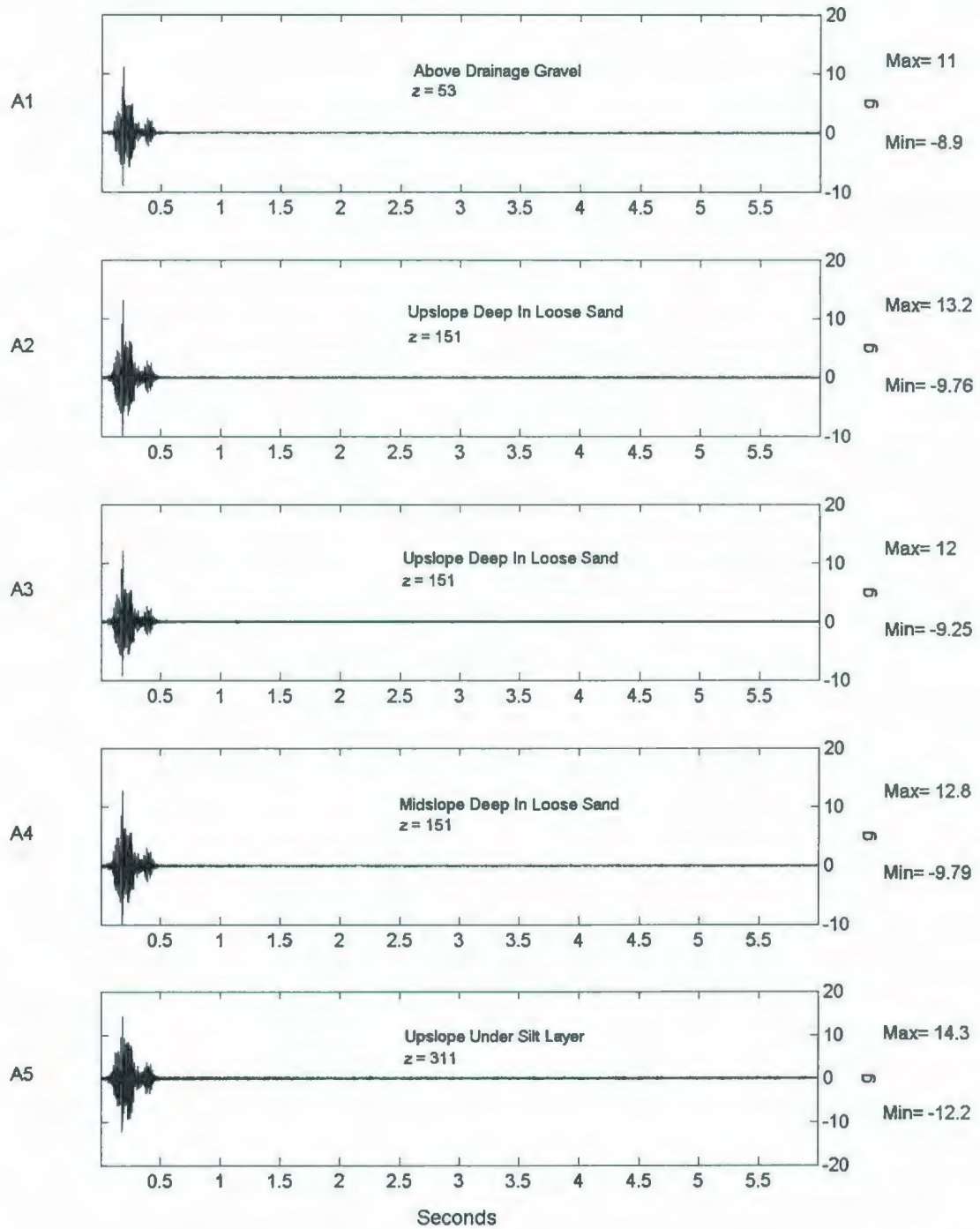
Figure 6.117: COSTA-E A475-3 Long-Term Accelerometer Response for A1-A5.
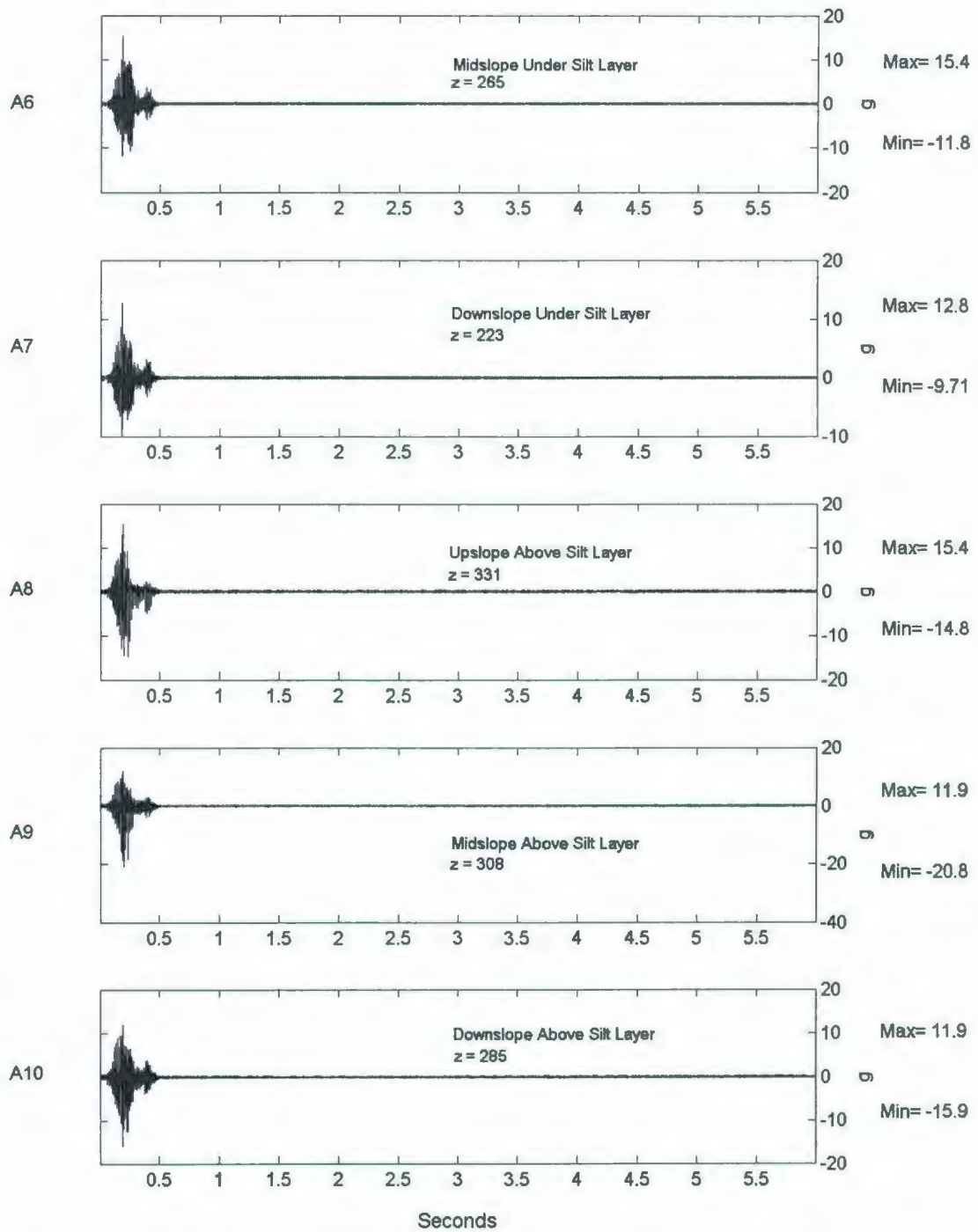
Figure 6.118: COSTA-E A475-3 Long-Term Accelerometer Response for A6-A10.

305

P1

ru = 1.0 @ 270.8 kPa

ru line is outside vertical axis scale

Upslope Deep In Loose Sand
z = 151

Max= 158

Min= 140

kPa

P2

ru = 1.0 @ 275.2 kPa

ru line is outside vertical axis scale

Midslope Deep In Loose Sand
z = 151

Max= 161

Min= 147

kPa

P3

ru = 1.0 @ 268.5 kPa

ru line is outside vertical axis scale

Downslope Deep In Loose Sand
z = 151

Max= 193

Min= 183

kPa

P4

ru = 1.0 @ 48.8 kPa

Upslope Under Silt Layer
z = 326

Max= 48.9

Min= 37.5

kPa

P5

ru = 1.0 @ 77.6 kPa

Upslope of Midslope Under Silt Layer
z = 298

Max= 71.3

Min= 47.9

kPa

Seconds

Figure 6.119: COSTA-E A475-3 Long-Term PPT Response for P1-P5.
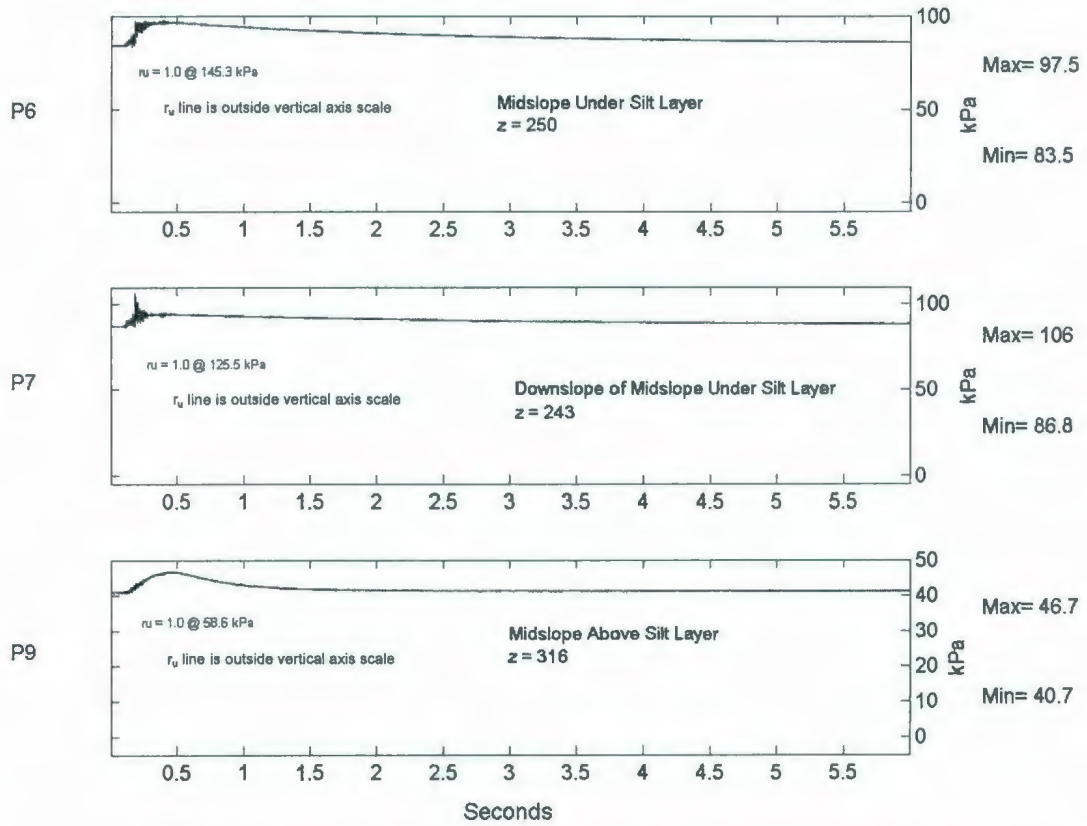
Figure 6.120: COSTA-E A475-3 Long-Term PPT Response for P6-P9.
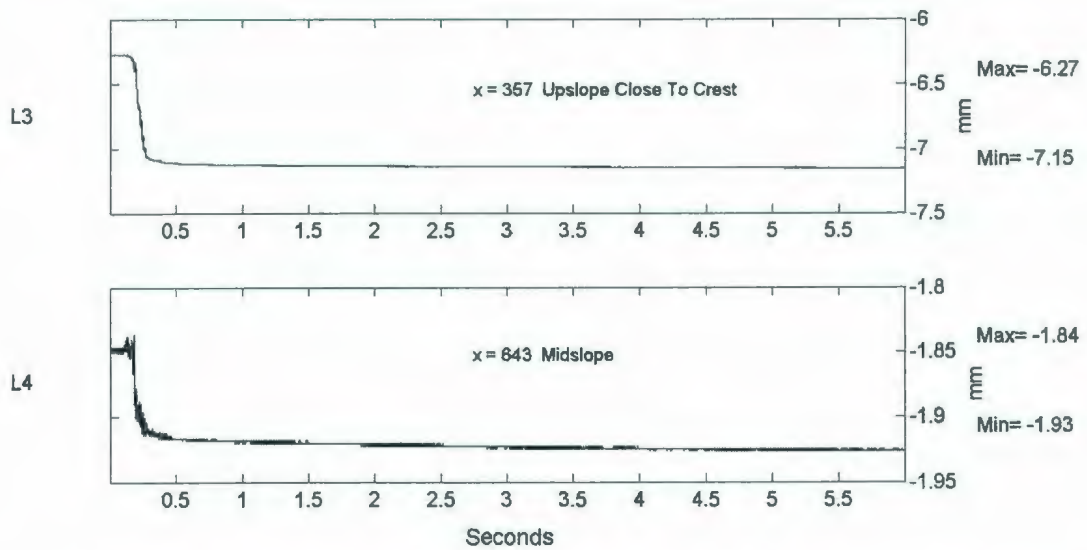
Figure 6.121: COSTA-E A475-3 Long-Term LVDT Deformation Response.

The long-term behaviour of the model during this third event was very similar to the previous event. Very little pore pressure is evident at deeper locations in the model, as shown by the relatively flat responses in P1, P2 & P3.

6.5.9 A475-4 Short-Term Testing Instrument Responses

All operating instruments were monitored during and shortly after the fourth A475 earthquake event. Figures 6.122 through 6.126 illustrate the observed responses in the various instruments during a 0.5 second period.
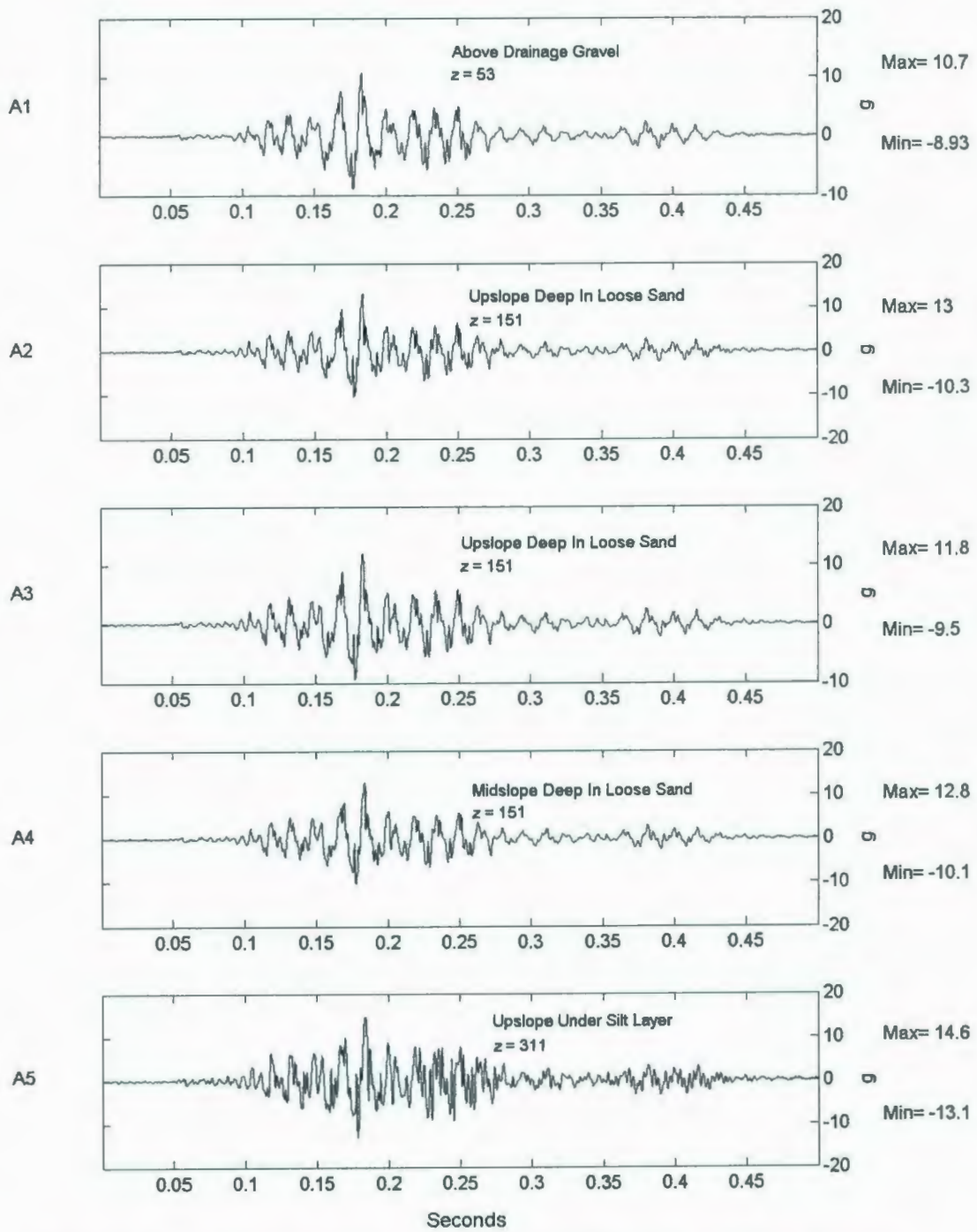
**Figure 6.122:** COSTA-E A475-4 Short-Term Accelerometer Response for A1-A5.
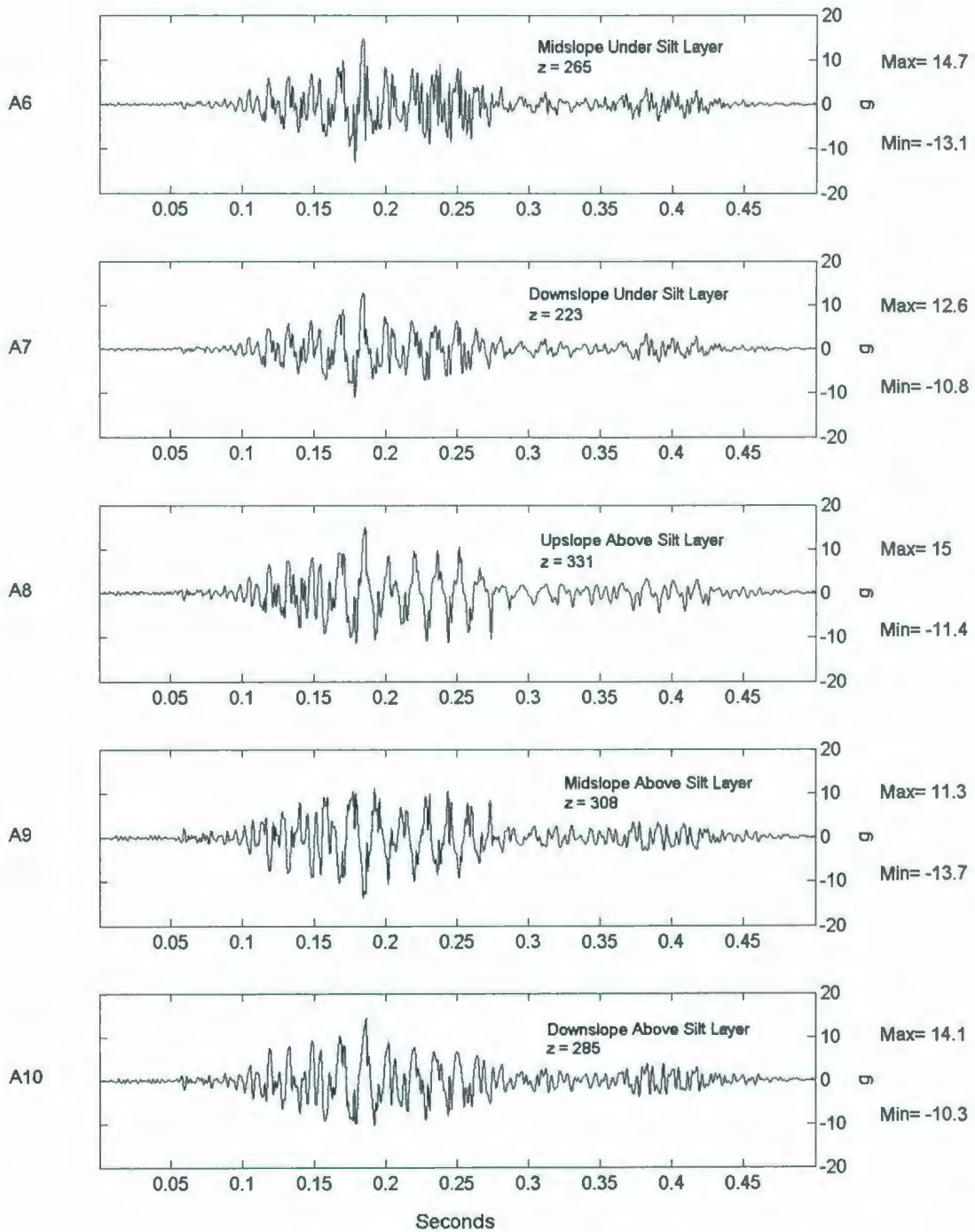
Figure 6.123: COSTA-E A475-4 Short-Term Accelerometer Response for A6-A10.
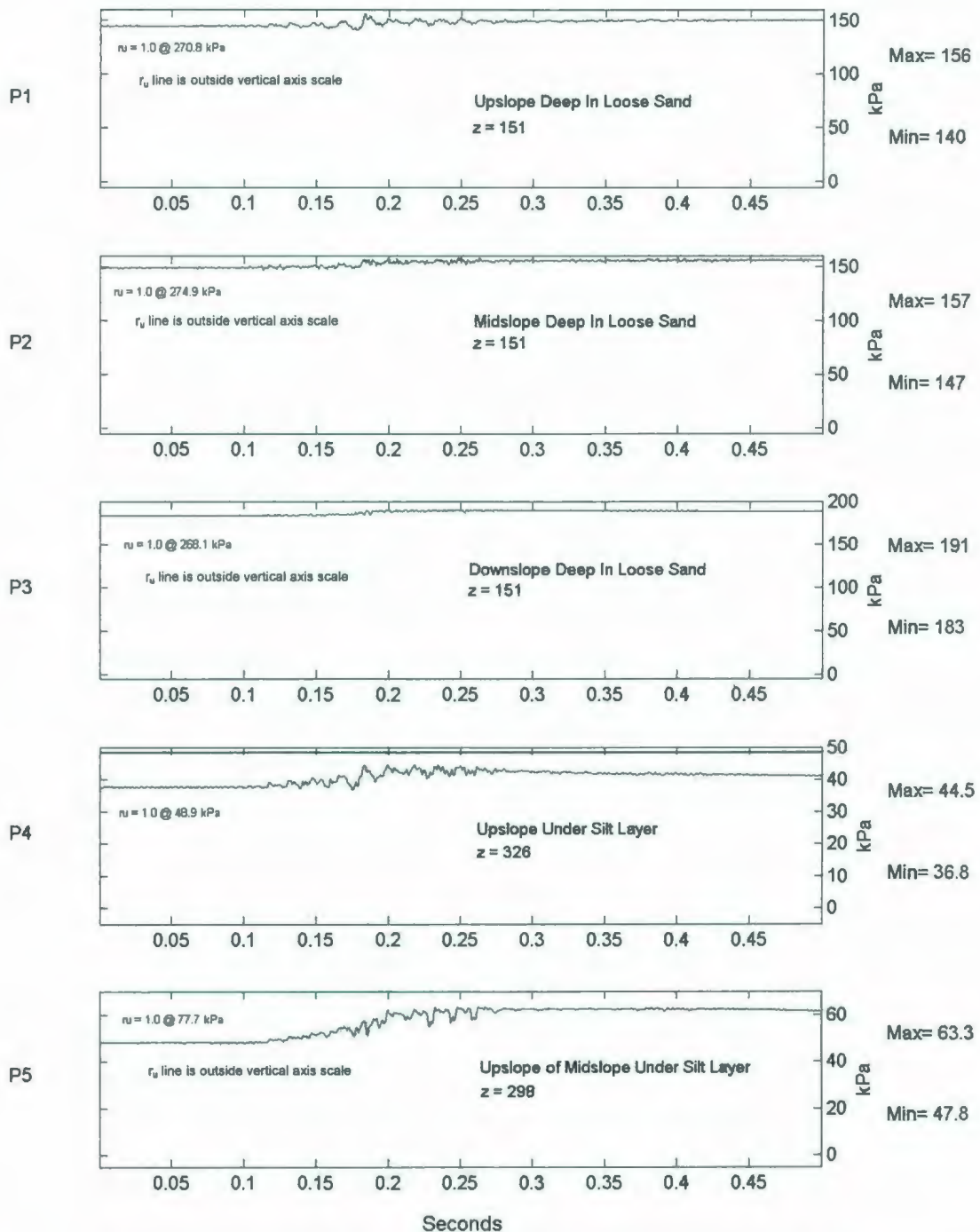
**Figure 6.124:** COSTA-E A475-4 Short-Term PPT Response for P1-P5.
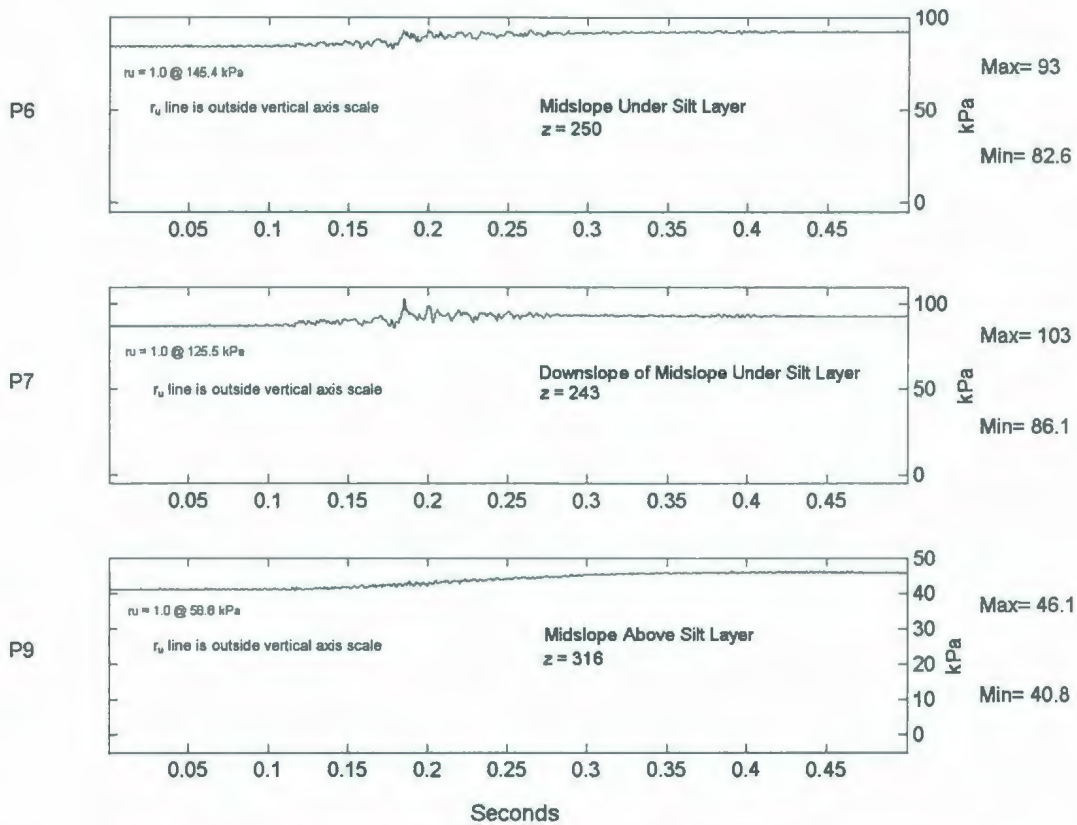
Figure 6.125: COSTA-E A475-4 Short-Term PPT Response for P6-P9.
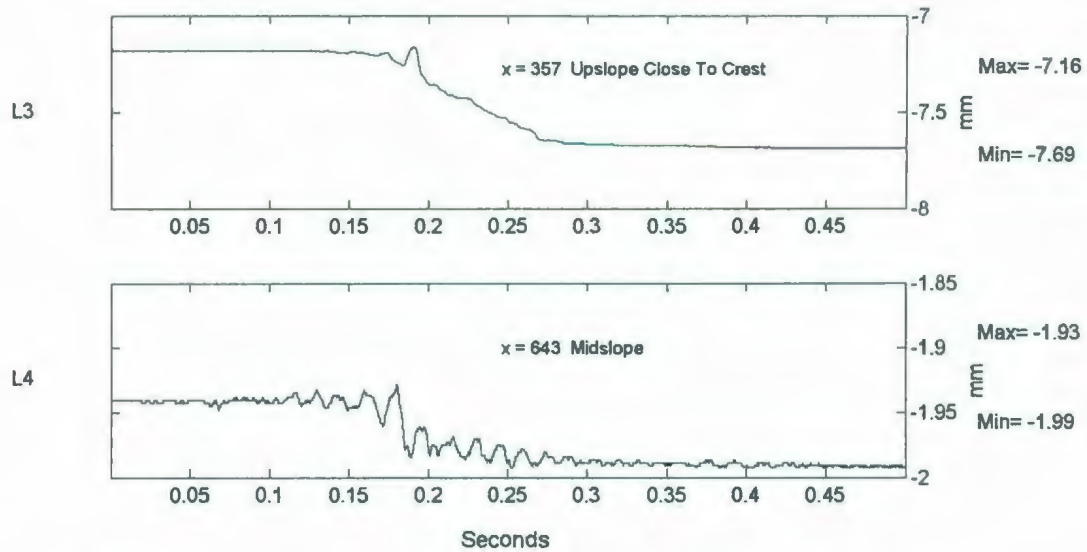
Figure 6.126: COSTA-E A475-4 Short-Term LVDT Deformation Response.

The responses in the instruments in the A475-4 event were very similar to the responses for the A475-3 event. The pore pressure generation continues to decrease for the most part in all PPTs. The vertical settlement also continues to decrease with successive shakings with the crest settling 0.53 mm and the midslope position settling 0.06 mm.

6.5.10 *A475-4 Long-Term Testing Instrument Responses*

The long-term responses were collected to examine the behaviour of the model for several seconds after the fourth A475 earthquake event. Figures 6.127 through 6.131 illustrate these responses. Evident on Figure 6.127 and 6.128 at approximately 3.9 seconds is a smaller secondary motion. This motion is attributable to the centrifuge payload and earthquake actuator recentralizing itself on the centrifuge swing after the earthquake actuation. This motion was not intended to occur in the model test and appears not to have any significant effect on the model in terms of long-term pore pressure or displacement response.
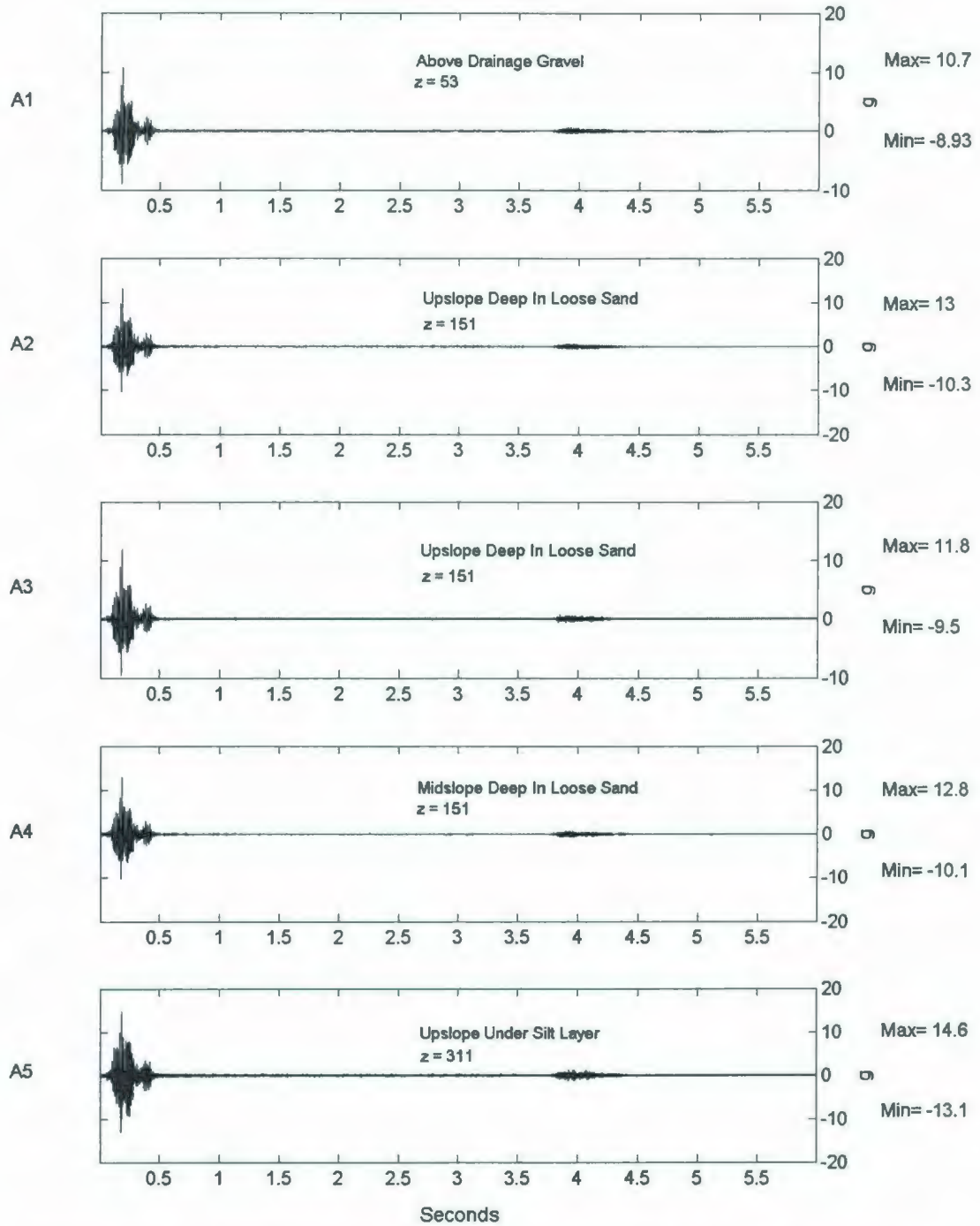
**Figure 6.127:** COSTA-E A475-4 Long-Term Accelerometer Response for A1-A5.
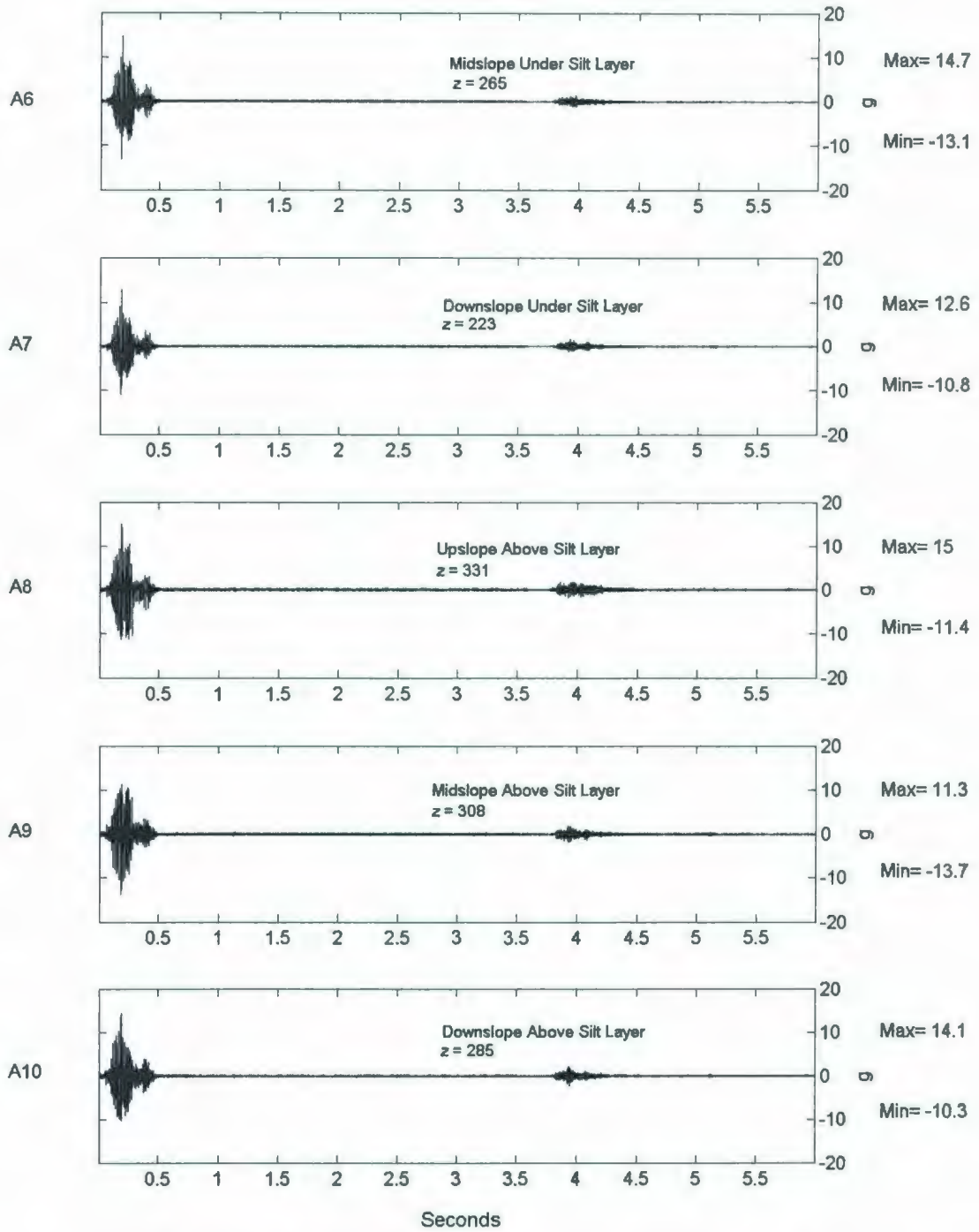
**Figure 6.128:** COSTA-E A475-4 Long-Term Accelerometer Response for A6-A10.
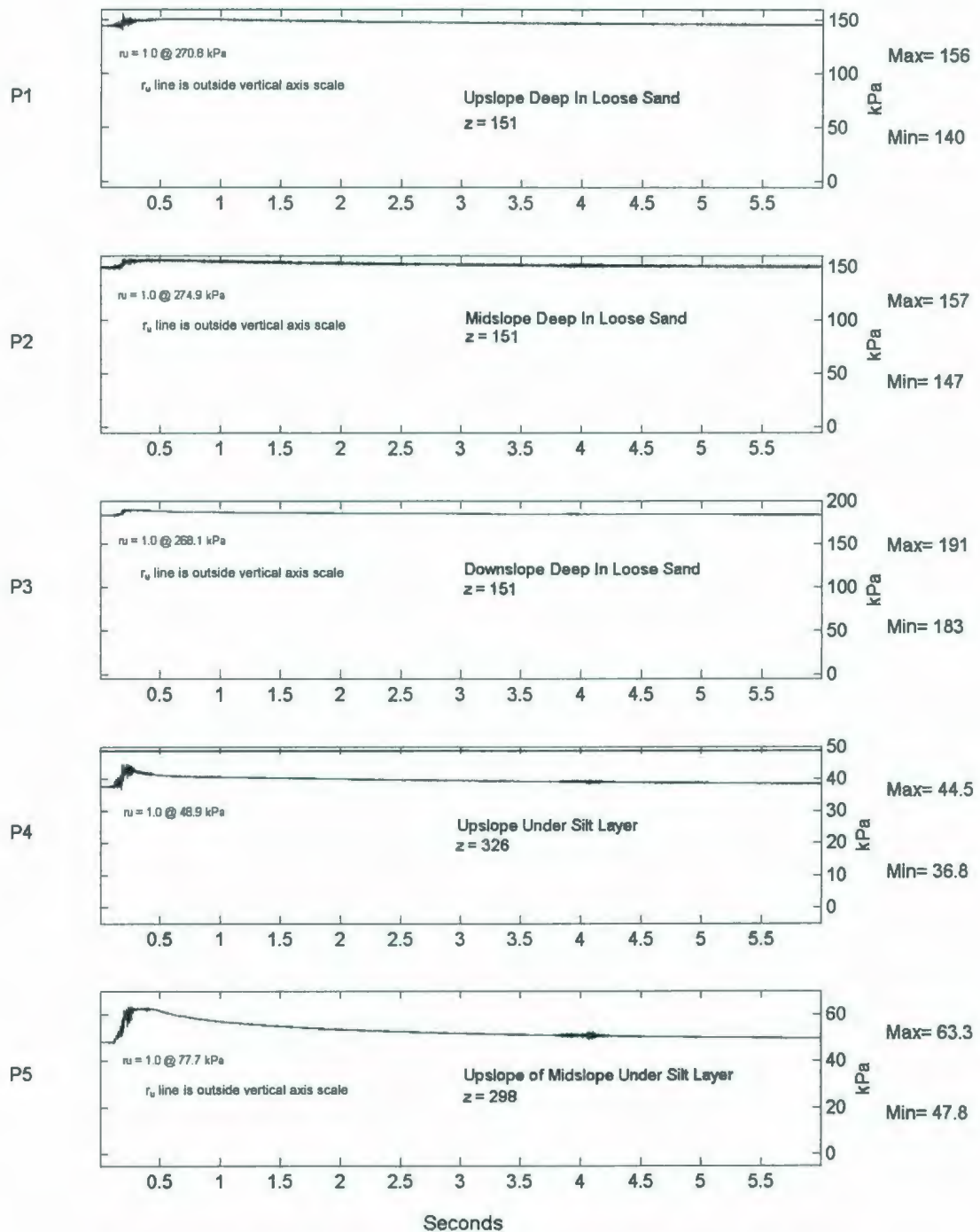
Figure 6.129: COSTA-E A475-4 Long-Term PPT Response for P1-P5.

P6 — ru = 1.0 @ 145.4 kPa
ru line is outside vertical axis scale
Midslope Under Silt Layer
z = 250
Max= 93
Min= 82.6

P7 — ru = 1.0 @ 125.6 kPa
ru line is outside vertical axis scale
Downslope of Midslope Under Silt Layer
z = 243
Max= 103
Min= 86.1

P9 — ru = 1.0 @ 58.8 kPa
ru line is outside vertical axis scale
Midslope Above Silt Layer
z = 316
Max= 46.1
Min= 40.6
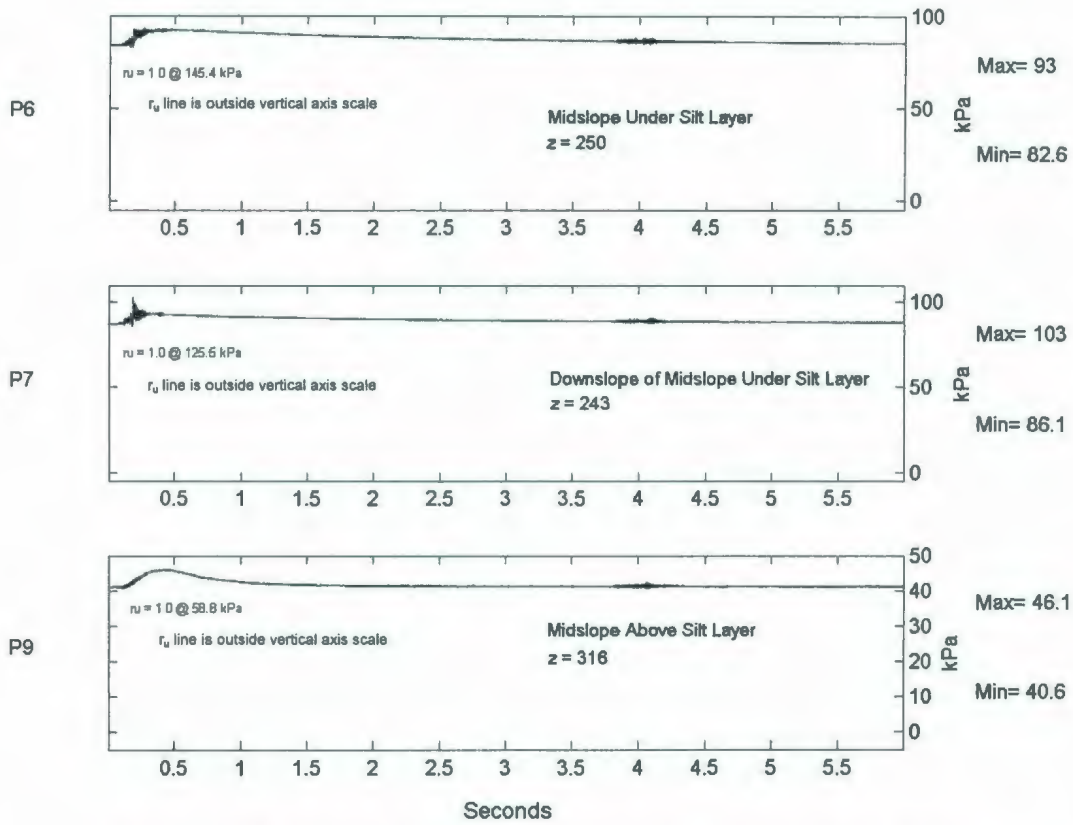
Figure 6.130: COSTA-E A475-4 Long-Term PPT Response for P6-P9.

L3 — x = 357 Upslope Close To Crest
Max= -7.16
Min= -7.71

L4 — x = 643 Midslope
Max= -1.93
Min= -2
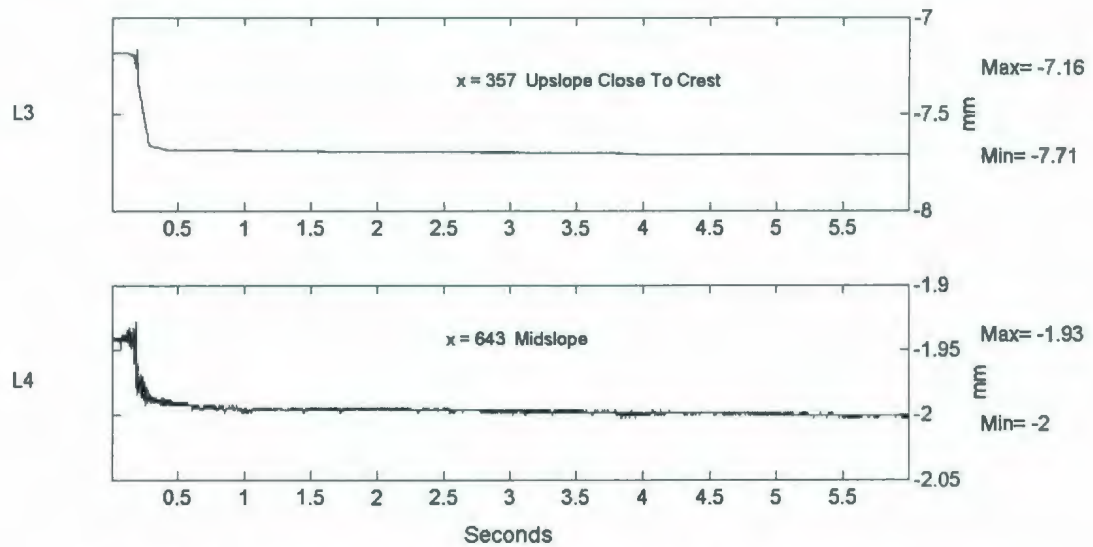
Figure 6.131: COSTA-E A475-4 Long-Term LVDT Deformation Response.

The long-term behaviour of the model during this fourth event was very similar to the previous event. Nevertheless, there was some observed attenuation in the magnitude of the negative acceleration observed in A8-10.

6.5.11 A475-5 Short-Term Testing Instrument Responses

All operating instruments were monitored during and shortly after the fifth A475 earthquake event. Figures 6.132 through 6.136 illustrate the observed responses in the various instruments during a 0.5 second period.
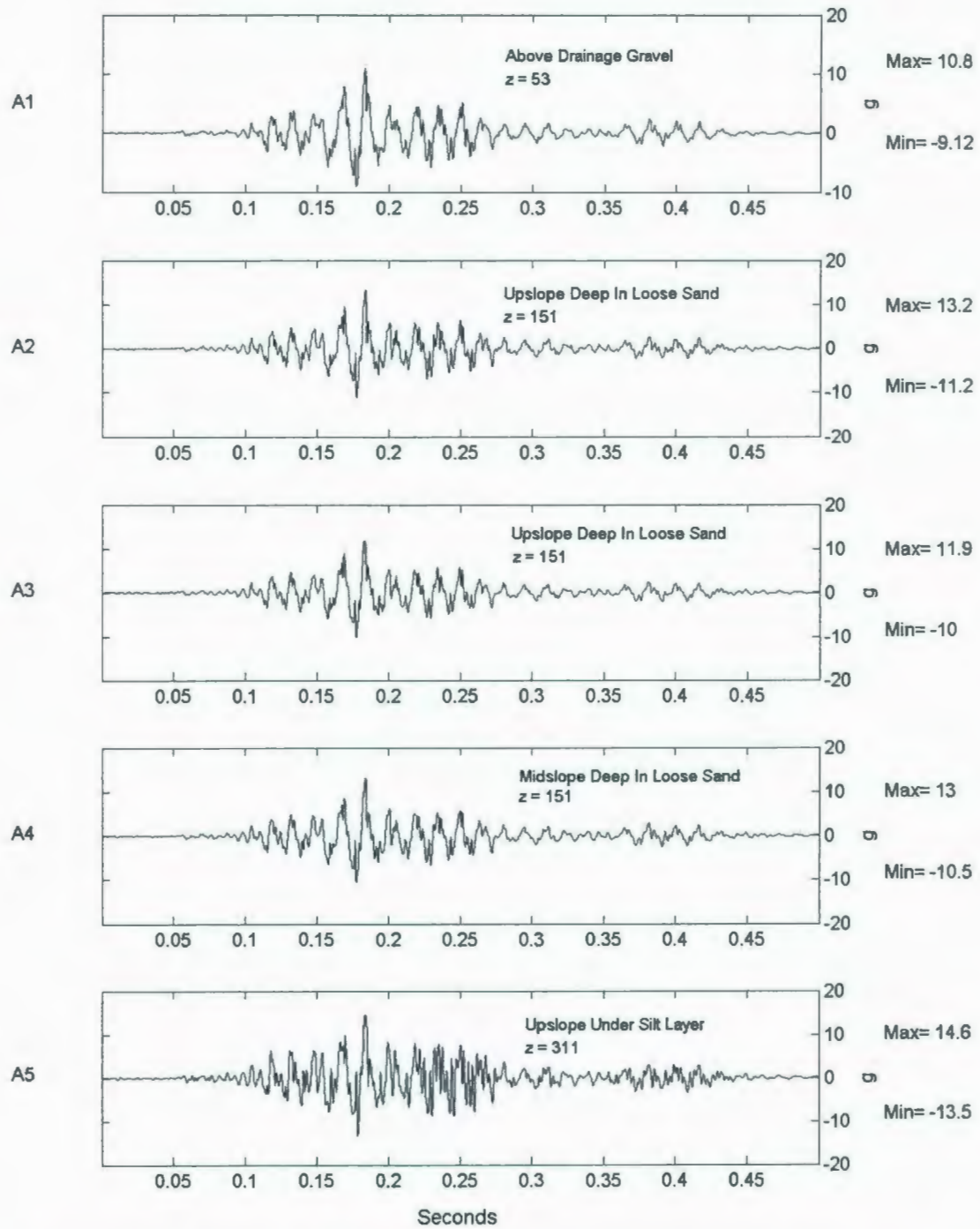
Figure 6.132: COSTA-E A475-5 Short-Term Accelerometer Response for A1-A5.

319
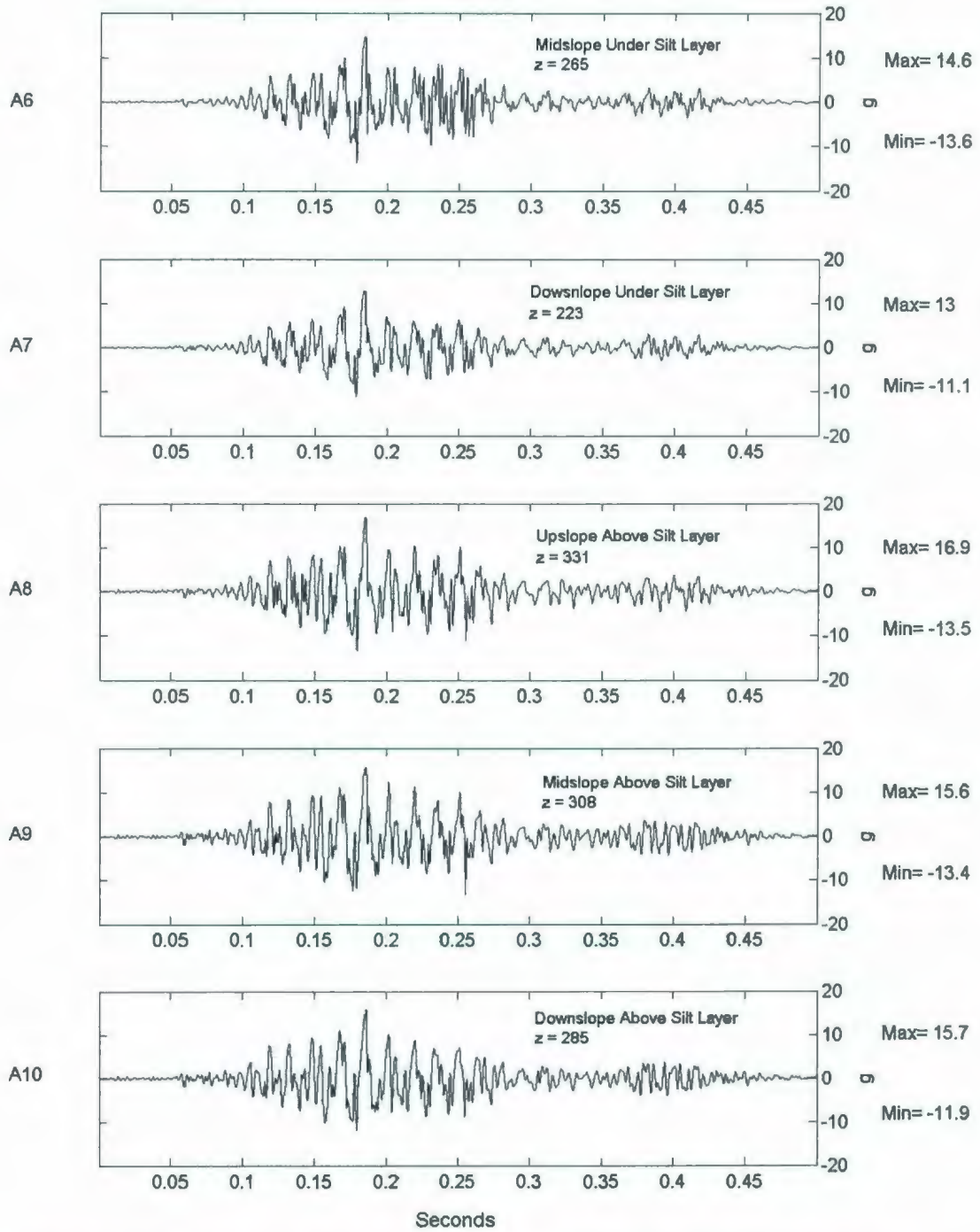
Figure 6.133: COSTA-E A475-5 Short-Term Accelerometer Response for A5-A10.
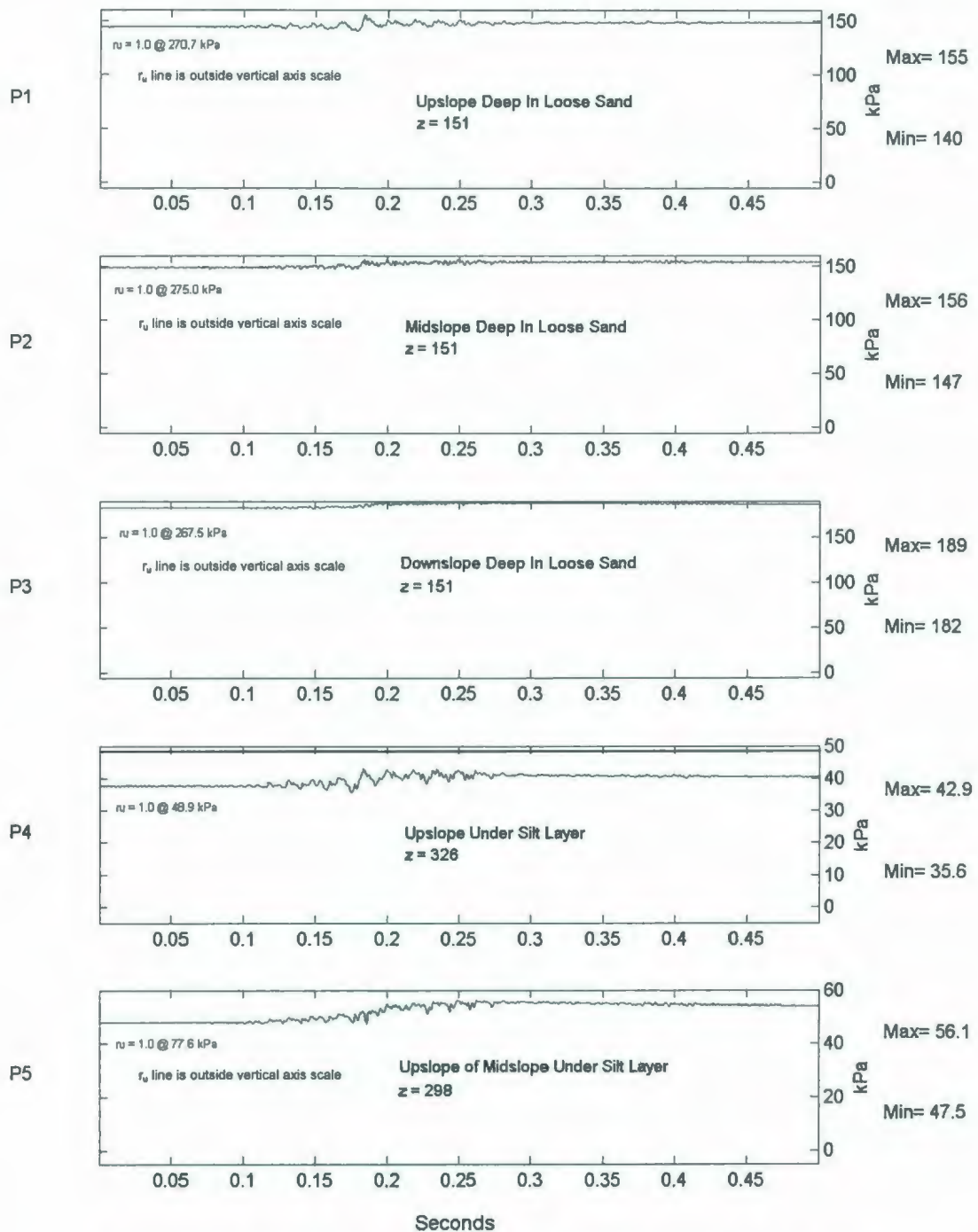
Figure 6.134: COSTA-E A475-5 Short-Term PPT Response for P1-P5.
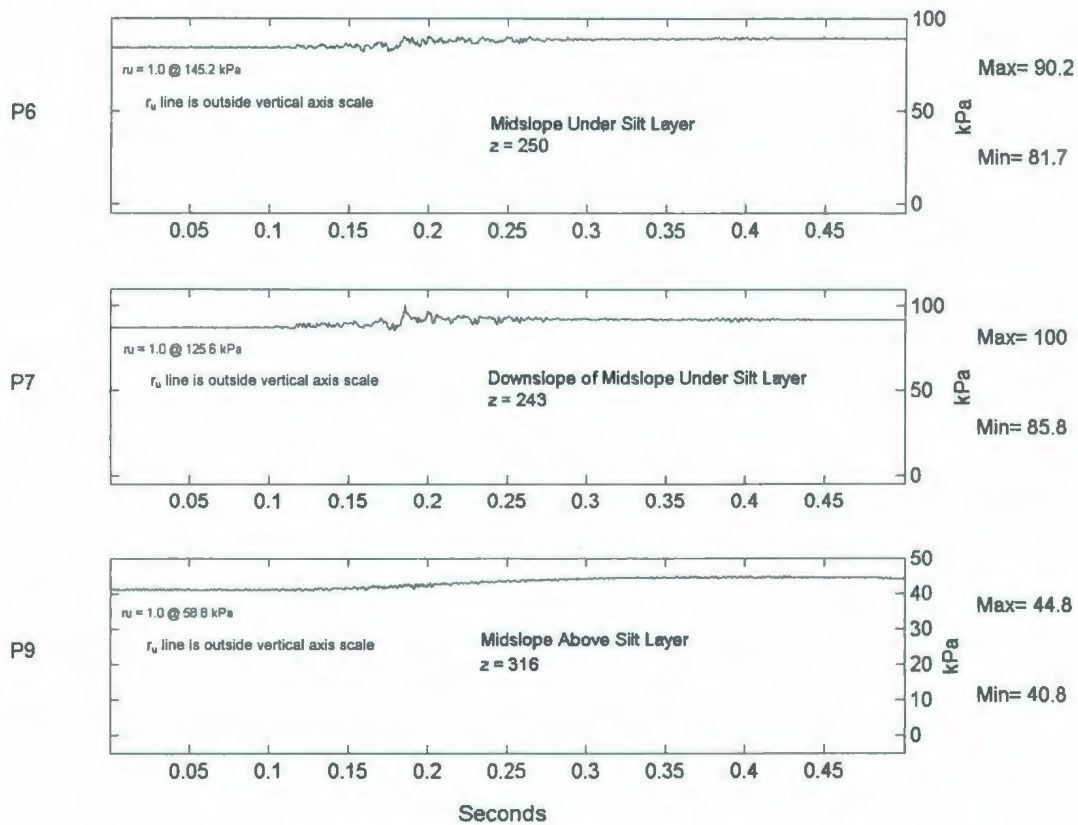
Figure 6.135: COSTA-E A475-5 Short-Term PPT Response for P6-P9.
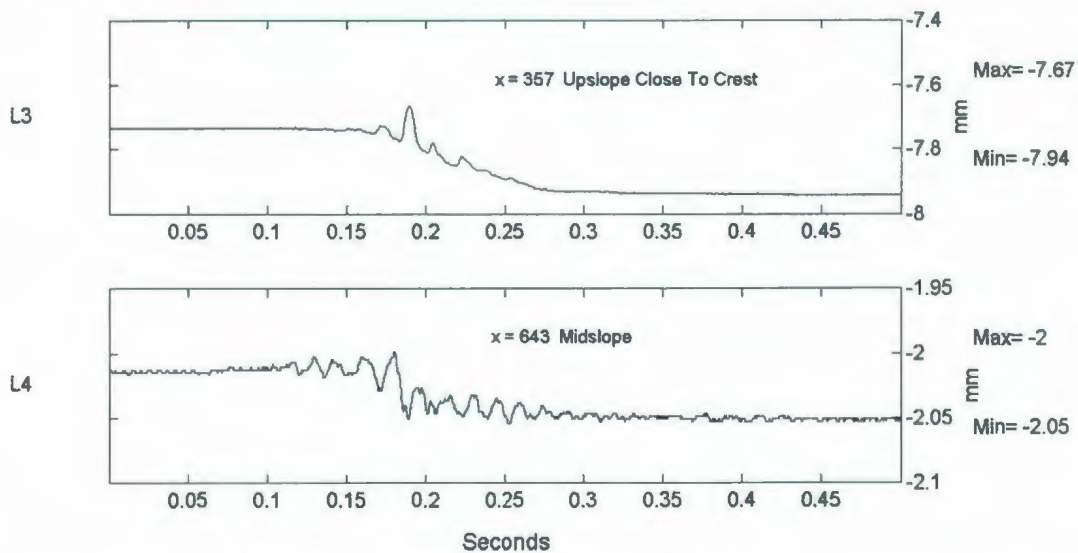
**Figure 6.136:** COSTA-E A475-5 Short-Term LVDT Deformation Response.

The responses in the instruments in the A475-5 event were very similar to the responses for the A475-4 event. Again, pore pressure dissipation continued to decrease, albeit just slightly. This reveals an overall trend in the decrease in generated excess pore pressure with successive shakings as all PPT instruments responded with decreased readings in each successive A475 earthquake. The vertical settlement, as shown in L3 and L4, also displays a similar trend over the five successive A475 earthquake events as the settlement in this event was further reduced to 0.27 and 0.05 mm in the crest and midslope positions respectively.

6.5.12 A475-5 Long-Term Testing Instrument Responses

The long-term responses were collected to examine the behaviour of the model for several seconds after the fifth A475 earthquake event. Figures 6.137 through 6.141 illustrate these responses.
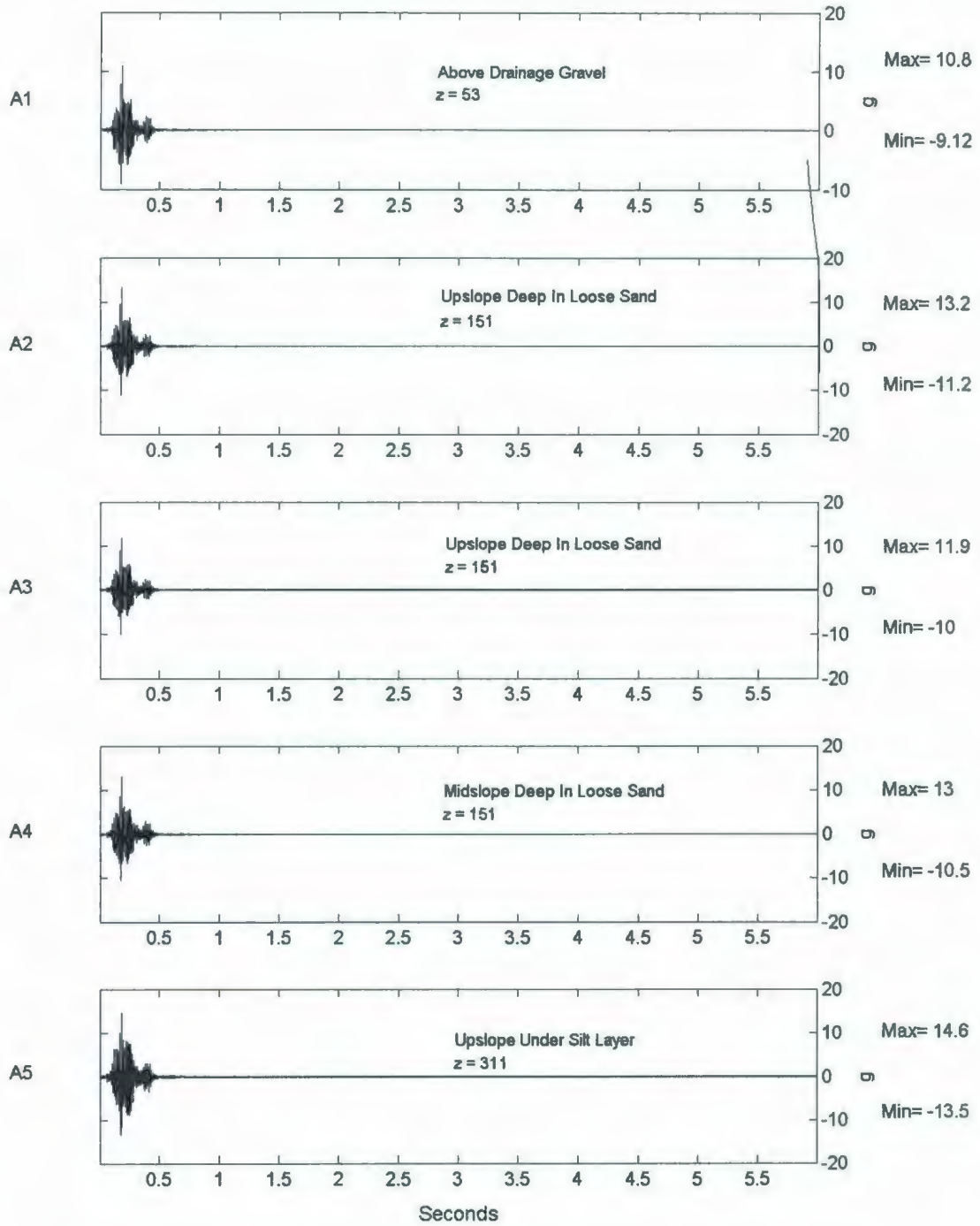
Figure 6.137: COSTA-E A475-5 Long-Term Accelerometer Response for A1-A5.
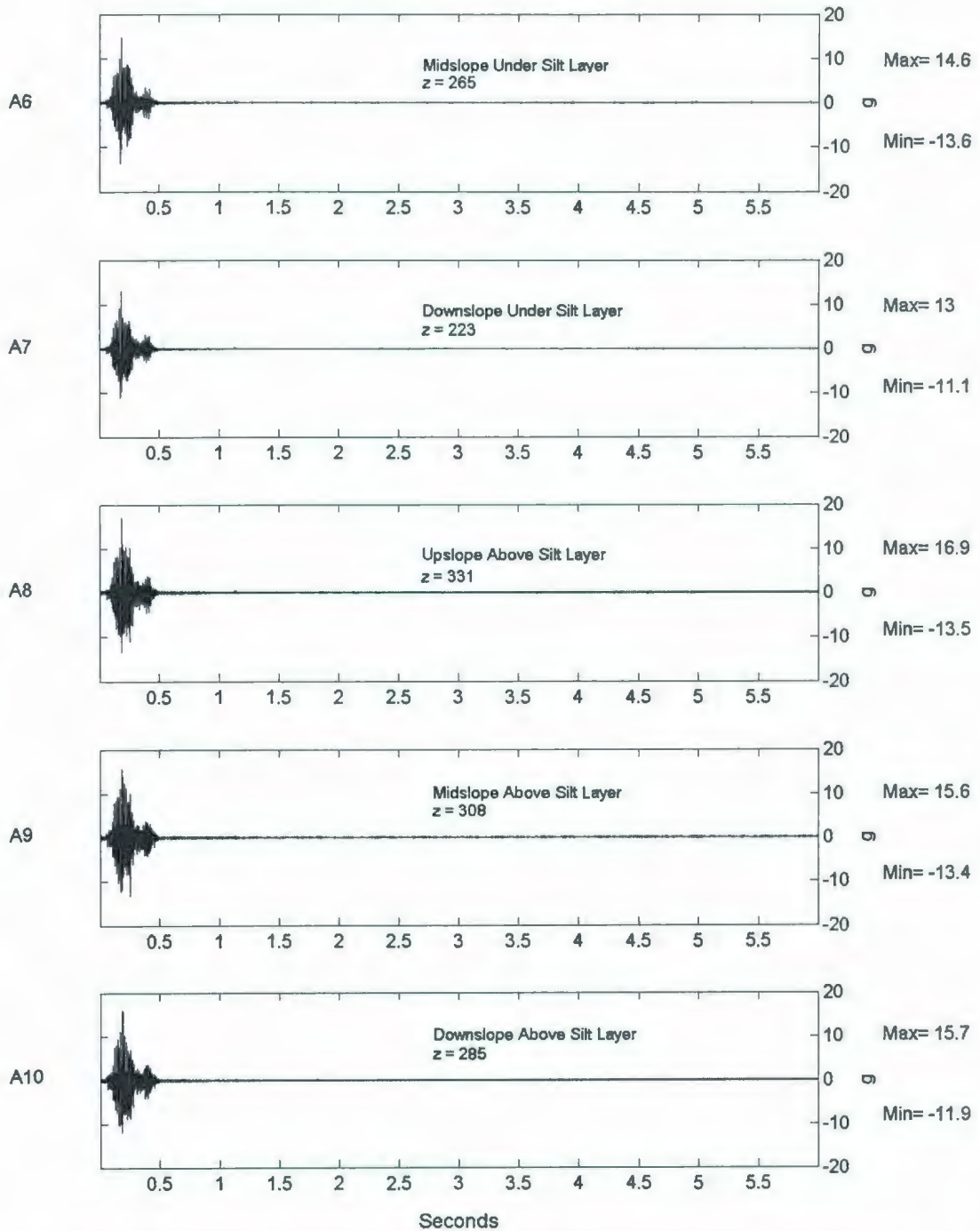
Figure 6.138: COSTA-E A475-5 Long-Term Accelerometer Response for A6-A10.
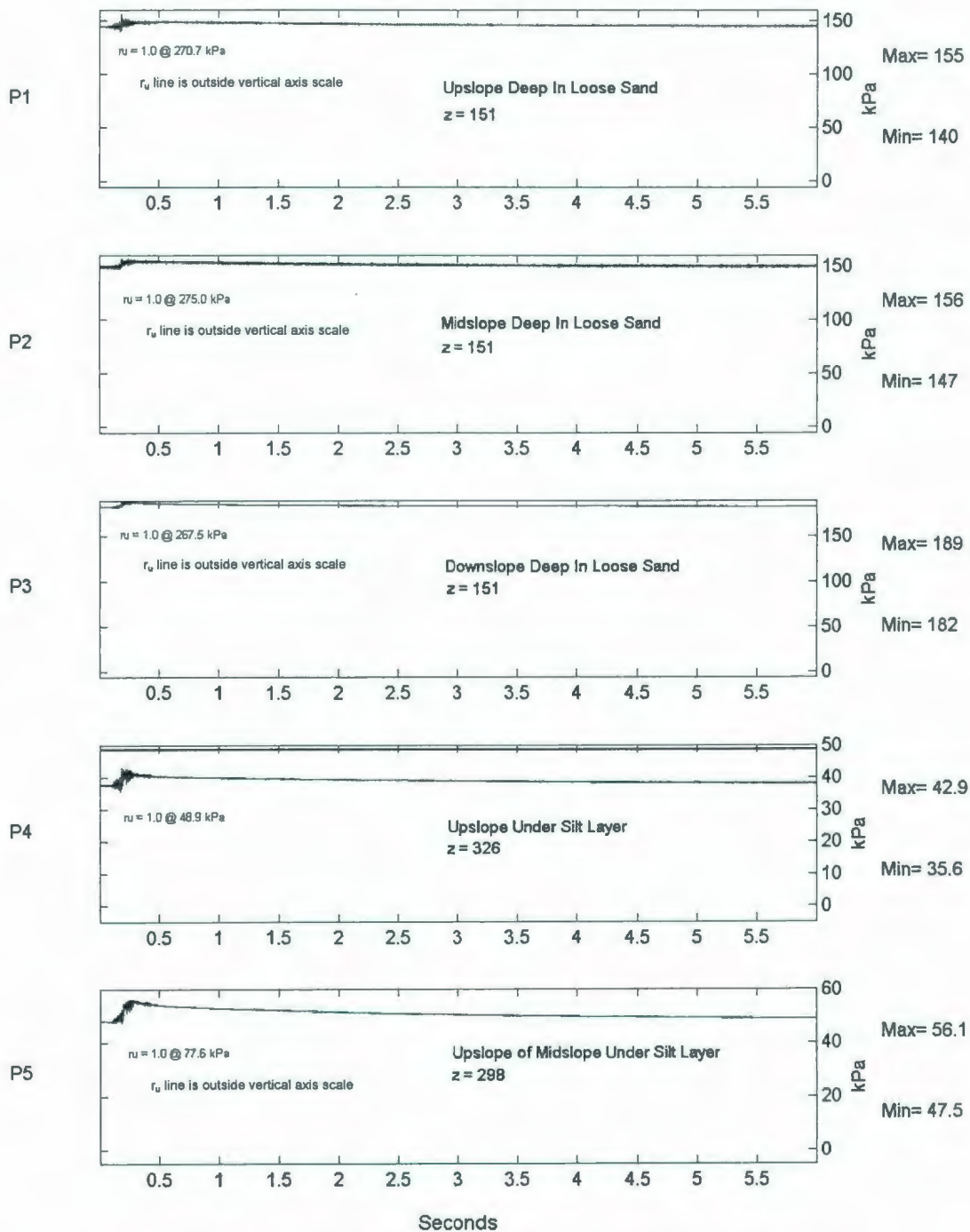
Figure 6.139: COSTA-E A475-5 Long-Term PPT Response for P1-P5.
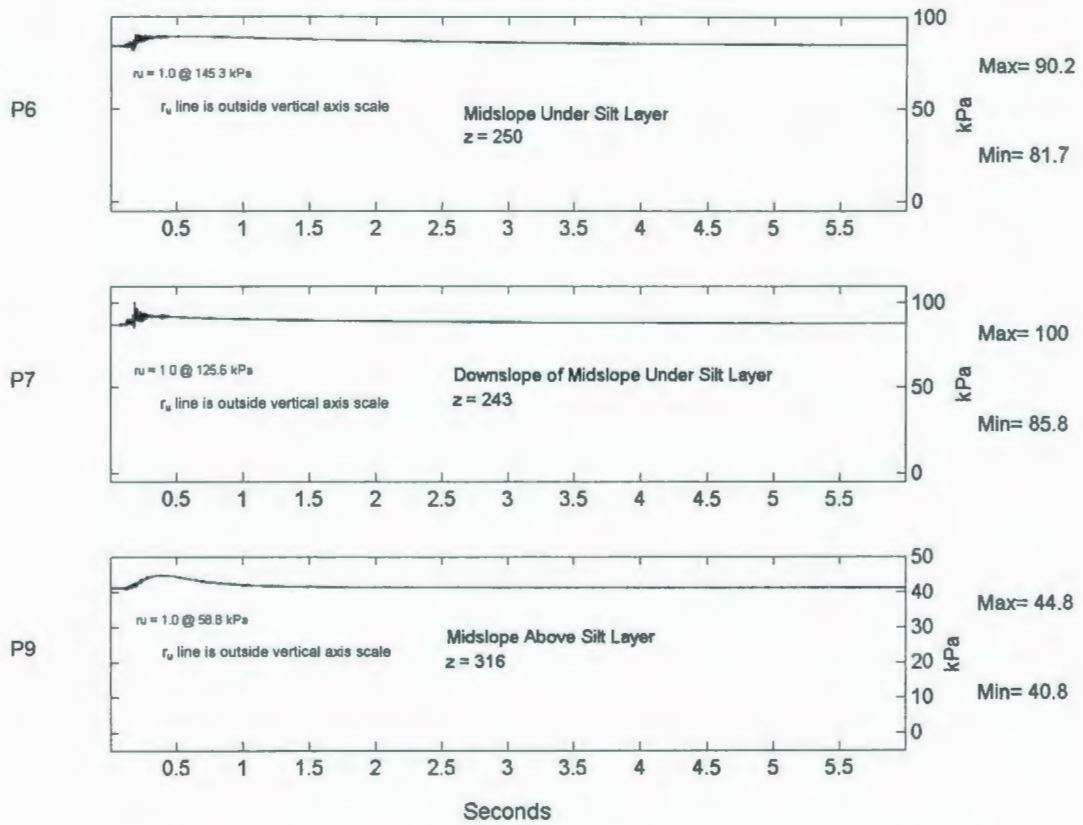
Figure 6.140: COSTA-E A475-5 Long-Term PPT Response for P6-P9.
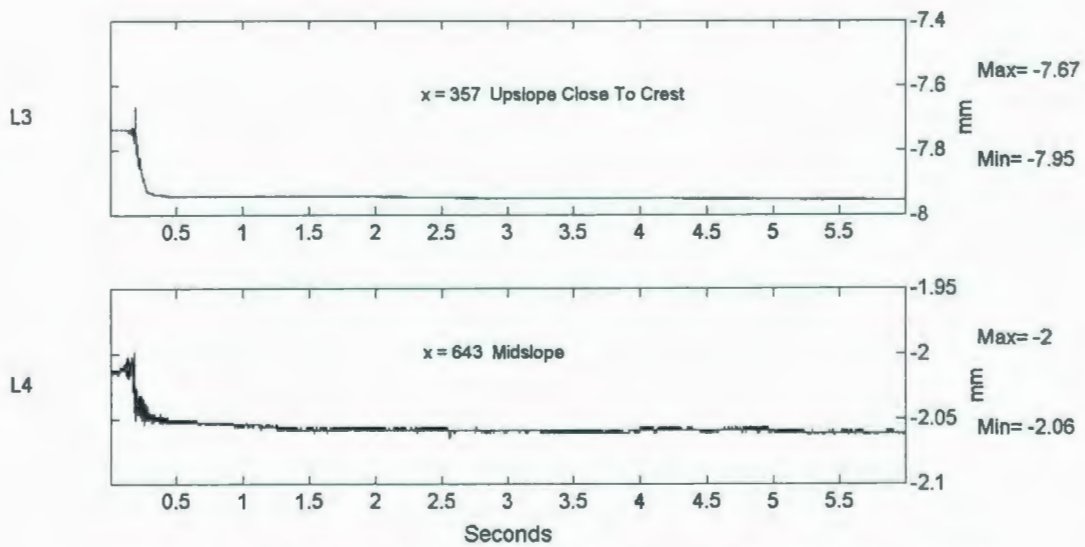
**Figure 6.141:** COSTA-E A475-5 Long-Term LVDT Deformation Response.

The final A475 event applied in this test also resulted in similar responses for all of the instruments to the responses observed in the A475-4 event as well as the other three previous events. The long-term PPT results show very little pore pressure generation with exposure to this earthquake.

6.5.13 2A2475 Short-Term Testing Instrument Responses

All operating instruments were monitored during and shortly after the 2A2475 earthquake event. Figures 6.142 through 6.146 illustrate the observed responses in the various instruments during a 0.5 second period.
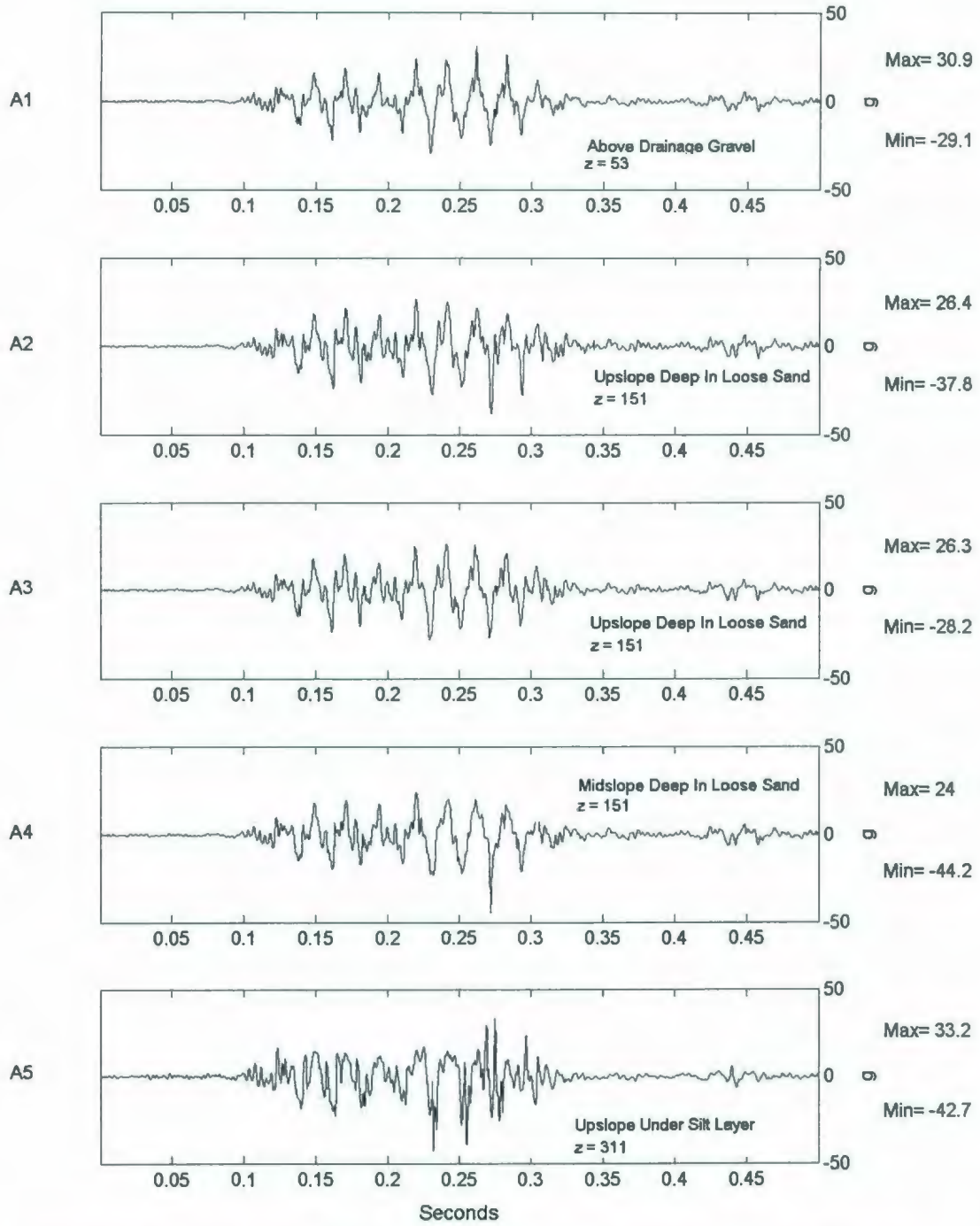
**Figure 6.142:** COSTA-E 2A2475 Short-Term Accelerometer Response for A1-A5.
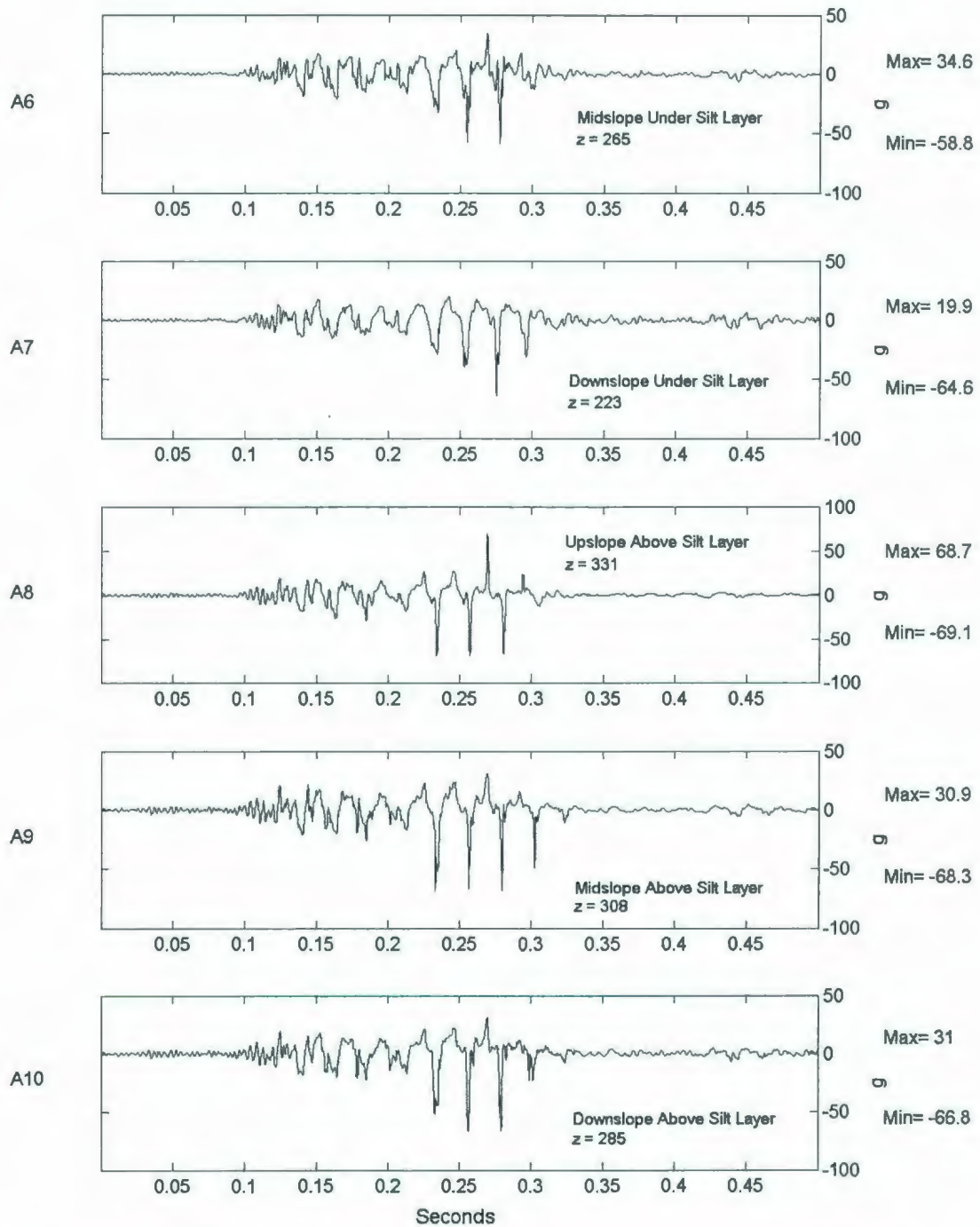
Figure 6.143: COSTA-E 2A2475 Short-Term Accelerometer Response for A6-A10.
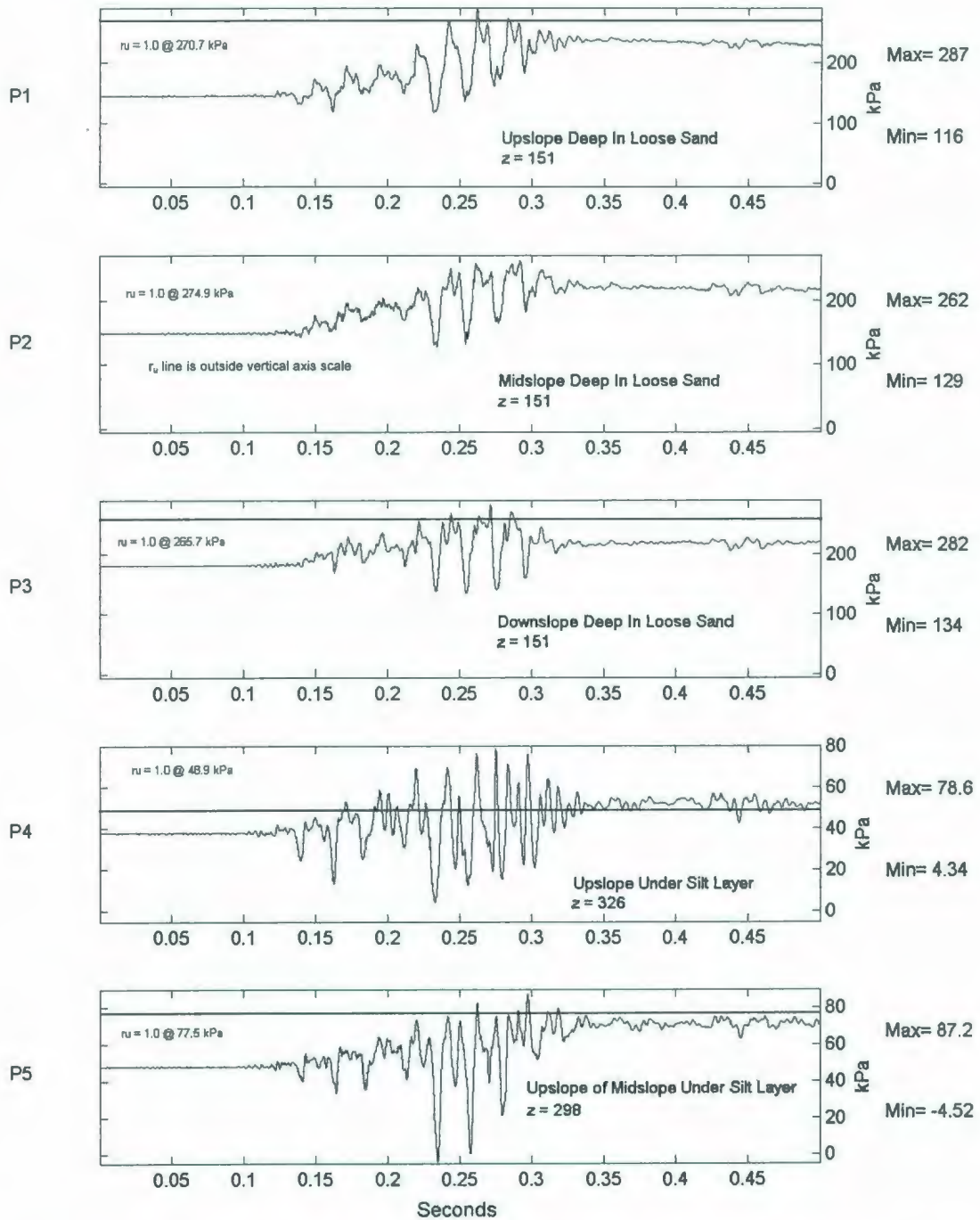
Figure 6.144: COSTA-E 2A2475 Short-Term PPT Response for P1-P5.
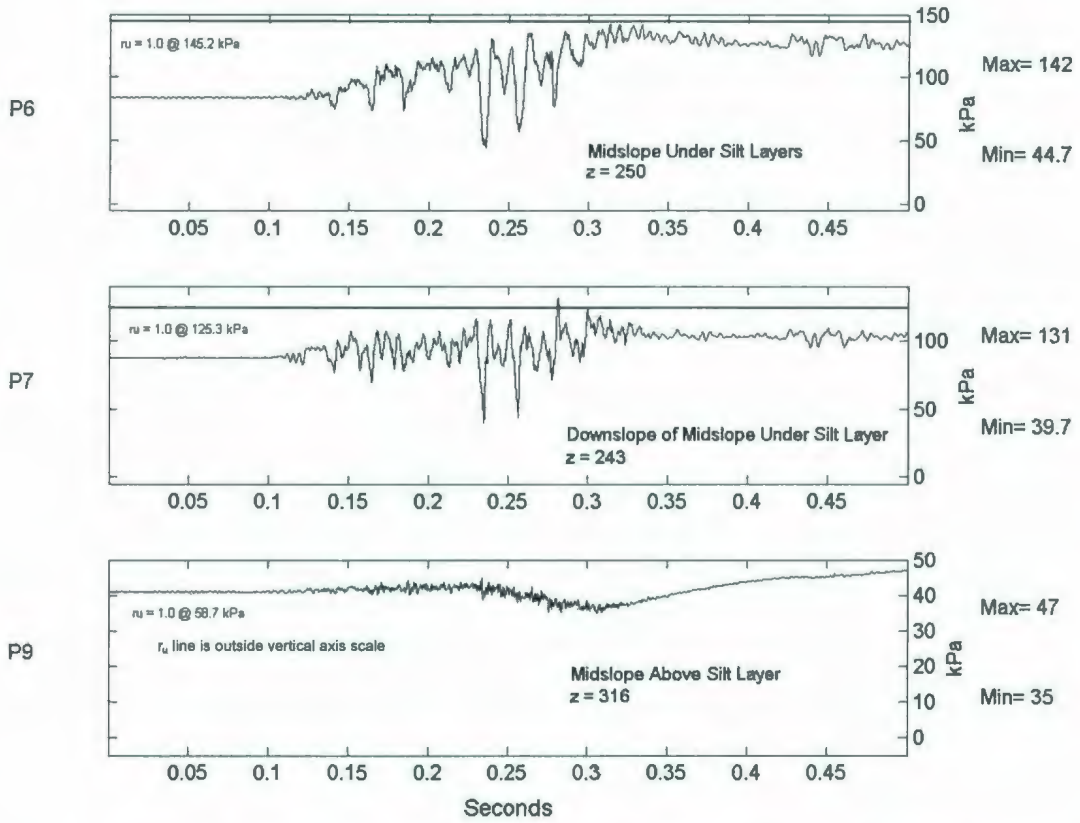
**Figure 6.145:** COSTA-E 2A2475 Short-Term PPT Response for P6-P9.
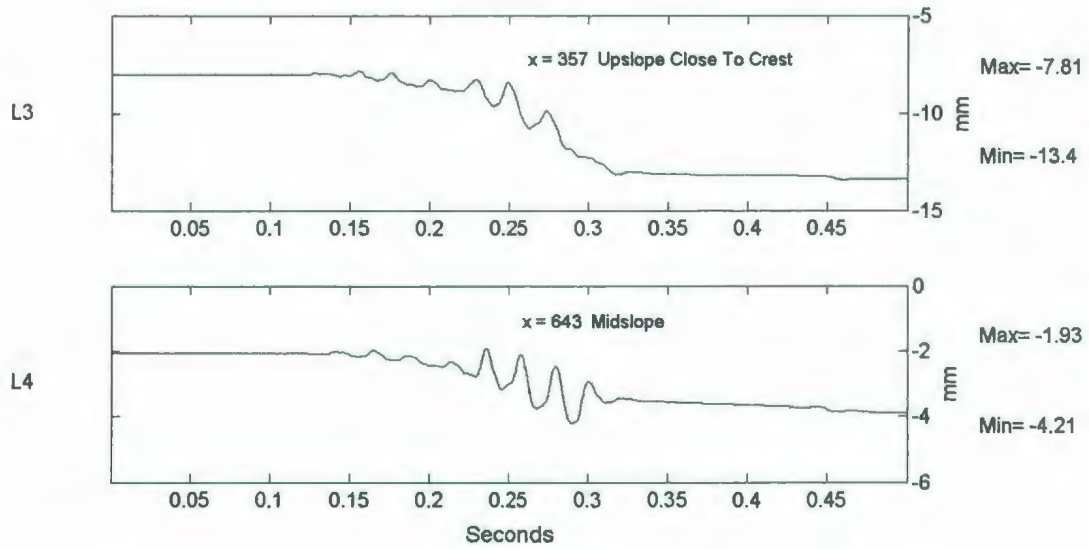
**Figure 6.146:** COSTA-E 2A2475 Short-Term LVDT Deformation Response.

Some of the trends observed following the smaller earthquakes event are also evident in this larger shaking event. There is a more pronounced increase in negative acceleration spikes as elevation increases in the model. Most noticeably is this behaviour in the accelerometers above the silt layer (A8, A9 & A10) where there are clear large dilation spikes of greater than 60 g, which is far beyond the magnitude of the maximum input acceleration of approximately 24 g.

In addition, below the silt layer, in P5, there is a distinct corresponding drop of pore pressure to below zero during the shaking event. Expectedly the generated pore pressures and accelerations are larger than in the smaller five earthquakes. Liquefaction conditions also appear at P4 under the silt layer at approximately 0.155 seconds and continue throughout the short-term observation period. Liquefaction also slightly occurs under the silt layer in the P5 position. The generated pore pressure also peaks over the liquefaction level deep in the sand model in both P1 and P3, however it does not occur at these locations until 0.25 seconds.

The LVDTs showed moderate response in surface settlement. The crest of the slope, as measured by L3, settled approximately 5.5 mm, while the slope face settled a little greater than 2 mm.

6.5.14 2A2475 Long-Term Testing Instrument Responses

The long-term responses were collected to examine the behaviour of the model for several seconds after the 2A2475 earthquake event. Figures 6.147 through 6.151 illustrate these responses.
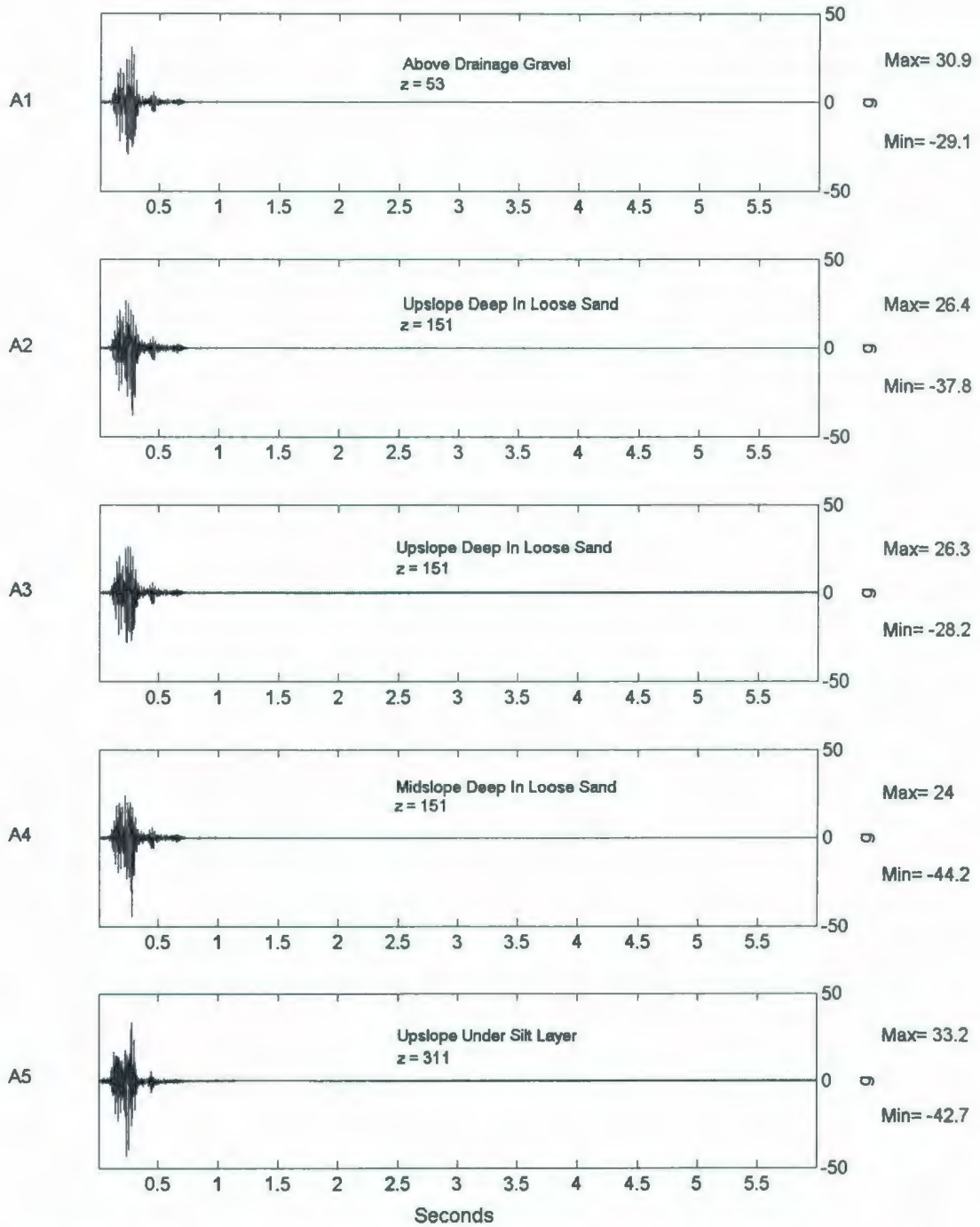
Figure 6.147: COSTA-E 2A2475 Long-Term Accelerometer Response for A1-A5.
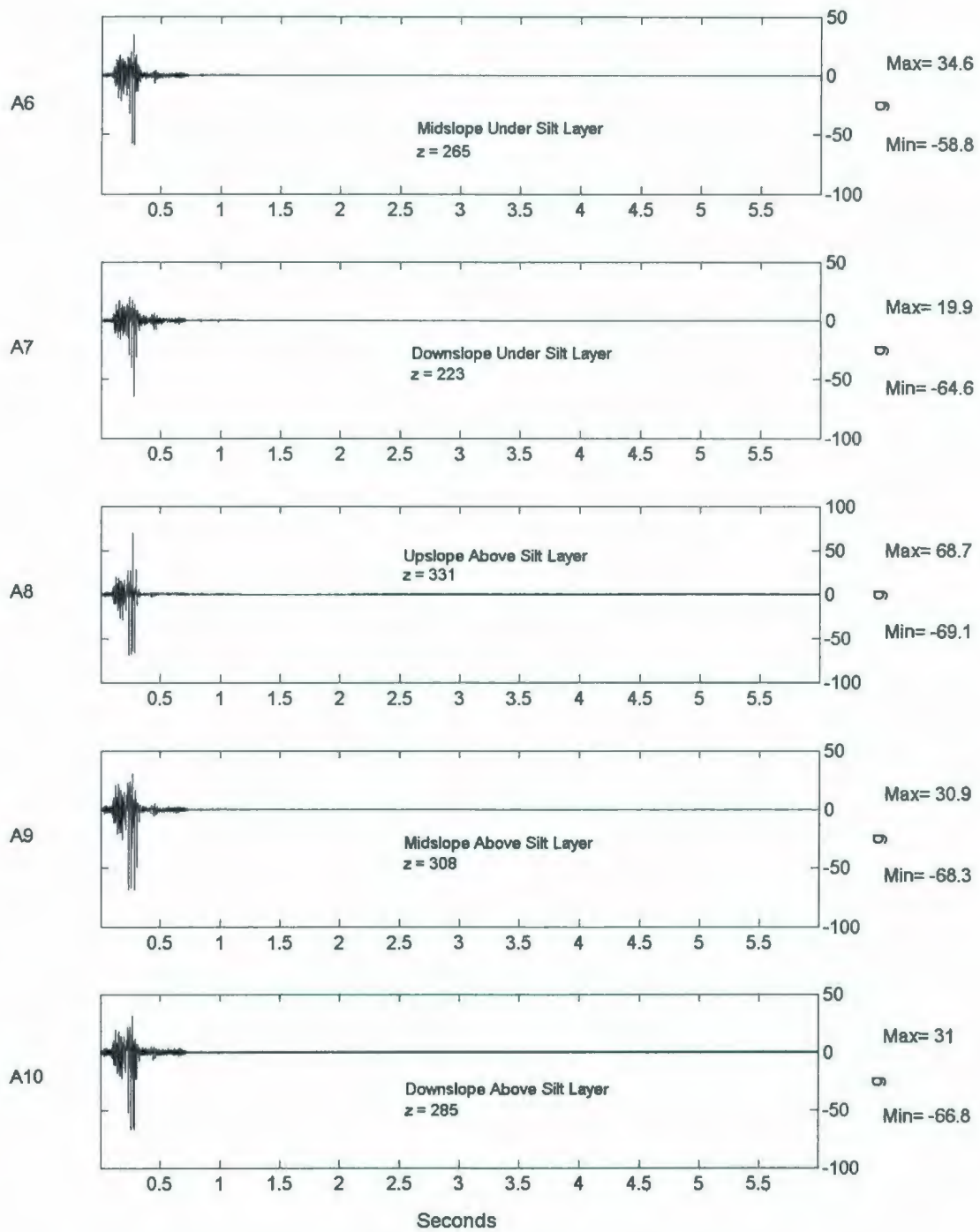
**Figure 6.148:** COSTA-E 2A2475 Long-Term Accelerometer Response for A6-A10.
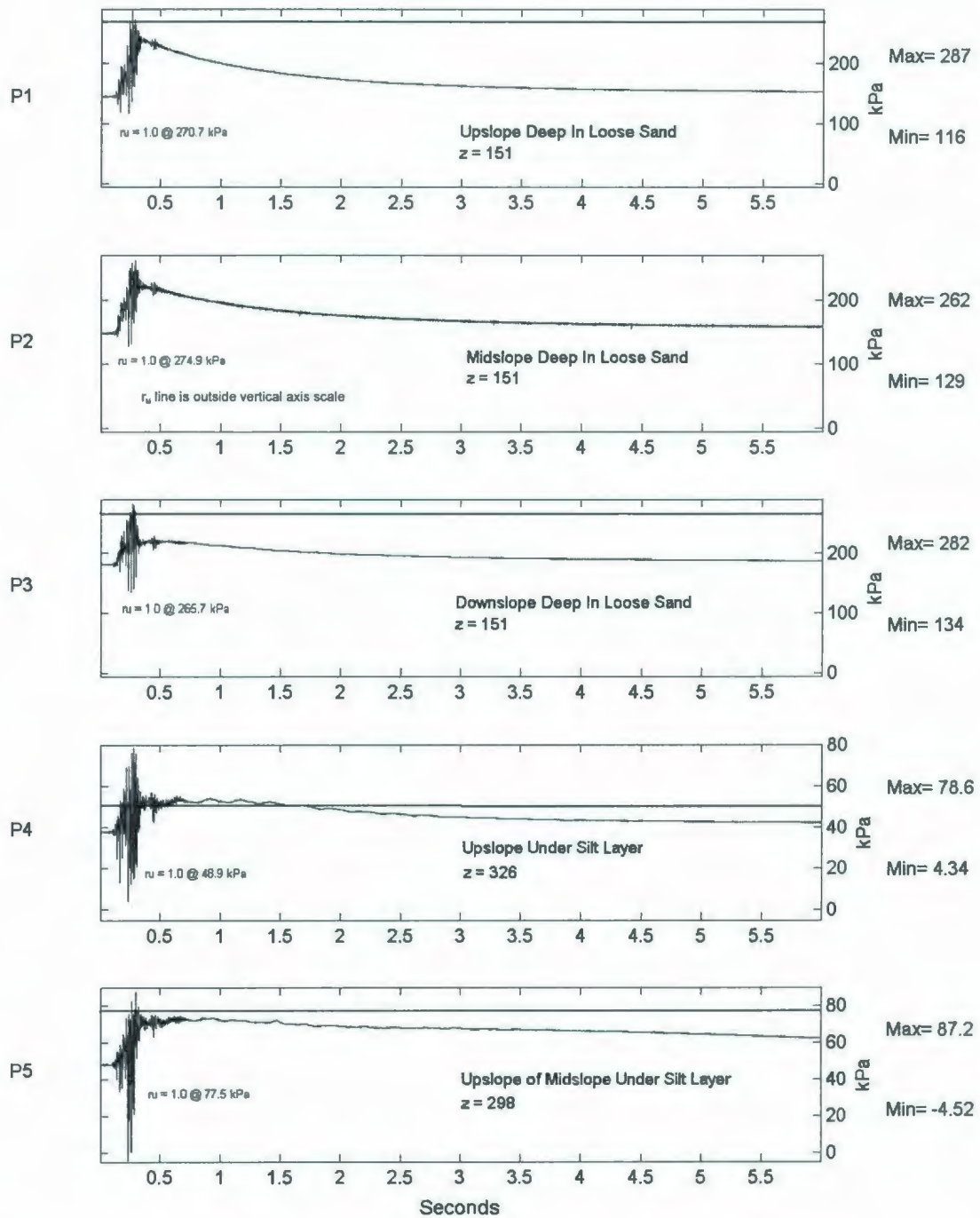
Figure 6.149: COSTA-E 2A2475 Long-Term PPT Response for P1-P5.
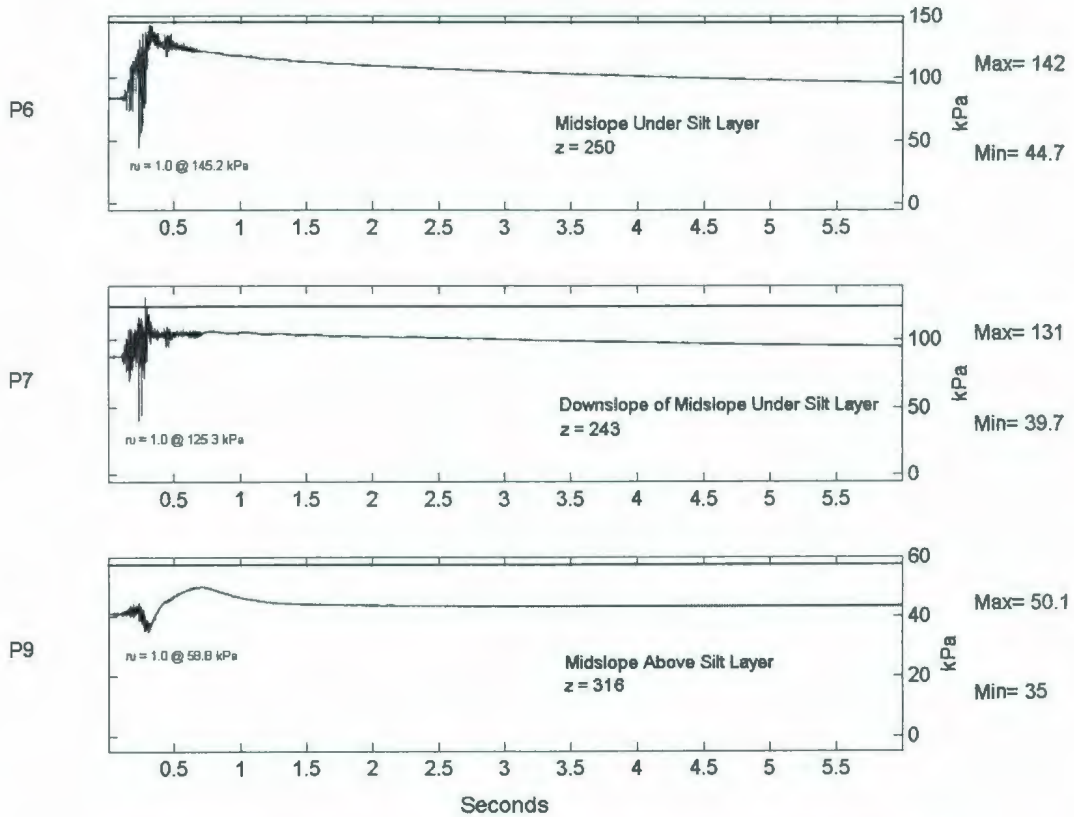
**Figure 6.150:** COSTA-E 2A2475 Long-Term PPT Response for P6-P9.
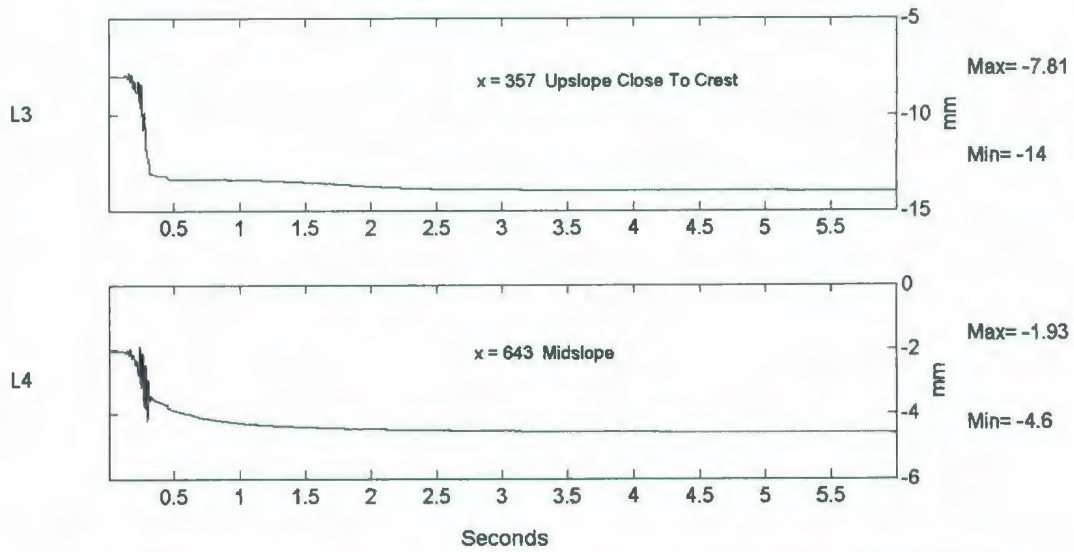
**Figure 6.151:** COSTA-E 2A2475 Long-Term LVDT Deformation Response.

338

The long-term accelerometer records further emphasize the negative spikes that were evident in the short-term records, especially in the A6 through A10 positions.

The long-term trends also show that there is prolonged dissipation of generated pore pressures. Nevertheless, the most notable PPT response in the long term is the initial decrease in pore pressure followed by a relatively large increase. In contrast to the pore pressure dissipation observed in the smaller A2475 events, the pore pressures observed after this event do not for the most part fully dissipate during the long-term observation period. Prolonged liquefaction is evident in P4, which continues until 1.75 seconds.

No significant vertical settlement occurs in L3 and L4 following the short-term observation period.

6.5.15 Post-Test Observations

Similarly to swing-up, the PPT and LVDT responses were monitored during swing-down to ensure integrity of the model and to observe any radical changes that may occur. All PPTs seem to experience the correct rate in reduction of pore pressure as the g-level decreases indicating that there were no large changes in pore pressure during swing-down. Most of the PPTs return to a value close to zero. The change from their original value could be caused by the movement of the PPT in the sand during shaking. However, it should be noted that the response of P3 did not completely return to a zero level. This most likely indicates that there is some electrical problem with the response of this

instrument. All LVDTs show little change during the swing-down period, but it appears that the model rebounds during swing-down about 1 mm or less in both functioning LVDTs.

Temperature measurements of the model were taken periodically before and after the loading of the model on to the centrifuge arm, as well as after the test. In previous tests warm oil circulating in the hydraulic mechanisms of the shaker have been observed to significantly effect the temperature of the model. A temperature probe was installed during pluviation deep in the loose sand. Table 6.23 displays these observed temperatures.

Table 6.23: COSTA-E Observed Model Temperature Response.

Time	Location	Comments	Temperature ($^{\circ}$C)
8:00 AM	On Lab Floor	Pre Loading	17.6
8:45 AM	On Arm	After Loading	20.8
11:15 AM	On Arm	Test Preparation	20.5
12:00 PM	On Arm	Pre-Test	20.3
1:20 PM	On Arm	Post-Test	21.3

After the centrifuge flight was completed, the profile of the model surface was measured while the model was still situated on arm. The results showed reduction in height on the upslope surface as well as some collection of material at the toe. Table 6.24 and Figure 6.152 illustrate these pre- and post- test conditions. No significant movement of the slope crest in the downslope direction was observed. Much like the response during COSTA-A

340

and COSTA-D only surface settlement, of approximately 10 mm, in the upslope farfield was observed with very little accumulation of material occurring at the toe.

Table 6.24: COSTA-E Post-Test Surface Profile.

Distance from Upslope End (mm)	Pre-Test Surface Height (mm)	Post-Test Surface Height (mm)
0	342	334
50	342	330
100	341	329
150	341	329
200	341	328
250	340	327
300	339	326
350	338	323
400	336	317
450	311	305
500	285	282
550	263	261
600	237	236
650	211	212
700	185	194
737	174	192
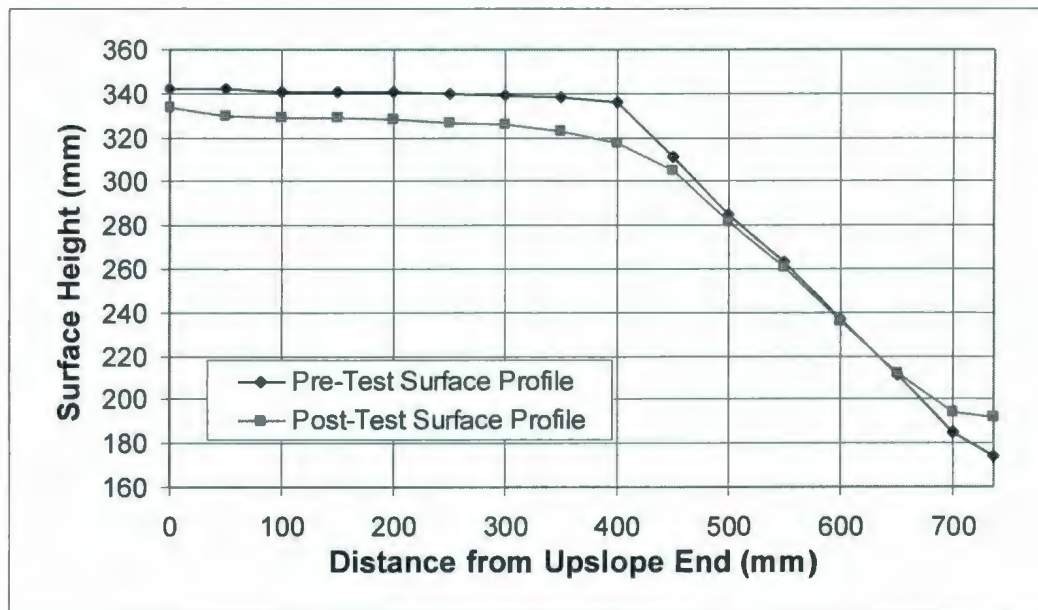
Figure 6.152: COSTA-E Post-Test Surface Profile.

Small white pieces of gravel were placed on the model slope face prior to saturation in a square grid measuring approximately 25 mm by 25 mm grid. A photograph of this grid as placed pre-test is shown in Figure 6.153. This was done to make qualitative comparisons of the movement of the slope face during the test.
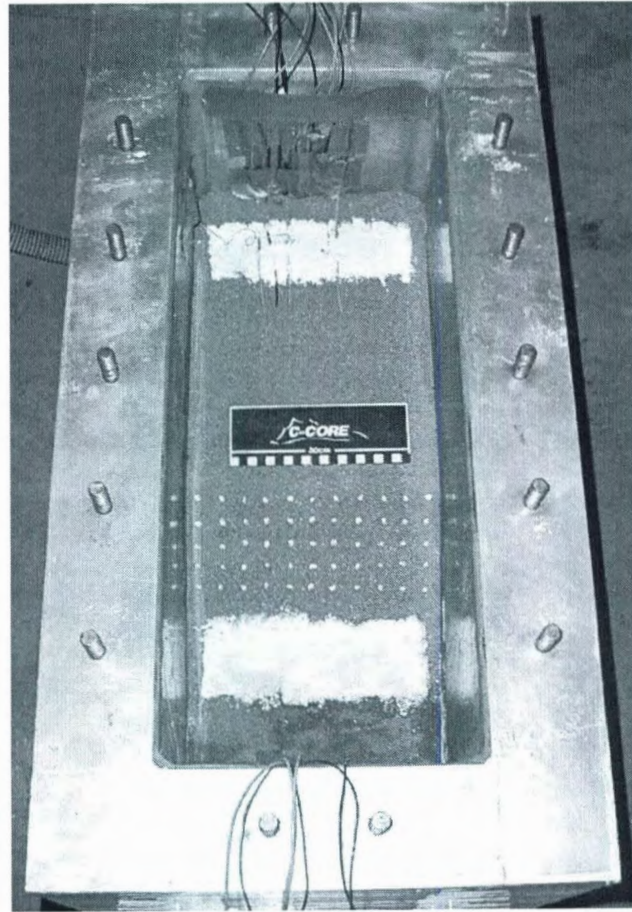
Figure 6.153: COSTA-E Pre-Test Slope Marker Grid.

Following the test a photograph of the model slope, similar to that shown in Figure 6.153 was also taken. The post-test marker grid conditions are shown in Figure 6.154. It is

shown that no some horizontal deformation of the marker grid occurred during slope failure, indicating there was a small amount of movement along the sidewalls compared to the centre of the model. This figure also shows that there was no significant movement or failure of the slope during the application of the earthquake events, further showing the conditioning of the model against failure for the applied shaking regime.
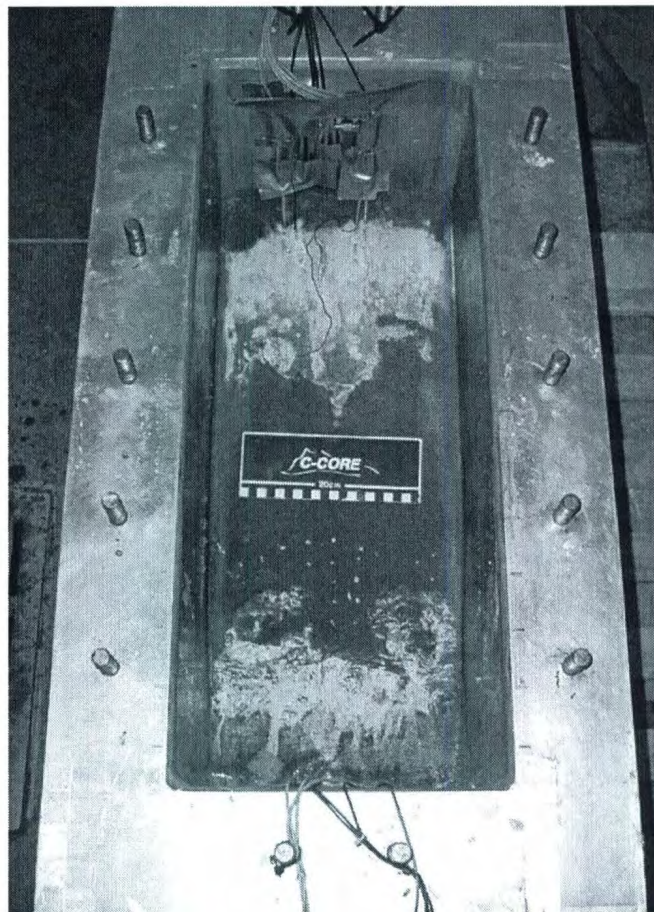
Figure 6.154: COSTA-E Post-Test Slope Marker Grid.

Following the test the model was transported off the centrifuge arm to the lab floor where it was drained and excavated. During excavation, the positions of the internal instruments were noted as shown in Chapter 5. Additionally, the location of the installed silt layer was measured and the height of this layer as well of a comparison with its intended position is given in Table 6.25 and Figure 6.155. The values presented are for the top of the silt layer. It was also observed that the silt layer had compressed slightly leaving it approximately 13-16 mm thickness in model scale. No significant mixing of the Fraser River sand and the Sil-Co-Sil silt was observed. No evidence was available to show that an earthquake induced failure had occurred. The large movement of the silt layer observed on COSTA-B and COSTA-C did not transpire in this test. The silt layer was not observed to have broken in any major way and some small downslope movement of the silt at the downslope breakout was observed to have taken place.

Table 6.25: COSTA-E Silt Layer Profile.

Distance from Upslope End (mm)	Pre-Test Silt Profile	Post-Test Silt Profile
50	343	330
100	343	329
150	339	323
200	330	317
250	321	311
300	312	304
350	303	298
400	294	291
450	284	283
500	275	271
550	265	264
600	242	244
650	--	232
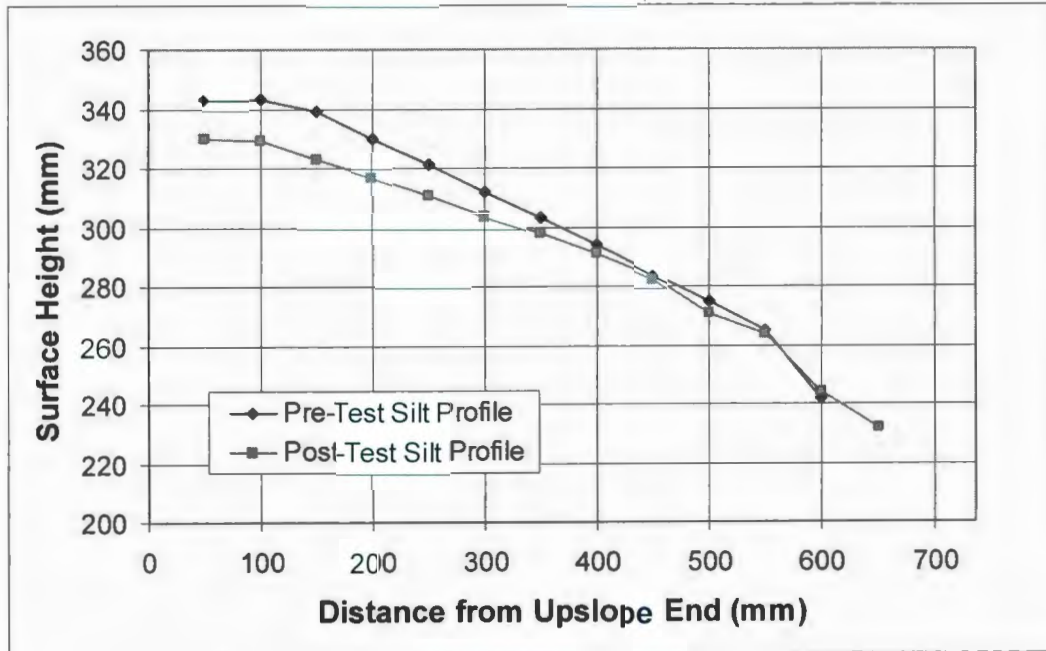
Figure 6.155: COSTA-E Silt Layer Profile.

7 EXPERIMENTAL TESTING ANALYSIS

7.1 Effect of Silt Layer

Overall, two major observations can be made from looking at the results of the COSTA-B and COSTA-C tests were that:

> (1) there is settlement in the upslope farfield during earthquake shaking; and
>
> (2) pore pressure migrates from deeper in the model upward after the earthquake shaking.

However, there are additional observations that can be made by examining the results.

The first observation that can be made by further examining the results of the centrifuge tests is a comparison of the short- and long-term results of the COSTA-C and COSTA-D tests in order to determine the effect of the presence of the relatively impermeable silt layer. These two models experienced the same earthquake shaking, the larger 2A2475 event, and the same test profile and geometry with the exception of the placement of a 5.5:1 sloped silt layer in the COSTA-C model.

The biggest characteristic difference between the results of COSTA-C and COSTA-D is the long-term response of L2, which measures the horizontal movement of the slope material above the silt layer location. A comparison of these responses is shown in Figure 7.1. In the COSTA-C test there is a large amount of downslope movement

following the completion of the earthquake event. This continued delayed slope movement is most likely due to the presence of the impermeable silt layer.

COSTA-C Silt Layer

COSTA-D No Silt Layer
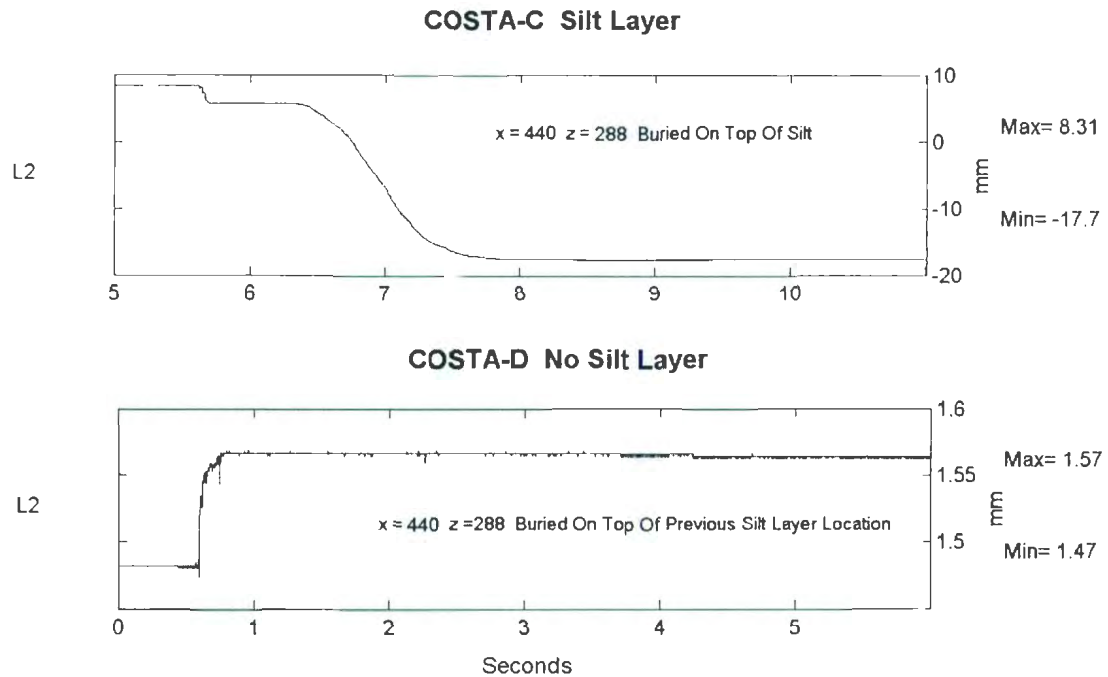
Figure 7.1: Comparison of Long-Term L2 Horizontal LVDT Deformation in COSTA-C & COSTA-D.

Comparing the short-term results of both the accelerometers and the PPTs for COSTA-C and COSTA-D does not reveal any effect of the presence of the silt layer. Figure 7.2 shows the short-term behaviour of A7 & A8, which are below and above the silt layer respectively for both COSTA-C and COSTA-D. The magnitudes of the accelerations are similar in both directions for the comparable locations for the two different geometries. In A7, for the COSTA-C test, there are slightly more pronounced negative spikes but the frequency of the response is similar in both tests at this location.

347

COSTA-C Silt Layer

A7

Downslope Under Silt Layer
z = 223

Max= 19.5

Min= -65.4

A8

Upslope Above Silt Layer
z = 331

Max= 20.5

Min= -37.9

COSTA-D No Silt Layer

A7

Downslope Under Previous Silt Layer Location
z = 223

Max= 19.9

Min= -64.6

A8

Upslope Above Previous Silt Layer Location
z = 331

Max= 20.2

Min= -33.7

Seconds
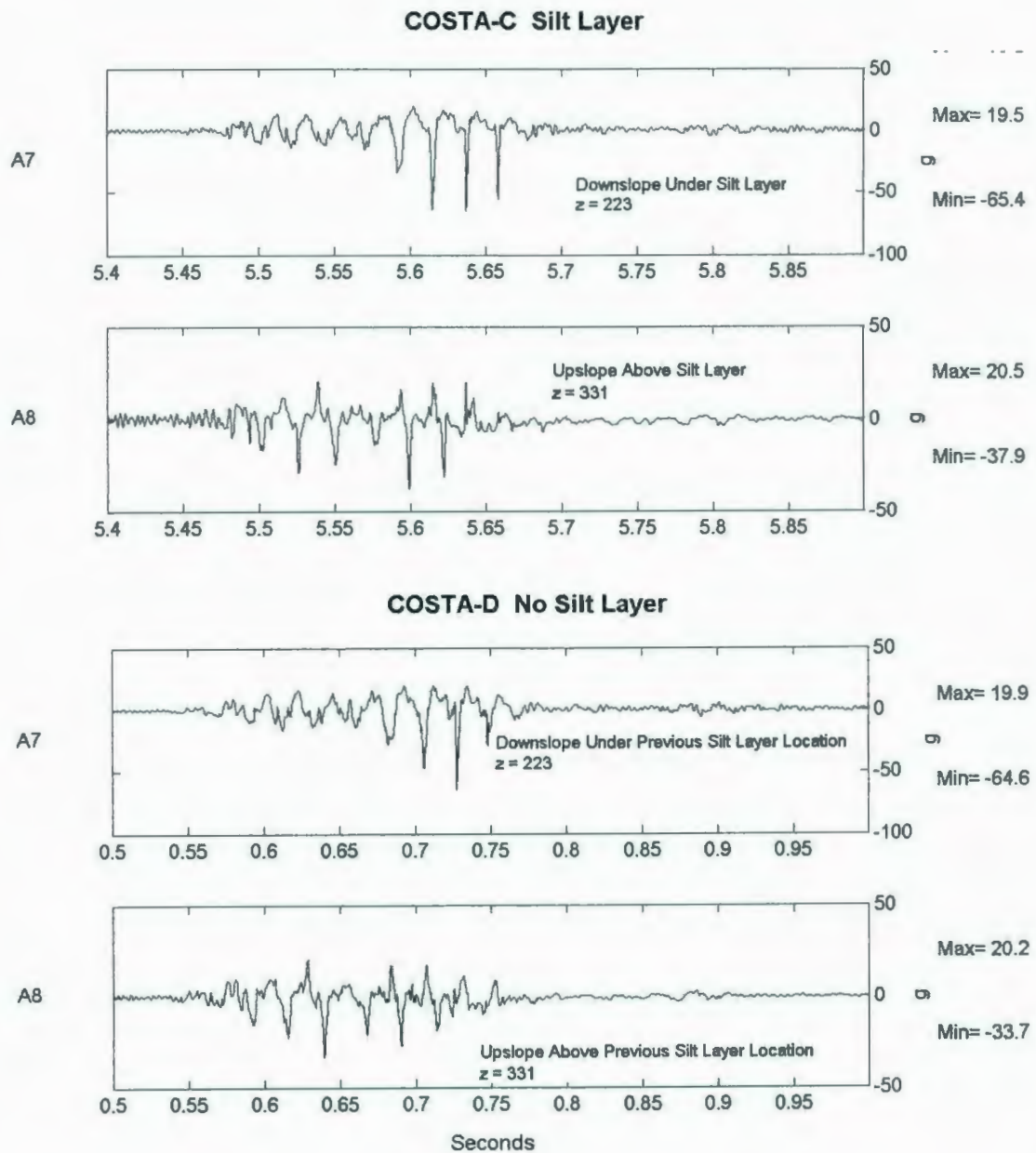
Figure 7.2: Comparison of Short-Term A7 & A8 Accelerometer Responses in COSTA-C & COSTA-D.

348

Looking at the short-term response of the PPTs, a similar comment can be made that there is little influence of the silt layer in terms of excess pore pressure generation. An example of this is the compared responses of P7 for both of these tests, which are very similar. This comparison is illustrated in Figure 7.3. Both tests feature the simultaneous negative spikes in both acceleration and pore pressure.
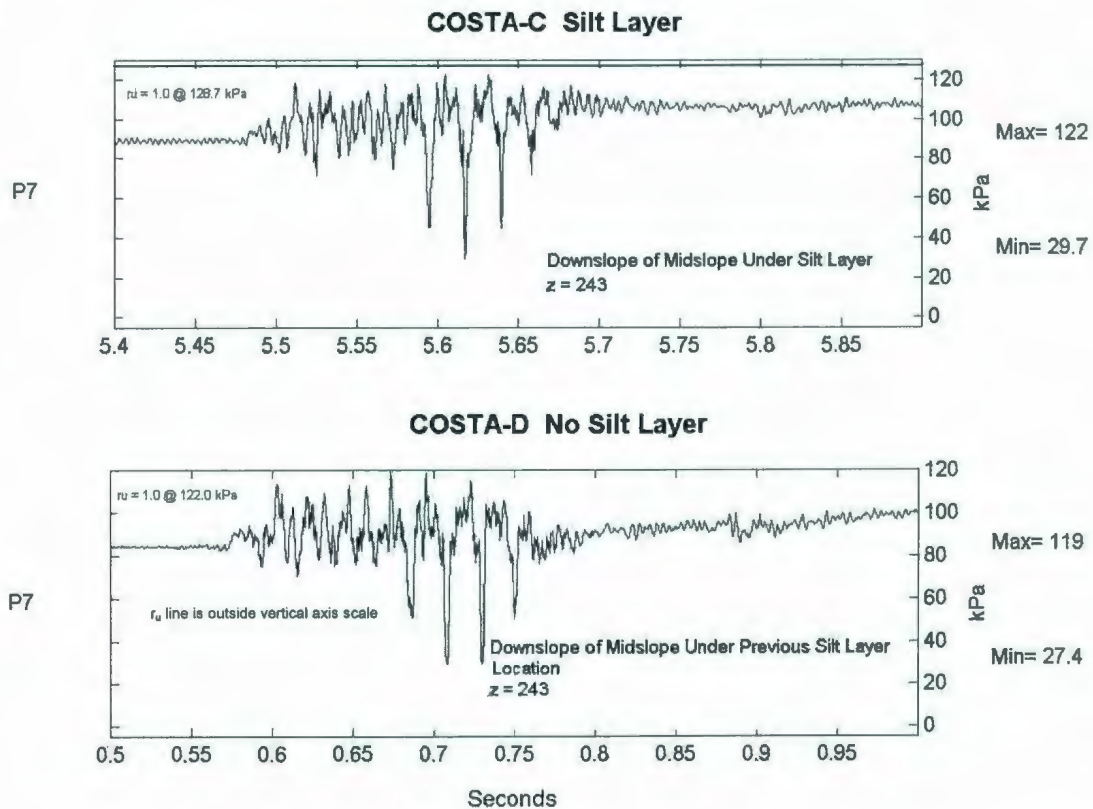
Figure 7.3: Comparison of Short-Term P7 PPT Responses in COSTA-C & COSTA-D.

There is evidence of an upslope migration under the silt layer, or in similar locations in the case of COSTA-D, of pore pressure in both tests as PPTs in the most downslope

locations, such as P7 and P8, seems to experience quicker dissipation that those in the upslope locations, such as P4 and P5. Therefore, it is evident that this effect is not directly contributory to instability.

The only noticeable difference in the short- and long-term responses of the PPTs and accelerometers occurs in the long-term behaviour of the PPTs that are placed directly beneath the silt layer. This is exemplified in Figure 7.4 where the PPT responses for P6 and P7 are illustrated for both tests. A thin line has been added to these figures to show the pre-shake pore pressure levels in each of these instruments. Any response above this level is the generated excess pore pressure. For these locations, it is shown that the dissipation of excess pore pressure occurs more quickly in COSTA-D, which features no buried silt layer. At the completion of the long-term observation period, both P6 and P7 have virtually returned to their pre-shake levels, indicating near total dissipation of excess pore pressure. In contrast, the response of P6 and P7 in the COSTA-C test shows delayed response and more significant residual excess pore pressure values at the completion of this long-term period. Since this effect is the only noteworthy difference in the responses of these instruments and slope failure was detected in COSTA-C, both by the response of L2 and in the post-test observations, it can be concluded that this long-term delayed dissipation of generated excess pore pressure is the cause of this observed failure.
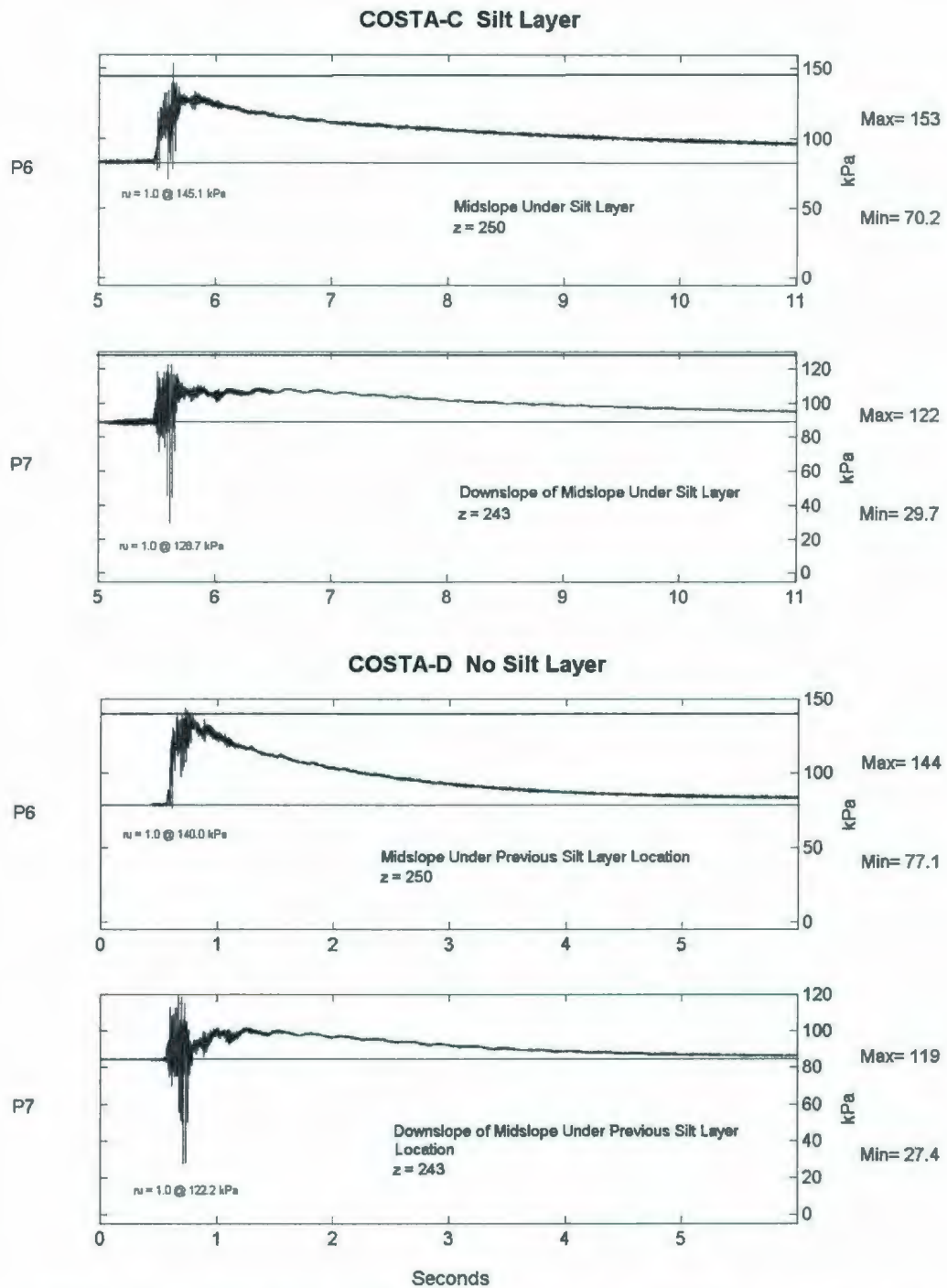
Figure 7.4: Comparison of Long-Term P6 & P7 PPT Responses for COSTA-C & COSTA-D.

However, the response of P5 through P8 does not exhibit prolonged liquefaction. The pore pressure ratio only rises above one in these instruments during the earthquake event. To examine the possible driving mechanism, a sliding block analysis can be undertaken to see if the increased pore pressure under the silt layer is a contributing factor. Referring to Figures 5.2 and 7.5 below, the effective weight (W') of the sliding block in the COSTA-C can be expressed as:

$$W' = An\gamma' \tag{7.1}$$

where A is the cross-sectional area and γ' is the effective unit weight of the soil, and can be calculated as:

$$W' = [(1/2)(0.1016m)(0.3556m)][70][9.4kN / m^3]$$
$$W' = 11.89kN / m$$
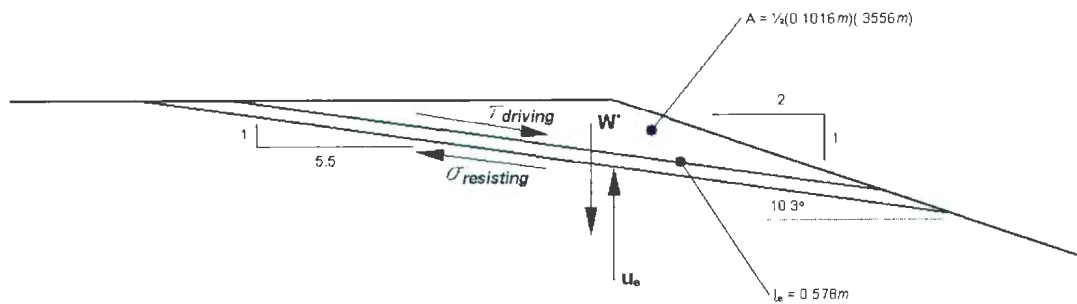
Figure 7.5: COSTA-C Sliding Block Geometry.

Following this, the driving stress ($\tau_{driving}$) can be expressed as:

$$\tau_{driving} = W'\sin\theta \qquad (7.2)$$

where θ is the slope angle, and can be calculated as:

$$\tau_{driving} = [11.89kN \,/\, m]\sin 10.3^{\circ}$$
$$\tau_{driving} = 2.13kN \,/\, m$$

Then, ignoring the side friction of the side container, the normal resisting force (σ_{normal}) can be expressed as:

$$\sigma_{normal} = [W'\cos\theta - u_e l_e]\tan\phi \qquad (7.3)$$

where l_e is the effective length of the silt in cross section upon which generated excess pore pressure is acting. Estimating an average generated excess pore pressure of 15 kPa, from looking at the response of P4 through P8 for COSTA-C and an effective shear stress parameter of 32° for the silt, σ_{normal} can be calculated as:

$$\sigma_{normal} = [(11.89kN \,/\, m)(\cos 10.3^{\circ}) - (15kPa)(0.578m)]\tan 32^{\circ}$$
$$\sigma_{normal} = 1.89kN \,/\, m$$

Since the normal resisting force has been found to be less than the resisting stress, a failure can be expected from the mechanism of excess generated pore pressure beneath the silt layer, which was observed in the COSTA-C test.

An additional effect that can be observed is in the COSTA-A test. Although there is increased prolonged excess pore pressure, and sometimes liquefaction, beneath the silt layer (as shown in the P2, P4, P5, P7, and P8 instruments in Figures 6.16 and 6.17), there is no slope failure. Although this type of increased pore pressure should serve as a

driving force for slope failure it is not large enough in this case to overcome the resisting force created by the shear resistance of the in liquefied overlying sand.

7.2 Effect of Earthquake Magnitude

Another set of observations that can be made is with respect to the effect of earthquake magnitude, as three different earthquakes of different magnitudes were applied to the same test geometry with a buried 5.5:1 sloped relatively impermeable silt layer. These comparable tests include: the first earthquake event of the COSTA-B test, where the A2475 earthquake was applied; the only earthquake applied during the COSTA-C test, where the 2A2475 earthquake was applied; and the first earthquake event of the COSTA-E test, where the smallest earthquake, the A475 earthquake was applied.

The accelerometer response of A1, which is the deepest placed accelerometer, in the COSTA-B A2475 and COSTA-C 2A2475 earthquakes is shown in Figure 7.6. These two earthquakes are identical in frequency but the 2A245 earthquake is exactly doubled in magnitude. The response for the A1 accelerometer shows that the input earthquake is very nearly doubled in magnitude as experienced at the base of the model, in terms of their maximum negative and positive accelerations, with some of the negative spiking behaviour that has been previously discussed beginning to appear in the COSTA-C response. The experienced maximum peak acceleration in the A2475 earthquake in the COSTA-B test is approximately 20% greater than the prescribed earthquake as shown in Figure 5.18, while the same response in the 2A2475 earthquake in the COSTA-C test is

354

approximately is also approximately 20% greater than the prescribed earthquake shown in Figure 5.19. This shows that there is very good agreement between the two tests in terms of the EQS reproducing the same earthquake motion at different magnitudes.

COSTA-B A2475 Earthquake

COSTA-C 2A2475 Earthquake
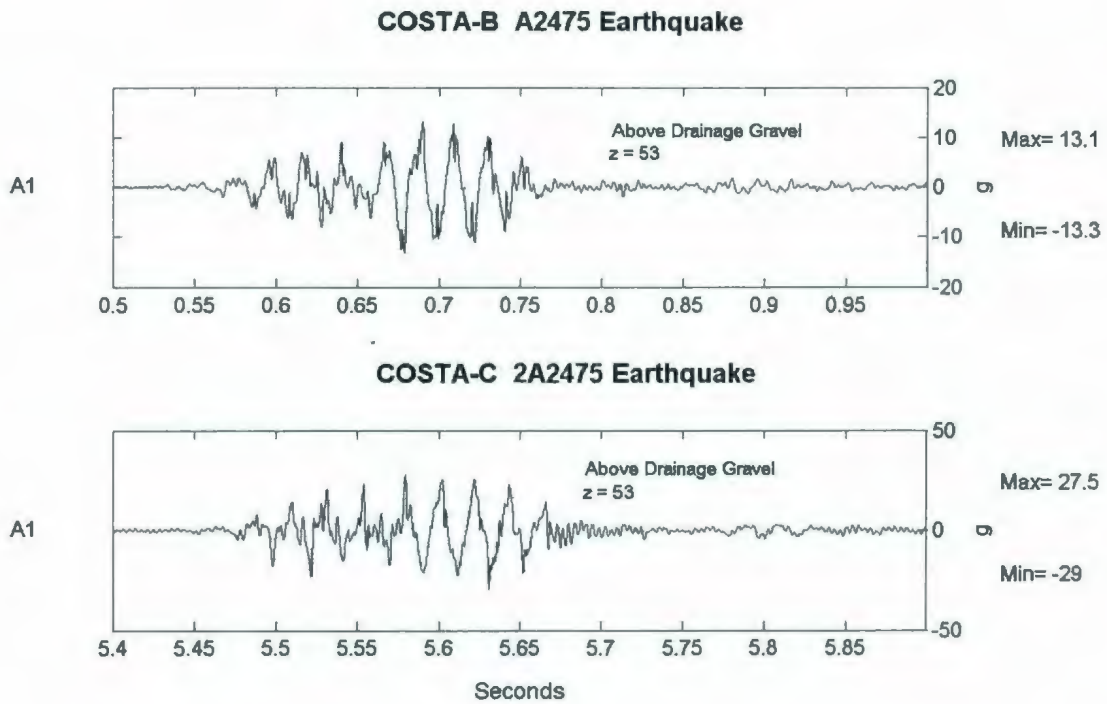
Figure 7.6: Comparison of Short-Term A1 Accelerometer Responses for COSTA-B A2475 & COSTA-C 2A2475.

Another effect that is apparent in the short-term responses of the accelerometers is with regard to the presence of the negative accelerometer spikes. In the A2475 earthquake in the COSTA-B test, these negative acceleration spikes are only present above the silt layer. However, with the increased acceleration of 2A2475 these negative acceleration spikes are evident both beneath the silt layer, such as in downslope locations in A6 and

A7 as well as upslope locations like A4, and in deeper locations, such as in A2 as shown in Figure 7.7 where its response is compared from COSTA-B to COSTA-C. Figure 7.7 also shows the response of this instrument for the first COSTA-E A475 earthquake. All accelerometers in all positions in this A475 earthquake event showed a virtually similar response in terms of frequency and magnitude, which in turn is very similar to the prescribed A475 earthquake signal shown in Figure 5.17. The A475 earthquake is about half the magnitude of the A2475 event in terms of peak acceleration, but is dissimilar in terms of frequency content. No negative spikes are apparent in the responses of the COSTA-E A475 earthquakes. These types of results show that these negative spikes, which have been attributed to dilative behaviour propagate deeper into the model with increased magnitude of earthquake shaking.
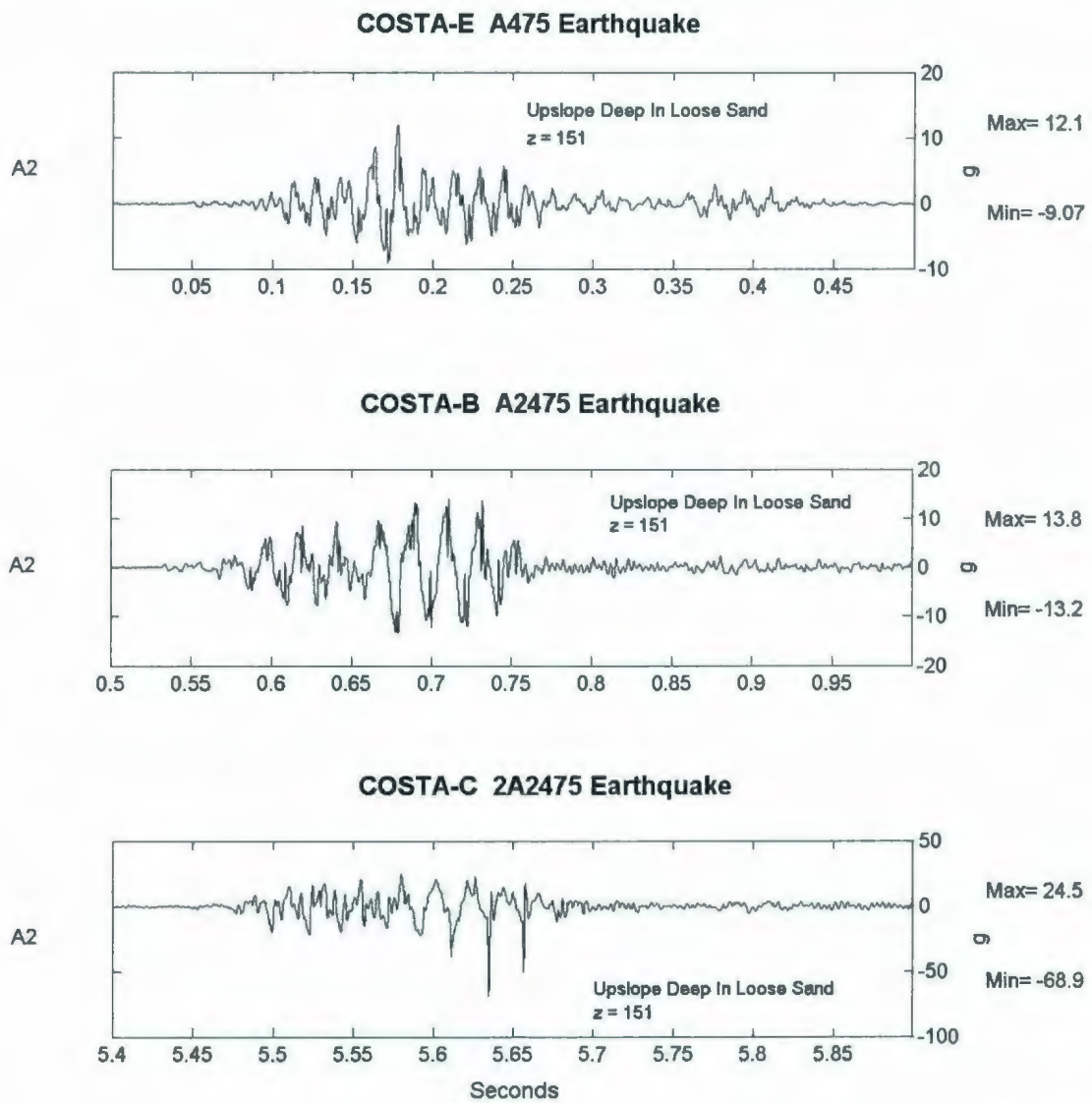
Figure 7.7: Comparison of Short-Term A2 Accelerometer Responses for COSTA-E
A475-1, COSTA-B A2475 & COSTA-C 2A2475.

In terms of a comparison of the short-term response of the PPTs it is evident that the
larger the earthquake in terms of peak acceleration, the higher the acceleration level the

357

greater excess pore pressure production and the higher frequency of response, which may however be related to the degree of saturation of the model. The COSTA-E A475 earthquake showed comparatively little PPT response as compared to the A2475 and 2A2475 earthquakes utilized in COSTA-B and COSTA-C respectively, especially above the silt layer where only a minor increase in pore pressure was recorded. This is in contrast to the responses in the larger quakes where some negative spiking was observed in conjunction with the negative spiking in the similarly placed accelerometers. Beneath the silt layer this dilative spiking is significantly more pronounced in the 2A2475 earthquake than it is in the A2475 earthquake, even though their maximum excess pore pressure level is similar, as shown in Figure 7.8.

COSTA-B A2475 Earthquake

P7

ru = 1.0 @ 124.2 kPa

Downslope of Midslope Under Silt Layer
z = 243

Max= 123

Min= 76.9

COSTA-C 2A2475 Earthquake

P7

ru = 1.0 @ 128.7 kPa

Downslope of Midslope Under Silt Layer
z = 243

Max= 122

Min= 29.7

Seconds
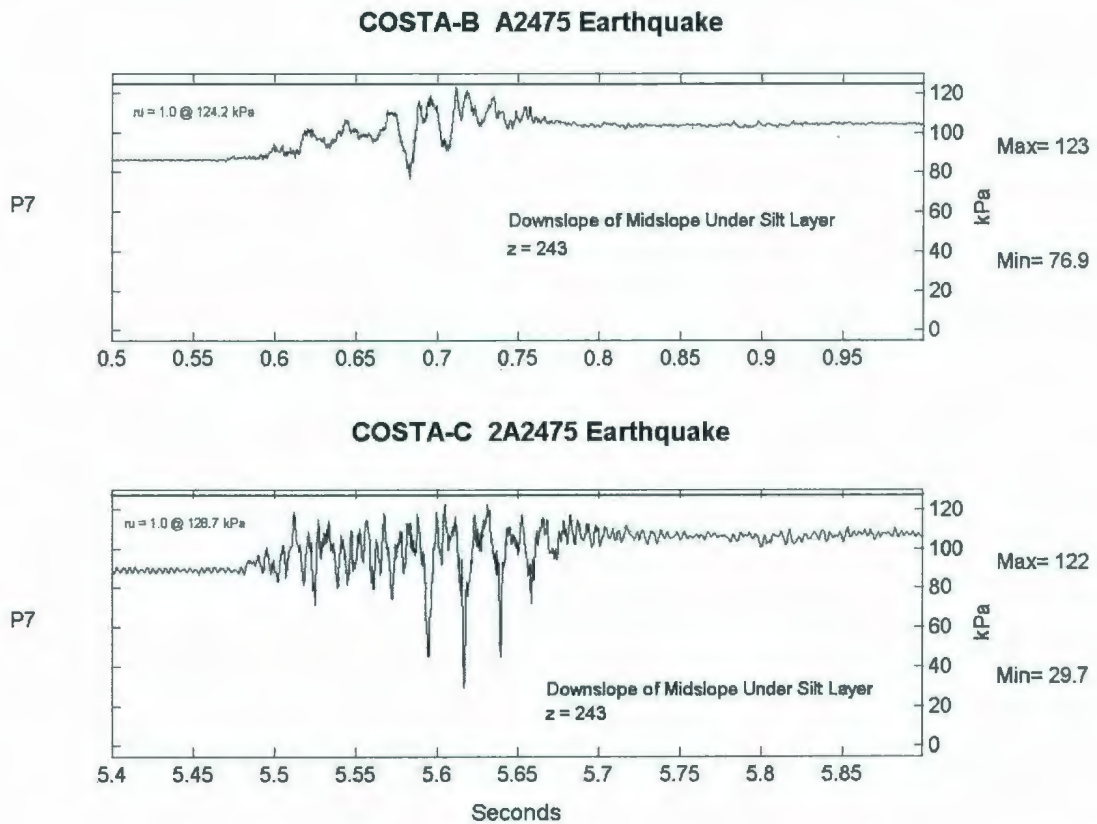
Figure 7.8: Comparison of Short-Term P7 PPT Responses for COSTA-B A2475 &
COSTA-C 2A2475.

Liquefaction is evident in upslope locations under the silt layer in both tests, but occurs
more readily in the model that experienced the larger earthquake, COSTA-C. Figure 7.9
illustrates how liquefaction occurs, with the r_u nearing a value of one, sooner in P4 in
COSTA-C and occurs totally in P5 in COSTA-C while it does not reach that level at all
in COSTA-B. Liquefaction also takes place in the deeper locations of the COSTA-C
model while excess pore pressure generation is rather tempered in comparison under
smaller earthquake loading in COSTA-B, as shown in Figure 7.10. These results suggest

359

a greater tendency for liquefaction at deeper locations, as well as at drainage boundaries, which include a relatively impermeable silt layer with increased shaking.

COSTA-B A2475 Earthquake
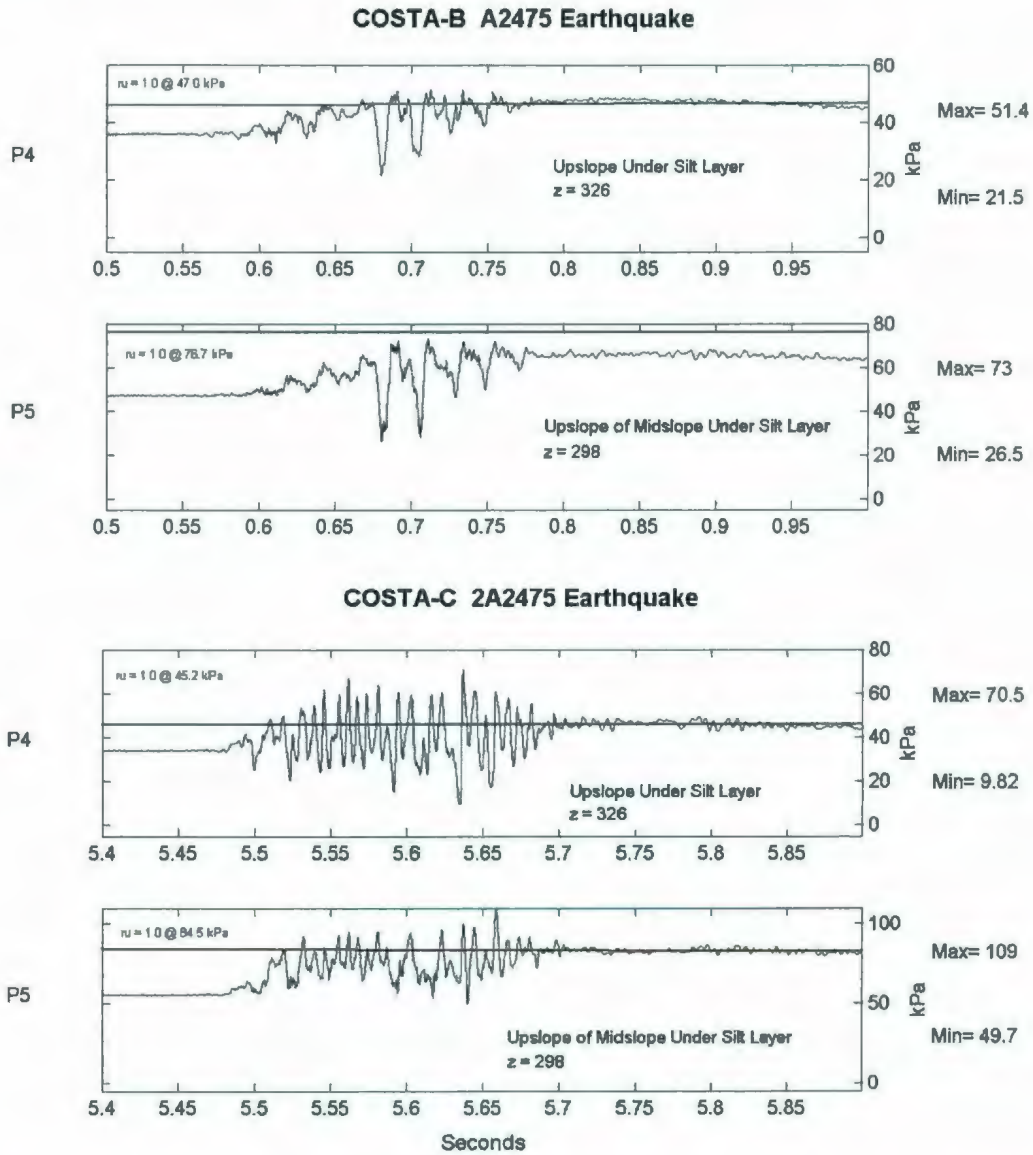
Figure 7.9: Comparison of Short-Term P4 & P5 PPT Responses for COSTA-B A2475 & COSTA-C 2A2475.

COSTA-B A2475 Earthquake

COSTA-C 2A2475 Earthquake
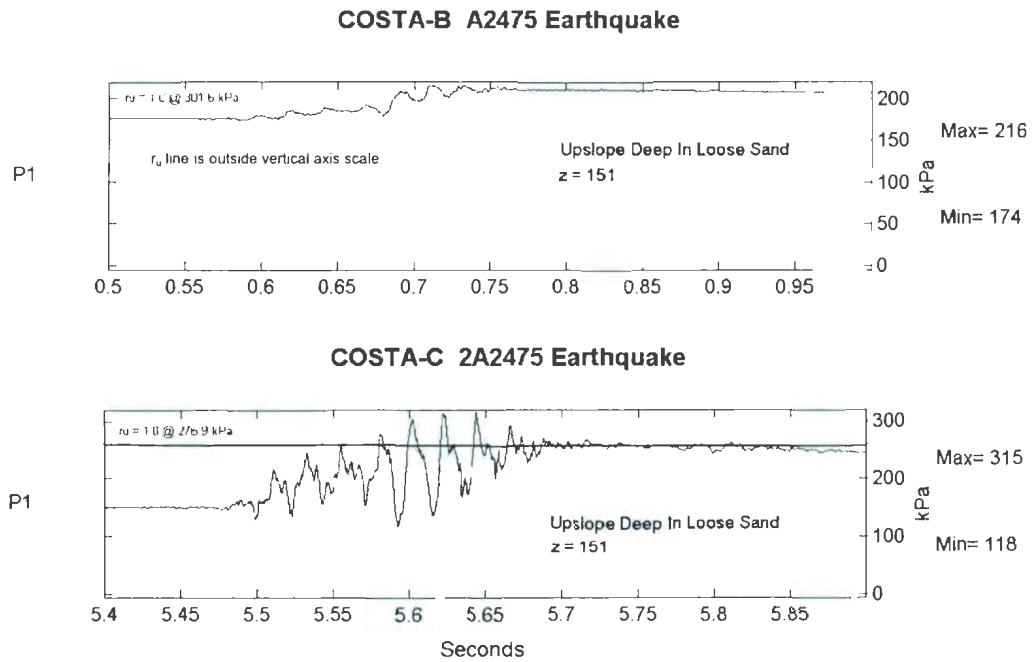
Figure 7.10: Comparison of Short-Term P1 PPT Responses for COSTA-B A2475 &
COSTA-C 2A2475.

Long-term PPT responses for both the COSTA-B A2475 and the COSTA-C 2A275 event
show the type of delayed pore pressure dissipation discussed in section 7.1, due to the
presence of the relatively impermeable silt layer.

The vertical LVDT displacements show settlement at both the farfield and crest locations,
as measured by L1 and L3 for both the 2A2475 earthquake events. Settlement was also
recorded in the COSTA-E A475-1 event, but no data was available for the farfield
location due to instrument malfunction. These results are tabulated in Table 7.1 for the
short-term observation periods. Also included in this table is the response of L4 for these

361

tests, which is placed on the slope face. This instrument experienced settlement in COSTA-B A2475 and COSTA-E A475-1, but experienced short-term heave in COSTA-C 2A475. The only other test in which short-term heave was experienced on the slope face was during the 2A2475 earthquake during the COSTA-B tests. These two tests, that featured heave on the slope face, were also the two tests where slope failure was observed from horizontal LVDT data and from post-observation tests. For this reason, short-term slope face heave can be correlated to eventual slope failure. The table shows that the settlement responses are increasingly larger for all locations with increased earthquake shaking magnitude, the only exception being with respect to the heave experienced in COSTA-C, which is most likely larger than measured, due to the burying of the LVDT pad.

Table 7.1: Summary of Vertical LVDT Responses in COSTA-E A475-1, COSTA-B A2475 & COSTA-C-2A2475.

Test	Earthquake	Instrument	Location	Response (mm)
COSTA-E	A475	L3	Crest	-1.8
		L4	Midslope	-0.2
COSTA-B	A2475	L1	Farfield	-1.8
		L3	Crest	-4.1
		L4	Midslope	-0.6
COSTA-C	2A2475	L1	Farfield	-4.5
		L3	Crest	-9.4
		L4	Midslope	>4.6

The only significant long-term observed response in the LVDTs, both horizontal and vertical, is in the COSTA-C 2A2475 earthquake as discussed previously in section 7.2 where there was observed delayed horizontal slope movement.

7.3 Effect of Multiple Earthquakes

The final type of comparison that can be made is regarding the effect of multiple earthquakes to the model geometry featuring a buried 5.5:1 sloped relatively impermeable silt layer. This can be accomplished by comparing and analyzing the results of COSTA-C test, test where the model experienced the 2A2475 earthquake event only, against the results obtained from the COSTA-E test where the model was pre-conditioned with five small A475 earthquake events before being exposed to the same 2A2475 earthquake event used in COSTA-C.

The contention of Lee et al. (2004) is that in submarine areas of large seismicity around the margins of the United States there seems to be an almost inverse relation to landslide occurrence. It has been postulated that seabed sediments in these areas become unusually strong due to the process termed "seismic strengthening". Due to the high seismicity of these areas, they are exposed to several low intensity earthquakes and with each passing of these earthquakes the excess pore pressure is increased, as experienced in all tests in this research. If these sediments do not fail immediately, the pore pressures will dissipate and the sediment will densify creating increased strength. The COSTA-E test was specifically configured to verify and examine this type of effect.

As previously discussed, in both Chapters 6 and 7, the results obtained during the progression of the application of the five smaller A475 earthquakes in the COSTA-E test had several notable characteristics. The observed acceleration records for all locations in

the model remain similar throughout each of the earthquakes, both in the short- and long-term observation periods. The acceleration records also posses the characteristic mode and frequency of the A475 input record shown in Figure 5.17. This would show that the A475 earthquake is not strong enough to induce any sort of movement from the generation and subsequent migration of excess pore pressure at any elevation of the model. The PPT responses show modest excess pore pressure generation, be it deep in the model, underneath the silt layer, or above the silt layer. With each successive A475 earthquake the maximum level of this pore pressure generation is observed to decrease. Figure 7.11 shows this pore pressure response for each consecutive earthquake for P6, which is situated at midslope beneath the silt layer. The maximum observed pore pressure decreases from 112 kPa in A475-1 to 90 kPa in A475-2. The reduced observed excess pore pressure with each passing earthquake is evidence that the sand is densifying and thus building resistance to failure. The long-term responses of pore pressure show full dissipation above the silt layer. Some small amount of excess pore pressure is still present below the silt layer and deep in the model, but this was allowed to fully dissipate by pausing for a period of one minute or more before applying the next earthquake.

COSTA-E A475-1 Earthquake

P6

ru = 1 0 @ 145.1 kPa

r_u line is outside vertical axis scale

Midslope Under Silt Layer
z = 250

Max= 112

Min= 83.2

100

50

0

kPa

0.05 0.1 0.15 0.2 0.25 0.3 0.35 0.4 0.45

COSTA-E A475-2 Earthquake

P6

ru = 1 0 @ 145.2 kPa

r_u line is outside vertical axis scale

Midslope Under Silt Layer
z = 250

Max= 104

Min= 83.8

100

50

0

kPa

0.05 0.1 0.15 0.2 0.25 0.3 0.35 0.4 0.45

COSTA-E A475-3 Earthquake

P6

ru = 1 0 @ 145.3 kPa

r_u line is outside vertical axis scale

Midslope Under Silt Layer
z = 250

Max= 97.5

Min= 83.5

100

50

0

kPa

0.05 0.1 0.15 0.2 0.25 0.3 0.35 0.4 0.45

COSTA-E A475-4 Earthquake

P6

ru = 1.0 @ 145.4 kPa

r_u line is outside vertical axis scale

Midslope Under Silt Layer
z = 250

Max= 93

Min= 82.6

100

50

0

kPa

0.05 0.1 0.15 0.2 0.25 0.3 0.35 0.4 0.45

COSTA-E A475-5 Earthquake

P6

ru = 1 0 @ 145.2 kPa

r_u line is outside vertical axis scale

Midslope Under Silt Layer
z = 250

Max= 90.2

Min= 81.7

100

50

0

kPa

0.05 0.1 0.15 0.2 0.25 0.3 0.35 0.4 0.45

Seconds

Figure 7.11: Progression of Pore Pressure Generation in COSTA-E A475 Earthquakes.

Settlement was observed in each of these five smaller earthquakes on both the slope face and at the slope crest. This settlement occurred almost exclusively during and immediately following the earthquake shaking. No significant delayed post-shake vertical movement was observed for any of the five A475 earthquakes. The relative density of the model can be estimated for each phase of the test using the crest settlement data, as well as the spin-up and pre-test observation data. The relative density increases from 49% before the earthquake to 57% after the fifth A475 earthquake. This confirms the densification effect discussed by Lee et al. (2004).

Table 7.2: Relative Density at Slope Crest Observed after COSTA-E A475 Earthquakes.

Condition	Settlement (mm)	Relative Density (%)
Post-Construction	N/A	34
Pre-Test	5.0	43
After Spin-Up	3.0	49
After A475-1	1.8	52
After A475-2	1.2	54
After A475-3	0.8	55
After A475-4	0.5	56
After A475-5	0.3	57

The negative dilative response of the accelerometers in the upslope direction that has been observed in this research is evident in both the COSTA-C and COSTA-E 2A2475 earthquakes. In post-test observations of the failure observed on COSTA-C occurred as the silt layer moved downslope due to the prolonged presence of excess generated pore pressure underneath the impermeable layer. A comparison of the short-term accelerometer responses above the silt layer between COSTA-C and COSTA-E for the larger earthquake shows that the negative spikes are more significant in the model that

366

has experienced previous earthquake loading. Figure 7.12 illustrates a comparison of these responses for the two tests for A8 and A9. These stronger upslope spikes in the model that experienced smaller previous earthquakes indicates that there is a reduction in permanent lateral displacement as compared to the model that did not receive any "seismic strengthening."
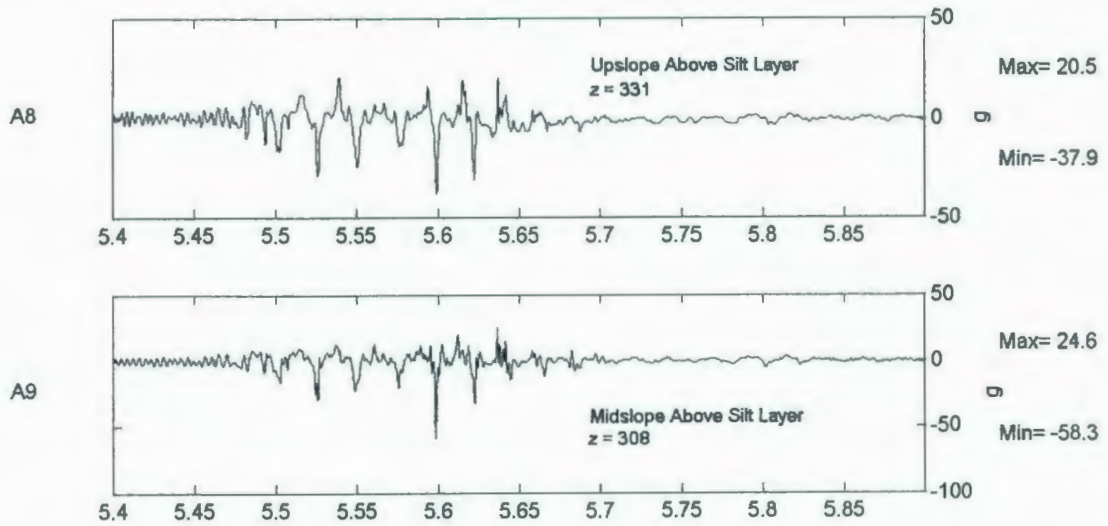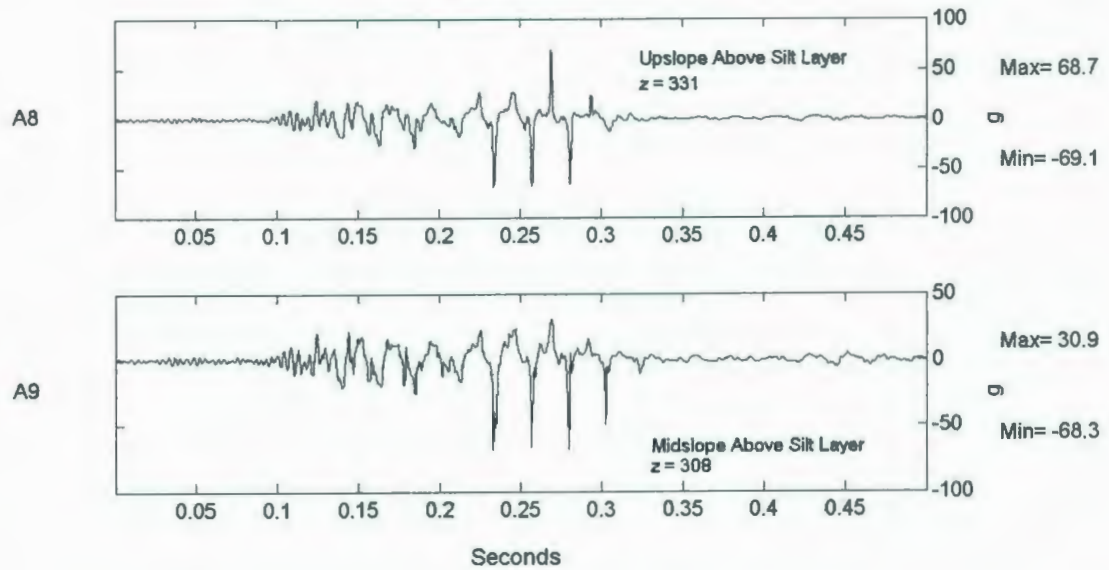
Figure 7.12: Comparison of Short-Term A8 & A9 Accelerometer Responses for COSTA-C 2A2475 & COSTA-E 2A2475.

Underneath the silt layer excess pore pressure generation is typically less in the COSTA-E 2A2475 earthquake than it was in the COSTA-C 2A2475 earthquake. This is due to the densification that occurred during the exposure to the previous small earthquakes. However, there is a noticeable effect of more significant dilative behaviour under the silt layer in the COSTA-E model, further serving to restrict significant horizontal movement. Figure 7.13 exemplifies this response for P5, where peak pore pressure levels are higher in the non-preconditioned model but the negative spikes are larger in the preconditioned model.
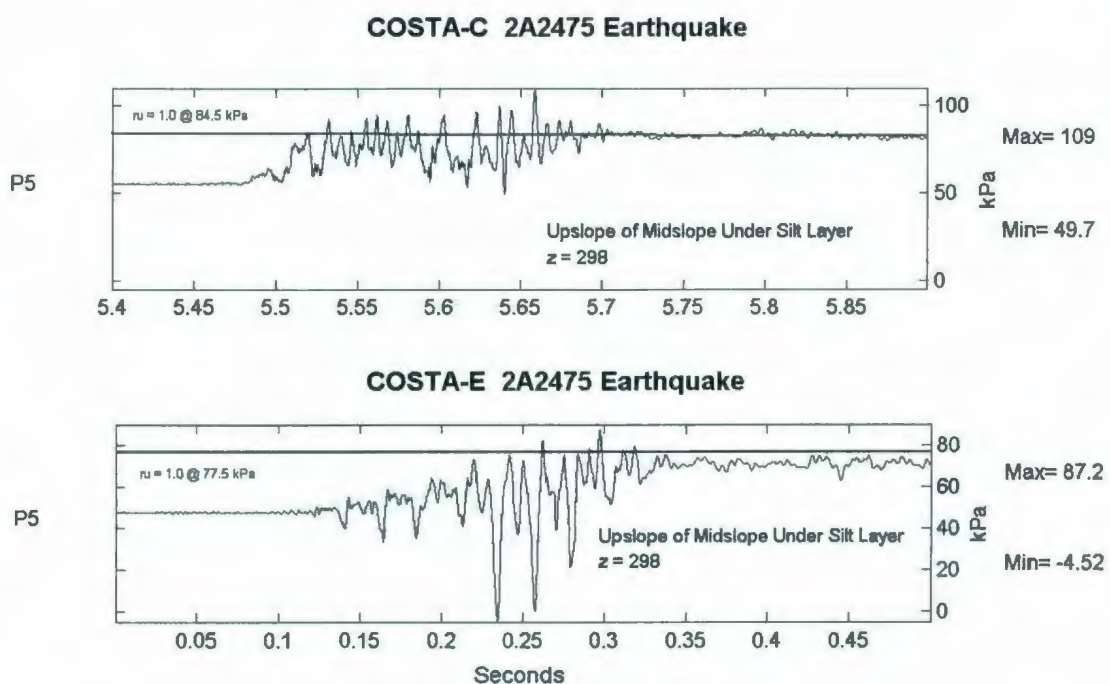
Figure 7.13: Comparison of Short-Term P5 PPT Responses for COSTA-C 2A2475 & COSTA-E 2A2475.

369

Unfortunately, no comparison of horizontal slope movement between these two models is possible, due to the malfunction of L2 during the COSTA-E test. However, there is a notable difference in the response of L4 between the two models. The short-term response of this instrument, which measures the vertical displacement of the surface of the model on the slope face, indicated 4.6 mm of heave in the COSTA-C test as compared to 2.3 mm of settlement in the COSTA-E test. The difference in vertical response is most likely attributable to the increased resistance to failure from densification and subsequent increased dilation effects. Figure 7.14 presents these L4 responses.

COSTA-C 2A2575 Earthquake

COSTA-E 2A2475 Earthquake
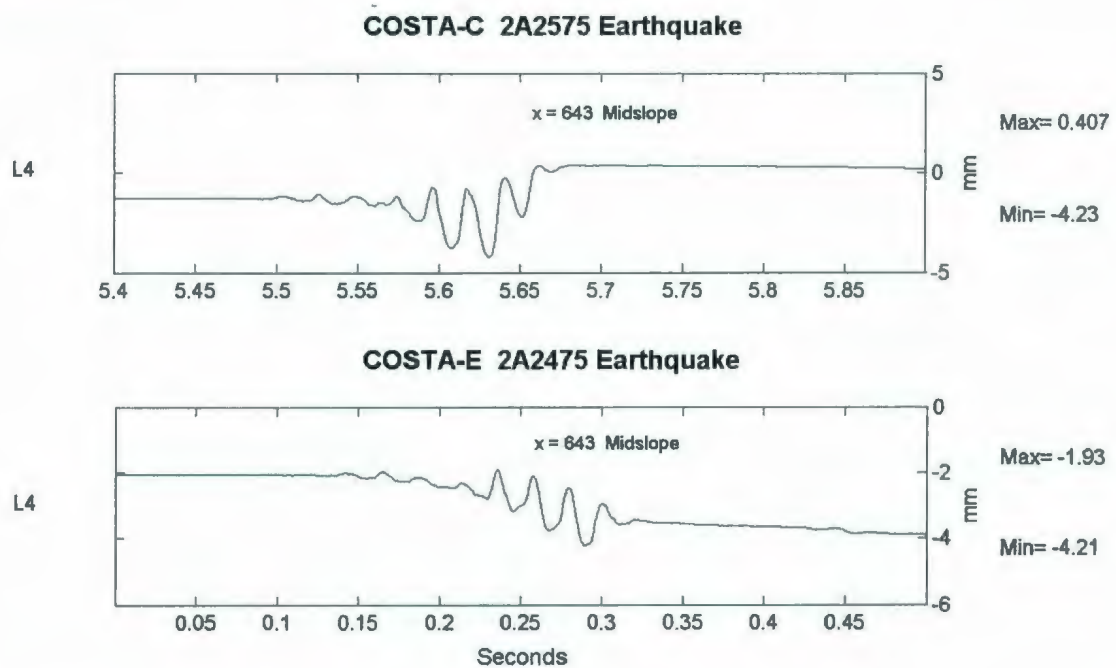
Figure 7.14: Comparison of Short-Term L4 Vertical LVDT Deformation in COSTA-C 2A2475 & COSTA-E 2A2475.

370

In terms of long-term pore pressure dissipation, the response of the two tests is similar, with delayed pore pressure dissipation occurring following the 2A2475 earthquakes in both the COSTA-C and COSTA-E tests. Nevertheless, with less excess pore pressure being generated in the COSTA-E test, this delayed dissipation has less of an impact on the stability of the slope.

No long-term vertical deformations were detected in COSTA-E for the two instruments that were functioning, L3 & L4. This is in contrast to the observed response for the COSTA-D 2A2475 earthquake, where some crest movement was detected in the two seconds following the cessation of the earthquake as displayed in Figure 7.15 below.

COSTA-C 2A2475 Earthquake

COSTA-E 2A2475 Earthquake
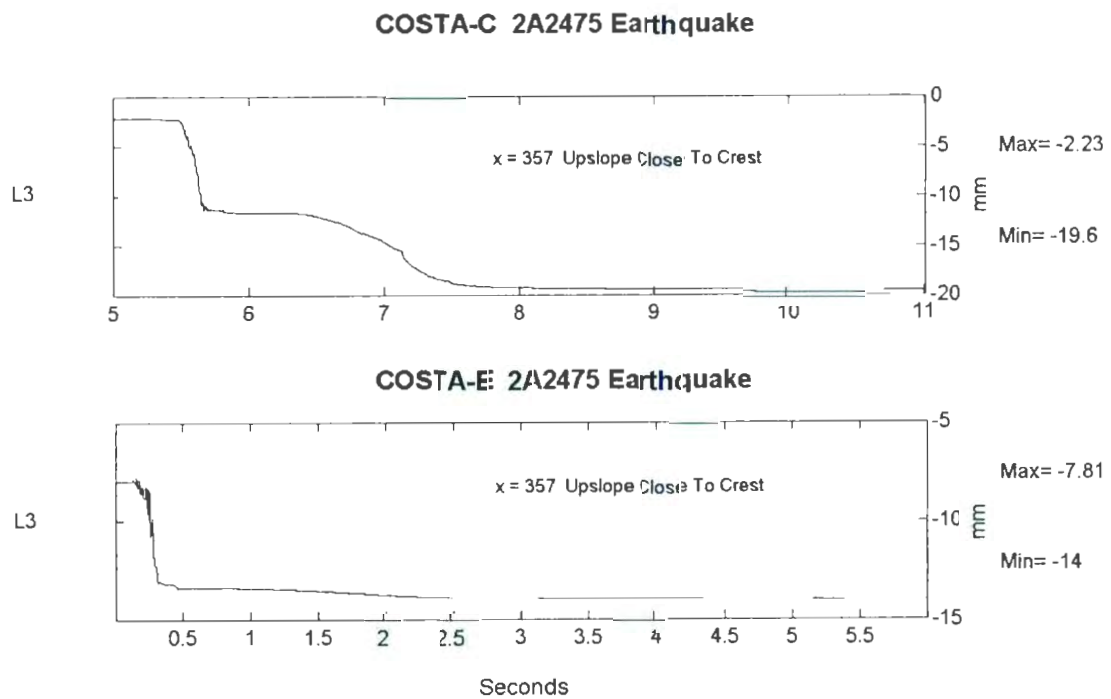
Figure 7.15: Comparison of Long-Term L3 Vertical LVDT Deformation in COSTA-C 2A2475 & COSTA-E 2A2475.

7.4 Comparison of Results to FEA Analyses

As mentioned at the beginning of Chapter 5 one of the purposes of this research was to compare the results of the centrifuge testing to finite element analyses. The full scale comparison of these two analytical methods, physical versus numerical, is beyond the scope of this research but is fully investigated by the doctoral research of Earthquake Induced Damage Mitigation from Soil Liquefaction Project that is being completed jointly by researchers at the University of British Columbia and the Memorial University of Newfoundland.

However, it is possible to take a brief look at how these analyses compare. For comparison purposes, the COSTA-D homogeneous sand centrifuge test was identical to the CT6 test undertaken in the above mentioned project. Before this test was completed, Naesgaard et al. (2005) presented a Class A Prediction of the testing results completed using the software program FLAC and the UBCSAND constitutive effective stress model.

The short-term predicted responses of accelerometers A1 through A10, pore pressure transducers P1 through P9, and displacement transducers L1 through L5 are shown below in Figures 7.15, 7.16, and 7.17 respectively. It should be noted that displacements and accelerations, as well as time are shown in prototype scale. These results can be directly

372

compared to the results presented in Section 6.4.3 in order to understand the relationship

between a finite element analysis prediction and a centrifuge model test.
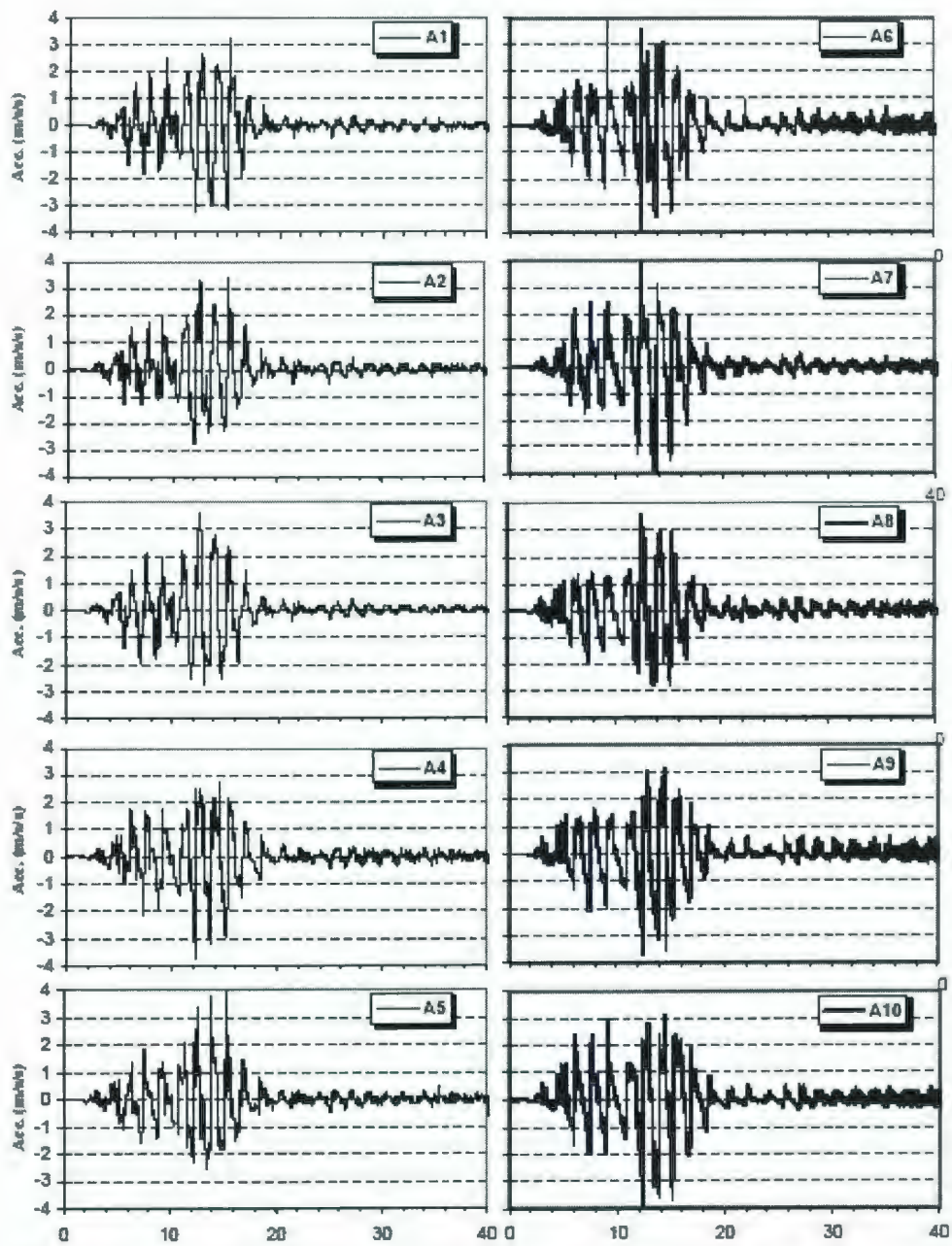
Figure 7.16: CT6/COSTA-D Predicted Accelerometer Responses.
After Naesgaard et al. (2005).

374
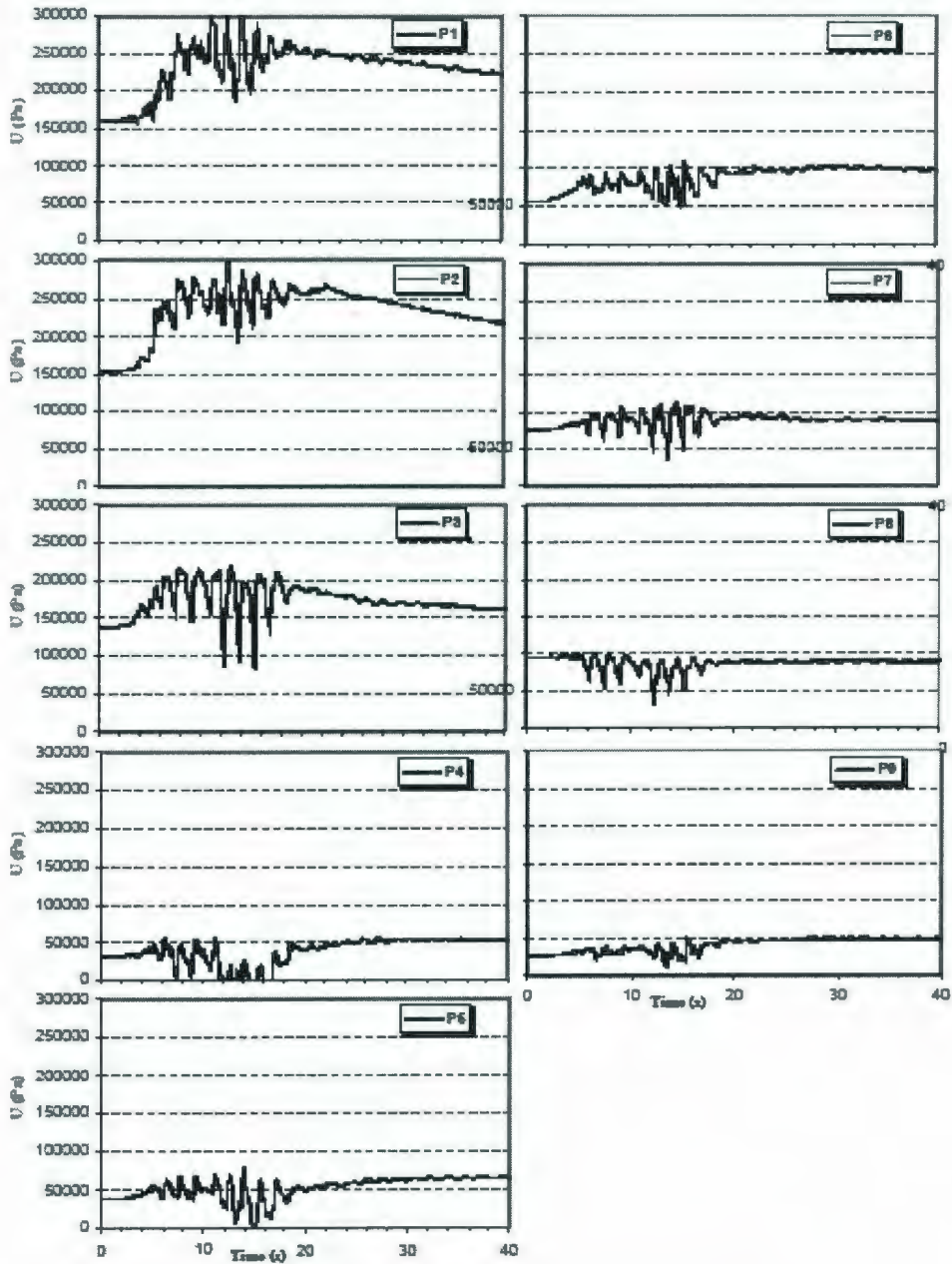
Figure 7.17: CT6/COSTA-D Predicted PPT Responses.
After Naesgaard et al. (2005).
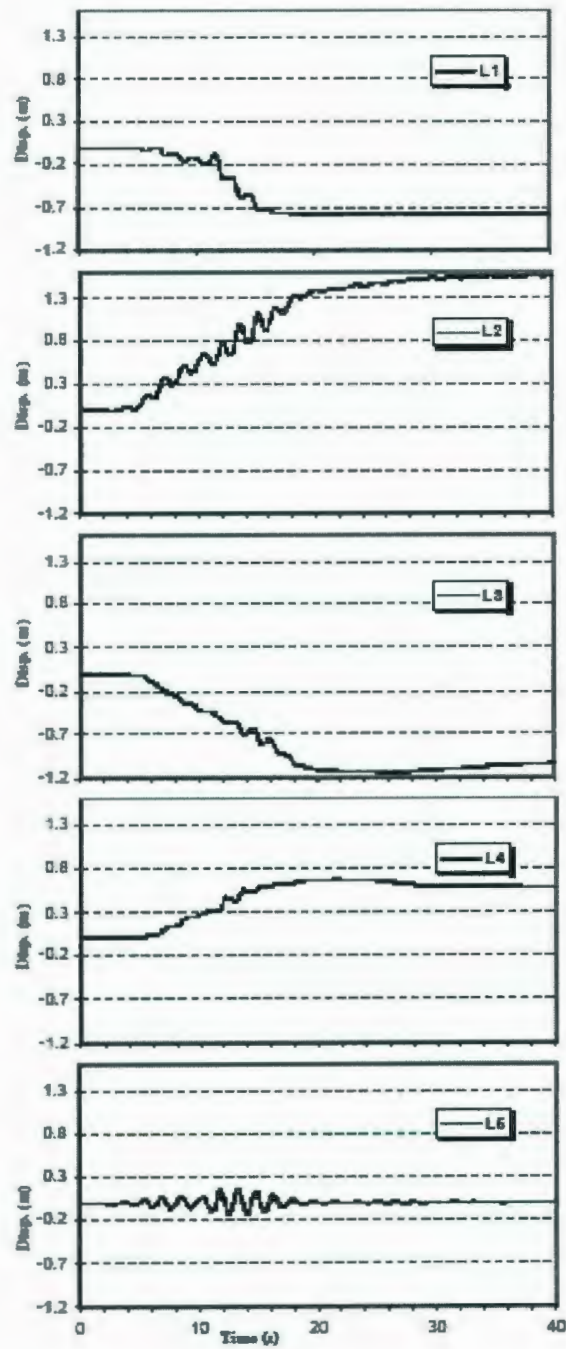
Figure 7.18: CT6/COSTA-D Predicted Displacement Transducer Responses. After Naesgaard et al. (2005).

376

In terms of acceleration response, there is not a great deal of agreement between the predicted movements shown in Figure 7.15 and the observed responses shown in Figures 6.77 and 6.78. Almost all of the predicted responses show an identical response in terms of mode, but with increased acceleration magnitude closer to the surface of the model. However, this is not the case in the observed responses, where the instruments show negative acceleration tendencies, which is most pronounced towards the surface of the model. The prescribed base motion was matched fairly well by the EQS, as shown in Figure 6.75, so there is not enough a discrepancy to explain these differences.

The PPT response shown in Figure 7.16, however, shows some interesting similarities. The deeper PPTs, P1 through P3 match well for magnitude of generated excess pore pressure and match the trend shown in the experiments, in Figure 6.79, of prolonged delayed pore pressure generation following the earthquake event. The upslope PPTs, that would be situated under the silt layer in other tests, also match well for the magnitude of excess generated pore pressure and show prolonged elevated pore pressure, as the instrument responses show in Figures 6.79 and 6.80. P4 matches well with the prediction, but higher levels of post-test sustained excess pore pressure existed in the model test at the P5 and P6 locations than in the predictions. Downslope and near surface PPTs, P7 through P9 also matched the predictions well in the sense that they showed little to no post-test elevated pore pressure reading as compared to the pre-test static levels.

In terms of displacement transducers, only L2, L4, and L5 functioned properly, as shown in Figure 6.81, limiting the amount of comparison to the predicted responses. The in-slope horizontal displacement transducer, L2, was predicted to move approximately 1.5 m in prototype scale, while in the model this movement was measured to be approximately 0.1 mm in model scale, or 0.007 m in prototype scale, far less than predicted. In the test, L4 showed approximately 5 mm of midslope settlement in model scale, which is completely contrary to the predicted heave. However, the movement of L5, which tracks the horizontal movement of the model itself, matched the predictions well.

The comparison of finite element analysis predictions to the observed experimental results show that some instruments responded as predicted and others did not, in the case of the COSTA-D test. Pore pressure responses matched well, while observed acceleration throughout the model showed a phenomenon of negative spiking that was not predicted. There could be several reasons for these discrepancies, not the least of which would be the full understanding of how the physical boundary conditions of the centrifuge modelling container affect the observed results. A full comparison of numerical modelling methods and physical modelling methods would be available in the results and reports of the Earthquake Induced Damage Mitigation from Soil Liquefaction Project.

7.5 Comparison to Other Work

The results of this work indicate the observation of similar phenomenon investigated by other researchers, both in the areas of the effect of saturation, the seismic behaviour of layered saturated soils, as well as with regard to the effects of seismic strengthening.

Mehrabadi (2006) discusses the effects of incomplete saturation on these types of centrifuge models. Since the degree of saturation was unknown in the experiments conducted in this research it is important to realize the impact this may have upon the results. Mehrabadi (2006) notes a good agreement between the numerical results obtained assuming perfect saturation and their experimental counterparts, supporting the conclusion that the centrifuge models were well saturated. The models used by Mehrabadi (2006) were prepared and constructed in an identical way under identical conditions in the same facility as the centrifuge tests discussed in the chapters above. These results would seem to indicate that the COSTA-Canada centrifuge results were adequately saturated, despite direct experimental evidence supporting this conclusion.

As stated by Kokusho (2003), it was found that sand deposits of different permeability are prone to develop post-liquefaction void distribution, stable water films, or transient turbulence, at sublayer boundaries, which may serve as a sliding surface in flow failure even after the end of earthquake shaking. This is the same type of movement found in both the COSTA-B and COSTA-C tests. If this movement is observed in sand deposits with sublayers of differing permeabilities, it would serve to reason that the same effect

could be extended to a silt layer embedded in a sand deposit, but with more pronounced effects, as observed in this work with noticeable downslope movement. Additionally, it was found by Kokusho (2003) that this water film mechanism can facilitate large flow displacements without mobilization of liquefaction dilatancy. This is because the developed water film serves as a shear stress isolator, but in a uniform sand deposit, such as in COSTA-D, flow displacement would only occur because of dilatancy. Kokusho and Kojima (2002) further state that these water films are easily formed beneath a sandwiched less permeable layer in a short time period, but a simple two-layer system, will not result in a stable water film but only a short-lived turbulence at the layer boundary. However, a three-layer system, such as presented here in the COSTA tests, with a sandwiched middle layer of finer soil can generate a stable water film beneath the middle layer. The results observed in the COSTA tests where movement was observed seem to fit this mechanism, a stable build up of pore pressure beneath the silt layer creating flow displacement not only owed to the dilatancy of the soil itself.

Malvick et al. (2002) and Kulasingam et al. (2004) have also found a number of factors that can influence the amount of void redistribution of water film generation, including: relative density, seismic event duration, volume of sand below lower permeability layer, shaking sequence, permeability contrast of the soils, maximum excess pore pressure ratio developed during shaking, slope geometry, and soil stratigraphy; some of which have been investigated in this research. These include, permeability contrast of the soils as analyzed in Section 7.1, seismic event duration or magnitude as discussed in Section 7.2,

380

and finally shaking sequence as presented in Section 7.3. This research appears to further confirm the work of these researchers with respect to these variables.

The seismic strengthening effects mentioned in Section 7.3 also seem to expand upon the ideas of past research, specifically that of Lee et al. (2004) where a real-life natural situation is discussed where an unfailed slope lies between two large slope failures in the seabed off the coast of California. It is suggested that this unfailed slope has survived failure due to the process of seismic strengthening, increasing the sediment's excess pore pressure with each passing earthquake then allowing the sediment to densify as pore pressure increases if failure does not occur. Laboratory simulations by Lee et al. (2004) serve to confirm this hypothesis.

8 CONCLUSIONS & RECOMMENDATIONS

8.1 Conclusions

According to the results obtained from the centrifuge modelling of the seismic initiation of the instability of submarine slopes, the following conclusions can be drawn:

(1) Submarine slope centrifuge models have been successfully constructed at the C-CORE Centrifuge Centre. Construction and saturation methods have been refined and improved with each successive test to ensure minimal disturbance and subsequent negative effect on the obtained relative density of the model sand during model preparation.

(2) The C-CORE EQS has been proven to reasonably reproduce the given earthquake motions on a model scale in a reliable fashion. This reproduction is done with respect to peak acceleration levels, signal frequency, and the experienced acceleration in instruments placed close to the bottom of the model.

(3) No significant frictional sidewall effects were observed. This was determined through the placement of a gravel marker grid upon the face of the slope. The minimization of these effects was accomplished with the application of petroleum jelly as well as very fine sand at the interface of the silt layer with the sidewall boundaries.

(4) Slope failure was only observed in models exposed to the 2A2475 earthquake motion. This was only evident in the COSTA-B & COSTA-C tests, where slope

movements were detected in post-test observations as well as in the responses of testing instruments.

(5) Test results showed that excess pore pressure and subsequent liquefaction occurred first in downslope and deeper areas and progressed upslope and upwards to the drainage boundary at the most upslope area of the model. This was experienced in models that included a silt layer as well as for the model that did not contain a silt layer.

(6) The presence of a silt layer impeded long-term dissipation of generated excess pore pressures as compared to models that did not posses a silt layer configuration. This delayed pore pressure generation was observed to be a contributing factor in models where failure was achieved. In addition, pore pressure transducers that were placed above the silt layer also experienced more rapid dissipation.

(7) A dilative response, characterized by large upslope (negative) spikes in the accelerometer records coupled with negative spikes in pore pressure were induced by the exposure of the models to the A2475 and 2A2475 earthquake signals. This dilative behaviour serves to reduce permanent lateral displacements.

(8) A small amount of short-term surface heave was observed on the slope face of models that were observed to have failed. This heaving was typically followed by long-term settlement.

(9) Movement of the slope, both horizontally and vertically, was detected after the cessation of the earthquake following shaking in the COSTA-B and COSTA-C tests. This was detected using LVDTs to measure these movements.

(10) In the tests in which failure was observed, COSTA-B and COSTA-C, post-test observations revealed that the silt layer slid down the underlying sand slope acting as one single unit. No breakage of the silt layer was observed to have taken place. When this happened, the silt layer slid until its movement was impeded by the downslope endwall of the model container where the silt proceeded to accumulate. This movement was most likely caused by the prolonged presence of the excess pore pressure under the silt layer, as compared to the lack of failure in COSTA-A where the overlying sand provided an overriding driving force

(11) The dilative response and upslope migration of excess pore pressures was observed with or without the presence of a relatively permeable silt layer.

(12) The tendency towards stronger negative acceleration spikes was observed to increase with increased elevation in the model.

(13) Larger earthquake magnitude, in terms of peak acceleration levels, induces the propagation of dilative behaviour to greater depths in the sand layer beneath the impermeable silt layer. Increased earthquake magnitude was also observed to have created increased excess pore pressure generation during the earthquake shaking as well as increased vertical surface settlement, except when failure occurred and the short-term heaving was observed.

(14) Liquefaction was found to occur more readily in larger earthquake motions both at deeper locations in the model as well as at drainage boundaries.

(15) Densification and seismic strengthening of the model was experienced with the exposure to a series of smaller seismic motions. This was concluded from surface

settlement data as well as the decreased excess pore pressure generation that was caused in each successive smaller earthquake. No failure was observed in the model that had been exposed to this series of smaller earthquakes, either during the application of the series of small A475 earthquakes or during the subsequent application of the larger more significant 2A2475 earthquake.

(16) A larger dilative response was observed in the seismically strengthened model during the application of the large 2A2475 earthquake. Since this dilation has been found to lead to indicate failure resistance in the model, this response is logical with the conclusion that the densification leads to strengthening of the slope.

(17) The increase in failure resistance caused by the dilative response was overcome by the delayed dissipation of the generated excess pore pressure underneath the silt layer. Failure was then characterized by long-term slope movements, short-term slope face surface heave, and the evidence of silt layer movement in post-test observations.

8.2 Recommendations

In this research, centrifuge tests were carried out to investigate the behaviour of submarine slopes under seismic loading. Good data and results have been obtained throughout this program. According to the results and experience obtained in this research, it is recommended that future research on the seismic initiation of submarine instability should be concentrated on the following aspects:

(1) Further investigation should be undertaken to further characterize the influence of seismic strengthening. One such area would be to determine the threshold earthquake magnitude whereby significant instability occurs instead of strengthening effects.

(2) Centrifuge tests may be carried out to determine the effect of the depth of the silt layer and conversely the thickness of the deep sand below the relatively impermeable silt layer. It has been discussed during this research that the thickness of the sand beneath the impermeable layer may have an effect on the magnitude of the generated excess pore pressure.

(3) Additionally, centrifuge tests may be carried out to determine the behaviour of a stratified soil geometry consisting of various "permeable" and "impermeable" layers. This type of testing would have a similar effect to the centrifuge testing regime suggested above. A layered profile would feature thinner sand layers and would produce results also indicating the effects of less sand material below a relatively impermeable layer. The stratified profile would also possibly give results that further characterize the nature of these types of failures by offering some sort of correlation between the level of excess pore pressure and slope movement.

(4) Further work should be carried out to minimize boundary effects caused by the modeling limitations themselves, as drainage boundaries and seismic reflections can cause effects on the observed effects.

In addition to the above testing recommendations, further suggestions can be made in general with respect to the seismic centrifuge testing of submarine slopes:

(1) The EQS at C-CORE, while providing reasonably reliable and well produced earthquake signals for this research, should continue to be refined and advanced to provide more reliable and greatly replicated earthquake motions within its designed performance envelope.

(2) A system should be developed to more accurately characterize the degree of saturation of the model immediately prior to the earthquake actuation. This is especially important since the stability of submarine slopes has been shown to be especially sensitive to the degree of saturation. This can most likely be utilized using the characteristics of acoustic waves by apply them to and observing there response in the model, as previously discussed in the available literature. Basic observations using this type of system are presented in this thesis, but the full development of this system is beyond the scope of this research.

(3) Further work should be performed to develop saturation procedures that ensure a greater degree of saturation with a substitute pore fluid that more accurately reflects prototype conditions, even though this work is more idealized in nature. Better saturation can perhaps be achieved through the application of greater vacuum pressure during the saturation process.

REFERENCES

Anadarajah, A. and Bardet, J.P. (1993). "Comparison of Numerical Predictions and Experimental Observations for Model 7." *VELACS*, Davis, USA, pp.1571-1582.

Andersen, A. and Bjerrum, L. (1967). "Slides in Subaqueous Slopes in Loose Sand and Silt." *Marine Geotechnique.* Urbana, USA, pp. 221-239.

Arulanandan, K., Canclini, J., and Anadarajah, A. (1982). "Simulations of Earthquake Motions in the Centrifuge." *J. Geotech. Eng. Div.,* ASCE, Vol. 114, pp. 1442-1449.

Arulanandan, K., Manzari, M., Zeng, X., Fagan, M., Scott, R.F., and Tan, T.S. (1994) "What the VELACS Project Has Revealed." *Centrifuge 94, Singapore,* pp. 25-32.

Arulanadan, K., Yogachandran, C., Muraleetharan, K.K., Kutter, B.L., and Chang, G.S. (1988). "Seismically Induced Flow Slide on Centrifuge." *J. Geotech. Eng.,* ASCE, Vol. 114, No. 12, pp. 1442-1449.

Arulanandan, K. and Zeng, X. (1993). "Mechanism of Flow Slide – Experimental Results of Model No. 6." *VELACS*, Davis, USA, pp.1543-1551.

Astaneh, S.M.F. (1993). *Effects of Earthquake on Saturated Soil Embankments.* Ph.D. Thesis, University of Colorado, Boulder, USA.

Astaneh, S.M.F., Ko, H.Y., and Sture, S. (1994). "Assessment of Earthquake Effects on Soil Embankments." *Centrifuge 94*, Singapore, pp. 221-226.

Atkinson, J.H. (1981). *Foundations and Slopes.* McGraw-Hill, London, UK.

Aubry, D., Benzenati, I., and Modaressi, A. (1993). "Overview of Model No. 2 for VELACS Project." *VELACS*, Davis, USA, pp.1383-1400.

Azizian, A. and Popescu, R. (2001). "Backanalysis of the 1929 Grand Banks Submarine Slope Failure." *Proc. 54th Can. Geotech. Conf.,* Calgary, Canada, pp. 808-815.

Azizian, A. and Popescu, R. (2003). "Finite Element Simulation of Retrogressive Failure of Submarine Slopes." *1st Int. Symp. Submarine Mass Movements and Their Consequences,* Kluwer Acadmeic, Dordrecht, Netherlands, pp. 11-20.

388

Batterson, M., Liverman, D.G.E., Ryan, J., and Taylor, D. (1999). "The Assessment of Geological Hazards and Disasters in Newfoundland: An Update." *Geological Survey Report 99-1*, Newfoundland Department of Mines and Energy.

Been, K., Conlin, B.H., Crooks, J.H.A., Fitzpatrick, S.W., Jefferies, M.G., Rogers, B.T., and Shinde, S. (1987). "Discussion: Back Analysis of the Nerlerk Berm Liquefaction Analysis." *Can. Geotech. J.*, Vol. 24, pp. 170-179

Been, K. and Jefferies, M.G. (1985). "A State Parameter for Sands." *Geotechnique*, Vol. 35, No. 2, pp. 99-112.

Bennett, R.H., Burns, J.T., Clarke, T.L., Faris, J.R., Forde, E.B., and Richards, A.F. (1980). "Piezometer Probes for Assessing Effective Stress and Stability in Submarine Sediments." *NATO Workshop on Marine Slides and Other Mass Movements*, Algarve, Portugal, pp. 129-161.

Bishop, A.W. (1955). "The Use of the Slip Circle in the Stability Analysis of Slopes." *Geotechnique*, Vol. 5, No. 1, pp. 7-17.

Bjerrum, L. (1971). "Subaqueous Slope Failures in Norwegian Fjords." *Norwegian Goetechnical Institute Publication No. 88.*

Boulanger, E., Konrad, J.M., Locat, J., and Lee, H. (1998). "Cyclic Behaviour of Eel River Margin Sediments: A Possible Explanation for the Paucity of Submarine Landslide Features." *Proc. AGU 1998 Fall Meeting, EOS Abstracts.*

Brennan, A.J. and Madabhushi, S.P.G. (2002). "Design and Performance of a New Deep Model Container for Dynamic Centrifuge Testing." *ICPMG 02*, St. John's, Canada, pp. 183-188.

Bugge, K., Befring, S., Belderson, R.H., Eidvin, T., Jansen, E., Kenyon, N.H., Holtedahl, H., and Sejrup, H.P. (1987). "A Giant Three-stage Submarine Slide off Norway." *Geo-Marine Letters*, Vol. 7, pp. 31-64.

Campbell, D.J., Cheney, J.A., and Kutter, B.L. (1991). "Boundary Effects in Dynamic Centrifuge Model Tests." *Centrifuge 91*, Boulder, USA, pp.441-448.

Chaney, R.C. and Fang, H.Y. (1991). "Liquefaction in the Coastal Environment: An Analysis of Case Histories." *Marine Geotechnology*, Vol. 10, pp.343-370.

Cheney, J.A., and Fragaszy, R.J. (1984). "The Centrifuge as a Research Tool." *Geotech. Test. J.*, Vol. 7, No. 4, pp.182-187.

Chen, R.H. (1975). *Limit Analysis and Soil Plasticity*. Elsevier, New York, USA.

Chen, Z.Y. and Morgenstern, N.R. (1983). "Extensions to the Generalized Method of Slice for Stability Analysis." *Can. Geotech. J.*, Vol. 20, pp. 104-119.

Chillarige, A.V., Morgenster, N.R., Robertson, P.K., and Christian, H.A. (1997). "Seabed Instability due to Flow Liquefaction in the Fraser River Delta." *Can. Geotech. J.*, Vol. 34, pp. 520-533.

Christian, J.T. (1996). "Reliability Methods for Stability of Existing Slopes." *Proc. Uncertainty Geol. Env.*, ASCE Spec. Pub., No. 58, Vol. 1, pp. 409-418.

Christian, J.T., Ladd, C.C., Baecher, G.B. (1994). "Reliability Applied to Slope Stability Analysis." *J. Geotech. Eng.*, ASCE, Vol. 120, No. 2, pp. 2180-2207.

Christian, J.T. and Urzua, A. (1998). "Probabilistic Evaluation of Earthquake Induced Slope Failure." *J. Geotech. & Geoenv. Eng.*, ASCE, Vol. 124, No. 11, pp. 1140-1143.

COSTA-Canada. (2001). Online Resource: http://www.costa-canada.ggl.ulaval.ca

Craig, R.F. (1997). *Soil Mechanics*. E & FN Spon, London, UK.

Desgagnes, P., Locat, J., Lee, H.J., Leroueil, S., Alexander, A., Mountain, G., and Pratson, L. (2000). "Geotechnical Properties of a Mass Flow Deposit on the Hudson Apron, Off New Jersey, U.S.A." *Proc. 53rd Can. Geotech. Conf.*, Montreal, Canada, pp. 137-144.

Dewoolkar, M.M., Ko, H.Y., Stadler, A.T., and Astaneh, S.M.F. (1999a). "A Substitute Pore Fluid for Seismic Centrifuge Modeling." *Geotech. Test. J.*, Vol. 22, No. 3, pp. 196-210.

Dewoolkar, M.M, Ko, H.Y., and Pak, R.Y.S. (1999b). "Centrifuge Modelling of Models of Seismic Effects on Saturated Earth Structures." *Geotechnique*, Vol. 49, No. 2, pp. 247-266.

Dimakis, P, Elverhoi, A., Hoeg, K., Solheim, A., Harbitz, C., Laberg, J.S., Vorren, TO., and Marr, J. (2000). "Submarine Slope Stability on High-latitude Glaciated Svalbard-Barents Sea Margin." *Marine Geology*, Vol. 162, pp. 303-316.

Dobry, R. and Liu, L. (1992). "Centrifuge Modelling of Soil Liquefaction." *Proc. 10th World Conf. Earthq. Eng.*, Madrid, Spain, pp.6801-6809.

Dobry, R. and Taboada, V.M. (1993). "Possible Lessons From VELACS Model No. 2 Results." *VELACS*, Davis, USA, pp.1341-1352.

Driscoll, N.W. (2000). "Potential for Large-scale Submarine Slope Failure and Tsunami Generation Along the U.S. Mid-Atlantic Coast." *Geology*, Vol. 28, No. 5, pp. 407-410.

Drucker, D.C. and Prager, W. (1952). "Soil Mechanics and Plastic Analysis of Limit Design." *Quart. App. Math.*, Vol. 10, No. 2, pp. 157-165.

Dupperret, A., Lagabrielle, Y., Bourgois, J., and Suess, E. (1993). "Large Scale Polyphased Submarine Slope Failure Induced by Subsidence Along the Northern Peruvian Margin." *Proc. 2nd Int. Symp. Geodynamics*, Oxford, UK, pp. 85-87.

Elgamal, A.W., Adalier, K., and Zeghal, M. (1993). "Overview and Relevance of Experimental Data from VELACS Project, Models 4A, 4B, and 6." *VELACS*, Davis, USA, pp.1681-1702.

Embley, R.W. (1980). "Anatomy of Some Atlantic Margin Sediment Slides and Some Comments on Ages and Mechanisms." *NATO Workshop on Marine Slides and Other Mass Movements*, Algarve, Portugal, pp. 189-213.

Fellenius, W. (1936). "Calculation of the Stability of Earth Dams." *Proc. 2nd Congress on Large Dams*, Washington, USA, pp. 445-459.

Fiegel, G.L., Hudson, M., Idriss, I.M., Kutter, B.L. and Zeng, X. (1994) "Effect of Model Containers on Dynamic Soil Response." *Centrifuge 94*, Singapore, pp. 145-150.

Fiegel, G.L. and Kutter, B.L. (1994). "Liquefaction Mechanism for Layered Soils." *J. Geotech. Eng.*, ASCE, Vol. 120, No. 4, pp. 737-755.

Figueroa, J.L, Saada, A.S., Dief, H., and Dietz, C.P. (1998). "Development of the Geotechnical Centrifuge at Case Western Reserve University." *Centrifuge 98*, Tokyo, Japan, pp. 3-8.

Fugslang, L.D. and Ovesen N.K. (1988). "The Application of the Theory of Modelling of Models to Centrifuge Studies." *Centrifuges in Soil Mechanics*, Rotterdam, Netherlands, pp.119-138.

Fujii, N. (1991). "Development of an Electromagnetic Centrifuge Earthquake Simulator." *Centrifuge 91*, Boulder, USA, pp. 351-354.

Gardner, J.V., Prior, D.B., and Field, M.E. (1999). "Humboldt Slide – A Large Shear-Dominated Retrogressive Slope Failure." *Marine Geology*, Vol. 154, pp. 323-338.

Goodings, D.J. (1985). "Relationships for Centrifugal Modelling of Seepage and Surface Flow Effects on Embankment Dams." *Geotechnique*, Vol. 32, pp. 149-152.

Goodings, D.J. and Gillette, D.R. (1996). "Model Size Effects in Centrifuge Models of Granular Slope Instability." *Geot. Test. J.*, Vol. 19, No. 3, pp. 277-285.

Griffiths, D.V. and Lane, P.A. (1999). "Slope Stability Analysis by Finite Elements." *Geotechnique*, Vol. 49, No. 3, pp. 387-403.

Haigh, S.K. and Madabhushi, S.P.G. (2002). "Dynamic Centrifuge Modelling of the Destruction of Sodom and Gomorrah." *ICPMG 02*, St. John's, Canada, pp. 507-511.

Hampton, M.A., Lee, H.J., and Locat, J. (1996). "Submarine Landslides." *Rev. of Geoph.*, Vol. 34, No. 1, pp. 33-59.

Hansen, A. (1984). "Landslide Hazard Analysis." *Slope Instability,* Wiley, New York, USA, pp. 523-602.

Harder, L.F. and Boulanger, R.W. (1997). " Application of K_σ and K_α Correction Factors." *Proc. NCEER Workshop on Eval. of Liq. Res. Of Soils,* Buffalo, USA, pp.167-190.

Hart, B., Masee, M., Locat, J., and Long, B. (2001). "High-Resolution Three-Dimensional Seismic Surveying of Submarine Landslides: Rationale and Challenges." *Proc. 54th Can. Geotech. Conf.,* Calgary, Canada, pp. 738-742.

Hassan, A.M. and Wolff, T.F. (2000). "Effect of Deterministic and Probabilistic Models On Slope Reliability Index." *Proc. GeoDenver 2000,* Denver, USA, pp. 194-208.

Hushmand, B. Scott, R.F., and Crouse, C.B. (1988). "Centrifuge Liquefaction Tests in a Laminar Box." *Geotechnique,* Vol. 38, No. 2, pp. 253-262.

Hutin, C., Perdriat, J., and Rames, D. (2002). "Dynamically Balanced Broad Frequency Earthquake Simulation." *ICPMG 02,* St. John's, Canada, pp. 175-178.

Imamura, S., Hagiwara, T., Ishihara, K., Tsukamoto, Y., and Kon, H. (2002). "Characteristics of Lateral Flows of Two-layered Slopes Due to Liquefaction in a Centrifuge." *ICPMG 02,* St. John's, Canada, pp. 501-506.

Inatmoi, T, Kazama, M., Iai, S., Kitazume, M., and Terashi, M. (1988). "Development of an Earthquake Simulator for the PHRI centrifuge." *Proc. Int. Conf. Geotech. Centrifuge Modelling.,* Paris, France, pp. 111-114.

Ishihara, K. (1996). *Soil Behaviour in Earthquake Geotechnics.* Oxford University Press, Oxford, UK.

Ishihara, K., Tatsuoka, F., and Yasuda, S. (1975). "Undrained Deformation and Liquefaction of Sand Under Cyclic Stresses." *Soils and Foundations.* Vol. 15, pp. 29-44.

Ishihara, K., Tsuchiya, H, Huang, Y., and Kamada, K. (2001). "Recent Studies on Liquefaction Resistance of Sand – Effect on Saturation." *Proc. 4th Int. Conf. Rec. Adv. Geotech. Earthq. Eng. and Soil Dynam.,* San Diego, USA, pp. 26-31.

Jenkins, C.J. and Keene, K.B. (1992). "Submarine Slope Failures of the Southeast Australian Continental Slope: A Thinly Sedimented Margin." *Deep Sea Research,* Vol. 39, No. 2, pp. 121-136.

Johns, M.W., Prior, D.B., Bornhold, B.D., Coleman, J.M., and Bryant, W.R. (1984). "Geotechnical Aspects of a Submarine Slope Failure, Kitimat Fjord, British Columbia." *Marine Geotechnology,* Vol. 6, No. 3, pp. 243-279.

Karlsrud, K. and Edgers L. (1980). "Some Aspects of Submarine Slope Stability." *NATO Workshop on Marine Slides and Other Mass Movements,* Algarve, Portugal, pp. 61-81.

Ko, H.Y. and Astaneh, S.M.F. (1993). "Overview of Experimental Results of Model No. 7." *VELACS,* Davis, USA, pp.1567-1570.

Ko, H.Y. (1994.) "Modeling Seismic Problems in Centrifuges." *Centrifuge 94, Singapore,* pp. 3-12. 1994.

Koga, Y., Matsuo, O., Koseki, J., Goto, Y., Kubodera, I., Suzuki, K., Fukada, H., and Okumura, R. (1991). "Applicability of the Dynamic Centrifuge Model Test Method in Developing Countermeasures Against Soil Liquefaction." *Centrifuge 91,* Boulder, USA, pp. 431-438.

Kokusho, T. (1999). " Water Film in Liquefied Sand and Its Effect on Lateral Spread." *J. Geotech. & Geoenv. Eng.,* ASCE, Vol. 125, No. 10, pp. 817-826.

Kokusho, T. (2001). "Simulation on Lateral Flow Mechanism in Layered Sand by 1G Shake Table and Other Tests." *Proc. NSF Int. Wksp. Earthq. Sim. Geotech. Eng.,* Cleveland, USA.

Kokusho, T. (2003). "Current State of Research on Flow Failure Considering Void Redistribution in Liquefied Deposits." *Soil Dynam. & Earthq. Eng.,* Vol. 23, pp. 585-603.

Kokusho, T. and Kojima, T. (2002). "Mechanism for Postliquefaction Water Film Generation in Layered Sand." *J. Geotech. & Geoenv. Eng.*, ASCE, Vol. 128, No. 2, pp. 129-137.

Koning, H.L. (1980). "On an Explanation of Marine Flow Slides in Sand." *NATO Workshop on Marine Slides and Other Mass Movements*, Algarve, Portugal, pp. 83-94.

Konrad, J.M. and Dubeau, S. (2002). "Cyclic Strength of Stratified Soil Samples." *Proc. 55th Can. Geotech. Conf.*, Niagara Falls, Canada, pp. 89-94

Kostaschuk, R.A. and McCann, S.B. (1989). "Submarine Slope Stability of a Fjord Delta: Bella Coola, British Columbia." *Geographie Physique et Quaternaire*, Vol. 43, No. 1, pp. 87-95.

Kulasingam, R., Malvick, E.J., Boulanger, R.W., and Kutter, B.L. (2004). "Strength Loss and Localization at Silt Interlayers in Slopes of Liquefied Sand." *J. Geotech & Geoenv. Eng.*, ASCE, Vol. 130, No. 11, pp. 1192-1202.

Kutter, B.L., Idriss, I.M., Khonke, T., Lakeland, J., Li, X.S., Sluis, W., Zeng, X., Tausscher, R.C., Goto, Y., and Kibodera, I. (1994). "Design of a Large Earthquake Simulator at UC Davis." *Centrifuge 94*, Singapore, pp. 169-175.

Lacy, S.J., Aubry, D., Benzenati, I., Modaressi, A., Roth, W., and Inel, S. (1993). "Overview of VELACS Model No. 2." *VELACS*, Davis, USA, pp.1369-1381.

Law, H., Ko, H.Y., Sture, S., and Pak, R. (1991). "Development and Performance of a Laminar Container for Earthquake Liquefaction Studies." *Centrifuge 91*, Boulder, USA, pp.369-376.

Law, H.K., Ko, H.Y., and Scavuzzo, R. (1994). "Simulation of O'Neill Forebay Dam, California, Subjected to the 1989 Loma Prieta Earthquake." *Centrifuge 94*, Singapore, pp. 245-250.

Lee, F.H. and Schofield, A.N. (1988). "Centrifuge Modelling of Sand Embankments and Islands in Earthquakes." *Geotechnique*, Vol. 38, No. 1, pp. 45-58.

Lee, F.H. (1990). "Frequency Response of Diaphragm Pore Pressure Transducers in Dynamic Centrifuge Model Test." *Geotech. Test. J.*, Vol. 13, pp. 201-207.

Lee, H.J. and Edwards, B.D. (1986). "Regional Method to Assess Offshore Slope Stability." *J. Geotech. Eng.,* ASCE, Vol. 112, No. 5, pp. 489-509.

Lee, H.J., Edwards, B.D., and Field, M.E. (1981). "Geotechnical Analysis of a Submarine Slump, Eureka, California." *Proc. 13th OTC,* Houston, USA, pp. 53-65.

Lee, H.J., Orzech, K., Locat, J., Boulanger, E., and Konrad, J.M. (2004). "Seismic Strengthening, A Conditioning Factor Influencing Submarine Landslide Development." *Proc. 57th Can. Geotech. Conf.,* Quebec, Canada.

Lemke, R.W. (1967). "Effects of the Earthquake of March 27, 1964, at Seward, Alaska." *U.S. Geological Survey Professional Paper 542-E.*

Leynaud, D. and Mienert, J. (2003). "Slope Stability Assessment of the Traenadjupet Slide Area Offshore the Mid-Norwegian Margin." *1st Int. Symp. Submarine Mass Movements and Their Consequences,* Kluwer Acadmeic, Dordrecht, Netherlands, pp. 255-265.

Liao, S. and Whitman, R.V. (1986). "Overburden Correction Factors for SPT in Sand." *J. Geotech. Eng.,* ASCE, Vol. 112, pp. 373-377.

Liquefaction Remediation Project. (2004). Online Resource: http://www.civil.ubc.ca/liquefaction/

Locat, J. and Lee, H.J. (2000). "Submarine Landslides: Advances and Challenges." *Proc. 8th Int. Symp. on Landslides,* Cardiff, UK, pp. 1-30.

Locat, J., Bornhold, B., Byrne, P., Hart, B., Hughes Clarke, J. Konrad, J.M., Lee, H., Leroueil, S., Long, B., Mosher, D., Piper, D., Phillips, R., Popescu, R., and Thomson, R. (2001). "COSTA-Canada, A Canadian Contribution to the Study of Continental Slope Stability: An Overview." *Proc. 54th Can. Geotech. Conf.,* Calgary, Canada, pp. 730-737.

Lykousis, V. (1991). "Submarine Slope Instabilities in the Hellenic Arc Region, Northeastern Mediterranean Sea." *Marine Geotechnology,* Vol. 10, pp. 83-96.

Madabhushi, S.P.G., Butler, G., and Schofield, A.N. (1998). :Design of an Equivalent Shear Beam Container for Use on the US Army Centrifuge." *Centrifuge 98,* Tokyo, Japan, pp. 117-122.

Madabhushi, S.P.G., Schofield, A.N., and Zeng, X. (1994). "Complimentary Shear Stresses in Dynamic Centrifuge Modeling." *Dynamic Geotechnical Testing II,* ASTM Publication 04-012130-38, Philadelphia, USA, pp. 346-359.

Malvick, E.J., Kulasingam, R., Kutter, B.L., and Boulanger, R.W. (2002). "Void Redistribution and Localized Shear Strains in Slopes During Liquefaction." *ICPMG 02*, St. John's, Canada, pp. 495-500.

Manzari, M.T. and Yogachandran, C. (1993). "An Overview of the Class-A Predictions for Model-6." *VELACS*, Davis, USA, pp.1553-1564.

Matsuo, O., Tsutsumi, T., Kondoh, K., and Tamoto, K. (1998). "The Dynamic Geotechnical Centrifuge at PWRl." *Centrifuge 98*, Tokyo, Japan, pp. 25-30.

Mehrabadi, A.J. (2006). *Seismic Liquefaction Countermeasures for Waterfront Slopes.* Ph.D. Thesis, Memorial University of Newfoundland, St. John's, Canada.

Moore J.G., Clague D.A., Holcomb R.T., Lipman P.W., Normark W.R., and Torresan M.E. (1989). "Prodigious Submarine Slides on the Hawaiian Ridge." *J. Geophys. Res.*, Vol. 94, No. 17, pp. 465-484.

Moran, K. (1993). "Offshore Site Investigations on Canadian Continental Margins." *Proc. 4th Can. Conf. Marine Geotech. Eng.*, pp. 977-997.

Morgenstern, N.R. and Price, V.E. (1965). "The Analysis of General Slip Surfaces". *Geotechnique*, Vol. 15, pp.79-93.

Morris, D.V. (1983). "An Apparatus for Investigating Earthquake-Induced Liquefaction Experimentally." *Can. Geotech. J.*, Vol. 20, pp. 840-845.

Mosher, D.C., Monahan, P.A., and Barrie, J.V.. (2001). "Submarine Failures in the Strait of Georgia, British Columbia: Landslides of the 1946 Vancouver Island Earthquake." *Proc. the 54th Can. Geotech. Conf.*, Calgary, Canada. pp. 744-751.

Mulder, T. and Cochonat, P. (1996). "Classification of Offshore Mass Movements." *J. Sedimentary Research*, Vol. 66, pp. 43-57.

Muraleetharan, K.K. and Arulanandan, K. (1991). "Dynamic Behaviour of Earth Dams Containing Stratified Soils." *Centrifuge 91*, Boulder, USA, pp. 401-408.

Murff, J.D. (1996). "The Geotechnical Centrifuge in Offshore Engineering." *Proc. 1996 OTC*, Houston, USA, pp. 675-689.

Naesgaard, E., Byrne, P.M., Seid-Karabasi, M., and Park, S.S. (2005). "Liquefaction Mitigation Project: Class A Prediction of Centrifuge Test CT-6." Self Published Project Report.

Nagase, H., Ko, H.Y., Law, H.K., and Pak, R.Y.S. (1994). "Permanent Displacement of Sloping Ground Due to Liquefaction." *Centrifuge 94*, Singapore, pp. 239-244.

Nagura, K., Tanaka, M., Kawasaki, K., and Higuchi, Y. (1994). "Development of an Earthquake Simulator for the TAISEI Centrifuge." *Centrifuge 94*, Singapore, pp. 151-156.

Newmark, N.M. (1965). "Effects of Earthquakes on Dams and Embankments." *Geotechniqe*, No. 15, Vol. 2, pp. 137-160.

Nitzsche, M. (1989). "Submarine Slope Instability: Eastern Banda Sea." *Netherlands Journal of Sea Research*, Vol. 24, No. 4, pp. 431-436.

Noornay, I. (1984). "Phase Relations in Marine Soils." *J. Geotech. Eng.*, ASCE, Vol. 110, No. 4, pp. 539-543.

Noornay, I. (1989). "Classification of Marine Sediments." *J. Geotech. Eng.*, ASCE, Vol. 115, No. 1, pp. 23-37.

Norris, R.D. Firth, J., Blusztain, J.S., and Ravizza, G. (2000). "Mass Failure of the North Atlantic Margin Triggered By the Cretaceous-Palogene Bolide Impact." *Geology*, Vol. 28, No. 12, pp. 1119-1122.

O'Reilly, M.P. and Brown, S.F. (1991). *Cyclic Loading of Soils: From Theory to Design*, Blackie and Son Ltd., Glasgow, UK.

O'Reilly, M.P., Brown, S.F., and Overy, R.F. (1991). "Cyclic Loading of Silty Clay With Drainage Periods." *J. Geotech. Eng.*, ASCE, Vol. 117, pp. 354-362.

Orange, D.L. (1992). "Submarine Slope Failure Caused by Excess Pore Pressure Gradients." *Proc. 1992 Fall Meeting U.S. Geological Association*, pp. 228.

Ovesen, N.K. (1979). "The Scaling Law Relationship – Panel Discussion." *Proc. 7th Eur. Conf. Soil Mech. Found. Eng.*, Brighton, UK, No. 4, pp. 319-323.

Paull, C.K., Ussler III, W., and Dillon, W.P. (2000). "Potential Role of Gas Hydrate Decomposition in Generating Slope Failures." *Natural Gas Hydrates in Oceanic and Permafrost Environment*, Kluwer Academic Publishers, Dordrect, Netherlands, pp. 149-156.

Perdriat, J., Phillips, R., Font, J.N., and Hutin, C. (2002). "Dynamically Balanced Broad Frequency Earthquake Simulation System." *ICPMG 02*, St. John's, Canada, pp. 169-173.

Phillips, R. (1993). "Centrifuge Modelling for Offshore Development." *Proc. 1993 NOIA Conf.*, St. John's Canada, pp. 136-149.

Phillips, R., Clark, J.I., Paulin, M.J., Meaney, R., Millan, D.E.L., and Tuff, K. (1994). "Canadian National Centrifuge Centre with Cold Regions Capabilities." *Centrifuge 94*, Singapore, pp. 57-62.

Phillips, R., Coulter, S.E., and Tu, M. (2004). "Earthquake Simulator Development for the C-CORE Geotechnical Centrifuge." *Proc. 57th Can. Geotech. Conf.*, Quebec, Canada.

Piper, D.J.W., Cochonat, P., and Morrison, M.L. (1999). "The Sequence of Events Around the Epicentre of the 1929 Grand Banks Earthquake: Initiation of Debris Flows and Turbidity Current Inferred From Sidescan Sonar." *Sedimentology*, 46, pp. 79-97.

Piper, D.J.W. and McCall, C. (2003). "A Synthesis of the Distribution of Submarine Mass Movements on the Eastern Canadian Margin." *1st Int. Symp. Submarine Mass Movements and Their Consequences*, Kluwer Acadmeic, Dordrecht, Netherlands, pp. 291-298.

Poulos, H.G. (1988). *Marine Geotechnics*. Unwin Hyman, London, UK.

Poulos, S.J. (1981). "The Steady State of Deformation." *J. Geotech Eng.*, ASCE, Vol. 107, No. 5, pp. 553-562.

Prevost, J.H. and Scanlan, R.H. (1983). "Dynamic Soil-Structure Interaction: Centrifugal Modeling." *Soil Dynam. & Earthq. Eng.*, Vol. 2, No. 4, pp. 212-221.

Prior, D.B. and Coleman, J.M. (1984). "Submarine Slope Instability." *Slope Instability*, Wiley, New York, USA, pp. 419-445.

Robertson, P.K. and Wride, C.E. (1998). "Evaluating Cyclic Liquefaction Potential Using the Cone Penetration Test." *Can. Geotech. J.* Vol. 35, 442-459.

Ryan, W.B.F. (1980). "Imaging of Submarine Landslides with Wide-Swath Sonar." *NATO Workshop on Marine Slides and Other Mass Movements*, Algarve, Portugal, pp. 175-188.

Santamarina, J.C. and Goodings, D.J. (1989). "Centrifuge Modeling: A Study of Similarity." *Geotech. Test. J.*, Vol. 12, No. 2, pp. 163-166.

Schofield, A.N. (1980). "Cambridge Geotechnical Centrifuge Operations." *Geotechnique*, Vol. 30, No. 3, pp. 227-268.

Schofield, A.N. (1981). "Dynamic and Earthquake Geotechnical Centrifuge Modelling." *Proc. Int. Conf. Recent Adv. Geotech. Earthq. Eng. Soil Mech.*, pp. 1081-1100.

Schofield, A.N. (1988). "An Introduction to Centrifuge Modelling." *Centrifuges in Soil Mechanics*, Rotterdam, Netherlands, pp.1-9.

Schwab, W.C., Danforth, W.W., Scanlon, K.M., and Masson, D.G. (1991). "A Giant Submarine Slope Failure on the Northern Insular Slope of Puerto Rico." *Marine Geology*, Vol. 96, pp. 237-246.

Scott, R.F. (1993). "Lessons Learned From VELACS Project." *VELACS*, Davis, USA, pp.1773-1779.

Seed, R.B., and Harder, L.F. (1990). "SPT-Based Analysis of Cyclic Pore Pressure Generation and Undrained Residual Strength." *Proc. Mem. Symp. For H.B. Seed.*, Vol. 2, pp. 351-376.

Seed, H.B. and Idriss, I.M. (1971). "Simplified Procedure for Evaluating Soil Liquefaction Potential." *J. Geotech. Eng. Div.*, ASCE, Vol. 97, 1249-1273.

Seed, H.B. and Idriss, I.M. (1982). "Ground Motions and Soil Liquefaction During Earthquakes." *Earthq. Eng. Res. Inst. Monograph*, Oakland, USA.

Seed, H.B., Lee, K.L., Idriss, I.M., and Makidisi, F.I. (1975). "The Slides on the San Fernando Dams During the Earthquake of February 9, 1971." *J. Geotech. Eng. Div.*, ASCE, Vol. 101, pp. 651-688.

Spencer, E. (1967). "A Method of Analysis of the Stability of Embankments Assuming Parallel Inter-slice Forces." *Geotechnique*, Vol. 17., No. 1, pp. 11-26.

Stark, T.D. and Olson, S.M. (1995). "Liquefaction Resistance Using CPT and Field Case Histories." *J. Geotech. & Geoenv. Eng.*, ASCE, Vol. 121, No. 12, pp. 856-869.

Stewart, D.P. (1988). "Experience With the Use of Methylcellulose as a Viscous Pore Fluid in Centrifuge Models." *Geotech. Test. J.*, Vol. 21, No. 4, pp. 365-369.

Swan, D. (1979). "Large Submarine Landslide, Kitimat Arm, B.C." *Proc 1st Can. Conf. Marine Geotech. Eng.*, Calgary, Canada, pp. 131-139.

Taboada-Urtuzuastegui, V.M. and Dobry, R. (1998). "Centrifuge Modeling of Earthquake-Induced Lateral Spreading in Sand." *J. Geotech. & Geoenv. Eng.*, ASCE, Vol. 124, No. 12, pp. 1195-1206.

Taboada-Urtuzuastegui, V.M., Martinez-Ramirez, G., and Abdoun, T. (2002). "Centrifuge Modeling of Seismic Behaviour of a Slope in Liquefiable Soil." *Soil Dynam. & Earthq. Eng.*, Vol. 22, pp. 1043-1049.

Tang, W.H., Stark, T.D., Angulo, M. (1999). "Reliability in Back Analysis of Slope Failures." *Soils and Foundations*, Vol. 39, No. 5, pp. 73-80.

Taylor, R.N., ed. (1995) *Geotechnical Centrifuge Technology*, Blackie Academic & Professional, London, UK.

Terzaghi, K. (1956). "Varieties of Slope Failures." *Proc. 8th Texas Conf. Soil Mech.& Found. Eng.*, Austin, USA, pp. 1-41.

Tu, M. (2004). *Evaluation of Remediation Against Seismic Induced Liquefaction*. Ph. D. Proposal, Memorial University of Newfoundland, St. John's, Canada.

Ueno, K. (1998). "Methods of Preparation of Sand Samples." *Centrifuge '98*, Tokyo, Japan, pp. 1047-1055.

Urgeles, R., Locat, J., Lee, H., Martin, F., and Konrad, J.M. (2001). "The Saguenay Fjord: Integrating Marine Geotechnical and Geophysical Data for Spatial Slope Stability Hazard Analysis." *Proc. 54th Can. Geotech. Conf.*, Calgary, Canada, pp. 768-775.

U.S. Silica. (2004). Online Resource: http://www.u-s-silica.com/

Vaid, Y.P. and Sivathayalan, S. (1996). "Static and Cyclic Liquefaction Potential of Fraser Delta Sands in Simple Shear and Triaxial Tests." *Can. Geotech. J.*, Vol. 33, pp. 281-289.

Van Laak, P.A., Taboada, V.M., Dobry, R., and Elgamal, A.W. (1994a). "Earthquake Centrifuge Modeling Using a Laminar Box." *Dynamic Geotechnical Testing II*, ASTM Publication 04-012130-38, Philadelphia, USA, pp. 370-384.

Van Laak, P.A., Elgamal, A.W., and Dobry, R. (1994b). "Design and Performance of an Electrohydraulic Shaker for the RPI Centrifuge." *Centrifuge 94*, Singapore, pp.139-144.

Whitman, R.V. and Lambe, P.C. (1986). "Effect of Boundary Conditions Upon Centrifuge Experiments sing Ground Motion Simulation," *Geotech. Test. J.*, Vol. 9, No.2, pp. 61-71.

Wilson, D.W., Farrell, T.M., and Kutter, B.L. (1993). "An Overview and Relevance of Experimental Data from VELACS Project Model Nos. 7, 11, and 12." *VELACS*, Davis, USA, pp.1657-1680.

Youd, T.L., Idriss, I.M., Andrus, R.D., Arangi, I., Castro, G., Christian, J.T. Dobry, R., Finn, W.D.L., Harder, L.F., Hynes, M.E., Ishihara, K., Koester, J.P., Liao, S.S.C., Marcuson, W.F., Martin, G.R., Mitchell, J.K., Moriwaki, Y., Power, M.S., Robertson, P.K., Seed, R.B., and Stokoe, K.H. "Liquefaction of Soils: Summary Report from the 1996 NCEER and 1998 NCEER/NSF Workshops on Evaluation of Liquefaction Resistance of Soils." (2001). *J. Geotech. & Geoenv. Eng.*, ASCE, Vol. 127, No. 10, pp. 817-833.

Yu, S.H., Salgado, R., Sloan, S.W., and Kim, J.M. (1998). "Limit Analysis Versus Limit Equilibrium for Slope Stability." *J. Geotech. & Geoenv. Eng.*, ASCE, Vol. 124, No. 4, pp. 1-11.

Zelikson, A., Devaure, B., and Badel, D. (1981). "Scale Modeling of Soil Structure Interaction Using a Programmed Series of Explosions During Centrifugation." *Proc. Int. Conf. Recent Adv. Geotech. Earthq. Eng. & Soil Mech.*, pp. 361-366.

Zen, K. & Yamakazi, H. (1990). "Mechanism of Wave-Induced Liquefaction and Densification in Seabed." *Soils & Foundations*, Vol. 30, No. 4. pp. 90-104.

Zen, K. & Yamakazi, H. (1991). "Field Observation and Analysis of Wave-Induced Liquefaction in Seabed." *Soils & Foundations*, Vol. 21, No.4. pp. 161-179.

Zeng, X. and Schofield, A.N. (1996). "Design and Performance of an Equivalent Shear Beam Container for Earthquake Centrifuge Modelling." *Geotechnique*, Vol. 46, No. 1, pp.83-102.

Zhou, S.H., Liu, J.G., Wang, B.L., Yang, L.C., and Gong, Q.M. (2002). "Centrifugal Model Test on the Stability of Underwater Slope." *ICPMG 02*, St. John's, Canada, pp. 759-764.

APPENDIX A

TESTING INSTRUMENT SPECIFICATIONS

DRUCK PDCR 81 Miniature Pore Pressure Transducer

PDCR 81

Dimensions:	6.5 x 11.7 mm
Operating Pressure Ranges:	100 and 200 psi
Excitation Voltage:	5 volts 6 ma nominal
Output Voltage:	75 mV
Zero Offset:	± 10 mV maximum
Span Setting:	± 20% of nominal output
Output Impedence:	1000 ohms
Load Impedence:	Greater than 100 kohms
Resolution:	Infinite
Operating Temperature:	-5 ^{O} to 250°F
Mechanical Shock:	1000 g for 1 ms in each axes will not affect calibration
Weight:	1.05 oz with 15 feet of cable

For additional information consult:
http://www.druck.com/usa/products/MiniatureSeries.pdf

PCB Piezotronics 353B18 Miniature High-Frequency Quartz ICP Accelerometer

Mass:	1.8 grams
Dimensions:	7.1 x 18.8 mm
Voltage Sensitivity:	10 mV/g ± 5%
Measurement Range:	± 500g peak
Frequency Range:	1 to 10000 Hz ± 5%
Mounted Resonance Frequency:	> 70 kHz
Broadband Resolution:	0.005 g rms
Operating Temperature Range:	-65 to 250°F
Sensing Element:	Quartz Shear
Electrical Connector:	10-32 Coaxial/Top
Mounting Thread:	5-40 Male

For additional information consult:
http://www.pcb.com/products/svs/svs353b18.html

Trans-Tek Series 240 General Purpose CV LVDT

Working Range:	± 25.4 mm
Maximum Working Range:	± 38.1 mm
Input:	6 to 30 VDC
Nominal Output:	4.6 to 24.8 VDC
Input Current:	8.3 – 52 mA
Non-Linearity:	± 0.5% over working range, ± 1% over usable range
Internal Carrier Frequency:	3200 Hz
% Ripple:	0.8
Output Impedance:	5600 Ohms
Frequency Response:	100 Hz
Temperature Range:	-54 to 121°C
Resolution:	Infinite

For additional information consult:
http://www.transtekinc.com/Catalog_PDFs-01/LVDTs/Ser240_01F.pdf

Bäumer OADM 2014460/S14C Laser Distance Sensor

Dimensions:	20.4 mm x 50 mm x 65 mm
Measuring Range:	30 to 130 mm
Resolution:	< 0.06 mm
Linearity Error:	± 0.2 mm
Response Time:	< 10 ms
Sensing Element:	Photoelectric Array
Output:	Analog / 4-20 mA / 0-10 VDC
Switching Current:	< 100 mA
Indicators:	LED Green (Power On) & LED Red (Soiled Lens)
Voltage Supply:	12 to 28 VDC
Maximum Supple Current:	< 120 mA
Light Source:	Pulsed Red Laser Diode
Laser Class:	2
Wavelength:	675 nm
Operating Temperature Range:	0 to 5°C
Laser Beam Diameter:	2 … 1 mm
Connectors:	ES 34C

For additional information consult:
http://www.baumersensorsolutions.com/product.html?id=fee12f83fd3a8a221b206c359a0
8c629&lang=en&product=34336&category=33&sub=222

GS Sensors Amplified Triaxial Accelerometer GSA3206
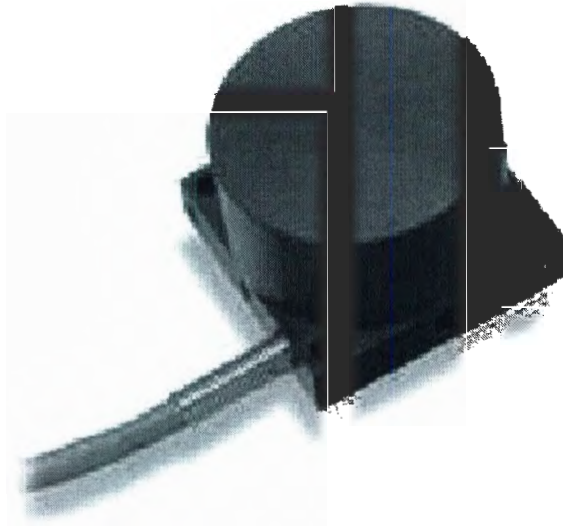
Dimensions:	30 mm x 30 mm x 25 mm
Mass:	30 grams
Excitation:	10 to 36 VDC
Offset at Zero:	2.5 VDC
Output Impedence:	10 ohms nominal
Linearity:	± 2%
Transverse Sensitivity:	< 3%
Operating Temperature Range:	-40 to 80°C
Frequency Response:	500 Hz in z-axis, 100 Hz in x-axis, 1000 Hz in y-axis

For additional information consult:

http://www.gssensors.com/catalogue/index_prod.php3